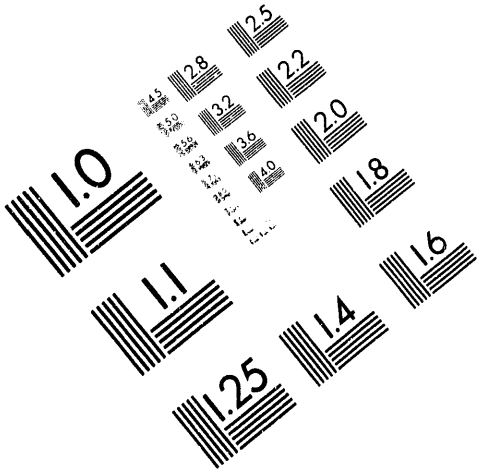

Association for Information and Image Management

1100 Wayne Avenue, Suite 1100
Silver Spring, Maryland 20910

301/587-8202

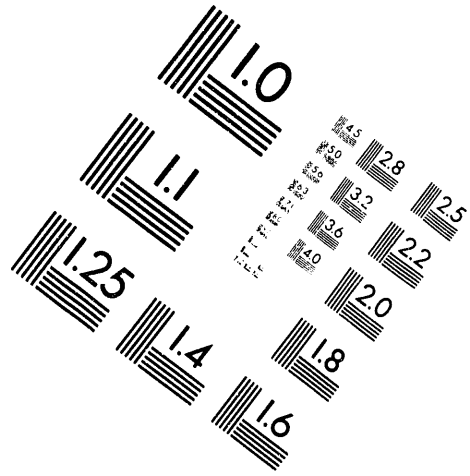

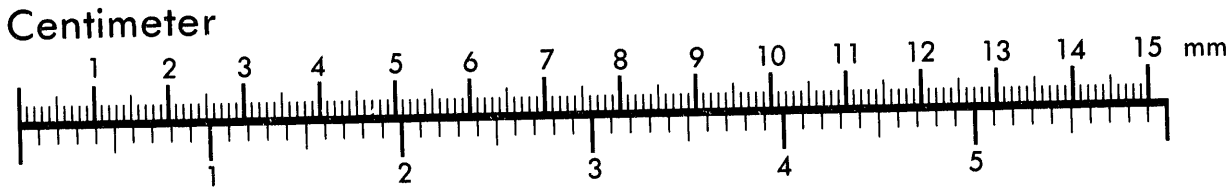

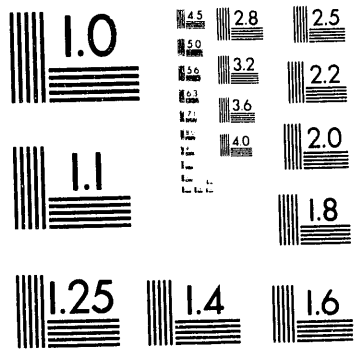

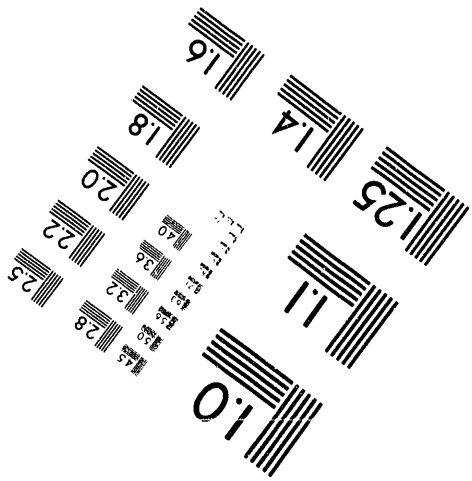

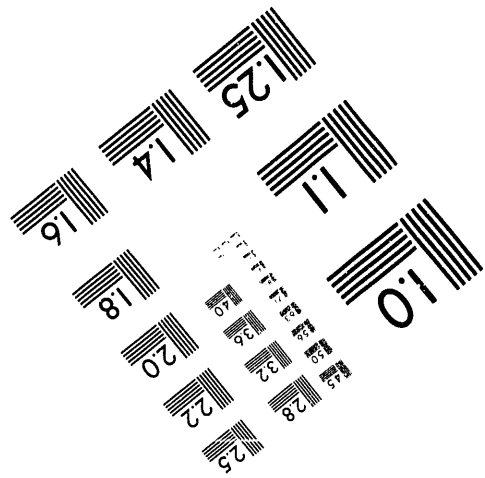

1 of 4

DOE/PC/88933-T2
(DE93012403)
Distribution Category UC-113

ALKALI/TX_2 CATALYSTS FOR CO/H_2 CONVERSION TO C_1-C_4 ALCOHOLS

Final Technical Progress Report

September 1, 1988 to August 31, 1991

Kamil Klier and Richard G. Herman
with
Michelle Richards-Babb, Roy Bastian, and Mark Kieke

Zettlemoyer Center for Surface Studies
and Department of Chemistry
Lehigh University
Bethlehem, PA 18015

March 1993

PREPARED FOR THE UNITED STATES
DEPARTMENT OF ENERGY

Under Contract No. DE-FG22-88PC88933

Acknowledgements

In addition to the support of the U.S. Department of Energy-Pittsburgh Energy Technology Center for this research, we appreciate the support of the sponsors of the following fellowships and scholarships for Michelle Richards-Babb: Heim Fellowship, Texaco Philanthropic Fellowship, Buch Fellowship, and University Graduate Fellowship.

TABLE OF CONTENTS

LIST OF FIGURES

LIST OF TABLES

ABSTRACT

The objective of this research is to determine the patterns of variations of catalyst activity and selectivity for the synthesis of alcohols from H_2/CO synthesis gas over a series of A/TX_2 compounds, where A is a heavy alkali dopant (i.e. Cs), T is a transition metal, and X is the chalcogenide sulfur. The benefit of this research rests in providing a scientific foundation and a database for catalytic processes leading to high octane oxygenated fuels such as ethanol/methanol/propanol mixtures, as well as to low olefins obtained by further catalytic dehydration of the C_2-C_4 alcohols. Since the source of carbon can be coal-derived synthesis gas, this research makes a contribution to the technology for high quality clean transportation fuels and for basic chemicals from coal.

The catalysts that were prepared during this research project were principally based on MoS_2, RuS_2, TaS_2, and NbS_2. Catalytic testing of these materials was carried out both before and after surface doping with Cs, and the results have been reported in available (NTIS) quarterly technical progress reports. Compared with the previously established catalytic behavior of Cs/MoS_2 catalysts (e.g. as in our previous DOE-PETC Final Report DOE/PC/80014-F (December 1988)), it was found that the activities and selectivities of the newly prepared catalysts were the same (MoS_2, DOE/PC/88933-2), had similar selectivity but much lower activity (RuS_2, DOE/PC/88933-3), or tended to preferentially form hydrocarbons (TaS_2, DOE/PC/88933-1). Dispersion of the alkali on the surface of the MoS_2 catalyst *via* crown ether complexes did not yield better catalysts, apparently because of the decomposition of the crown ether complex (DOE/PC/88933-7). Therefore, much of our research concentrated on understanding the fundamental surface chemistry of these catalysts so that scientific design of better catalysts could subsequently be achieved.

In alcohol synthesis, as well as in a large number of other hydrogenation-based catalytic processes, activation of hydrogen by the catalyst surface is essential. In the present case, knowledge of transition metal disulfide surface properties is important before the mechanism of hydrogen dissociation can be addressed. For this reason, the electronic structures of MoS_2, RuS_2, and NbS_2 were studied both theoretically and experimentally. For example, experimental valence bands were obtained by high resolution electron spectroscopy for chemical analysis (HR-ESCA, also referred to as X-ray photoelectron spectroscopy) and theoretical valence bands were calculated using solid state extended Hückel theory. Comparison of two-dimensional (2-D) MoS_2 theoretical valence bands with the experimental HR-ESCA valence bands of polycrystalline MoS_2 led to parametrization of the S 3s, S 3p, and Mo 4d atomic ionization potentials and Slater-type coefficients and exponents. The S 3s and S 3p parameters obtained for MoS_2 were used to obtain the NbS_2 and RuS_2 theoretical valence bands. The theoretical valence bands and modified atomic orbital populations (MAOPOPs) calculated in this way qualitatively reproduced the experimental HR-ESCA valence bands for these three sulfides.

The electronic structure of MoS_2 was studied in greater detail by obtaining theoretical energy dispersion curves. Curvatures and energetic positions of theoretical energy dispersion curves approximated those of experimental curves obtained by ultraviolet photoelectron spectroscopy (UPS). A direct gap ($K \rightarrow K$) was calculated for 2-D MoS_2

while an indirect gap ($\Gamma \rightarrow K$) was calculated for 3-D MoS_2. The indirect gap in 3-D MoS_2 was shown to arise from antibonding interactions of crystal orbitals across the Van der Waals gap at Γ. Crystal orbital pictures identifying the nature of the energy dispersion were also obtained from extended Hückel calculations.

Electronic structure studies of 1-D $(MoS_2)_5$ systems led to the conclusion that addition of edges to the basal plane surface results in the formation of unoccupied edge states at and above the Fermi level. HR-ESCA valence band comparisons of single crystal MoS_2 and polycrystalline MoS_2 show higher intensity on the low binding energy side of the highest occupied band (Mo $4d_{z2}$) in the sample containing the higher number of edge sites, i.e. polycrystalline MoS_2. The theoretical calculations show that occupation of edge states will contribute to higher intensity on the low binding energy side of the highest occupied band. These edge states possess mainly Mo 4d character.

Theoretical binding enthalpies for hydrogen adsorption on molybdenum and sulfur sites on various molybdenum disulfide systems were calculated. Of the sulfur sites, fully coordinated basal plane sites were favored over 1-coordinate and 2-coordinate edge sites. However, basal plane S sites on systems terminating in edges were favored over basal plane sites of an infinite sheet. Of the molybdenum sites, 2-, 3-, 4-, and 5-coordinate edge sites were favored in that order over fully coordinated basal plane sites. Overall, the order of stability for dissociative chemisorption of hydrogen (in terms of binding enthalpy) was shown to be 2-coordinate edge Mo > 3-coordinate edge Mo > 3-coordinate basal plane S > 1- and 2-coordinate edge S > 4-coordinate edge Mo > 5-coordinate edge Mo > 6-coordinate basal plane Mo. The theoretical results are in general agreement with the present experimental evidence that suggests hydrogen molecules are dissociated on MoS_2 edges. Subsequent transfer of hydrogen atoms from edge sites to basal plane sites enables the edge planes to dissociate additional hydrogen molecules. The theoretical calculations show that binding of hydrogen to basal plane sulfur atoms is thermodynamically favorable. Thus, it is probable that H_2 is initially dissociated on 2-, 3-, 4-, and 5-coordinate Mo edge sites, with subsequent transfer of H atoms from the edge sites to basal plane S sites.

Angle-resolved HR-ESCA (AR-ESCA or AR-XPS) of single crystal MoS_2 showed the existence of forward focusing of ejected photoelectrons at a polar angle of $\approx 49°$ and at azimuthal angles separated by 60°. Forward focusing of second atomic layer molybdenum photoelectrons by the first atomic layer sulfur atoms is shown to occur at the following azimuthal angles: 0°, 120°, and 240° (with arbitrary designation of 0°). Forward focusing of fifth atomic layer Mo photoelectrons by the fourth atomic layer of S is shown to occur at the following azimuthal angles: 60°, 180°, and 300°. Thus, in MoS_2 it is demonstrated that forward focusing predominates even when the Mo atom is located 7.73 Å from the surface.

A brief discussion of some of this work has been published in the paper "Structure and Surface Properties of Sulfides," K. Klier, M. Richards, and R. G. Herman, in "*Synthesis and Properties of New Catalysts: Utilization of Novel Materials, Components, and Synthetic Techniques*," ed. by E. W. Corcoran, Jr., M. J. Ledoux, and J. R. Knox, Materials Research Society, 157 (1990). Additional publications will be forth-coming.

Chapter 1
INTRODUCTION

Transition metal disulfides, TS_2, have recently been investigated for a variety of catalytic processes. Hydrodesulfurization and hydrodenitrogenation are just two of the major catalytic processes studied using TS_2 species.[1,2] Another more recent catalytic process involves the production of C_1-C_4 alcohols from synthesis gas, CO/H_2, using an alkali doped TS_2 species, namely Cs-doped MoS_2.[3] C_1-C_4 alcohols can be used as fuel additives to boost the overall octane rating and percent oxygen containing components (oxygenates) of a hydrocarbon-based fuel. The addition of oxygenates to hydrocarbon based fuels is environmentally beneficial in that CO and hydrocarbon emissions are reduced at higher air to fuel ratios.[4] Pure methanol can be used as a neat fuel or can be used as a reactant in the production of high octane methyl tertiary butyl ether, MTBE. The Cs-doped MoS_2 used in this process is referred to as a bifunctional catalyst. The proposed role of the alkali component, Cs, is to activate the CO via formation of a formate-type intermediate, $HCOO^-$, by the combination of a OH^- (the counter ion associated with the Cs^+) and a reactant CO molecule. The proposed role of the MoS_2 is to activate the H_2 by either heterolytic or homolytic dissociation of the H_2 on the MoS_2 surface.

Other research on molybdenum-sulfur catalysts has focused on methane coupling in a H_2 reducing environment to produce C_{2+} hydrocarbons over molybdenum-sulfur clusters encapsulated in a molecular sieve.[5] This catalyst involves the synthesis of small particles of a molybdenum-sulfur species (molecular cluster size) inside the supercages of a Y type zeolite. Particles of this size maximize the number of edge Mo and S atoms. The catalytic processes mentioned above all involve one common factor. In some manner, hydrogen must be activated on the surface of the catalyst and be made available for hydrogenation of the intermediate carbon-containing species. Knowledge of the surface properties of the transition metal disulfide species is important before the mechanism of hydrogen dissociation can be addressed. For instance, on the surface of MoS_2 the specific site at which H_2 is activated depends on the electronic properties of the sample.

It is the intent of this investigation to study in detail the bulk and surface electronic structure of the following transition metal disulfides: NbS_2, MoS_2, and RuS_2. These three disulfides have been chosen for the following reasons: NbS_2, exhibits metallic behavior due in part to the d^1 configuration of Nb^{+4} and possesses the layer-type bulk structure typical of many transition metal disulfides; MoS_2, exhibits semiconductor behavior due in part to the d^2 configuration of Mo^{+4}, possesses the layer-type structure, and is the most active disulfide used for alcohol synthesis; and RuS_2, exhibits semiconductor behavior due in part to the d^6

configuration of Ru^{+2}, possesses the pyrite-type structure typical of many transition metal disulfides, and is active as a HDS catalyst indicating a large amount of hydrogenation ability.

The electronic structure of the three disulfides were studied in detail both experimentally and theoretically. Experimental studies of the valence band of the disulfides were carried out using high resolution electron spectroscopy for chemical analysis (HR-ESCA) also referred to as high resolution x-ray photoelectron spectroscopy (HR-XPS). However, the valence bands of disulfides obtained via HR-ESCA are combinations of the atomic valence levels of sulfur and the transition metal. The HR-ESCA experiment does not resolve the valence band into contributions due to the atomic valence levels from different atoms. Theoretically calculated valence bands were used to interpret the HR-ESCA experimental results. A solid state adaptation of the extended Hückel theory is a very simple method that will calculate the density of states, as well as the contributions of the valence atomic orbitals to the density of states. Theoretical studies of the valence bands of the disulfides were carried out using the extended Hückel method applied to solid state systems. Once, an understanding of the electronic structure of the bare disulfide surface was achieved, hydrogen adsorption on the same surfaces was examined. Molybdenum disulfide was extensively studied in terms of hydrogen adsorption in an attempt to understand the nature of the hydrogen dissociation. Another feature that was studied theoretically, was the nature of the edge sites on MoS_2. The high surface area basal plane of MoS_2 is considered to be relatively inert, thus most of the catalysis is thought to occur on edge planes of polycrystalline MoS_2. This study will focus on the most stable type of edge planes and changes in the electronic structure and hydrogen adsorption properties upon the addition of the edge planes.

The electronic properties of MoS_2 have been reported in the literature by a variety of researchers. Theoretical methods of studying the band structure of MoS_2 include the following: semiempirical tight binding method,[6,7] simplified linear combination of muffin-tin orbitals method,[8] pseudopotential form of the linear combination of atomic orbitals (LCAO) neglecting three-center terms,[9] augmented-spherical-wave method,[10,11] and the atom superposition and electron delocalization molecular orbital method (ASED-MO)[12]. The theoretical method used in this study is the extended Hückel method applied to solid state systems which takes into account the periodicity of the lattice. Comparisons of the limitations of each of the theoretical methods mentioned previously as applied to extended systems will be discussed below. The choice of the extended Hückel method was based on the need for a very simple theory that could be used to calculate the electronic structure of a variety of systems to the same level of approximation. Some of the systems under study include the following: stoichiometric clusters

of MoS_2, two-dimensional infinite sheets of MoS_2, and one dimensional infinite sheets of MoS_2 with various types of exposed edge planed. Changes in the electronic structure of MoS_2 upon the introduction of different types of edge planes can be studied to obtain information on possible surface states. A knowledge of the surface states on a specific edge can lead to further investigations into the chemisorption preference of H_2 and CH_x for the molybdenum and sulfur edge atoms. The extended Hückel method with solid state applications can be used to theoretically study the electronic structure of all of the systems considered above.

The band structure of 2H-MoS_2 was studied theoretically by Bromley et al. in 1972 using a semiempirical tight binding method.[6,7] This method calculated matrix elements such as overlap considering only nearest neighbor interactions. As a result, molybdenum or sulfur overlap with molybdenum or sulfur atoms separated by a unit cell vector were neglected in this type of calculation. The semiempirical nature of this calculation arises from the fitting of theoretical energy gaps to experimental energy gaps observed in optical absorption studies of 2H-MoS_2. As a result large corrections to the matrix elements were made. In 1973, Kasowski theoretically calculated the energy bands of 2H-MoS_2 using the ab initio method of simplified linear combination of muffin-tin orbitals.[8] In this work, only the energy dispersion curves for the Mo4d-S3p valence bands and lower portion of the conduction bands are shown. Dispersion of the S3s bands is not shown. In 1978, Bullett studied the band structure of 2H-MoS_2 using a standard LCAO approach neglecting three-center terms.[9] In this study, a pseudopotential form of the Hamiltonian was used such that the Hamiltonian consisted of two parts, an atomic-like part centered on a particular atom and a perturbation from a second atom. Interactions between atoms separated by greater than 5.0 Å were neglected in this calculation. The d-electron charge was adjusted self-consistently so that the input neutral atom d-configuration energy levels were made consistent with the output occupation. Ab initio self-consistent band structure calculations using the augmented-spherical-wave method were performed by Coehoorn et al. in 1987.[10,11] In order to achieve self-consistency, the parameter u, corresponding to the degree of sulfur elevation above and below the plane of molybdenum atoms, was varied from the experimental value of 0.129 to a value of 0.121 for the calculations. One of the most recent studies of the electronic structure of MoS_2 was carried out by Anderson et al. using the atom superposition and electron delocalization molecular orbital method (ASED-MO).[12] This study used molybdenum-sulfur clusters such as MoS_6^{8-}, $Mo_7S_{18}^{8-}$, and $Mo_7S_{24}^{20-}$ to model the electronic structure of an MoS_2 species containing both bulk and edge molybdenum and sulfur atoms. The valence orbitals of molybdenum and sulfur were modeled by Slater-type orbitals. The valence state ionization potentials and slater orbital exponents were varied to achieve proper charge transfer between diatomic fragments. Theoretical hydrogen adsorption on MoS_2

was studied on edge and basal surfaces of the idealized clusters. Heterolytic H_2 adsorption on 5-coordinate Mo^{4+} edge sites was supported by these calculations.

One of the reasons for theoretically studying the electronic structure of MoS_2 using the extended Hückel method applied to solid state systems is because a very simple description of the band structure in terms of atomic orbitals is obtained. Using this method the nature of the dispersion in the experimental valence bands and E(**k**) curves can be evaluated. The previous theoretical studies concentrated mainly on accurately reproducing the optical band gaps and energy dispersion curves of 2H-MoS_2. The experimental valence band obtained via photoelectron spectroscopy is generally not compared to densities of states obtained for the aforementioned theoretical calculations. The theoretical study of Bullett does calculate the density of states. However, this density of states appears very different from the experimental valence band in terms of intensities of the various bands. One of the motivating reasons for this theoretical study is to decipher the MoS_2 valence band obtained via photoelectron spectroscopy. For example, the dispersion of the experimental S3s region is such that this level can't be considered a semi-core level but rather should be considered as a semi-valence level. The experimental S3s dispersion is explained by the extended Hückel theory used in this study. Another motivating factor for this study focuses on the experimental photoelectron spectroscopy of polycrystalline MoS_2 vs a single crystal of MoS_2. The theoretical difference between the valence bands of polycrystalline MoS_2 and a single crystal of MoS_2 can be obtained by studying a one-dimensional infinite sheet of MoS_2 with different exposed edge planes (modeling the edges of polycrystalline MoS_2) and a two-dimensional infinite sheet of MoS_2 with no edge planes (modeling single crystal MoS_2). Recent interest in MoS_2 has focused on the site of dissociation of H_2 on the surface. Previous investigators have studied this system in an attempt to elucidate whether the site of dissociation occurs on the molybdenum sites, sulfur sites or on both molybdenum and sulfur sites. The question of whether hydrogen dissociates by a heterolytic or a homolytic pathway on the MoS_2 surface is also still unanswered. The extended Hückel method applied to solid state systems can be used as a theoretical tool to examine the above mentioned systems.

The study mentioned previously involving the theoretical energy band comparison between a two-dimensional infinite sheet and a one-dimensional sheet (with terminating edge planes) of MoS_2 was prompted by the investigations of Roxlo et al.[13] This study looked at the effect on the optical absorption of introducing an increasing number of edge sites onto a thin MoS_2 single crystal. Below the energy of the indirect band gap, the amount of absorption increased as the number of edge impurity levels was increased. This result indicates that with

the addition of edges unoccupied surface states are appearing in the band gap region. A theoretical study of the band structure of two- and one-dimensional MoS_2 systems can be used to probe this experimental result. In an earlier study, Liang et al focused on the photoemission of poorly crystallized MoS_2.[14] Poorly crystallized MoS_2 was obtained in situ by first thermally decomposing ammonium thiomolybdate, $(NH_4)_2MoS_4$, to MoS_3. The second step involved heating of the resultant MoS_3 with H_2 at elevated temperature to obtain the desired product, poorly crystallized MoS_2. Ultraviolet photoemission spectroscopy (UPS) of this sample showed a tail on the lower binding energy side of the experimental d_{z2} band in the valence band region. The origin of this tail was thought by Liang et al. to be due to dimerization of molybdenum atoms on reconstructed edge planes.

Recently, angle resolved ultraviolet photoelectron spectroscopy (ARUPS) has been used by Mamy et al to experimentally determine the energy dispersion on the surface of natural molybdenite, 2H-MoS_2.[15] This study used both of the helium lines (He(I), 21.2 eV; He(II), 40.8 eV) as incident radiation in order to rule out effects due to $k_\perp$ dispersion. The data were obtained in the directions Γ to M, K to Γ, and M to K in polar angle increments of 5°. This resulted in experimental energy dispersion curves consisting of approximately ten points for the Γ to M and K to Γ directions. Previous theoretical calculations were used to connect the experimental points in the aforementioned directions of the first Brillouin zone. Energy dispersion curves for the S3s region of MoS_2 were not obtained in this study. Energy dispersion curves obtained from electronic structure calculations of two-dimensional MoS_2 can be compared to the experimental energy dispersion curves of 2H-MoS_2.

Hydrogen adsorption on polycrystalline MoS_2 has been studied by a number of research groups. In 1980, Wright et al studied the sorption of hydrogen onto MoS_2 surfaces prepared from the thermal reduction of MoS_3 by H_2 at 400°C.[16] Since sample preparation involved exposure to H_2, the preparation was followed by degassing of the sample in vacuum at 300°C. However, the resulting sample still retained hydrogen to the amount of 0.011 moles H per mole of MoS_2 ($H_{0.011}MoS_2$). In this study, it was found that MoS_2 surfaces sorbed approximately three times more hydrogen than was accessible to N_2. The dependence of H_2 sorption on the pressure of H_2 was also studied at a constant temperature of 300°C. As the hydrogen pressure was increased from 400 torr to 670 torr, the amount of hydrogen sorbed also increased with no sign of leveling off at higher pressures. At 670 torr, the resulting composition was the following: $H_{0.089}MoS_2$.

Other investigations of hydrogen sorption on amorphous MoS_2 surfaces prepared from nonaqueous preparations of the molybdenum chloride and lithium sulfide were carried out by

Sampson et al.[17] and Vasudevan et al[18]. The samples used in these studies were also exposed to H_2 during the pretreatment procedure which involved heating at 250°C in a 20% H_2S/H_2 mixture. Results from differential scanning calorimetry (DSC) indicate that two different hydrogen sorption sites exist on amorphous MoS_2. The first site is populated at H_2 pressures of 0.66 atm and temperatures below 150°C. At temperatures near 150°C, the sorption of H_2 increases very rapidly. The second site is populated at temperatures above 150°C and only becomes saturated at H_2 pressures of ca. 50 atm. Sorption of H_2 by the second site was found to be accompanied by an exotherm in the DSC; the magnitude of this exotherm increased with increasing pressure. IINS experiments of H_xMoS_2 samples in which only the first site was populated resulted in excitations at 662 cm^{-1} and 872 cm^{-1}. The 662 cm^{-1} excitation was assigned to a S–H deformation mode of hydrogen bonded to a single sulfur atom on the surface. The 872 cm^{-1} excitation was assigned to deformation modes of either Mo–O–H or Mo–H. The Mo–O–H deformation mode was thought to be the more likely cause of the 872 cm^{-1} excitation since this excitation persisted even after exposure of the hydrogen sorbed MoS_2 sample to air for a period of four weeks. Also, if the MoS_2 sample was not resulfided prior to hydrogen adsorption, the scattering intensity of the 872 cm^{-1} mode relative to the 662 cm^{-1} mode was higher. IINS experiments of H_xMoS_2 samples with population of both first and second sites indicated an additional excitation near 400 cm^{-1} that increased in intensity as the pressure of H_2 was increased. X-ray investigations of the two sites showed that population of the second site resulted in an additional diffraction peak corresponding to a **c** lattice spacing of 15.6 Å. The **c** lattice spacing of bare MoS_2 ranges from 12.3–12.6 Å and thus population of the second site by hydrogen involved an expansion of the lattice in the **c** direction, perpendicular to the S–Mo–S layers.

Blackburn and Sermon in 1983 studied the rate of hydrogen sorption by polycrystalline MoS_2 at 101 kPa and 52°C.[19] MoS_2 was found to sorb H_2 to the extent of 15.29 cm^3/gm to yield a stoichiometry of $H_{0.22}MoS_2$ at infinite time. The rate of H_2 sorption by MoS_2 was found to be slow. After 60 min. exposure of the surface to H_2, $H_{0.1}MoS_2$ was produced. Jones et al studied the adsorption of H_2 on MoS_2 on both adsorption sites by inelastic neutron scattering.[20] The results of their investigation confirmed the identification of the first hydrogen site as due to an Mo–S–H surface species indicating dissociation of H_2 on the MoS_2 surface. The second site was attributed to adsorbed molecular hydrogen. The theoretical ASED–MO study of hydrogen adsorption on molybdenum–sulfur clusters performed by Anderson et al supports the heterolytic dissociation mechanism of hydrogen at five–coordinate edge Mo sites.[12] However, the second hydrogen adsorption site (populated at temperatures above 150°C) on MoS_2 surfaces is attributed to the diffusion of hydrogen atoms from edge molybdenum atoms to sulfur anion

basal plane sites and not molecularly adsorbed hydrogen.

A more recent study of hydrogen adsorption on microcrystalline MoS_2 and single crystal MoS_2 was carried out by Komatsu and Hall in 1991.[21] Microcrystalline MoS_2 was prepared from ammonium tetrathiomolybdate by rapid heating of the precursor from 22°C to 350°C in a flow of 14%H_2S/H_2. This treatment was followed by passivation of the MoS_2 in 10%O_2/He at -196°C (30 min) and then at 22°C (30 min), in situ resulfidation in 14%H_2S/H_2 at 400°C (1 hr), reduction in dry H_2 500°C (1 hr), and flushing with purified He or N_2 at 450°C (1.5 hr). The sample resulting from this pretreatment procedure was referred to as fresh microcrystalline MoS_2 and was shown to contain no adsorbed hydrogen. Adsorption of hydrogen on fresh MoS_2 at a pressure of 0.72 atm was shown to occur rapidly at -196°C; this was followed by desorption of hydrogen at -78°C. Adsorption at -196°C was attributed to molecular hydrogen adsorption. At temperatures above 27°C, adsorption again occurred. Hydrogen adsorption on this sample was also studied at a pressure of 1 atm and temperatures in the range of 350°C to 773°C. Adsorption of hydrogen at each temperature was monitored by temperature programmed desorption, microbalance and isotope dilution to yield the following moles of hydrogen x in the formula H_xMoS_α: 0.044, 350°C; 0.038, 400°C; 0.030, 450°C; and 0.019, 500°C. Thus, the number of moles of hydrogen adsorbed at p_{H2}=1 atm decreased as the adsorption temperature was increased from 350°C to 500°C. The stoichiometry of the microcrystalline sample also changed such that the number of moles of sulfur α in H_xMoS_α decreased from its initial value of 1.983 to a value of 1.953 after H_2 adsorption at a temperature of 500°C. When the aforementioned H_xMoS_α samples were heated from 22°C to 400°C in flowing N_2, the TPD profile indicated the start of hydrogen desorption at 97°C and the desorption of H_2 as one broad peak centered at 247°C. Adsorption of hydrogen at higher H_2 pressures and 180°C indicated an increase in hydrogen uptake (up to ca. x=0.06) with increasing H_2 pressures (up to 35 atm). The amount of hydrogen adsorption also increased with increasing MoS_2 surface area. Extrapolations of the hydrogen uptake to zero surface area indicated a significant amount of uptake (x>0). This result supports previous investigations which indicate that hydrogen may exist within the Van der Waals gap. Variability in the hydrogen uptake x from that of previous investigations is attributed to different edge/basal plane ratios and different sulfur deficiencies α resulting from the different preparation procedures and formation of H_2S due to lack of thorough pretreatment. The ^1H NMR of H_xMoS_α samples gave a Gaussian shaped peak of FWHM ca. 25 ppm located at a chemical shift of ca. 2 ppm. This value is consistent with H bound to S in organic compounds. Adsorption of hydrogen onto a natural single crystal of 2H-MoS_2 did occur although a measurable BET surface area was not obtained. The MoS_2 single crystal was found to adsorb 0.001 moles of H at 1 atm and 180°C and 0.005 moles of H at 35 atm and 180°C.

Assuming a surface area of 1 m^2/gm and a basal plane sulfur concentration of 1.2×10^{15} atoms/cm^2, the authors determined a ratio of >2 hydrogen atoms/surface sulfur atom were adsorbed at $p(H_2)$=35 atm. Komatsu and Hall conclude from this set of experiments that when the surface area of the catalyst is 55 m^2/gm and at $p(H_2)$=1 atm, 86% of the hydrogen is held by the MoS_2 surface. The ^1H NMR work deserves special notice; only one peak corresponding to a S-H species is detected. The authors argue that reductive adsorption of hydrogen could lead to reduction of Mo^{+4} to Mo^{+3} producing H bonded to paramagnetic Mo^{+3}. The ^1H NMR signal of Mo^{+3}-H species would be broadened beyond recognition. However, this argument would also lead to broadening of the ^1H NMR peak due to the S-H species. The authors then suggest that the electron originating from the hydrogen may not be localized on an adjacent Mo atom but rather is injected into the conduction band of the extended system. This issue will be addressed by theoretical hydrogen adsorption on 1-D $(MoS_2)_5$ and $(MoS_2)_{19}$ clusters. The overall conclusion of Komatsu and Hall in this study is that hydrogen dissociates heterolytically on edge sites containing sulfur vacancies. Edge dissociation of hydrogen is followed by diffusion of hydrogen atoms to other locations at temperatures of 77°C.

Activation of hydrogen on the MoS_2 surface is of central importance in the catalytic processes discussed previously. The above discussion shows the different opinions about the second hydrogen adsorption site. The second site may very well play the more active role in catalytic reactions since for example in alcohol synthesis the partial pressure of reactant H_2 over MoS_2 is ca. 41 atm. Thus, further study of hydrogen adsorption over MoS_2 and related disulfide catalysts is needed for an understanding of hydrogen dissociation.

The electronic structure of RuS_2 has been studied recently using the self-consistent field scattered wave X_α (SCF-SW-Xα) method on clusters of RuS_6^{10-}.[22] The negative charge on the cluster serves to keep the sulfur atoms in an oxidation state of -2. However, the formal charge on each sulfur in the solid state RuS_2 system is -1 because of the formation of sulfur dimer pairs, S_2^{-2}. Thus, this study looks at a cluster as representative of the solid state system and discrete energy levels instead of energy bands are calculated. A more recent investigation of the RuS_2 electronic structure used self-consistent density-functional theory.[23] This method is much more rigorous and incorporates the solid state structure of the RuS_2 system into the calculation. A theoretical density of states was calculated and compared to an experimental XPS valence band of polycrystalline RuS_2. The experimental valence band and theoretical density of states agree in terms of energetic positions of the bands. However, the zero of energy in the theoretical calculations was placed at the highest occupied crystal orbital energy. Intensity ratios of the various energy bands in the theoretical density of states are not correct

when compared to the experimental valence band due to the differing photoelectron cross-sections of the S3s, S3p, and Ru4d orbitals.

This research effort has been undertaken to obtain more information on the electronic structure of the transition metal disulfides, NbS_2, MoS_2, and RuS_2. This information is necessary for a thorough understanding of the catalytic activity exhibited by each catalyst. The electronic structures of NbS_2, MoS_2, and RuS_2 were studied in great detail in order to answer the following questions:

1. What is the cause (in terms of orbital character) of the energy dispersion with wavevector, $E(\mathbf{k})$ vs. $\mathbf{k}$, for 2H-MoS_2?

2. What is the nature of the unoccupied surface states that reside in the band gap region of a MoS_2 sample possessing a significant number of coordinately unsaturated edge atoms?

3. Which hydrogen adsorption sites are thermodynamically stable? Are sulfur sites preferred over molybdenum sites; are basal plane sites preferred over edge plane sites?

4. Can the extended Hückel theory applied to solid state systems be parametrized in terms of the S3s, S3p, and Mo4d atomic ionization potentials, H_{ii}, and Slater-type orbital coefficients, c_i, and exponents, ζ_i, so that the experimental valence band of MoS_2 is theoretically reproduced?

5. Can the S3s and S3p ionization potentials, H_{ii}, and Slater-type orbital coefficients, c_i, and exponents, ζ_i, used to reproduce the MoS_2 experimental valence band be used to also reproduce the features of the NbS_2 and RuS_2 experimental valence bands?

6. Can the theoretical charges on the transition metal and sulfur of the NbS_2, MoS_2, and RuS_2 systems calculated by the theory be related to the binding energy shifts of the appropriate core levels found from HR-ESCA analysis of the polycrystalline samples?

As mentioned previously, Cs-doped MoS_2 is an important catalyst. The Cs is present on the surface of this catalyst in two forms: agglomerated particles and a surface dispersed species. Location of the Cs on the surface of this catalyst is an important issue. Another important issue is the coordination of molybdenum atoms on the edges of the crystalline catalyst particles, i.e. is the majority of edge molybdenum atoms coordinated by four of five sulfur atoms? A relatively new technique, angle resolved ESCA, has been developed by a variety of investigators.[24,25] In angle resolved ESCA, the intensity of the photoelectron signal due to core levels is enhanced in directions connecting the emitting atom with a neighboring surface atom.

This phenomenon is generally referred to as forward focusing. Angle resolved ESCA can be used to study the coordination of the molybdenum atoms on both the basal and edge planes. The Cs atom positions could also be determined from the difference between an angle resolved ESCA study of Cs-doped and Cs-free MoS_2 specimens.

Forward focusing or forward scattering of photoelectrons originating from near surface atoms (the emitter) occurs due to the attractive potential of neighboring atom cores (scatterer). This process produces enhanced photoelectron intensity along a line connecting the emitter to the scatterer. The line connecting the emitter and scatterer is experimentally defined by the azimuthal and polar angles. In most angle resolved XPS experiments, the sample is rotated since the detector axis is fixed. The polar angle is defined as the angle between the surface normal and the detector. The azimuthal angle is defined as the angle of rotation about the surface normal from an arbitrarily redefined point on the sample surface. Some prerequisites for observation of forward scattering are that the emitter-scatterer distances must be small, the sample surface must be ordered, the photoelectrons must be of high kinetic energy ($\sim$ 1 keV), and the emitter and scatterer atoms must be located close to the sample surface. Multiple scattering of forward scattered photoelectrons will occur if the emitter and scatterer lie too far from the surface. Multiple scattering by overlying atom cores is caused by deflection or defocusing of the forward scattered photoelectrons from their original trajectory. Thus, strong forward scattering is only observed for the top most surface layers of an ordered sample. Background information for this section was found in References 24a, 24b, 25. 26, 27, and 28.

The basal plane of single crystal MoS_2 is expected to exhibit forward focusing of the photoelectrons from Mo at polar angles of 49.1° because of the surface layer of coordinated S atoms. The polar angle is defined as the angle between the surface normal and the ESCA detector. Different polar angles are achieved by tilting of the sample surface since the detector position is fixed in the SCIENTA ESCA-300 system. Three azimuthal directions containing the Mo-S bond and separated by 120° (corresponding to rotation of the sample about the surface normal) should exhibit enhanced intensity at polar angles of 49.1°. Single crystals of MoS_2 can be obtained as the naturally occurring mineral, molybdenite. A preliminary angle resolved ESCA study was carried out on the basal plane of MoS_2. This study was used to check the feasibility of using the forward focusing technique on less than ideal single crystal surfaces of MoS_2. Up to this point, the majority of the angle resolved ESCA studies have been carried out on adsorbed species residing on single crystal surfaces consisting of one type of atom. The angle resolved ESCA study on MoS_2 was also used to test the applicability of this technique to crystals made up of more than one type of atom. Results of an angle resolved HR-ESCA study

on the basal plane of single crystal MoS_2 will be presented in this work. The applicability of this technique to studies of the edge Mo coordination is not feasible at the present time. Uniform edge planes of MoS_2 larger than the spot area analyzed by HR-ESCA have not been synthesized due to the large stability of the basal plane.

Chapter 2
EXPERIMENTAL

A description of the experimental techniques used to study the transition metal disulfides is presented in this section. The valence band spectra of single crystal MoS_2 and polycrystalline MoS_2, RuS_2 and NbS_2 were obtained by means of high resolution x-ray photoelectron spectroscopy (HR-XPS), also known as high resolution electron spectroscopy for chemical analysis (HR-ESCA). Orientation of the MoS_2 single crystal was achieved by Laue diffraction. Valence bands used to calculate the energy dispersion of MoS_2 were obtained by angle-resolved ultraviolet photoelectron spectroscopy (ARUPS).

2.1 Sample Preparation

2.1.1 Molybdenum Disulfide Single Crystal.

The MoS_2 single crystal was obtained from a natural source, Bear Lake, Canada, as the mineral molybdenite. X-ray diffraction (XRD) of a crushed portion of this specimen verified that the MoS_2 obtained was of the hexagonal modification. This modification is generally referred to as 2H-MoS_2 indicating that there are two MoS_2 units per hexagonal unit cell. The procedure for preparation of the crystal for XPS measurements involved cleavage of the crystal to expose a fresh basal plane, in an inert atmosphere (a N_2 filled glove bag). While inside the N_2 filled glove bag, the freshly cleaved crystal was mounted on an XPS sample holder and the sample and holder were placed in a N_2 filled bottle. The nitrogen filled bottle was then transferred to a glove bag attached to the XPS fast entry chamber. This glove bag was flushed with N_2 several times. The fast entry chamber was then vented with N_2 and opened to the N_2 filled glove bag. The sample was then transferred from the bottle to the fork in the fast entry chamber. This procedure minimized exposure of the freshly cleaved basal plane to contaminants found in air. Some of the experiments involving XPS and UPS, specifically in the studies of forward focusing of core level photoelectrons and energy dispersion curves, required orientation of the crystal by Laue diffraction after sample cleavage but prior to sample analysis. Thus, samples oriented by Laue diffraction were exposed to air for a short period of time prior to analysis. In the case of XPS analysis of core levels and valence bands, this exposure was not of great consequence.

2.1.2 Polycrystalline Molybdenum Disulfide.

Polycrystalline MoS_2 was obtained from J. G. Santiesteban. This sample was prepared by the thermal decomposition of molybdenum trisulfide, MoS_3.[29] The starting materials used

in this preparation were ammonium heptamolybdate, $(NH_4)_6Mo_7O_{24} \cdot H_2O$ and ammonium sulfide, $(NH_4)_2S$. These reactants were mixed in an aqueous solution to obtain the product $(NH_4)_2MoS_4$. Acidification of this product led to the precipitation of MoS_3, which after filtering and drying was decomposed to MoS_2 and S by heating under a flow of nitrogen. The MoS_2 resulting from this type of preparation was highly stoichiometric and poorly crystalline with a surface area of $\sim 60\ m^2/gm$. A more detailed description of this preparation is given in Reference 29. Since these samples were not prepared fresh, pretreatment of the samples prior to analysis was necessary. Pretreatment consisted of heating the polycrystalline MoS_2 sample in a quartz tube at 400°C for 1 hr in a 2.04% H_2/N_2 gas flow of $\sim$ 1cc/sec. Exposure of the polycrystalline samples to air prior to analysis was avoided by removing the sample from the quartz tube in a N_2 filled glove box.

Polycrystalline MoS_2 was mounted on an XPS sample holder through the use of indium foil. A drawing of the XPS sample holder is given in Figure 1. A wafer of clean indium foil was placed on top of a clean XPS sample holder. A small amount of polycrystalline MoS_2 was then spread over the surface of the indium foil. The polycrystalline MoS_2 was pressed into the indium foil to produce a smooth continuous layer of MoS_2. The sample and holder were enclosed in a N_2 filled bottle. The N_2 filled bottle was then transferred to a glove bag attached to the fast entry chamber of the XPS apparatus. The polycrystalline sample was then transferred under N_2 from the bottle to the fast entry chamber fork as described in Section 2.1.1.

2.1.3 Polycrystalline Ruthenium Disulfide.

Polycrystalline RuS_2 was prepared by the method of Pecoraro and Chianelli.[30] This method was modified slightly in that ethyl acetate was replaced by methanol as the solvent and $RuCl_4$ was replaced by α-$RuCl_3$ as the ruthenium source. Methanol was preferred because very pure RuS_2 without Li or Cl impurities was desired. Solubilities of the various reactants, products, and impurities, present at some point in the preparation, in CH_3OH are given as follows: α-$RuCl_3$, slightly soluble; Li_2S, very soluble; LiCl, soluble to 42.36g/100cc; RuS_2, insoluble; LiOH, slightly soluble.[31] The entire preparation procedure was carried out in a nitrogen filled glove box to avoid exposure to air. The air exposure was avoided not only to minimize oxidation of the ruthenium sulfide surface but also because of the pyrophoric nature of the intermediate ruthenium sulfide product. Stoichiometric polycrystalline RuS_2 was obtained by first partially dissolving a weighed amount of ruthenium chloride, α-$RuCl_3$, in a large amount of CH_3OH (approximately 300 ml CH_3OH) while stirring. Lithium sulfide, Li_2S, was

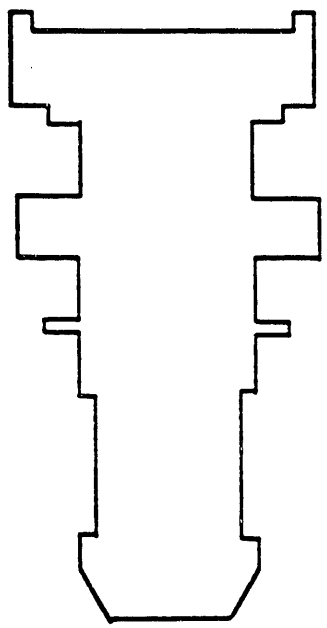

Figure 1. XPS sample holder used for polycrystalline samples. Polycrystalline MoS_2 was pressed onto the surface of clean In foil residing on the top of the XPS sample holder.

dissolved in approximately 100 ml of CH_3OH in a separate beaker. The methanolic solution of lithium sulfide was then filtered to remove any LiOH formed by the reaction of Li_2S with residual H_2O present in the methanol. The filtered methanolic solution of lithium sulfide was then added to the methanolic solution of ruthenium chloride with stirring. This solution was allowed to react for longer than 16 hr. When the reaction was complete, the ruthenium sulfide precipitate was allowed to settle (4–16 hr) for easier decantation of the liquid. After decantation of the liquid, the ruthenium sulfide precipitate was filtered and subsequently washed with fresh CH_3OH. After washing, the ruthenium sulfide precipitate was dried at room temperature in N_2.

Conversion of the intermediate ruthenium sulfide precipitate to the final form of ruthenium disulfide was accomplished by sulfidization under a 14.8% H_2S/H_2 gas mixture. In the sulfidization procedure a dispersion of an ca. 2 g portion of the precipitate over quartz beads in a quartz tube was used. Glass wool in the ends of the tube held the beads and precipitate in place. Swagelock valves placed on both ends of the quartz tube were used to avoid air exposure when transferring the tube from the N_2 filled glove box to the heating apparatus. A mixture of 14.8% H_2S/H_2 was then attached to one end of the quartz tube and a gas flow of ca. 1 cc/sec (as measured by a bubble meter attached to the other end of the tube) was attained at room temperature. Once the desired gas flow was set, it was maintained throughout the rest of the sulfidization process. The temperature of the quartz tube was then elevated to ca. 120 °C (a temperature above the boiling point of the solvent, CH_3OH, 64.5 °C). This temperature was maintained for ca. 15 min. in order to drive off any remaining solvent before further temperature increase. The temperature was then increased to 500 °C in a time period approximately 15 min. This temperature was then maintained for 1 hr. During this time the H_2S/H_2 flow was checked periodically to ensure a constant flow rate. The temperature was then lowered to room temperature under the same gas flow rate. When the tube had cooled sufficiently, the valves on both ends were closed and the tube was transferred into the N_2 filled glove box. The whole sulfidization procedure was carried out in a laboratory hood.

Ruthenium disulfide, RuS_2, resulting from the preparation discussed above was nearly stoichiometric and highly crystalline. XRD confirmed the presence of RuS_2. In some cases, small amounts of Ru(0) were also detected by XRD. However, XRD is a bulk technique and it seems likely that any Ru(0) present existed mainly in the bulk. The sulfidization procedure probably sulfided the surface of any Ru(0) present in the precipitate. The presence of Ru(0) in the RuS_2 sample prepared can probably be attributed to bulk Ru(0) present in the starting material, α–$RuCl_3$. This seems to be the most likely explanation since α–$RuCl_3$ is synthesized from ruthenium metal and Cl_2. A second possible origin of Ru(0) could be the actual reaction

of α–$RuCl_3$ with Li_2S. The exact stoichiometry of the reaction that occurs has not been presented in the literature. Due to the pyrophoric nature of the intermediate precipitate, it seems likely that the use of α–$RuCl_3$ (instead of $RuCl_4$) may result in the formation of highly dispersed Ru(0), equation 1a. A reaction scheme in which $RuCl_3$ reacts with Li_2S to form RuS_2

$$4\ RuCl_3(s) + 6\ Li_2S(s) \rightarrow 3\ RuS_2(s) + Ru^0(s) + 12\ LiCl(s) \qquad (1a)$$

$$Ru^0(s) + 2\ H_2S(g) \rightarrow RuS_2(s) + 2\ H_2(g) \qquad (1b)$$

$$\text{NET: } 4\ RuCl_3(s) + 6\ Li_2S(s) + 2\ H_2S(g) \rightarrow 4\ RuS_2(s) + 12\ LiCl(s) + 2\ H_2(g) \qquad (1c)$$

and Ru(0) in a 3:1 ratio, equation 1a, is likely. Sulfidization of the Ru(0) obtained from reaction 1a should then produce RuS_2, reaction 1b. Addition of reactions 1a and 1b leads to the net balanced equation, reaction 1c, for the production of RuS_2 from α–$RuCl_3$, Li_2S, and H_2S. According to reaction 1a and an incomplete course of reaction 1b, reaction of $RuCl_3$ with Li_2S could account for the presence of Ru(0) in the bulk, since sulfidization may occur preferentially on the surface of the Ru(0).

Typical surface areas of the RuS_2 obtained from this preparation were in the range of 7–10 m^2/gm. Surface areas were experimentally determined on an automated Digisorb 2500 by obtaining a 5-point adsorption isotherm using N_2 as the adsorbate. The volume of adsorbed gas for monolayer coverage of the solid sample, V_{mon}, was calculated using the BET equation 2 from the slope m and intercept b of a plot of $z/[(z-1) \times V]$ vs. z.[32] The surface area was then calculated from the monolayer volume of N_2, V_{mon} and the area per N_2 molecule.

$$\frac{z}{(1-z)V} = \frac{1}{cV_{mon}} + \frac{(c-1)z}{cV_{mon}} \qquad (2)$$

where

$z = \frac{p}{p_o}$ = ratio of equilibrium pressure to bulk vapor pressure

V = volume of adsorbed gas at pressure p

V_{mon} = volume of adsorbed gas for monolayer coverage $= \frac{1}{(m+b)}$

$m = \frac{(c-1)}{cV_{mon}}$; $b = \frac{1}{cV_{mon}}$

2.1.4 Polycrystalline Niobium Disulfide

The preparation of stoichiometric niobium disulfide, NbS_2, was investigated M. Kieke.[33] The synthesis of highly stoichiometric NbS_2 was found not to be possible by wet chemistry methods similar to those used in the cases of MoS_2 and RuS_2. Therefore, niobium sulfide, $NbS_{1.75}$, was purchased from the ALFA company. This sample was synthesized from the elements. Elemental analysis of this sample revealed that its stoichiometry actually consisted of 1.55 sulfurs to 1 niobium atoms. Thus, this sample is metal rich. Previous reports in the literature indicate that extra Nb atoms reside in the van der Waals gap existing between adjacent S-Nb-S sandwiches. HR-ESCA valence band analysis of this sample must be interpreted with caution, since stoichiometric NbS_2 was not examined. In the remainder of the text this sample will be referred to as $NbS_{(2-x)}$.

2.2 Laue Diffraction

Orientation of the MoS_2 single crystals used in the HR-ESCA forward focusing and UPS energy dispersion experiments was necessary for accurate interpretation of the experiments. In the case of the forward focusing experiment, the azimuthal direction of the Mo-S bond needed to be known in order to prove that forward focusing was occurring on the MoS_2 surface. In the case of the UPS experiment, energy dispersion curves along the high symmetry directions, $\Gamma \rightarrow M$, $\Gamma \rightarrow K$, and $K \rightarrow M$, in the first Brillouin zone needed to be investigated. These directions can be located by obtaining a picture of the crystal surface by Laue back diffraction. This section describes some of the principles of back-reflection Laue. Background information on this technique was obtained from Reference 34.

2.2.1 Principles of Laue Diffraction

In the back-reflection Laue method, incident radiation of variable wavelength, λ, is allowed to fall on a single crystal surface. The source of this variable wavelength radiation is the continuous radiation from a tungsten, W, x-ray tube. An x-ray tube consists of a source of electrons and two metal electrodes. High voltage applied across the two electrodes draws electrons to the tungsten anode target. X-rays are produced by the impact of the accelerated (typically 5-40 keV) electrons on the target metal. A continuous spectrum of x-rays results from the rapid deceleration of the electrons by the target. The total intensity, I, of the radiation is proportional to the atomic number Z of the target metal. Thus, the higher is the atomic number of the metal, the higher is the total intensity of radiation obtained. W has a high atomic number (Z=74) and thus produces high intensity continuous radiation.

In this experiment, the Bragg angle, θ, is fixed for each set of planes of spacing, d, in the single crystal. Each set of planes then diffracts the component of incident radiation with wavelength λ that satisfies the Bragg law, equation 3, for the fixed values of θ and d.[34] In this equation, the integer n is referred to as the diffraction order. The {hkl} and {nh nk nl} sets of planes are parallel but are situated so that the distance between {hkl} planes is d_{hkl} and the distance between {nh nk nl} planes is d_{hkl}/n. In the back-reflection Laue method, the photographic film and single crystal surface are placed perpendicular to the incident beam. The photographic film is placed between the crystal and source such that the incident radiation passes through a hole in the film. Spots recorded on the photographic film are due to beams diffracted backwards by the crystal. A schematic representation of the back-reflection laue diffractometer is shown in Figure 2. Sets of planes in the crystal cause the diffraction spots. A more detailed explanation of the back-reflection Laue method can be found in Reference 34.

$$n\lambda = 2d_{hkl}(\sin \theta) \tag{3}$$

2.2.2 Orientation of MoS_2 Single Crystal

The procedure used for orientation of an MoS_2 single crystal by Laue diffraction is given in the following paragraph. A suitable single crystal of MoS_2 was obtained by cleaving several pieces of MoS_2 with a clean, sharp edge. The cleaved crystals were examined for cleanliness and flatness of the basal plane. The best samples were pressed between two clean microscope slides and saved for Laue diffraction. A back-reflection Laue diffractometer containing a W x-ray source was used for the analysis. A single crystal of MoS_2 was taken from the microscope slides and pressed into the Laue sample holder which was then placed in the instrument. Typical settings used for the generator were the following: 20 nA, 30 kV and 10 min exposure time. Once a good picture was obtained, the crystal was oriented by rotation of the sample holder according to information obtained from the Laue picture. A typical Laue picture for the samples of 2H-MoS_2 used in this study is shown in Figure 3. The Laue picture consists of 3 distinct rows of spots, 60° apart and 6 spots, 60° apart. The four black spots near the center of the picture, when connected, mark the vertical and horizontal axes of the camera. The angles of rotation of a row of spots from the vertical (or horizontal) axis can then be measured from the picture. Rotation of the sample must be opposite that of rotation as measured from the picture. For example, if the picture indicates that a row of spots must be rotated clockwise by 10° to line up with the vertical axis, then the sample must be rotated counterclockwise by 10°. The sample holder was marked in 2° increments so that accurate rotation of the sample was achieved. Once

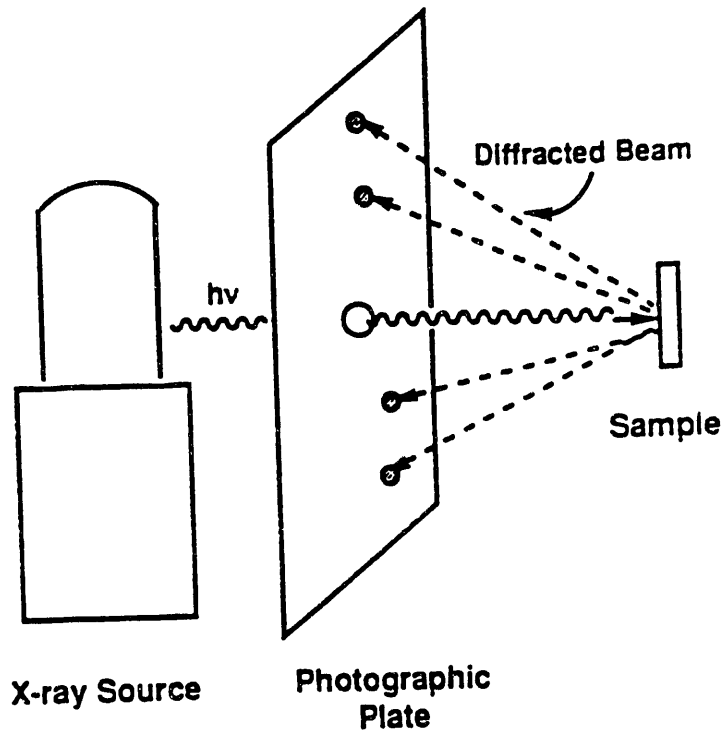

Figure 2. Schematic representation of the back-reflection laue diffractometer.

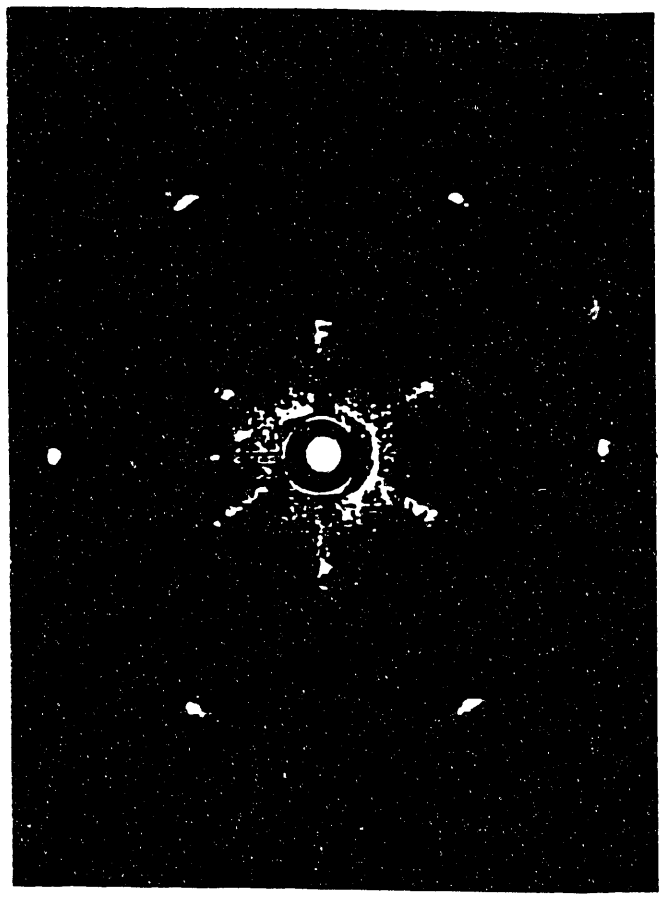

Figure 3. Experimental back-reflection Laue photograph of the (0002) plane of a natural single crystal of 2H-MoS_2.

orientation of the sample was achieved, a scribe mark was placed on the sample to indicate the position of the sample in relation to the Laue picture. Note that samples oriented by Laue diffraction were exposed to air for an extended period of time.

2.2.3 Interpretation of Laue Pattern for the Orientation of 2H-MoS_2

The (0002) plane of 2H-MoS_2 was the plane obtained upon cleavage of natural crystals. Thus, the (0002) plane was oriented perpendicular to the beam of incident radiation in the Laue experiment. Diffraction of x-rays from this plane could in principle produce a spot on the photographic film called the zone center. However, since the diffraction beam from this plane occurs in the same direction as the incoming beam of x-rays, the (0002) spot is absent. Location of this spot, the zone center, was found by drawing perpendicular lines between the four black spots near the center of the photograph.

A set of planes that all intersect the same straight line are said to belong to the same zone and are called planes of a zone. The intersecting straight line contained in the planes of a zone is called the zone axis, Z_{uvw}. Figure 4, shows the relationship between planes belonging to the same zone and the corresponding zone axis. If the zone axis of this set of planes is parallel to the crystal surface, then diffracted beams from the planes of this zone will produce a set of spots that lie on a straight line and contain the zone center, the (0002) diffraction spot. Planes of a zone containing a zone axis that is perpendicular to the (0002) surface will not produce Laue spots on the film. As mentioned previously, there are three straight lines of spots present on the Laue photograph of (0002) 2H-MoS_2, Figure 3. Planes causing a diffraction spot on one of the straight line of spots contain the same zone axis and obey equations 4a and 4b below. In

$$G_{hkl} \cdot Z_{uvw} = (h\mathbf{a}^* + k\mathbf{b}^* + l\mathbf{c}^*) \cdot (u\mathbf{a} + v\mathbf{b} + w\mathbf{c}) = 0 \quad (4a)$$

$$G_{hkl} \cdot Z_{uvw} = hu + kv + lw = 0 \quad (4b)$$

Solutions of 4a and 4b are:

$$u = kl' - lk' \quad (4c)$$

$$v = lh' - hl' \quad (4d)$$

$$w = hk' - kh' \quad (4e)$$

this equation, the reciprocal lattice vector, G_{hkl}, is perpendicular to the real space (hkl) plane and to the vector defining the zone axis, Z_{uvw}. Thus, if the hkl indices of two planes on the straight lines of spots (belonging to the same zone axis) are known, then the u, v, w indices of

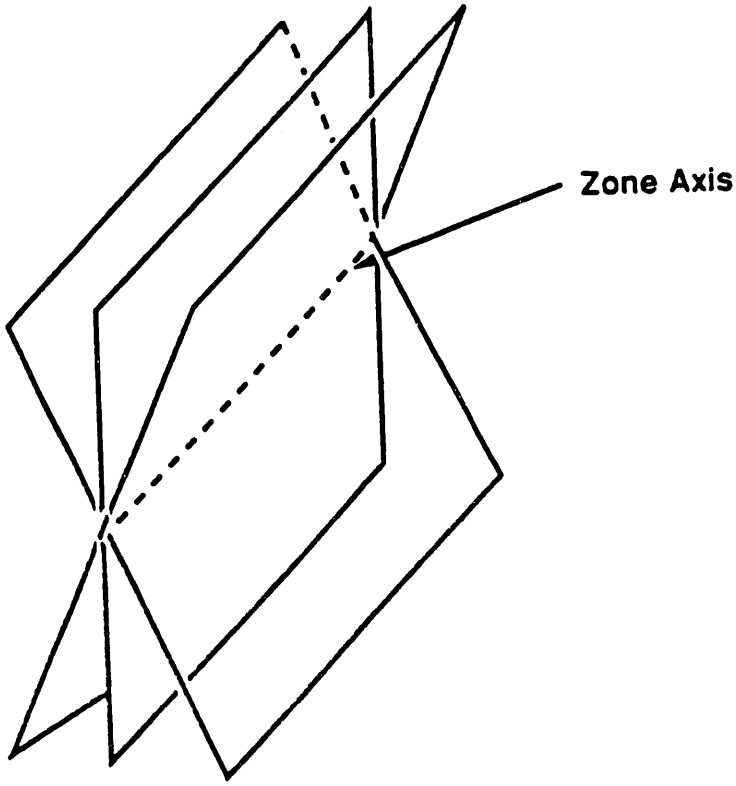

Figure 4. Planes of a zone parallel to the same zone axis.

the zone axis can be found from equations 4c, 4d, and 4e. In these equations, h′, k′, and l′ are coordinates of another vector G′ perpendicular to the h′, k′, l′ plane of the zone. Once the zone axis, Z_{uvw}, is found, conditions for the h, k, l indices of other planes belonging to the same zone axis can be found from the equations given above. Background information for this section was obtained from Reference 34.

In MoS_2 forward focusing directions with respect to the (0002) basal plane are expected to occur in the direction of Mo–S bonds of the first atomic layer sulfur and the second atomic layer molybdenum. The following set of planes are perpendicular to the (0002) surface and contain the Mo–S bonds: $(\bar{1}2\bar{1}0)$, $(\bar{1}\bar{1}20)$, and $(2\bar{1}\bar{1}0)$ or $(1\bar{2}10)$, $(11\bar{2}0)$, and $(\bar{2}110)$ respectively. This set of planes also defines the direction Γ→K (or $G_{\bar{1}2\bar{1}0}$) in the first Brillouin zone since this direction is perpendicular to the $\{\bar{1}2\bar{1}0\}$ set of planes. A schematic representation of the (0002) MoS_2 surface showing the forward focusing atoms in the above planes is shown in Figure 5a. Figure 5b shows the directions Γ→M ($G_{\bar{1}100}$), Γ→K ($G_{\bar{1}2\bar{1}0}$), and K→M ($G_{\bar{1}2\bar{1}0}$) in the first Brillouin zone with respect to the real lattice. Directions where forward focusing is <u>not</u> expected to occur correspond to the following set of planes: $(\bar{1}100)$, $(10\bar{1}0)$, $(01\bar{1}0)$ or $(1\bar{1}00)$, $(\bar{1}010)$, and $(0\bar{1}10)$ respectively. These planes are also perpendicular to the (0002) surface but do not contain Mo–S bonds. This set of planes corresponds to the direction Γ→M ($G_{\bar{1}100}$) in the first Brillouin zone. These planes are shown in Figure 5c. Γ→M and Γ→K directions are located 30 ° from each other as measured about the surface normal. No diffraction spots appear on the Laue film for either of the sets of planes discussed above since both sets of planes are perpendicular to the (0002) surface. However, each of these planes belongs to a set of planes which possess a zonal axis that is parallel to the (0002) surface. Thus, if other planes of this zone axis produce diffraction spots on the film, then the planes discussed above can be located. A standard stereogram of 2H–MoS_2, available in the literature, can be used to identify the planes responsible for the Laue diffraction spots.[35]

Based on measurements of spot distances obtained from the stereographic projection of MoS_2, Reference 35 , the three straight lines of spots are due to planes belonging to the following zone axes: [0n0], [n00], and [nn0] (where n can be any integer number). Substitution of the coordinates of the zone axes into equation 4b results in the following conditions for the hkl indices of the planes belonging to that zonal axis: k=0, h=0, h=-k, and l arbitrary. The four-index notation for hexagonal systems, (hkil) where i=-(h+k) will be used throughout the rest of the text. The third index i is redundant and not needed for defining a plane but is included to show that certain planes form a symmetric set. The $(10\bar{1}0)$, $(01\bar{1}0)$, and $(1\bar{1}00)$ planes satisfy the specified conditions and thus belong to these zones. Thus, each of these planes

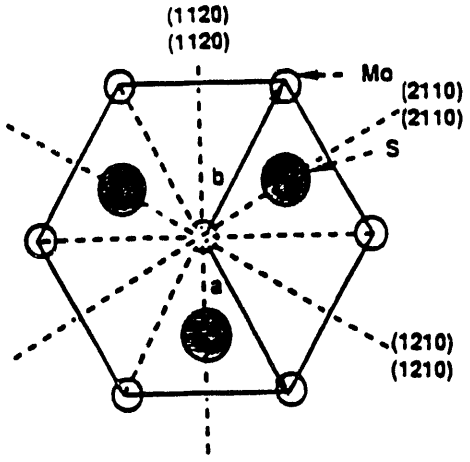

Figure 5a. Schematic representation of the (0002) MoS_2 plane and the planes along which forward focusing occurs. (white circles=second atomic layer Mo; black circles=first atomic layer S)

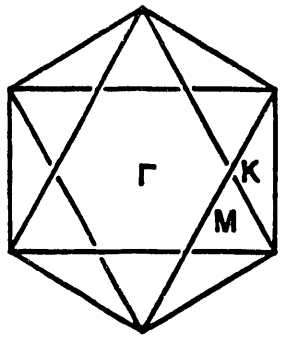

Figure 5b. First Brillouin zone showing the following directions: Γ—M, Γ—K, and K—M. Note that the orientation of the hexagonal Brillouin zone is the same as the real lattice.

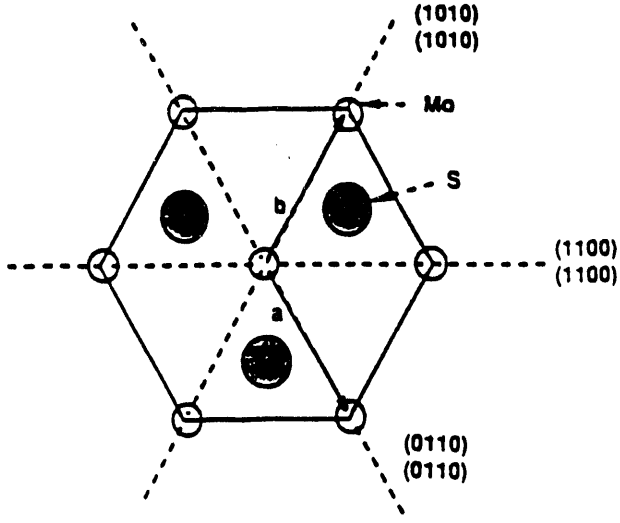

Figure 5c. Schematic representation of the (0002) MoS_2 plane and the planes along which forward focusing does <u>not</u> occur. (white circles=second atomic layer Mo; black circles=first atomic layer S)

is perpendicular to one of the straight lines of spots and to the (0002) surface. Analysis of the same projection also indicates that the spots (6 spots located 30° from the straight lines of spots) are due to planes belonging to the following zone axes: $[\bar{n}\ n\ 0]$, $[2n\ n\ 0]$, and $[n\ 2n\ 0]$. Conditions for the hkl indices of the real lattice planes belonging to this set of zonal axes are the following: h=k, 2h=-k, -h=2k, and l arbitrary. Thus, the $(\bar{1}\bar{1}20)$, $(\bar{1}2\bar{1}0)$, and $(2\bar{1}\bar{1}0)$ planes satisfy the conditions and are each perpendicular to a line connecting two of the spots through the zone axis. This set of planes contains the Mo-S bond and as a result is parallel to the direction of forward focusing. Thus, forward focusing directions are located parallel to the straight lines of spots (located every 60°) and perpendicular to lines connecting the 6 spots through the zone axis. Located 30° from this direction, are the non-forward focusing directions.

2.3 High Resolution Electron Spectroscopy for Chemical Analysis, (HR-ESCA)

2.3.1 Principles of HR-ESCA

In the HR-ESCA method, high intensity x-rays impinging on a sample surface cause ejection of core and valence level electrons, photoelectrons, into the vacuum. Photoelectrons resulting from this process are emitted with a specific kinetic energy, E_k, that depends to a first approximation on the energy of the incident x-rays, $h\nu$, and the binding energy of the electron to surface, E_b. The detector system detects the number of photoelectrons at each kinetic energy and the result is a spectrum of photoelectron intensity vs. photoelectron kinetic energy, E_k. A schematic representation of the HR-ESCA system is shown in Figure 6. To a first approximation, equation 6 can be used to obtain the binding energy, E_b, of the electrons. Thus, a spectrum of the photoelectron intensity vs. photoelectron binding energy, E_b, can be obtained.

$$E_b = h\nu - E_k \tag{5}$$

However, the situation is actually more complicated than this. Photoelectrons ejected from the solid must overcome forces due to the surface that lower the experimentally obtained kinetic energy. These forces are called the work function, ϕ, of the surface. The work function is defined as the difference between the chemical potential, μ, of electrons inside the surface at the Fermi level, E_f, and the electrostatic potential of electrons just outside the surface at the vacuum energy, E_v.[36] Also, for semiconductor and conductor samples in contact with the instrument, the Fermi level, E_f, of the sample and instrument are the same. The instrument is calibrated with a good metallic conductor in such a way that the Fermi level, E_f, of the instrument appears at a binding energy of zero eV. Thus binding energies measured in this way are measured from the Fermi level, E_f, instead of the vacuum level, E_v. The Fermi level, E_f,

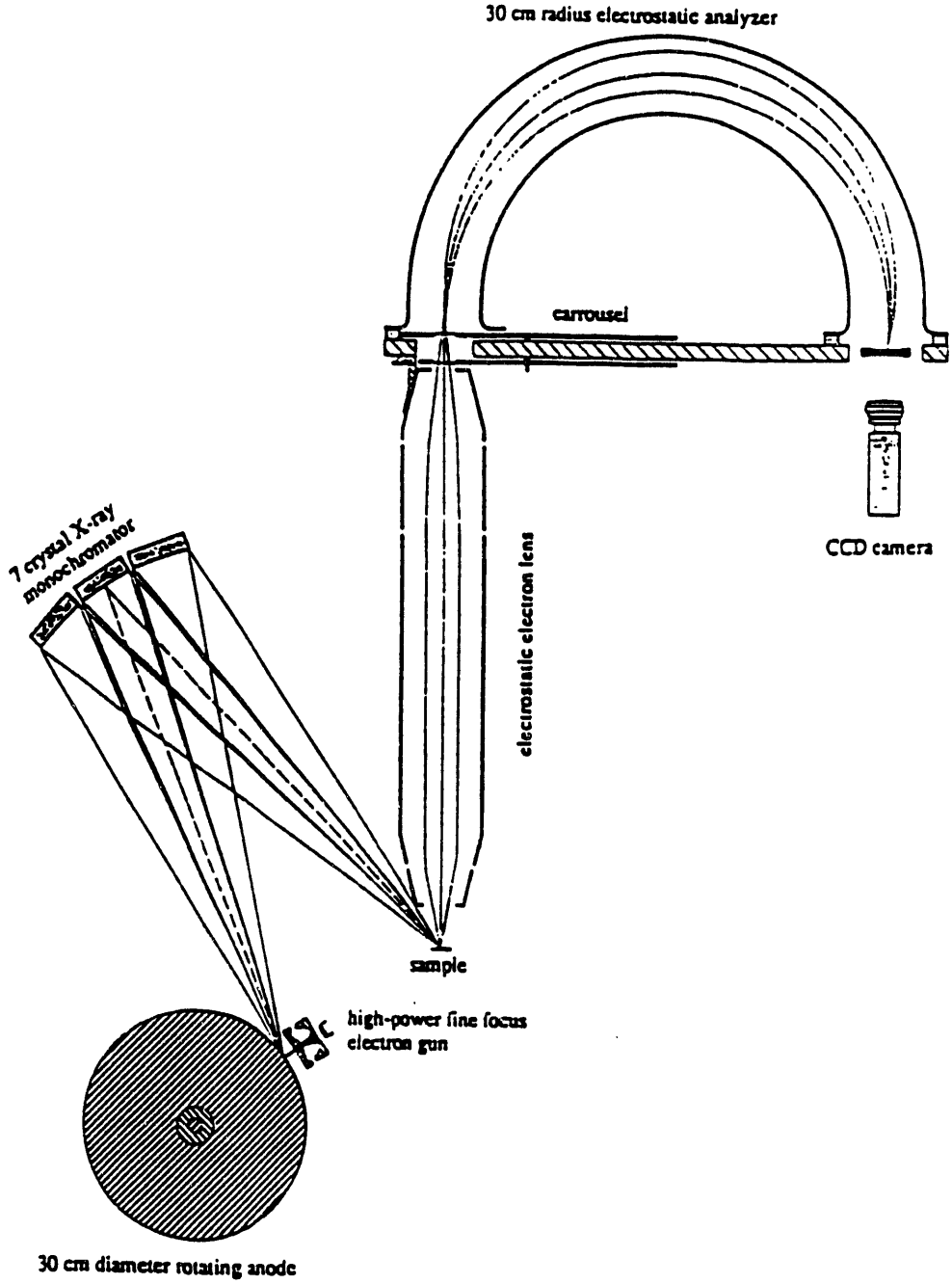

Figure 6. Schematic representation of the HR-ESCA system used to obtain core and valence level spectra.

and vacuum level, E_v, energies are related to each other by the work function as indicated in equation 6. For metals, the Fermi level is located at the top of the valence band.

$$E_f - E_v = \phi \tag{6}$$

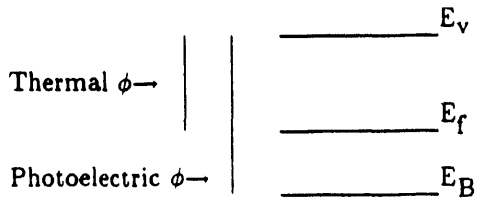

For semiconductors, the Fermi level is located in the region of the gap that exists between the valence and conduction bands. Thermionic emission of electrons measures the thermal work function of the sample as defined in equation 6. Photoelectron spectroscopy measures the photoelectric work function of the sample which is defined as the difference between the highest occupied crystal orbital located at an energy E_B and the vacuum level.

Other effects that change the photoelectron kinetic energy, E_k, are final state effects. Once the photoelectron is emitted from the sample surface, a positive hole is left behind. Thus the final state consists not only of an outgoing photoelectron but also of a positive hole. This positive hole attracts the outgoing photoelectron and the electrons left behind on the surface. Relaxation of the electrons left behind on the surface to decrease the energy of the system also occurs. This relaxation energy decreases the binding energy, thus increasing the kinetic energy of the outgoing photoelectron.

When samples are analyzed via HR-ESCA, information on elemental composition and oxidation states is obtained from the surface. HR-ESCA is a surface sensitive technique because photoelectrons emitted from atoms beneath the surface must travel a certain distance through the lattice before reaching the surface and eventually being detected. The escape depth or attenuation length, λ_m, is used to define the distance a photoelectron can travel through the lattice before it loses energy or is scattered by other atoms of the lattice and is no longer detected. The escape depth has been studied in detail by Seah and Dench for elements, inorganic compounds and organic compounds.[37] In general the escape depth varies with photoelectron kinetic energy, such that the lowest escape depths (most surface sensitive) are found for photoelectrons possessing kinetic energies of 30 eV--40 eV. For inorganic compounds, Seah and Dench obtained a universal equation 7 from a universal curve of experimentally

determined escape depths. In MoS_2, the monolayer thickness a is calculated to be ca. 2.6 Å.

$$\lambda_m = \frac{2170}{(E)^2} + 0.72 \times (aE)^{\frac{1}{2}} \tag{7a}$$

$$\lambda_n = a \times \lambda_m \tag{7b}$$

where λ_m = escape depth in monolayers
λ_n = escape depth in nanometers
E = photoelectron kinetic energy
a = monolayer thickness

The experimental valence band of MoS_2 extends from a binding energy of ca. 20 eV to 0 eV, as measured with respect to the Fermi level. Thus, photoelectrons ejected from the valence band region of MoS_2 by monochromatic Al K_α radiation of energy 1486.6 eV have kinetic energies (prior to leaving the surface) extending from 1486.6 eV to 1466.6 eV. Using equations 7a and 7b above these kinetic energies correspond to an escape depth of ca. 14 monolayers or 38 Å for the valence band region. The Mo 3d, Mo 3p and S 2p core levels were also studied in many of the experiments discussed in the following sections. Approximate photoelectron kinetic energies and escape depths for the Mo $3d_{5/2}$, Mo $3p_{3/2}$ and S $2p_{3/2}$ core levels are as follows: 1258 eV, 35 Å; 1091 eV, 32 Å; and 1325 eV, 36 Å. Photoelectrons ejected from the valence band region of MoS_2 by He I radiation of energy 21.22 eV have kinetic energies (prior to leaving the surface) extending from ca. 21 eV to 0 eV. Again, using the equations above, these kinetic energies correspond to an escape depth of ca. 6.6 monolayers or 18 Å at 21 eV. However, a dramatic increase in the escape depth occurs as the kinetic energy is lowered further so that at 5 eV, the escape depth is 88 monolayers or 230 Å. The equations of Seah and Dench only typify a general trend in the behavior of photoelectron escape depth vs. energy. Thus, escape depths calculated from the Seah and Dench equations should not be viewed as absolute numbers. However, the discussion above shows that photoelectron spectroscopy is a surface sensitive technique.

2.3.2 Description of HR-ESCA Instrument

The instrument used for HR-ESCA analysis of the core levels and valence bands of transition metal disulfides was the SCIENTA ESCA-300 that is located in the Zettlemoyer Center for Surface Studies at Lehigh University. The SCIENTA ESCA-300 is equipped with a water-cooled high intensity rotating Al K_α anode (a Cr anode is also available). The x-rays resulting from this source are monochromatized by seven quartz crystals and are impinging on the sample at an angle of 45° from the detector axis. The high intensity and monochromaticity

of the source make analysis of valence bands a routine procedure. The detector system consists of a large radius (60 cm) hemispherical analyzer combined with a multichannel plate detector. High sensitivity and high energy resolution are achieved with this type of detector system.

The HR-ESCA instrument is also equipped with a sample stage that is manually controlled. The sample stage can be translated in the x, y, and z directions and rotated about the azimuthal and polar axes. The orientation of the analyzer, x-ray source, and sample in terms of the x, y, and z axes is shown in Figure 7. The analyzer entrance is parallel to the z-axis and the incoming x-rays approach the sample surface in the xz-plane at an angle of 45° from the sample surface when the surface is orientated perpendicular to the detector. A microscope used for sample observation is located in the yz-plane. The portion of the HR-ESCA instrument used for sample transfer is divided into three main chambers separated by gate valves. The first chamber, the fast entry chamber, is used for introduction of the sample into the vacuum system. Initial pump down of the sample to pressures in the low 10^{-6} torr range is carried out in this chamber. Retractable forks are used for sample transfer between the various chambers in the HR-ESCA instrument. Transfer to the second chamber, the preparation chamber, is carried out after the fast entry chamber is at a pressure in the low 10^{-6} torr range. The sample resides in the preparation chamber until pressures in the low 10^{-8} torr range are reached. Argon bombardment and heating of samples can be carried out in the preparation chamber to obtain cleaner surfaces and better vacuum. Transfer to the third chamber, the sample chamber, is then carried out. Analysis of the sample takes place in the sample chamber. Due to the nature of the sample transfer system, pressure in the sample chamber remains low, in the low 10^{-9} to 10^{-10} torr range. One advantage of this type of sample transfer system is that introduction of contaminants into the sample chamber is minimized. A second advantage is that the amount of time between introduction of the sample and analysis of the sample is decreased. Typical times (depending on the amount of sample degassing) between introduction and analysis of a sample are 20–30 min.

The SCIENTA ESCA-300 is also equipped with a spatial lens, a prelens. When in place, the prelens decreases the area of the sample from which photoelectrons are detected. Essentially, the prelens magnifies the area sampled. In the spatial mode a rectangular spot size, 3.9 mm × 110 μ, can be sampled. Spatial mode was used in the forward focusing studies to obtain information on the directionality of the bonds.

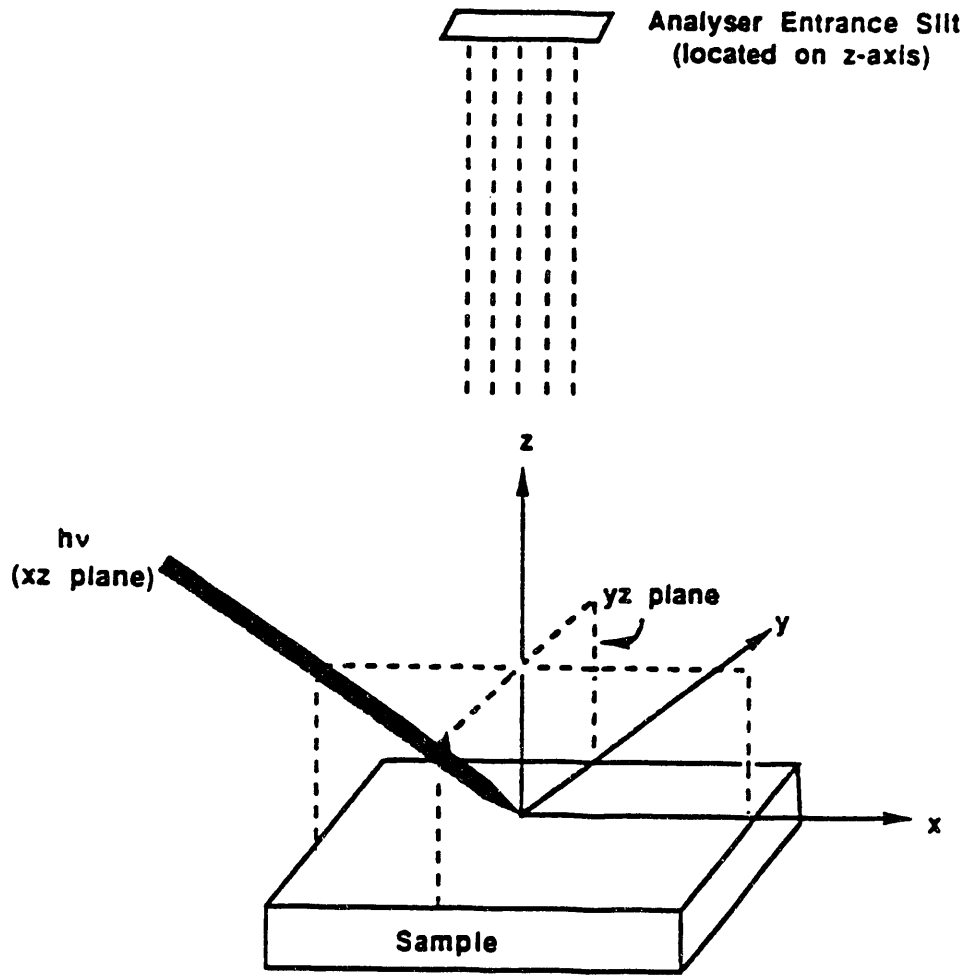

Figure 7. Orientation of the HR-ESCA analyzer, x-ray source, and sample in terms of x, y, and z axes.

2.3.3 Core Level and Valence Band Analysis by HR-ESCA

Cleanliness and stoichiometry of the transition metal disulfides was examined by core level analysis via HR-ESCA. Instrumental parameters such as pass energy, E_p, step size, time/step, slit width, and mode of operation (either high transmission mode or high spatial mode) are set prior to analysis. The pass energy, E_p, is the constant energy to which the photoelectrons are retarded for detection by the hemispherical analyzer. During an analysis, the pass energy is set to a specific value. Thus, only photoelectrons that possess a kinetic energy equal to the pass energy are detected. However, photoelectrons are emitted from the sample with a range of kinetic energies. Emitted photoelectrons are slowed down or retarded by an applied voltage to attain the specified pass energy. The retardation voltage, R_V, is related to the photoelectron kinetic energy, E_K, and the pass energy, E_p, by the following equation: $E_K=R_V+E_p$. The retardation voltage is scanned over an energy range specified by the binding energy range. For example, in a typical survey scan, the pass energy is set to 300 eV and the binding energy range is from 1000 eV - 0 eV. The corresponding kinetic energy range is from ca. 486 eV - 1486 eV. Using the equation defined above, the retardation voltage is scanned from 186 eV - 1186 eV. The step size indicates the width of the energy step between each retardation scan. Thus, if a range of 1000 eV is scanned with a step size of 0.5 eV, then the retardation voltage will be incremented 2000 times by 0.5 eV each time. The time/step indicates how long the detector collects counts at each specific scan. If there are 2000 steps and a time/step of 0.02 sec, then one entire scan of the defined region will take a minimum of 40 seconds. The slit width defines the physical width of a slit that is positioned in front of the detector entrance. The smaller (larger) the slit the greater (lower) the resolution and the lower (higher) the intensity. Transmission mode is characterized by high intensity but low spatial resolution. Spatial mode is obtained by placing the spatial lens (prelens) in front of the detector entrance. In this mode optimal spatial resolution is achieved at the expense of photoelectron intensity.

Typical instrumental parameters used for obtaining survey scans were the following: pass energy, E_p, 300 eV (or 150 eV); step size, 0.5 eV; time/step, 0.02 sec; slit width, 1.1 mm; number of scans, 5; binding energy range, 1000 eV - 0 eV; and transmission mode. Typical instrumental parameters used for obtaining core level scans were the following: pass energy, E_p, 75 eV; step size, 0.05 eV; time/step, 0.04 sec; slit width, 1.1 mm; number of scans, 4-5; and transmission mode. Survey scans were initially run for carbon and oxygen contaminants. If the carbon and oxygen contaminants were present but their concentrations were low, core level regions of the TS_2 (where T=transition metal, Nb, Mo, Ru, Fe) and the contaminants were

recorded in detail. For example, on a typical sample of MoS_2 the following core level regions were obtained: Mo 3d, S 2p, C 1s, and O 1s. A rough estimate of the amount of carbon and oxygen surface contaminants was then obtained from the C 1s (O 1s) and Mo 3d areas and photoelectron cross-sections.

As mentioned previously, analysis of photoemission from valence bands is a routine procedure with the SCIENTA ESCA-300 instrument when angular resolution is not required. Measurement times for valence band analyses varied from 1 hr to 4 hr, according to the amount of detail required from the spectrum. Typical instrumental parameters used for obtaining valence bands of transition metal disulfides, TS_2, were the following: pass energy, E_p, 75 eV; step size, 0.05 eV; time/step, 0.4 sec; slit width, 1.1 mm; binding energy range, 20 eV — -1 eV; and number scans, ca. 50.

2.3.4 Angle Resolved HR-ESCA

MoS_2 single crystals used in the angle resolved study were first oriented by Laue diffraction as described in Section 2.2.2. Due to the nature of the orientation procedure, the crystals used in this study were exposed to ambient atmosphere. The oriented MoS_2 single crystal was placed on an ESCA sample holder such that the scribe mark on the crystal lined up with a scribe mark on the sample holder. Two small screws and a Be-Cu spring clip were used to fasten the sample to the sample holder. The sample holder assembly used in this study is shown in Figure 8. The ESCA sample holder was scribed every 30°. The sample holder was machined to a height such that the single crystal surface was located at the epicenter of the polar angle axis. In this way, the crystal did not swing through an arc with incrementing the polar angle. Thus, photoelectrons were detected from the same spot on the sample surface.

A survey and detailed core level spectra (Section 2.3.3) were obtained to check for contaminants, carbon and oxygen, and the surface stoichiometry. The sample used in this study contained small amounts of surface carbon and oxygen. However, the stoichiometry of the surface was such that only one species of molybdenum and sulfur were present. Sample heating in vacuum, at temperatures in the range of 300° - 600°C, was attempted in order to remove the carbon contaminants from the surface. Heating alone was not useful for removing carbon from the surface. Heating in oxygen to remove surface carbon was avoided to minimize oxidation of the surface. Heating in hydrogen was avoided because a second experiment aimed at understanding hydrogen adsorption on the MoS_2 surface was planned.

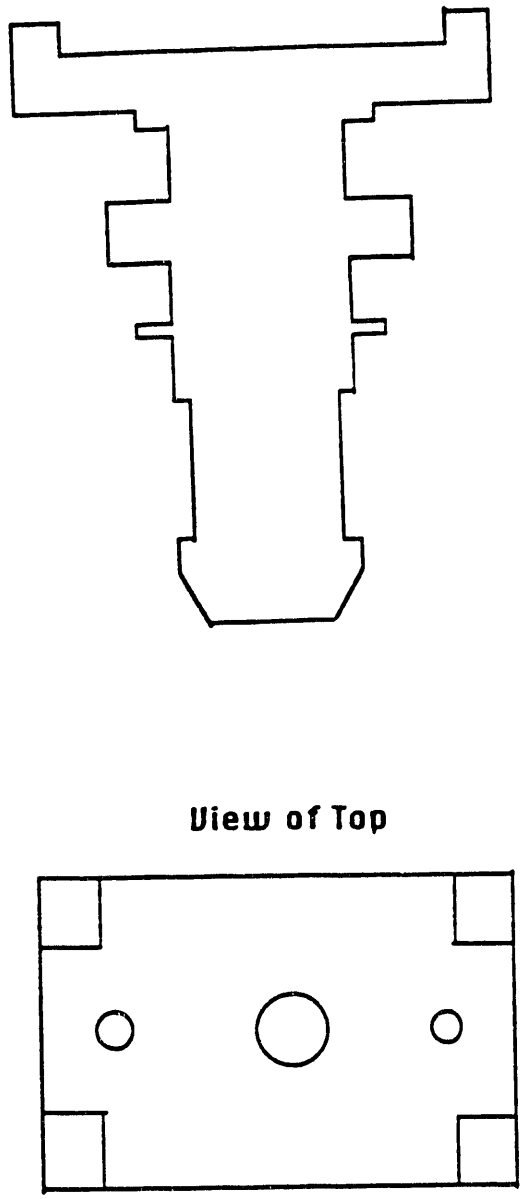

Figure 8. Sample holder assembly used in angle resolved HR-ESCA studies of MoS_2 single crystals. The oriented MoS_2 single crystal was placed on top of the sample holder shown. Two small screws and a Be-Cu spring clip were used to fasten the single crystal in place.

Since very accurate angular information was needed for the forward focusing experiment, the spectra were obtained in the spatial mode. This mode decreases the area on the sample surface in terms of photoelectron detection. Spatial resolution is increased while photoelectron intensity is decreased in this mode of operation. Thus, the sample must be positioned at the focal point of the detector lens system for maximum intensity detection. The sample position was maximized by translating the sample along the y (perpendicular to the detector axis) and z (parallel to the detector axis) axes until maximum photoelectron intensity was obtained for the Mo $3d_{5/2}$ peak. The y and z settings found from this maximization procedure were kept constant throughout the forward focusing experiment.

Calibration of the rotational axis knob was accomplished using the accurate scribe marks present on the sample holder. Rotation of this knob by 2.041 units rotated the sample by 30°. Rotation of the knob to higher (lower) numbers rotated the sample clockwise (counterclockwise). A microscope is located parallel to the detector axis in the sample chamber of the HR-ESCA for sample monitoring. The scribe mark on the sample surface was lined up parallel to the detector using cross-hairs in the microscope, this rotational position was given an arbitrary azimuthal angle designation of 0°. The rotational setting at this point was 10.35 units.

The first angular resolved HR-ESCA experiment performed was a study of the variation in photoelectron core level peak intensity vs. azimuthal angle, ϕ, at a constant polar angle, θ, of 49°. The azimuthal angle, ϕ, and polar angle, θ, as measured from the sample surface are shown in Figure 9. A constant polar angle of 49° was chosen because for the (0002) plane of 2H-MoS_2, forward focusing of an Mo photoelectron by nearest-neighbor sulfur is expected at an angle of 49.1° from the surface normal. Core level regions examined in this study were the following: Mo $3d_{5/2}$, Mo $3p_{3/2}$ and S 2p. The pass energy, E_p, was increased to 150 eV and the number of scans for each region was decreased to one without loss of information. The rotational control knob was rotated in increments of 0.25 units from an initial setting of 4.25 units to a final setting of 13.00 units. This corresponded to incrementating the azimuthal angle by 3.67° from an initial setting of 89.7° to a final setting of -39.0°. Sample rotation occurred in a clockwise direction. During this study, the rotational knob was always incremented in the same direction to avoid backlash. Reproducibility of the results was examined by obtaining duplicate regional spectra at azimuthal angles of +30°, 0°, and -30°. Reproducibility ranged from 3% to 17% in the Mo $3d_{5/2}$ peak areas. The major reason for low reproducibility in this study resides in the inaccuracies existing in the rotational knob. The rotational knob is believed to be fairly reproducible when rotation occurs in the same direction, however rotation of the knob back does not necessarily reproduce the original sample position. Care was taken to avoid errors by

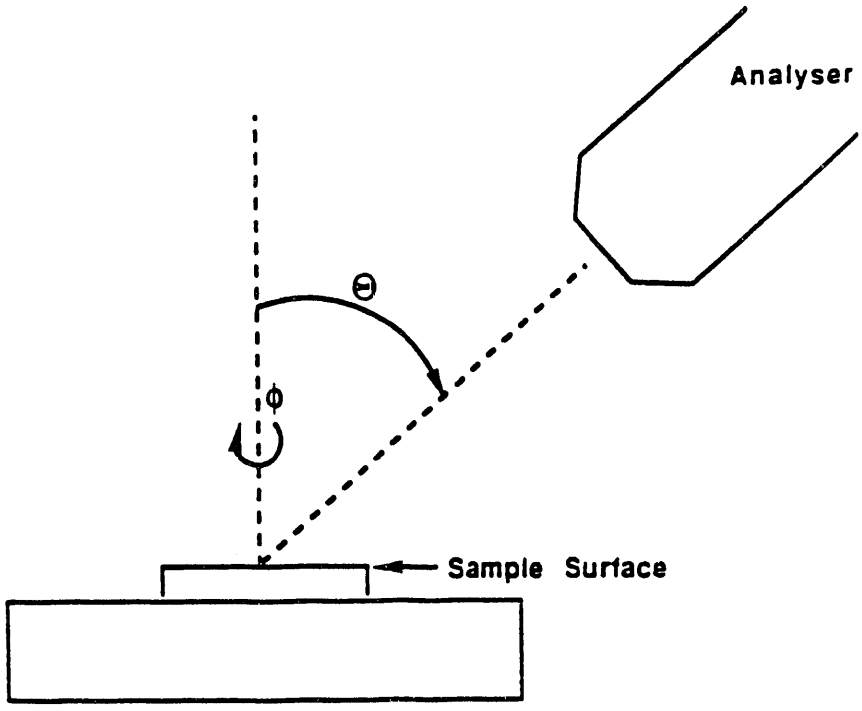

ϕ = Azimuthal Angle - angle measured from an arbitrary position about the surface normal.

Θ = Polar Angle - angle between the analyser and the surface normal.

Figure 9. Geometry of the HR-ESCA system for angular studies. The azimuthal angle, o, is measured from an arbitrary position about the surface normal and the polar angle, θ, is the angle existing between the analyzer and the surface normal.

examining the sample position in relation to a set of cross-hairs located in the microscope.

The second set of experiments examined the variation of photoelectron core level peak intensity vs. polar angle at constant azimuthal angles of 0°, 30°, and 60°. The polar angle was incremented by 2° from an initial setting of -10° to +60°. The Mo $3d_{5/2}$ core level region was the only region examined.

2.3.5 HR-ESCA of Polycrystalline MoS_2 Exposed to Hydrogen.

Core level and valence band regions of bare and hydrogen adsorbed polycrystalline MoS_2 surfaces were obtained by HR-ESCA. A freshly prepared sample of polycrystalline MoS_2 was used for this study. The polycrystalline sample was obtained from the thermal decomposition of MoS_3 to MoS_2 and S under a nitrogen flow (discussed in detail in Section 2.1.2). One important feature of this sample was that exposure to pretreatment procedures involving hydrogen were avoided since the adsorption of hydrogen was under study. The sample was then transferred to a nitrogen filled glove box minimizing exposure to air. Sample mounting of the polycrystalline MoS_2 sample onto an ESCA sample holder took place inside the nitrogen filled glove box. Since heating of the sample inside the HR-ESCA fast entry chamber was necessary, indium foil was not used to hold the MoS_2 powder sample in place. Instead the surface of a clean silicon wafer was roughened with a diamond tip pen to produce scratches into which the MoS_2 polycrystalline sample was pressed to form a smooth relatively thin layer of sample. The MoS_2 covered silicon wafer was then mounted with screws onto a gold-plated ESCA sample holder. The sample and holder were then transferred (under nitrogen) to a nitrogen filled glove bag attached to the HR-ESCA fast entry chamber. Thus, sample preparation and transfer were carried in the absence of air.

Survey and valence band spectra as well as Mo3d, S2p, C1s, and O1s core level spectra of the bare polycrystalline MoS_2 surface were carried out as indicated in Section 2.3.3. Spectra of the bare surface were obtained at both normal incidence and grazing angles of detection (8° takeoff angle). After HR-ESCA analysis of the bare MoS_2 surface was complete, the sample was transferred to the fast entry chamber where hydrogen exposure was carried out. The sample was exposed to ~ 1 atm of pure H_2 (99.999% H_2) at room temperature for a period of one hour. Immediately following hydrogen exposure, the fast entry chamber was evacuated until a pressure of 5×10^{-6} torr was reached. Survey and valence band spectra as well as core level spectra were obtained at normal and grazing angles of incidence following transfer of the sample to the HR-ESCA analysis chamber. After this second HR-ESCA analysis, the sample was transferred back to the fast entry chamber where it was again exposed to ~ 1 atm of hydrogen

at $\sim$ 125° C for one hour. Sample heating was carried out by resistive heating of the sample holder. Survey and valence band spectra as well as core level spectra were obtained at normal and grazing angles of detection following transfer of the sample to the HR-ESCA analysis chamber. After the third HR-ESCA analysis, the sample was transferred back to the fast entry chamber where it was again exposed to $\sim$ 1 atm of hydrogen at $\sim$ 350-389° C for one hour. Survey and valence band spectra as well as core level spectra were obtained at normal and grazing angles of detection following transfer of the sample to the HR-ESCA analysis chamber.

2.4 Angle Resolved Ultraviolet Photoelectron Spectroscopy, ARUPS

2.4.1 Description of ARUPS

The apparatus used for ARUPS experiments consists of an attachment to the HR-ESCA system discussed in Section 2.3.2. A windowless VG MICROTECH ultraviolet source that can be operated with a variety of gases was previously installed in the HR-ESCA system. The source is essentially a gas discharge lamp that when used with ultra-high purity helium gas becomes a source of ultraviolet radiation. This source is positioned so that the angle between the detector and source is 45°, as in the case of the monochromatized x-ray Al K_α source. Because the He source is windowless, a high UV flux that results in high sensitivity is achieved. Use of ultra-high purity helium gas produces the He I and He II lines at 21.22 eV and 40.8 eV, respectively. A two-stage differential pumping unit is used to pump away the helium gas such that sample chamber pressures of 1.0×10^{-9} torr are reached.

2.4.2 ARUPS Experiment for the Determination of Energy Dispersion Curves

Energy dispersion curves were obtained from an ARUPS study of the valence band of single crystal 2H-MoS_2. As mentioned previously, natural single crystals of 2H-MoS_2 were cleaved such that the (0002) basal plane was exposed. The crystal used in this study was oriented by Laue diffraction as described previously, section 2.2.2. Thus, exposure of the surface to air was not avoided. Mounting of the sample onto the ESCA sample holder was achieved as discussed in section 2.3.4. Since, the azimuthal direction of forward focusing along the Mo–S bond corresponds to the direction $\Gamma \rightarrow K$ in the first Brillouin zone, forward focusing was used to pinpoint the $\Gamma \rightarrow K$ direction more exactly. Thus, an angle resolved HR-ESCA experiment was carried out first by monitoring the Mo $3d_{5/2}$ photoelectron intensity vs. azimuthal angle at a constant polar angle of 49°. The rotational knob controlling the azimuthal angle was incremented by 0.1 units (1.47°) from an initial setting of 13.70 units (-10.4°) to a final setting of

12.30 units (10.215°). These rotational units do not tally with those of the previous angle resolved HR-ESCA study, Section 2.3.4, because the sample and rotational knob were moved between the two studies. In this way, the Γ—M direction was located from the maximum Mo $3d_{5/2}$ photoelectron intensity. The Γ—K direction was located at azimuthal angles of ± 30° from the Γ—M direction.

UPS valence bands were obtained with the following instrumental parameters: pass energy, E_p, 10 eV; step size, 0.04 eV; time/step, 0.5 sec; slit width, 1.1 mm; and number of scans, 1. Transmission mode was used with the spatial lens physically placed in front of the detector entrance. UPS valence bands were obtained in azimuths corresponding to the Γ—M and Γ—K directions. ARUPS experiments were carried out at polar angle increments of 2° starting at −10° and ending at +60°. The K—M direction was also obtained since this direction is just an extension of Γ—K.

Chapter 3
THEORETICAL METHOD

A description of the theoretical method used for calculations of the electronic structure of various transition metal disulfide species is given in this section. The theoretical method used was actually a solid state adaptation of the extended Hückel method. A computer program entitled Extended Hückel Molecular, Crystal and Properties Package (EHMACPP) was obtained from the Quantum Chemistry Program Exchange (QCPE) and was used for a calculation of the electronic structures.[38] The electronic structure of the MoS_2 surface was calculated using various models for the surface. Some of the models are listed in the following: two-dimensional molybdenum disulfide, 2-D MoS_2; three-dimensional molybdenum disulfide, 3-D MoS_2; and one-dimensional $(MoS_2)_5$ structures, 1-D $(MoS_2)_5$, terminating in $(10\bar{1}0)$ and $(10\bar{1}1)$ edges. The structure and purpose of these models will be discussed below. Adsorption of hydrogen on the MoS_2 surface was also studied theoretically by placing hydrogen atoms at various positions on the model surfaces. The validity of this method was checked by also calculating the electronic structure of related transition metal disulfide species, specifically, NbS_2 and RuS_2.

3.1 Description of the Solid State Adaptation of the Extended Hückel Method.

As mentioned previously, the theoretical method used in this study was the extended Hückel method applied to solid state systems. Actual calculations were carried out on the Lehigh University VAX 8530 system using the computer program EHMACPP. Some features of this program are the ability to calculate the density of states, energy dispersion curves, orbital character of energy bands, total energy, and electron population for a variety of systems, all to the same level of approximation. This theory is basically empirical in nature, meaning that the results depend on the input parameters. Specifically, the results depend to a large degree on the atomic ionization potentials, H_{ii}, and the Slater-type atomic orbital radial exponents, ζ_i and orbital coefficients, c_i. Agreement with experiment can be improved by an adjustment of the input parameters, H_{ii}, ζ_i, and c_i, of the atomic orbitals used as the basis.

The approach of this theory is to define a set of local molecular orbitals, $\psi_j(r)$, that consist of contributions from the valence atomic orbitals, χ_μ, of the atoms in the primitive cell of the solid under study. The form of the local molecular orbitals is shown in equation 8a. In this equation χ_μ denotes the atomic orbitals of the primitive cell; n, the number of atomic orbitals in the primitive cell; μ, the index of the atomic orbital; j, the index of the molecular orbital; $\mathbf{R}_{\mu,p}$, the vector denoting the position of the μ^{th} atomic orbital in the p^{th} primitive cell in the lattice and $c^{k}_{j,\mu}$, the coefficient indicating the contribution of the μ^{th} atomic orbital to

the j^{th} molecular orbital ($\psi_j(\mathbf{r}-\mathbf{R}_p)$). Born-Kármán boundary conditions are imposed on the molecular orbitals within the primitive cells resulting in the formation of crystal molecular orbitals (also called the Bloch molecular orbitals), $\phi_j^{\mathbf{k}}(\mathbf{r})$, having the form given in equation 8b. In this equation $\mathbf{k}$ denotes the momentum vector (propagation vector) specified in equation 8d; $N=N_A N_B N_C$, the number of primitive cells in the crystal; $\mathbf{R}_p$, the lattice vector denoting the position of the p^{th} primitive cell in the lattice and p, the index of the primitive cell. Substitution of equation 8a into 8b leads to equation 8c.

$$\psi_j(\mathbf{r}-\mathbf{R}_p) = \sum_{\mu=1}^{n} c_{j,\mu}^{\mathbf{k}} \chi_\mu(\mathbf{r}-\mathbf{R}_{\mu,p}) \tag{8a}$$

$$\phi_j^{\mathbf{k}}(\mathbf{r}) = \frac{1}{\sqrt{N}} \sum_{p=1}^{N} \exp(i\mathbf{k}\cdot\mathbf{R}_p)\psi_j(\mathbf{r}-\mathbf{R}_p) \tag{8b}$$

$$\phi_j^{\mathbf{k}}(\mathbf{r}) = \frac{1}{\sqrt{N}} \sum_{\mu,p}^{n,N} c_{j,\mu}^{\mathbf{k}} \exp(i\mathbf{k}\cdot\mathbf{R}_p)\chi_\mu(\mathbf{r}-\mathbf{R}_{\mu,p}) \tag{8c}$$

$$\mathbf{k} = 2\pi\left(\frac{n_A}{N_A}\times\mathbf{a}^* + \frac{n_B}{N_B}\times\mathbf{b}^* + \frac{n_C}{N_C}\times\mathbf{c}^*\right) \tag{8d}$$

The next step is to solve the Schrödinger equation for the crystal Bloch molecular orbitals as shown in equation 9a. Crystal Bloch molecular orbital energies, $\epsilon(\mathbf{k})$, and coefficients, $c_{j,\mu}^{\mathbf{k}}$, making up the local molecular orbitals are given by solution of equation 9b. The Coulomb, resonance and overlap type integrals are defined in equation 9c and 9d. These integrals are parametrized in the extended Hückel solid state procedure. The overlap, $S_{\mu,\nu}$, is calculated explicitly (equation 9d) using the atomic orbital basis (the Slater-type single or double zeta basis set). In place of calculating the coulomb, $H_{\mu,\mu}$, and resonance, $H_{\mu,\nu}$, integrals explicitly using equation 9c, these integrals are chosen according to the method of Hoffmann.[39] The coulomb integrals, $H_{\mu,\mu}^{EH}$, used in the EHMACPP program are chosen to be the valence state ionization potentials; the resonance type integrals, $H_{\mu,\nu}^{EH}$, are calculated from the components $H_{\mu,\mu}^{EH}$ and $S_{\mu,\nu}$. Equation 9e shows the assumed empirical relationship between these quantities (K is generally taken to be 1.75) for obtaining values of $H_{\mu,\nu}^{EH}$ from the Wolfsberg-Helmholtz formula. The program actually allows the user to specify one of two ways to calculate the $H_{\mu,\nu}^{EH}$ the normal Wolfsberg-Helmholz formula, equation 9e, or a weighted $H_{\mu,\nu}^{EH}$ defined in equation 9f. Wolfsberg-Helmholz $H_{\mu,\nu}^{EH}$ are obtained from weighted $H_{\mu,\nu}^{EH}$ by neglecting the second and third terms under the brackets in equation 9f. The momentum vector $\mathbf{k}$ gives the directions in which crystal properties propagate. For example, crystal orbital energies, $\epsilon(\mathbf{k})$, obtained from this solution show dispersion with variation of $\mathbf{k}$. The wavevector, $\mathbf{k}$, maps the momentum

space around a single diffraction spot (or a single G–vector of the reciprocal lattice) called the Brillouin zone and is determined by crystal geometry as above. All crystal properties including the crystal orbital energies are periodic with the G–vector, e.g. $\epsilon(\mathbf{k})=\epsilon(\mathbf{k}+\mathbf{G})$. The density of states is obtained when the $\epsilon(\mathbf{k})$ curves are integrated over the whole Brillouin zone. The density of states, $dN(\epsilon)$, is proportional to the derivative, $d\mathbf{k}/d\epsilon$. In reality, the density of states is computed from a grid of special points in the first Brillouin zone according to the method of Cohen et al.[40] Extended Hückel theory applied to solid state systems is essentially an empirical one–electron theory in which correlation effects are not taken into account. However, one feature of this theory is that overlap interactions other than nearest–neighbor atoms are taken into account.

$$\hat{H}\phi_j^{\mathbf{k}}(\mathbf{r}) = \epsilon(\mathbf{k})\phi_j^{\mathbf{k}}(\mathbf{r}) \tag{9a}$$

$$| H_{\mu,\nu}(\mathbf{k}) - S_{\mu,\nu}(\mathbf{k})\epsilon(\mathbf{k}) | = 0 \tag{9b}$$

$$H_{\mu,\nu}(\mathbf{k}) = \frac{1}{N}\sum_{p,q}\exp[i\mathbf{k}\cdot(\mathbf{R}_q-\mathbf{R}_p)]\int \chi_\mu(\mathbf{r}-\mathbf{R}_{\mu,p})\,\hat{H}\,\chi_\nu(\mathbf{r}-\mathbf{R}_{\nu,q})\,d\mathbf{r} \tag{9c}$$

$$S_{\mu,\nu}(\mathbf{k}) = \frac{1}{N}\sum_{p,q}\exp[i\mathbf{k}\cdot(\mathbf{R}_q-\mathbf{R}_p)]\int \chi_\mu(\mathbf{r}-\mathbf{R}_{\mu,p})\,\chi_\nu(\mathbf{r}-\mathbf{R}_{\nu,q})\,d\mathbf{r} \tag{9d}$$

$$H_{\mu,\nu}^{EH} = \tfrac{1}{2}K\,(H_{\mu,\mu}^{EH} + H_{\nu,\nu}^{EH})S_{\mu,\nu} \tag{9e}$$

$$H_{\mu,\nu}^{EH} = \left\{\tfrac{1}{2}K + \tfrac{1}{2}\left(\frac{H_{\mu,\mu}^{EH}- H_{\nu,\nu}^{EH}}{H_{\mu,\mu}^{EH}+H_{\nu,\nu}^{EH}}\right)^2 + \left(\tfrac{1}{2} - \tfrac{1}{2}K\right)\left(\frac{H_{\mu,\mu}^{EH}- H_{\nu,\nu}^{EH}}{H_{\mu,\mu}^{EH}+H_{\nu,\nu}^{EH}}\right)^4\right\}(H_{\mu,\mu}^{EH} + H_{\nu,\nu}^{EH})S_{\mu,\nu} \tag{9f}$$

As mentioned previously, input parameters for the program include the following: Slater–type radial exponents, ζ_i, and coefficients, c_i; atomic ionization potential of valence orbitals, H_{ii}; cartesian coordinates, x_i, y_i, and z_i, of the atoms contained in one primitive cell of the model system; and the position and weighting factor of the k–points at which the calculation is to be carried out. A discussion of the Slater–type orbitals used in the calculations is given is Section 3.2. Section 3.3 discusses the sets of **k**–points used in calculations of energy dispersion curves and density of states.

3.2 Parametrization of the Atomic Radial Functions Via Comparison With Experiment.

Radial orbitals used in the EHMACPP program are the single and double zeta Slater–type orbitals (STO's). Single and double zeta functions are approximate atomic orbitals in

which a given electron orbital is described by one or two Slater-type functions, respectively. The single and double zeta STO forms of the radial functions are shown in equations 10a and 10b, respectively. Some of the parameters shown in these equations are defined as follows: R_{SZ}, single zeta STO; R_{DZ}, double zeta STO; r, distance of electron from the nucleus; n, principal quantum number of the atomic orbital; and N_i, normalization constant for the radial function as defined in equation 10c. Thus, once values for ζ_i and c_i are found, the radial functions are obtained.

$$R_{SZ} = r^{n-1} \times \left(Ne^{-\zeta r}\right) \tag{10a}$$

$$R_{DZ} = r^{n-1}\left(N_1 c_1 e^{-\zeta_1 r} + N_2 c_2 e^{-\zeta_2 r}\right) \tag{10b}$$

$$N_i = \frac{(2\zeta_i)^{n+\frac{1}{2}}}{[(2n)!]^{\frac{1}{2}}} \tag{10c}$$

where N_i is N_1, N_2 or N and ζ_i is ζ_1, ζ_2 or ζ

The basis orbitals used for calculating the electronic structure of MoS_2 were the Mo 5s, Mo 5p, Mo 4d and the S3s, S3p valence orbitals. Similar orbitals were used for the transition metal atoms in NbS_2 and RuS_2; however, in the case of Nb and Ru the metal 5p orbitals were neglected. Initial input parameters for the STO's of MoS_2 were obtained from a study performed by Hughbanks and Hoffmann on the Chevrel phases of a molybdenum-sulfur system.[41] These parameters will be referred to as the H&H radial parameters and are given in Table 1. Table 1 also lists a second set of STO input parameters obtained from the SCF computed, tabulated list of Slater-type orbital double zeta coefficients, exponents and valence shell ionization potentials of Clementi and Roetti.[42] These parameters will be referred to as C&R radial parameters. Asterisks after the coefficients indicate that the values of these parameters were changed in the program so that normalized radial functions resulted. The values of the coefficients taken directly from the C&R tables were not normalized because these functions actually contained small contributions from atomic orbitals of lower n value for the purpose of orthogonalization. Normalization of the atomic radial functions was checked by the EHMACPP program. The normalization condition for double zeta functions is given in equation 11a and 11b (S is defined in equation 11c). To obtain equation 11b, equation 10b is substituted for the radial portion of the wavefunction and equation 10c is substituted for the N_i of the double zeta function. If the double zeta radial function is not normalized ($N' \neq 1$) when

Table 1

STO radial wavefunction parameters for Nb, Mo, Ru, and S valence orbitals. Values in parentheses indicate the value of i for the double zeta coefficients, c_i, and exponents, ζ_i.

Atom	Orbital	H_{ii}(eV)	ζ_i	c_i
Mo	5s (H&H)	-8.77	1.96	1.00
	5p (H&H)	-5.60	1.90	1.00
	4d (H&H)	-11.06	4.54 (1)	0.5899 (1)
			1.90 (2)	0.5899 (2)
Nb	5s(H&H)	-10.10	1.89	1.00
	5p(H&H)	-6.86	1.85	1.00
	4d(H&H)	-12.10	4.08(1)	0.64010(1)
			1.64(1)	0.55160(2)
Ru	5s(H&H)	-8.310	2.078	1.00
	5p(H&H)	-3.280	2.043	1.00
	4d(H&H)	-10.740	5.378(1)	0.53399(1)
			2.303(2)	0.63649(2)
S	3s (H&H)	-20.0	1.817	1.00
	3p (H&H)	-13.3	1.817	1.00
Mo	5s (C&R)	-5.8789	1.94119 (1)	0.54776 (1)
			1.10333 (2)	0.57494 (2)
	4d (C&R)	-9.4728	3.81446 (1)	0.50051* (1)
			1.86369 (2)	0.62684* (2)
Nb	5s(C&R)	-5.6805	1.84738(1)	0.54046*(1)
			1.06545(2)	0.55624*(2)
	4d(C&R)	-7.9241	3.59080(1)	0.47775*(1)
			1.71750(2)	0.65431*(2)
Ru	5s(C&R)	-5.8443	2.04429(1)	0.52381(1)
			1.13104(2)	0.59975(2)
	4d(C&R)	-10.860	4.25911(1)	0.53422*(1)
			2.09384(2)	0.59271*(2)
S	3s (C&R)	-23.918	2.66221 (1)	0.55645* (1)
			1.68771 (2)	0.48731* (2)
	3p (C&R)	-11.890	2.33793 (1)	0.52120* (1)
			1.33331 (2)	0.54431* (2)

H&H = parameters obtained from Hughbanks and Hoffmann.
C&R = parameters obtained from Clementi and Roetti.
* = coefficients obtained after normalization by the program.

input into the program, the program normalizes the function by changing the coefficients, c_1 and c_2, to c_1' and c_2' as indicated in equation **11d**. The double and single zeta STO functions tabulated by C&R contain the correct number of nodes due to contributions from atomic orbitals of lower n value. Atomic orbitals of lower n value are more contracted (possess larger ζ_i) and thus contribute to the overall radial function at distances close to the atomic nucleus. Orbital coefficients of some of the more contracted atomic orbitals are negative leading to nodes in the overall double and single zeta radial functions tabulated by C&R. The radial functions obtained from the parameters of H&H do not contain any nodes. Since, the EHMACPP program only accepts single or double zeta functions, contributions from atomic orbitals of lower n value were neglected when using the parameters of C&R. Thus, the radial functions obtained from C&R did not contain any nodes.

$$\int \psi^* \psi \, d\tau = N' \qquad \text{where } \psi = Y_m^l \times R_{DZ} \tag{11a}$$

$$N' = c_1^2 + c_2^2 + 2 S c_1 c_2 \tag{11b}$$

$$S = \left\{ \frac{4\zeta_1\zeta_2}{(\zeta_1+\zeta_2)^2} \right\}^{(n+\frac{1}{2})} \tag{11c}$$

$$c_1' = \frac{c_1}{\sqrt{N'}} \quad ; \quad c_2' = \frac{c_2}{\sqrt{N'}} \tag{11d}$$

Many of the calculations were carried out using the radial parameters of H&H. However, a better theoretical valence band was achieved through the use of the C&R double zeta parameters. By parametrizing the C&R radial functions according to the HR-ESCA valence band experiment a good description of the experimental valence band was obtained. The input parameters, specifically H_{ii}, were varied to match the position of the valence levels in the HR-ESCA experiment. Variation of H_{ii} caused a corresponding variation in the overlap matrix elements. Thus the Slater type orbital coefficients, c_i, were adjusted to acnieve the best overlap by varying the radius of the valence shell. An example of this occurs for the shifting of the S3s levels in MoS_2. Initially, the theoretical position for the S3s levels (C&R) was at -23.918 eV. A comparison of the theoretically calculated and experimentally determined valence band in this region shows that theoretically this level has approximately the correct shape and width. After parametrization of the S3s H_{ii} to HR-ESCA valence band, the S3s level is shifted from -23.918 eV to -17.80 eV. The S3s region calculated with this H_{ii} has a smaller full width

at half maximum (FWHM). To correct for this smaller width, the contribution, c_2, of the more diffuse part of the radial function (with lower ζ value, ζ_2) was increased. Consequently the contribution, c_1, of the more contracted part of the radial function (with higher ζ, ζ_1) was decreased due to normalization. Thus only the Slater-type double zeta coefficients c_i were varied, but the double zeta exponents were not varied from the values given by C&R.

The original HR-ESCA valence band spectrum of MoS_2 was shifted to higher binding energies by the work function of the sample. Work function measurements obtained from the literature vary from 4.1 eV[15] through 4.55 ± 0.1 eV[43] to 4.8 ± 0.05 eV[44]. The two lowest values were obtained from UPS experiments, while the 4.8 eV value was obtained using a retarding potential method with an electron gun with subsequent comparison to a standard of known work function. The 4.1 eV work function is a thermal work function (E_v-E_f) while the other two are photoelectric work functions (E_v-E_B, see Section 2.3.1). The HR-ESCA valence band spectra were corrected by the most recently obtained value of the work function 4.1 eV in order to obtain accurate values for the valence state ionization potentials, H_{ii}. The experimentally obtained H_{ii} were subsequently used as input for the electronic structure calculations of MoS_2. Experimental and theoretical valence bands were compared in a qualitative manner only, no attempt at quantitative self-consistency was made. At this point in the investigation, qualitative explanations of the electronic structure are the desired result.

3.3 Method of Obtaining Theoretical Valence Bands (TVB).

The theoretical calculations discussed above provide the MoS_2 density of states. A theoretical valence band is desired for a comparison with the HR-ESCA experimental valence band. An experimental valence band is actually a density of states modified by the sensitivity of the photoelectrons to detection and convoluted with the final states. For XPS, final states are known to vary smoothly with energy, and hence their effect on the structure of the valence band is small. Sensitivity of the photoelectrons to detection depends on a number of parameters such as the energy of the incident x-rays and the atom type and orbital from which the photoelectrons originate. This sensitivity is quantified and referred to as the photoelectron cross-section. Values of the photoelectron cross-sections have been theoretically calculated by Scofield and are tabulated in Reference 45. Table 2 reproduces the Scofield cross-sections relevant to this study. In the core level analysis, the ratios of atoms on the surface can be obtained in an approximate manner through modification of the core level areas by the appropriate photoelectron cross-sections. This type of analysis would in principle be possible for the valence band of MoS_2. However, the valence band region of MoS_2 is complicated by overlap

interactions between the valence atomic levels. Theoretical calculations are needed to dissect the valence band region into contributions due to the different valence atomic levels.

The theoretical MoS_2 density of states can be partitioned into atomic orbital populations (AOPOP's), which are defined as contributions to the density of states due to the valence atomic levels in the basis. The resulting sum of the AOPOP's is the density of states. Modification of the individual AOPOP's by the appropriate Scofield cross-sections with subsequent summation of the modified AOPOP's will result in a calculation of the theoretical valence band. The theoretical valence band can then be compared with greater accuracy to the experimental valence band. AOPOP's that have been multiplied by the appropriate Scofield cross-section will be referred to as modified AOPOP's (MAOPOP's) in the rest of the text. This method of modifying the density of states is based on an approach, developed by Gelius, that is used for the molecular orbitals of molecules.[46] In this study the major contributions to the density of states are due to the S3s, S3p and Mo 4d valence levels. The Mo 5s, Mo 5p levels contribute a small amount to the density of states with an even smaller contribution to the valence band due to the small photoelectron cross-sections involved. For this reason, the Mo 5s, 5p levels have been neglected in calculations of the theoretical valence band. Scofield cross-sections and their ratios for Nb, Mo, Ru and S used in electronic structure calculations are listed in Table 2. The Mo 4d to S3p cross-section ratio is 4.08. Thus the Mo 4d AOPOP is effectively multiplied by 4.09 relative to the S3p AOPOP.

3.4 Structural Models of MoS_2 Studied.

3.4.1 Bulk Structure of MoS_2

Molybdenum disulfide, MoS_2, forms a layer structure similar to graphite but with two crystal modifications. These modifications are the hexagonal structure denoted 2H-MoS_2 and the rhombohedral structure denoted 3R-MoS_2. The number in front of the letter in this designation specifies the number of MoS_2 molecules per unit cell, two for the hexagonal modification and three for the rhombohedral modification. The focus of this research has been on the hexagonal modification since this is the structure of the synthesized polycrystalline samples as well as of the naturally grown single crystals of MoS_2. Thus, the rest of this discussion will focus on the bulk structure of 2H-MoS_2. Background information on the transition metal disulfides structures is obtained from Wilson and Yoffe.[47]

Table 2.

Photoelectron Scofield cross–sections for Al K_α radiation.

Atom	Orbital	Cross-Section
Nb	$4d_{3/2}$	0.0812
	$4d_{5/2}$	0.1166
	4d	0.1978
	$5s_{1/2}$	0.0157
Mo	$4d_{3/2}$	0.1298
	$4d_{5/2}$	0.1864
	4d	0.3162
	$5s_{1/2}$	0.0157
Ru	$4d_{3/2}$	0.274
	$4d_{5/2}$	0.393
	4d	0.667
	$5s_{1/2}$	0.0188
S	$3s_{1/2}$	0.1465
	$3p_{1/2}$	0.0262
	$3p_{3/2}$	0.0512
	3p	0.0774

Ratios:
$$\frac{\text{Nb 4d}}{\text{S3p}} = \frac{0.1978}{0.0774} = 2.56$$
$$\frac{\text{Mo 4d}}{\text{S3p}} = \frac{0.3162}{0.0774} = 4.09$$
$$\frac{\text{Ru 4d}}{\text{S3p}} = \frac{0.667}{0.0774} = 8.62$$

In 2H-MoS_2, the molybdenum atoms are coordinated to six sulfur atoms in a trigonal prismatic environment. The sulfur atoms are each coordinated to three molybdenum atoms. Formal charges of molybdenum and sulfur are generally given as +4 and -2, respectively. However, as will be discussed later, MoS_2 is actually a fairly covalent compound that shares its electrons between the molybdenum and sulfur atoms substantially more than indicated by the formal charges. Calculated charges on molybdenum and sulfur are much smaller than the formal charges indicated.

2H-MoS_2 forms a layer structure with two molecules of MoS_2 per unit cell. Three atomic layers consisting of first atomic layer sulfur, second atomic layer molybdenum and third atomic layer sulfur make up one layer of MoS_2. One MoS_2 unit translated in two-dimensions within the layer by a linear integral combination of primitive translations **a** and **b** forms the infinite single sheet structure. Three-dimensional crystals are produced by stacking of the MoS_2 layers. The three-dimensional crystal is held together by weak van der Waals forces between the sulfur atoms on adjacent MoS_2 layers. In the three dimensional crystal the real lattice vector, **c**, is perpendicular to the real lattice vectors, **a**, **b**, and to the direction of propagation of the MoS_2 layers. The second MoS_2 molecule in 2H-MoS_2 resides in a second MoS_2 layer. This second MoS_2 layer is offset from the first such that molybdenum atoms in the second are beneath (or above) sulfur atoms in the first while sulfur atoms in the second are beneath (or above) molybdenum atoms in the first layer. Real lattice vectors for 2H-MoS_2 are given in equations 12a, 12b, and 12c. A picture of the 2H-MoS_2 lattice is given in Figure 10. Table 3 lists the positions of the atoms in one unit cell of 2H-MoS_2 in terms of the real lattice vectors, **a**, **b**, **c**. The length of the real lattice vectors **a** and **b** is the same and equal to 3.16 Å. An angle between the vectors **a** and **b** is 120°. The length of **c** is 12.30 Å. The parameter u, equal to 0.128252, is defined as the elevation of the sulfur atoms above and below the plane of molybdenum atoms in terms of **c**. Thus the two atomic layers of sulfurs in one MoS_2 layer are located 1.5775 Å and -1.5775 Å above and below the atomic layer of molybdenums. The distance between the layers of sulfur belonging to two different MoS_2 layers, the Van der Waals gap, is defined as h and is equal to 0.243496 or in actual units, 2.995 Å.

$$\mathbf{a} = \frac{|\mathbf{a}|}{2}\left(\hat{x} - \sqrt{3}\hat{y}\right) \tag{12a}$$

$$\mathbf{b} = \frac{|\mathbf{a}|}{2}\left(\hat{x} + \sqrt{3}\hat{y}\right) \tag{12b}$$

$$\mathbf{c} = |\mathbf{c}|\hat{z} \tag{12c}$$

where $\hat{x}$, $\hat{y}$, $\hat{z}$ are unit vectors along the cartesian axes.

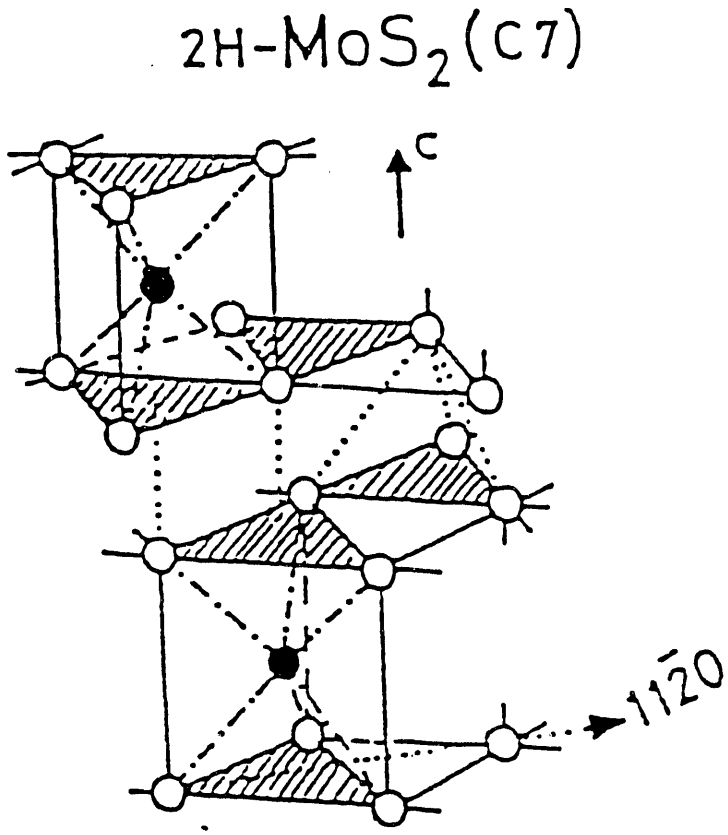

J.A. Wilson and A.D. Yoffe, Advan. Phys., 18, 193 (1969).

Figure 10. Representation of the bulk structure of 2H–MoS_2.

Table 3.
Positions of the atoms in one unit cell of 2H-MoS_2 in terms of the real lattice vectors, **a**, **b**, **c**. (u = 0.128252)

Atom	Position
Mo	(0, 0, 0)
S	$(\frac{1}{3}, -\frac{1}{3}, u)$
S	$(\frac{1}{3}, -\frac{1}{3}, -u)$
Mo	$(\frac{1}{3}, -\frac{1}{3}, \frac{1}{2})$
S	$(0, 0, \frac{1}{2}+u)$
S	$(0, 0, \frac{1}{2}-u)$

Reciprocal lattice vectors can be calculated, using equations 13a, 13b, and 13c, from the real lattice vectors defined above.[48] The reciprocal lattice vectors are given in equation 14a, 14b, and 14c. A set of parallel real lattice planes defined in terms of the Miller indices (hkl) has a vector in the reciprocal lattice, $G_{hkl} = h\mathbf{a}^* + k\mathbf{b}^* + l\mathbf{c}^*$, that is perpendicular to this set of planes. This point is important in interpretation of Laue back-reflection patterns. The reciprocal lattice basis vectors $\mathbf{a}^*$, $\mathbf{b}^*$ are equal in length and subtended by an angle of 60°. The reciprocal lattice is rotated by 30° when compared to the real lattice. Figures 11a and 11b show the relationship between the real lattice vectors, **a**, **b** and the reciprocal lattice vectors, $\mathbf{a}^*$, $\mathbf{b}^*$, for the 2H-MoS_2 system. The vectors **c** and $\mathbf{c}^*$ are not shown but are simply perpendicular to the first two vectors.

$$\mathbf{a}^* = \frac{\mathbf{b} \times \mathbf{c}}{\mathbf{a} \cdot (\mathbf{b} \times \mathbf{c})} \tag{13a}$$

$$\mathbf{b}^* = \frac{\mathbf{c} \times \mathbf{a}}{\mathbf{a} \cdot (\mathbf{b} \times \mathbf{c})} \tag{13b}$$

$$\mathbf{c}^* = \frac{\mathbf{a} \times \mathbf{b}}{\mathbf{a} \cdot (\mathbf{b} \times \mathbf{c})} \tag{13c}$$

$$\mathbf{a}^* = \frac{1}{|\mathbf{a}|}\left(\hat{x} - \frac{\hat{y}}{\sqrt{3}}\right) \tag{14a}$$

$$\mathbf{b}^* = \frac{1}{|\mathbf{a}|}\left(\hat{x} + \frac{\hat{y}}{\sqrt{3}}\right) \tag{14b}$$

$$\mathbf{c}^* = \frac{\hat{z}}{|\mathbf{c}|} \tag{14c}$$

The first Brillouin zone can be found from the reciprocal lattice by finding the smallest volume enclosed by the perpendicular bisectors of the reciprocal lattice vectors. The first Brillouin zone is the momentum space surrounding a single diffraction spot. This momentum space is mapped by the wavevector, **k**. The wavevector gives directions in which crystal properties propagate. For example, crystal orbital energies, $\epsilon(\mathbf{k})$, show dispersion with the wavevector, **k**. In Figure 11c is shown the two-dimensional first Brillouin zone of 2H-MoS_2. It is noted that the orientation of the first Brillouin zone is rotated 30° from that of the reciprocal lattice. Thus, the first Brillouin zone has the same orientation as the real lattice. Some high symmetry points are indicated as Γ, K and M. These points are defined in terms of fractional coordinates of the reciprocal lattice vectors, $\mathbf{a}^*$, $\mathbf{b}^*$, $\mathbf{c}^*$. In terms of the reciprocal lattice vectors the coordinates of these points are as follows: Γ, (0, 0, 0); K, $(\frac{1}{3}, \frac{1}{3}, 0)$; and M, $(\frac{1}{2}, 0, 0)$. Points in the first Brillouin zone actually represent points in the **k**-space. Therefore, the K point actually represents the wavevector $\mathbf{k}_K = \frac{1}{3}\mathbf{a}^* + \frac{1}{3}\mathbf{b}^* = \frac{2}{3|\mathbf{a}|}\hat{x}$, with origin at the Γ point. The length of this vector, $\mathbf{k}_K$, is $\frac{2}{3|\mathbf{a}|}$.

3.4.2 Two-Dimensional MoS_2 Model

A two-dimensional infinite sheet of MoS_2 was used to model one layer of a 2H-MoS_2 single crystal. This structure excluded effects due to Van der Waals interactions between MoS_2 layers. One molecule of MoS_2 translated in both the **a** and **b** directions produces the two-dimensional layer. The structural parameters, cartesian coordinates in Å, used in this calculation are given in Table 4. The atoms Mo_1, S_2 and S_3 define the MoS_2 repeat unit in two-dimensions whereas the Mo-a and Mo-b atoms are used to define the real lattice vectors in two-dimensions. Interactions were included up to four neighbors in each direction, **a** and **b**.

3.4.3 Three-Dimensional MoS_2 Model

Three-dimensional infinite structure of MoS_2 was used to model single crystals of MoS_2. In this model, the layers discussed for the 2-D MoS_2 (Section 3.4.2) model were stacked in the third direction, the **c** direction. Thus, the Van der Waals interactions were taken into account. As discussed previously, in Section 3.4.1, the layers are offset such that molybdenum atoms in adjacent layers are beneath (or above) sulfur atoms in the first layer. The structural parameters, cartesian coordinates in Å, of the two molybdenum and four sulfur atoms representing one unit cell of the 3-D structure are given in Table 4. In this calculation, interactions were included up to four nearest neighbor cells in each of the directions, **a**, **b**, and **c**.

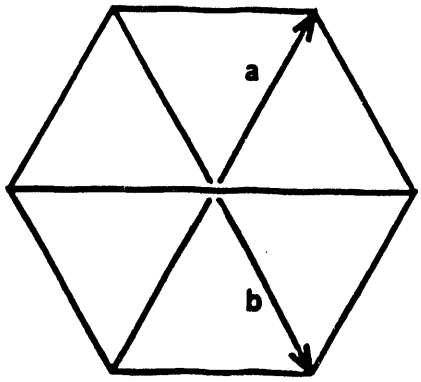

Figure 11a. Real lattice vectors a and b for $2H-MoS_2$.

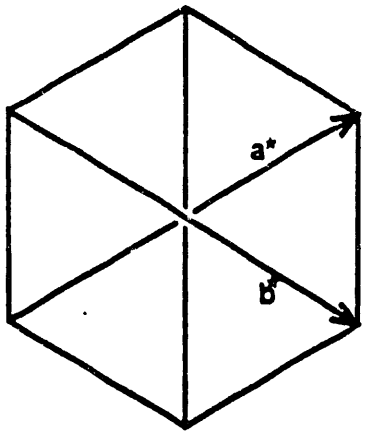

Figure 11b. Reciprocal lattice vectors a^* and b^* for $2H-MoS_2$.

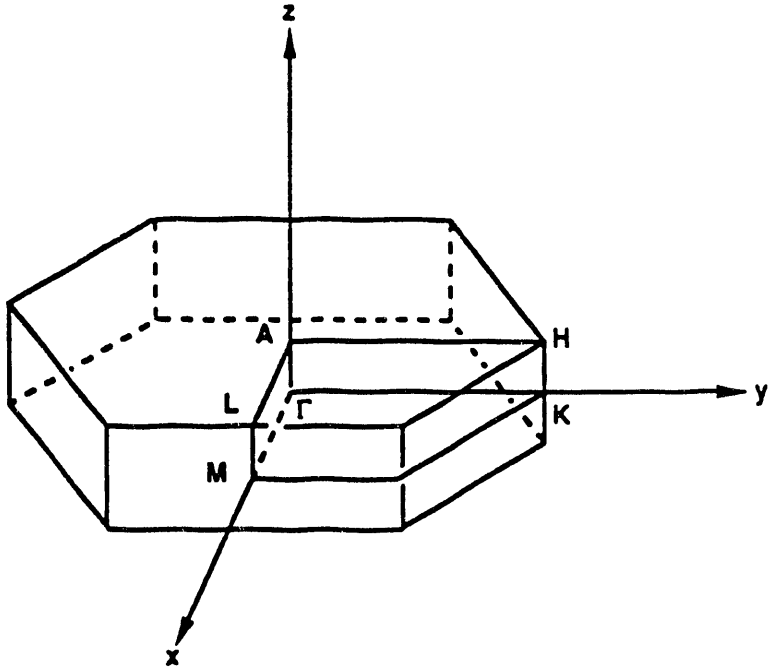

Figure 11c. First Brillouin zone for $2H-MoS_2$.

Table 4.

Structural parameters used in electronic structure calculations of 2-D MoS_2 and 3-D MoS_2. (units are in Å)

	Atom	x	y	z
	Mo_1	0.	0.	0.
Layer 1 →	S_2	0.	-1.8244269	1.5775
	S_3	0.	-1.8244269	-1.5775
	Mo_4	0.	-1.8244269	6.1500
Layer 2 →	S_5	0.	0.	7.7275
	S_6	0.	0.	4.5725
	Mo-a	1.5800	-2.7366403	0.
Real Lattice	Mo-b	1.5800	2.7366403	0.
Vectors	Mo-c	0.	0.	12.3000

3.4.4 1-D $(MoS_2)_5$ Models Terminating at the $(10\bar{1}0)$ and $(10\bar{1}1)$ Edges

The 2-D infinite layer of MoS_2 discussed previously was terminated at different edge planes to theoretically study the changes in electronic structure produced by the addition of edges. Structures with two different edges, $(10\bar{1}0)$ and $(10\bar{1}1)$, were studied. A structure with $(10\bar{1}0)$ edges was produced by theoretically terminating the 2-D infinite sheet with edges perpendicular to the basal plane (0002). A structure with $(10\bar{1}1)$ edges was produced by theoretically terminating the 2-D infinite sheet with inclined edges. The result in both cases was a unit cell of 5 MoS_2 units that when propagated in one-direction, the $\hat{x}$ direction, produced a sheet of infinite in the $\hat{x}$ direction but of finite width in the $\hat{y}$ direction. Table 5a gives the structural parameters of the 1-D $(MoS_2)_5$ model terminating in $(10\bar{1}0)$ edges. Figures 12a and 12b show the 1-D $(MoS_2)_5$ system terminating at the $(10\bar{1}0)$ edges as viewed parallel to the x-axis (side view) and z-axis (top view), respectively. Table 5b gives the structural parameters of the 1-D $(MoS_2)_5$ model terminating in $(10\bar{1}1)$ edges. Figures 12c and 12d show the 1-D $(MoS_2)_5$ system terminating at the $(10\bar{1}1)$ edges as viewed parallel to the x-axis (side view) and z-axis (top view), respectively. The only difference in the structural parameters of these two models occurs in those of sulfur atom S-0601. In the structure terminating by the $(10\bar{1}0)$ edges, the S-0601 atom is located on the same edge as S-0501. However, in the structure terminating by the $(10\bar{1}1)$ edges, the S-0601 atom is located on the opposite edge.

The structures discussed above expose molybdenum and sulfur atoms with different degrees of coordination on edge planes. In 2H-MoS_2, the molybdenum atoms are coordinated to 6 sulfur atoms while the sulfur atoms are coordinated to 3 molybdenum atoms. Addition of

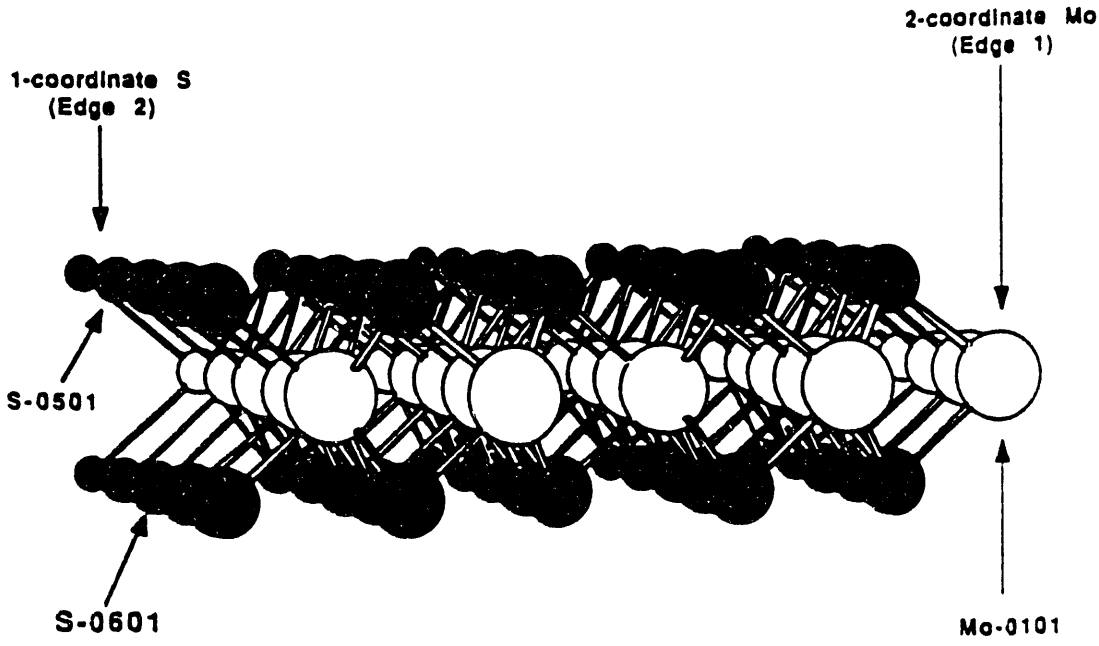

Figure 12a. Side view (parallel to the x-axis) of the 1-D $(MoS_2)_5$ system terminating at the $(10\bar{1}0)$ edges. The $(10\bar{1}0)$ structure was terminated in straight edges perpendicular to the basal plane.

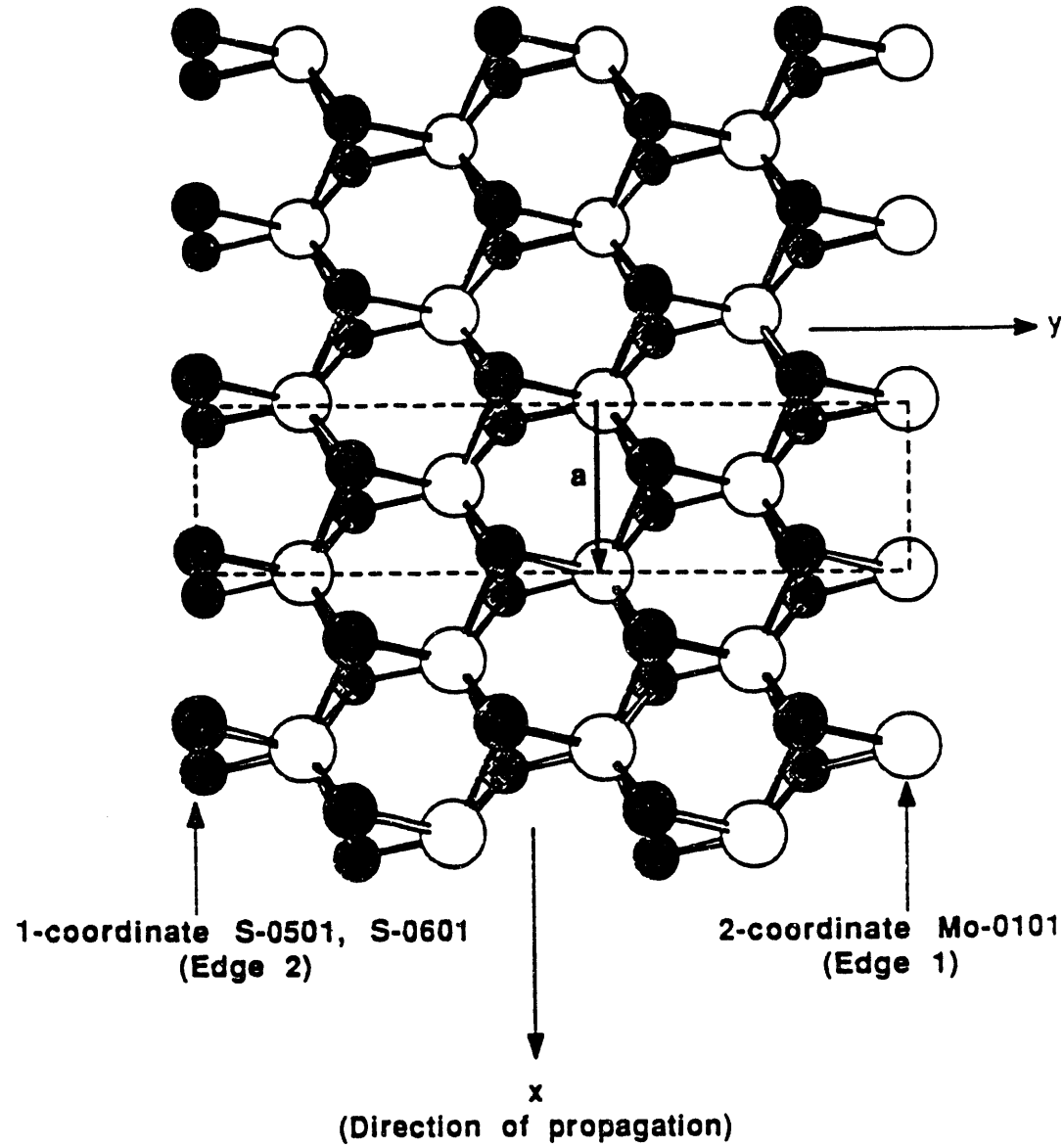

Figure 12b. Top view (parallel to the z-axis) of the 1-D $(MoS_2)_5$ system terminating at the $(10\bar{1}0)$ edges.

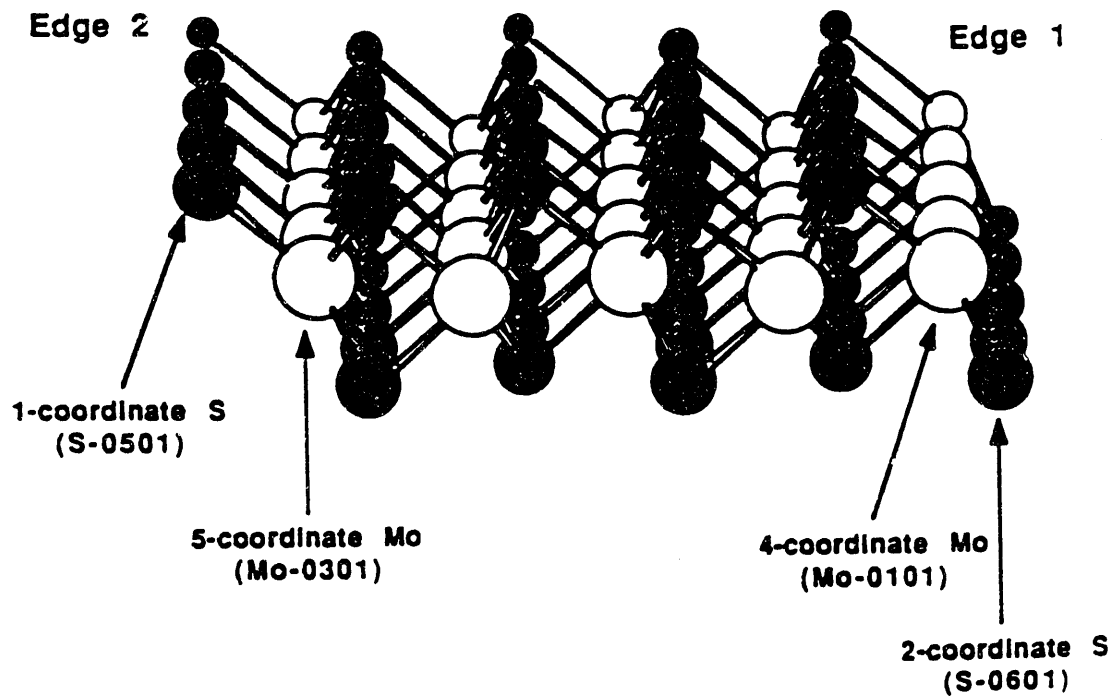

Figure 12c. Side view (parallel to the x-axis) of the 1-D $(MoS_2)_5$ system terminating at the $(10\bar{1}1)$ edges. The $(10\bar{1}1)$ structure was terminated in edges inclined to the basal plane.

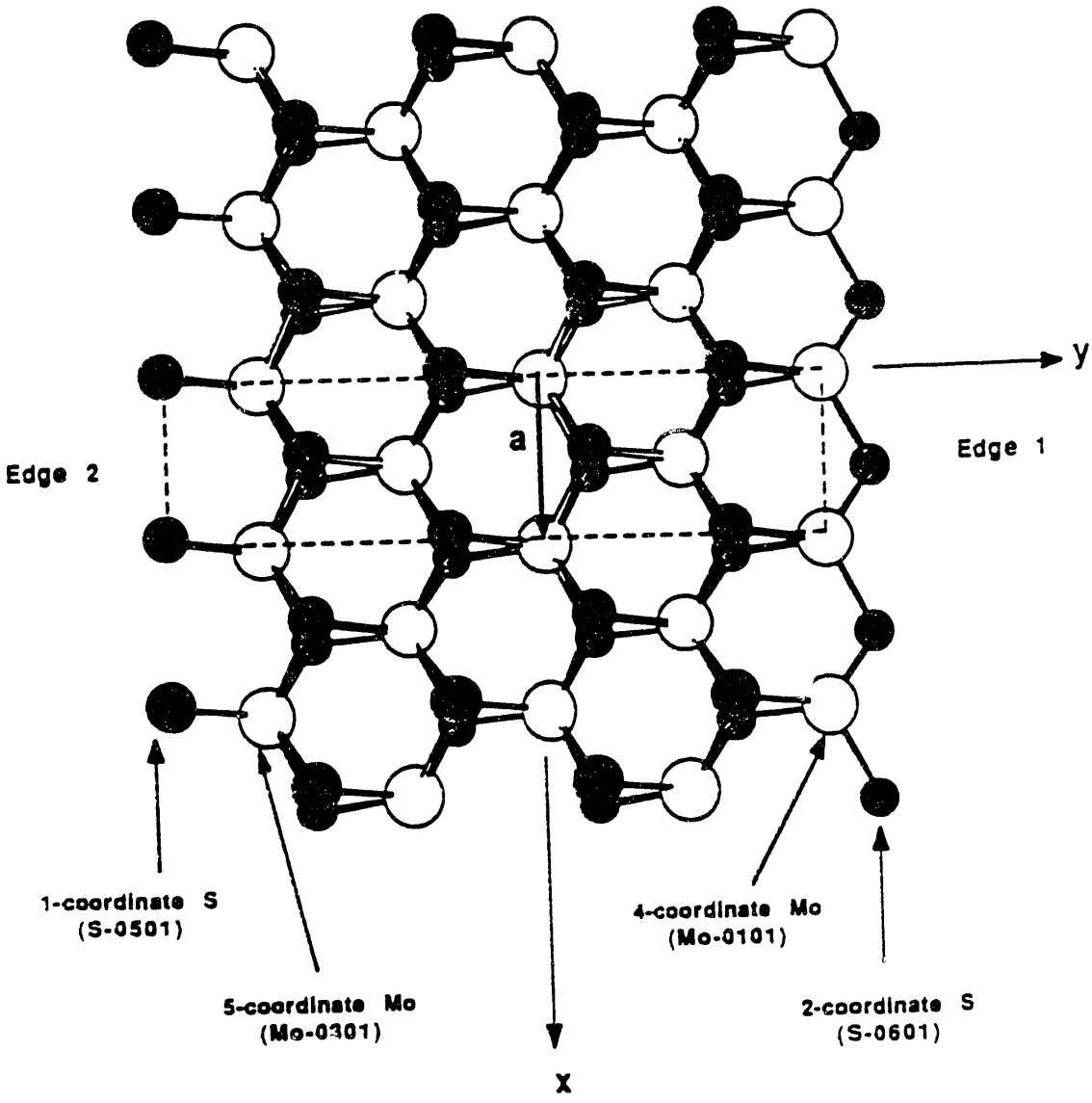

Figure 12d. Top view (parallel to the z-axis) of the 1-D $(MoS_2)_5$ system terminating at the $(10\bar{1}1)$ edges.

Table 5a.

Structural parameters of 1-D $(MoS_2)_5$ terminating in $(10\bar{1}0)$ edges.
(units are in Å)

Atom	x	y	z
Mo-0101	0.	5.473281	0.
Mo-0201	0.	0.	0.
Mo-0301	0.	-5.473281	0.
Mo-0401	1.580	2.736640	0.
Mo-0501	1.580	-2.736640	0.
S-0101	0.	3.648854	1.5775
S-0201	0.	3.648854	-1.5775
S-0301	0.	-1.824427	1.5775
S-0401	0.	-1.824427	-1.5775
S-0501	0.	-7.297707	1.5775
S-0601	0.	-7.297707	-1.5775
S-0701	1.580	0.912213	1.5775
S-0801	1.580	0.912212	-1.5775
S-0901	1.580	-4.561067	1.5775
S-1001	1.580	-4.561067	-1.5775
Mo-a	3.160	0.	0.

Table 5b.

Structural parameters of 1-D $(MoS_2)_5$ terminating in $(10\bar{1}1)$ edges.
(units are in Å)

Atom	x	y	z
Mo-0101	0.	5.473281	0.
Mo-0201	0.	0.	0.
Mo-0301	0.	-5.473281	0.
Mo-0401	1.580	2.736640	0.
Mo-0501	1.580	-2.736640	0.
S-0101	0.	3.648854	1.5775
S-0201	0.	3.648854	-1.5775
S-0301	0.	-1.824427	1.5775
S-0401	0.	-1.824427	-1.5775
S-0501	0.	-7.297707	1.5775
S-0601	1.580	6.385494	-1.5775
S-0701	1.580	0.912213	1.5775
S-0801	1.580	0.912212	-1.5775
S-0901	1.580	-4.561067	1.5775
S-1001	1.580	-4.561067	-1.5775
Mo-a	3.160	0.	0.

edges into these structures exposes atoms that are not fully coordinated. Addition of $(10\bar{1}0)$ edges exposes two different edges. The first edge consists of two-coordinate molybdenum atoms; the second edge consists of one-coordinate sulfur atoms (in the first and third atomic layers). Addition of $(10\bar{1}1)$ edges also exposes two different edges. The first edge consists of two-coordinate sulfur atoms and four-coordinate molybdenum atoms. The second edge consists of one-coordinate sulfur atoms (first atomic layer only) and five-coordinate molybdenum atoms.

3.4.5 2-D H-MoS_2 Model

Hydrogen adsorption on 2-D MoS_2 was studied by theoretically placing a hydrogen atom at different spots on the basal plane. Since the 2-D MoS_2 structure contained no edges, only two types of hydrogen sites were calculated. In the first structure a hydrogen atom was placed directly above a basal plane sulfur atom such that the S-H distance was 1.35 Å (+z direction). This S-H distance was chosen because the S-H distance in an inorganic SH_2 molecule is 1.3455 Å.[3] In the second structure a hydrogen atom was placed directly above a molybdenum atom such that the Mo-H distance was 1.7 Å (+z direction). Due to the trigonal prismatic coordination of molybdenum, hydrogen atoms in the second structure were also located 1.83 Å away from three equivalent sulfur atoms. These structures are highly saturated with hydrogen because there is one hydrogen atom per unit of MoS_2. Figures 13a and 13b show the position of hydrogen theoretically adsorbed on basal plane sulfur atoms and molybdenum atoms in 2-D MoS_2. The structural parameters used in the 2-D H-MoS_2 calculations are given in Tables 6a and 6b.

Table 6a.
Structural parameters used in electronic structure calculations of 2-D H-MoS_2 with hydrogen directly above basal plane sulfur atoms. (d_{S-H}=1.35 Å, d_{Mo-H}=3.45 Å)

Atom	x	y	z
Mo-0101	0.	0.	0.
S-0201	0.	-1.8244269	1.5775
S-0301	0.	-1.8244269	-1.5775
H-0401	0.	-1.8244269	2.9275

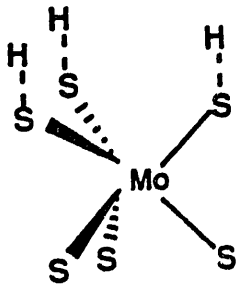

Figure 13a. Hydrogen theoretically adsorbed on basal plane sulfur atoms in 2-D MoS_2.

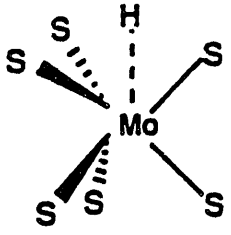

Figure 13b. Hydrogen theoretically adsorbed on basal plane molybdenum atoms in 2-D MoS_2.

Table 6b.

Structural parameters used in electronic structure calculations of 2-D H-MoS_2 with hydrogen directly above molybdenum atoms. (d_{Mo-H}=1.7 Å, d_{S-H}=1.83 Å)

Atom	x	y	z
Mo-0101	0.	0.	0.
S-0201	0.	-1.8244269	1.5775
S-0301	0.	-1.8244269	-1.5775
H-0401	0.	0.	1.7

3.4.6 1-D H-$(MoS_2)_5$ Model Terminating in $(10\bar{1}1)$ Edges

Hydrogen adsorption on the 1-D $(MoS_2)_5$ model terminating in $(10\bar{1}1)$ edges was studied theoretically by placing hydrogen atoms at various sites on the edge and basal plane atoms. The structure terminating in $(10\bar{1}1)$ edges was chosen since this structure was found to be energetically more stable than the structure terminating in $(10\bar{1}0)$ edges. Insight into possible sites for hydrogen adsorption was obtained from a study of the electronic structure of the bare 1-D $(MoS_2)_5$ surface. For instance, on the edge with 2-coordinate sulfur atoms (S-0601) exposed, dangling sulfur p_y-type orbitals are present at the top of the valence band. Thus, theoretically placing a hydrogen atom 1.35 Å away from this sulfur atom, in the +y direction, seems like a good site for hydrogen to adsorb. These structures are not as highly saturated with hydrogen as in the previous case of 2-D H-MoS_2 because there is one hydrogen atom per five units of MoS_2. The structural parameters of the hydrogen atom for each of the 11 different locations are shown in Table 7. The structures of hydrogen adsorbed on the four edge locations (Cases A-D) and two of the basal plane locations (Cases E and I) are shown in Figures 14a-14f.

3.5 Structural Models of NbS_2 Studied.

3.5.1 Bulk Structure of NbS_2

The bulk structure of 2H-NbS_2 is very similar to that of 2H-MoS_2. Again, a number of different NbS_2 modifications exist. However, this study focused on the hexagonal modification. 2H-NbS_2 forms a layer structure in which the niobium atoms are coordinated to 6 sulfur atoms in a trigonal prismatic environment. Each sulfur atom is coordinated to 3 niobium atoms. As described previously for 2H-MoS_2, Section 3.4.1, sandwiches of NbS_2 propagate in two-dimensions in the directions of the real lattice basis vectors, **a** and **b**. Stacking of the NbS_2 layers in the third direction, **c**, perpendicular to **a** and **b** produces the three-dimensional crystal. The definition of the real lattice and reciprocal lattice vectors, given in Section 3.4.1, is the same

Table 7.

Structural parameters of the hydrogen atoms placed on a 1-D $(MoS_2)_5$ model terminating in $(10\bar{1}1)$ edges. The structural parameters for bare 1-D $(MoS_2)_5$ are given in Section 3.4.4. Also shown is the name of the nearest neighbor, NN, atom in each case and the closest distances, d_{S-H}, d_{Mo-H}. (units are in Å)

Case	Atom	x	y	z	NN Atom	d_{S-H}	d_{Mo-H}	Site
A	H-0101	1.58	7.735494	-1.5775	S-0601(+y)	1.35	3.18	Edge 1
B	H-0101	0.	7.173281	0.	Mo-0101(+y)	2.37	1.7	Edge 1
C	H-0101	0.	-7.297707	2.9275	S-0501(+z)	1.35	3.45	Edge 2
D	H-0101	0.	-5.473281	-1.7	Mo-0301(-z)	1.83	1.7	Edge 2
E	H-0101	0.	3.648854	2.9275	S-0101(+z)	1.35	3.45	Basal
F	H-0101	0.	-1.824427	2.9275	S-0301(+z)	1.35	3.45	Basal
G	H-0101	1.58	0.912213	2.9275	S-0701(+z)	1.35	3.45	Basal
H	H-0101	1.58	-4.561067	2.9275	S-0901(+z)	1.35	3.45	Basal
I	H-0101	0.	0.	1.7	Mo-0201(+z)	1.83	1.7	Basal
J	H-0101	1.58	2.736640	1.7	Mo-0401(+z)	1.83	1.7	Basal
K	H-0101	1.58	-2.736640	1.7	Mo-0501(+z)	1.83	1.7	Basal

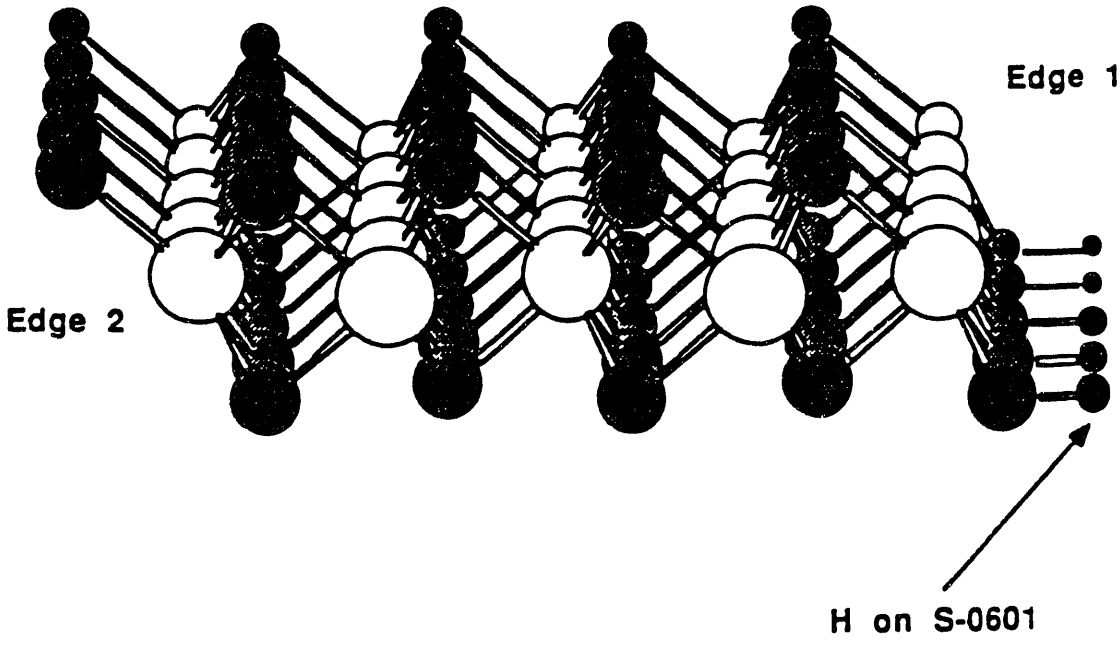

Figure 14a. Hydrogen theoretically adsorbed on edge plane S-0601 in the 1-D $(MoS_2)_5$ structure terminating at the $(10\bar{1}1)$ edges. (Case A)

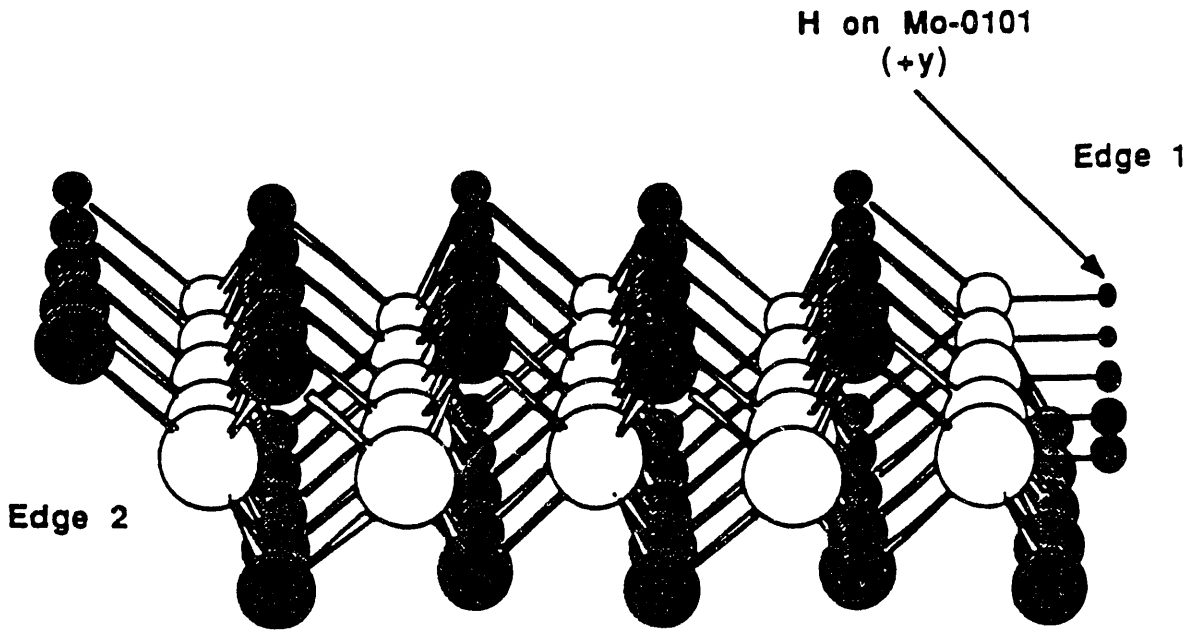

Figure 14b. Hydrogen theoretically adsorbed on edge plane Mo-0101 in the 1-D $(MoS_2)_5$ structure terminating at the $(10\bar{1}1)$ edges. (Case B)

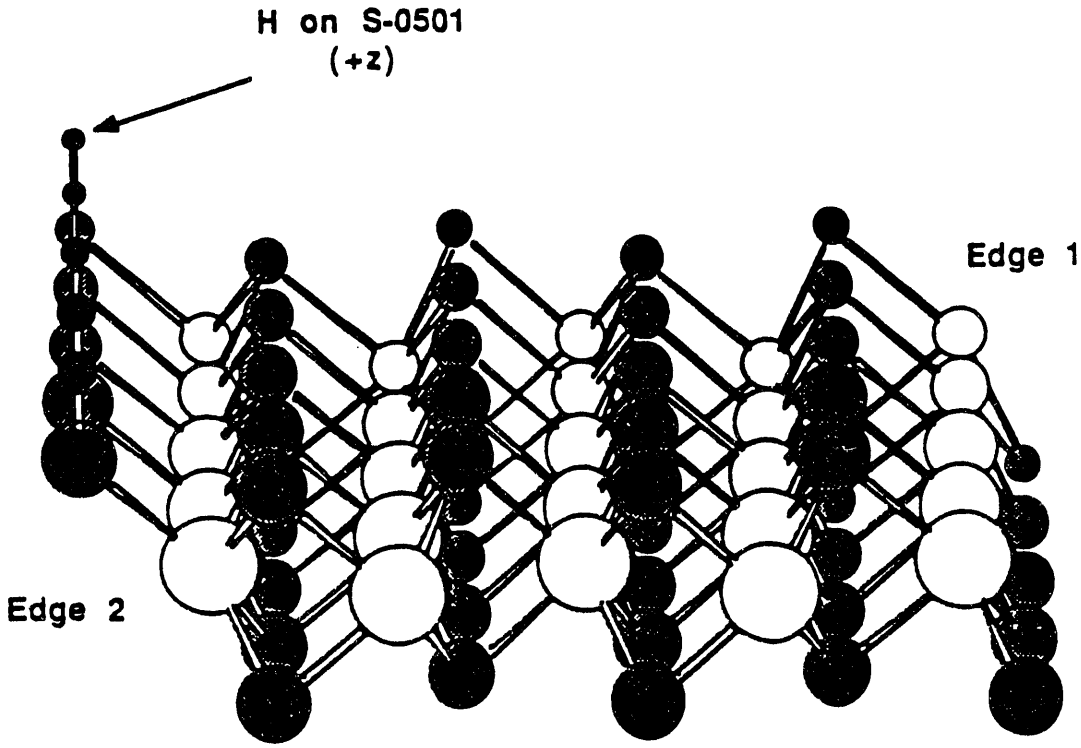

Figure 14c. Hydrogen theoretically adsorbed on edge plane S-0501 in the 1-D $(MoS_2)_5$ structure terminating at the $(10\bar{1}1)$ edges. (Case C)

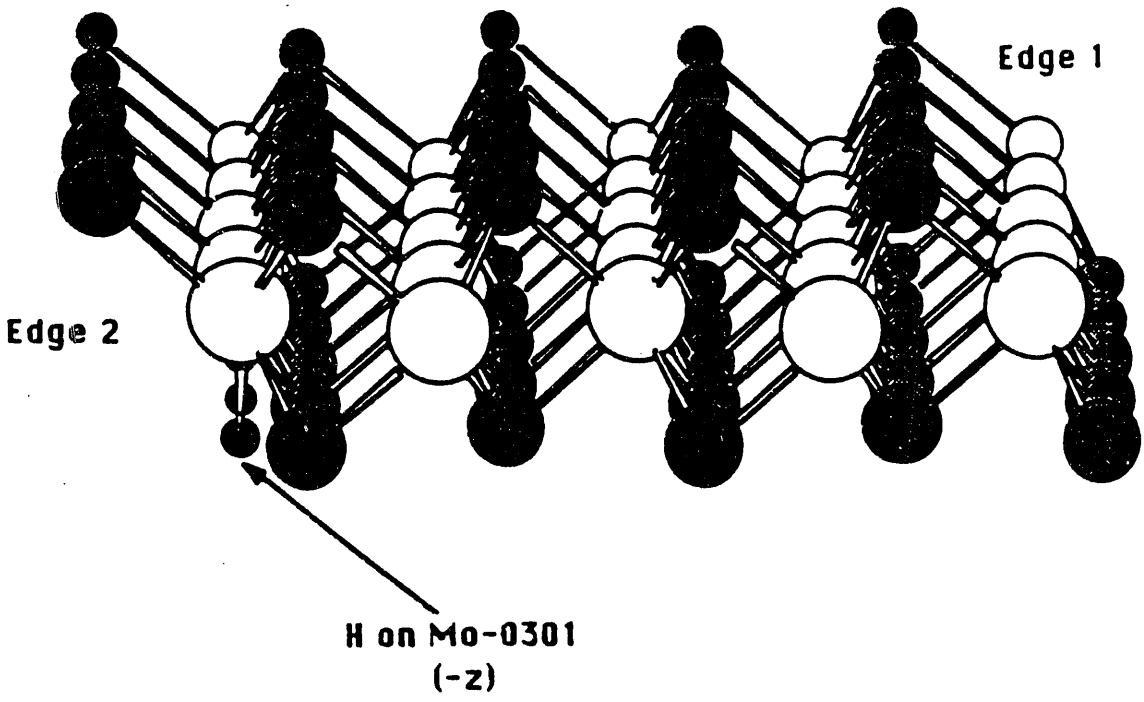

Figure 14d. Hydrogen theoretically adsorbed on edge plane Mo-0301 in the 1-D $(MoS_2)_5$ structure terminating at the $(10\bar{1}1)$ edges. (Case D)

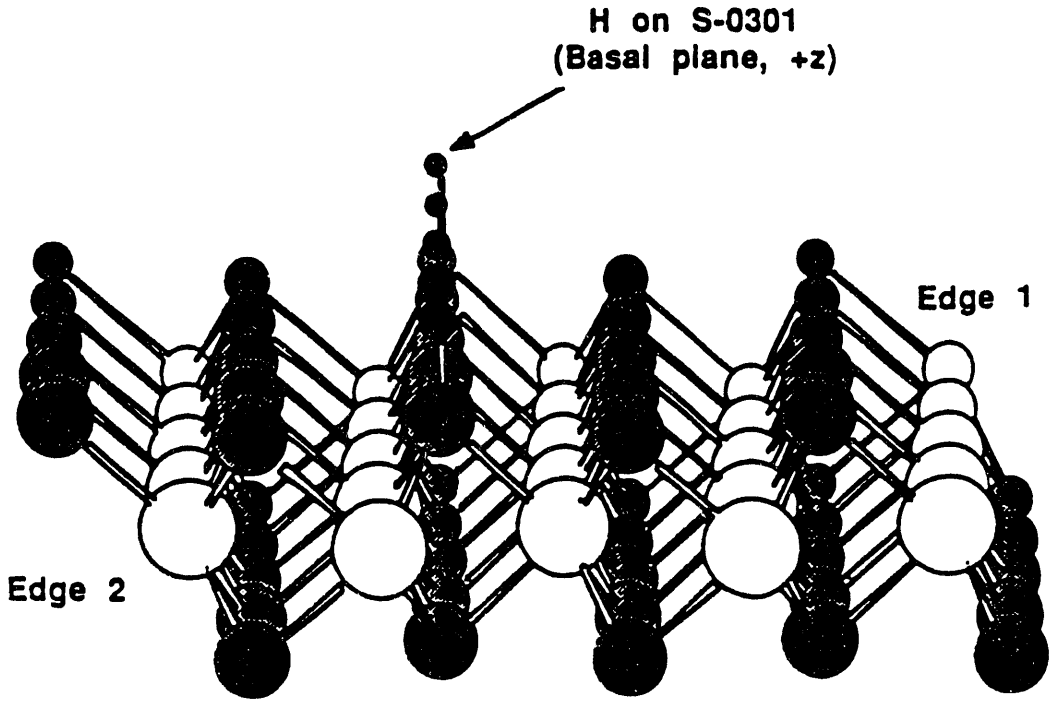

Figure 14e. Hydrogen theoretically adsorbed on basal plane S-0301 in the 1-D $(MoS_2)_5$ structure terminating at the $(10\bar{1}1)$ edges. (Case E)

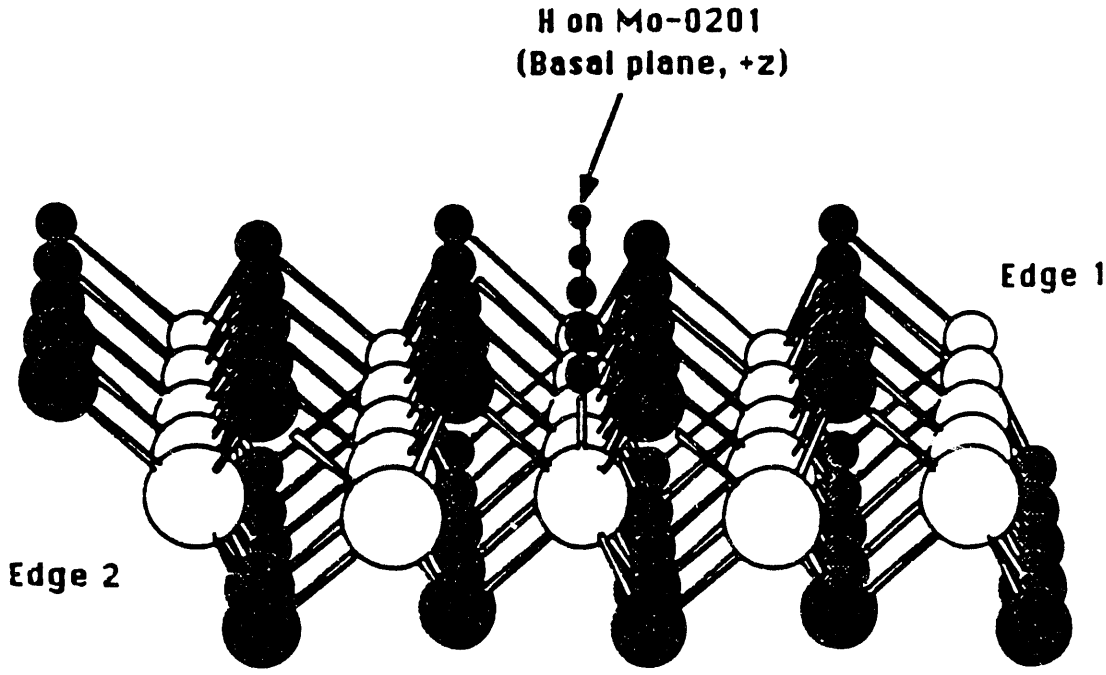

Figure 14f. Hydrogen theoretically adsorbed on basal plane Mo-0201 in the 1-D $(MoS_2)_5$ structure terminating at the $(10\bar{1}1)$ edges. (Case I)

for both 2H-NbS_2 and 2H-MoS_2. In the case of 2H-NbS_2, the following structural parameters are defined: |**a**|=|**b**|=3.31 Å, |**c**|=11.89 Å, u=0.125 (u|**c**|=1.48625 Å), and h=0.250 (h|**c**|=2.9725 Å).

The main difference between the bulk structures of 2H-NbS_2 and 2H-MoS_2 is in the orientation of the second NbS_2 layer. In 2H-NbS_2, the layers are stacked such that niobium atoms in adjacent layers lie above or below niobium atoms in the first layer. Table 8 lists the positions of the atoms in one unit cell of 2H-NbS_2 in terms of the real lattice vectors, **a**, **b**, and **c**.

Table 8.
Positions of the atoms in one unit cell of 2H-NbS_2 in terms of the real lattice vectors, **a**, **b**, and **c**. (u=0.125)

Atom	Position
Nb	(0, 0, 0)
S	$(\frac{1}{3}, -\frac{1}{3}, u)$
S	$(\frac{1}{3}, -\frac{1}{3}, u)$
Nb	$(0, 0, \frac{1}{2})$
S	$(-\frac{1}{3}, \frac{1}{3}, \frac{1}{2}+u)$
S	$(-\frac{1}{3}, \frac{1}{3}, \frac{1}{2}-u)$

3.5.2 2-D NbS_2 Model

Structural parameters used in the electronic structure calculations of one layer of NbS_2 are listed in Table 9. Again, this structure neglected the Van der Waals interactions between adjacent layers. Interactions were calculated up to four nearest neighboring unit cells in the directions of **a** and **b**.

Table 9.
Structural parameters used in electronic structure calculations of one NbS_2 layer. (units are in Å)

Atom	x	y	z
Nb-0101	0.	0.	0.
S-0201	0.	-1.9110294	1.48625
S-0301	0.	-1.9110294	-1.48625
Nb-a	1.655	-2.8665441	0.
Nb-b	1.655	2.8665441	0.

3.6 Structural Models of RuS_2 Studied.

3.6.1 Bulk Structure of RuS_2

The bulk structure of RuS_2 is very different than that of the layer compounds, 2H-NbS_2 and 2H-MoS_2, discussed previously. RuS_2 exists in the bulk as the pyrite structure. Many transition metal disulfides exhibit the pyrite structure. Some representative pyritic transition metal disulfides are the following: MnS_2, FeS_2, CoS_2, NiS_2, and RuS_2. The pyrite structure can be visualized as a derivation of the NaCl structure. Unit cells of both NaCl and transition metal disulfide pyrite compounds are face-centered cubic (fcc). The unit cell of NaCl is made of two interpenetrating fcc lattices, one of which contains only the Na^+ cations and a second contains only the Cl^- anions. The pyrite transition metal disulfides also contain two interpenetrating fcc lattices. The first fcc lattice contains only the transition metal, M. The second fcc lattice has lattice points that consist of the centers of S_2 dimers. Sulfur dimers are positioned such that the bond between dimers lies along one of the four equivalent (111) directions.[49] The formal charge on the transition metal, e.g. Ru, is +2 while that on the sulfur dimer pairs, S_2, is -2. Thus, each sulfur has an effective oxidation state of -1. One unit cell of the pyrite compound, RuS_2, is shown in Figure 15.[50]

There are four lattice points per unit cell in the pyrite structure. Each lattice point is made up of one transition metal atom and a sulfur dimer. The coordinates of the lattice points are listed in Table 10. The shift parameter, u, is designated such that if u=0, then the original NaCl type lattice is obtained. In the pyrite compounds this would lead to an empirical crystal formula of MS, instead of MS_2, due to coalescence of the sulfurs. When the value of $u=\frac{1}{2}$, the sulfurs coalesce with the metal atoms. Thus the range of u is defined for $0 < u < \frac{1}{2}$.

Table 10.

Positions of the atoms in one unit cell of a pyritic transition metal disulfide compound in terms of the lattice vectors, a, b, and c.

M	S_1	S_2
(0, 0, 0)	$(-u, -u, \frac{1}{2}+u)$	$(u, u, \frac{1}{2}-u)$
$(\frac{1}{2}, \frac{1}{2}, 0)$	$(\frac{1}{2}+u, \frac{1}{2}-u, \frac{1}{2}-u)$	$(\frac{1}{2}-u, \frac{1}{2}+u, \frac{1}{2}+u)$
$(0, \frac{1}{2}, \frac{1}{2})$	$(-u, \frac{1}{2}-u, 1-u)$	$(u, \frac{1}{2}+u, 1+u)$
$(\frac{1}{2}, 0, \frac{1}{2})$	$(\frac{1}{2}-u, u, 1-u)$	$(\frac{1}{2}+u, -u, 1+u)$

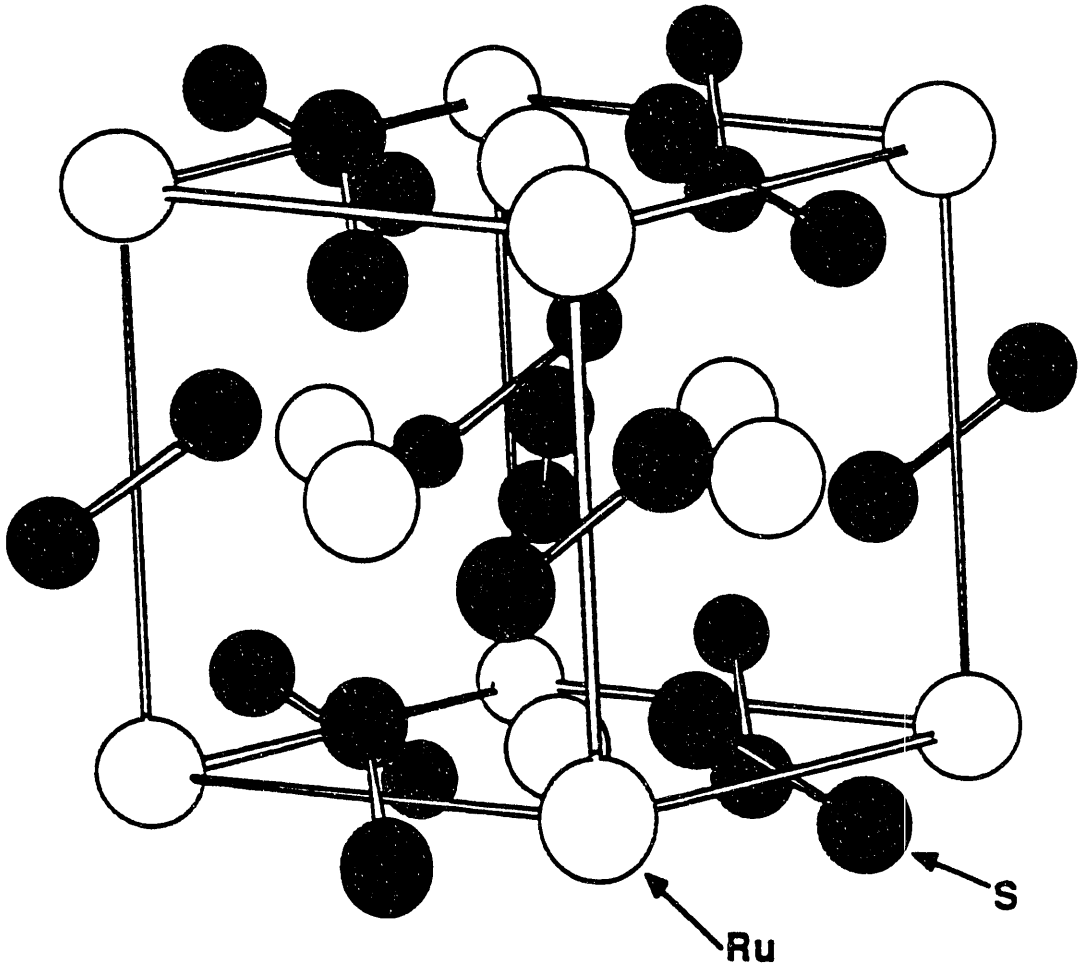

Figure 15. Unit cell of the pyritic transition metal disulfide RuS_2. In this cubic structure the lengths of the real lattice vectors, **a**, **b**, and **c** are all equal to 5.6095 Å. (White circles=sulfur atoms, black circles=ruthenium atoms.)

Each transition metal atom has six nearest neighbor sulfur atoms. The sulfur atoms surround the metal in a distorted octahedral array. Each sulfur atom is surrounded by 3 metal atoms and 1 sulfur atom in a distorted tetrahedral environment. The cell dimensions, shift parameter, u, S-S bond length and M-S bond length for the pyrite compounds, FeS_2 and RuS_2, are compared to the corresponding values for NbS_2 and MoS_2 in Table 11.

Table 11.
Cell dimensions, shift parameter, u, S-S, M-S and M-M bond length in pyrite compounds, MnS_2, FeS_2, CoS_2, NiS_2, and RuS_2, as compared to the hexagonal compounds 2H-NbS_2 and 2H-MoS_2. (RuS_2 parameters obtained from Reference 50 and MnS_2, FeS_2, CoS_2, NiS_2 parameters obtained from Reference 51)

MX_2	#d e⁻	|a|, |c| (Å)	u (Å)	S-S (Å)	M-S (Å)	M-M (Å)	
MnS_2	d^5 (Mn^{+2})	6.097	0.0988	2.086	2.590	4.311	
FeS_2	d^6 (Fe^{+2})	5.404	0.1160	2.171	2.259	3.821	Pyritic
CoS_2	d^7 (Co^{+2})	5.523	0.1110	2.124	2.315	3.905	
NiS_2	d^8 (Ni^{+2})	5.677	0.1050	2.065	2.396	4.014	
RuS_2	d^6 (Ru^{+2})	5.6095	0.1121	2.178	2.351	3.966	
2H-NbS_2	d^1 (Nb^{+4})	3.31, 11.89	0.125	2.97	2.42	3.31	Hexagonal
2H-MoS_2	d^2 (Mo^{+4})	3.16, 12.30	0.128252	3.16	2.41	3.16	

3.6.2 3-D RuS_2 Model

Since the RuS_2 structure does not exhibit a layer-type structure, only three-dimensional models of the bulk structure were studied. Structural parameters used in electronic structure calculations of 3-D RuS_2 are shown in Table 12.

3.7 Choice of Wavevectors Points, k-Points, in the First Brillouin Zone.

Prior to electronic structure calculations, a set of wavevector, **k**, points was chosen for each structure. This set of k-points defined the type of calculation to be carried out. A large set of k-points representative of the first Brillouin zone was used for calculations of the density of states and theoretical valence bands. A smaller subset of k-points propagating in one-direction of the first Brillouin zone was used for obtaining the energy dispersion curves. The calculation of energies and crystal Bloch orbitals was repeated for each k-point in the set. This section discusses the k-point sets used in electronic structure calculations.

Table 12.
Structural parameters used in electronic structure calculations of 3-D RuS_2. (units are in Å)

Atom	x	y	z
Ru-0101	0.	0.	0.
Ru-0201	2.804750	2.804750	0.
Ru-0301	0.	2.804750	2.804750
Ru-0401	2.804750	0.	2.804750
S-0501	-0.628825	-0.628825	3.433575
S-0601	0.628825	0.628825	2.175925
S-0701	3.433575	2.175925	2.175925
S-0801	2.175925	3.433575	3.433575
S-0901	-0.628825	2.175925	4.980675
S-1001	0.628825	3.433575	6.238325
S-1101	2.175925	0.628825	4.980675
S-1201	3.433575	-0.628825	6.238325
Ru-a	5.6095	0.	0.
Ru-b	0.	5.6095	0.
Ru-c	0.	0.	5.6095

3.7.1 The k-Point Sets Used in Calculations of the Density of States and Theoretical Valence Bands of 2H-NbS_2 and 2H-MoS_2

The density of states and theoretical valence bands of 2H-NbS_2 and 2H-MoS_2 were calculated using a very large set of **k**-points. As mentioned previously in Section 3.4.1, the two-dimensional first Brillouin zone of 2H-NbS_2 and 2H-MoS_2 is hexagonal. Due to the hexagonal symmetry, a triangular portion (1/12 of the Brillouin zone) can be used to represent the whole Brillouin zone. This portion is shown in the first Brillouin zone of 2H-MoS_2 (Section 3.4.1) as the area enclosed by the directions $\Gamma \rightarrow M$, $\Gamma \rightarrow K$, and $K \rightarrow M$. Two sets of **k**-points will be discussed in reference to calculations of the density of states and theoretical valence bands of 2H-NbS_2 and 2H-MoS_2. The first set is referred to as special **k**-points and the second set is referred to as a uniform grid of **k**-points.

The special set of **k**-points was obtained from a two-dimensional graphite example contained in the EHMACPP program. Since two-dimensional graphite, NbS_2, and MoS_2 exhibit the same two-dimensional hexagonal first Brillouin zone, the **k**-points from this example were used for electronic structure calculations of two-dimensional NbS_2 and MoS_2. This special set of **k**-points consisted of a total of 171 **k**-points. The **k**-points were input into the program in terms of $\mathbf{k}_1$, $\mathbf{k}_2$, and $\mathbf{k}_3$, defined as follows: $\mathbf{k}_1 = u\mathbf{a}^*$; $\mathbf{k}_2 = v\mathbf{b}^*$; and $\mathbf{k}_3 = w\mathbf{c}^*$ (where u, v, w are fractional coordinates). The fractional coordinates u, v and w were input into the program for each **k**-point to be calculated. A plot of the 171 special **k**-points is shown in Figure 16. These

plots were generated in terms of the vectors $\mathbf{k}_x$ and $\mathbf{k}_y$ because the vectors $\mathbf{k}_1$ and $\mathbf{k}_2$ are not perpendicular. These vectors are defined in the following: $\mathbf{k}_x=(u+v)\frac{\hat{x}}{|\mathbf{a}|}$; $\mathbf{k}_y=(v-u)\frac{\hat{y}}{|\mathbf{a}|\sqrt{3}}$. Thus, Figure 16 actually plots $|\mathbf{a}|\sqrt{3}\mathbf{k}_y$ vs. $|\mathbf{a}|\mathbf{k}_x$ or $(v-u)\hat{y}$ vs. $(u+v)\hat{x}$. However, the special points shown in Figure 16 still represent the area enclosed by the directions $\Gamma\rightarrow M$, $\Gamma\rightarrow K$, and $K\rightarrow M$ of the first Brillouin zone.

A uniform grid of **k**-points was derived from the set of special **k**-points discussed above. The plot of special **k**-points shows that every third row of **k**-points is missing in this set. Upon inclusion of the missing **k**-points a uniform grid of **k**-points consisting of a total of 271 **k**-points results. A plot of the uniform grid of 271 **k**-points is shown in Figure 17. From the figure it can be seen that the direction $\Gamma\rightarrow K$ lies along the k_x axis.

Most of the density of states and theoretical valence band calculations were carried out using the set of 171 special **k**-points instead of the uniform grid of 271 **k**-points. Use of special **k**-points resulted in a good description of the electronic structure without loss of information. Electronic calculations performed using both the uniform grid of 271 **k**-points and the special 171 **k**-points provided similar results. Thus, no information was lost when using the special **k**-points and substitution was permissible. Calculation of the density of states and theoretical valence bands using a limited set of 12 special **k**-points does, however, lead to a markedly different result. Thus, large sets of **k**-points are needed for accurate representation of the theoretical valence band.

3.7.2 The k-Point Sets Used in Calculations of 2H-MoS_2 Energy Dispersion Curves

Theoretical energy dispersion curves of two- and three-dimensional 2H-MoS_2 were calculated using the EHMACPP program. For these calculations, sets of **k**-points propagating in specific high symmetry directions were used. Energy dispersion curves for the following directions were calculated: $\Gamma\rightarrow K$, $\Gamma\rightarrow M$, and $K\rightarrow M$. The **k**-points along the $\Gamma\rightarrow M$ direction had values of $|\mathbf{k}|$ ranging from 0 at the Γ point to $\frac{1}{|\mathbf{a}|\sqrt{3}}$ at the M point. In this direction the values of $\mathbf{k}_1$, $\mathbf{k}_2$, and $\mathbf{k}_3$ have the ranges defined in the following: $\mathbf{k}_1=0\rightarrow 0.5\mathbf{a}^*$; $\mathbf{k}_2=0$; and $\mathbf{k}_3=0$. The **k**-points along the $\Gamma\rightarrow K$ direction had values of $|\mathbf{k}|$ ranging from 0 at the Γ point to $\frac{2}{|\mathbf{a}|3}$ at the K point. In this direction the values of $\mathbf{k}_1$, $\mathbf{k}_2$, and $\mathbf{k}_3$ have the ranges defined in the following: $\mathbf{k}_1=0\rightarrow\frac{1}{3}\mathbf{a}^*$; $\mathbf{k}_2=0\rightarrow\frac{1}{3}\mathbf{b}^*$; and $\mathbf{k}_3=0$. In general, calculations were carried out using 51 k-points in each direction to ensure better continuity of the resulting energy dispersion curves.

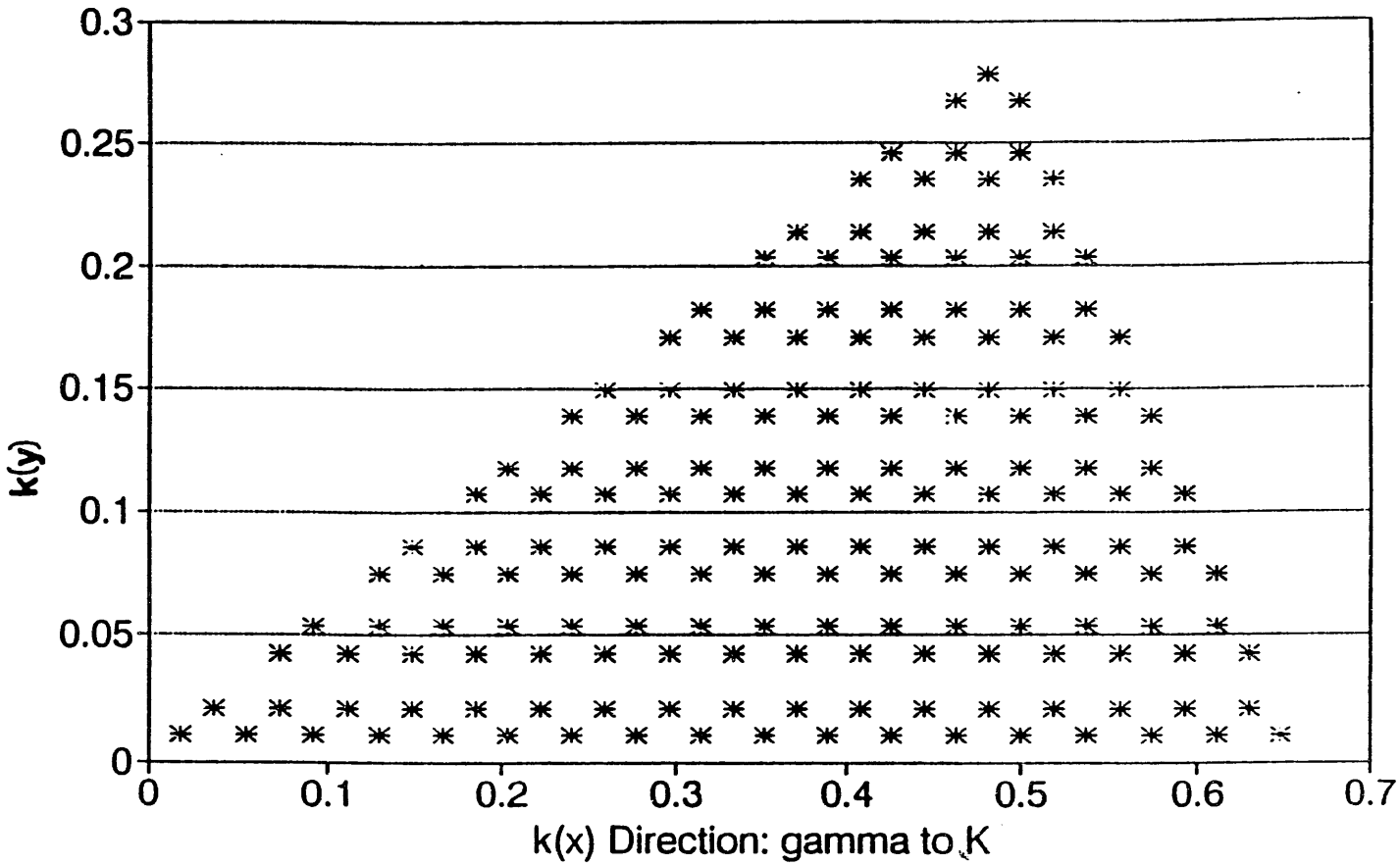

Figure 16. Plot of the special 171 k-points used in the electronic structure calculations of two-dimensional 2H-NbS_2 and 2H-MoS_2. Actual plot is of $|a|\sqrt{3}k_y$ vs. $|a|k_x$ or $(v-u)\hat{y}$ vs. $(u+v)\hat{x}$. (The units of k_x, k_y are Å^{-1}.)

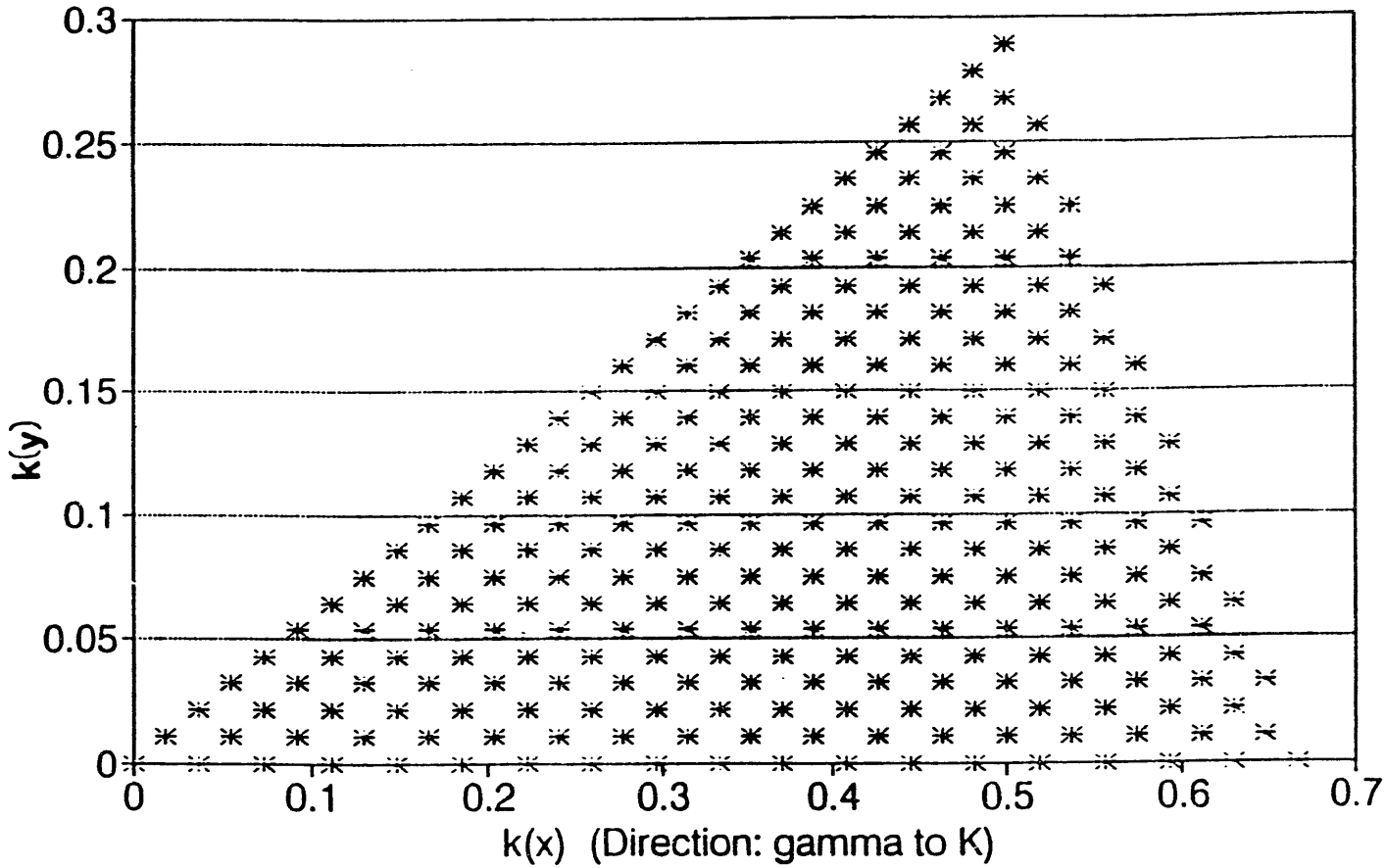

Figure 17. Plot of the uniform grid of 271 k points used in the electronic structure calculations of two dimensional 2H MoS_2. Actual plot is of $|a|\sqrt{3}k_y$ vs. $|a|k_x$ or $(v\ u)\hat{y}$ vs. $(u+v)\hat{x}$. (The units of k_x, k_y are Å^{-1}.)

Chapter 4
EXPERIMENTAL RESULTS

4.1 HR-ESCA Analysis of Polycrystalline $NbS_{(2-x)}$, MoS_2, and RuS_2.

4.1.1 Core Level Analysis Polycrystalline MoS_2

Prior to HR-ESCA analysis of the valence bands of polycrystalline samples, the surface composition was probed by obtaining survey and core level spectra. Survey spectra followed by detailed core level spectra were obtained as indicated in Section 2.3.3. Core level spectra collected were the following: transition metal T, 3d; S, 2p; C, 1s; and O, 1s. The carbon and oxygen regions were recorded to probe the cleanliness of the surface. Approximate surface atom ratios could be found from a ratio of the core level peak areas multiplied by the inverse of the respective Scofield cross-sections. Homogeneous composition and oxidation states of the transition metal disulfide surface were judged from the transition metal 3d and S 2p regions. If core levels due to only one type of oxidation state were present, the surface was assumed to be uniform.

A survey spectrum of polycrystalline MoS_2, prepared as described in Section 2.1.2, is shown in Figure 18a. The survey spectrum showed that molybdenum and sulfur atoms were the predominant chemical species present on the surface but small amounts of carbon and oxygen were also present. This sample was pretreated prior to HR-ESCA analysis with a 2.04 % H_2/N_2 gas mixture. The sample was not exposed to air after the pretreatment procedure.

Regional scans of individual core levels for polycrystalline MoS_2 are shown in Figures 18b, 18c, 18d, and 18e. The carbon 1s and oxygen 1s regions, Figures 18b and 18c, indicate surface contamination by carbon and oxygen species. The symmetries and narrow peaks in the Mo 3d region shown in Figure 18d indicate the presence of only one molybdenum oxidation state. The raw data show a Mo $3d_{5/2}$ peak at 229.03 eV and a $3d_{3/2}$ peak at 232.18 eV. To check the spectrometer calibration, a regional scan of the Au 4f core levels was obtained. The Au $4f_{7/2}$ peak should appear at 83.98 eV. In this case, the Au $4f_{7/2}$ peak appeared at 83.96 eV, a difference of -0.02 eV. Thus, on comparison with the Au region all of the peak positions were shifted to higher binding energy by +0.02 eV, to 229.05 eV (Mo $3d_{5/2}$) and 232.20 eV (Mo $3d_{3/2}$). The spin-orbit splitting between the two Mo 3d peaks is 3.15 eV. In molybdenum metal, the Mo $3d_{5/2}$ peak appears at 227.7 eV with a 3d splitting of 3.15 eV.[52] Thus in polycrystalline MoS_2, molybdenum appears at a higher binding energy relative to a molybdenum species in the metallic state but with the same spin-orbit splitting. The 3d shifts can be interpreted by looking at the charge potential model developed by Siegbahn and

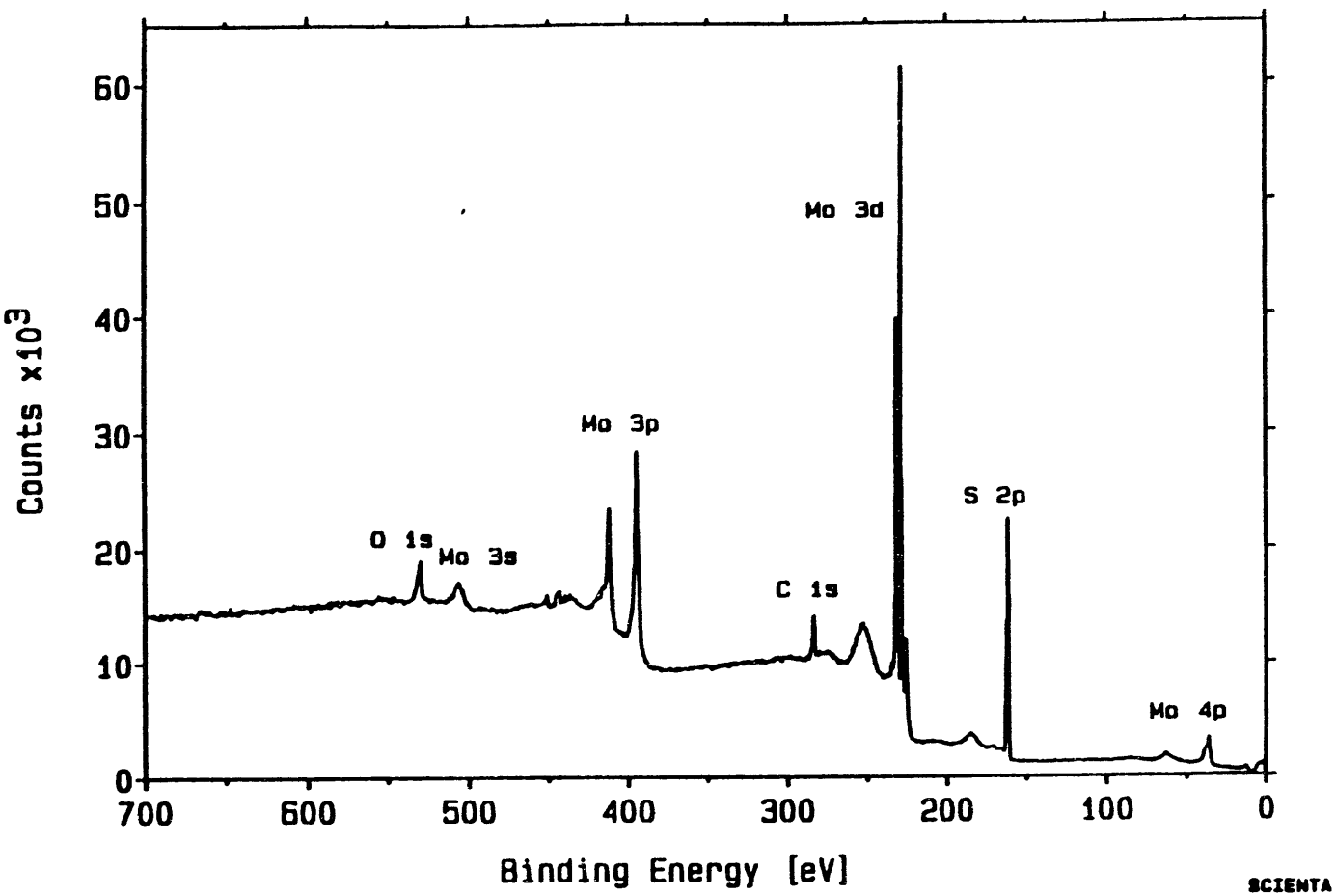

Figure 18a. Survey spectrum of polycrystalline MoS_2. Spectral parameters were the following: pass energy, E_p, 150 eV; step size, 0.5 eV; time/step; slit width, 1.1 mm; and transmission mode.

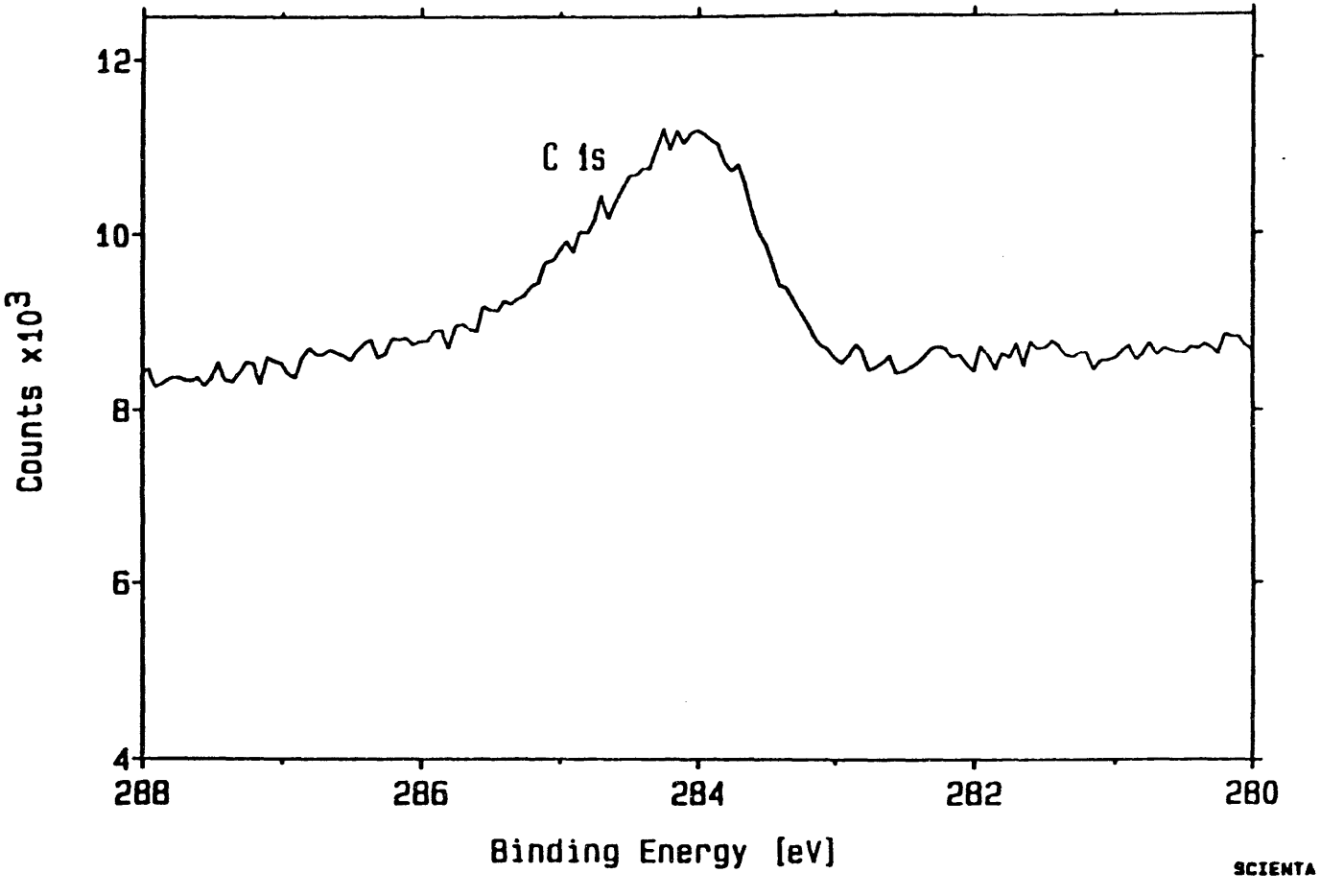

Figure 18b. Core level carbon 1s region of polycrystalline MoS_2. Spectral parameters were the following: pass energy, E_p, 75 eV; step size, 0.05 eV; time/step, 0.04 sec; slit width, 1.1 mm; and transmission mode.

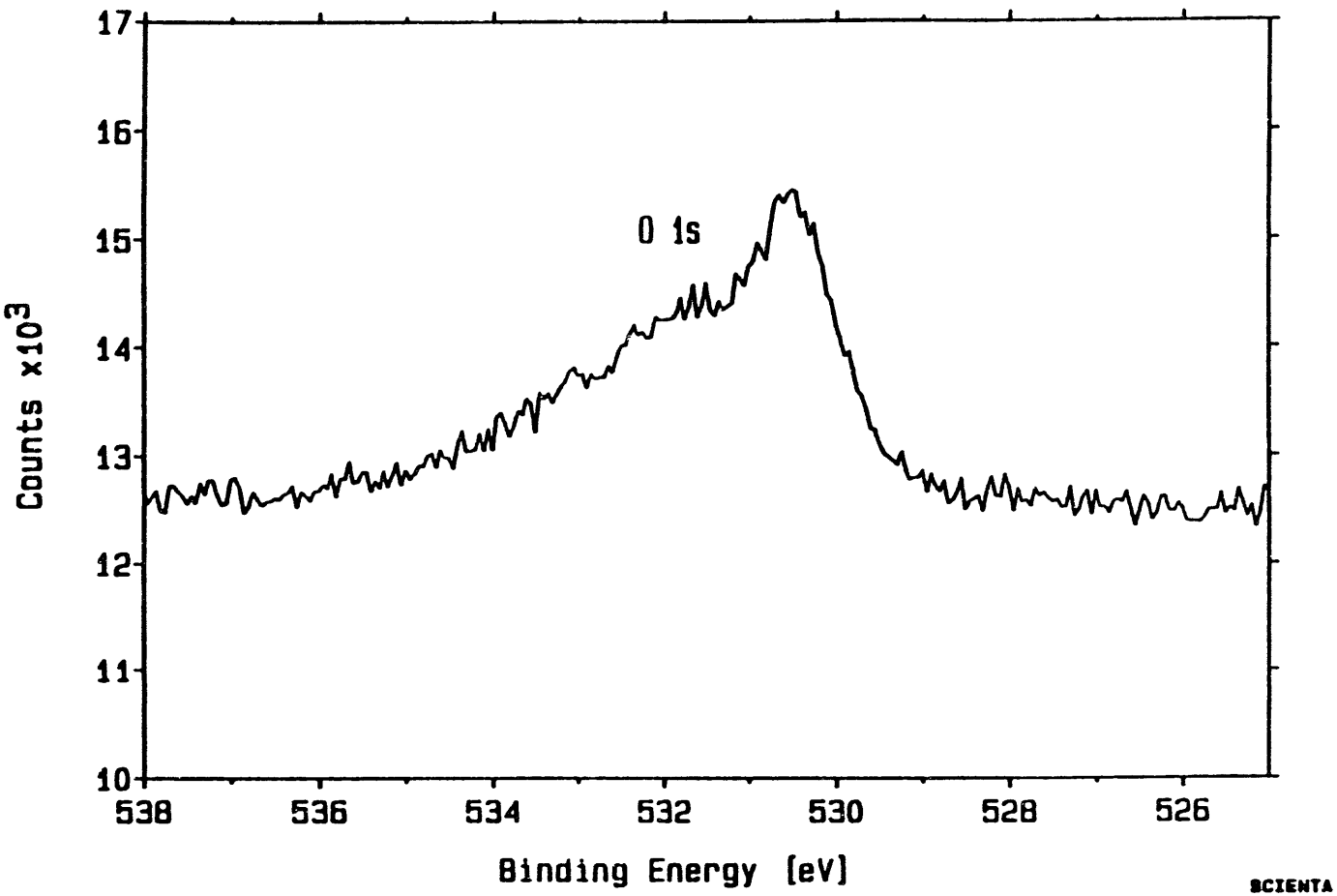

Figure 18c. Core level oxygen 1s region of polycrystalline MoS_2. Spectral parameters were the following: pass energy, E_p, 75 eV; step size, 0.05 eV; time/step, 0.04 sec; slit width, 1.1 mm; and transmission mode.

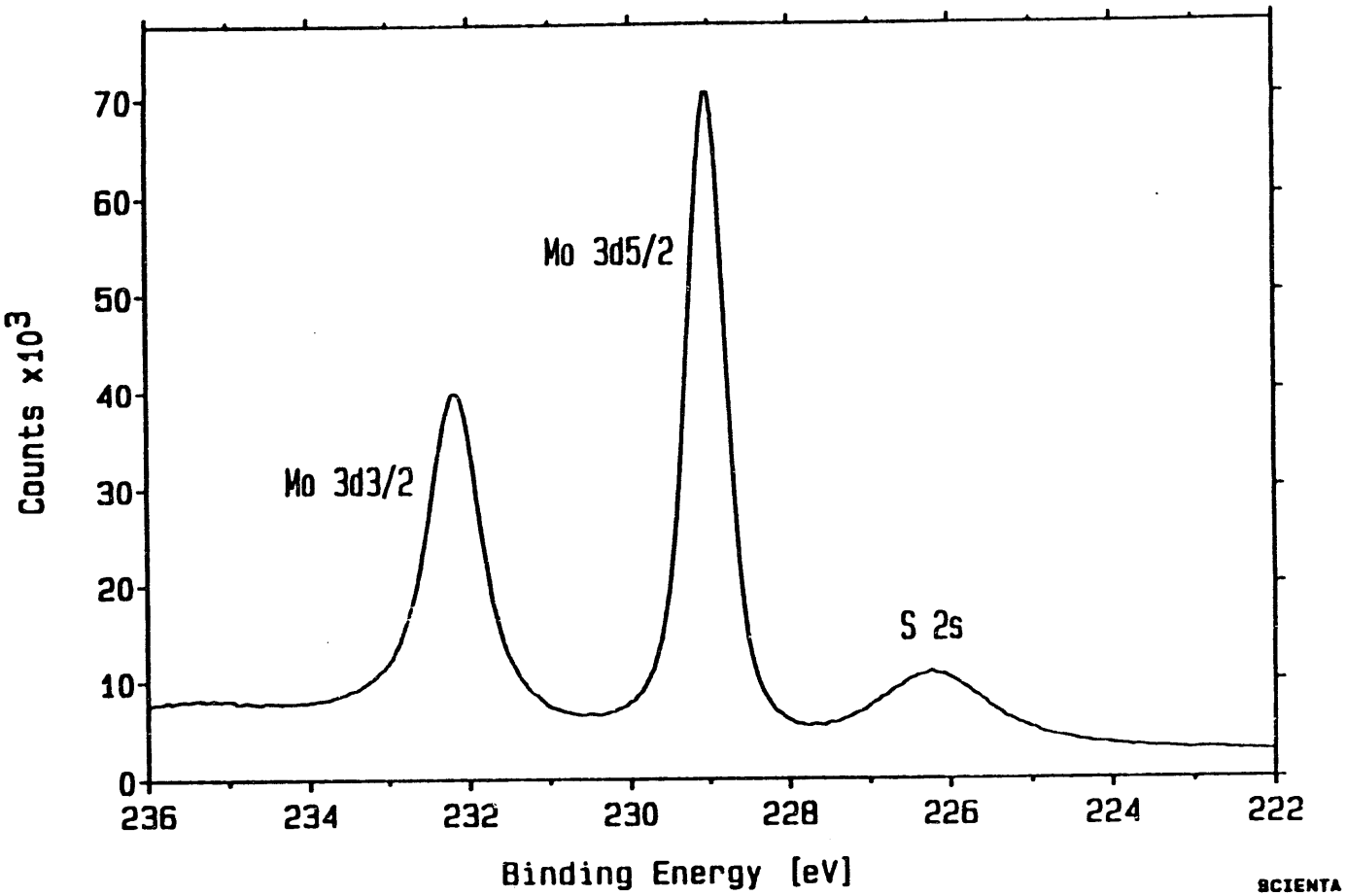

Figure 18d. Core level molybdenum 3d region of polycrystalline MoS_2. Spectral parameters were the following: pass energy, E_p, 75 eV; step size, 0.05 eV; time/step, 0.04 sec; slit width, 1.1 mm; and transmission mode.

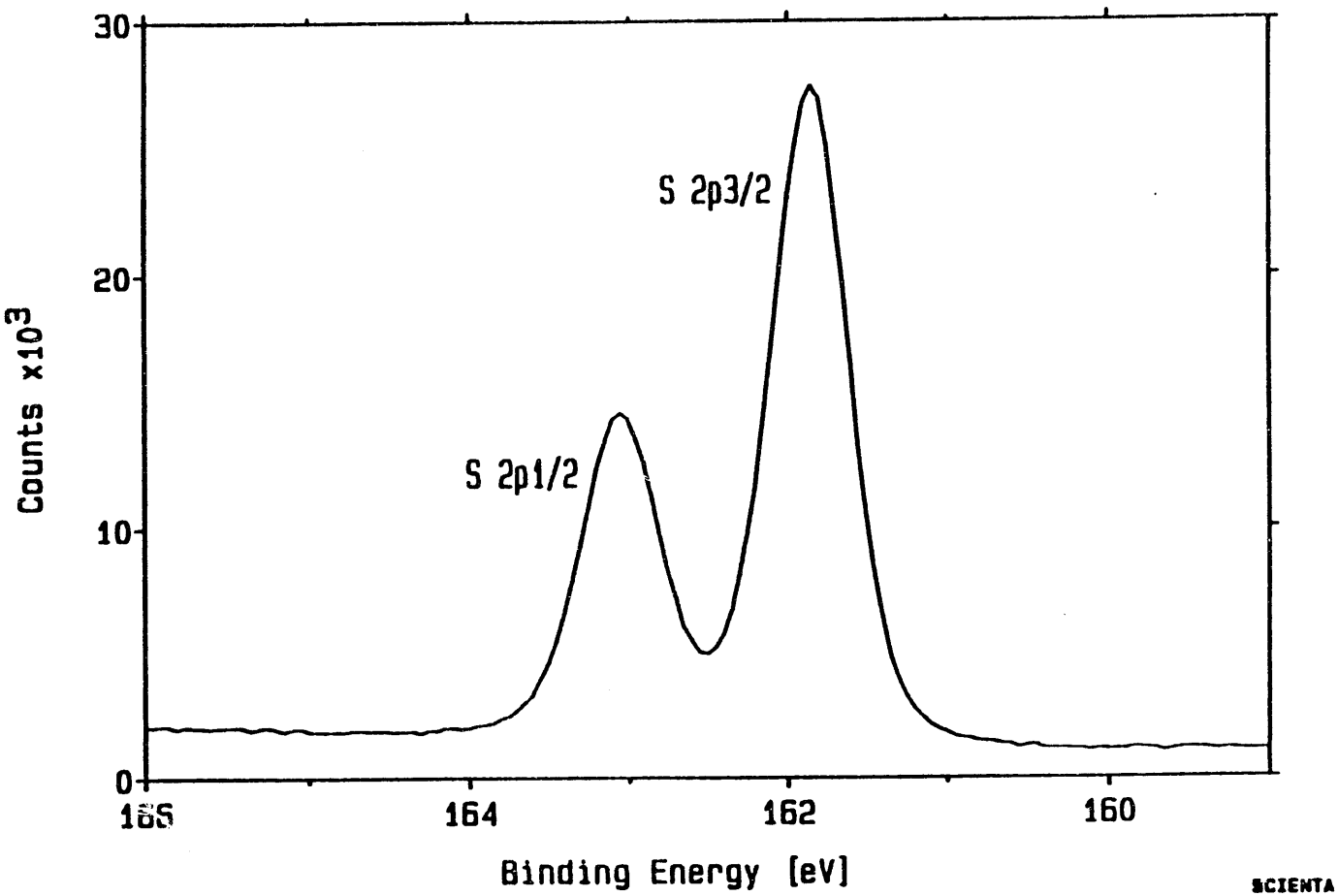

Figure 18e. Core level sulfur 2p region of polycrystalline MoS_2. Spectral parameters were the following: pass energy, E_p, 75 eV; step size, 0.05 eV; time/step, 0.04 sec; slit width, 1.1 mm; and transmission mode.

discussed in Reference 53. The charge potential model relating binding energies of a specific core level photoelectron ejected from same atom in two different environments, $E_i^{(j)}$, to the corresponding charges, $q_i^{(j)}$, and potentials in ionic solids, $V_i^{(j)}$, is shown in 15. For an atom existing in two different oxidation states in separate compounds with

$$E_i^{(1)} - E_i^{(2)} = k(q_i^{(1)} - q_i^{(2)}) + (V_i^{(1)} - V_i^{(2)}) \qquad (15)$$

where $q_i^{(j)}$= charge on atom i

k = constant

$E_i^{(j)}$=binding energy

$V_i^{(j)}$=potential in ionic solids. Summation extending over the whole lattice and closely related to the Madelung energy.

$q^{(1)}>q^{(2)}$ (or $q^{(1)}<q^{(2)}$), then the binding energy of a core level photoelectron ejected from the first compound, $E^{(1)}$, will be larger (smaller) than the binding energy of a core level photoelectron ejected from the atom in the second compound, $E^{(2)}$. Thus, Mo 3d electrons from the more positively oxidized species will require more energy to be removed from the atom and the Mo 3d photoelectron peaks will appear at higher binding energy relative to a zero valent molybdenum species.

The symmetric and narrow peaks in the S 2p region shown in Figure 18e indicate the presence of only one sulfur oxidation state. The binding energies of the S 2p emission range from approximately 160 eV to 170 eV.[50] Sulfate, $(SO_4)^{-2}$, species generally appear at higher binding energies near $\sim$ 167–169 eV. This region was monitored and sulfate type species were not detected. The S $2p_{3/2}$ and S $2p_{1/2}$ peaks in the present sample appear at 161.86 eV and 163.05 eV with a splitting of 1.19 eV. When shifted by +0.02 eV (consistent with the Au calibration), the peaks appear at 161.88 eV and 163.07 eV, respectively. The S 2p peaks of a sulfur, S_n, species appear at $\sim$ 164 eV (literature peaks of S 2p region are unsplit due to lower spectrometer resolution).[50] Compared to a sulfur, S_n species, the sulfur in MoS_2 is reduced.

A rough estimate of the carbon and oxygen contamination levels on the polycrystalline MoS_2 surface can be obtained from the corresponding photoelectron peak areas and Scofield cross–sections. The ratio of molybdenum to carbon surface atoms was found to be approximately 1.8. The ratio of molybdenum to oxygen surface atoms was found to be approximately 3.0. Although this sample was not exposed to air after the pretreatment procedure, it seems likely that this procedure was not effective enough to remove all of the impurities.

4.1.2 Core Level Analysis of Polycrystalline $NbS_{(2-x)}$

Polycrystalline $NbS_{(2-x)}$ was also studied via HR-ESCA. As discussed in Section 2.1.4, this sample was not stoichiometric and contained a large amount of excess niobium. Pretreatment of this sample in a 14.8 % H_2S/H_2 gas mixture prior to HR-ESCA analysis was carried out in the hope of creating a homogeneous NbS_2 surface. HR-ESCA analysis revealed the presence of a large amount of surface oxygen and small amount of surface carbon. However, the most disturbing feature about this sample was the presence of 2-3 different niobium oxidation states and 2 different sulfur oxidation states.

Curve fitting of the Nb 3d region indicated that the largest contribution was derived from a Nb $3d_{5/2}$ peak situated at a binding energy of 203.45 eV. This oxidation state was attributed to niobium atoms in stoichiometric NbS_2. Other niobium species were located at higher binding energies and could probably be attributed to non-stoichiometric niobium oxide and niobium sulfide species. In Nb(0) metal, the Nb $3d_{5/2}$ peak appears at a binding energy between 201.6 eV and 202.4 eV.[25] Thus, niobium atoms in the sulfide are oxidized relative to niobium atoms in the metal.

Curve fitting of the S 2p region of $NbS_{(2-x)}$ (Figure 19) showed the presence of two different sulfur oxidation states. However, no sulfate-type species were found on this sample. The two S $2p_{3/2}$ peaks were situated at binding energies of 160.83 eV and 161.82 eV. The peak at 161.82 eV had an area approximately double that of the peak at 160.83 eV. Thus, by comparison to the S $2p_{3/2}$ peak of MoS_2 situated at 161.88 eV, the peak at 161.82 eV was attributed to sulfur atoms in NbS_2. The peak at 160.83 eV could be attributed to sulfur atoms in non-stoichiometric niobium sulfide. A second form of niobium sulfide, Nb_2S_5, is relatively stable and may have formed in conjunction with NbS_2.

4.1.3 Core Level Analysis of Polycrystalline RuS_2

A survey spectrum of polycrystalline RuS_2, prepared as described in Section 2.1.3, is shown in Figure 20a. This sample was loaded into the HR-ESCA instrument under N_2 immediately following the pretreatment procedure and was not exposed to air prior to HR-ESCA analysis. As indicated in the survey spectrum, the surface of this sample consisted of ruthenium and sulfur atoms. A small amount of oxygen was also present on the surface. An approximate estimate of the surface atom ratio of ruthenium to oxygen was obtained from the photoelectron peak areas and Scofield cross-sections. The surface ruthenium to oxygen atom ratio was found to be ~ 1.6. Due to the use of α-$RuCl_3$ as a starting material for RuS_2,

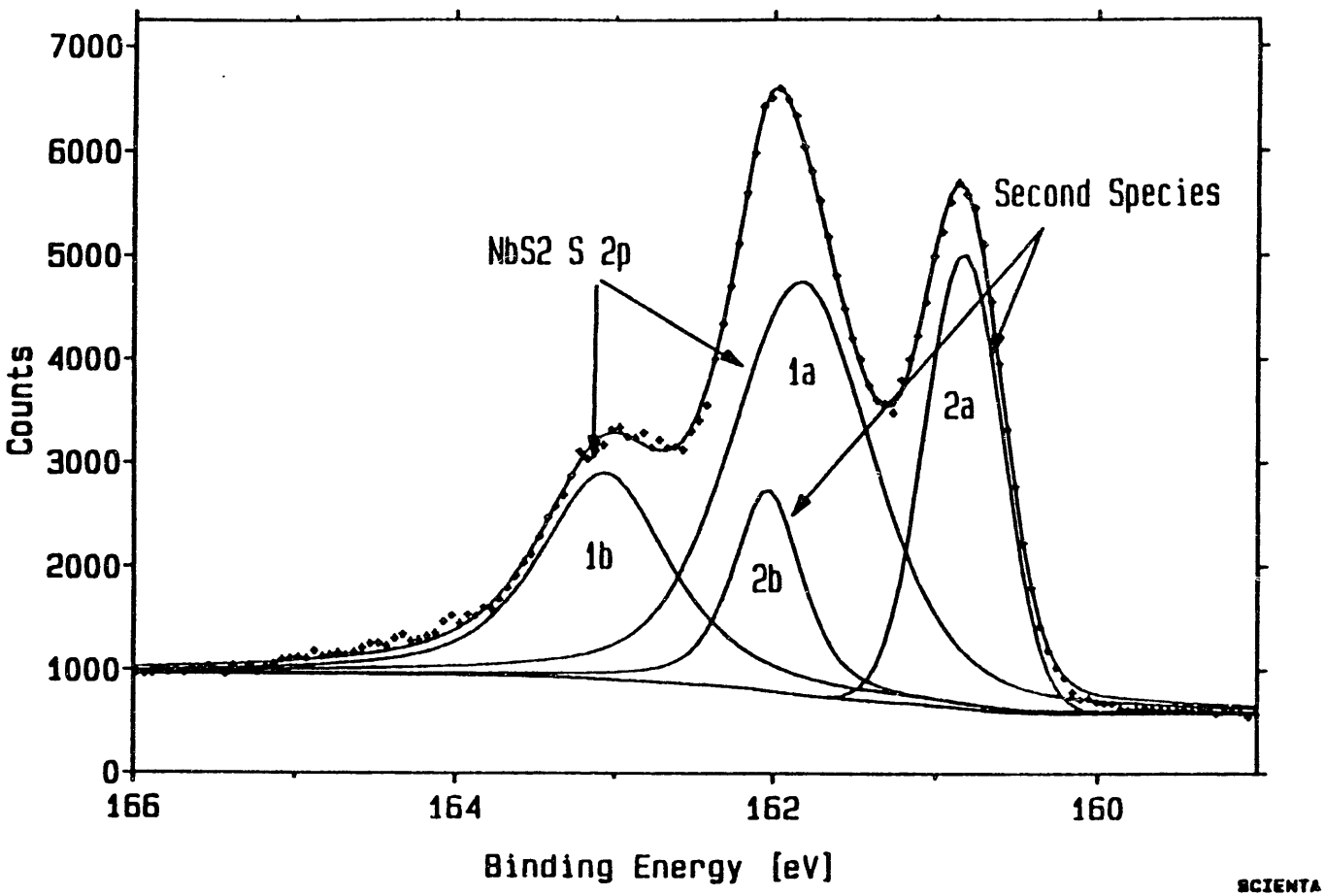

Figure 19. Curve fitting of the S2p region of $NbS_{(2-x)}$ showing the presence of two different sulfur oxidation states 1 and 2. The $S2p_{3/2}$ and $S2p_{1/2}$ levels of Site 1 are attributed to sulfur atoms in NbS_2. The $S2p_{3/2}$ and $S2p_{1/2}$ levels of Site 2 are attributed to sulfur atoms in non-stoichiometric niobium sulfide.

contamination by chlorine was also expected. However, no significant signal due to Cl 2p photoelectrons was observed at binding energies around 200 eV.

Regional scans of individual core levels of polycrystalline RuS_2 are shown in Figures 20b, 20c, and 20d. In the case of RuS_2, the C 1s peak ($\sim$ 284 eV) overlaps with the Ru $3d_{3/2}$ peak (284.05 eV). Thus, carbon contamination could not be monitored by obtaining the C 1s region. However a carbon Auger transition, $KL_{23}L_{23}$, located at approximately 1226 eV was used to check for the presence of surface carbon.[50] The carbon auger region is shown in Figure 20b. The line shown indicates the approximate position that the carbon auger transition would appear if carbon was present. No significant amount of carbon was found to be present on this surface. This region does show a Ru MNN Auger transition at $\sim$ 1214 eV.

The Ru 3d region, as shown in Figure 20c, indicates the presence of only one ruthenium oxidation state. The Ru $3d_{5/2}$ and Ru $3d_{3/2}$ peaks appear at 279.96 eV and 284.05 eV, respectively. Thus, the Ru 3d level is split by 4.09 eV. HR-ESCA analysis of both ruthenium metal, Ru(0), and ruthenium oxide, RuO_2, was also carried out such that a comparison of the Ru 3d peak positions could be made. Peak positions and splittings of the Ru 3d region for RuS_2, Ru(0), and RuO_2 are given in Table 13. As indicated in the Table 13, the Ru $3d_{5/2}$ peaks in RuS_2 and Ru(0) occur at a binding energies of 279.96 eV and 280.05 eV, respectively. Ruthenium in the sulfide appears to lie very close in binding energy to the zero-valent ruthenium in the metal. From simple electrostatic arguments, the ruthenium in RuS_2 seems to be slightly reduced relative to a ruthenium atom in Ru(0) metal since the binding energy of the Ru $3d_{5/2}$ peak is less for the sulfide than for the metal. However, ruthenium atoms in RuO_2 are oxidized relative to a ruthenium atom in Ru(0) metal since the binding energy of the Ru $3d_{5/2}$ peak is greater for the oxide than for the metal. This result comes as a surprise because the formal oxidation state of the ruthenium atoms in the sulfide is supposed to be +2. These results indicate that RuS_2 is held together by largely covalent instead of ionic forces. The ruthenium atoms in RuS_2 may actually exhibit a very small positive or zero charge.

Table 13.

Peak positions and splitting of the Ru 3d region obtained via HR-ESCA for the following polycrystalline compounds: RuS_2, Ru(0), and RuO_2.

	Peak Positions (eV)		Spin Orbit
Sample	Ru $3d_{3/2}$	Ru $3d_{5/2}$	Splitting (eV)
RuS_2	284.05	279.96	4.09
Ru(0)	284.17	280.05	4.12
RuO_2	284.93	280.70	4.23

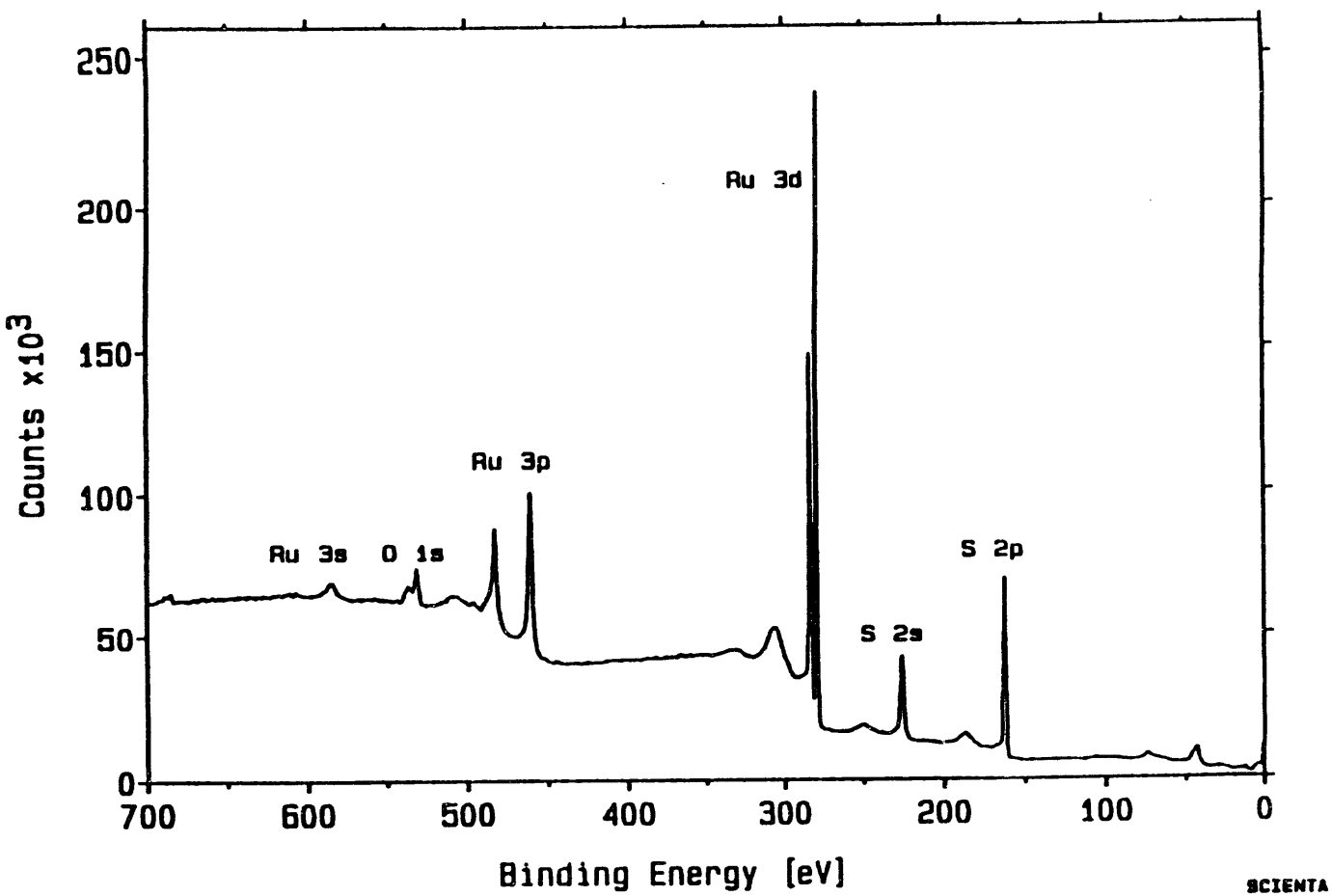

Figure 20a. Survey spectrum of polycrystalline RuS_2. Spectral parameters were the following: pass energy, E_p, 300 eV; step size, 0.6 eV; slit width, 1.1 mm; and transmission mode.

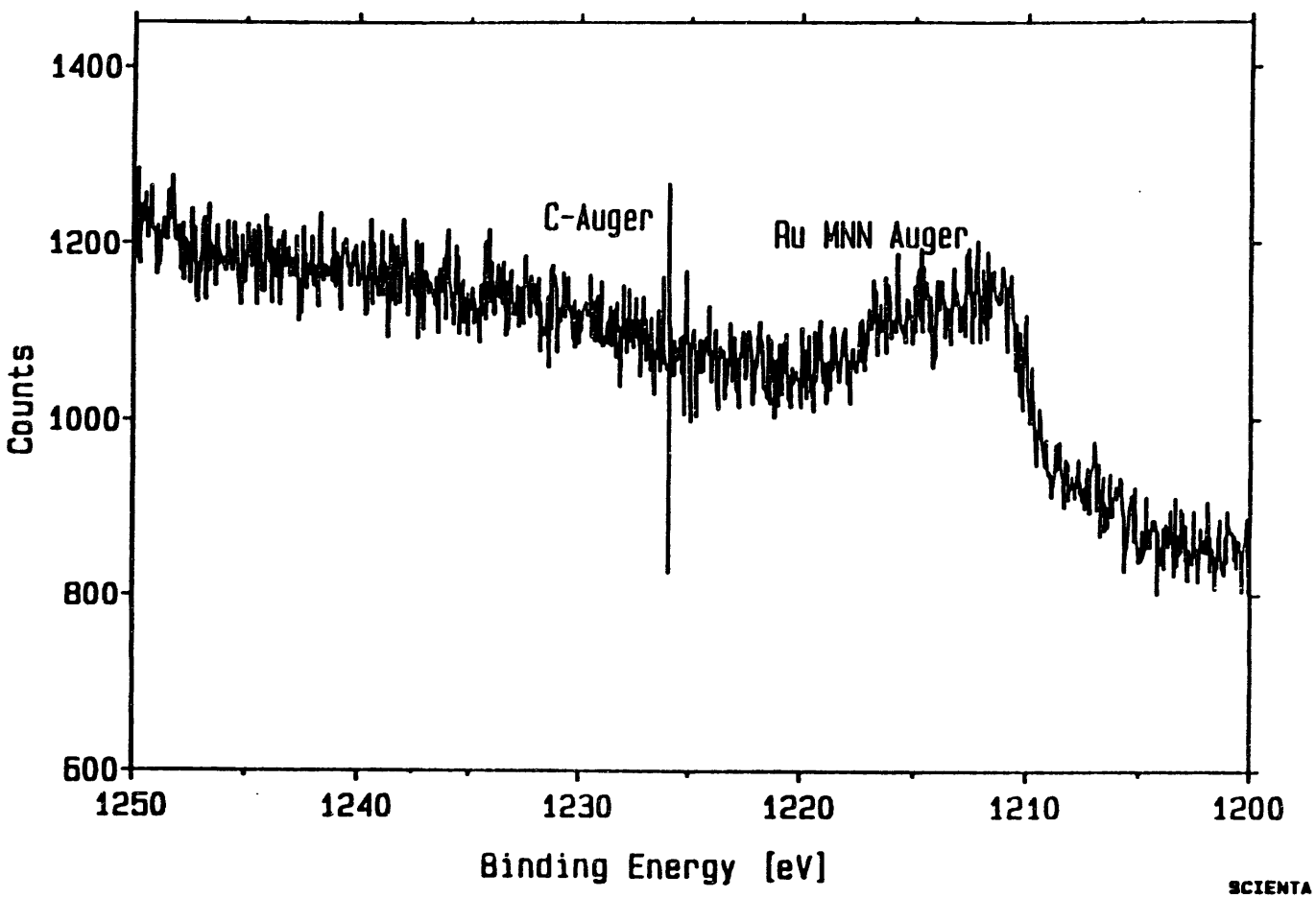

Figure 20b. Carbon Auger region of polycrystalline RuS_2. Spectral parameters were the following: pass energy, E_p, 75 eV; step size, 0.05 eV; time/step, 0.04 sec; slit width, 1.1 mm; and transmission mode.

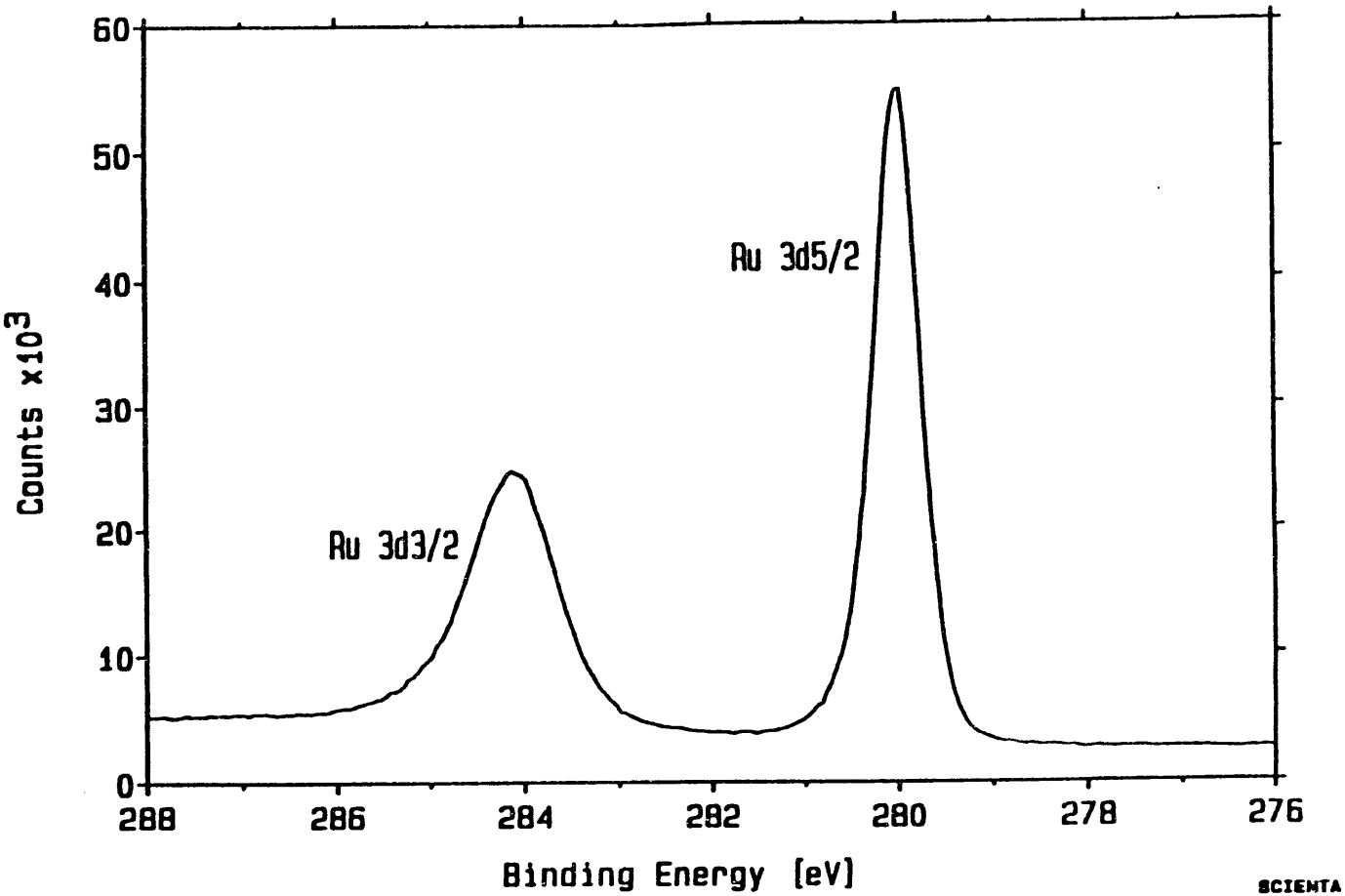

Figure 20c. Core level ruthenium 3d region of polycrystalline RuS_2. Spectral parameters were the following: pass energy, E_p, 75 eV; step size, 0.05 eV; time/step, 0.04 sec; slit width, 1.1 mm; and transmission mode.

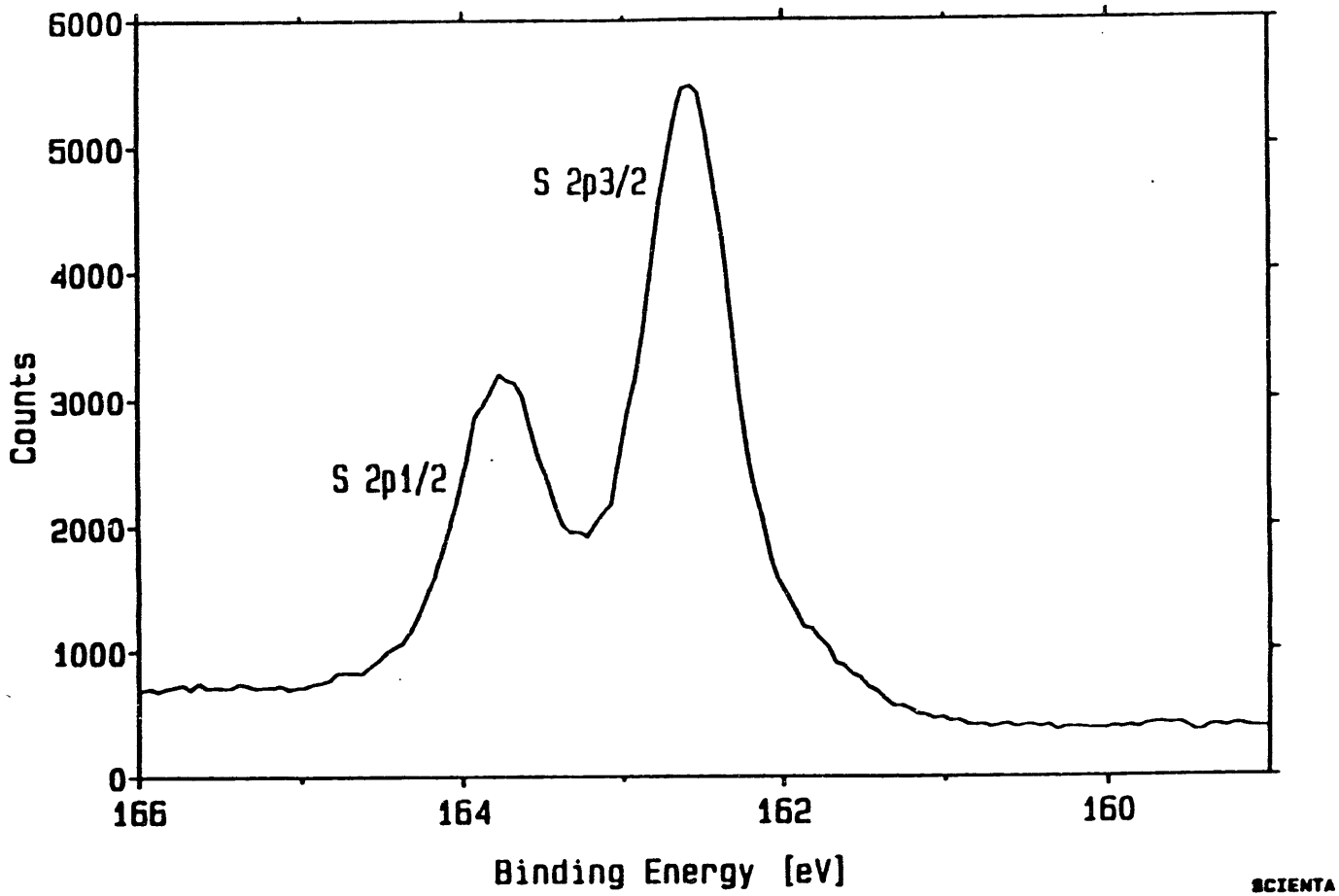

Figure 20d. Core level sulfur 2p region of polycrystalline RuS_2. Spectral parameters were the following: pass energy, E_p, 75 eV; step size, 0.05 eV; time/step, 0.04 sec; slit width, 1.1 mm; and transmission mode.

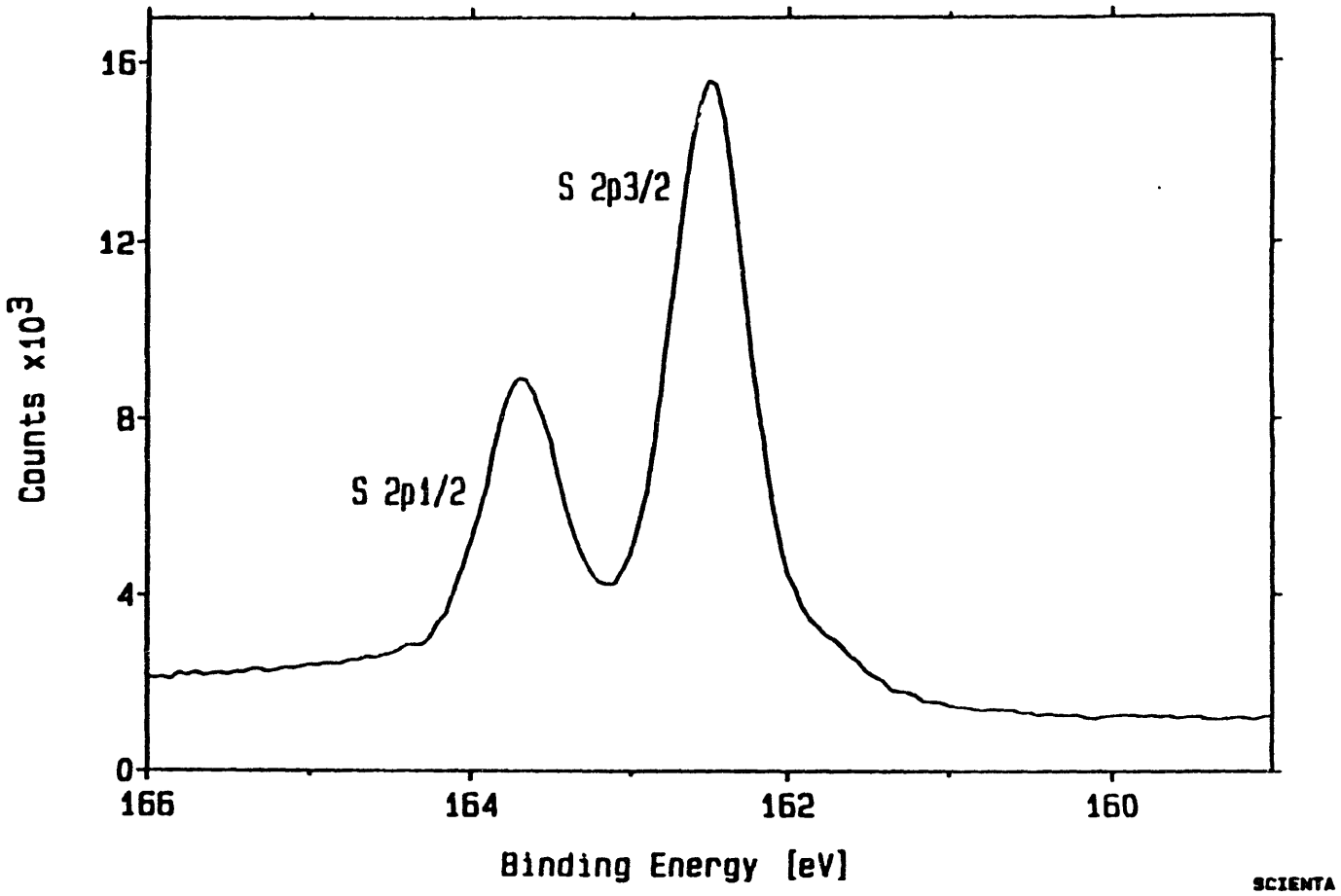

Figure 20e. Core level sulfur 2p region of single crystal (100) FeS_2. Spectral parameters were the following: pass energy, E_p, 75 eV; step size, 0.05 eV; time/step, 0.04 sec; slit width, 1.1 mm; and transmission mode.

The symmetric and narrow peaks in the S 2p region shown in Figure 20d indicate the presence of only one oxidation state of sulfur. No sulfate–type species were found to be present on the surface of this sample. A qualitative analysis of the sulfur to ruthenium atomic surface ratio using corresponding photoelectron areas and Scofield cross–sections resulted in a value of ca. 2 sulfur atoms per ruthenium atom on the surface. The S $2p_{3/2}$ and $2p_{1/2}$ peaks appear at 162.59 eV and 163.73 eV with a splitting of 1.14 eV. The S $2p_{3/2}$ peak in polycrystalline MoS_2 appears at 161.88 eV. Thus, the sulfur atoms in pyritic RuS_2 are oxidized relative to sulfur atoms in layered MoS_2 but reduced relative to a sulfur, S_n, species. Formal oxidation states for sulfur atoms in layered MoS_2 and pyritic RuS_2 are -2, from S^{2-} species, and -1, from $(S_2)^{2-}$ species, respectively. The binding energies of the S 2p region follow the change in oxidation state on moving from a layered to a pyritic transition metal disulfide.

To investigate the changes in binding energies (and hence oxidation states) of the transition metal and sulfur on proceeding from layered to pyritic structures, a second type of pyritic material, naturally occurring pyrite, FeS_2, was studied via HR–ESCA. A natural single crystal of pyrite, FeS_2, was obtained from Ward's Natural Science Establishment. This crystal was obtained naturally in the cubic modification. Thus, simply cutting the surface parallel to one of the cubic planes gave the (100) surface of FeS_2. Back–reflection Laue was used to verify the assignment of (100) to the FeS_2 surface.

HR–ESCA analysis of the Fe 2p region of this sample indicated the existence of only one iron oxidation state. The Fe $2p_{3/2}$ peak in the sulfide appeared at a binding energy of 707.08 eV. Literature values for the Fe $2p_{3/2}$ peak in metallic iron, Fe(0), and FeS_2 are 706.8 eV and 706.5 eV, respectively.[52] Thus, iron in the sulfide appears at approximately the same position as iron in the metallic state. This situation is similar to that of the ruthenium in pyritic RuS_2.

The S 2p region of pyritic FeS_2, as shown in Figure 20e, indicates the presence of only one sulfur oxidation state. The S $2p_{3/2}$ and S $2p_{1/2}$ peaks appear at 162.48 eV and 163.68 eV with a splitting of 1.20 eV. The S $2p_{3/2}$ peak in pyritic RuS_2 appeared at 162.59 eV. Thus, the binding energies of the S 2p peaks are very similar for pyritic compounds.

Table 14 lists the S 2p binding energies for a variety of TS_2 compounds as obtained via HR–ESCA analysis. As mentioned previously, the S 2p peaks of a zero–valent sulfur species, S_n, appear at $\sim$ 164 eV. Thus, sulfur atoms in both the layered and the pyritic structures are reduced relative to a zero–valent species. However, sulfur atoms in layered compounds are reduced to a greater extent than sulfur atoms in pyritic compounds. The S 2p region of pyritic RuS_2 and layered MoS_2 are compared in Figure 21. Thus, the S 2p region can be used to

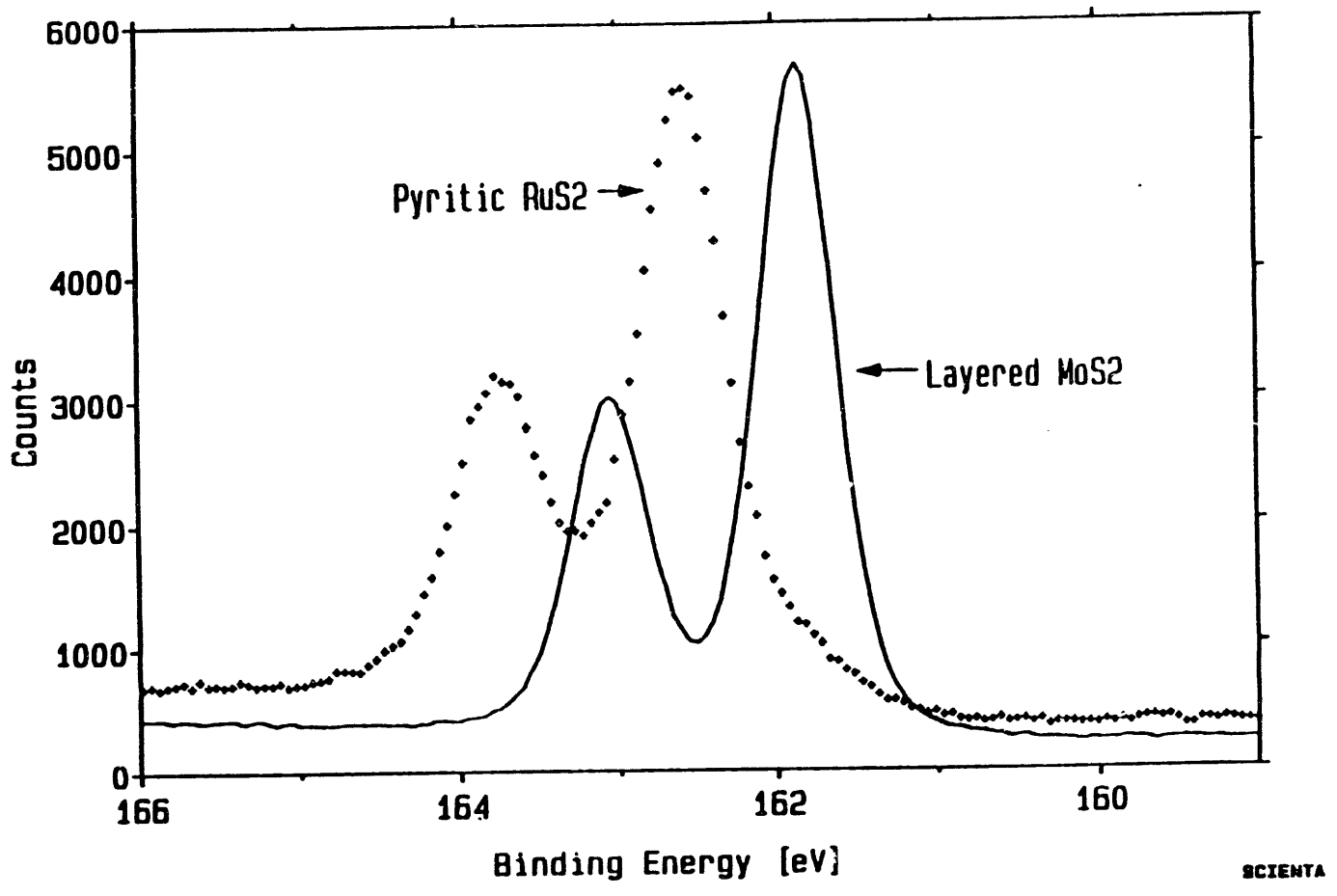

Figure 21. Comparison of the S 2p region of pyritic RuS_2 and layered MoS_2.

distinguish pyritic-type sulfur from layered-type sulfur. To summarize the HR-ESCA results discussed above, S $2p_{3/2}$ photoelectron peaks for pyritic and layered compounds appear at $\sim$ 162.5 eV and 161.8 eV, respectively. Also, the 3d peaks of transition metals in pyritic TS_2 compounds appear at approximately the same position as a zero-valent species; the 3d peaks of transition metals in layered TS_2 compounds appear at higher binding energy (positive oxidation state) when compared to zero-valent species.

Table 14.

Binding energies and splittings of the S $2p_{1/2}$ and $2p_{3/2}$ photoelectron peaks for the listed TS_2 compounds. Note the difference between pyritic and layer compounds. (S 2p binding energy for WS_2 obtained from Reference 50, units are eV.

TS_2	Structure	S $2p_{1/2}$	S $2p_{3/2}$	Spin Orbit Splitting
RuS_2	Pyritic	163.73	162.59	1.14
FeS_2	Pyritic	163.68	162.48	1.20
NbS_{2-x}	Layered	163.06	161.82	1.24
MoS_2	Layered	163.07	161.88	1.19
WS_2	Layered		161.8[25]	

4.2 Valence Band Analysis of Polycrystalline $NbS_{(2-x)}$, MoS_2, and RuS_2.

Valence band spectra of polycrystalline samples were acquired for longer periods of time compared to the corresponding core levels discussed above. In general valence levels exhibit very low intensity. The intensity of the valence levels compared to the core levels can be seen on the survey scans of MoS_2 and RuS_2 discussed in the preceding sections (Sections 4.1.1 and 4.1.3). Comparison of the valence region between binding energies of $\sim$ 20 eV - 0 eV to that of the transition metal 3d core levels shows the low intensity of the valence band region compared to the core levels.

Using Al K_α radiation as the source of x-rays, valence levels appear at low binding energies, $\sim$ 20 eV - 0 eV, with high kinetic energies, $\sim$ 1466 eV - 1486 eV. Analysis of the universal curve for attenuation length, λ, of photoelectrons vs. photoelectron kinetic energy, shows that photoelectrons from the valence band (using Al K_α radiation) originate from approximately 14 monolayers.[54] Thus, valence band spectrum obtained using Al K_α radiation are fairly representative of the bulk compound. Small amounts of surface contaminants such as carbon and oxygen do not affect the appearance of the valence band to a great extent. Thus, in this section, the valence band of the non-stoichiometric polycrystalline $NbS_{(2-x)}$ will be used to

represent the valence band of NbS_2.

Valence bands obtained with the use of the present HR-ESCA for $NbS_{(2-x)}$, MoS_2, RuS_2, and FeS_2 are shown in Figures 22a, 22b, 22c, and 22d, respectively. The valence bands shown reflect the difference in structure, layered for NbS_2 and MoS_2 and pyritic for RuS_2, and the difference in the number of 4d electrons. The valence bands of $NbS_{(2-x)}$ and MoS_2 show two distinct regions. The first region appears at approximately 14 eV binding energy, this region will be referred to as the S3s valence band region. The second region extends from approximately 0 eV (the Fermi level of the instrument) to 8 eV. This region is generally referred to as the metal 4d-S3p region. In both cases, the metal 4d-S3p region consists of 4 distinct peaks. In the case of $NbS_{(2-x)}$, the topmost peak extends past 0 eV and exhibits a sharp drop at the Fermi level identifying this sample as metallic. Stoichiometric NbS_2 is known to possess metallic conductivity. MoS_2 is known to be a small band gap semiconductor. The valence band region of MoS_2 shown in Figure 22b does not possess significant electron density above 0 eV binding energy, confirming the semiconducting nature of this sample. The upper portion of the valence band regions, metal 4d-S3p region, for both $NbS_{(2-x)}$ and $\overline{MoS_2}$ are plotted together in Figure 22e. Differences in the topmost portion of valence band (near 0 eV) are more apparent in Figure 22e.

The valence band of polycrystalline pyritic RuS_2, as shown in Figure 22c, is quite different from the valence bands of the layered compounds, NbS_2 and MoS_2. Again, the valence band consists of two distinct regions. The S3s region centered at approximately 14 eV, is dispersed into two or more different peaks due to the association of the sulfurs into dimer pairs, $(S_2)^{2-}$. As indicated in Section 3.6.1, the closest sulfur–sulfur distance, d_{S-S}, in RuS_2 is 2.178 Å. In NbS_2 and MoS_2, the closest sulfur–sulfur distances, d_{S-S}, are 2.97 Å and 3.16 Å, respectively. Thus, the sulfur 3s valence orbitals in pyritic RuS_2 interact to a greater extent than in the layered compounds.

The upper portion of the RuS_2 valence band, Ru4d-S3p region, extends from approximately 0 eV to 10 eV. This region is dominated by a peak at the top of the valence band centered at ~ 2 eV. Ruthenium species in RuS_2 have a formal oxidation state of +2, leaving the Ru with a d^6 configuration. Thus, contribution of Ru 4d electrons to the valence band region is high compared to the layered compounds (Nb^{+4}, d^1; Mo^{+4}, d^2). The peak centered at ~ 2 eV is generally attributed to the Ru 4d orbitals. RuS_2 is known to be a small band gap semiconductor. The valence band region, shown in Figure 22c, does not possess significant electron density beyond 0 eV. Pyritic FeS_2 exhibits a valence band similar to that of RuS_2. The valence band of FeS_2 is shown in Figure 22d.

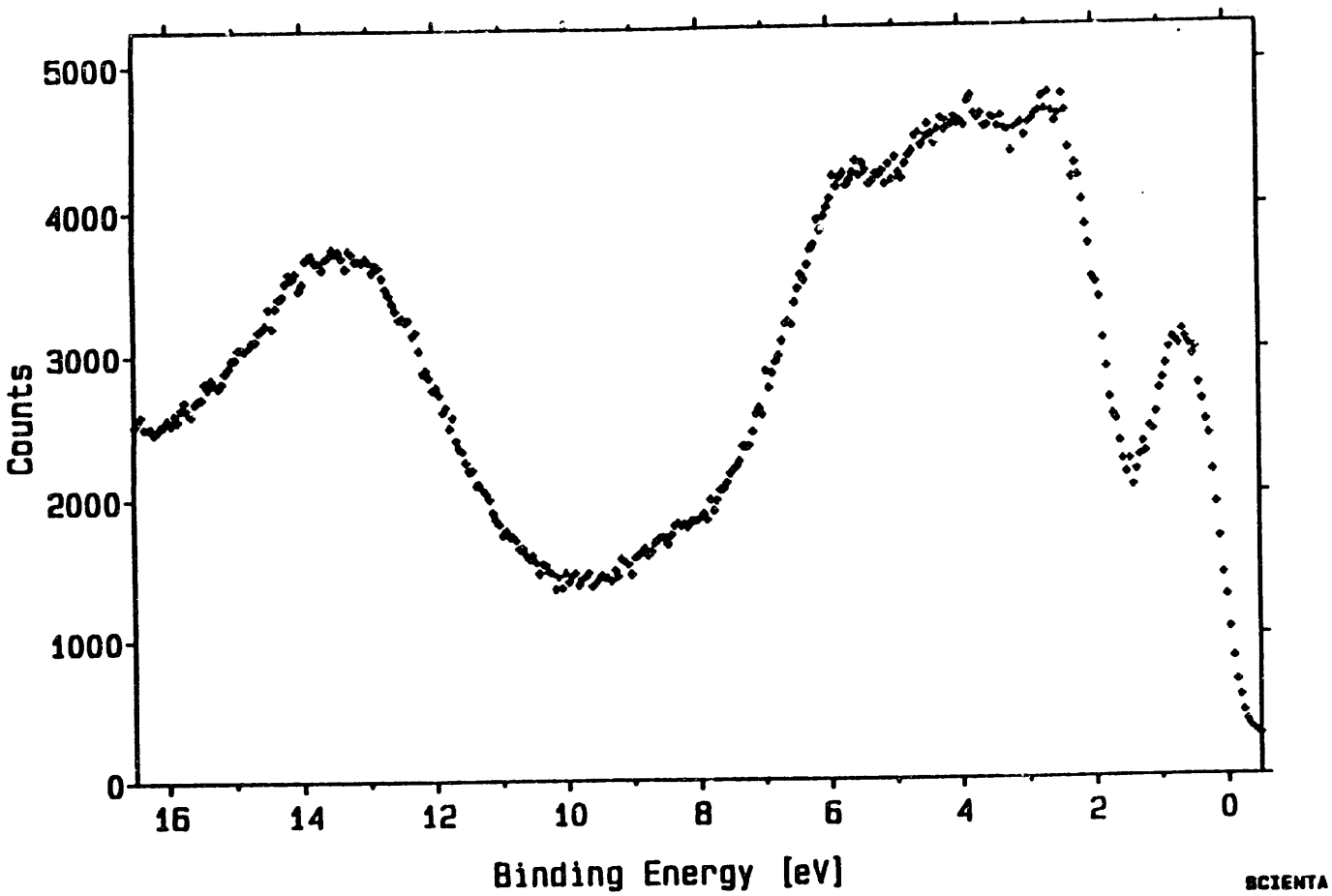

Figure 22a. Valence band region of polycrystalline $NbS_{(2-x)}$. Spectral parameters were the following: pass energy, E_p, 75 eV; step size, 0.05 eV; slit width, 1.1 mm; and transmission mode.

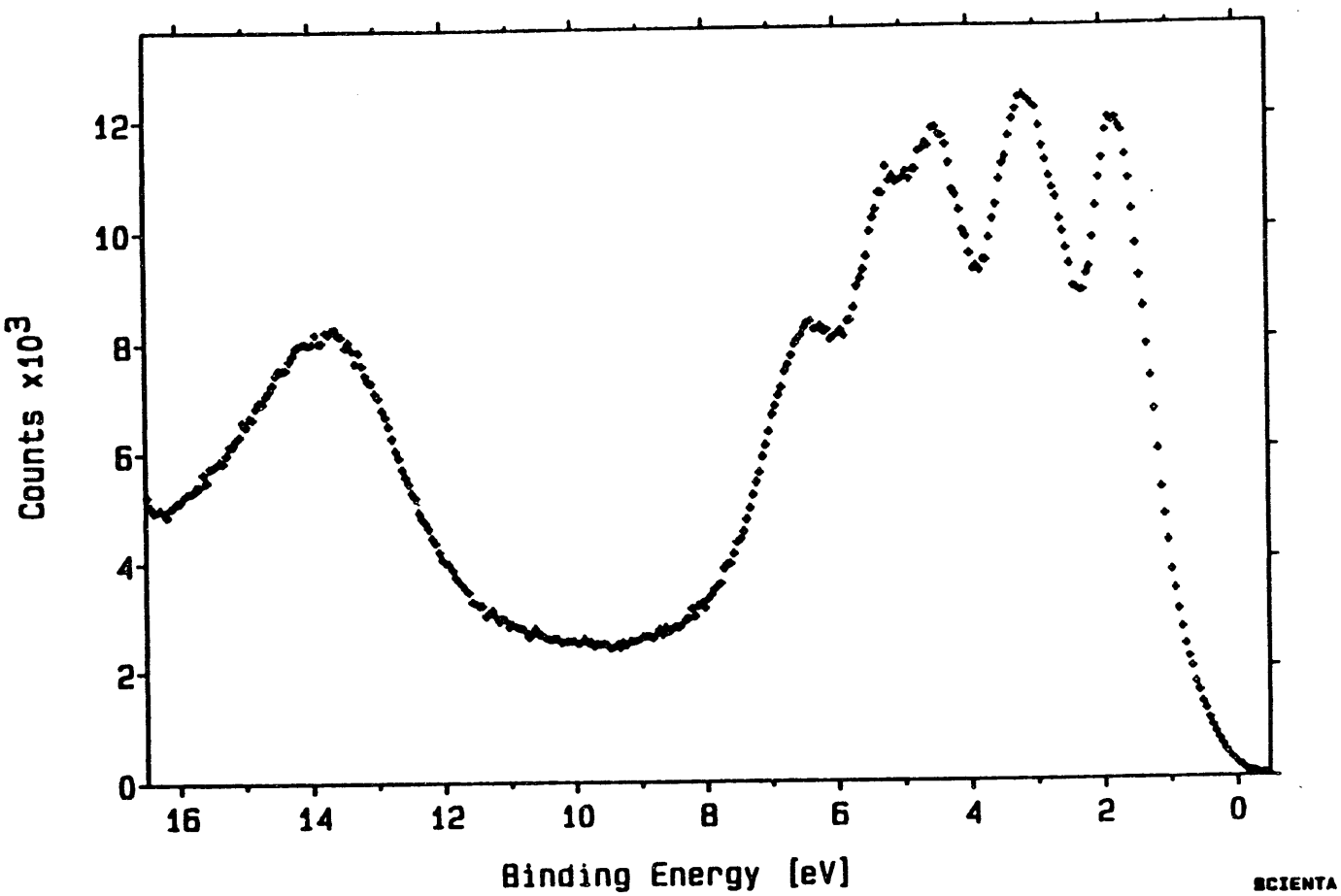

Figure 22b. Valence band region of polycrystalline MoS_2. Spectral parameters were the following: pass energy, E_p, 75 eV; step size, 0.05 eV; slit width, 1.1 mm; and transmission mode.

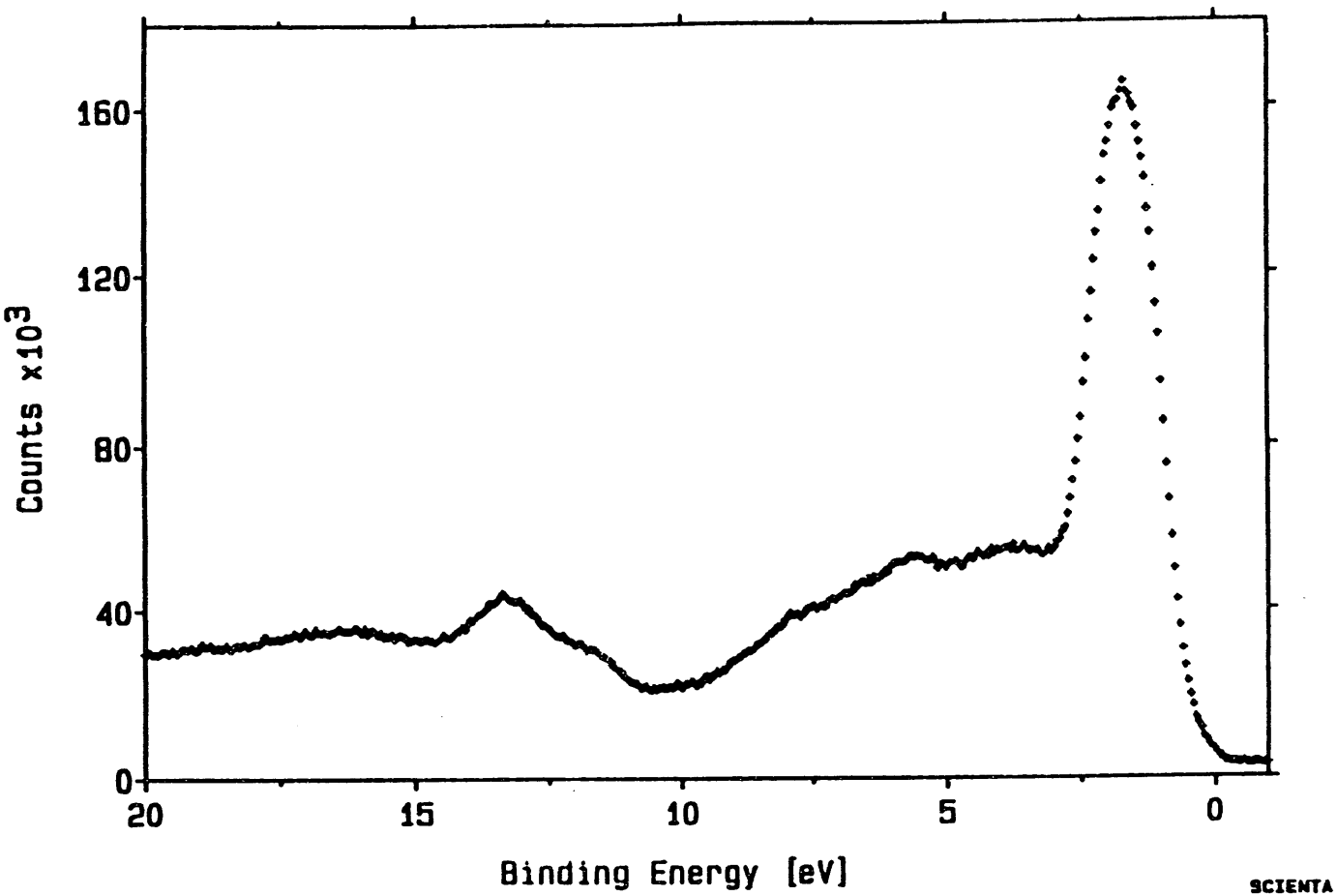

Figure 22c. Valence band region of polycrystalline RuS_2. Spectral parameters were the following: pass energy, E_p, 75 eV; step size, 0.05 eV; slit width, 0.8 mm; and spatial mode.

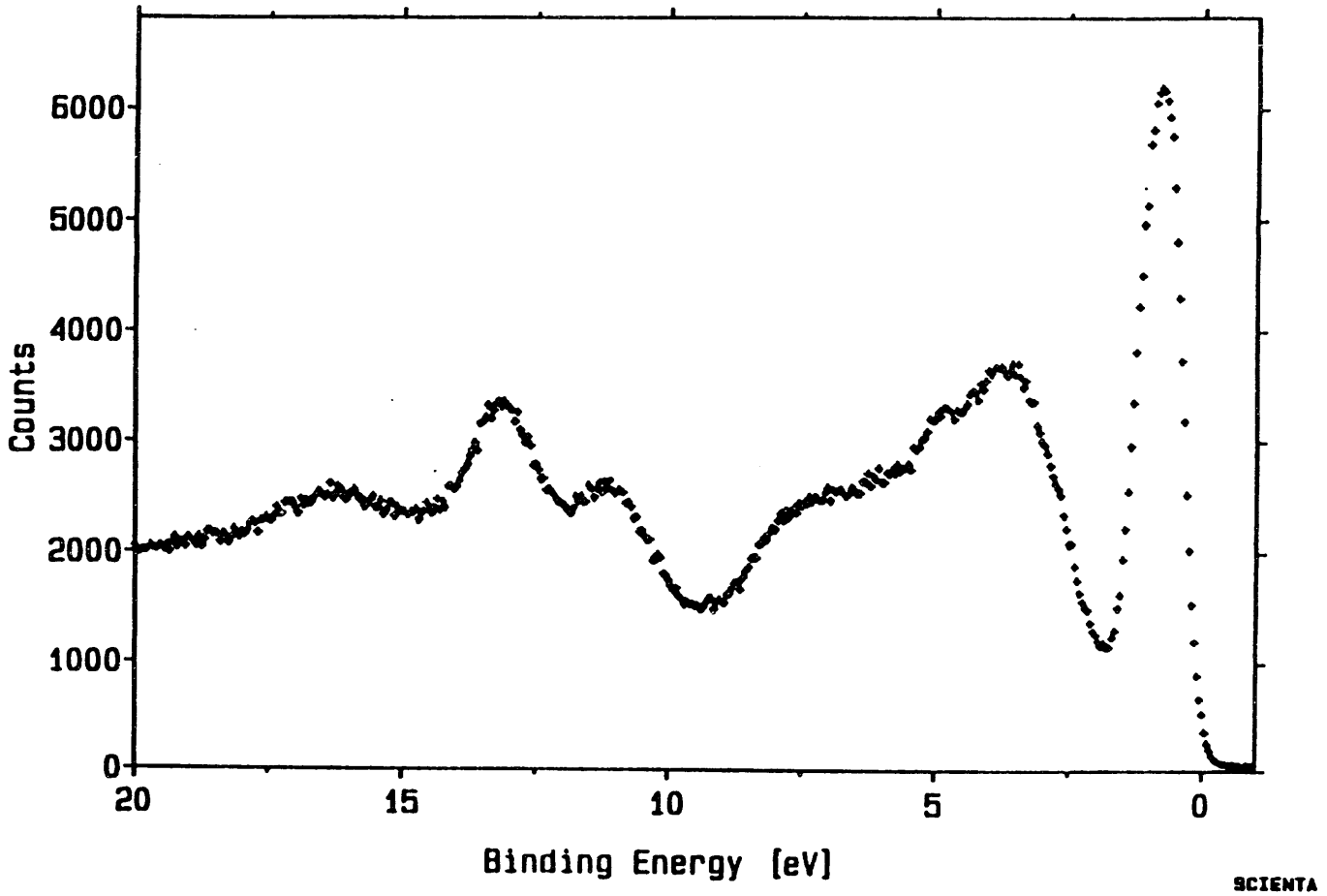

Figure 22d. Valence band region of single crystal FeS_2. Spectral parameters were the following: pass energy, E_p, 75 eV; step size, 0.05 eV; slit width, 1.1 mm; and spatial mode.

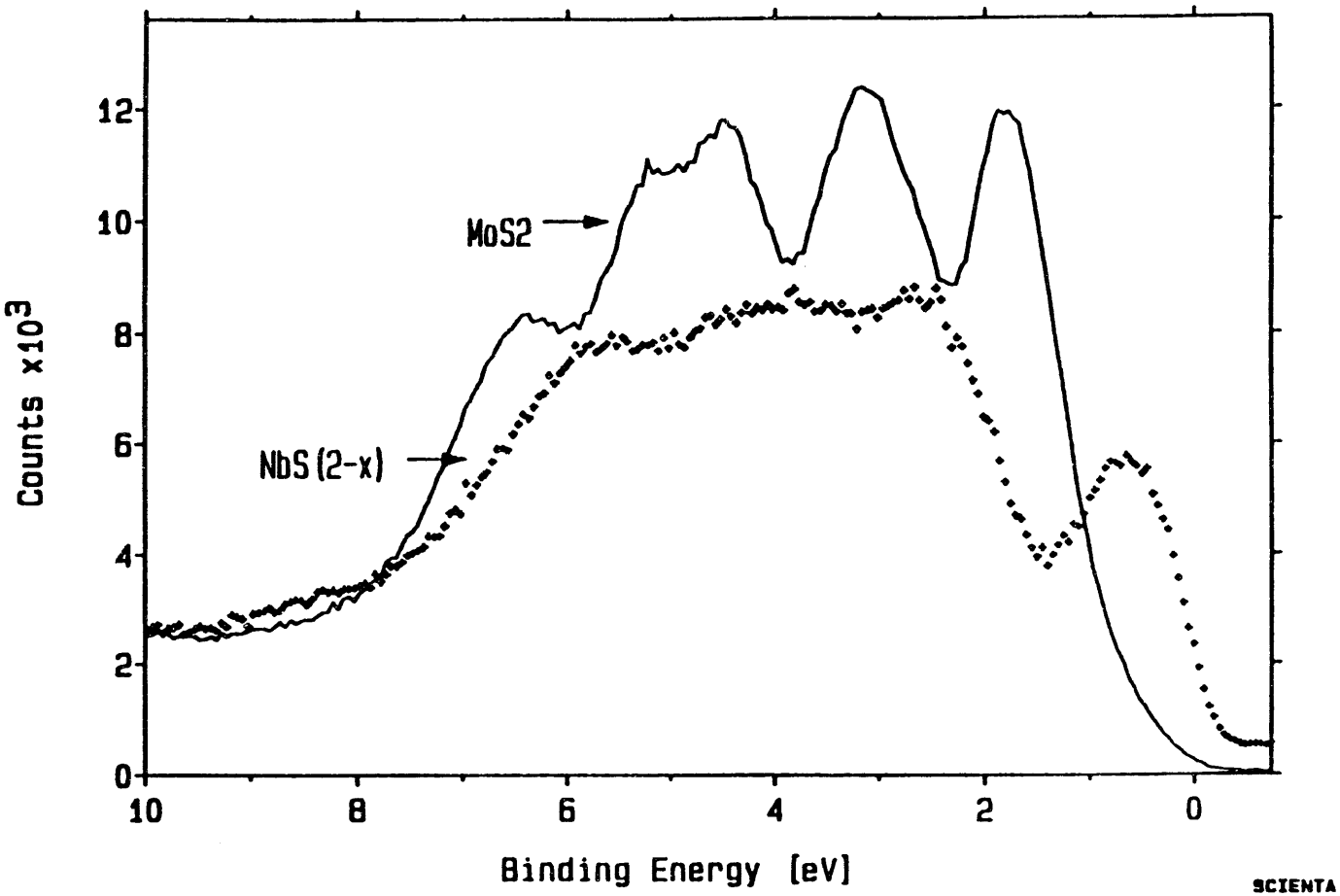

Figure 22e. Upper portion of the valence band region, metal 4d-S3p region, for both polycrystalline $NbS_{(2-x)}$ and MoS_2. Note the difference in electron density at the very top of the valence band for each compound.

Valence band regions of the polycrystalline samples will be discussed in more detail in Chapter 6. Chapter 5 presents theoretical results of an electronic study of NbS_2, MoS_2, and RuS_2 using the EHMACPP program discussed previously (Chapter 3). Discussion, Chapter 6, will bring together experimental results (Chapter 4) and theoretical results (Chapter 5) for a better understanding of the electronic structure of the transition metal disulfides, NbS_2, MoS_2, and RuS_2.

4.3 HR-ESCA of Polycrystalline MoS_2 Exposed to Hydrogen.

4.3.1 Analysis of the Bare MoS_2 Surface.

Exposure of the polycrystalline MoS_2 used in this study was rigorously excluded prior to HR-ESCA analysis. However, small amounts of oxygen and carbon did remain on the sample surface and were not removed even by exposure of the sample surface to ~ 1 atm of hydrogen at 350°-389° C. The Mo3d region (spectra similar to Figure 19d) of the bare MoS_2 surface showed the presence of only one molybdenum oxidation state with $Mo3d_{5/2}$ and $Mo3d_{3/2}$ peaks at 229.00 and 232.17 eV. The S2p region (spectra similar to Figure 19e) showed the presence of one sulfur oxidation state with $S2p_{3/2}$ and $S2p_{1/2}$ peaks at 161.86 and 163.05 eV respectively. Au4f core levels of gold plated onto the sample holder were also monitored to assure accurate instrumental calibration during the duration of the hydrogen adsorption experiment. Prior to hydrogen adsorption, the $Au4f_{7/2}$ level appeared at 83.97 eV. A valence band spectra of this sample similar to that of Figure 22b was also obtained for this sample.

4.3.2 Analysis of the Hydrogen Exposed MoS_2 Surface.

Exposure of the MoS_2 sample to ~ 1 atm of hydrogen at room temperature for one hour resulted in only minor shifts in the Mo3d and S2p core levels. The Mo3d region of the hydrogen adsorbed sample again showed the presence of only one molybdenum oxidation state with $Mo3d_{5/2}$ and $Mo3d_{3/2}$ peaks at 229.07 and 232.23 eV respectively. The S 2p region showed the presence of one sulfur oxidation state with $S2p_{3/2}$ and $S2p_{1/2}$ peaks at 161.92 and 163.11 eV respectively. Both Mo3d and S2p core levels shifted to higher binding energy by $\sim +0.06 \rightarrow +0.07$ eV. Figures 23a and 23b show the Mo3d and S2p core levels respectively for the bare MoS_2 surface and the surface exposed to hydrogen at room temperature. Although the shift to higher binding energies upon hydrogen adsorption is small, this shift is easily seen for the $Mo3d_{5/2}$ and $S2p_{3/2}$ core levels. Analysis of the gold plated on the sample holder indicated no corresponding shift to higher binding energy of the $Au4f_{7/2}$ core level. The $Au4f_{7/2}$ level appeared at 83.98 eV after exposure of the sample to hydrogen. Figure 23c shows the two Au4f

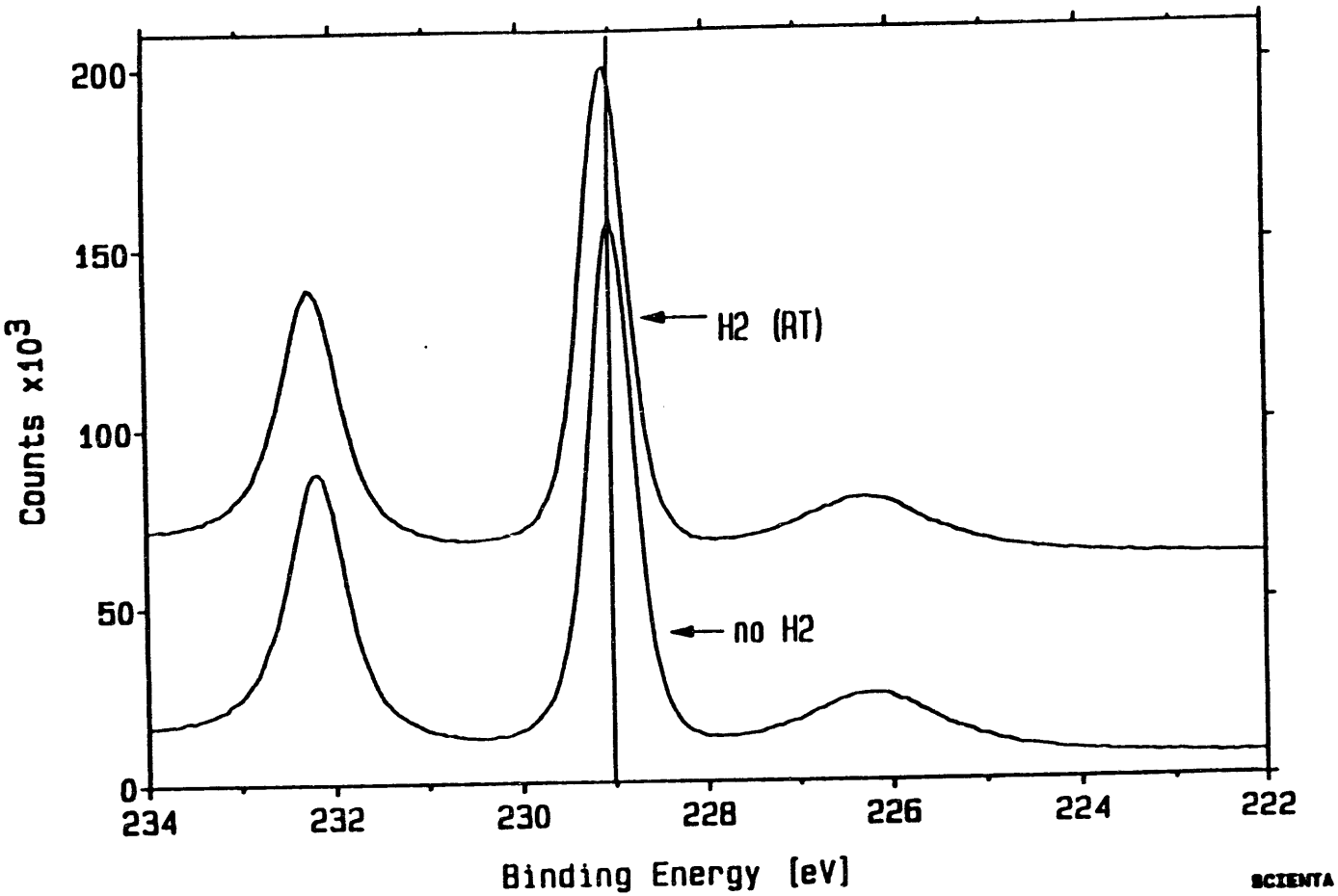

Figure 23a. Core level Mo3d region of polycrystalline MoS_2 obtained via HR-ESCA. The lower spectrum shows the Mo3d region of the bare surface while the upper spectrum show the Mo3d region of the surface after exposure to hydrogen at room temperature for a period of one hour. (RT=room temperature)

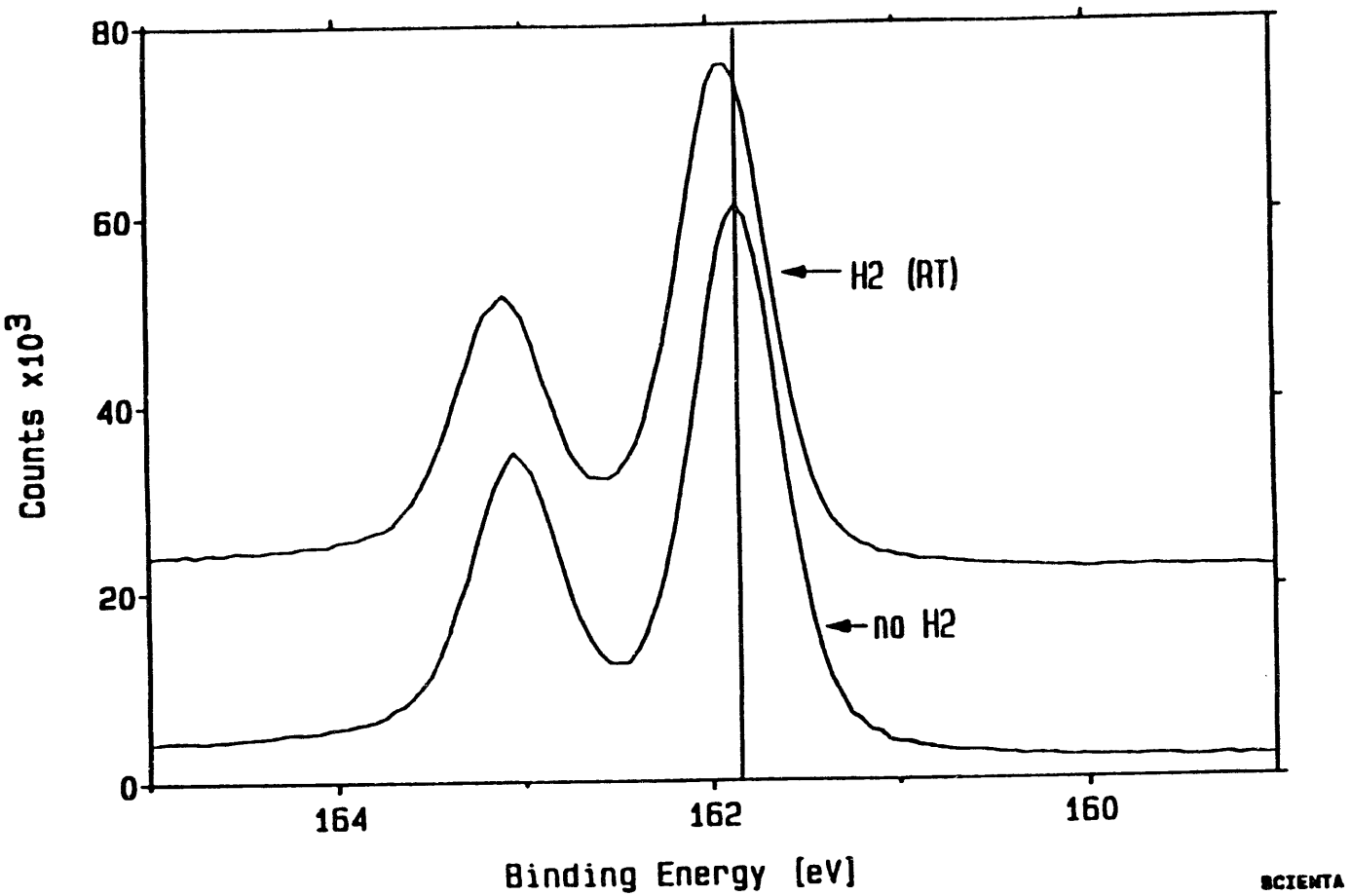

Figure 23b. Core level S2p region of polycrystalline MoS_2 obtained via HR-ESCA. The lower spectrum shows the S2p region of the bare surface while the upper spectrum shows the S2p region of the surface after exposure to hydrogen at room temperature for a period of one hour. (RT=room temperature)

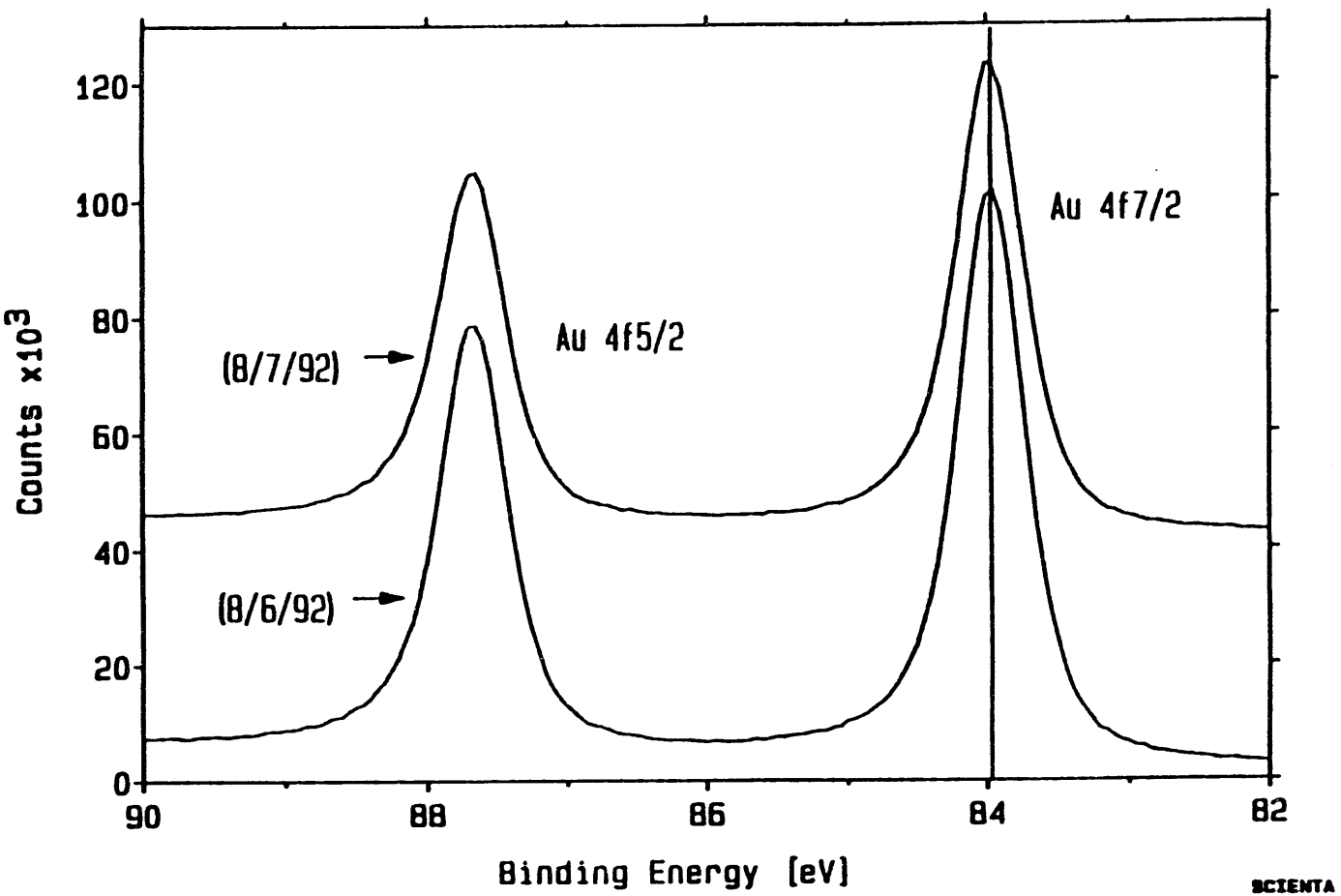

Figure 23c. Core level Au4f region of gold plated onto the sample holder. The lower spectrum was obtained prior to exposure of the sample to hydrogen (8/6/92) while the upper spectrum was obtained after exposure of the sample to hydrogen (8/7/92) at room temperature for a period of one hour.

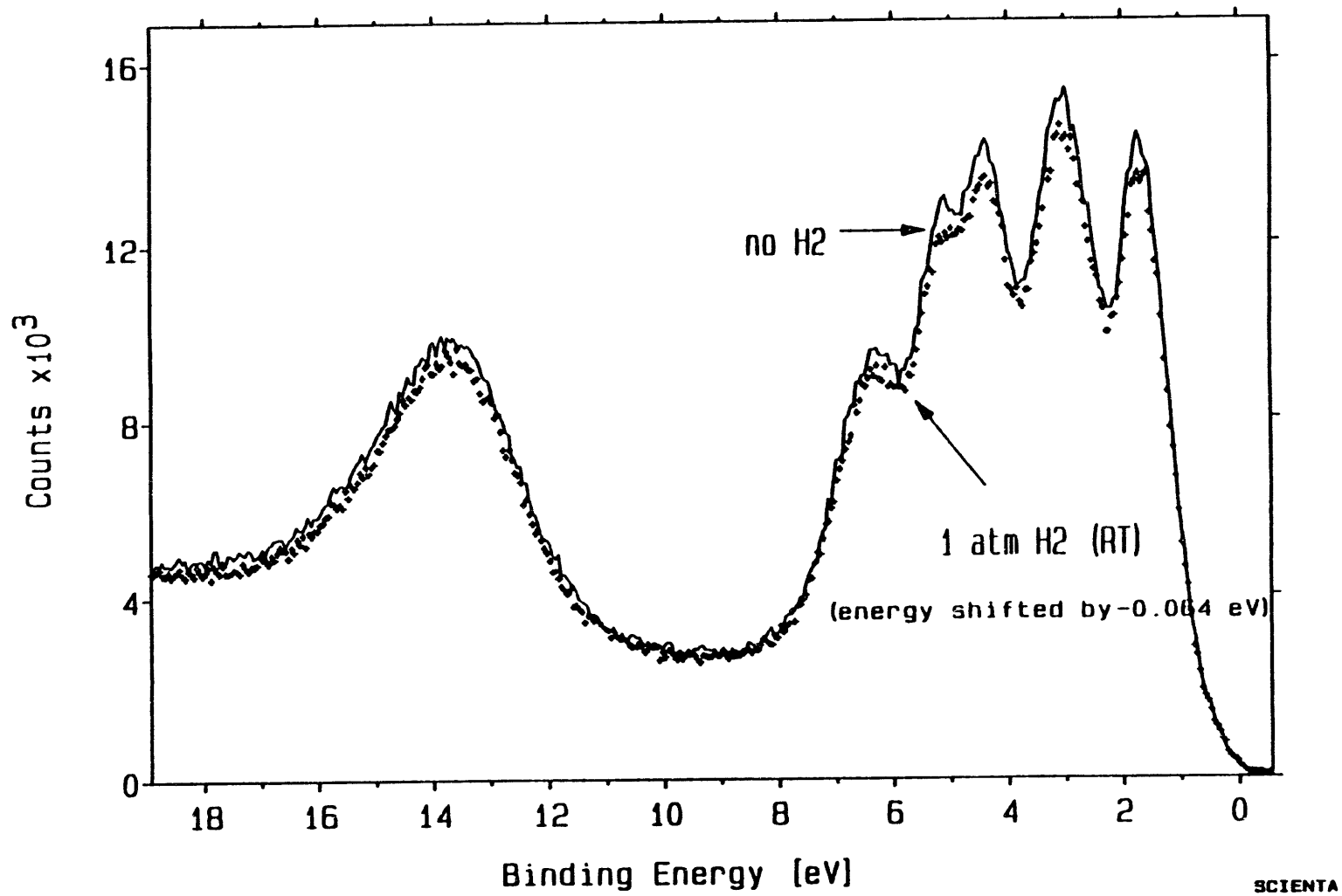

Figure 23d. Valence band regions of the bare MoS_2 surface (solid line) and the surface exposed to hydrogen at room temperature for a period of one hour (crosses). The valence band spectrum of the hydrogen adsorbed sample was shifted by -0.064 eV to lower binding energies for ease of comparison (RT=room temperature).

regions obtained at different points in the experiment. The Au4f spectrum obtained on 8/6/92 was obtained prior to hydrogen adsorption, while the Au4f spectrum obtained on 8/7/92 was obtained after exposure of the sample to hydrogen. Thus, changes in the instrumental calibration can be ruled out as the origin in the Mo3d and S2p binding energy shifts. Exposure of the sample to hydrogen also seemed to shift the entire valence band to higher binding energies by $\sim +0.06$ eV. Figure 23d shows the two valence band regions obtained for the bare MoS_2 surface and the surface exposed to hydrogen at room temperature. The valence band of the hydrogen exposed sample was shifted by -0.064 eV so that a qualitative comparison of the positions, intensities and widths could be carried out. The positions of the five major bands that makeup the Mo4d-S3p valence band are very similar after the -0.064 eV shift of the hydrogen adsorbed sample. The Mo4d-S3p band width is also very similar in both cases. Specifically, there is no widening of the Mo4d-S3p band at the top of the valence band and there is no widening of the Mo4d-S3p band at the bottom of this band. Thus, hydrogen adsorption at room temperature caused all of the levels to shift to higher binding energies by $\sim +0.06 \rightarrow +0.07$ eV. A shift of this type indicates that charging of the MoS_2 surface may be occurring upon exposure of the surface to hydrogen.

Exposure of the sample to ~ 1 atm of hydrogen at 125° C and 350°-389° C resulted in similar binding energy shifts of the Mo3d and S2p core levels. Binding energies and full widths at half maximum (FWHM) of the Mo3d and S2p core level regions obtained at normal incidence for the bare and hydrogen exposed MoS_2 surface tabulated in Table 15. Exposure of the sample

Table 15.

Binding energies (BE) and full widths at half maximum (FWHM) of the Mo3d and S2p core level regions obtained at normal incidence for the bare and hydrogen exposed MoS_2 surface. Hydrogen exposure was carried under ~ 1 atm H_2 for a period of one hour at room temperature, 125°C, and 350°-389°C. (Units are eV)

Level	Parameter	Bare	H_2, RT	H_2, 125°C	H_2, 350°-389°C
$Mo3d_{5/2}$	BE	229.00	229.07	229.07	229.04
	FWHM	0.57	0.59	0.58	0.56
$Mo3d_{3/2}$	BE	232.17	232.23	232.24	232.20
	FWHM	0.74	0.76	0.74	0.75
$S2p_{3/2}$	BE	161.86	161.92	161.93	161.91
	FWHM	0.56	0.58	0.58	0.57
$S2p_{1/2}$	BE	163.05	163.11	163.12	163.10
	FWHM	0.56	0.58	0.61	0.57

to hydrogen at room temperature caused a $\sim +0.06-+0.07$ eV shift to higher binding energies that remained throughout the experiment. No significant widening of the Mo3d and S2p core levels, as evidenced by the FWHM's given in the table above, was observed. Thus, at normal incidence only one Mo3d and one S2p oxidation state was present on the sample surface for both hydrogen exposed and bare surfaces. Again, the valence bands of the samples exposed to hydrogen at 125°C and 350°C-389°C were similar to the valence band of the bare MoS_2 surface except for the small shift to higher binding energies.

Binding energies and full widths at half maximum (FWHM's) of the Mo3d and S2p core level regions obtained at grazing angles of detection (82° off normal) are shown in Table 16. Exposure of the sample to ~ 1 atm hydrogen at 125°C shifted the Mo3d and S2p core levels obtained at grazing angle by +0.06 eV to higher binding energies. A shift to higher binding energies upon exposure of the sample to hydrogen at 350°C is not as apparent in the spectrum obtained at grazing angle. The sample used in this experiment was polycrystalline MoS_2 in the form of a powder. Due to the requirement of sample heating during hydrogen exposure, the MoS_2 powder was mounted onto a silicon wafer by pressing the powder into scratches resident on the wafer surface. Initially a smooth, continuous layer of MoS_2 powder was present on the wafer surface. The frequent hydrogen exposures, sample heating and sample transfers inside the HR-ESCA chambers caused the continuous layer of powder to crack and thin with subsequent loss of MoS_2 powder from the sample holder. After exposure of the sample to hydrogen at 350°C-389°C, only a small amount of MoS_2 powder remained on the sample holder. Extensive sample manipulation was necessary to obtain a survey spectrum that did not record core levels due to the underlying silicon wafer. Thus, core level and valence band peak intensities obtained at grazing angle of detection after hydrogen exposure at 350°C-389°C were not as intense as for bare MoS_2. However, the peak positions and full widths at half maximum can still be compared. The valence band regions obtained at grazing angle of detection for the bare MoS_2 surface and the same surface exposed to hydrogen at 350°C-389°C are shown in Figure 24. The valence band of the hydrogen exposed surface was multiplied by 1.18 so that the background intensity of the two spectra was similar. The two spectra are very similar except that the hydrogen exposed sample exhibits extra intensity at the top of the valence band (at ~ 0 eV). This extra intensity at the top of the valence band could be attributed to the filling of previously empty states at the top of the valence band or to destabilization of the highest occupied crystal orbitals upon hydrogen adsorption. Possible origins of the valence band and core level changes upon hydrogen exposure will be addressed in the Discussion of Chapter 6.

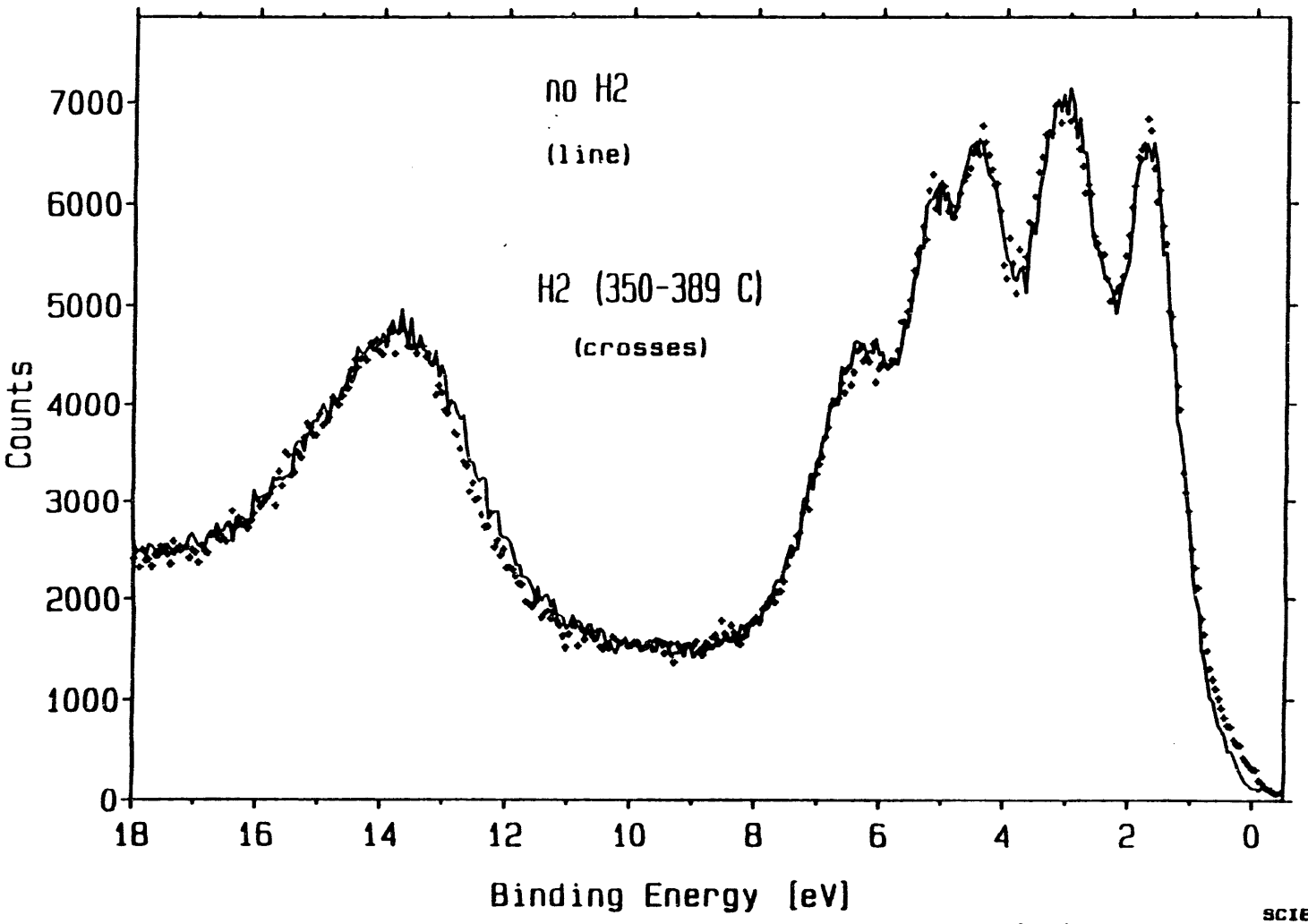

Figure 24. Valence band regions obtained at grazing angle of detection for the bare MoS_2 surface and the same surface exposed to hydrogen at 350°C 389°C. The valence band region of the hydrogen exposed surface was multiplied by 1.18 so that a similar background intensity was achieved.

Table 16.

Binding energies (BE) and full widths at half maximum (FWHM) of the Mo3d and S2p core level regions obtained at grazing angle of detection (82° of normal) for the bare and hydrogen exposed MoS_2 surface. Hydrogen exposure was carried under ~ 1 atm H_2 for a period of one hour at 125°C and 350°-389°C. (Units are eV)

Level	Parameter	Bare	H_2, 125°C	H_2, 350°-389°C
$Mo3d_{5/2}$	BE	229.03	229.09	229.04
	FWHM	0.59	0.60	0.58
$Mo3d_{3/2}$	BE	232.20	232.25	232.21
	FWHM	0.76	0.77	0.77
$S2p_{3/2}$	BE	161.89	161.95	161.91
	FWHM	0.59	0.60	0.58
$S2p_{1/2}$	BE	163.07	163.13	163.10
	FWHM	0.64	0.65	0.58

4.4 HR-ESCA Analysis of MoS_2 Single Crystal.

4.4.1 Analysis of Surface Contamination

As indicated in Section 2.1.1, the MoS_2 single crystal used for the angle resolved studies was oriented by back reflection Laue diffraction. Thus, this crystal was exposed to air prior to analysis via HR-ESCA. A survey spectrum of the MoS_2 single crystal is shown in Figure 25a. The surface of this sample consists mainly of molybdenum and sulfur atoms with minor contamination by carbon and oxygen. A rough estimate of the level of the carbon impurity gave a surface composition of ~ 2.4 molybdenum atoms per carbon atom.

Regional scans of the Mo 3d and S 2p peaks are shown in Figure 25b and 25c. The Mo $3d_{5/2}$ and $3d_{3/2}$ peaks occur at 229.06 eV and 232.24 eV, respectively, with a splitting of 3.18 eV. These binding energies were corrected for the Au calibration by shifting the peaks by -0.3 eV. The Mo $3d_{5/2}$ peak position in polycrystalline MoS_2 occurred at 229.05 eV, thus the values for single crystal MoS_2 are in good agreement with those of the polycrystalline sample.

The symmetric and narrow peaks in the S 2p region for single crystal MoS_2, shown in Figure 25c, indicate the presence of only one sulfur oxidation state. No sulfate species were found on this surface even though the surface was exposed to air. S $2p_{3/2}$ and $2p_{1/2}$ peaks are situated at binding energies of 161.91 eV and 163.11 eV (corrected by the -0.3 eV of Au calibration), respectively, with a splitting of 1.20 eV. The S $2p_{3/2}$ peak of polycrystalline MoS_2 was found at a binding energy of 161.88 eV. Thus, this surface, as expected, has characteristics similar to those of the polycrystalline, layered MoS_2 discussed in Sections 4.1.1 and 4.1.3.

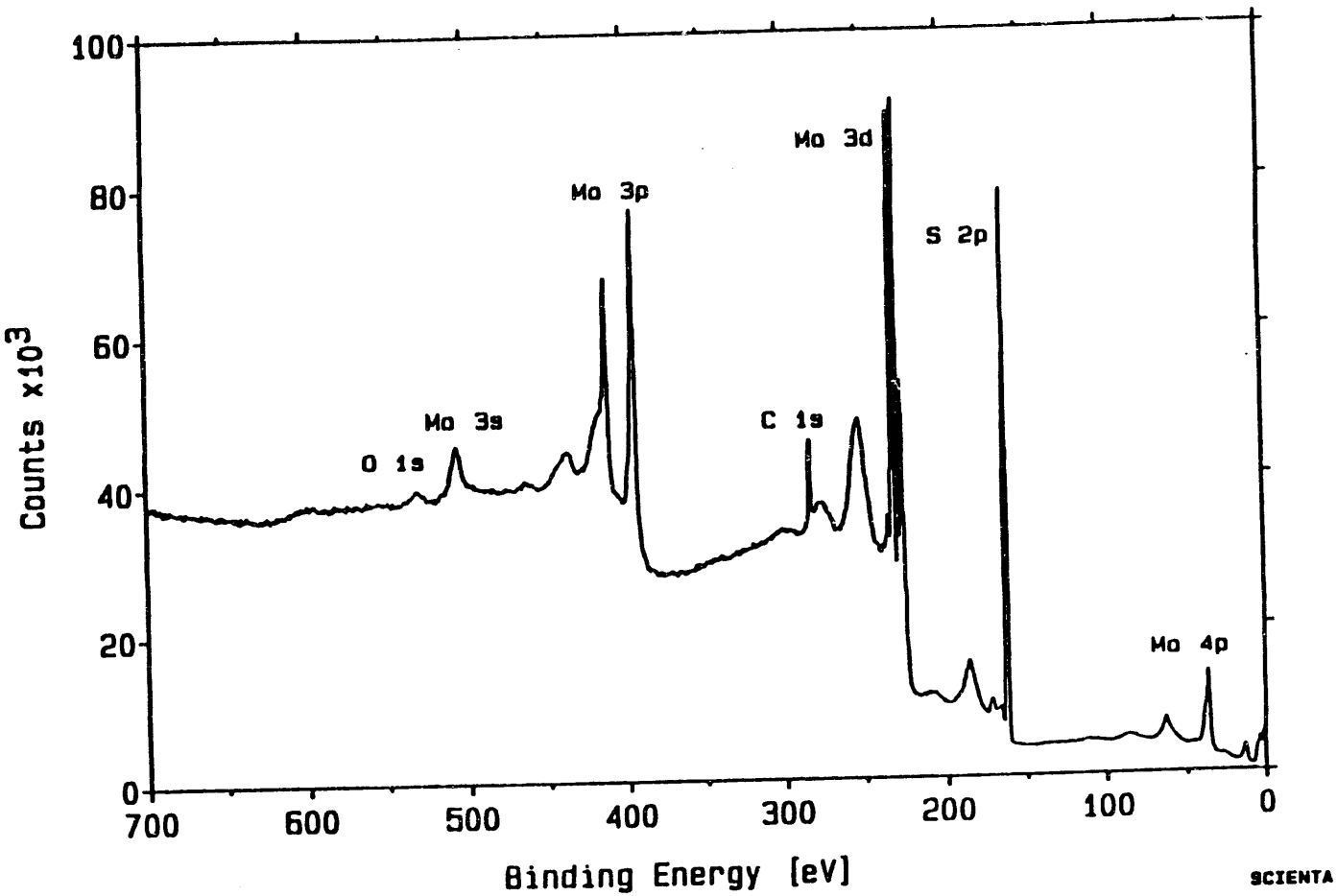

Figure 25a. Survey spectra of MoS_2 single crystal. Spectral parameters were the following: pass energy, E_p, 300 eV; step size, 0.5 eV; slit width, 1.1 mm; and transmission mode.

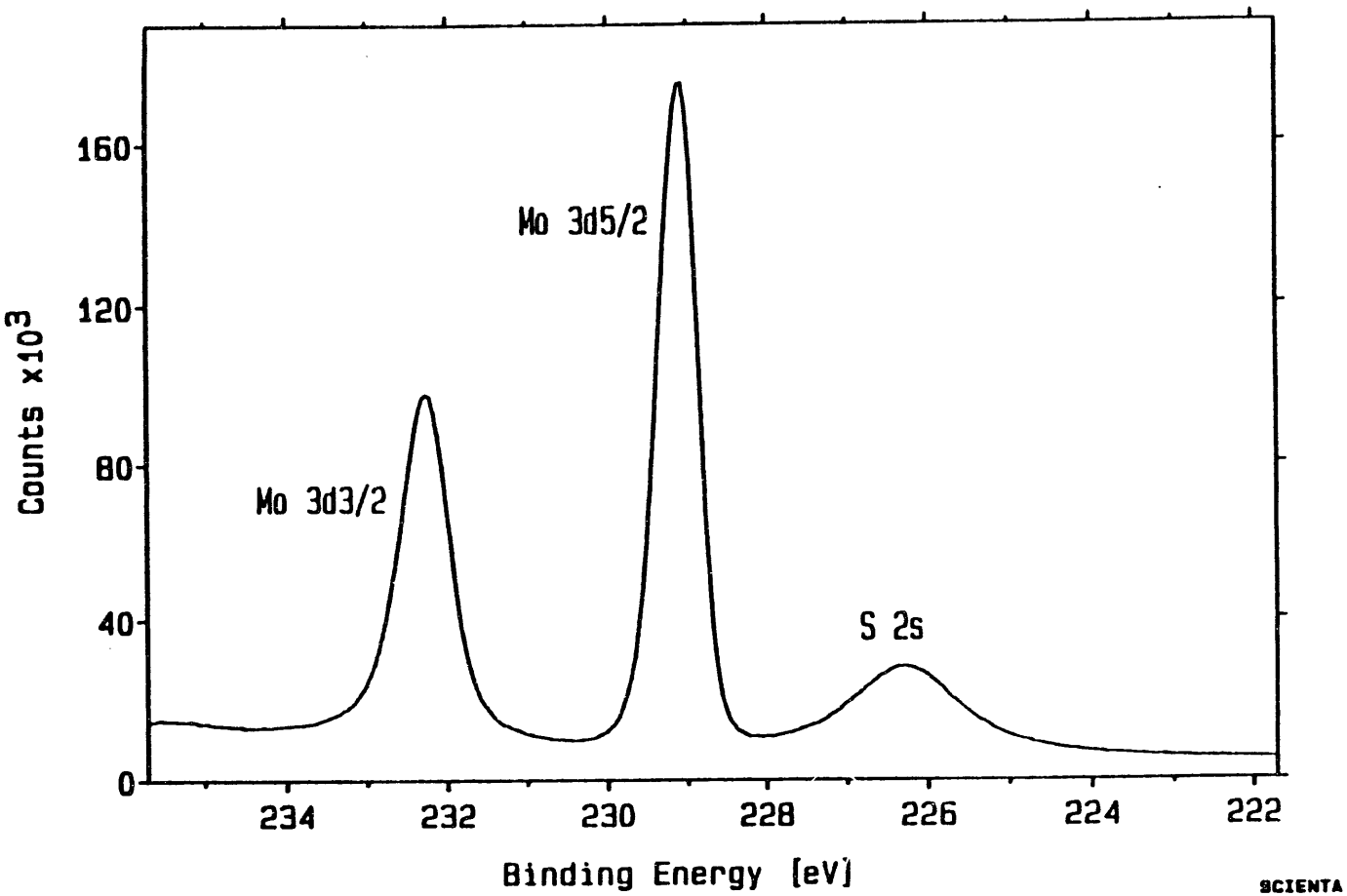

Figure 25b. Core level molybdenum 3d region of single crystal MoS_2. Spectral parameters were the following: pass energy, E_p, 75 eV; step size, 0.5 eV; time/step, 0.4 sec; slit width, 1.1 mm; and transmission mode.

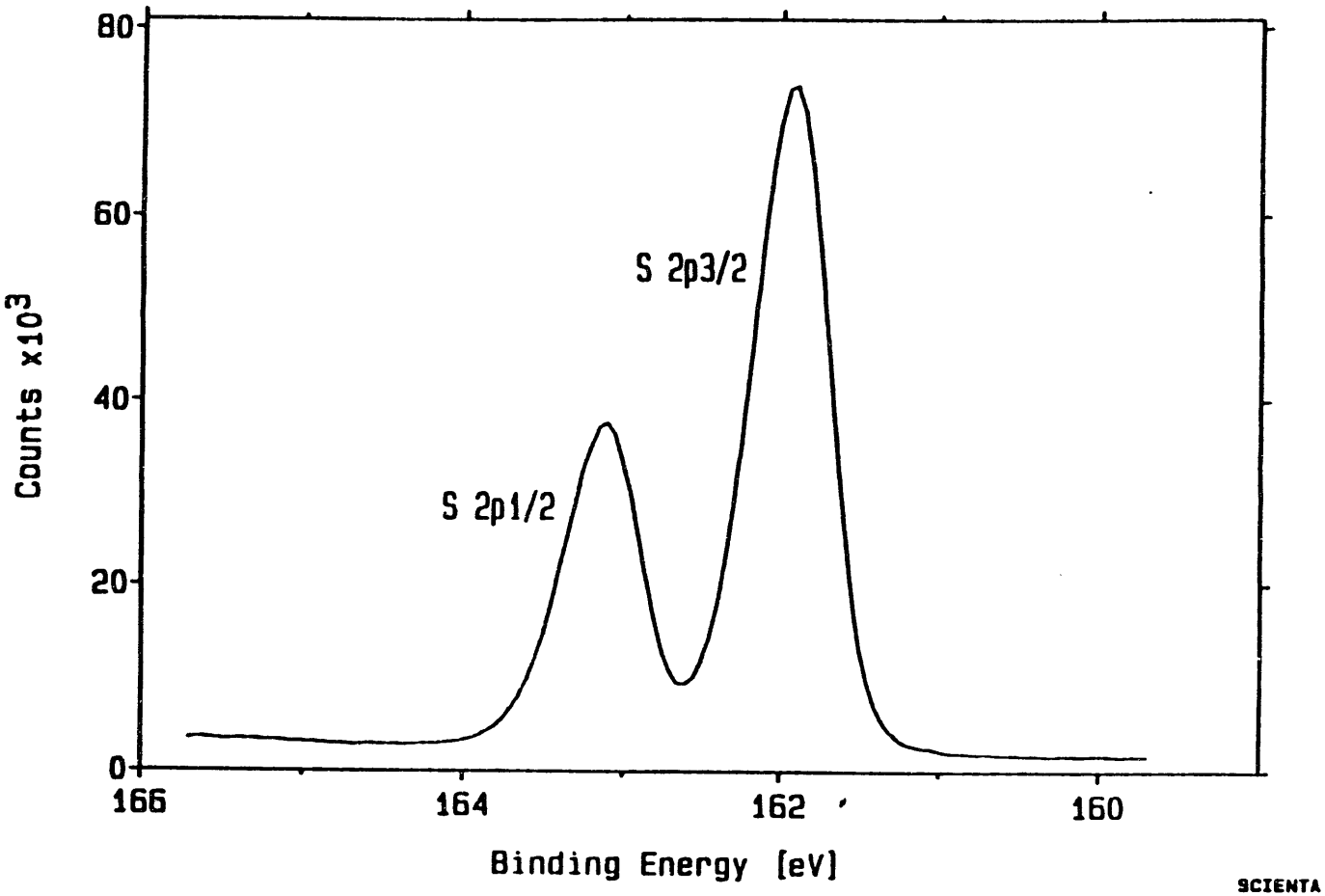

Figure 25c. Core level sulfur 2p region of single crystal MoS_2. Spectral parameters were the following: pass energy, E_p, 75 eV; step size, 0.5 eV; time/step, 0.4 sec; slit width, 1.1 mm; and transmission mode.

4.4.2 Valence Band Analysis

Valence band analysis of single crystal MoS_2 was carried out as indicated in Section 2.3.3. As discussed in the previous section, this sample did possess small amounts of surface carbon. However, this carbon did not affect XPS analysis of the valence band region due to the low carbon 2s and 2p cross-sections and the large escape depth of photoelectrons originating from the valence band region (using Al K_α radiation).

The valence band region of the single crystal MoS_2 is shown in Figure 26a. The single crystal valence band is similar to that of polycrystalline MoS_2 with some minor differences. For instance, in polycrystalline MoS_2 the intensity of the top two peaks is very close. However, in the single crystal, the intensity of the first band is greater than that of the second band. Figure 26b shows the valence bands of the single crystal and polycrystalline MoS_2 samples plotted on the same energy scale (each corrected using Au calibration). The differences in intensity are more apparent when plotted in this way. The S3s region is similar in both samples. Only the Mo 4d-S3p valence band region varies on going from polycrystalline to single crystal MoS_2. Possible explanations for the valence band differences will be discussed in more detail in Chapter 6.

4.4.3 Angle Resolved HR-ESCA

As discussed in Section 2.3.4, the MoS_2 single crystal used in the angle resolved HR-ESCA study was first oriented by Laue diffraction. Thus, the freshly cleaved surface was exposed to air prior to the angle resolved HR-ESCA study. The major contaminant was carbon as indicated in Section 4.2.1. However, the presence of the carbon overlayer was not believed to affect the results of the angle resolved study significantly since carbon is believed to be a weak scatterer of high kinetic energy photoelectrons.

On the (0002) surface of MoS_2, forward focusing of second atomic layer molybdenum photoelectrons by first atomic layer sulfurs is expected to occur at a polar angle of 49.1° along the $(\bar{1}2\bar{1}0)$, $(\bar{1}\bar{1}20)$, and $(2\bar{1}\bar{1}0)$ (or $\perp$ to (1010), (1100), and (1100) planes) azimuthal directions (see Figure 3a). These directions are located 120° apart. Orientation of the MoS_2 crystal by back-reflection Laue diffraction was used to locate these directions. A scribe mark placed on the sample surface was used to reference one of these directions. This direction was parallel to the $\{\bar{1}2\bar{1}0\}$ set of planes and will be referred to in the rest of the text as azimuthal angle equal to 0°.

Most of the angle resolved ESCA studies done previously have been performed on single crystals consisting of one type of atom or on metal overlayers on a metallic single crystal

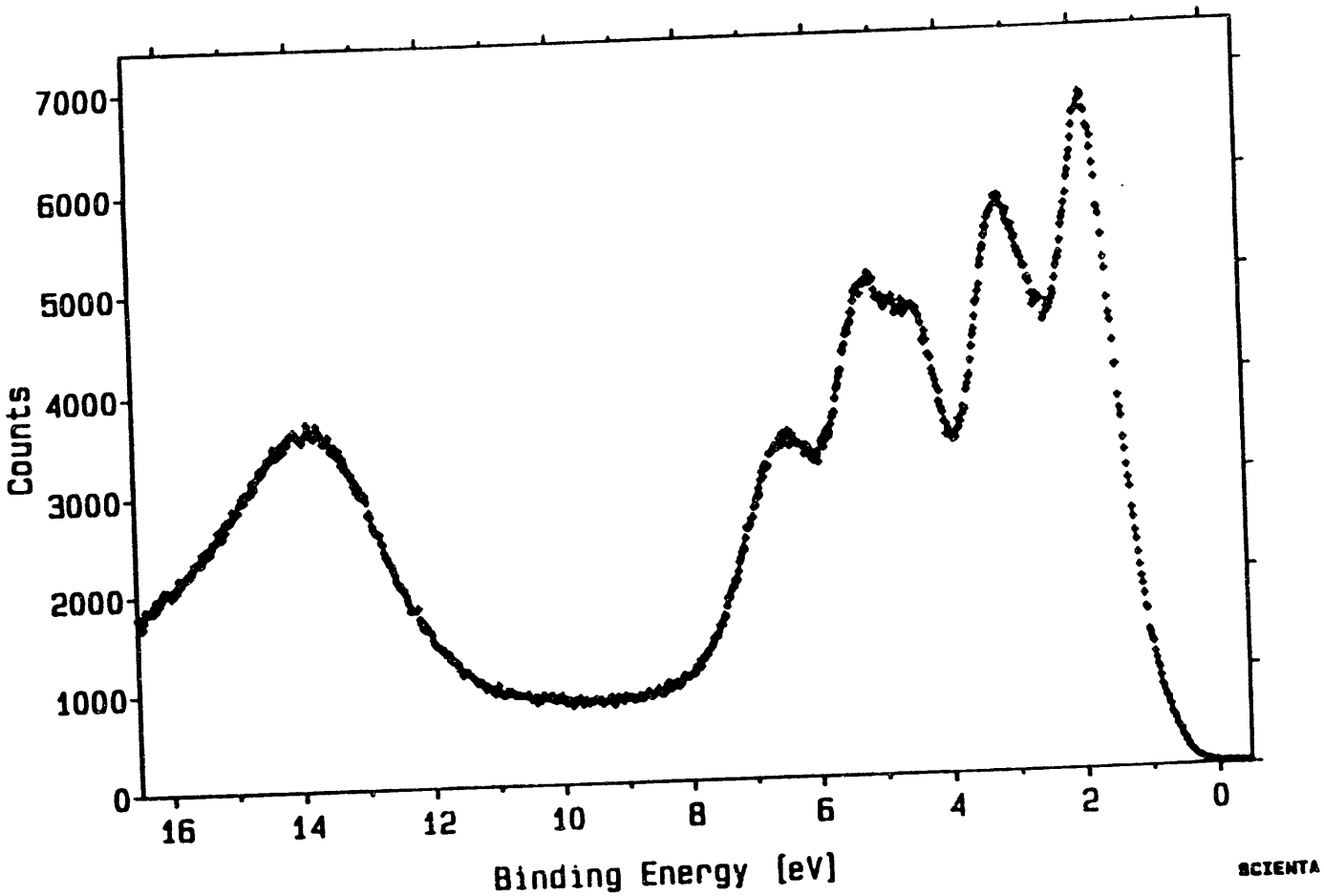

Figure 26a. Valence band region of single crystal MoS_2. Spectral parameters were the following: pass energy, E_p, 75 eV; step size, 0.02 eV; slit width, 1.1 mm; and transmission mode.

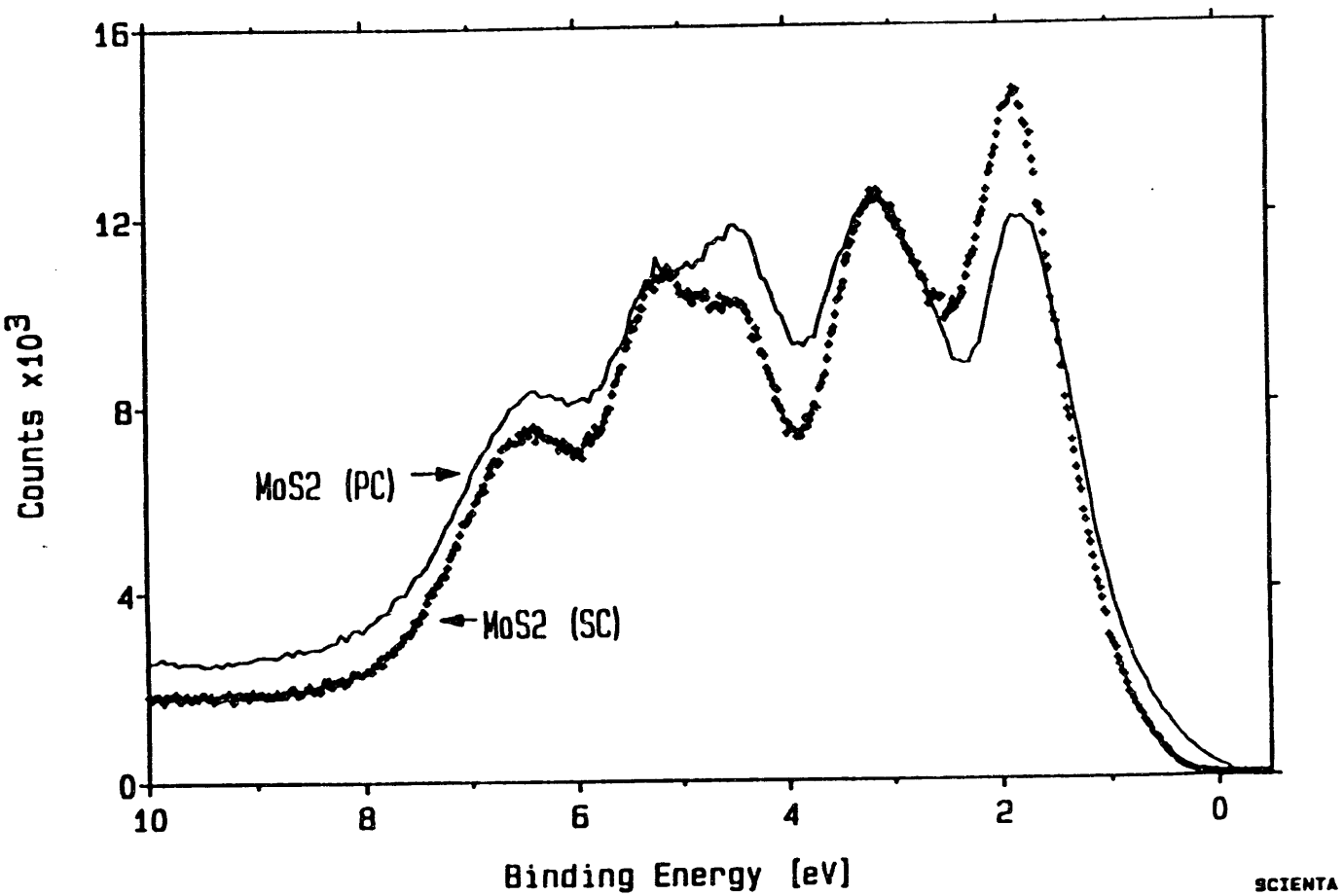

Figure 26b. Comparison of the valence band regions of single crystal and polycrystalline MoS_2. Spectral parameters for both samples were the following: pass energy, E_p, 75 eV; slit width, 1.1 mm; and transmission mode. Step size for single crystal and polycrystalline MoS_2 was 0.02 eV and 0.05 eV, respectively.

surface. Thus, this is one of the first angle resolved HR-ESCA investigations of forward focusing in a compound exhibiting a complex structure. Prior to presenting the experimental results, it seems reasonable to investigate the structure of the (0002) MoS_2 surface in terms of all geometrically possible forward focusing directions. Table 17a tabulates all geometrically possible polar angles at which forward focusing could occur for Mo photoelectrons. The corresponding azimuthal angles at which this forward focusing would be detected is also tabulated along with the distance, d_{Mo-SC}, between the Mo photoelectron emitter and the scatterer. Table 17b tabulates all geometrically possible polar angles at which forward focusing could occur for S photoelectrons. The corresponding azimuthal angles of detection along with the distance, d_{S-SC}, between the sulfur photoelectron emitter and scatterer are also given. This geometrical study was carried out down to fifth atomic layer molybdenum assuming position of all atoms as in bulk crystal structure (see Figure 7 and Section 3.4.1).

As indicated in Table 17a and 17b, forward focusing of Mo and S photoelectrons by molybdenum and sulfur atoms residing in the rest of the structure is very complicated. However, forward focusing by near-surface atoms at short distances from the emitters is expected to dominate. This study primarily focused on a polar angle of 49°. As indicated in Table 17a, forward focusing of second atomic layer molybdenum photoelectrons by first atomic layer sulfur atoms will occur at azimuthal angles of 0°, 120°, and 240°. However, the same type of forward focusing will occur for fifth atomic layer molybdenum photoelectrons by fourth atomic layer sulfur atoms at azimuthal angles of 60°, 180°, 300°, shown in Figure 27. If the surface is considered to consist of first layer sulfur atoms then a fifth layer molybdenum atom resides 7.73 Å from the surface. Thus, if both types of forward focusing occur, then at a constant polar angle of 49.1°, maxima in Mo 3d photoelectron intensity will be present at the following arbitrary azimuthal angles: 0°, 60°, 120°, 180°, 240°, and 300°. Minima are expected to occur in between the listed azimuthal directions. A similar type of forward focusing of third atomic layer sulfur 2p photoelectrons by second layer molybdenum atoms is expected to occur at a polar angle of 49.1° at the following azimuthal angles: 60°, 180°, 300°.

Results of the angle resolved HR-ESCA experiments obtained at constant azimuthal angles are shown in Figures 28a, 28b, and 28c. This set of experiments is described in Section 2.3.4. Figures 28a, 28b, and 28c plot the area of the molybdenum photoelectron peak (Mo $3d_{5/2}$ or Mo $3p_{3/2}$) vs. polar angle for constant azimuthal angles designated as 0°, 30°, and 60°. The directions represented by the 0° and 60° azimuths correspond to one of the azimuthal directions represented by the following planes which contain the Mo-S bond and are thus parallel to the forward focusing directions: $(\bar{1}2\bar{1}0)$, $(\bar{1}\bar{1}20)$, and $(2\bar{1}\bar{1}0)$ or $(1\bar{2}10)$, $(11\bar{2}0)$, and

Table 17a.

Tabulation of polar angles, azimuthal angles, and distance between emitter and scatterer, d_{Mo-SC}, for forward focusing of Mo photoelectrons. (AL=Atomic Layer, E=Emitter, SC=Scatterer)

Description	d_{Mo-SC} (Å)	Polar Angle	Azimuthal Angles
5^{th} AL Mo by 3^{rd} AL S	4.57	0°	All
5^{th} AL Mo by 1^{st} AL S	7.73	0°	All
5^{th} AL Mo by 2^{nd} AL Mo	6.41	16.5°	60°, 180°, 300°
5^{th} AL Mo by 1^{st} AL S	8.35	22.2°	30°, 90°, 150°, 210°, 270°, 330°
5^{th} AL Mo by 2^{nd} AL Mo	7.15	30.7°	0°, 120°, 240°
5^{th} AL Mo by 3^{rd} AL S	5.56	34.6°	30°, 90°, 150°, 210°,270°, 330°
5^{th} AL Mo by 1^{st} AL S	9.47	35.3°	0°, 60°, 120°, 180°, 240°, 300°
5^{th} AL Mo by 2^{nd} AL Mo	7.82	38.1°	40.9°, 79.1°, 160.9°, 199.1°, 280.9°, 319.1°
5^{th} AL Mo by 1^{st} AL S	9.98	39.3°	30°, 90°, 150°, 210° 270°, 330°
5^{th} AL Mo by 2^{nd} AL S	9.00	46.9°	46.1°, 73.9°, 166.1°, 193.9°, 286.1°, 313.9°
5^{th} AL Mo by 1^{st} AL S	11.38	47.2°	10.9°, 49.1°, 70.9°, 109.1°, 130.9°, 169.1° 190.9°, 229.1°, 250.9° 289.1°, 310.9°, 349.1°
2^{nd} AL Mo by 1^{st} AL S	2.41	49.1°	0°, 120°, 240°
5^{th} AL Mo by 4^{th} AL S	2.41	49.1°	60°, 180°, 300°
5^{th} AL Mo by 2^{nd} AL Mo	9.54	49.9°	60°, 180°, 300°
5^{th} AL Mo by 3^{rd} AL S	7.13	50.1°	0°, 60°, 120°, 180°, 240°, 300°
5^{th} AL Mo by 1^{st} AL S	12.23	50.8°	30°, 90°, 150°, 210°, 270°, 330°
5^{th} AL Mo by 2^{nd} AL Mo	10.05	52.3°	36.6°, 83.4°, 156.6°, 203.4°, 276.6°, 323.4°

Table 17a (cont).

Tabulation of polar angles, azimuthal angles, and distance between emitter and scatterer, d_{Mo-SC}, for forward focusing of Mo photoelectrons. (AL=Atomic Layer, E=Emitter, SC=Scatterer)

Description	d_{Mo-SC} (Å)	Polar Angle	Azimuthal Angles
5^{th} AL Mo by 3^{rd} AL S	7.80	54.1°	30°, 90°, 150°, 210°, 270°, 330°
5^{th} AL Mo by 1^{st} AL S	13.40	54.8°	0°, 60°, 120°, 180°, 240°, 300°
5^{th} AL Mo by 1^{st} AL S	13.77	55.8°	16.1°, 43.9°, 76.1°, 103.9°, 136.1°, 163.9° 196.1°, 223.9°, 256.1° 283.9°, 316.1°, 343.9°
5^{th} AL Mo by 2^{nd} AL Mo	11.00	56.0°	0°, 120°, 240°
5^{th} AL Mo by 2^{nd} AL Mo	11.45	57.5°	19.1°, 100.9°, 139.1°, 220.9°, 259.1°, 340.9°
5^{th} AL Mo by 1^{st} AL S	14.81	58.6°	30°, 90°, 150°, 210°, 270°, 330°
5^{th} AL Mo by 1^{st} AL S	15.79	60.7°	6.6°, 53.4°, 66.6°, 113.4°, 126.6°, 173.4° 186.6°, 233.4°, 246.6° 293.4°, 306.6°, 353.4°
5^{th} AL Mo by 2^{nd} AL Mo	12.69	61.0°	
5^{th} AL Mo by 3^{rd} AL S	9.53	61.3°	(12 Azimuths)
5^{th} AL Mo by 2^{nd} AL Mo	13.45	62.8°	
5^{th} AL Mo by 1^{st} AL S	16.94	62.8°	
2^{nd} AL Mo by 1^{st} AL S	3.98	66.6°	60°, 180°, 300°
5^{th} AL Mo by 4^{th} AL S	3.98	66.6°	0°, 120°, 240°

Table 17b.

Tabulation of polar angles, azimuthal angles, and distance between emitter and scatterer, d_{S-SC}, for forward focusing of S photoelectrons. (AL=Atomic Layer, E=Emitter, SC=Scatterer)

Description	d_{S-SC} (Å)	Polar Angle	Azimuthal Angles
3rd AL S by 1st AL S	3.15	0°	All
4th AL S by 2nd AL Mo	4.57	0°	All
4th AL S by 1st AL S	6.41	16.5°	0°, 120°, 240°
4th AL S by 1st AL S	7.15	30.7°	60°, 180°, 300°
4th AL S by 3rd AL S	3.51	31.3°	0°, 120°, 240°
4th AL S by 2nd AL Mo	5.56	34.6°	30°, 90°, 150°, 210°, 270°, 330°
4th AL S by 1st AL S	7.82	38.1°	19.1°, 100.9°, 139.1°, 220.9°, 259.1°, 340.9°
3rd AL S by 1st AL S	4.46	45.0°	30°, 90°, 150°, 210°, 270°, 330°
4th AL S by 1st AL S	9.00	46.9°	46.1°, 73.9°, 166.1°, 193.9°, 286.1°, 313.9°
3rd AL S by 2nd AL Mo	2.41	49.1°	60°, 180°, 300°
4th AL S by 1st AL S	9.54	49.9°	0°, 120°, 240°
4th AL S by 2nd AL Mo	7.13	50.1°	0°, 60°, 120°, 180° 240°, 300°
4th AL S by 3rd AL S	4.72	50.6°	60°, 180°, 300°
4th AL S by 1st AL S	10.05	52.3°	23.4°, 96.6°, 143.4°, 216.6°, 263.4°, 336.6°

Table 17b (cont).

Tabulation of polar angles, azimuthal angles, and distance between emitter and scatterer, d_{S-SC}, for forward focusing of S photoelectrons. (AL=Atomic Layer, E=Emitter, SC=Scatterer)

Description	d_{S-SC} (Å)	Polar Angle	Azimuthal Angles
4^{th} AL S by 2^{nd} AL Mo	7.80	54.1°	30°, 90°, 150°, 210°, 270°, 330°
4^{th} AL S by 3^{rd} AL S	5.68	58.2°	19.1°, 100.9°, 139.1°, 220.9°, 259.1°, 340.9°
3^{rd} AL S by 1^{st} AL S	6.32	60.0°	0°, 60°, 120°, 180°, 240°, 300°
3^{rd} AL S by 1^{st} AL S	7.06	63.5°	30°, 90°, 150°, 210°, 270°, 330°
3^{rd} AL S by 2^{nd} AL Mo	3.98	66.6°	0°, 120°, 240°

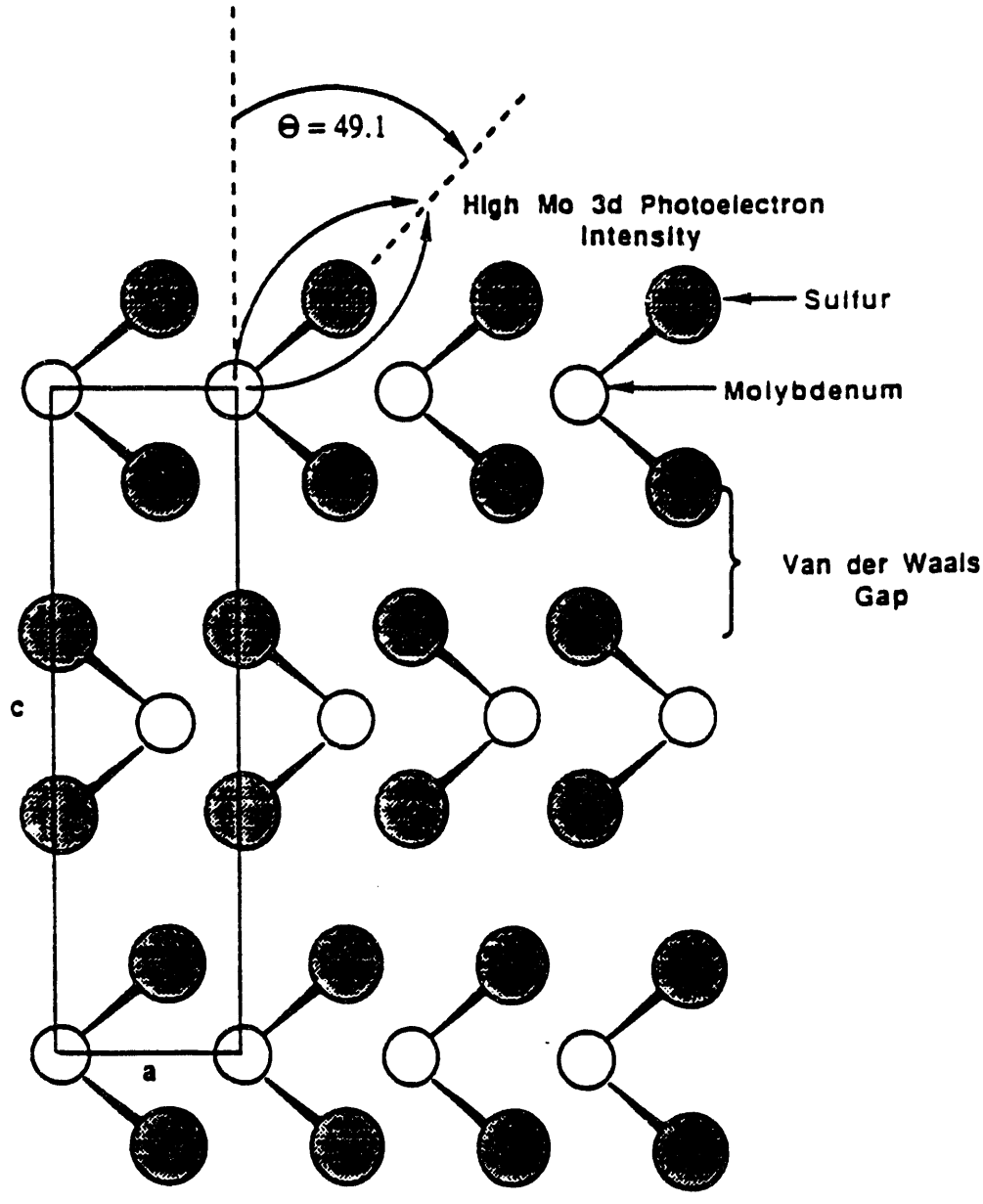

Figure 27. Azimuthal directions of forward focusing at a constant polar angle of 49.1° for second atomic layer molybdenum photoelectrons by first atomic layer sulfur atoms and for fifth atomic layer molybdenum photoelectrons by fourth atomic layer sulfur atoms.

($\bar{2}110$). As indicated above, a maximum in Mo photoelectron intensity is expected at a polar angle of 49.1° for every 60° azimuthal rotation of the sample. However, back-reflection Laue diffraction can not distinguish the direction of the Mo-S bond arising from second atomic layer molybdenum atoms from that arising from fifth atomic molybdenum atoms because both Mo-S bonds lie parallel to the $\{\bar{1}2\bar{1}0\}$ set of planes (see Figure 18). Thus, forward focusing due to second layer and fifth layer molybdenum photoelectrons can not be differentiated. Intense maxima are present at polar angles of 0° and 48° for the 0° azimuth as shown in Figure 28a. For the 30° azimuth, as shown in Figure 28b, one intense maximum is present at a polar angle of approximately -3°. A smaller maximum is present at a polar angle of 36°. For the 30° azimuth, maximum in Mo photoelectron area is absent near a polar angle of 49°. For the 60° azimuth, as shown in Figure 28c, intense maxima are present at polar angles of -3° and 47°.

The result of an angle resolved HR-ESCA study performed at a constant polar angle of 49° is shown in Figure 28d. In this study the azimuthal angle was incremented by 3.67° as described in Section 2.3.4. Intense maxima in Mo photoelectron area occur at approximate azimuthal angles of 5° and 72°. The difference between these two directions is 67° which is very to the expected difference of 60°. As mentioned previously, this study may not be as accurate as the previously discussed studies involving incrementation of the polar angle since the azimuthal rotational control was not as precise.

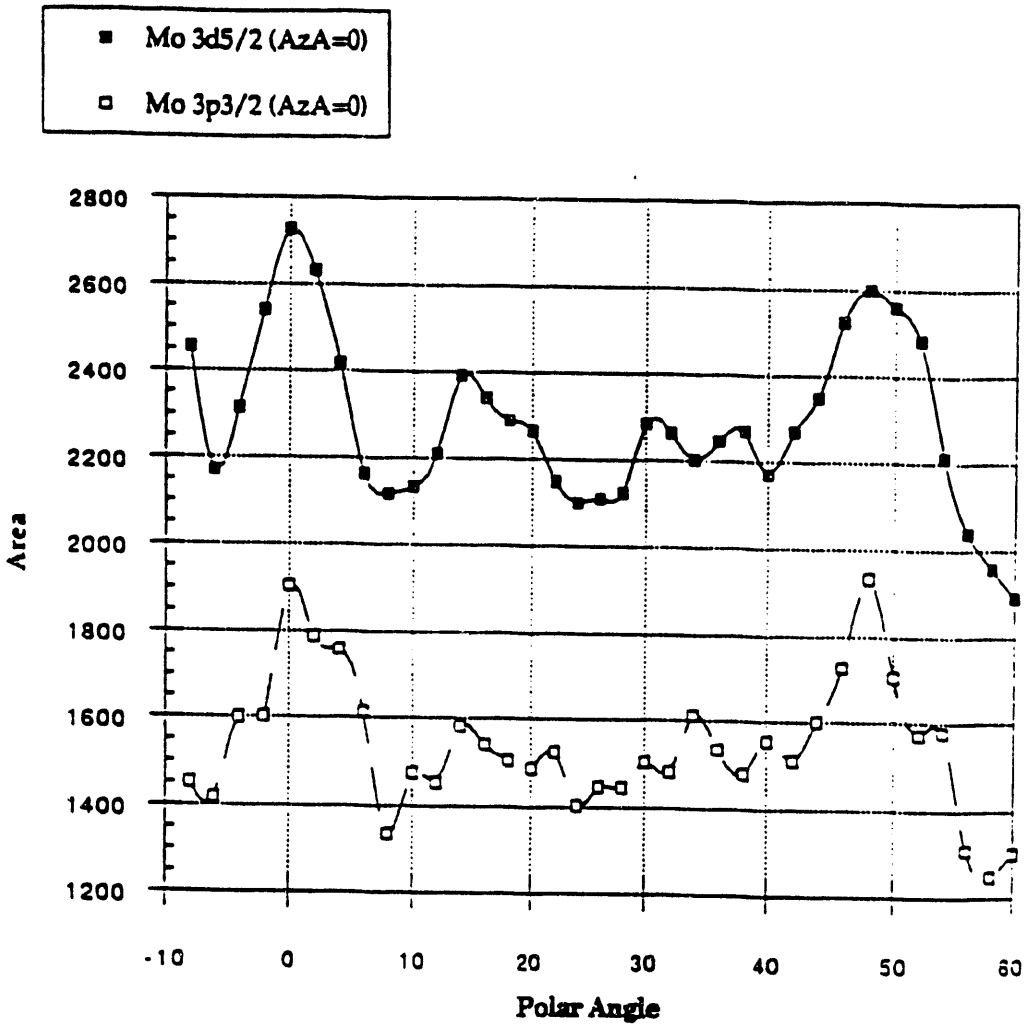

Figure 28a. Angle resolved HR-ESCA study of (0002) plane of natural molybdenite, 2H-MoS_2. Plotted is the Mo $3d_{5/2}$ and Mo $3p_{3/2}$ photoelectron peak area vs. polar angle for the 0° azimuth.

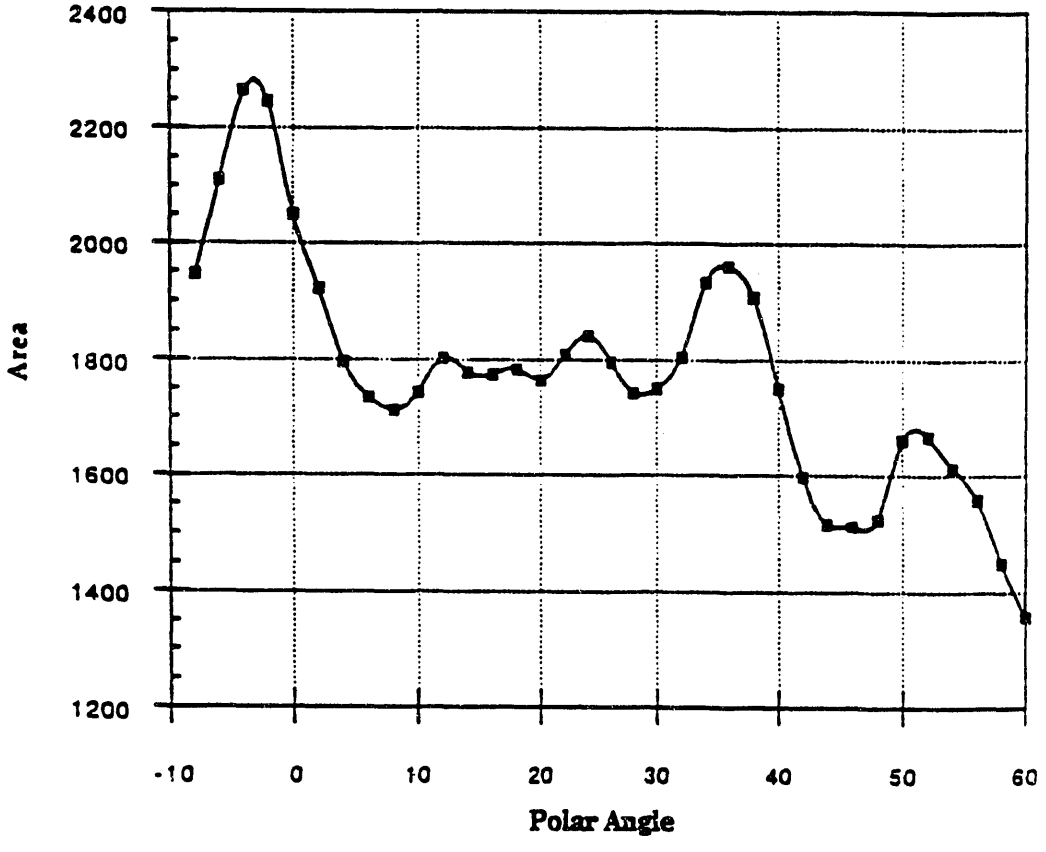

Figure 28b. Angle resolved HR-ESCA study of (0002) plane of natural molybdenite, 2H-MoS_2. Plotted is the Mo $3d_{5/2}$ photoelectron peak area vs. polar angle for the 30° azimuth.

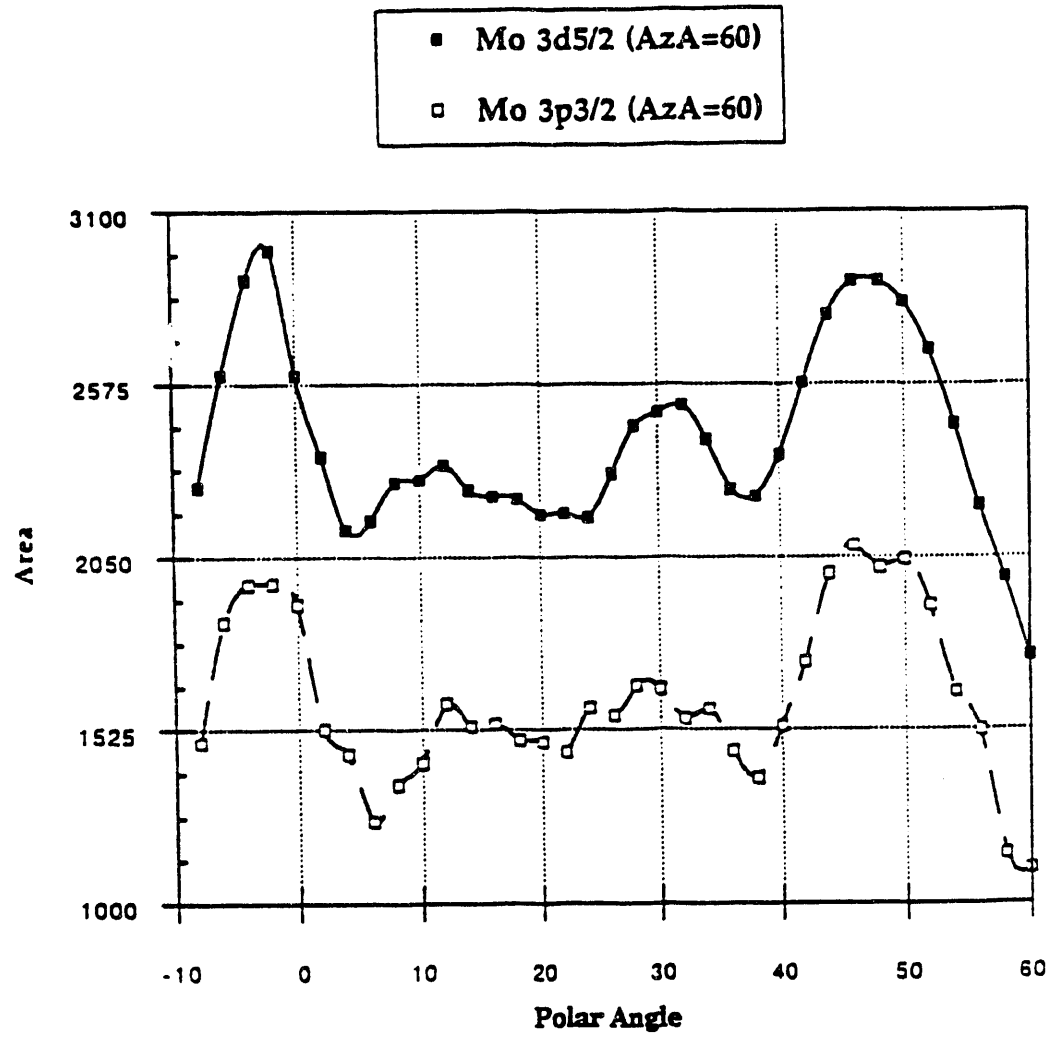

Figure 28c. Angle resolved HR-ESCA study of (0002) plane of natural molybdenite, 2H-MoS_2. Plotted is the Mo $3d_{5/2}$ and Mo $3p_{3/2}$ photoelectron peak area vs. polar angle for the 60° azimuth.

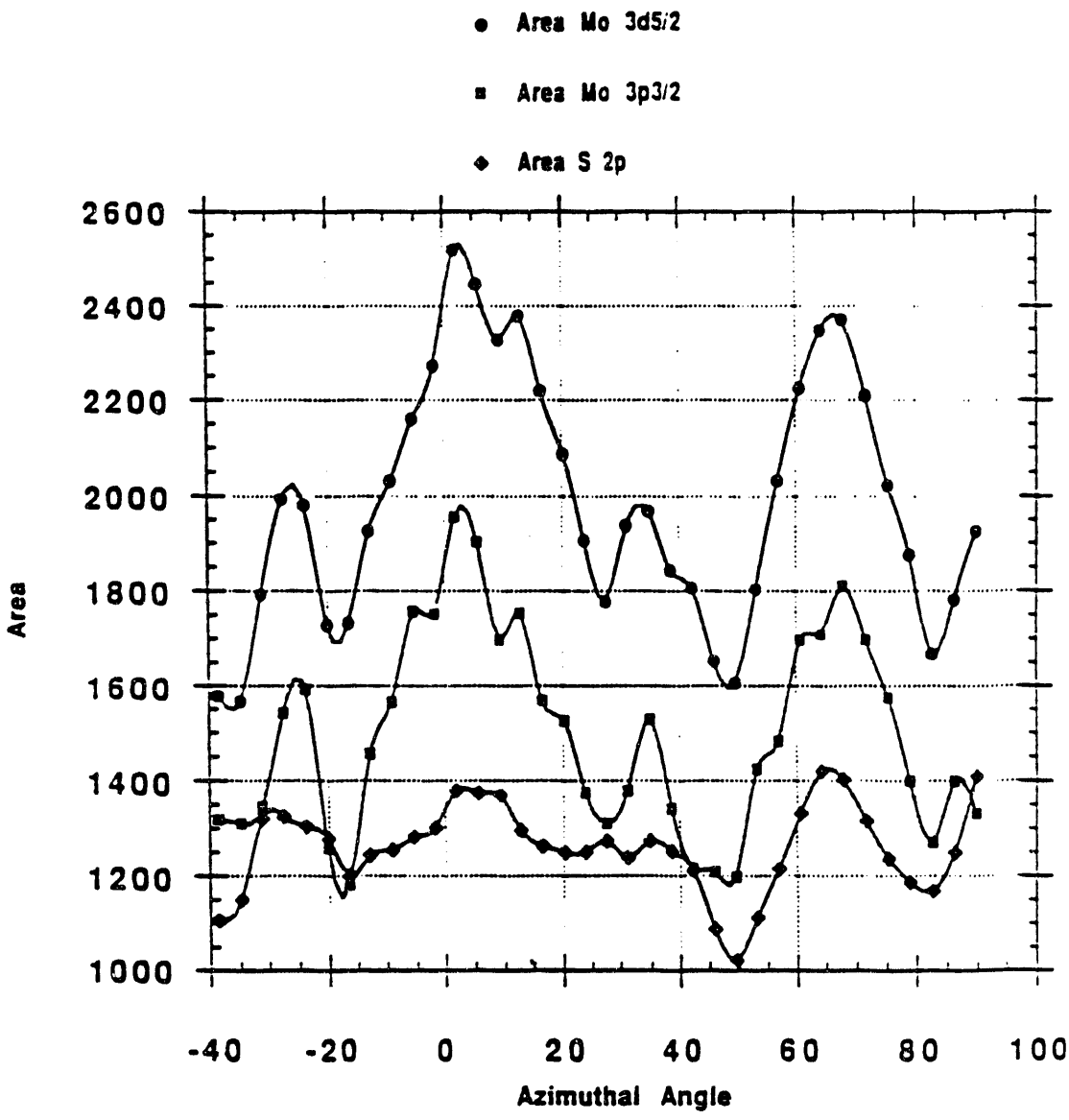

Figure 28d. Angle resolved HR-ESCA study of (0002) plane of natural molybdenite, 2H-MoS_2. Plotted is the Mo $3d_{5/2}$ photoelectron peak area vs. azimuthal angle for a constant polar angle of 49°.

Chapter 5
THEORETICAL RESULTS

5.1 Electronic Structure of 2-D MoS_2.

Two-dimensional MoS_2, consisting of one MoS_2 per unit cell, was modeled as described in Section 3.4.2. A set of 171 special **k**-points, described in Section 3.7.1, was used in the calculation of the theoretical valence band. Radial functions for the valence orbitals involved in this study were represented by Slater-type orbitals using the parameters of Hughbanks and Hoffmann, Section 3.2. These parameters are for single zeta S3s, S3p and Mo5s, Mo5p and double zeta Mo4d radial functions.

5.1.1 Theoretical Valence Band

A two-dimensional infinite sheet of MoS_2 was used to model one layer of 2H-MoS_2. A description of this structure as well as the structural coordinates of the atoms is given in Section 3.4.2. Initially, the density of states (and theoretical valence band) was studied using the set of 171 special **k**-points described in Section 3.7.1. The first set of studies used the atomic parameters of Hughbanks and Hoffmann, discussed in Section 3.2, for the S3s, S3p and Mo4d atomic orbitals. A theoretical valence band was obtained by summation of the S3s, S3p and Mo4d modified atomic orbital populations, MAOPOP's, as described in Section 3.3.

The density of states and theoretical valence band of 2-D MoS_2 are shown together in Figure 29a. Figure 29b shows the theoretical valence band of 2-D MoS_2 scaled to the experimental valence band of MoS_2 obtained via HR-ESCA shown in Section 4.2. Modified atomic orbital populations, MAOPOP's, for the Mo4d and S3s, S3p orbitals are shown in Figure 29c. The theoretical density of states shows a large number of states in the center of the Mo4d-S3p valence band. When the density of states is modified by the Scofield photoelectron cross-sections (Reference 18) to obtain a theoretical valence band, the contribution of the states in the center of the Mo4d-S3p valence band is decreased. This decrease occurs because much of the contribution in this region comes from the S3p orbitals. S3p orbitals have a low photoelectron cross-section compared to the Mo4d orbitals, 0.2448 S3p/Mo4d. Thus, the theoretical valence band not the density of states is compared to the experimental valence band. Some of the features of the experimental valence band (Section 4.2) are reproduced in the theoretical valence band. For instance, the broad band located at $\sim$-22 eV in the theoretical valence band consists of mainly S3s character. This band has a similar dispersion in both theoretical and experimental valence bands. However, the S3s band is located too close to the upper portion of

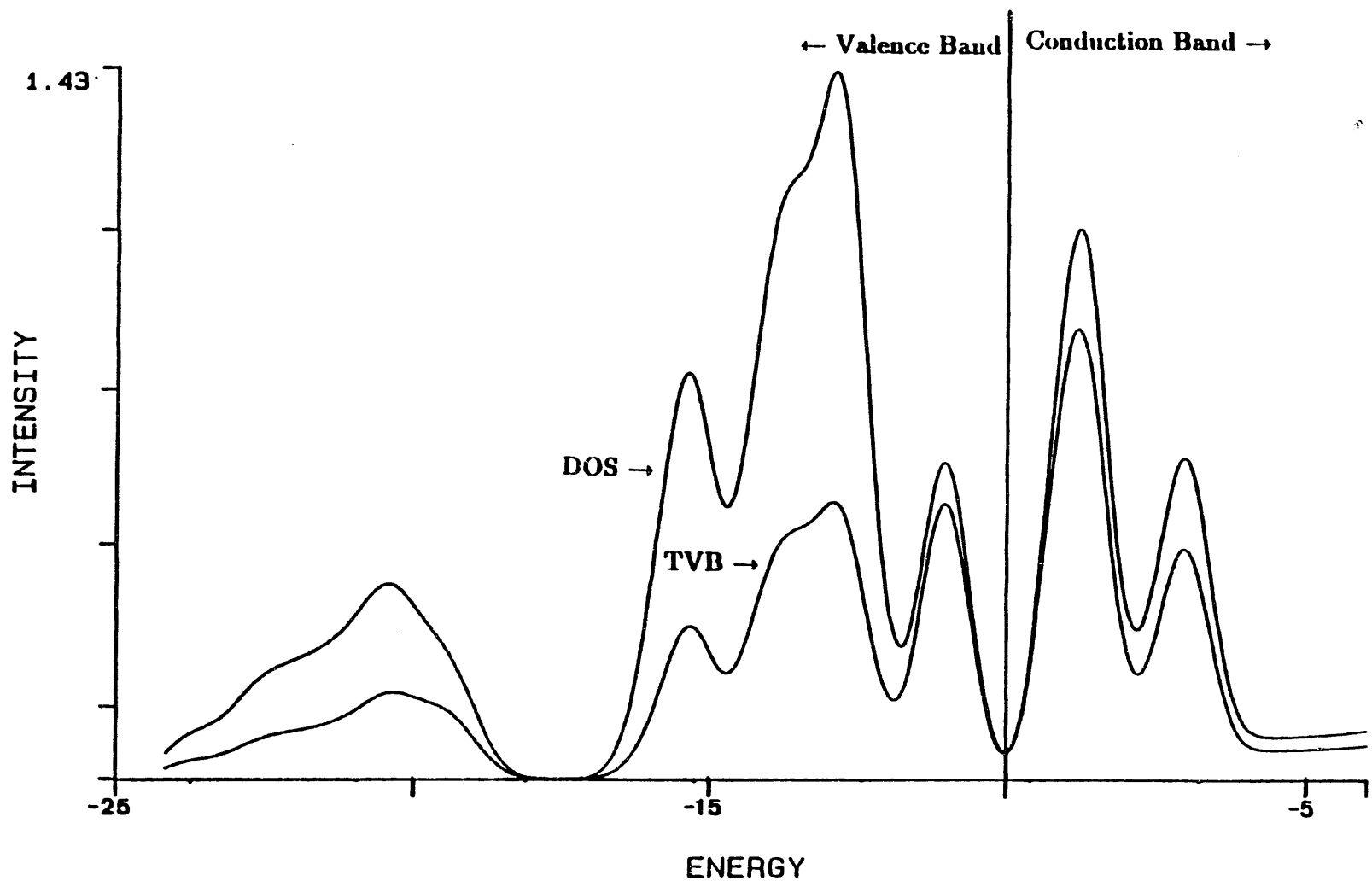

Figure 29a. Comparison of theoretical density of states (DOS) and theoretical valence band (TVB) of 2 H MoS_2. The 171 special k-point set and S3s, S3p and Mo4d atomic parameters of Hughbanks and Hoffmann were used for this calculation.

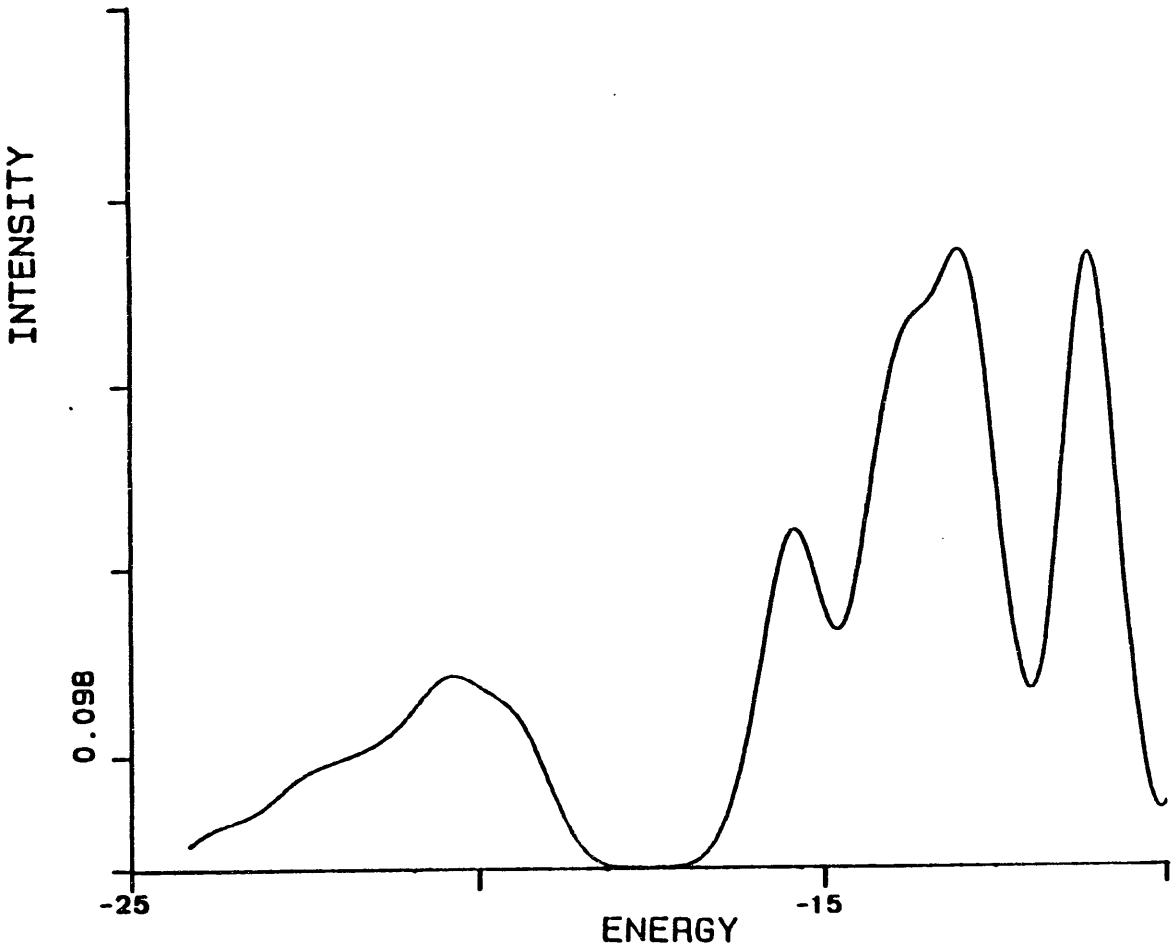

Figure 29b. Theoretical valence band of 2-D MoS_2. The 171 special k-point set and S3s, S3p and Mo4d atomic parameters of Hughbanks and Hoffmann were used for this calculation.

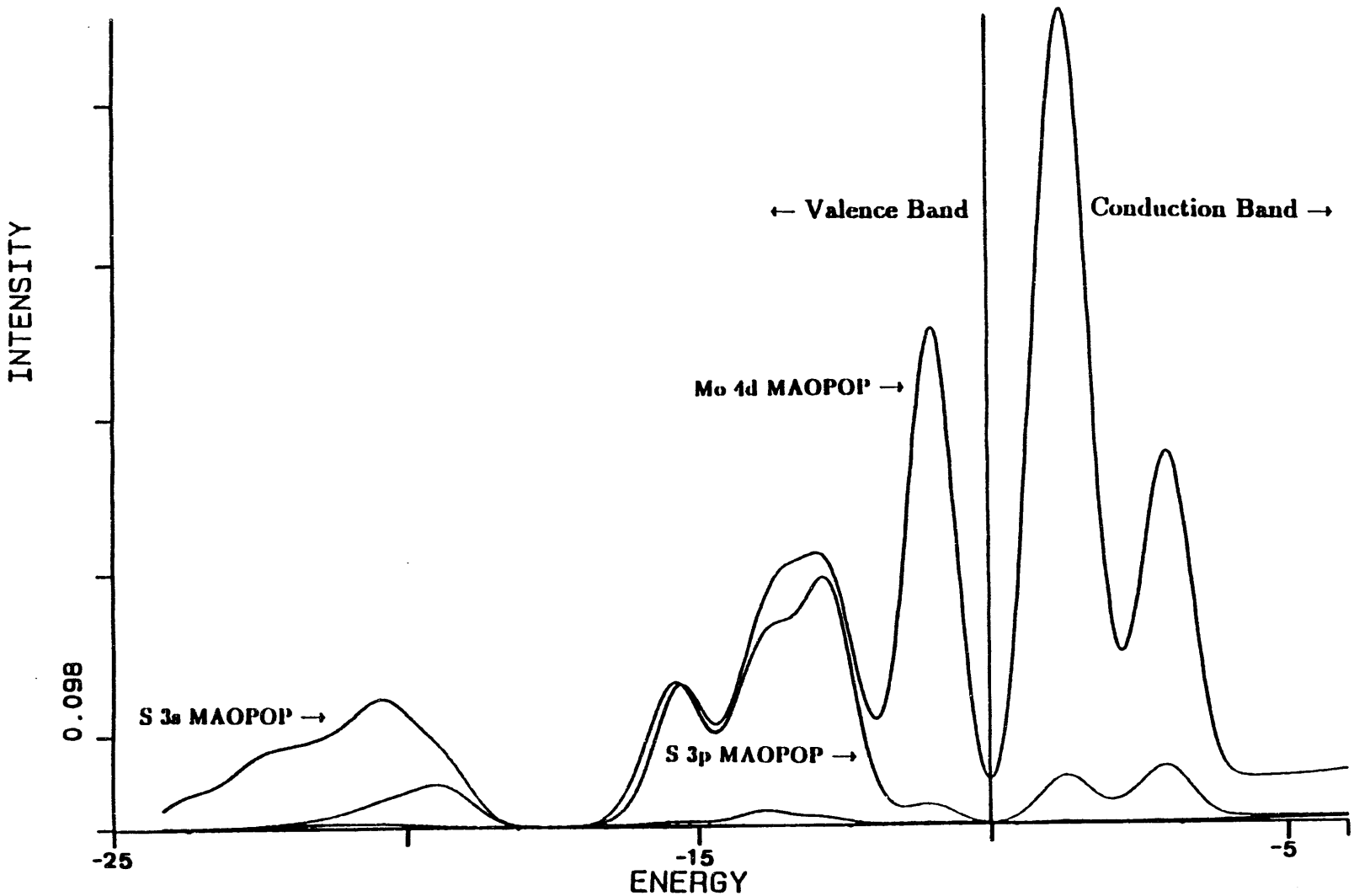

Figure 29c. Theoretical modified atomic orbital populations, MAOPOP's, for the Mo4d and S3s, S3p orbitals. The 171 special k point set and S3s, S3p and Mo4d atomic parameters of Hughbanks and Hoffmann were used for this calculation.

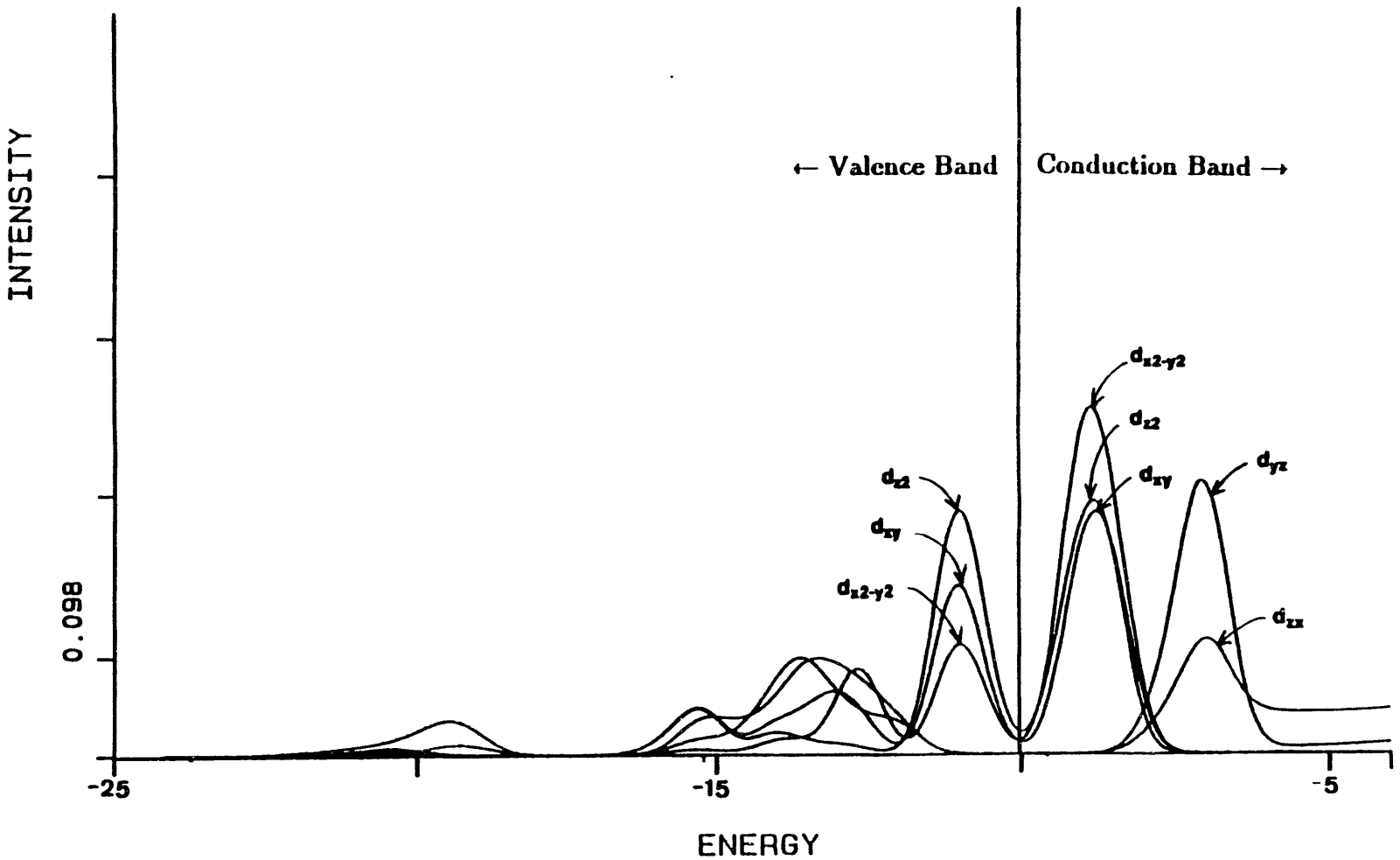

Figure 29d. Theoretical modified atomic orbital populations, MAOPOP's, for the Mo $4d_{z2}$, $4d_{xy}$, $4d_{x2\ y2}$, $4d_{zx}$, and $4d_{yz}$ orbitals. The 171 special k-point set and S3s, S3p and Mo4d atomic parameters of Hughbanks and Hoffmann were used for this calculation.

the valence band (Mo4d-S3p) compared to the experimental valence band. Also, the Mo4d-S3p portion of the experimental valence band consists of 4 distinct bands. In the theoretical valence band the Mo4d-S3p region consists of 3 bands with the center band indicating a certain amount of splitting. The energies obtained from the theoretical calculation indicate that this particular system is a semiconductor. Prior to gaussian smoothing, the top of the valence band is located at -10.656 eV. However, the theoretical valence band, Figure 29b, shows a small number of bands present at the Fermi level. These bands are an artifact of the Gaussian smoothing functions imposed on the energy levels by the EHMACPP program. The EHMACPP program calculates discrete energy levels for each **k**-point in the Brillouin zone that is input for the particular structure under study. Gaussian functions ($\exp[-(E-E_i)^2/\delta^2]$) are placed on the energy levels with a certain standard deviation defined by a factor delta, δ. Wider gaussians and more smoothing result through the use of larger delta values. In all of the theoretical calculations discussed, a value of delta equal to 0.5 eV was used. This value was chosen because it leads to a peak width at the top of the theoretical MoS_2 valence band similar to that of the experimental MoS_2 valence band.

The modified atomic orbital populations, MAOPOP's, for the Mo4d and S3s, S3p orbitals as shown in Figure 29c indicate the breakdown of the theoretical valence band. The lowest energy band consists of mainly S3s orbitals with a small amount of contribution from the Mo4d orbitals. This band will be referred to as the S3s band. The upper part of the valence band consists of mainly S3p and Mo4d orbitals and will be referred to in the rest of the text as the Mo4d-S3p valence band. The highest occupied band (at the top of the valence band) consists of mainly Mo4d character. MAOPOP's of the individual Mo4d orbitals are shown in Figure 29d. Mo $4d_{z2}$, $4d_{xy}$, and $4d_{x2-y2}$ orbitals contribute to the highest occupied band of the valence band such that the contribution of $d_{z2} > d_{xy} > d_{x2-y2}$. Two intense bands form the lowest unoccupied portion of the conduction band. The lowest unoccupied band (at the bottom of the conduction band) has mainly Mo4d character also. Again, Mo $4d_{z2}$, $4d_{xy}$, and $4d_{x2-y2}$ orbitals contribute such that $d_{x2-y2} > d_{z2} \simeq d_{xy}$. The next lowest unoccupied band consists of Mo $4d_{yz}$ and $4d_{zx}$ character such that the contribution of $d_{yz} > d_{zx}$. Crystal field splitting of the d orbitals in a transition metal coordinated by ligands in a trigonal prismatic environment occurs such that d_{z2} is lowest in energy followed by degenerate d_{xy} and d_{x2-y2} orbitals and the highest energy degenerate d_{yz} and d_{zx} orbitals. The Mo4d orbital contributions in 2-D MoS_2 follow the crystal field splitting to a limited extent. The d_{xy} and d_{x2-y2} orbitals mix with the d_{z2} orbitals to a large degree in the valence band. However, the d_{yz} and d_{zx} orbitals are well separated from the rest of the d orbitals at the top of the valence band.

S3p orbitals contribute primarily to the lower and center portions of the Mo4d-S3p valence band. The highest occupied band has almost no contribution from the S3s or S3p orbitals. One important feature in the electronic structure calculations is the degree of dispersion of the S3p orbitals. Using the single zeta radial functions obtained from the work of Hughbanks and Hoffmann, the S3p MAOPOP exhibits a dispersion consisting of two major peaks. This leads to the three-peaked nature of the Mo4d-S3p valence band. Thus, dispersion of the S3p orbitals has a major effect on the appearance of the valence band in this region. Calculations involving the double zeta functions obtained from Clementi and Roetti will be discussed in Section 5.6.

A similar calculation was carried out using the 271 **k**-points of a two-dimensional uniform grid, Section 2.7.1. The uniform grid was used in place of the 171 special **k**-point set to see if any information was lost by using the smaller set of **k**-points. This calculation revealed that no information was lost through the use of the 171 special **k**-points. Since the amount of cpu time increased with the number of **k**-points calculated, the smaller set was used.

5.1.2 Theoretical Energy Dispersion Curves

Energy dispersion curves for 2-D MoS_2 in the $\Gamma \rightarrow M$, $\Gamma \rightarrow K$, and $K \rightarrow M$ directions were also calculated using the atomic parameters of Hughbanks and Hoffmann, discussed in Section 3.2. The **k**-point sets used in these calculations are described in Section 3.7.2. The 2-D MoS_2 energy dispersion curves are shown in Figures 30a and 30b. Figure 30a shows the energy dispersion of the S3s and Mo4d-S3p portion of the valence band as well as the lower portion of the conduction band. Figure 30b shows the upper Mo4d-S3p portion of the valence band compared to the experimental energy dispersion curves of 2H-MoS_2 obtained by Mamy et al.[15]

The theoretical energy dispersion curves indicate correctly that 2-D MoS_2 is a small band gap semiconductor. The highest energy point of the occupied valence band and the lowest energy point of the unoccupied conduction band occurs at the K point. Thus, for the theoretical system, 2-D MoS_2, the band gap is direct with an energy of 1.19 eV. Optical experiments indicate that the band gap of 2H-MoS_2 is actually indirect with a gap of ~ 1.25 eV.[13] STM experiments also show the presence of a 1.35 eV indirect gap in 2H-MoS_2.[55] Previous theoretical work on MoS_2 positions the indirect gap as occurring from the top of the valence band at Γ to the bottom of the conduction band at T (1/2 $\Gamma \rightarrow$K).[8,9,10]

The theoretical energy dispersion curves also show the presence of an energy gap between the highest occupied valence band (band #9) and the lower Mo4d-S3p bands (bands

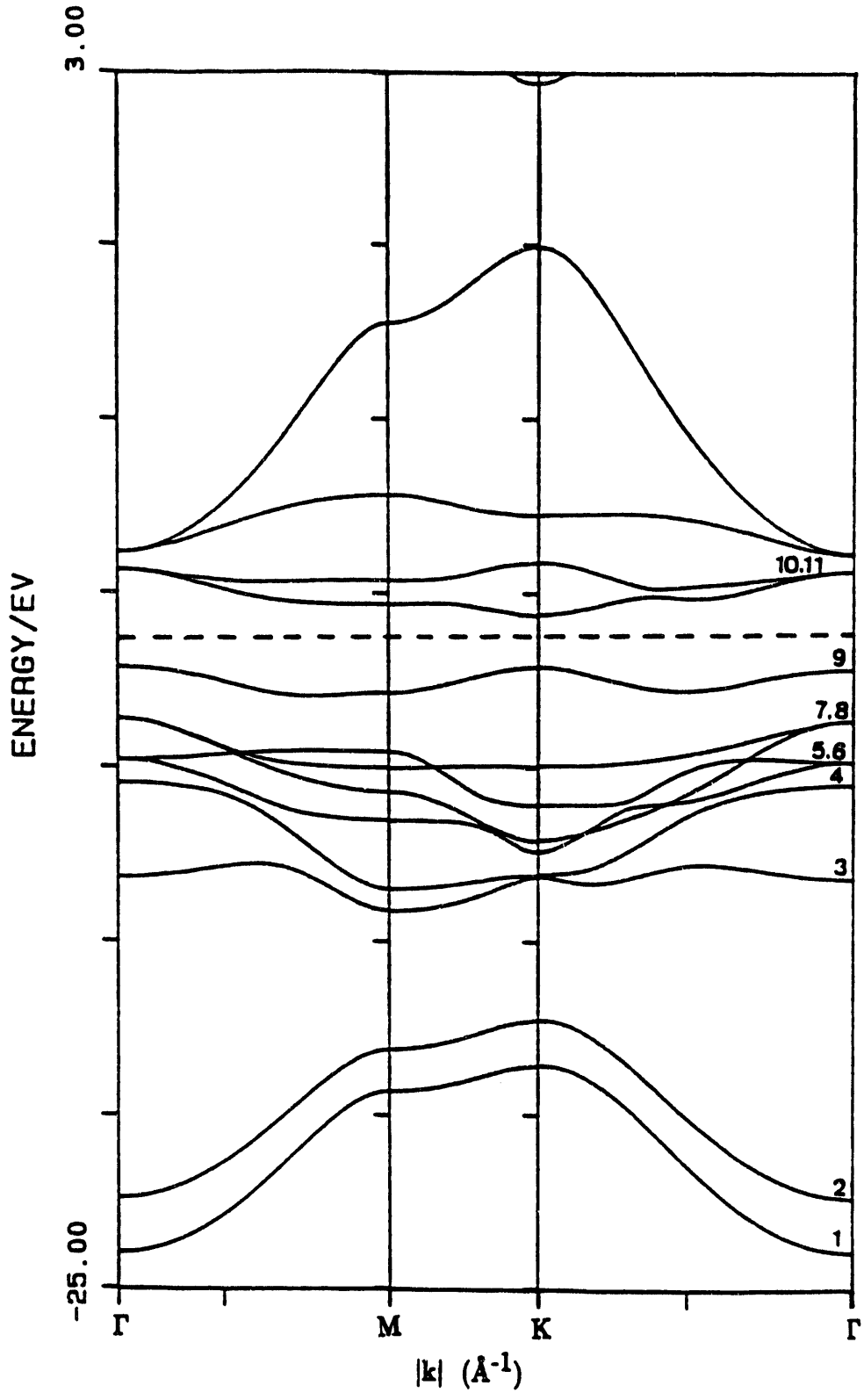

Figure 30a. Theoretical energy dispersion curves of 2-D MoS_2. S3s and Mo4d-S3p valence bands as well as the lowest energy portion of the conduction bands are shown. Note the presence of a direct gap at the K point.

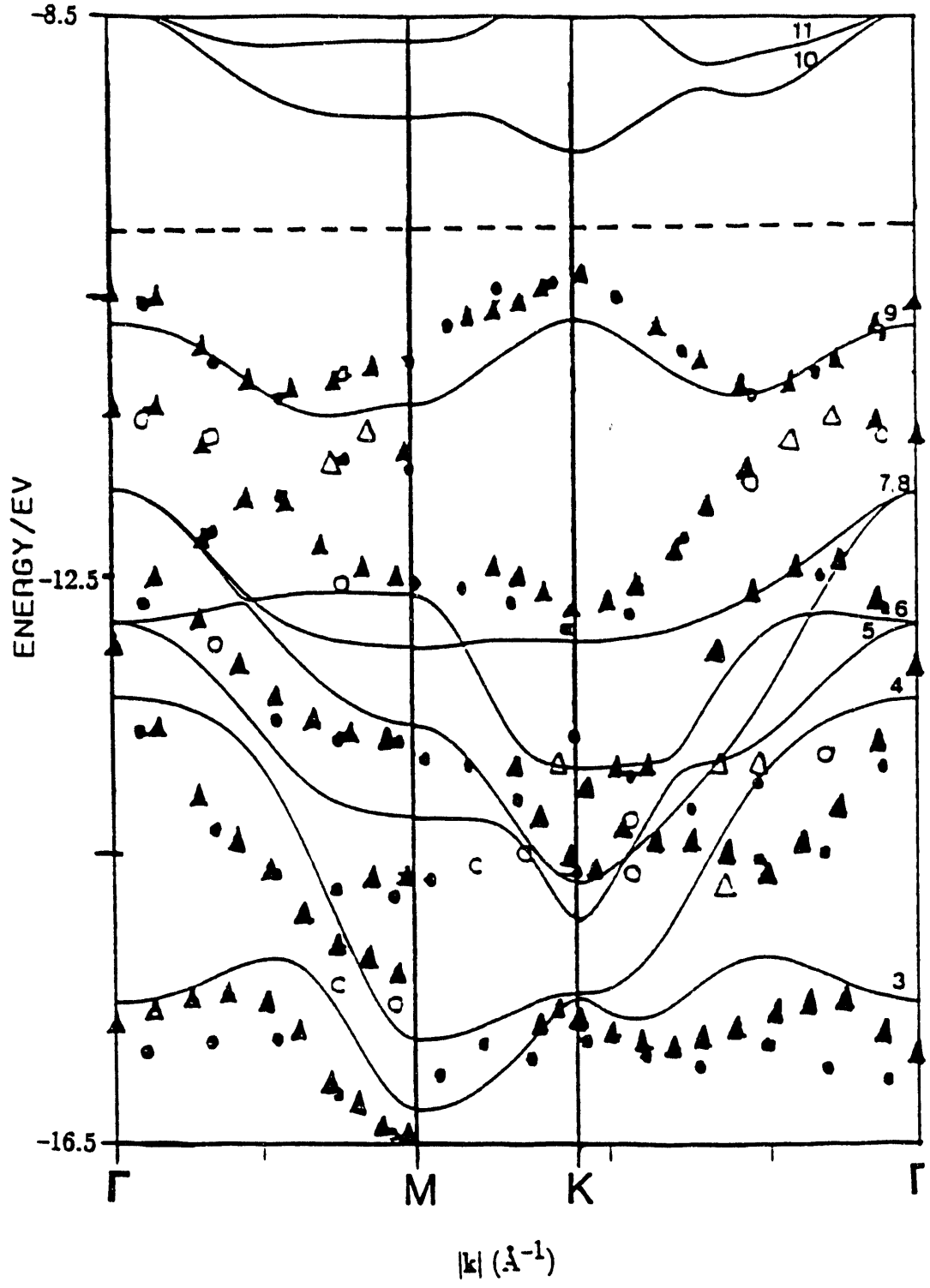

Figure 30b. Theoretical energy dispersion curves of 2-D MoS_2 (solid lines) compared to the experimental energy dispersion curves of Mamy et al. (triangles and circles). Only the upper portion of the valence band is shown. the S3s bands have not been obtained experimentally.

#3-#8). An energy gap in the energy dispersion curves indicates no overlap between these bands. Thus, the valence band should exhibit a well separated band at the top of the valence band. The theoretical valence band for this system does exhibit a band at the top of the valence band that is well separated from the rest of the Mo4d-S3p bands. However, the experimental valence band exhibits a band just below the Fermi level that has a large degree of overlap with the lower Mo4d-S3p bands. Also, the experimental energy dispersion curves of Mamy et al., reproduced in Figure 30b, do not show a significant gap between the highest occupied band and the lower portion of the Mo4d-S3p valence band. Curvature of the energy bands at the top and bottom of the Mo4d-S3p valence band is very similar for both theory and experiment.

In summary, the theoretical valence band and energy dispersion curves of 2-D MoS_2 were obtained using the atomic parameters of Hughbanks and Hoffmann. The following features of the experimental energy dispersion curves were reproduced by the theory: semiconductor nature of 2H-MoS_2, energy dispersion of the S3s bands and curvature of the energy bands, specifically at the top and bottom of the Mo4d-S3p valence band. The following features were not reproduced by the theory: indirect gap from $\Gamma \rightarrow T$ and overlap between the highest occupied valence band and the lower Mo4d-S3p bands.

5.2 Electronic Structure of 3-D MoS_2.

Three-dimensional MoS_2, consisting of two MoS_2's per unit cell, was modeled as described in Section 3.4.3. Since this calculation included the lattice vector c, the set of k-points also had to include points in the direction of c^* or $k_3=wc^*$. A set of 855 special k-points was used in the three-dimensional calculation of the theoretical valence band. These points were obtained by repeating the 171 special k-points (used in the two-dimensional case) in the k_3 (or c^*) direction such that k_3 was incremented by $0.1c^*$ from an initial value of 0 to $0.4c^*$ ($k_3=0.5c^*$ was not included due to a maximum number of k-points of 1000 set by the EHMACPP program). The calculations discussed in this section again used the atomic parameters of Hughbanks and Hoffmann, given in Section 3.2. Interactions were included up to four neighbors in each direction.

5.2.1 Effect of Van der Waals Interactions

Prior to analysis of an infinite 3-D MoS_2 structure, the effect of Van der Waals interactions between adjacent MoS_2 layers was studied. As discussed previously, one layer of MoS_2 with no Van der Waals interactions was studied, next four MoS_2 layers, $(MoS_2)_4$, with three Van der Waals interactions was studied. These systems were propagated in only two

dimensions. Three-dimensional MoS_2, propagated in 3 directions, with an infinite number of Van der Waals interactions between the layers, was the last system studied.

The most interesting result of this study comes from a comparison of the standard energy of formation, ΔU_f°, per MoS_2 unit for each system. The energies of formation for the three systems discussed above are given in Table 18. A description of the method used for determining the energies of formation is given in Appendix A. Comparison of the energies shows that 2-D MoS_2 is the most stable system. Theoretically, the addition of three Van der Waals interactions, as in 2-D $(MoS_2)_4$, and an infinite number of Van der Waals interactions, as in 3-D MoS_2, causes a destabilization of the system. Thus, theoretically 2-D MoS_2 is more stable than 2-D $(MoS_2)_4$ which is more stable than 3-D MoS_2. 3-D MoS_2 is destabilized by 9.84 kcal/mole when compared to 2-D MoS_2. These theoretical results indicate that 3-D MoS_2 should not form because of the stability of the 2-D form. However, in nature 3-D MoS_2 is the form that actually exists. Van der Waals interactions should stabilize not destabilize the 3-D MoS_2 structure.

Table 18.

Standard energy of formation, ΔU_f°, per MoS_2 unit for the following systems: 2-D MoS_2, 2-D $(MoS_2)_4$, 3-D MoS_2, and 1-D $(MoS_2)_5$ terminating in $(10\bar{1}0)$ and $(10\bar{1}1)$ edges. The 1-D $(MoS_2)_5$ systems are discussed in Section 5.3. Appendix A gives a description of the method used for determining the energies of formation. Units are in kcal/mol.

System	Edges	# Sheets	ΔU_f° (kcal/mol of MoS_2)
2-D MoS_2	None	1	-463.58
2-D $(MoS_2)_4$	None	4	-456.24
3-D MoS_2	None	∞	-453.74
1-D $(MoS_2)_5$	$(10\bar{1}0)$	1	-435.75
1-D $(MoS_2)_5$	$(10\bar{1}1)$	1	-447.28

Energy destabilization due to the addition of Van der Waals interactions between successive layers is also obtained in calculations of graphite using the EHMACPP program. The hexagonal layer structure of graphite consists of 4 carbons per unit cell. Two carbons repeat in the first layer and the remaining two carbons repeat in the second layer. Calculations similar to those for MoS_2 were carried out such that the energies of formation for 2-D graphite containing 1, 2, and 4 layers of carbon atoms (thus 0, 1, and 3 Van der Waals interactions) could be compared. The energies of formation for 2-D graphite containing 1, 2, and 4 layers of carbon

were found to be -254.57 kcal/mole, -253.71 kcal/mole, and -253.28 kcal/mole, respectively. Theoretically, the graphite structure containing 1 carbon layer is the most stable structure, as the number of Van der Waals interactions and carbon layers increases, the graphite structure was destabilized in energy. Thus, solid state extended Hückel theory, in general, does not accurately calculate the small energies of Van der Waals interactions.

5.2.2 Theoretical Valence Band of 3-D MoS_2

The theoretical valence band of three-dimensional MoS_2 was calculated using the structural parameters referred to in Section 3.4.3. A set of 855 special **k**-points and the atomic parameters of Hughbanks and Hoffmann were used for this calculation. The theoretical valence band of 3-D MoS_2 is shown in Figure 31. Large differences between the theoretical valence bands of the 2-D and 3-D MoS_2 systems are not present. The only difference seems to be a smoothing out of levels in the 3-D case. Thus, in calculations of the theoretical valence band of MoS_2, the 2-D system results in similar structure as the 3-D system.

5.2.3 Theoretical Energy Dispersion Curves

Energy dispersion curves for 3-D MoS_2 were calculated in the following directions: $\Gamma \rightarrow M$, $\Gamma \rightarrow K$, $K \rightarrow M$, and $\Gamma \rightarrow A$. The **k**-point sets used in this calculation were the same as those used in the 2-D case and are described in Section 3.7.2. Figure 32 shows the theoretical energy dispersion curves of 3-D MoS_2. S3s and Mo4d-S3p valence bands as well as the lower portion of the conduction bands are shown. One immediately obvious feature is that the number of bands in the 3-D case is twice that of the 2-D case. The 2-D case involved only one MoS_2 per unit cell; the 3-D case involves two MoS_2's per unit cell. The number of crystal energies output depends on the number of atomic orbitals input. There are 9 atomic orbitals per Mo atom (one, 5s; three, 5p; and five, 4d) and 4 atomic orbitals per S atom (one, 3s and three, 3p). Thus, for the 2-D system, 17 atomic orbitals are input resulting in the calculation of 17 crystal energies and 17 energy bands. For the 3-D system, 34 atomic orbitals are input resulting in the calculation of 34 crystal energies and energy bands.

The lowest energy bands, S3s bands, run almost parallel in some directions indicating a splitting of the bands due to the addition of the third dimension. For instance, focusing on the lowest S3s energy band (band #1), this band has been split from one band in the 2-D case to two bands in the 3-D case. One of the 2 bands was stabilized in energy while the other was destabilized in energy. The largest degree of splitting between the two bands occurs at the Γ point. At the K point the S3s bands become degenerate. The reason for this splitting can be

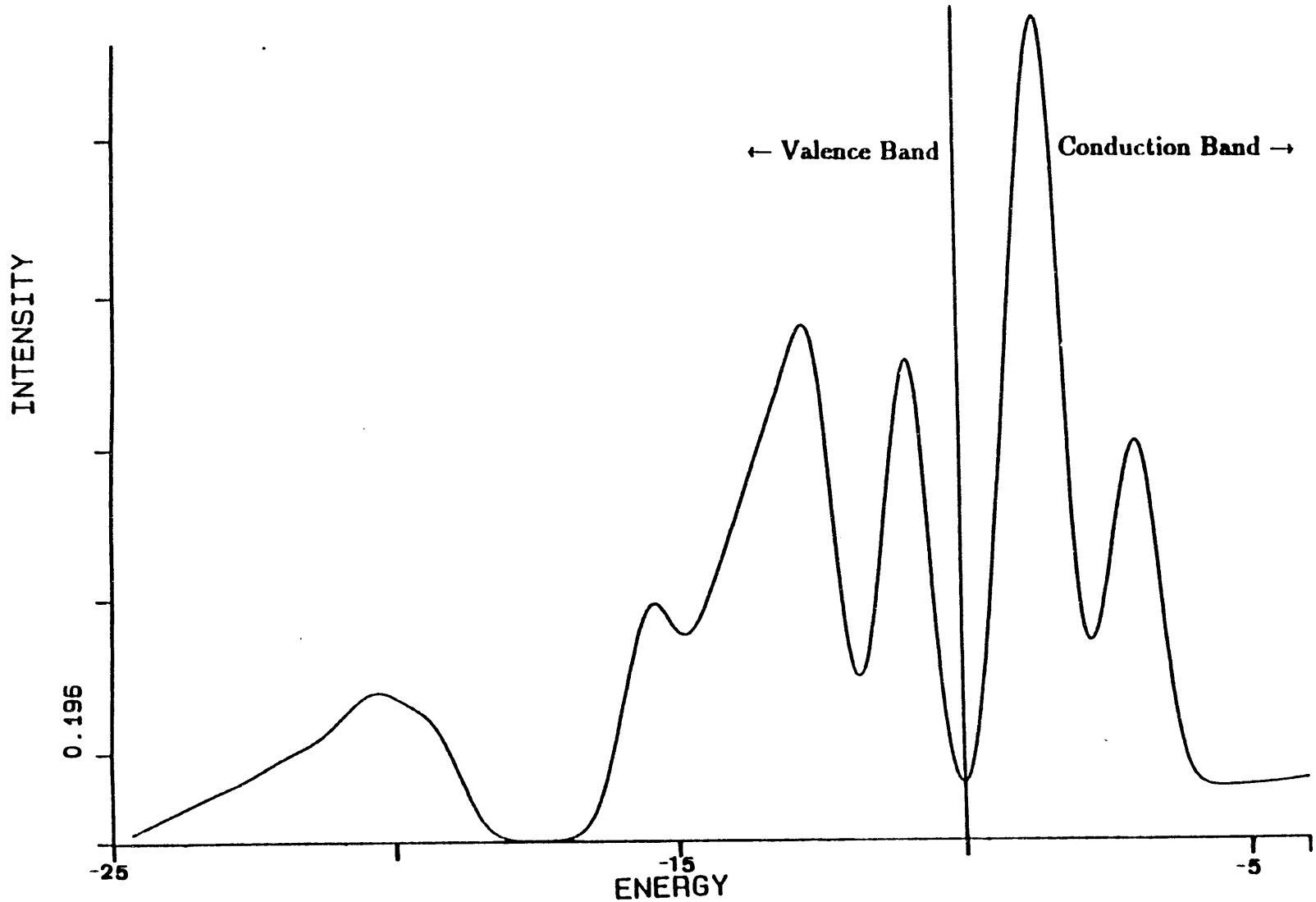

Figure 31. Theoretical valence band of 3-D MoS_2. A set of 855 special k-points and the S3s, S3p and Mo4d atomic parameters of Hughbanks and Hoffmann were used in this calculation.

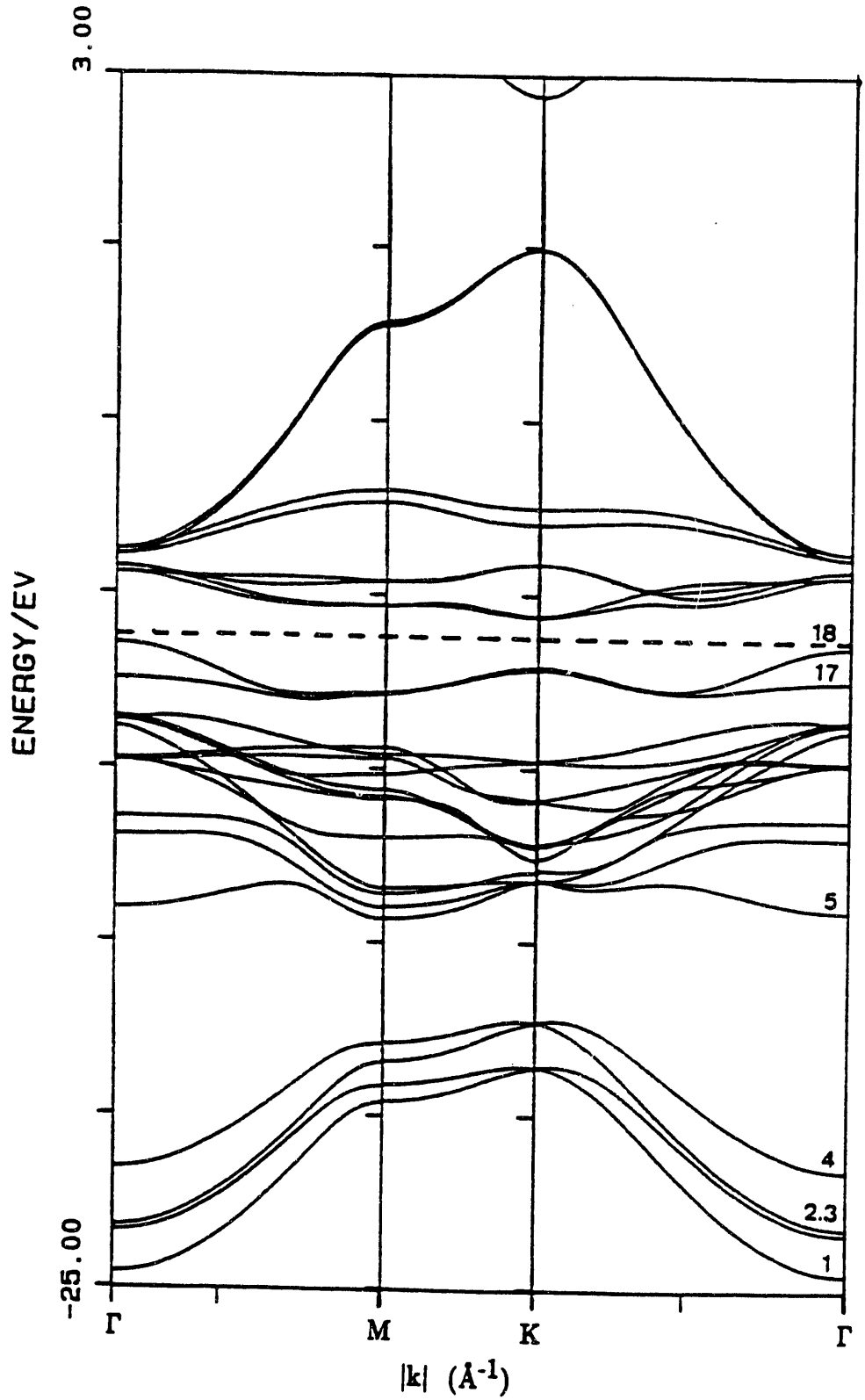

Figure 32. Theoretical energy dispersion curves of 3-D MoS_2. S3s and Mo4d-S3p valence bands as well as the lowest energy portion of the conduction bands are shown. Note the presence of an indirect gap from Γ—K.

explained by looking at the atomic orbital character of the crystal orbitals responsible for the energy dispersion of the S3s bands. Addition of the third dimension adds MoS_2 layers in the c direction. Adjacent MoS_2 layers result in Van der Waals interactions between the layers. If the atomic orbitals involved in a particular band do not possess a significant component in the c direction (or $\hat{z}$ direction), for instance p_x, p_y, d_{xy} or d_{x2-y2}, then these orbitals will not interact across the wide Van der Waals gap to a significant extent. If the atomic orbitals involved in a particular band do possess a component in the c direction, for instance p_z, d_{z2}, d_{zx}, and d_{yz}, then these orbitals will interact more across the Van der Waals gap. The orbital character of the crystal orbitals responsible for the energy dispersion will be discussed in detail in Chapter 6.

Addition of the third dimension into the calculation of the energy dispersion curves dramatically affects the band gap of the MoS_2 system. From Figure 32, it can be seen that the highest energy point of the valence band is now located at Γ. The previous calculation on 2-D MoS_2 resulted in this point being located at K, see Figure **30a**. The lowest point of the conduction band in the 3-D system (as well as the 2-D system) occurs at the K point. An indirect band gap from the highest occupied band at Γ to the lowest unoccupied band at K of 0.68 eV is the smallest energy gap in the 3-D system. Thus, on proceeding from the 2-D to the 3-D system, the band gap changes from direct (K→K) to indirect (Γ→K) and narrows from 1.19 eV to 0.68 eV. In all cases for the MoS_2 system, addition of the third dimension results in an indirect band gap.

Splitting of the highest energy valence band at the Γ point results in the formation of the indirect gap. As described for the S3s bands, this band is split into two bands at Γ. One band is stabilized in energy while the other is destabilized in energy. The band that is destabilized in energy causes the indirect gap. The cause of the destabilization can be obtained from the orbital character of the crystal orbitals and will be discussed in Chapter 6. One other feature to notice is that the band destabilized in energy is destabilized more than the band that is stabilized in energy. This results in a net destabilization of the 3-D structure when compared to the 2-D structure. Thus, addition of Van der Waals interactions into the system causes a net destabilization of the energy, as indicated by the energies Section 5.2.1. Addition of Van der Waals interactions should actually stabilize the structure. Thus, solid state extended Hückel theory does not accurately calculate Van der Waals interactions.

Energy dispersion in the direction Γ→A is shown in Figure 33. In this direction, the value of the wavevector ranges from $\mathbf{k}=0$ to $\mathbf{k}=\frac{1}{2}\mathbf{c}^*$. Energy dispersion in this direction is relatively flat, such that no curvature of the bands is evident. Again as in the previous directions, the largest amount of splitting is present at Γ. For example the highest crystal band,

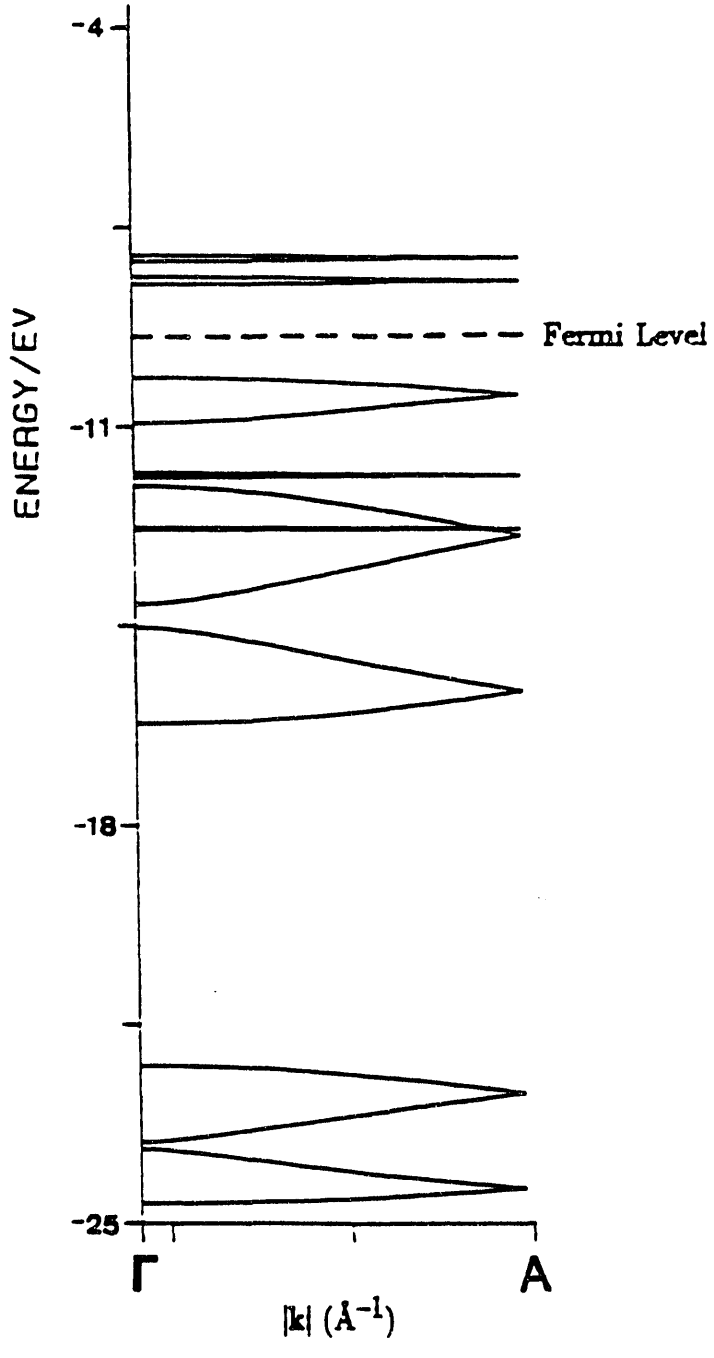

Figure 33. Theoretical energy dispersion curves of 3-D MoS_2 in the direction Γ—A. S3s and Mo4d-S3p valence bands as well as the lowest energy portion of the conduction bands are shown.

Band #9 in 2-D MoS_2, is split into two bands #17 and #18 in 3-D MoS_2. As one proceeds from Γ to A, the bands begin to decrease in the amount of splitting until at A the bands are degenerate. For example, Bands #17 and #18 have energies of -10.93 eV and -10.13 eV at Γ respectively. At A, Bands #17 and #18 are degenerate and have an energy of -10.43 eV. This energy is close to the energy of Band #9 at Γ in 2-D MoS_2 of -10.68 eV. As will be discussed in Chapter 6, splitting of the bands on proceeding from 2-D to 3-D MoS_2 occurs mainly due to bonding and antibonding interactions of the sulfur orbitals across the Van der Waals gap. The degeneracies present at A indicate that an equal number of antibonding and bonding interactions are present in both bands due to the value of the phase factor at A. Thus degeneracy of the bands results at A.

5.3 Electronic Structure of 1-D $(MoS_2)_5$ Terminating in $(10\bar{1}0)$ and $(10\bar{1}1)$ Edges.

The electronic structures of two systems having a repeat unit of five MoS_2's per unit cell, $(MoS_2)_5$, and terminating in different edge planes were studied. Systems terminating in $(10\bar{1}0)$ and $(10\bar{1}1)$ edges were studied. A description of these models is given in Section 3.4.4. The purpose of this study was to look at changes in the electronic structure produced upon the addition of edges. Since the $(MoS_2)_5$ unit was propagated in one-dimension parallel to the Γ→K, the set of **k**-points for the calculations ranged from $\mathbf{k}_1$=0 to $\mathbf{k}_1$=0.5$\mathbf{a}^*$ in increments of 0.05$\mathbf{a}^*$. Atomic parameters used for the Slater-type radial functions were those obtained from Hughbanks and Hoffmann, Section 3.2.

5.3.1 1-D $(MoS_2)_5$ Terminating in $(10\bar{1}0)$ Edges

The first 1-D $(MoS_2)_5$ system studied was the system terminating at the $(10\bar{1}0)$ edges. As discussed previously, addition of $(10\bar{1}0)$ edges exposes two different edges. The first edge consists of two-coordinate molybdenum atoms; the second edge consists of one-coordinate sulfur atoms (in both the first and third atomic layer). The energy of formation, ΔU_f°, of the 1-D $(MoS_2)_5$ systems containing edges must be compared to the energy of formation of the 2-D MoS_2 system containing no edges. This is a correct comparison since these structures each contain one MoS_2 layer such that Van der Waals interactions are not present. The energy of formation of 1-D $(MoS_2)_5$ containing $(10\bar{1}0)$ is -435.75 kcal/mole while that of 2-D MoS_2 is -463.58 kcal/mole as shown in Table 18 Section 5.2.1. Thus, addition of $(10\bar{1}0)$ edges destabilizes the structure. Addition of these edges also leads to edge states that widen the S3s valence band, specifically at the K point. Surface states also appear at the top of the valence band leading to overlap of the conduction and valence bands.

The theoretical valence band of the 1-D $(MoS_2)_5$ system terminating at the $(10\bar{1}0)$ edges is shown in Figure 34a. Modified atomic orbital populations for the Mo4d, S3s, and S3p orbitals and Mo $4d_{z2}$, $4d_{xy}$, $4d_{x2-y2}$, $4d_{zx}$, and $4d_{yz}$ orbitals are shown in Figures 34b and 34c, respectively. The theoretical valence band indicates that the valence and conduction bands overlap to a large degree. In 2-D and 3-D MoS_2 systems, a small energy gap existed between the valence and conduction bands. Thus, semiconductor behavior is not present in the 1-D $(MoS_2)_5$ system terminating at the $(10\bar{1}0)$ edges. Prior to gaussian smoothing by the program, the top of the valence band is located at -10.769 eV for the $(10\bar{1}0)$ system. Thus, the highest occupied levels of the $(10\bar{1}0)$ system lie lower in energy than those of the 2-D MoS_2 system in which the top of the valence band occurs at -10.656 eV. This indicates that surface states due to the addition of edges are unoccupied. Most of the changes in the theoretical valence band can be attributed to changes in the Mo4d MAOPOP. The S3s and S3p MAOPOP's are similar for both the 2-D MoS_2 and 1-D $(MoS_2)_5$ systems. However, the Mo4d MAOPOP has changed dramatically so that the valence and conduction bands overlap. A comparison of the Mo4d contributions in both cases shows that most of the valence band changes occur because of changes in the Mo $4d_{zx}$ and $4d_{yz}$ MAOPOP's. The $Mo4d_{xz}$ orbitals now contribute to the highest occupied valence band and the $Mo4d_{yz}$ orbitals contribute to the region between the highest occupied valence band and lowest unoccupied conduction band.

5.3.2 1-D $(MoS_2)_5$ Terminating in $(10\bar{1}1)$ Edges

A 1-D $(MoS_2)_5$ system terminating at the $(10\bar{1}1)$ edges was also studied. As discussed previously, Section 3.4.4, addition of $(10\bar{1}1)$ edges also exposes two different edges. The first edge consists of two-coordinate sulfur atoms (third atomic layer only) and four-coordinate molybdenum atoms. The second edge consists of one-coordinate sulfur atoms (first atomic layer only) and five-coordinate molybdenum atoms. Thus, Mo atoms residing on $(10\bar{1}1)$ edges have a higher degree of coordination than atoms residing on $(10\bar{1}0)$ edges. Theoretically, the energy of formation of the 1-D $(MoS_2)_5$ structure was found to be more stable by 11.5 kcal/mole when it terminated $(10\bar{1}1)$ edges rather than $(10\bar{1}0)$ edges. For these structures, the energies of formation were -447.28 kcal/mole and -435.75 kcal/mole for the $(10\bar{1}1)$ and the $(10\bar{1}0)$ edges shown in Table 18 Section 5.2.1. Both of the structures with edges were found to be less stable when compared to the 2-D MoS_2 system possessing no edges.

Since the 1-D $(MoS_2)_5$ system terminating in $(10\bar{1}1)$ edges was found to be the more stable structure, this structure was studied in greater detail. Addition of these edges leads to a widening of the S3s valence band particularly at the K point. Surface states are also introduced

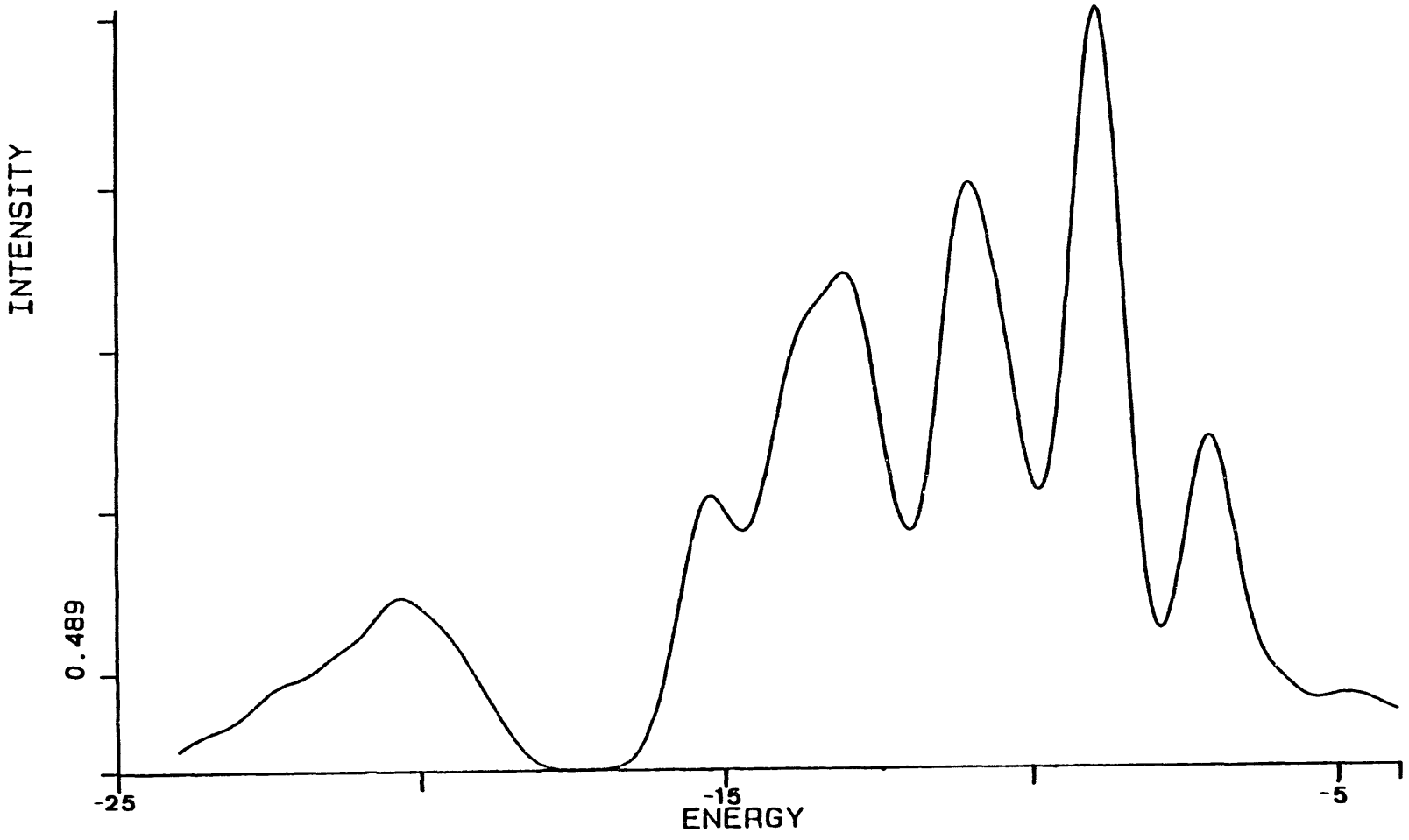

Figure 34a. Theoretical valence band of 1-D $(MoS_2)_5$ system terminating in $(10\bar{1}0)$ edges. The atomic parameters of Hughbanks and Hoffmann were used in this calculation.

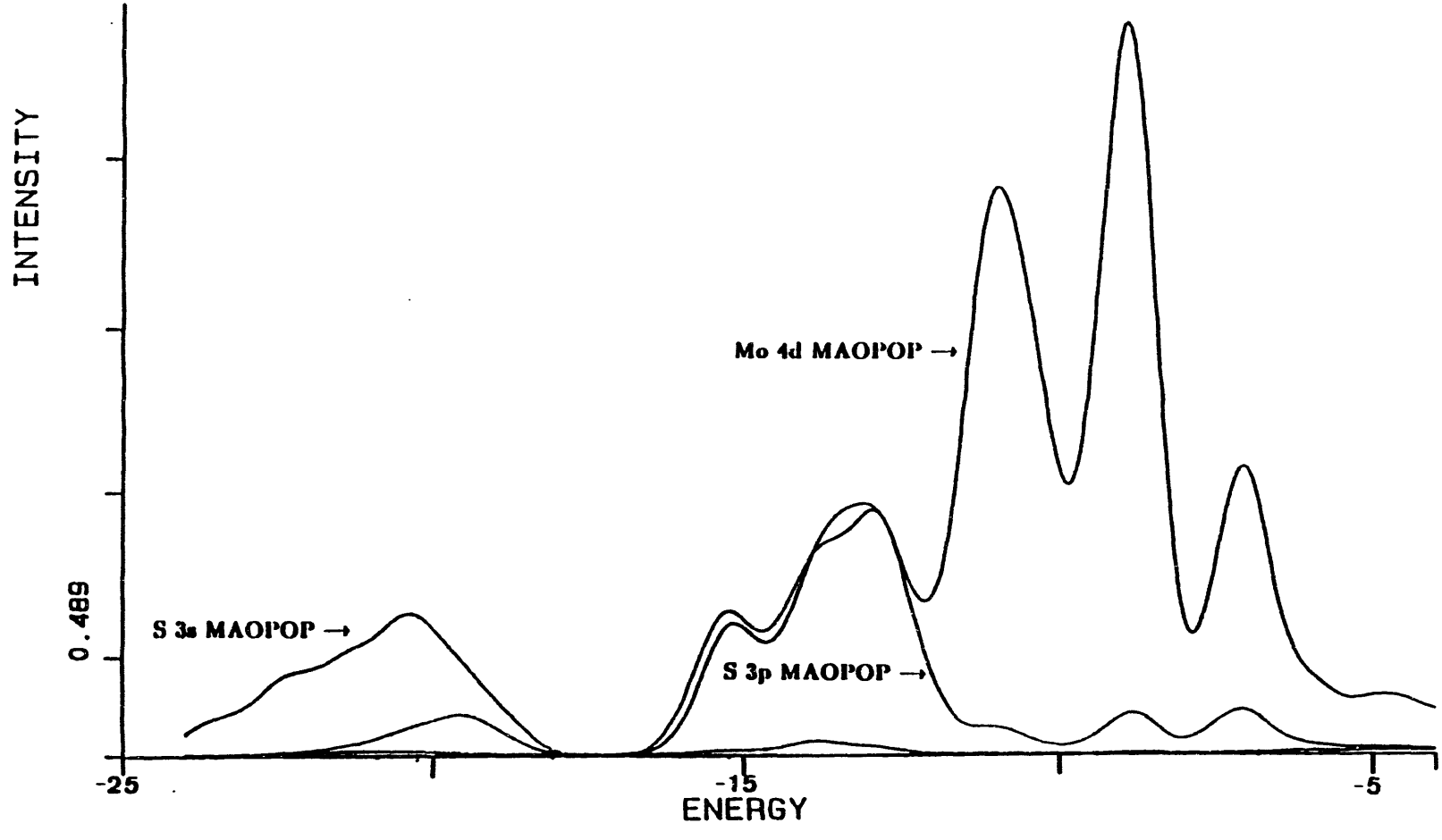

Figure 34b. Modified atomic orbital populations for the Mo4d, S3s and S3p orbitals. The atomic parameters of Hughbanks and Hoffmann were used in this calculation.

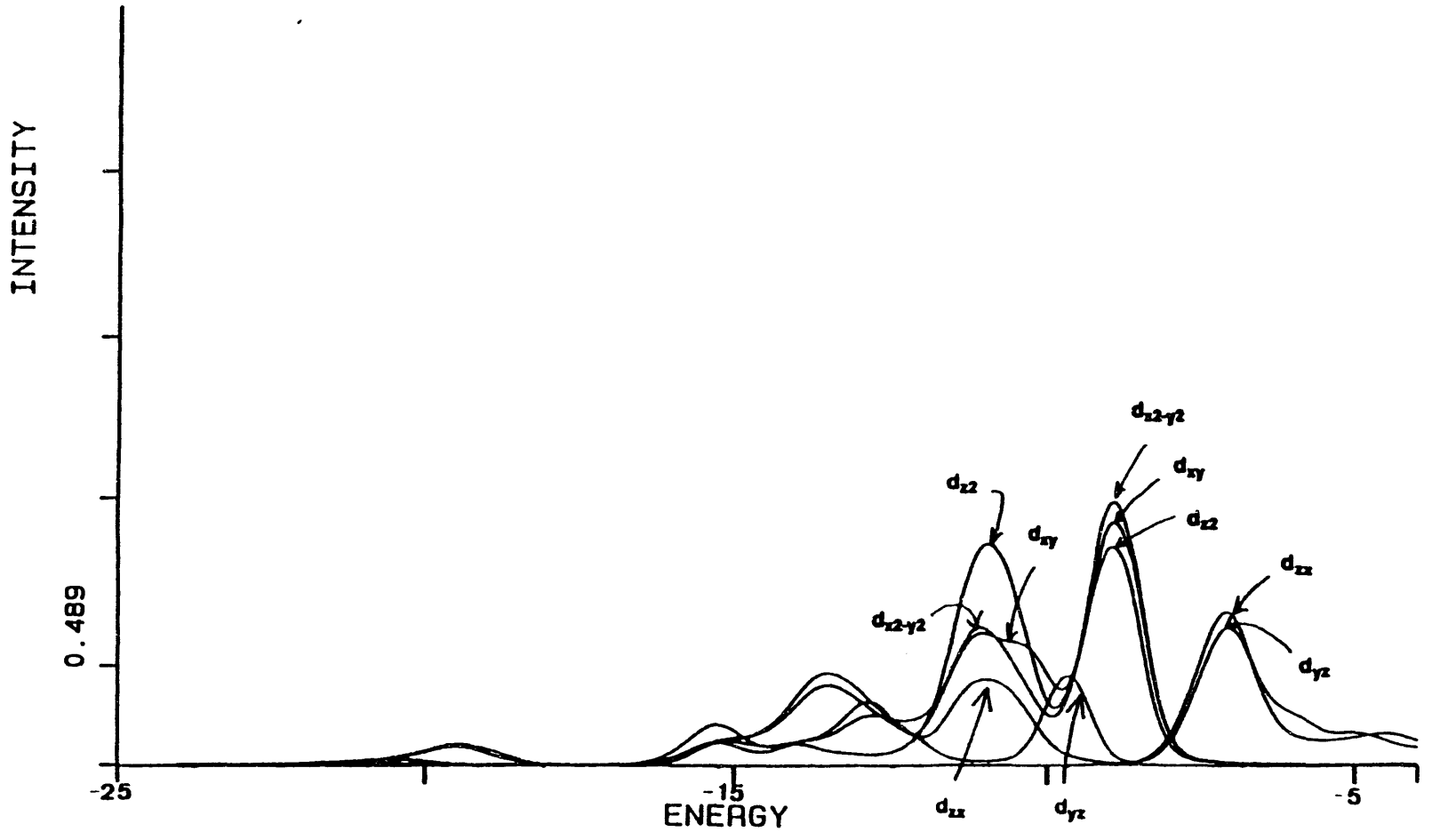

Figure 34c. Modified atomic orbital populations for the Mo $4d_{z2}$, $4d_{xy}$, $4d_{x2-y2}$, $4d_{zx}$, and $4d_{yz}$ orbitals. The atomic parameters of Hughbanks and Hoffmann were used in this calculation.

at the top of the valence band such that the valence band and the conduction bands overlap.

The orbital character of the surface states can be obtained from the coefficients of the crystal orbitals. A more detailed analysis of the coefficients will be discussed in Chapter 6. The theoretical valence band of the 1-D $(MoS_2)_5$ system terminating in $(10\bar{1}1)$ edges is shown in Figure 35a. The modified atomic orbital populations for the Mo4d, S3s, and S3p orbitals and the individual Mo4d contributions to the valence band are shown in Figures 35b and 35c. Again, the theoretical valence band overlaps with the conduction band changing the behavior of the system from semiconductor to metallic. In this system, the top of the valence band is located at -10.645 eV which is slightly above that of the 2-D MoS_2 system which occurs at -10.769. This may indicate that unlike the $(10\bar{1}0)$ system, the $(10\bar{1}1)$ system possesses a small amount of occupied surface states. Thus, if a real system possessed a large amount of $(10\bar{1}1)$ edges, XPS valence band analysis of this system would show extra intensity at the top of the valence band due to electrons residing in surface states at the top of the valence band. This result will be discussed in more detail in Chapter 6 where it will be used to explain differences in the XPS valence bands of polycrystalline and single crystal MoS_2. The behavior of the S3s and S3p MAOPOP's is similar in both the 2-D MoS_2 system and the 1-D $(MoS_2)_5$ edge terminated systems. Changes in the theoretical valence band can be attributed to changes in the Mo4d MAOPOP. Major changes occur in the MAOPOP's of the Mo $4d_{zx}$ and Mo $4d_{yz}$ orbitals. In the 2-D MoS_2 system, these orbitals were well separated from the other three Mo4d orbitals at the top of the valence band and the bottom of the conduction band. Addition of $(10\bar{1}1)$ edges leads to a mixing of the d_{zx} and d_{yz} orbitals with the d_{z2}, d_{xy}, and d_{x2-y2} orbitals.

5.3.3 Comparison of Theoretical Charges

The EHMACPP program also provides an option for calculating the overall electron population on the atoms (over the filled crystal orbitals). Electron populations can be used to obtain average charges on the atoms contained in one unit cell. For example, in the case of 2-D MoS_2, electron populations were calculated for each of the 171 special **k**-points. Since the repeat unit was one MoS_2, these populations were calculated for one molybdenum atom (Mo_1) and two sulfur atoms (S_2 and S_3). Individual electron populations obtained at each **k**-point were averaged over all of the 171 special **k**-points, to obtain an average electron population for each atom. Average charges were found by subtraction of the average electron population from the number of valence electrons on the bare atom. In 2-D MoS_2, average electron populations on the atoms were the following: Mo_1, 5.442790; S_2, 6.278607; and S_3, 6.278607. Molybdenum atoms ($5s^14d^5$) and sulfur atoms ($3s^23p^4$) each possess 6 valence electrons. Consequently,

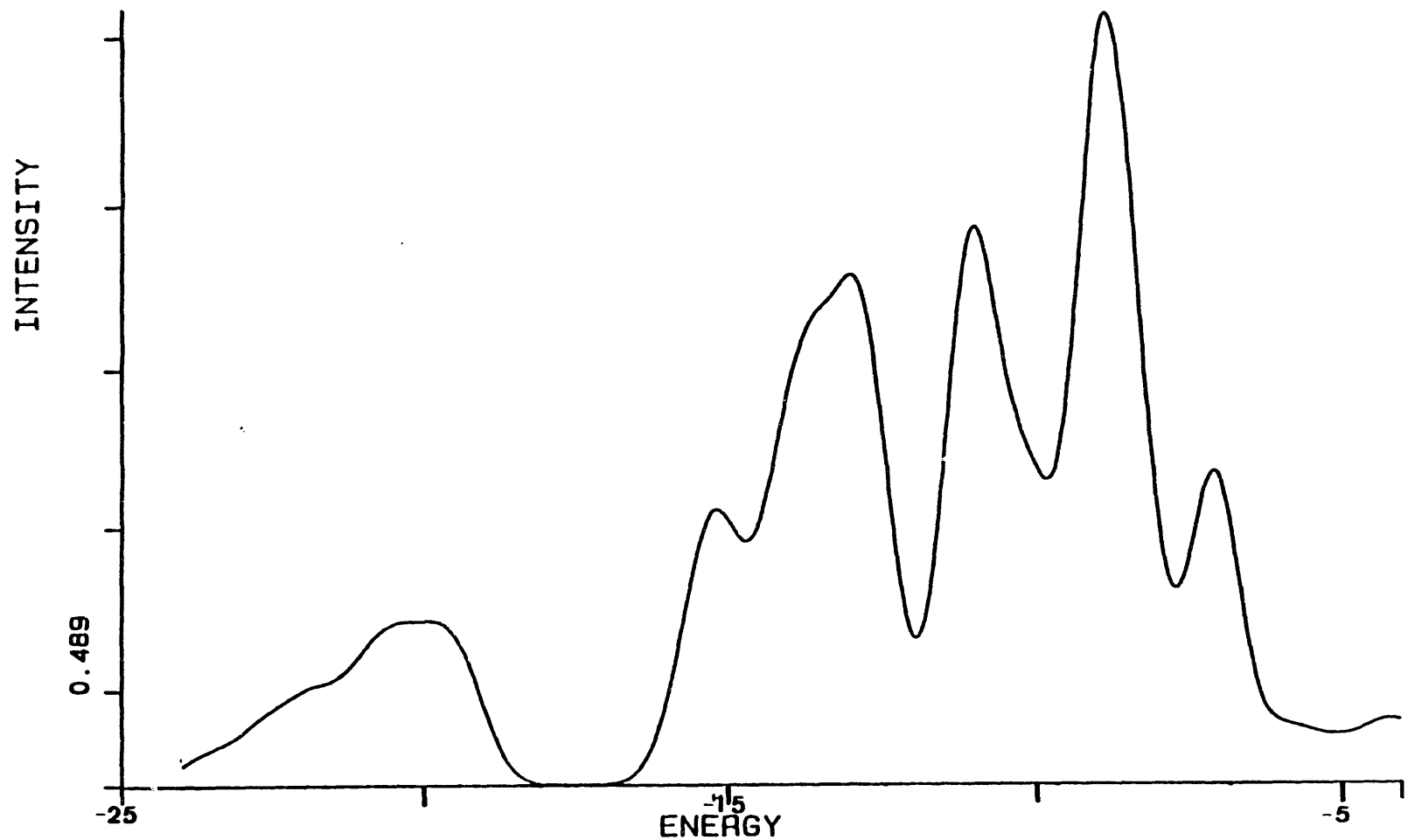

Figure 35a. Theoretical valence band of 1-D $(MoS_2)_5$ system terminating in $(10\bar{1}1)$ edges. The atomic parameters of Hughbanks and Hoffmann were used in this calculation.

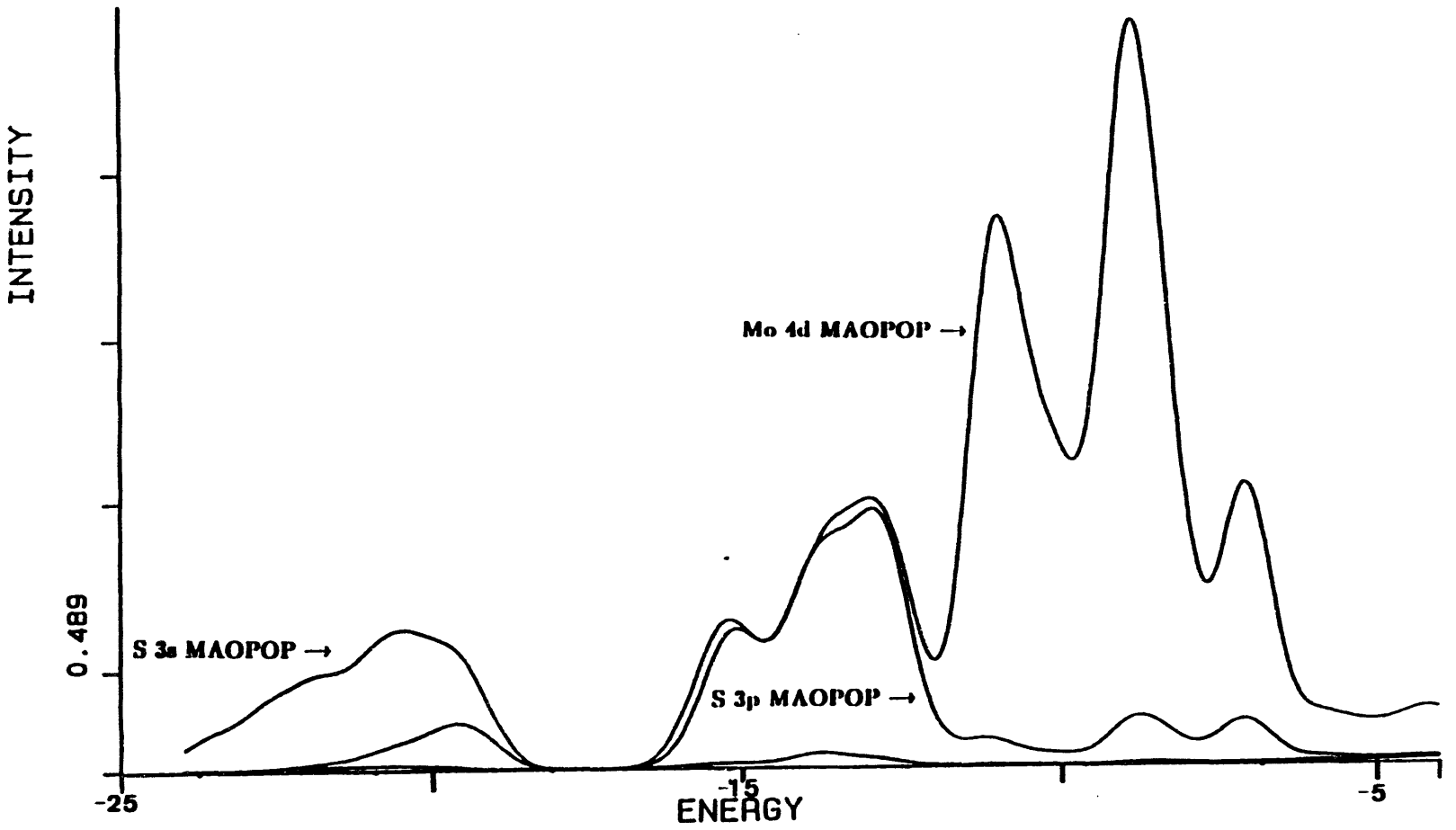

Figure 35b. Modified atomic orbital populations for the Mo4d, S3s and S3p orbitals. The atomic parameters of Hughbanks and Hoffmann were used in this calculation.

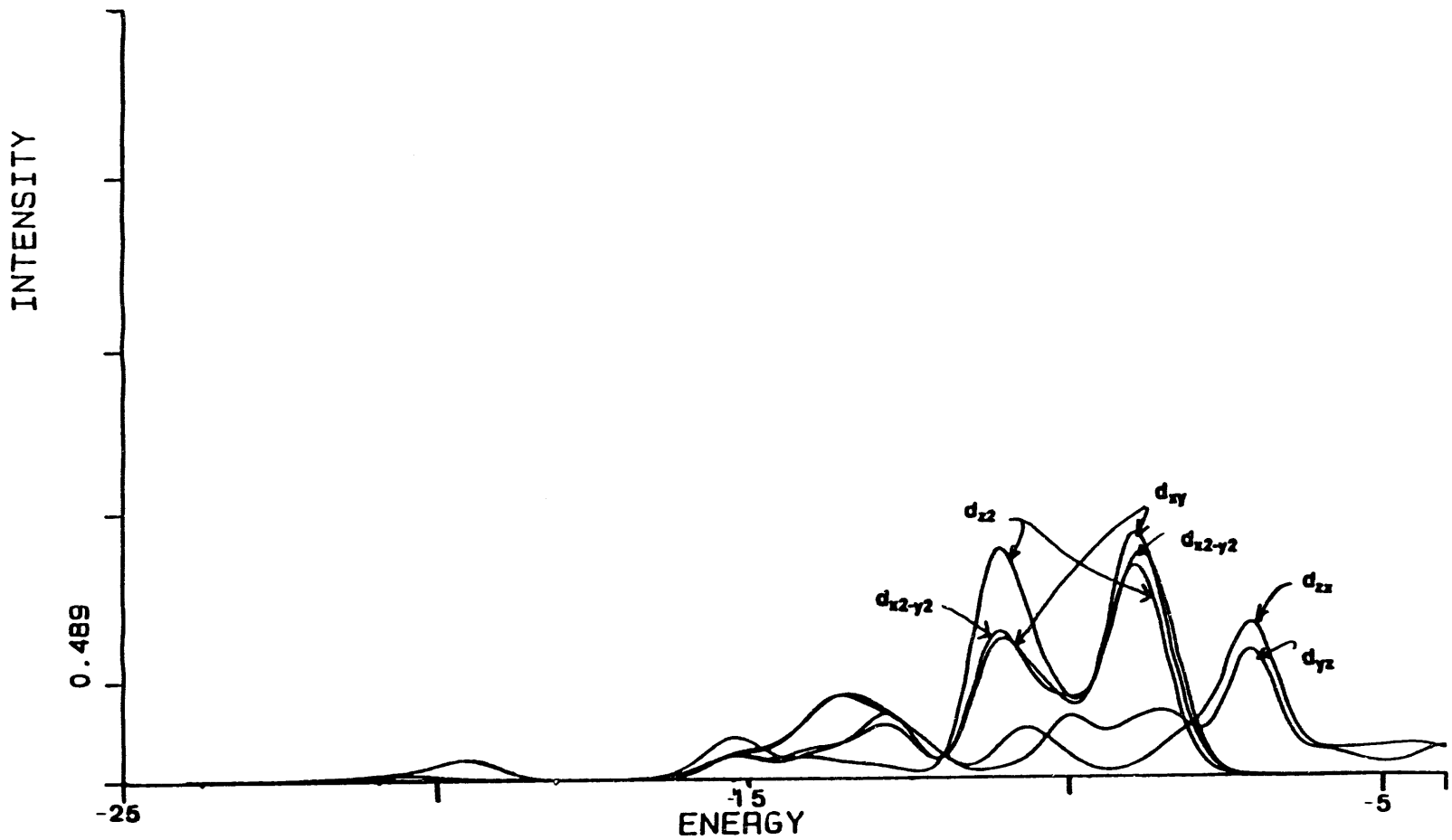

Figure 35c. Modified atomic orbital populations for the Mo $4d_{z2}$, $4d_{xy}$, $4d_{x2-y2}$, $4d_{zx}$, and $4d_{yz}$ orbitals. The atomic parameters of Hughbanks and Hoffmann were used in this calculation.

average charges are the following: Mo_1, +0.56; S_2, -0.28; and S_3, -0.28. Average charges on the molybdenum and sulfur atoms in the 3-D MoS_2 system were also calculated. Average charges for the atoms of the 3-D system are the following: Mo_1, +0.74, S_2,-0.37; S_3, -0.37; Mo_4, +0.74; S_5, -0.37; and S_6, -0.37. The theoretical average charges are much different than the formal oxidation states assigned to the atoms in MoS_2. The formal oxidation state of Mo is +4 while that of S is -2. Thus, these results indicate that the bonding in MoS_2 is largely covalent in nature.

On the 1-D $(MoS_2)_5$ structures, average charges are more complicated. In each unit cell there are 5 different Mo species and 10 different S species due to termination of the structure with edges. Average molybdenum and sulfur charges for the 15 atoms can be obtained by averaging the individual charges at each **k**-point. The resulting average charges are given in Table 19. As indicated in the table, molybdenum atoms in 1-D $(MoS_2)_5$ systems are more positively charged when compared to the corresponding 2-D MoS_2 system. Sulfur atoms are also less negatively charged when compared to the 2-D system, except for coordinately

Table 19.

Average charges for 2-D MoS_2 and 1-D $(MoS_2)_5$ systems terminating in $(10\bar{1}0)$ and $(10\bar{1}1)$ edges. Coordination of the atoms is shown in parentheses.

Atom	2-D MoS_2	1-D $(MoS_2)_5$ $(10\bar{1}0)$ edges	1-D $(MoS_2)_5$ $(10\bar{1}1)$ edges
Mo-0101	+0.56 (6)	+0.87 (2)	+0.69 (4)
Mo-0201		+0.70 (6)	+0.65 (6)
Mo-0301		+1.47 (6)	+1.25 (5)
Mo-0401		+0.92 (6)	+0.64 (6)
Mo-0501		+0.65 (6)	+0.71 (6)
S-0101	-0.28 (3)	-0.22 (3)	-0.27 (3)
S-0201	-0.28 (3)	-0.22 (3)	-0.19 (3)
S-0301		-0.27 (3)	-0.26 (3)
S-0401		-0.27 (3)	-0.27 (3)
S-0501		-1.30 (1)	-1.21 (1)
S-0601		-1.30 (1)	-0.68 (2)
S-0701		-0.26 (3)	-0.27 (3)
S-0801		-0.26 (3)	-0.27 (3)
S-0901		-0.25 (3)	-0.21 (3)
S-1001		-0.25 (3)	-0.29 (3)

unsaturated edge sulfur atoms. Edge sulfur atoms are more negative when compared to sulfur in 2-D MoS_2. In the structure terminating in $(10\bar{1}0)$ edges, the two one-coordinate edge sulfur atoms (S-0501 and S-0601) possess an average charge of -1.30 as compared to -0.28 for the 2-D system. Two-coordinate edge molybdenum atoms possess an average charge of +0.87 as

compared to +0.56 for molybdenum atoms in the 2-D system. Thus, termination of MoS_2 layers in $(10\bar{1}0)$ edges results in one positively charged edge and one negatively charged edge. It is interesting to note that the most positively charge molybdenum atoms are not two-coordinate edge molybdenums but rather six-coordinate molybdenum atoms (Mo-0301) bound to two one-coordinate sulfur atoms (S-0501 and S-0601). Thus, electrons are transferred from the molybdenum atoms (Mo-0301) toward the two one-coordinate sulfur atoms (S-0501 and S-0601).

In the structure terminating at the $(10\bar{1}1)$ edges, two-coordinate edge 1 sulfur atoms (S-0601) and one-coordinate edge 2 sulfur atoms (S-0501) possess average charges of -0.68 and -1.21, respectively. These charges are more negatively charged when compared to the sulfur charge of -0.28 in 2-D MoS_2. Four-coordinate edge 1 molybdenum atoms (Mo-0101) and five-coordinate edge 2 molybdenum atoms (Mo-0301) possess average charges of +0.69 and +1.25, respectively. Again, the molybdenum atoms are more positively charged when compared to the 2-D case. The most positively charged molybdenum atoms are edge 2 molybdenum atoms (Mo-0301) coordinated to a one-coordinate sulfur atom. A general trend seems to be that when molybdenum atoms are coordinated to one-coordinate sulfur atoms, electrons are transferred from the molybdenum to the sulfur. The structure terminating at $(10\bar{1}1)$ edges does not exhibit large edge charge separation as does the structure terminating at $(10\bar{1}0)$ edges. In the $(10\bar{1}0)$ structure, edge 1 consists of positively charged molybdenum atoms (+0.87) while edge 2 consists of negatively charged sulfur atoms (-1.30). There are two edge 2 sulfur atoms per one edge 1 molybdenum atom. Thus, the charge separation can be viewed as $|+0.87 - (2 \times -1.30)| = 3.47$ units of charge. In the $(10\bar{1}1)$ structure, edge 1 consists of negatively charged sulfur atoms (-0.68) and positively charged molybdenum atoms (+0.69). Edge 2 also consists of negatively charged sulfur atoms (-1.21) and positively charged molybdenum atoms (+1.25). Thus, the charge separation can be viewed as $|(-0.68 + 0.69) - (-1.21 + 1.25)| = 0.03$. Edge charge separation in the $(10\bar{1}0)$ structure is much greater than that in the $(10\bar{1}1)$ structure. This difference in edge charge separation could account for the large energy stabilization (by 11.53 kcal/mole) of the $(10\bar{1}1)$ structure compared to the $(10\bar{1}0)$ structure. Of course, this is a simplistic view of the edges since charges of fully coordinated atoms next to edge atoms were not considered. However, these results do explain the stability of one structure over another.

5.4 Electronic Structure of 2-D H-MoS_2.

Hydrogen adsorption on 2-D MoS_2 was studied by theoretically placing a hydrogen atom at different sites on the basal plane. Hydrogen was placed at two sites in this study, above

a basal plane sulfur atom and above a basal plane molybdenum atom. A more detailed discussion of these structures can be found in Section 3.4.5. For this calculation, the 171 special k-points were used, as well as the atomic parameters of Hughbanks and Hoffmann, Section 3.2.

5.4.1 Comparison of Energies

A description of the method used in determining the energies and enthalpies of formation and the binding enthalpies of the 2-D H-MoS_2 system is given in Section A.3 of Appendix A. As discussed in Appendix A, theoretical binding enthalpies can be obtained from the enthalpies of formation of the bare and hydrogen covered 2-D MoS_2 surface. The first reaction under consideration is the reaction of hydrogen atoms, H^0, with the basal plane of an MoS_2 surface, equation 16a. As indicated in Table 20, when the MoS_2 is theoretically exposed to hydrogen atoms, hydrogen preferentially adsorbs on exposed sulfur atoms. Molybdenum atoms are not a thermodynamically favored site for hydrogen adsorption in this study, since a positive enthalpy is calculated for reaction 16a. The next reaction under consideration is the reaction of hydrogen molecules, H_2, with the basal plane of an MoS_2 surface, equation 16c. This reaction was studied because most of the experimental results for hydrogen adsorption on MoS_2 were performed using hydrogen gas not hydrogen atoms. Again as indicated in Table 20, thermodynamically the most stable sites for hydrogen adsorption are the sulfur atoms.

$$H^0(g) + MoS_2(s) \rightarrow H\text{-}MoS_2(s) \qquad \Delta H_{10}=\text{see Table 20} \qquad (16a)$$

$$\tfrac{1}{2} H_2(g) \rightarrow H^0(g) \qquad \Delta H_{11}=52.10 \text{ kcal/mole} \qquad (16b)$$

$$\tfrac{1}{2} H_2(g) + MoS_2(s) \rightarrow H\text{-}MoS_2(s) \qquad \Delta H_{12}=\text{see Table 20} \qquad (16c)$$

Table 20.

Binding enthalpies of hydrogen atoms, ΔH_{10}, and molecules, ΔH_{12}, on the surface of 2-D MoS_2. The two sites studied were hydrogen on sulfur and hydrogen on molybdenum. (Units are in kcal/mole.)

Structure	Atom	Site	Coordination	ΔH_{10}	ΔH_{12}
2-D H-MoS_2	Mo	Basal	6	10.24	62.34
2-D H-MoS_2	S	Basal	3	-68.95	-16.85

5.4.2 Comparison of Theoretical Charges

When the surface of 2-D MoS_2 is theoretically covered with hydrogen atoms, the average charges are dramatically altered. Two cases of hydrogen adsorption were studied,

hydrogen above basal plane sulfur atoms (S_2) and hydrogen above basal plane molybdenum atoms (Mo_1). Average charges for these systems are shown in Table 21. When hydrogen was placed above basal plane sulfur atoms, the charge on this sulfur atom (S_2) changed from -0.28 to +0.54. The molybdenum atom charge changed from +0.56 to -0.27 and the charge on the opposite plane sulfur atom (S_3) changed from -0.28 to -0.36. The charge on the hydrogen atom was small, +0.1. A sulfur atom on the basal plane MoS_2 already has a full coordination of 3, thus inclusion of a hydrogen atom increases the number of atoms attached to this atom. The positive charge exhibited by the sulfur atom (S_2) with a coordinated hydrogen is counteracted by the more negative charges of the molybdenum and the remaining sulfur (S_3) atoms.

When the hydrogen atom is placed directly above a basal plane molybdenum atom, the charge on S_2 again becomes more positive, +0.078 compared to -0.28. The molybdenum atom becomes less positive changing from +0.56 to +0.018. Again, electron density is transferred away from the hydrogen adsorbed basal plane to the molybdenum atoms and to the opposite plane of sulfur atoms. In this case, the hydrogen atom is located in the center of a triangle of equivalent sulfur atoms, S_2's. Thus, these three sulfur atoms are sharing the positive charges imposed by the hydrogen covered surface.

Table 21.

Average charges on molybdenum, sulfur, and hydrogen atoms in 2-D H-MoS_2 systems. Two cases of hydrogen adsorption were studied, hydrogen above basal plane sulfur (d_{S-H}=1.35 Å, d_{Mo-H}=3.45 Å) and molybdenum atoms (d_{Mo-H}=1.7 Å, d_{S-H}=1.83 Å).

System	H Position	Mo Charge	S Charge	H Charge
MoS_2	None	+0.56	-0.28	———
H-MoS_2	S_2	-0.27	+0.54 (S_2) -0.36 (S_3)	+0.10
H-MoS_2	Mo_1	+0.02	+0.08 (S_2) -0.36 (S_3)	+0.27

5.4.3 Theoretical Valence Bands

Theoretical valence bands of 2-D H-MoS_2 are shown in Figures 36a and 36c. Modified atomic orbital populations of the Mo4d, S3s and S3p orbitals are shown in Figures 36b and 36d. In Figures 36a and 36b, hydrogen is located directly above basal plane sulfur atoms at a distance, d_{S-H}, of 1.35 Å. In Figures 36c and 36d, hydrogen is located directly above basal plane molybdenum atoms at a distance, d_{Mo-H}, of 1.7 Å. Theoretically, the valence bands have changed dramatically with the addition of hydrogen atoms to the surface.

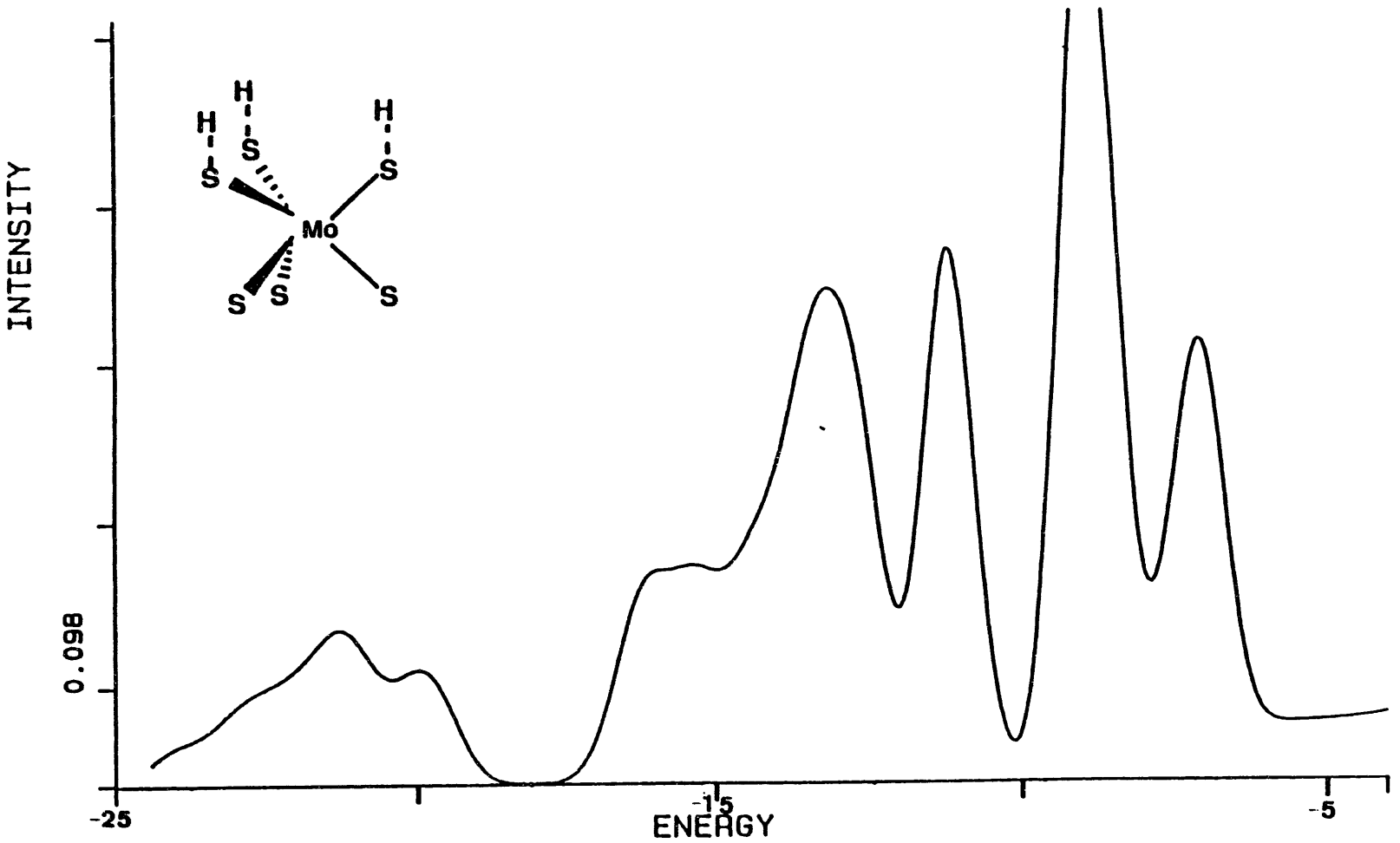

Figure 36a. Theoretical valence band of 2-D H-MoS_2 with hydrogen located directly above basal plane sulfur atoms.

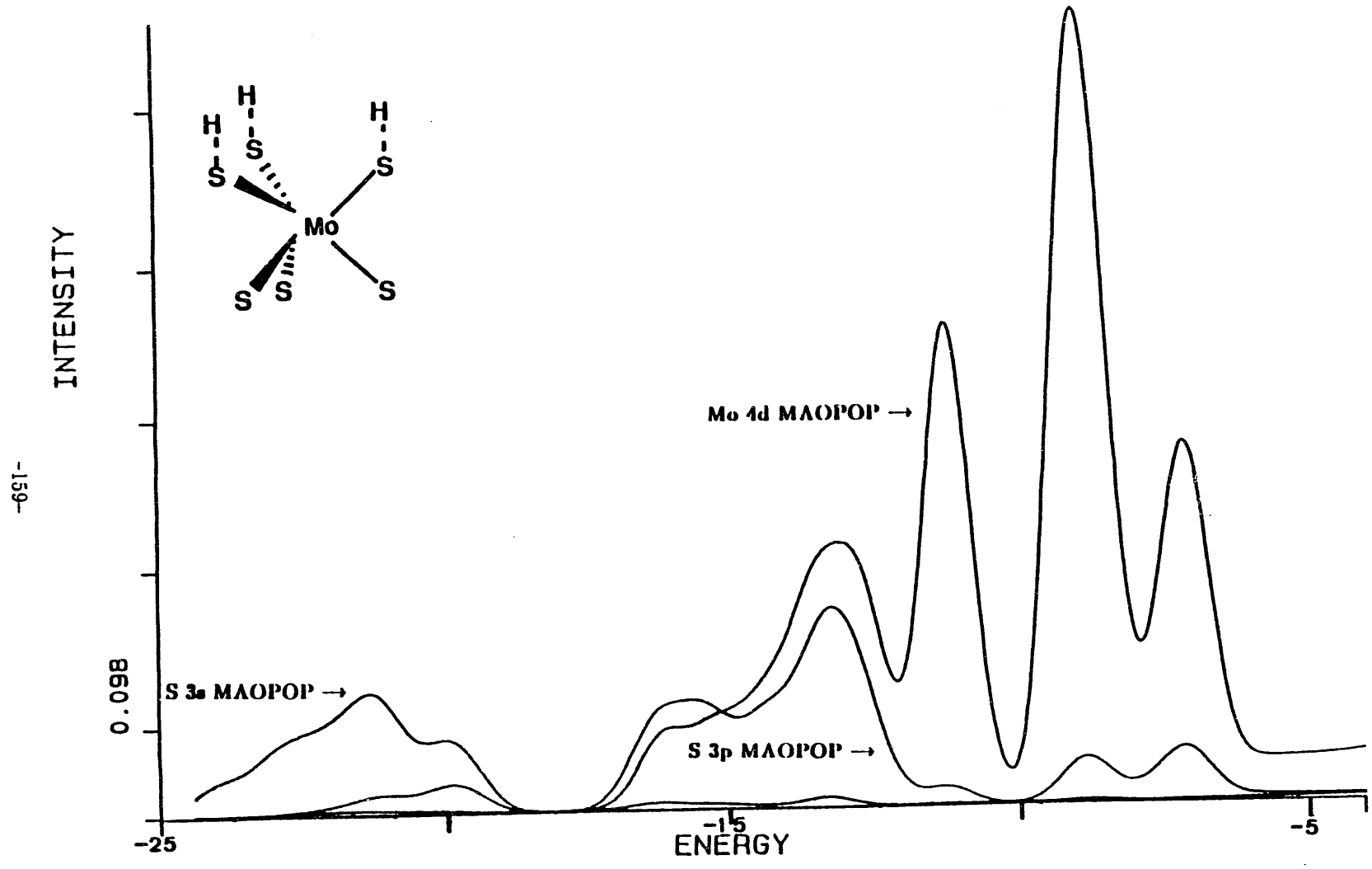

Figure 36b. Modified atomic orbital populations of 2-D H MoS_2 with hydrogen located directly above basal plane sulfur atoms.

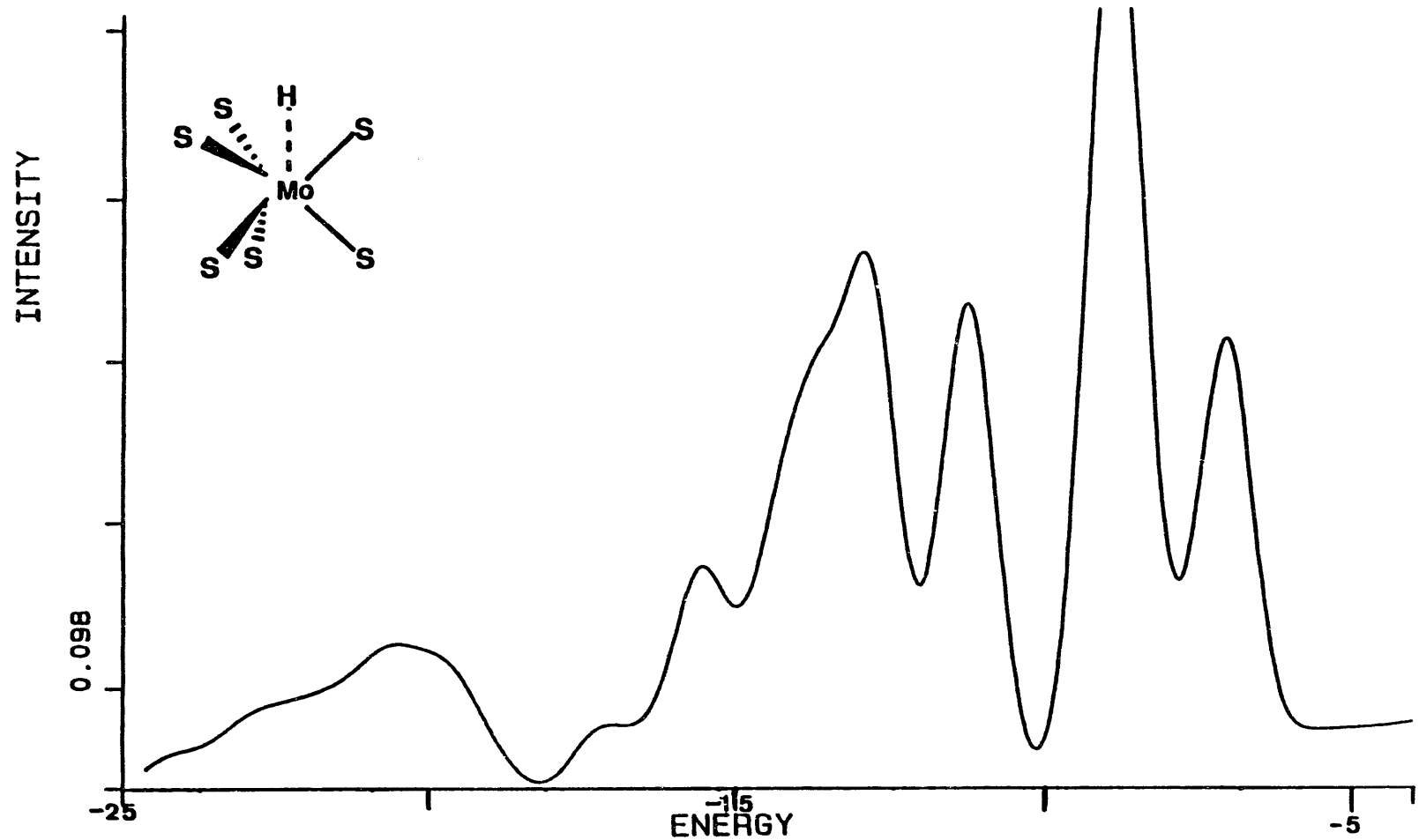

Figure 36c. Theoretical valence band of 2-D H-MoS_2 with hydrogen located directly above basal plane molybdenum atoms.

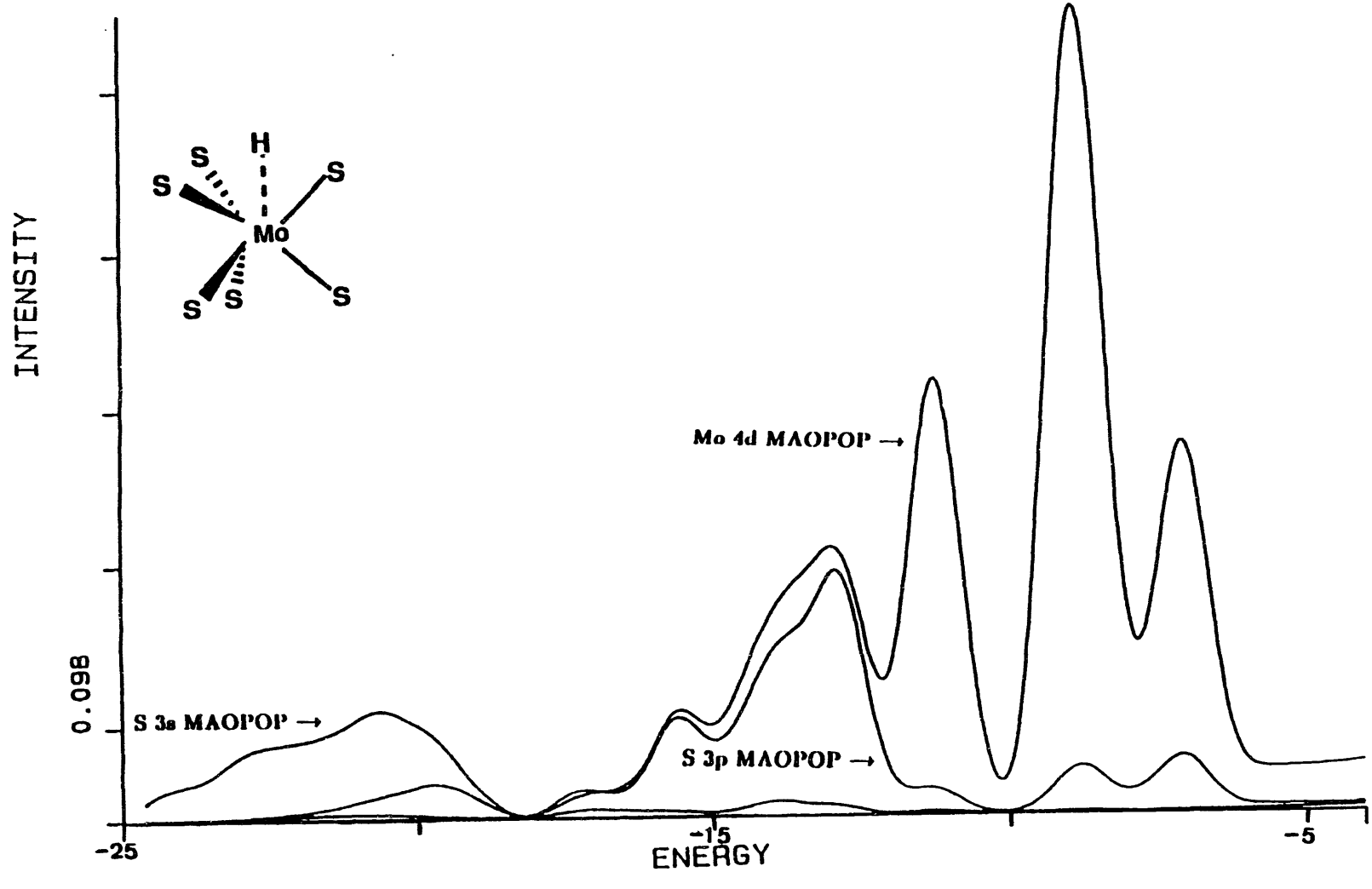

Figure 36d. Modified atomic orbital populations of 2-D II MoS_2 with hydrogen located directly above basal plane molybdenum atoms.

As indicated in Section 5.4.1, basal plane sulfur atoms are more thermodynamically favorable sites for hydrogen adsorption than molybdenum atoms. Addition of hydrogen to basal plane sulfur atoms causes some changes in the theoretical valence band shown in Figure 36a. Dispersion of the S3s band changes so that the maximum peak position is shifted to higher binding energies. A widening of the Mo4d-S3p valence band by ~ 0.8 eV occurs mainly at the bottom of the Mo4d-S3p valence band shown in Figure 36a. The band at the lower end of the Mo4d-S3p valence band is smoothed into a large shoulder. The top peak of the valence band has also shifted to higher binding energies by ~ 0.4 eV Also, a small portion of the conduction band is now filled due to the additional electron from the hydrogen atom.

The theoretical valence band obtained upon the addition of hydrogen to basal plane molybdenum atoms is shown in Figure 36c. Small changes in the dispersion of the S3s band result from the addition of hydrogen. An additional band at the bottom of the Mo4d-S3p valence band has appeared and the top peak of the valence band has shifted to higher binding energies by ~ 0.3 eV. Again, a portion of the conduction is occupied due to the additional electron from the hydrogen atom.

5.4.4 Theoretical Energy Dispersion Curves

The origin of the changes in the theoretical valence bands that occur upon the addition of hydrogen to 2-D MoS_2 can be explained by studying the energy dispersion curves. Energy dispersion curves for the H-MoS_2 systems with hydrogen adsorbed on basal plane sulfur and molybdenum atoms were calculated in the following directions: $\Gamma \rightarrow M$, $\Gamma \rightarrow K$, and $K \rightarrow M$. In Figure 37a are shown the energy dispersion curves for the system in which hydrogen resides on top of the basal plane sulfur atoms. In Figure 37b are shown the energy dispersion curves for the system in which hydrogen resides on top of the basal plane molybdenum atoms.

When hydrogen resides directly above the basal plane sulfur atoms, Figure 37a, the two S3s bands (bands #1 and #2) are lowered in energy in all of the directions calculated. A lowering in energy of the S3s dispersion curves results in the shift of the maximum to higher binding energy seen in the S3s valence band. The lowest band of the Mo4d-S3p valence band (band #3) is lowered in energy at Γ by ~ 1 eV. This results in a widening of the Mo4d-S3p valence band as described in Section 5.4.4. The highest fully occupied energy band (band #9) is lowered in energy at Γ by ~ 0.4 eV. The lowest energy conduction bands remain relatively unchanged.

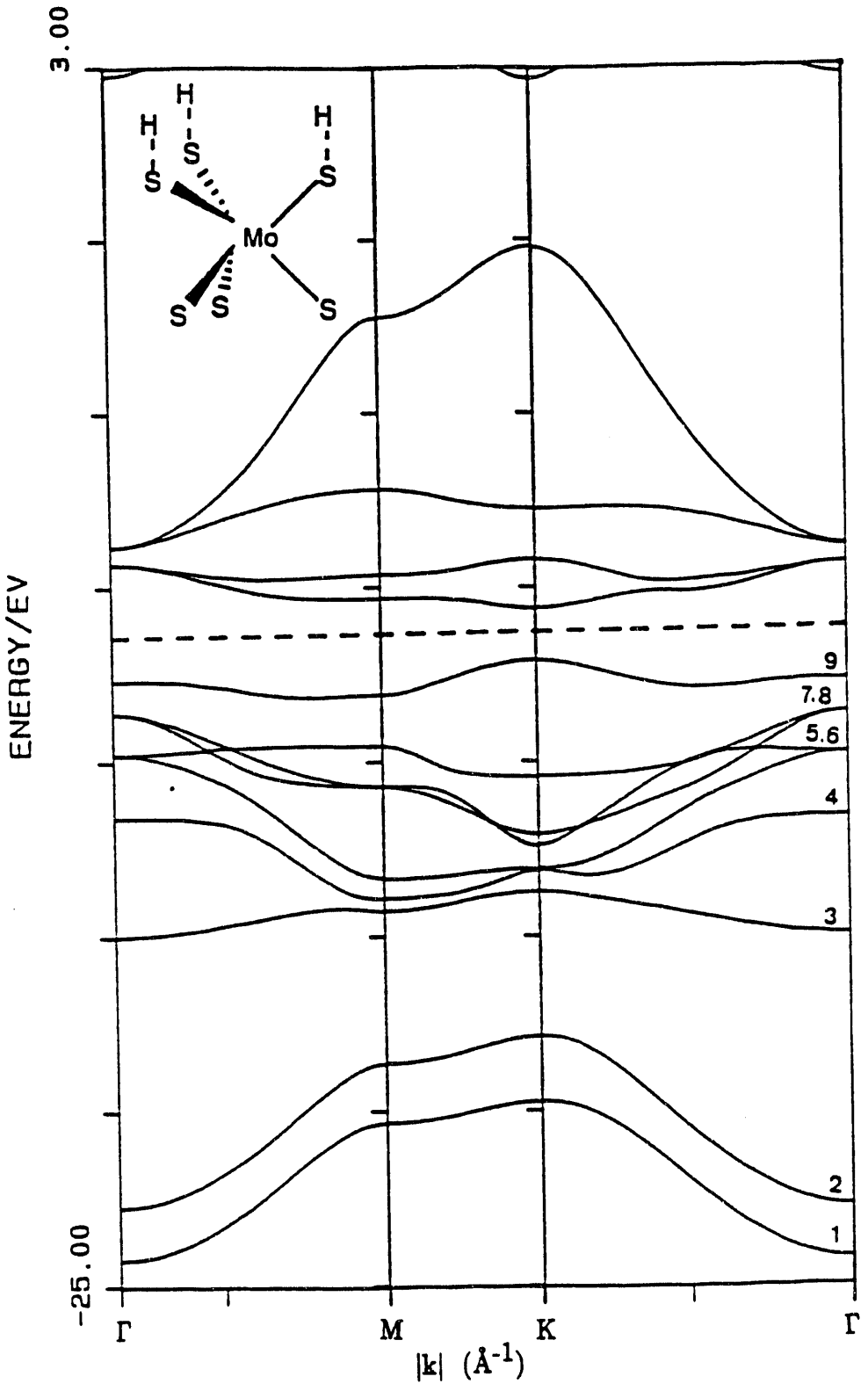

Figure 37a. Theoretical energy dispersion curves of 2-D H-MoS_2 with hydrogen located directly above the basal plane sulfur atoms.

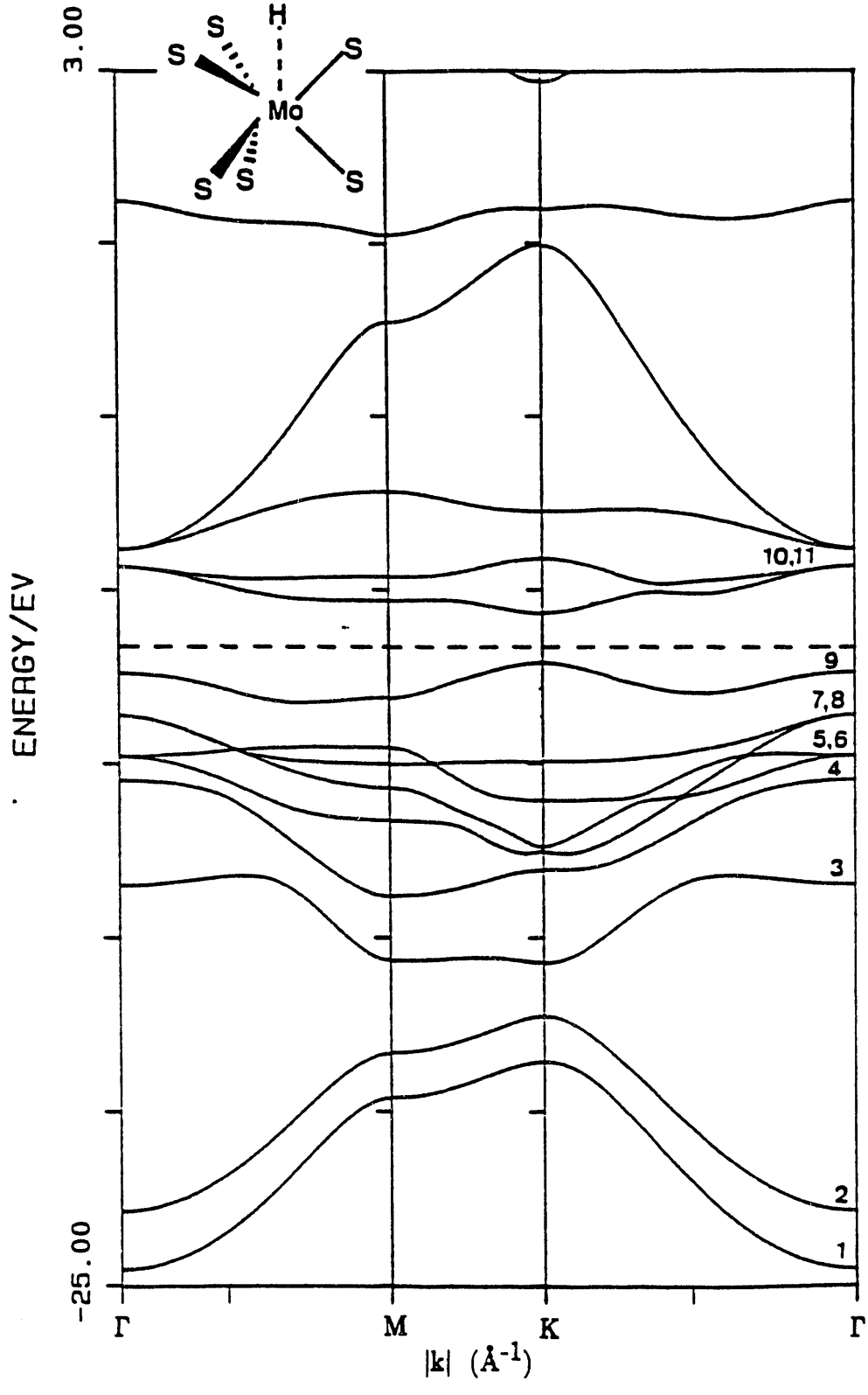

Figure 37b. Theoretical energy dispersion curves of 2-D H-MoS_2 with hydrogen located directly above the basal plane molybdenum atoms.

When hydrogen resides directly above the basal plane molybdenum atoms, Figure 37b, the two S3s bands (bands #1 and #2) are again lowered in energy, particularly at Γ. The S3s bands at K become degenerate for the two systems with and without hydrogen. This result implies no bonding interaction between the hydrogen and the S3s orbitals. The lowest band of the Mo4d-S3p valence band (band #3) is lowered in energy, especially in the direction K→M. This band is relatively dispersionless in the K→M direction and thus produces the new peak in the theoretical valence band, described in Section 5.4.3. The highest fully occupied energy band (band #9) is lowered in energy at Γ by ~ 0.3 eV. The lowest energy conduction band remains relatively unchanged.

Experimental photoelectron spectroscopy (HR-ESCA and UPS) can not be used to directly detect hydrogen adsorbed on a MoS_2 surface. However, the theoretical studies discussed above suggest that changes in the valence band and energy dispersion curves caused by hydrogen adsorption could be detected using photoelectron spectroscopy. If changes are found experimentally, the theoretical calculations described above may help identify the sites for hydrogen adsorption.

5.5 Electronic Structure of 1-D H-$(MoS_2)_5$ Terminating at the $(10\bar{1}1)$ Edges.

5.5.1 Comparison of Energies

The calculated binding enthalpies of hydrogen atoms, ΔH_{15}, on the 1-D $(MoS_2)_5$ structure terminating in $(10\bar{1}1)$ edges are given in Table 22. Theoretically on this surface, the most stable sites for hydrogen atoms are on the edge and basal plane sulfur atoms. Reaction 17c shows the reaction of hydrogen molecules with the 1-D $(MoS_2)_5$ surface. The enthalpies for this reaction, ΔH_{16}, are shown in Table 22. Again, the enthalpies indicate that edge and basal plane sulfur sites are the most thermodynamically favored for hydrogen adsorption. However, the four-coordinate edge molybdenum site is also thermodynamically favored for hydrogen adsorption. Five-coordinate edge and basal plane molybdenum atoms are not thermodynamically favorable sites for hydrogen adsorption.

One of the reasons for the unfavorable binding energy for hydrogen adsorption onto molybdenum basal plane sites could be the proximity of basal plane sulfur atoms. The basal plane of 2H-MoS_2 is generally thought to consist of sulfur atoms. Since, molybdenum atoms are coordinated to 6 sulfur atoms in a trigonal prismatic geometry, molybdenum atoms are buried beneath a surface of exposed atoms. Thus, when hydrogen adsorbs on a molybdenum atom it also resides close to 3 equivalent sulfur atoms. This may be the reason for the destabilization of the molybdenum basal plane sites compared to edge sites with smaller number

of coordinating sulfur atoms.

$$(MoS_2)_5(s) + H^0(g) \rightarrow H\text{-}(MoS_2)_5(s) \qquad \Delta H_{15}=\text{see Table 22} \quad (17a)$$

$$\tfrac{1}{2} H_2(g) \rightarrow H^0(g) \qquad \Delta H_{11}=52.10 \text{ kcal/mole} \quad (17b)$$

$$(MoS_2)_5(s) + \tfrac{1}{2} H_2(g) \rightarrow H\text{-}(MoS_2)_5(s) \qquad \Delta H_{16}=\text{see Table 22} \quad (17c)$$

Table 22.

Binding enthalpies of hydrogen atoms, ΔH_{15}, and molecules, ΔH_{16}, on the surface of 1-D $(MoS_2)_5$ with $(10\bar{1}1)$ edges. Four different edge sites and six basal plane sites were studied. (Units are in kcal/mole.)

Structure	Atom	Site	Coordination	ΔH_{15}	ΔH_{16}
1-D $(MoS_2)_5$	S-0601	Edge(1)	2	-90.30	-38.20
	Mo-0101	Edge(1)	4	-83.84	-31.74
	S-0501	Edge(2)	1	-92.14	-40.05
	Mo-0301	Edge(2)	5	-37.26	14.84
	S-0101	Basal	3	-98.01	-45.91
	S-0301	Basal	3	-101.60	-49.50
	S-0701	Basal	3	-101.87	-49.77
	S-0901	Basal	3	-101.70	-49.60
	Mo-0201	Basal	6	-22.73	29.37
	Mo-0401	Basal	6	-23.16	28.94
	Mo-0501	Basal	6	-22.88	29.22

The binding enthalpy for adsorption of hydrogen molecules onto basal plane sulfur atoms in the 2-D MoS_2 system and 1-D $(MoS_2)_5$ system is -16.85 kcal/mol and -49.50 kcal/mol, respectively. This result would lead one to believe that adsorption onto basal plane surfaces of MoS_2 containing a large ratio of edge to basal plane area would be more thermodynamically stable than adsorption onto basal plane surfaces with a smaller ratio of edge to basal plane area. However, the binding enthalpy comparison between the 2-D H-MoS_2 and the 1-D H-$(MoS_2)_5$ is not correct since the ratio of hydrogen atoms to MoS_2 units is 1 for the 2-D system and 0.20 for the 1-D system. Thus, the difference between the binding enthalpies for hydrogen adsorption onto basal plane Mo and S atoms may be due to a concentration effect. To check the validity of this statement, a second set of calculations was carried out on the 1-D system. In this set of calculations, hydrogen was first placed on five basal and edge plane sulfur

sites and then on five basal and edge plane molybdenum sites to obtain a ratio of one hydrogen per MoS_2. Binding enthalpies of these calculations are shown in Table 23. In both cases hydrogen adsorption onto the $(MoS_2)_5$ system with a ratio of one hydrogen atom per MoS_2 leads to stabilization of the overall binding enthalpy such that the values obtained are closer to the binding enthalpies for adsorption of hydrogen on basal plane atoms of the 1-D system. Thus, a concentration effect does not explain the binding enthalpy differences between the 2-D and 1-D systems. The only reasonable explanation for the stabilization is that the addition of edges to the 1-D system modifies not only edge plane atoms but also basal plane atoms such that these sites become more favorable for reactions with hydrogen. Thus, a MoS_2 system with a large number of edges (such as polycrystalline MoS_2) should adsorb hydrogen more readily than a system with a small number of edges (single crystal MoS_2).

Table 23.

Binding enthalpies of hydrogen atoms, ΔH_{10}, and molecules, ΔH_{12}, on the surface of 1-D $(MoS_2)_5$. The two sites studied were hydrogen on sulfur and hydrogen on molybdenum. In this study a ratio of one hydrogen per MoS_2 was used. (Units are in kcal/mole MoS_2.)

Structure	Atom	Site	ΔH_{10}	ΔH_{12}
1-D $(H\text{-}MoS_2)_5$	Mo	Basal and Edge	-36.50	15.60
1-D $(H\text{-}MoS_2)_5$	S	Basal and Edge	-93.84	-41.74

5.5.2 Comparison of Charges

Once the hydrogen atoms were placed on the 1-D $(MoS_2)_5$ structure terminating at the $(10\bar{1}1)$ edges, the distribution of average atomic charges was altered. Charges for each 1-D $H\text{-}(MoS_2)_5$ structure were calculated as indicated in Section 5.3.3. Average charges for 1-D $H\text{-}(MoS_2)_5$ systems with hydrogen residing on the edge plane atoms are given in Table 24a. Average charges for 1-D $H\text{-}(MoS_2)_5$ systems with hydrogen residing on the basal plane atoms are given in Table 24b.

When hydrogen atoms reside on Edge 1 two-coordinate sulfur atoms (S-0601), some changes in the average charges occur. The Edge 1 sulfur atoms are oxidized from -0.68 to +0.032. Edge 1 four-coordinate molybdenum atoms (Mo-0101) are reduced from +0.69 to -0.081. The hydrogen atom possesses a positive charge of +0.099. Edge 2 five-coordinate molybdenum atoms (Mo-0301) are also reduced from +1.25 to +1.17. Thus, electron density is transferred from the hydrogen atom through the sulfur atom (S-0601) to the molybdenum atom (Mo-0101). Edge 2 five-coordinate molybdenum atoms (Mo-0301) are reduced due to transfer

Table 24a.

Average charges for 1-D H-$(MoS_2)_5$ structures terminating in $(10\bar{1}1)$ edges with hydrogen residing on edge plane atoms.

Atom	$(MoS_2)_5$ Bare	H-$(MoS_2)_5$ with H on: S-0601	Mo-0101	S-0501	Mo-0301
Mo-0101	+0.69	-0.081	+0.88	+0.36	+0.51
Mo-0201	+0.65	+0.66	+0.68	+0.64	+0.67
Mo-0301	+1.25	+1.17	+1.29	+0.76	+0.86
Mo-0401	+0.64	+0.68	+0.68	+0.64	+0.68
Mo-0501	+0.71	+0.71	+0.79	+0.70	+0.73
S-0101	-0.27	-0.28	-0.29	-0.28	-0.27
S-0201	-0.19	-0.20	-0.25	-0.20	-0.19
S-0301	-0.26	-0.26	-0.26	-0.27	-0.27
S-0401	-0.27	-0.26	-0.26	-0.27	-0.27
S-0501	-1.21	-1.21	-1.20	-0.42	-1.23
S-0601	-0.68	+0.032	-0.72	-0.72	-0.70
S-0701	-0.27	-0.27	-0.27	-0.27	-0.27
S-0801	-0.27	-0.27	-0.27	-0.27	-0.27
S-0901	-0.21	-0.21	-0.19	-0.22	-0.22
S-1001	-0.29	-0.29	-0.26	-0.31	+0.11
H-0101	—	+0.099	-0.34	+0.12	+0.15

Table 24b.

Average charges for 1-D H-$(MoS_2)_5$ structures terminating in $(10\bar{1}1)$ edges with hydrogen residing on basal plane atoms.

Atom	$(MoS_2)_5$ Bare	H-$(MoS_2)_5$ with H on: S-0301	Mo-0201
Mo-0101	+0.69	+0.16	+0.17
Mo-0201	+0.65	+0.61	+0.88
Mo-0301	+1.25	+1.01	+1.00
Mo-0401	+0.64	+0.63	+0.63
Mo-0501	+0.71	+0.64	+0.67
S-0101	-0.27	-0.28	-0.28
S-0201	-0.19	-0.20	-0.20
S-0301	-0.26	+0.61	-0.12
S-0401	-0.27	-0.27	-0.27
S-0501	-1.21	-1.23	-1.23
S-0601	-0.68	-0.73	-0.73
S-0701	-0.27	-0.26	+0.018
S-0801	-0.27	-0.27	-0.27
S-0901	-0.21	-0.21	-0.22
S-1001	-0.29	-0.30	-0.30
H-0101	—	+0.098	+0.27

of electrons through the bulk-like lattice. This is similar to the situation for hydrogen residing on the basal plane sulfur in the 2-D H-MoS_2 system. Of the three sulfur sites studied on the $(10\bar{1}1)$ system, hydrogen on this sulfur site, two-coordinate edge S-0601 atoms, is the least stable. The binding enthalpy for a hydrogen molecule on this site is -38.20 kcal/mole.

Hydrogen atoms residing on the Edge 2 one-coordinate sulfur atoms (S-0501) also produce changes in the average charges of the atoms. Edge 2 one-coordinate sulfur atoms are oxidized from -1.21 to -0.42. Edge 2 five-coordinate molybdenum atoms (Mo-0301) are reduced from +1.25 to +0.76. Edge 1 four-coordinate molybdenum atoms (Mo-0101) are also reduced from +0.69 to +0.36. However, edge 1 two-coordinate sulfur atoms (S-0601) are slightly reduced from -0.68 to -0.72. The hydrogen atom possesses a positive charge of +0.12. Again, electron density is transferred from the hydrogen atoms through the sulfur atoms (S-0501) to the molybdenum atoms (Mo-0301). Edge 1 molybdenum (Mo-0101) and sulfur atoms (S-0601) are also reduced by transfer of electrons through the bulk-like lattice. Of the three sulfur sites studied, this sulfur site is intermediate in hydrogen binding enthalpy. The binding enthalpy for hydrogen molecule on this site is -40.05 kcal/mole.

The last sulfur site studied was hydrogen adsorption onto basal plane three-coordinate sulfur atoms (S-0301). This study was expected to parallel the behavior of hydrogen atoms residing on basal plane atoms in the 2-D H-MoS_2 system. Of the three sulfur sites studied, this site was the most stable for hydrogen adsorption. The binding enthalpy for a hydrogen molecule on this site is -49.50 kcal/mole. In this system, the fully coordinated basal plane sulfur atom (S-0301) is oxidized from -0.26 to +0.61. Basal plane and edge plane molybdenum atoms are reduced. Basal plane atoms Mo-0201 and Mo-0501 are reduced from +0.65 to +0.61 and from +0.71 to +0.64, respectively. Mo-0201 and Mo-0501 are directly connected to the hydrogen adsorbed basal plane sulfur atom (S-0301). Edge plane molybdenum atoms, Mo-0301 and Mo-0101, are also reduced from +0.69 to +0.16 and from +0.65 to +0.61. Edge plane sulfur atoms, S-0501 and S-0601, are reduced slightly from -1.21 to -1.23 and from -0.68 to -0.73, respectively. The hydrogen atom possesses a slight positive charge of +0.098. Thus, electrons are transferred from the hydrogen and sulfur (S-0301) atoms through basal plane molybdenum atoms (Mo-0201, Mo-0501 and Mo-0401) to edge plane molybdenum atoms (Mo-0101 and Mo-0301) and sulfur atoms (S-0601 and S-0501). One interesting feature present in the 2-D H-MoS_2 system with hydrogen adsorbed on basal plane sulfur atoms is not present in this system. In the 2-D H-MoS_2 system, electrons were transferred from hydrogen and first atomic layer sulfur atoms (S-0201) to molybdenum atoms (Mo-0101) and third atomic layer sulfur atoms (S-0301). Thus, sulfur atoms that did not possess hydrogen atoms were reduced from -0.28 to -

0.36. In the H-$(MoS_2)_5$ system terminating at the $(10\bar{1}1)$ edges and with hydrogen adsorbed on basal plane sulfur atoms (S-0301), third atomic layer sulfur atoms (S-0401) were not reduced significantly. Electrons are transferred to unsaturated edge plane atoms instead of to third atomic layer basal plane sulfur atoms.

When hydrogen is theoretically adsorbed onto Edge 1 four-coordinate molybdenum atoms (Mo-0101), all of the molybdenum atoms in the unit cell are slightly oxidized. Basal plane molybdenum atoms, Mo-0201, Mo-0401 and Mo-0501, are oxidized from +0.65 to +0.68, from +0.64 to +0.68, and from +0.71 to +0.79, respectively. Edge plane molybdenum atoms, Mo-0101 (4-coordinate) and Mo-0301 (5-coordinate), are oxidized from +0.69 to +0.88 and from +1.25 to +1.29, respectively. Only small changes occur in some of the sulfur atoms. Edge 1 two-coordinate sulfur (S-0601) and basal plane three-coordinate sulfur (S-0201) atoms are reduced from -0.68 to -0.72 and from -0.19 to -0.25, respectively. Both of these sulfur atoms are bound to Mo-0101. The hydrogen atom possesses a negative charge of -0.34 in this structure. Thus, electrons are transferred from second atomic layer molybdenum atoms to adsorbed hydrogen atoms. Edge 1 four-coordinate molybdenum atoms (Mo-0101) are the most stable molybdenum sites for hydrogen adsorption. The binding enthalpy for a hydrogen molecule on this site is -31.74 kcal/mole.

When hydrogen is theoretically adsorbed onto Edge 2 five-coordinate molybdenum atoms (Mo-0301), this atom is reduced from +1.25 to +0.86. Sulfur atoms attached to this molybdenum atom are S-0501 (1-coordinate), S-0901 (3-coordinate), and S-1001 (3-coordinate). S-0501 is reduced only slightly, however S-1001 is oxidized from -0.29 to +0.11. The charge on S-0901 is relatively unaffected by the addition of hydrogen atoms. S-1001 is strongly affected by the addition of hydrogen atoms to Mo-0301 because this atom is located only 1.83 Å away from the hydrogen atom. The hydrogen atom itself possesses a positive charge of +0.15. Edge 1 four-coordinate molybdenum atoms (Mo-0101) are also reduced from +0.69 to +0.51. Thus, electrons are transferred from the hydrogen atoms to the molybdenum atom it is attached to, Mo-0301. Also, electrons are transferred from sulfur atoms located close to the adsorbed hydrogen atoms, S-1001, to Mo-0301. The binding enthalpy of a hydrogen molecule on this site, Mo-0301, is 14.84 kcal/mole, an unfavorable process.

The last hydrogen adsorption site studied was hydrogen on basal plane molybdenum atoms, Mo-0201. This site was expected to exhibit behavior similar to hydrogen adsorbed on basal plane molybdenum in the 2-D H-MoS_2 system. In the 1-D H-$(MoS_2)_5$ system terminating in $(10\bar{1}1)$ edges, this site is thermodynamically less favorable than the previous sites. The binding enthalpy of a hydrogen molecule on this site is 29.37 kcal/mole. The charge on

Mo–0201 is increased from +0.65 to +0.88. Sulfur atoms attached to Mo–0201 include S–0301, S–0401, S–0701, and S–0801. Charges on S–0401 and S–0801 are not affected significantly by hydrogen adsorption, because these atoms are located on the bottom of the MoS_6 trigonal prism, away from the adsorbed hydrogen atom. However, charges on S–0301 and S–0701 change from –0.26 to –0.12 and from –0.27 to +0.018, respectively. Edge plane molybdenum atoms, Mo–0101 and Mo–0301, are reduced from +0.69 to +0.17 and from +1.25 to +1.00, respectively. The hydrogen atoms possesses a positive charge of +0.27. Thus, electrons are transferred from the hydrogen and basal plane sulfur (S–0301 and S–0701) and molybdenum (Mo–0201) atoms to edge plane unsaturated molybdenum atoms, Mo–0101 and Mo–0301. In the 2–D H–MoS_2 system with hydrogen adsorbed on basal plane molybdenum atoms, the molybdenum atom with hydrogen attached is reduced from+0.56 to +0.018. Basal plane sulfur atoms located on the same side as the hydrogen atoms are oxidized from –0.28 to +0.078. Basal plane sulfur atoms located on the opposite side are reduced from –0.28 to –0.36. The hydrogen atoms possess a positive charge of +0.27. Thus, electrons are transferred from hydrogen and basal plane sulfur atoms located on the same side to molybdenum atoms and sulfur atoms located on the opposite basal plane. The 2–D H–MoS_2 system has a binding enthalpy for hydrogen molecules on basal plane molybdenum atoms of 62.34 kcal/mole. Hydrogen adsorption onto basal plane molybdenum atoms in the 2–D MoS_2 system is thermodynamically less stable compared to hydrogen adsorption onto basal plane molybdenum atoms, Mo–0201, in the 1–D $(MoS_2)_5$ system terminating at the $(10\bar{1}1)$ edge. One reason for the difference in stability could be that the 2–D system has a ratio of one hydrogen per molybdenum but the 1–D $(MoS_2)_5$ system has a ratio of one hydrogen per 5 molybdenum atoms. The 1–D H–$(MoS_2)_5$ systems seem to transfer electrons to unsaturated edge atoms, while the 2–D H–MoS_2 systems transfer electrons to sulfur atoms on the opposite basal plane.

These results indicate that the most thermodynamically favorable site for hydrogen adsorption is on basal plane sulfur atoms in the 2–D and 1–D systems. Basal planes in 1–D systems terminating in edges are more favorable because electron transfer occurs to unsaturated edge molybdenum atoms instead of to basal plane sulfur atoms.

5.6 Parametrization of the MoS_2 Theoretical Valence Band.

As discussed in Section 5.1.1, the theoretical valence band of 2–D MoS_2, obtained using the atomic parameters of Hughbanks and Hoffmann, does not accurately represent the experimental valence band of MoS_2 obtained via HR–ESCA. One notable feature that is not reproduced by the theory using these parameters is the four–peaked nature of the upper portion

of the valence band (Mo4d-S3p region). Also, the S3s band is located too close to the upper Mo4d-S3p valence band. Thus, a theoretical calculation of 2-D MoS_2 was carried out using the atomic parameters of Clementi and Roetti, discussed in Section 3.2. Double zeta functions, instead of single zeta functions, were used for the S3s and S3p orbitals in an attempt to obtain the four-peaked nature of the upper Mo4d-S3p valence band. After the effect of double zeta functions was studied, the atomic parameters, H_{ii} and c_i, were adjusted to fit the experimental valence band. Ionization potentials, H_{ii}, were measured directly from the experimental valence band of MoS_2 (after shifting the entire experimental valence band by -4.1 eV, the work function of MoS_2).

5.6.1 Effect of S3p Double Zeta Functions

The effect of S3s, S3p double zeta functions on the theoretical valence band was investigated first. The double zeta functions and atomic ionization parameters of Clementi and Roetti, discussed in Section 3.2, were used for the S3s, S3p and Mo4d atomic orbitals. Energy dispersion curves obtained using the more diffuse S3p double zeta function show some differences. Curvature of the bands, particularly band #3, at the bottom of the Mo4d-S3p valence band becomes more pronounced. Overlap of the two highest occupied crystal bands, bands #8 and #9, of the Mo4d-S3p valence band now occurs. Previously, using the single zeta functions of Hughbanks and Hoffmann, bands #8 and #9 did not overlap but were separated by a gap. This gap between bands #8 and #9 led to the three-peaked nature of the theoretical valence band.

The theoretical valence band of 2-D MoS_2 obtained using the atomic parameters of Clementi and Roetti is shown in Figure 38a. Modified atomic orbital populations, MAOPOP's, for the S3s, S3p and Mo4d orbitals are shown in Figure 38b. The upper Mo4d-S3p theoretical valence band now consists of four distinct peaks, similar to the experimental valence band. The total width of the Mo4d-S3p theoretical valence band region is ca. 6 eV, the experimental width is also ca. 6 eV. However, the S3s band is separated from the bottom of the Mo4d-S3p valence band by ca. 9 eV. Experimentally, the S3s band is separated from the upper Mo4d-S3p valence band by ca. 6 eV. Thus, the atomic ionization potentials, H_{ii}, of Clementi and Roetti did not correctly match those needed to produce good agreement between theory and experiment.

The S3p double zeta functions are necessary for a better representation of the MoS_2 valence band. The use of more diffuse S3p double zeta functions increases the overlap between the S3p and Mo4d atomic orbitals leading to the four-peaked nature of the upper valence band.

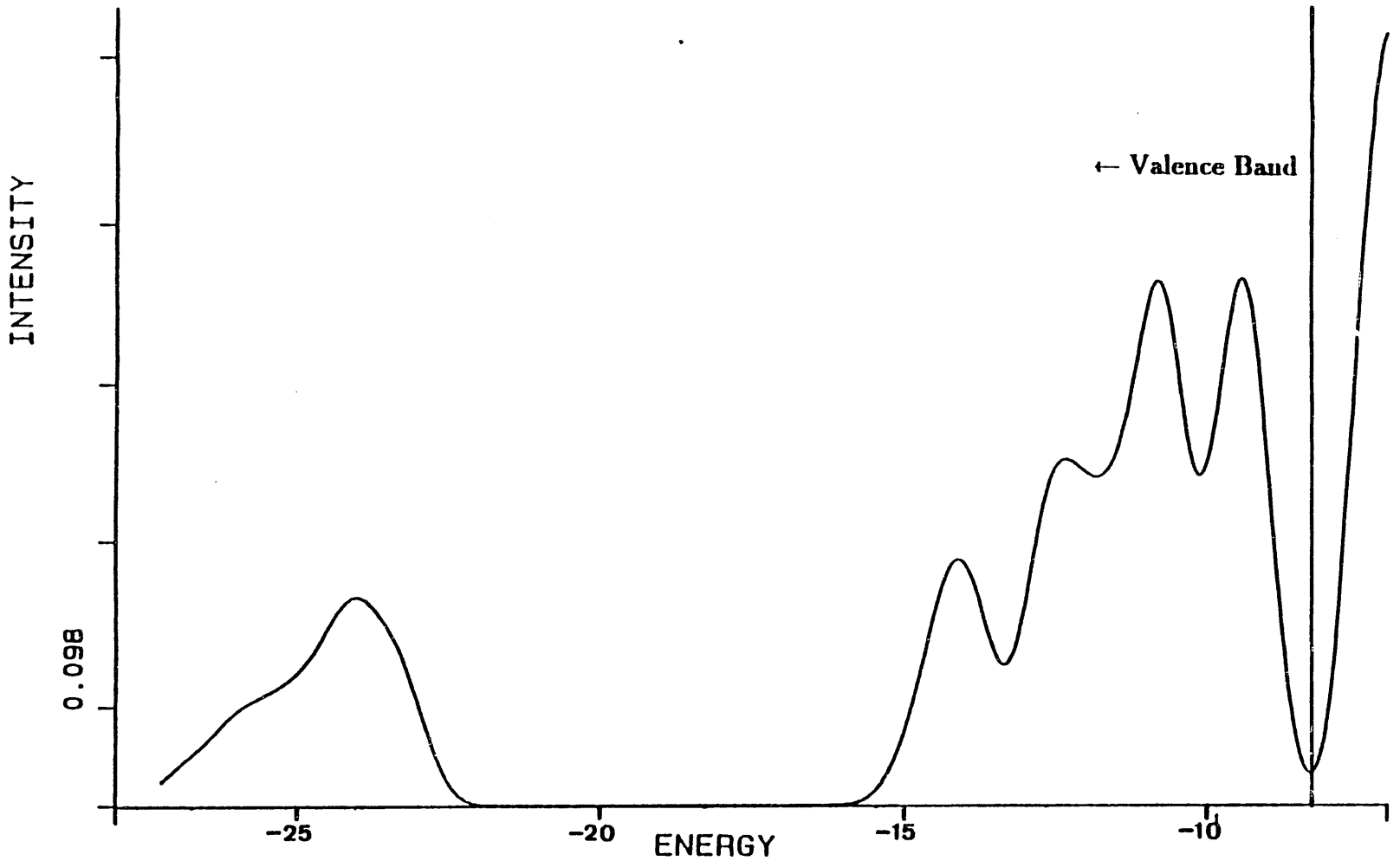

Figure 38a. Theoretical valence band of 2 D MoS_2. Atomic parameters and ionization potentials of Clementi and Roetti (Reference 42) were used in this calculation.

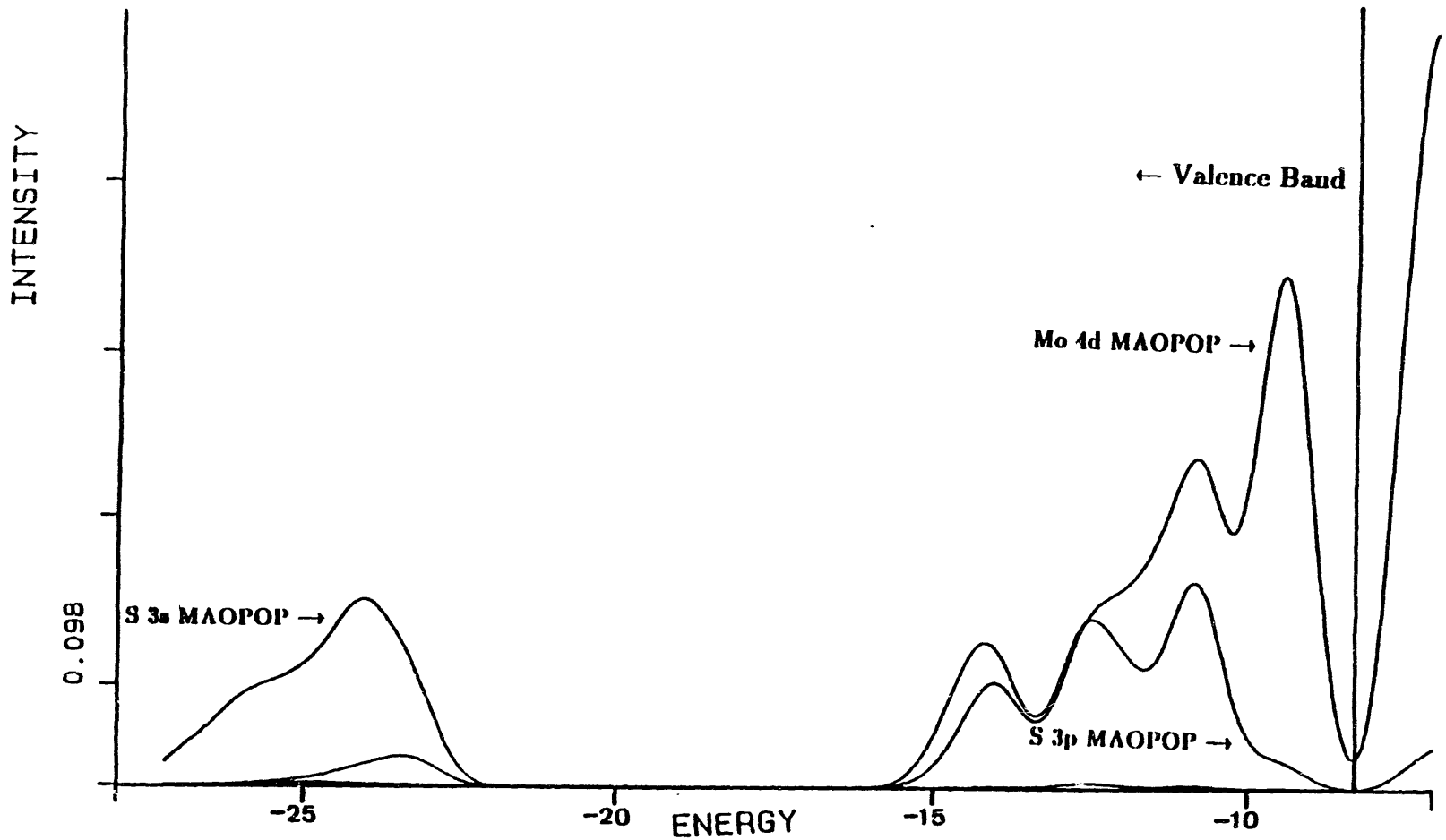

Figure 38b. Theoretical modified atomic orbital populations, MAOPOP's, for S3s, S3p and Mo4d orbitals. Atomic parameters and ionization potentials of Clementi and Roetti (Reference 42) were used in this calculation.

Representation of the S3p atomic orbitals with a very diffuse single zeta function instead of a double zeta function does not lead to an accurate representation of the valence band. The rest of the calculations discussed in Section 5.6.1 were performed using the atomic parameters including ionization potentials of Clementi and Roetti for all of the MoS_2 valence orbitals.

Charges obtained for the atoms using the parameters of Clementi and Roetti were very similar to those obtained using the parameters of Hughbanks and Hoffmann. The charge on the molybdenum was +0.55 while that on the sulfur atoms was -0.28. In previous calculations using the parameters of Hughbanks and Hoffmann, the molybdenum charge was +0.56 and the sulfur charges were -0.28. Thus, these calculations produce the same type of charge distribution probably due to the similar atomic ionization potentials of the Mo4d and S3p orbitals. The energy of formation of 2-D MoS_2 obtained using the parameters of Clementi and Roetti was -371.02 kcal/mole. Thus the total energy changed from -463.58 kcal/mole using Hughbanks and Hoffmann parameters to -371.02 kcal/mole using Clementi and Roetti parameters.

5.6.2 Parametrization of Atomic Parameters, H_{ii} and c_i

As discussed previously, Section 5.6.1, the relative positions of the S3s and Mo4d-S3p valence bands were not theoretically reproduced using the atomic ionization potentials of Clementi and Roetti. For this reason, parametrization of the atomic ionization potentials, H_{ii}, was carried out as discussed in Section 3.2. Changes in the atomic ionization potentials, H_{ii}, caused overlaps to become smaller leading to bands with smaller widths. To correct for this smaller width, the contribution of the more diffuse part of for example the S3p radial function, c_2, was increased. Once the atomic ionization potentials were set by comparison with experiment, the new theoretical valence band obtained with these parameters was compared to the experimental valence band. A set of theoretical calculations were carried out in which only one parameter was varied for each run. This set of calculations led to a set of atomic parameters that qualitatively reproduced the experimental valence band. These parameters are shown in Table 25. The 2-D MoS_2 theoretical valence band obtained with the new set of parameters is shown in Figure 39a. The modified atomic orbital populations, MAOPOP's, are shown in Figure 39b. Comparison of the theoretical valence band to the experimental valence band is shown in Figure 39c. Modified atomic orbital populations, MAOPOP's, of the individual Mo4d contributions are shown in Figure 39d.

An increase of the more diffuse part of a double zeta function involves an increase in c_2 with a corresponding decrease in c_1, due to normalization requirements. The initial parameters, ζ_i and c_i, for Slater-type double zeta functions were obtained from Clementi and Roetti. The

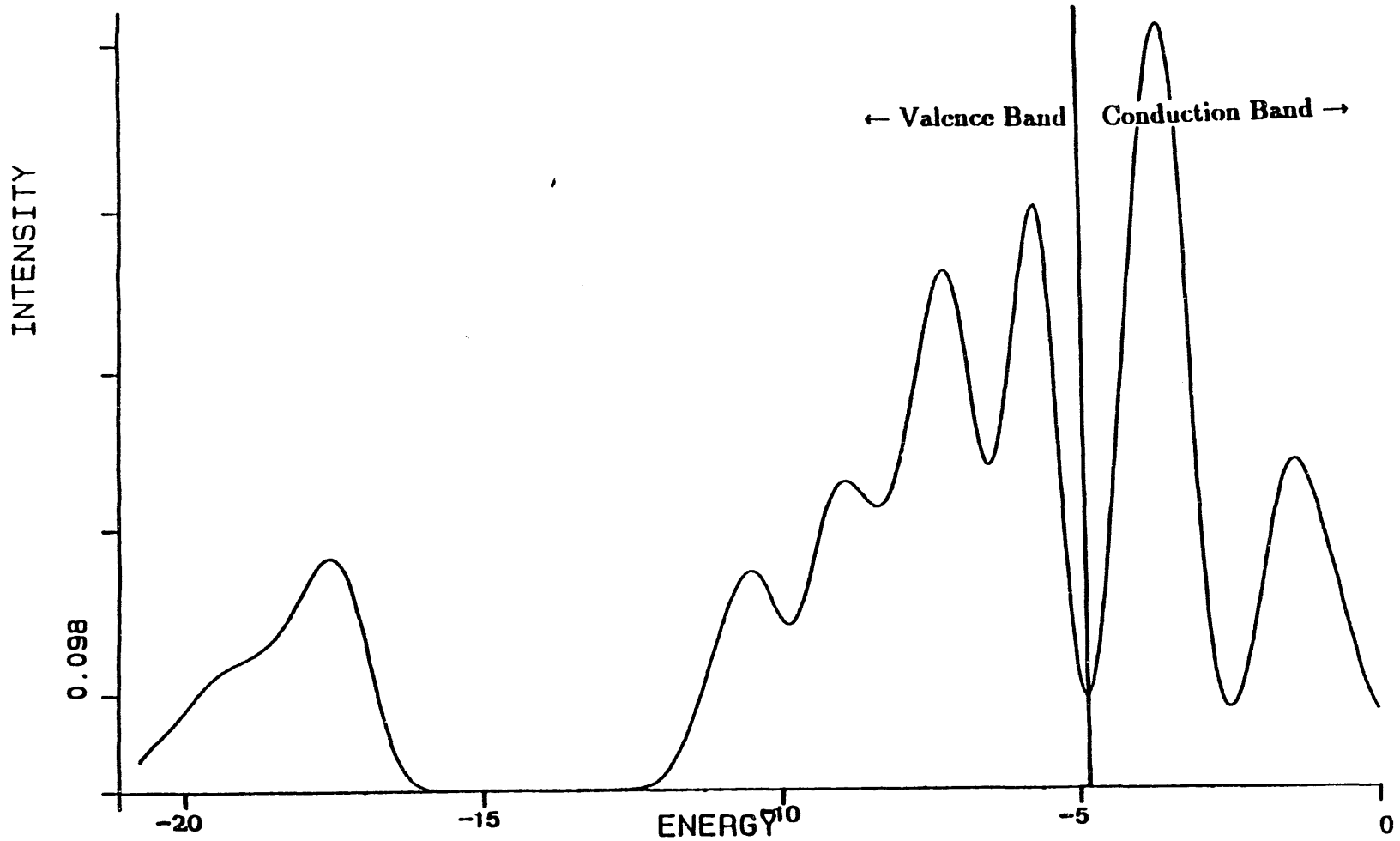

Figure 39a. Theoretical valence band of 2-D MoS_2 calculated using the 171 special k-points. Atomic parameters used in this calculation are given in Table 25.

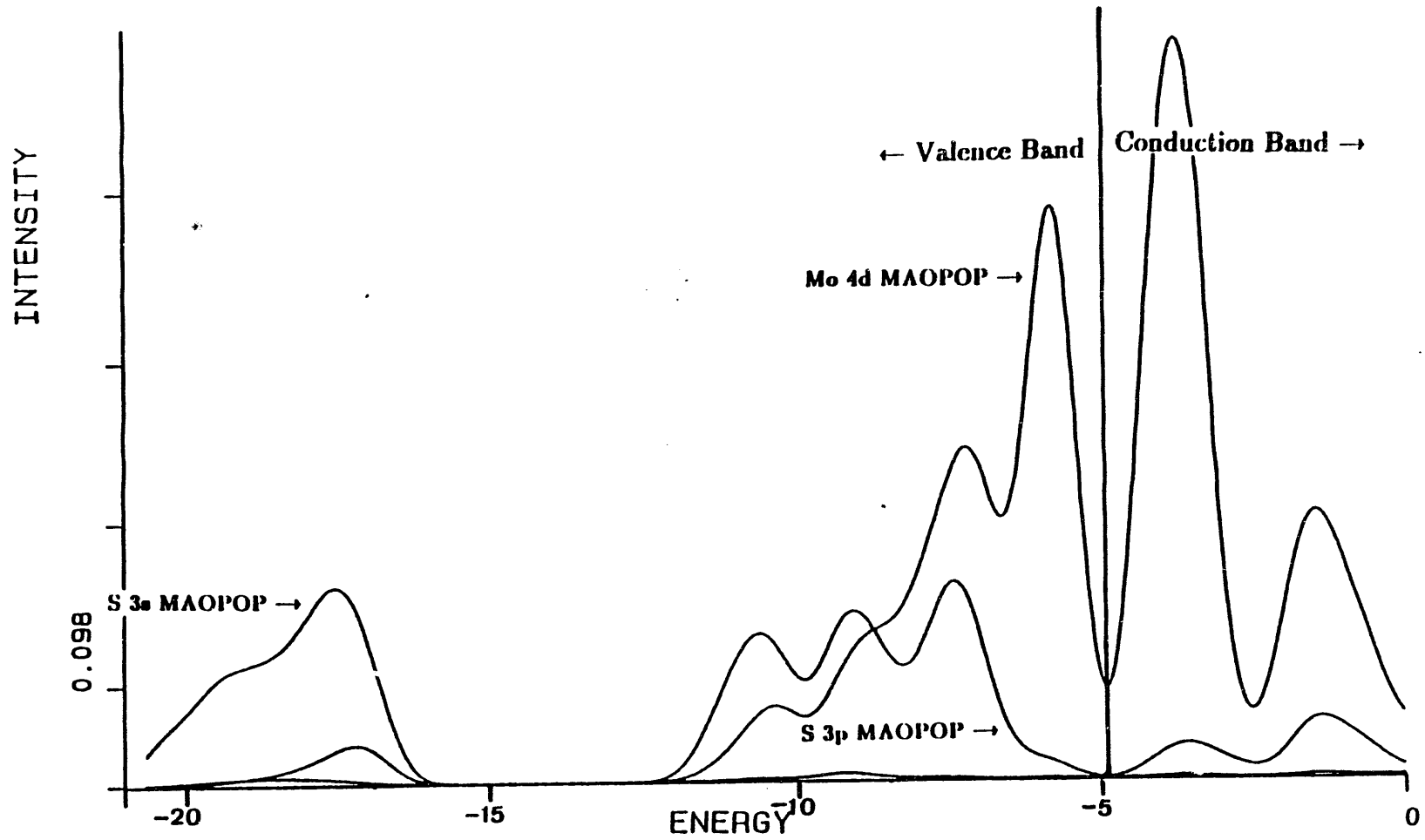

Figure 39b. Modified atomic orbital populations, AOPOP's, of 2 D MoS_2. Modified AOPOP's shown are for S3s, S3p and Mo4d contributions to the theoretical valence band. The 171 special k points and atomic parameters of Table 25 were used in this calculation.

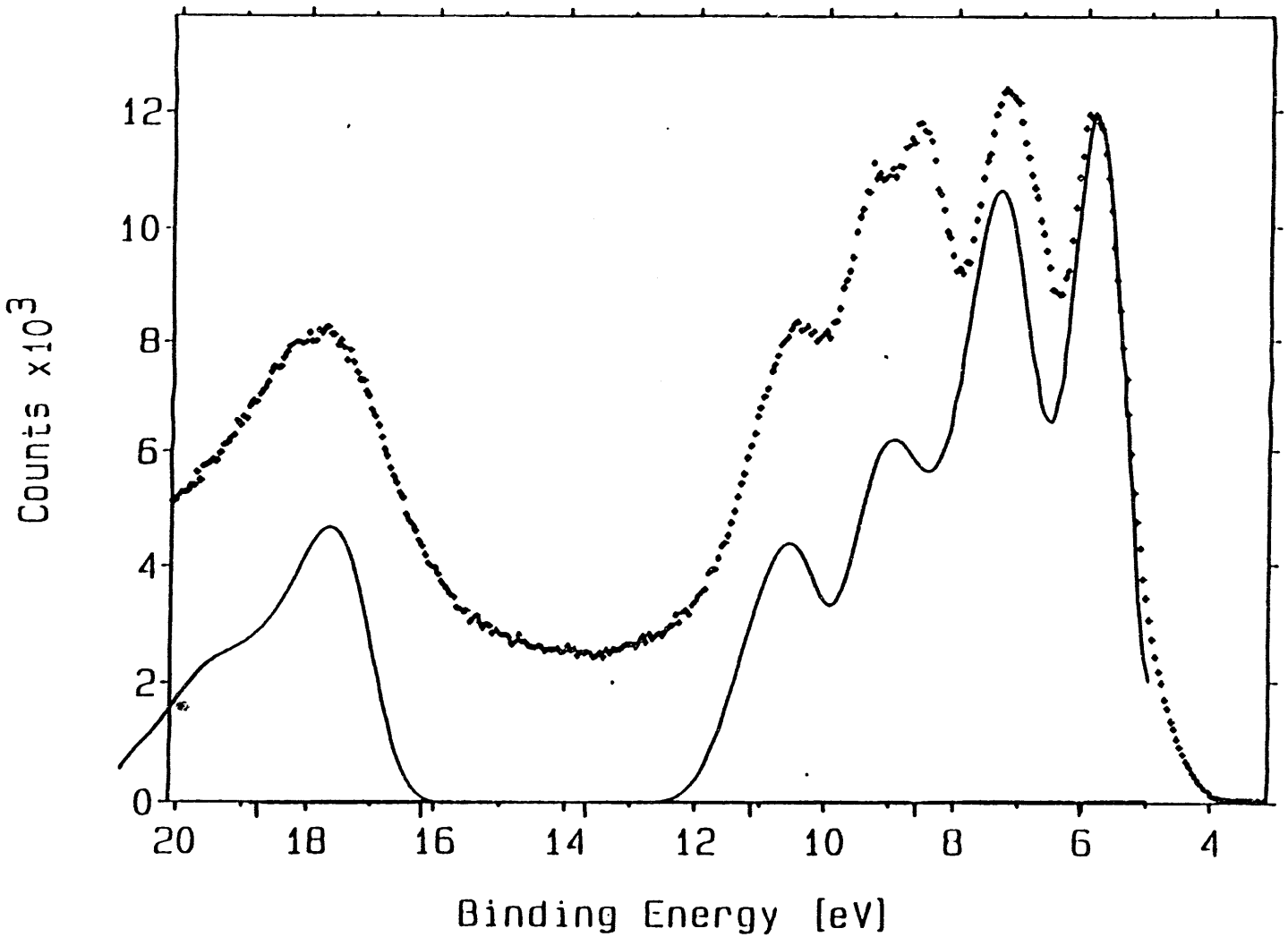

Figure 39c. Comparison of the theoretical and experimental valence bands of MoS_2.

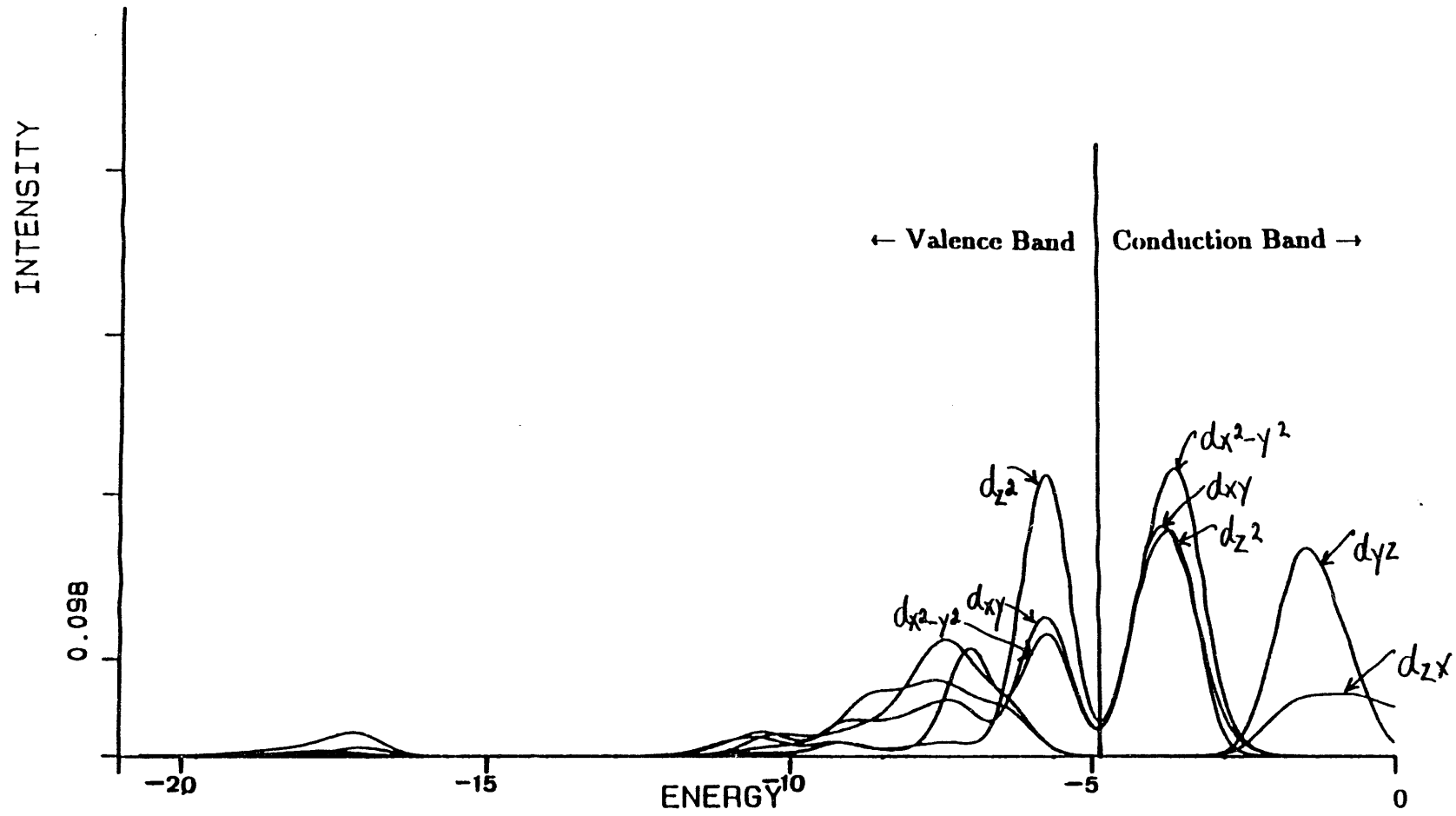

Figure 39d. Modified atomic orbital populations, MAOPOP's, of 2-D MoS_2 for the individual Mo4d orbitals. The 171 special k-points and atomic parameters of Table 25 were used in this calculation.

Table 25.

Radial parameters, H_{ii}, ζ_i, and c_i, for the Mo4d, S3s, and S3p atomic orbitals. Parametrization of theoretical and experimental valence bands led to the parameters listed in this table. The numbers in parentheses indicate the value i.

Atom	Orbital	H_{ii}(eV)	ζ_i	c_i
Mo	4d	-6.00	3.81446 (1)	0.38841 (1)
			1.86369 (2)	0.72684 (2)
S	3s	-17.80	2.66221 (1)	0.43538 (1)
			1.68771 (2)	0.60731 (2)
S	3p	-8.845	2.33793 (1)	0.35338 (1)
			1.33331 (2)	0.70431 (2)

most probable radius of the S3s orbitals was located at 1.32 au (0.698 Å). An increase of c_2 from 0.48731 to 0.60731 led to a most probable radius of 1.40 au (0.741 Å). The new set of parameters for the S3s orbitals leads to a broader S3s band in the theoretical valence band. The resulting S3s theoretical band width is comparable to the experimental S3s band width, as seen in Figure 39c.

The most probable radius of the Mo4d orbitals was located initially at 1.32 au (0.698 Å). An increase in c_2 from 0.62684 to 0.72684 led to a most probable radius of 1.48 au (0.783 Å). The more diffuse Mo4d atomic orbitals led to changes in the conduction band and only small changes in the valence band. The bottom of the conduction band (band #10) was destabilized (snifted upwards) in energy by ~ 0.4 eV. The top of the valence band was also destabilized by ~ 0.05 eV for a net change of ~ 0.35 eV. Thus, the band gap between the valence and conduction bands was increased by the use of more diffuse Mo4d zeta functions. However, the direct gap located at K still remains since this calculation was performed on the two-dimensional MoS_2 model. The nature of the Mo4d-S3p valence band was not changed through the use of more diffuse Mo4d radial functions.

The most probable radius of the S3p orbitals was located initially at 1.70 au (0.900 Å). An increase in c_2 from 0.54431 to 0.70431 led to a most probable radius of 1.74 au (0.921 Å). The more diffuse S3p atomic orbitals led to a greater degree of overlap between the sulfur and molybdenum orbitals. Four definite peaks in the Mo4d-S3p valence band were obtained in this calculation. The width of this band also increased by ~ 0.45 eV due to a lowering at the bottom of the Mo4d-S3p valence band of ~ 0.4 eV and a raising of the top of the valence band of ~ 0.05 eV. The raising of the top of the valence band results in a decreased direct band gap at K. More diffuse S3p zeta functions result in a splitting of the central Mo4d-S3p peak into

two peaks in the valence band region. The nature of the radial part of the S3p atomic functions has the greatest effect on the Mo4d-S3p valence band.

This set of studies found that diffuse S3p double zeta functions are needed to produce a theoretical valence band that is in qualitative agreement with the experimental valence band. In 2H-MoS_2 the closest Mo-S distance is 2.41 Å, the most probable radius of the more diffuse Mo4d and S3p orbitals are 0.741 Å and 0.921 Å, respectively. The sum of these two most probable radii is 1.662 Å, approximately 69 % of the closest Mo-S distance. The size of the band gap is largely dependent on the diffuseness of the Mo4d orbitals. As the diffuseness of the Mo4d orbitals is increased the size of the band gap increases. This increase is mainly due to destabilization of the lowest energy conduction band (band #10). Diffuse S3s double zeta functions widen the S3s band but do not affect the rest of the valence band.

Theoretical energy dispersion curves for the 2-D MoS_2 system using the parameters given in Table 25 were calculated for the following directions: Γ—M, Γ—K, and K—M. The energy dispersion curves are shown in Figures 40a and 40b. Figure 40a shows the dispersion of the S3s, Mo4d-S3p valence bands and the bottom of the conduction bands. Figure 40b shows the dispersion of the Mo4d-S3p bands compared to the experimental energy dispersion curves obtained by Mamy et al.[15] Overlap between the top of the valence band (band #9) and the rest of the Mo4d-S3p valence band (specifically bands #7 and #8) can be seen in the energy dispersion curves. This overlap occurs between band #9 at the M point and bands #7 and #8 at the Γ point. Thus, a large gap between the top of the valence band and the rest of the Mo4d-S3p valence band is not present in the theoretical valence band. As in the previous calculations involving the 2-D MoS_2 system, the top of the valence band and bottom of the conduction band are located at the K point resulting in a direct gap. A calculation using the parameters given in Table 25 for 3-D MoS_2 results in the formation of an indirect gap occurring from the top of the valence band at Γ to the bottom of the conduction band at K.

The energy dispersion curves, especially of the bands with a large amount of S3p contribution show a greater amount of dispersion or curvature with energy. Overall, curvature of the energy dispersion curves obtained using the parameters of Table 25 (and thus double zeta S3p radial functions) is more pronounced than that of the energy dispersion curves obtained using the parameters of Hughbanks and Hoffmann (single zeta S3p radial functions). The total width of the Mo4d-S3p bands is similar to that of the experimental energy dispersion curves.

The energy of formation of the 2-D MoS_2 system obtained using the parameters given in Table 25, was found to be -247.58 kcal/mol. The energy calculated using the parameters of

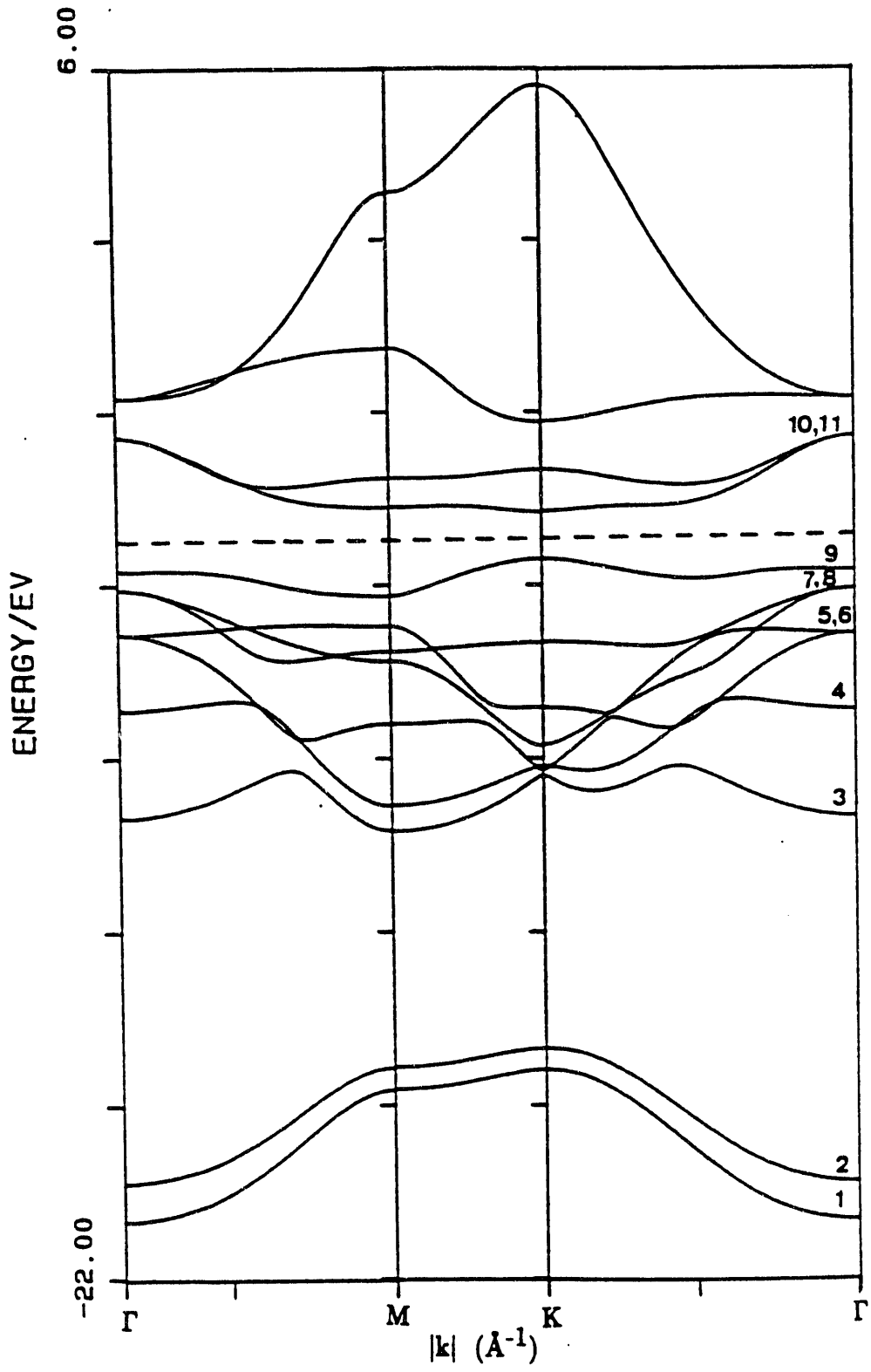

Figure 40a. Theoretical energy dispersion curves of 2-D MoS_2. S3s and Mo4d - S3p valence bands as well as the lowest energy portion of the conduction band are shown. Parameters of Table 25 were used for this calculation.

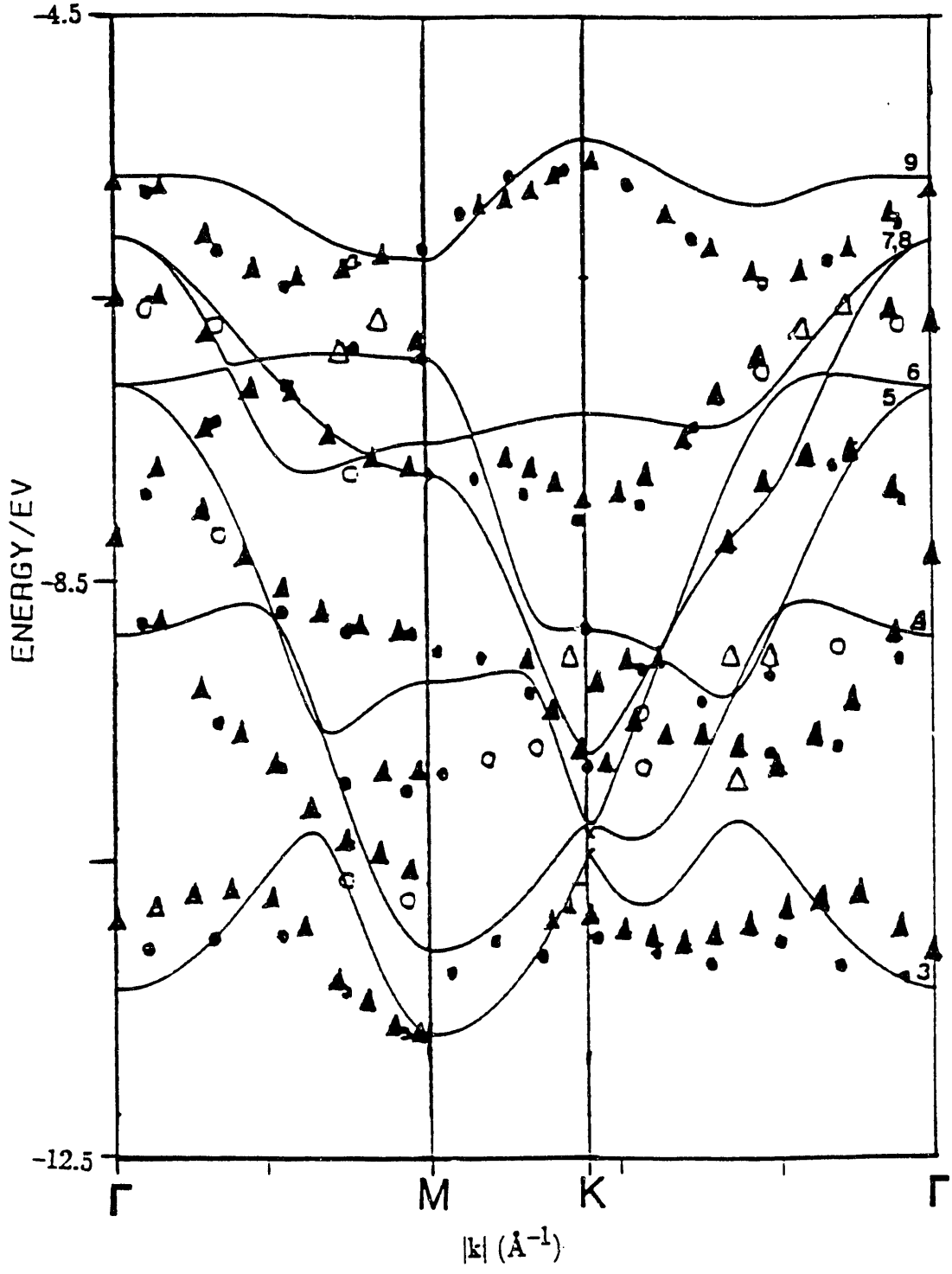

Figure 40b. Theoretical energy dispersion curves of 2-D MoS_2 (solid lines) compared to the experimental valence energy dispersion curves of Mamy et al. (triangles and circles).[15] Only the upper portion of the valence band is shown, the S3s bands have not been obtained experimentally.

Hughbanks and Hoffmann, Section 5.2.1, was -463.58 kcal/mol. Table 26 lists the energies and enthalpies of formation as well as the molybdenum and sulfur charge for the three different sets of basis sets used in calculations of the electronic structure. Thus, changes in the atomic ionization potentials produce large changes in the energies. However, changes in the energies produced on the introduction of Van der Waals interactions between the layers and termination in edge planes are expected to follow the same trends. For example, a 3-D MoS_2 calculation was carried out using the atomic parameters given in Table 22 and a set of 12 special k-points. The calculated energy of formation for this calculation was -241.54 kcal/mole. As discussed in Section 5.2.1, introduction of Van der Waals interactions between the MoS_2 layers destabilized the structure by 6.0 kcal/mole. The enthalpy of formation of bulk MoS_2 as calculated from thermodynamic data is -356.37 kcal/mole.[56a,b] Thus, neither set of parameters calculates the enthalpy of formation of MoS_2 correctly.

Table 26.

Energies of formation and charges obtained for the three sets of calculations involving different basis sets. H&H=parameters obtained from Hughbanks and Hoffmann, C&R=parameters obtained from Clementi and Roetti, ESCA=parameters obtained by parametrization with the ESCA valence band of MoS_2.

Basis Set	$\Delta U_f^\circ(\frac{kcal}{mol})$	$\Delta H_f^\circ(\frac{kcal}{mol})$	Mo Charge	S Charge
H&H	-463.58	-465.36	+0.56	-0.28
C&R	-371.02	-372.80	+0.55	-0.28
ESCA	-247.58	-249.36	+0.99	-0.50
Experimental	——	-356.37		

Charges were also increased by parametrization of the atomic ionization parameters with experiment. In the 2-D MoS_2 system calculated using the parameters given in Table 22 the charges are the following: Mo, +0.99; S_2, -0.50; and S_3, -0.50. Thus, the molybdenum charge was increased from a value of +0.56 obtained with the parameters of Hughbanks and Hoffmann to +0.99. The sulfur charges were decreased from a value of -0.28 to -0.50. Charges of the 3-D MoS_2 system calculated using the parameters of Table 22 are the following: Mo, +1.33; S, -0.67. Thus on proceeding from the 2-D to 3-D system, the molybdenum was oxidized from +0.99 to +1.33 and the sulfur was reduced from -0.50 to -0.67.

5.6.3 Effect of Nodes on the Theoretical Valence Band.

As mentioned in Section 3.2, the Mo4d, S3s, and S3p radial functions used in calculations of the electronic structure of MoS_2 did not contain any nodes. The number of nodes in a true radial function should be equal to the principal quantum number of the orbital, n, minus the azimuthal quantum number of the orbital, l, minus one or $n-l-1$. Thus, the Mo4d radial function should possess $4-2-1 = 1$ node; the S3p radial function should possess $3-1-1 = 1$ node; and the S3s radial function should possess $3-0-1 = 2$ nodes. Addition of a node to the S3p radial function was carried out by changing the sign of the coefficient belonging to the more contracted zeta function of the double zeta STO. However, simply changing the sign of one of the coefficients produces a very different radial function. Thus, the coefficients and zeta values were also changed to produce a S3p double zeta function that had most probable radius close to 1.74 au (similar to that of the S3p orbitals given in Table 27) and contained one node close to the atomic center. Inclusion of the node did not affect the theoretical valence band or energy dispersion curves. However, the total radial function at large distances from the atomic center now resembled a single zeta function as used by Hughbanks and Hoffmann. The resulting theoretical valence band possessed a three-peaked nature in the Mo4d-S3p valence band. A gap between the highest occupied crystal band (band #9) and the lower Mo4d-S3p (specifically bands #7 and #8) was also present in the theoretical energy dispersion curves.

From the above discussions, addition of nodes does not affect the valence band or energy dispersion curves. The characteristic shape of the MoS_2 valence band was only achieved when double zeta S3p radial functions containing no nodes were used as the basis. Inclusion of nodes with retention of the double zeta character of the S3p orbitals could be carried out by using a S3p radial function that included more than two STO's. However, at this time, the EHMACPP program only allows double zeta STO's.

5.7 Electronic Structure of 2-D NbS_2

Two-dimensional (2-D) NbS_2, consisting of one NbS_2 per unit cell, was modeled as described in Section 3.5.2. The set of 171 special **k**-points, described in Section 3.7.1, was used in the calculation of the theoretical valence band. Initially, a theoretical calculation was carried out using radial functions for the valence orbitals that were represented by Slater-type orbitals using the parameters of Hughbanks and Hoffmann for the S3s, S3p and Nb4d orbitals, Section 3.2. A second theoretical calculation was carried out using the parameters of Clementi and Roetti, Section 3.2. A third theoretical calculation was carried out using the S3s and S3p atomic parameters obtained from the parametrization of the MoS_2 valence band, Section 5.6.2

and Table 25. The ionization potential, H_{ii}, and coefficients, c_i, for the Nb4d orbital were obtained by comparison with an experimentally obtained XPS valence band of polycrystalline NbS_{2-x}, Section 4.2.

5.7.1 Theoretical Valence Band.

The theoretical valence band for NbS_2 was obtained by first modifying the S3s, S3p, and Nb4d atomic orbital populations by their corresponding photoelectron cross-sections to obtain modified atomic orbital populations, MAOPOP's. Subsequent summation of the S3s, S3p and Nb4d MAOPOP's leads to a NbS_2 theoretical valence band. This method is described in Section 3.3. The ratio of Nb4d to S3p photoelectron cross-sections is 2.56. This ratio is approximately 1/3 lower than that of Mo4d to S3p photoelectron cross-sections. Thus in NbS_2, the Nb4d orbitals will contribute less to the upper Nb4d-S3p valence band region in NbS_2 than the Mo4d orbitals contribute to the upper Mo4d-S3p valence band region in MoS_2. The valence of 2-D NbS_2 is shown in Figure 41a. S3s, S3p and Nb4d modified atomic orbital populations, MAOPOP's, for 2-D NbS_2 are shown in Figure 41b. The theoretical valence band of NbS_2 was obtained using the parameters given in Table 27. The ionization potentials and atomic parameters of the S3s, S3p orbitals obtained by parametrization of the MoS_2 theoretical valence band were used for this calculation, Section 5.6.2. Nb4d double zeta exponents, ζ_i, were obtained from tabulations of Clementi and Roetti. The Nb4d ionization potential and double zeta coefficients were parametrized according to the experimentally obtained XPS valence band of NbS_{2-x}. This set of parameters is referred to as the ESCA atomic parameters.

Table 27.

Radial parameters, H_{ii}, ζ_i, and c_i, for the Nb4d, S3s, and S3p atomic orbitals. Parametrization of theoretical and experimental valence bands led to the parameters listed in this table. The numbers in parentheses indicate the value of i.

Atom	Orbital	H_{ii}(eV)	ζ_i	c_i
Nb	4d	-5.53	3.59080(1)	0.36188(1)
			1.71750(2)	0.75431(2)
S	3s	-17.80	2.66221(1)	0.43538(1)
			1.68771(2)	0.60731(2)
S	3p	-8.845	2.33793(1)	0.35338(1)
			1.33331(2)	0.70431(2)

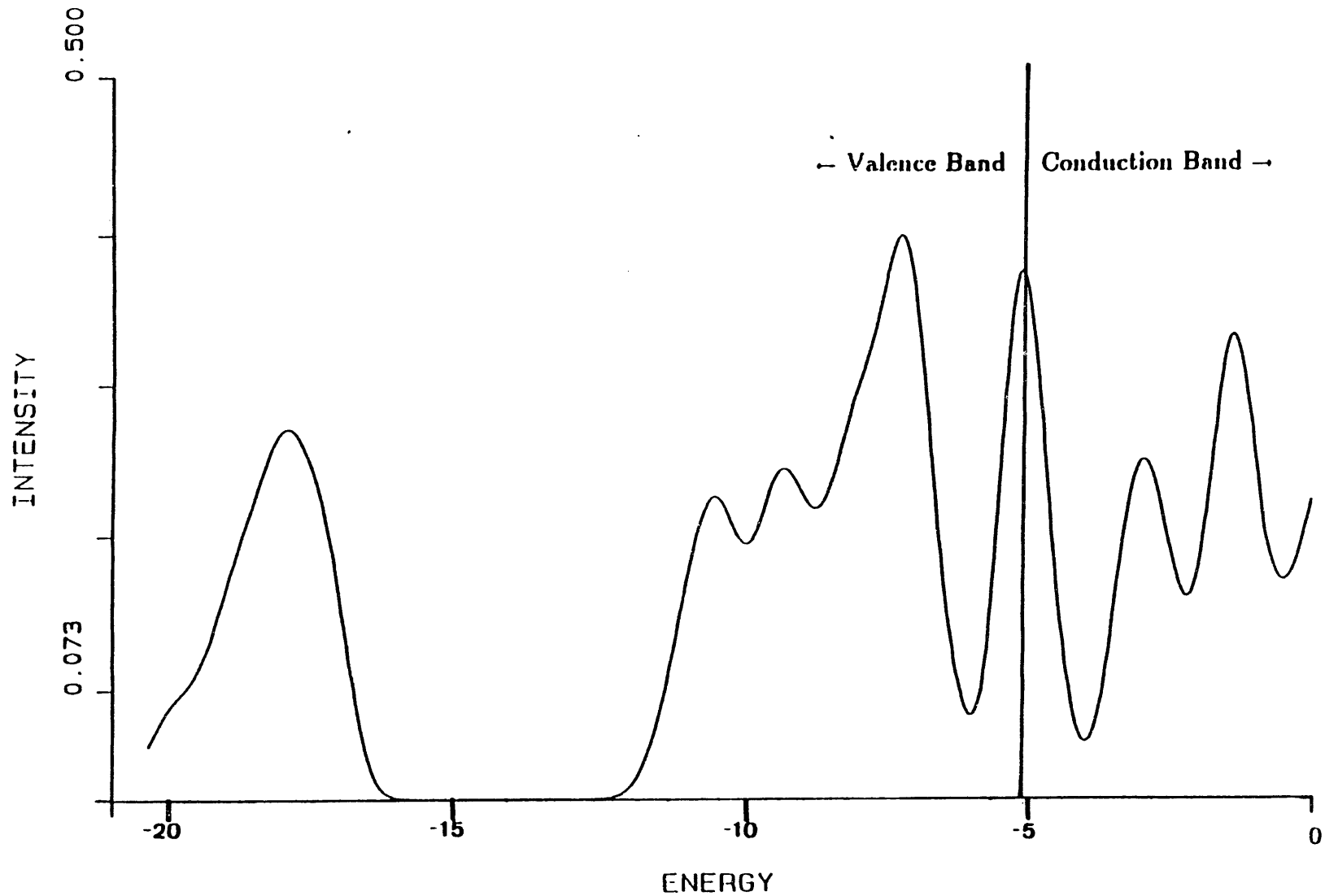

Figure 41a. Theoretical valence band of 2 D NbS_2. The 171 special k-point set and S3s, S3p, and Nb4d ESCA atomic parameters given in Table 27 were used for this calculation.

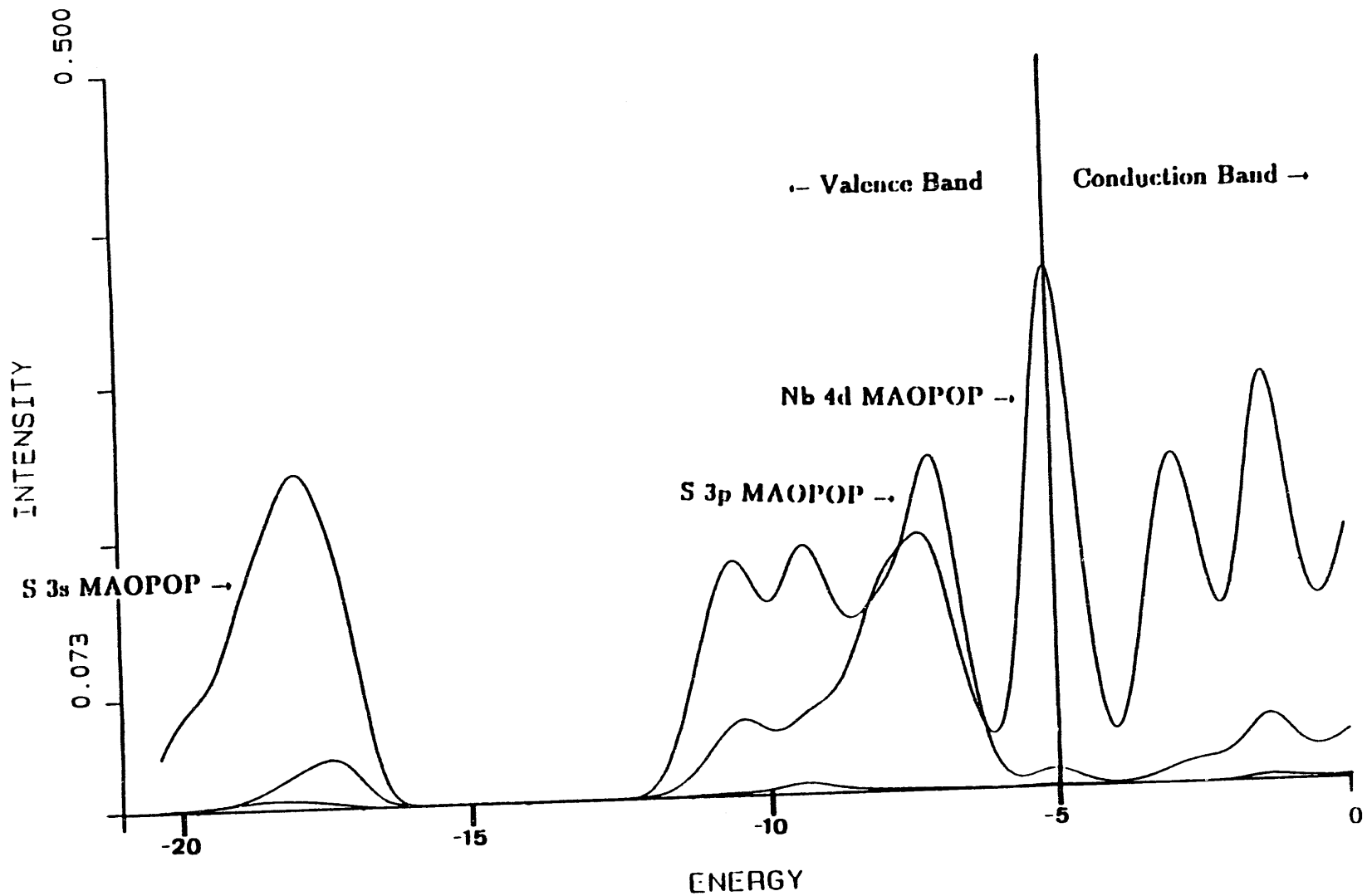

Figure 41b. Theoretical modified atomic orbital populations, MAOPOP's, for the Nb4d and S3s, S3p orbitals of 2 D NbS_2. The 171 special k point set and S3s, S3p, and Nb4d ESCA atomic parameters given in Table 27 were used for this calculation.

The theoretical valence band of 2-D NbS_2 is very similar to that of 2-D MoS_2. The valence band consists of a single S3s band located at ca. 18 eV and an upper Nb4d-S3p band. The S3s band of 2-D NbS_2 has less dispersion (FWHM of S3s band less) than the S3s band of 2-D MoS_2. The loss of S3s dispersion in 2-D NbS_2 can be attributed to the longer S-S bond distance within the sulfur atomic layers of NbS_2. In NbS_2 the S-S bond distance within the sulfur atomic layers is 3.31 Å, whereas in MoS_2 this distance is 3.16 Å. The highest occupied band is only occupied by 1/2 (or one electron per NbS_2) and as a result 2-D NbS_2 possesses metallic conductivity.

5.7.2 Comparison of Energies and Charges.

Energies and charges were obtained for each of the theoretical calculations involving different atomic basis sets. The charges and energies for the three sets of calculations are given in Table 28. Calculations involving the atomic parameters of Hughbanks and Hoffmann give

Table 28.

Energies of formation and charges obtained for the three sets of calculations involving different basis sets. H&H=parameters obtained from Hughbanks and Hoffmann, C&R=parameters obtained from Clementi and Roetti, ESCA=parameters obtained by parametrization with the ESCA valence band of NbS_{2-x}.

Basis Set	$\Delta U_f^\circ(\frac{kcal}{mol})$	$\Delta H_f^\circ(\frac{kcal}{mol})$	Nb Charge	S Charge
H&H	-533.37	-535.14	-0.43	+0.21
C&R	-321.97	-323.74	+1.13	-0.56
ESCA	-277.74	-279.52	+1.75	-0.87
Experimental	——	-391.57		

unrealistic negative niobium and positive sulfur charges of -0.43 and +0.21, respectively. As discussed in Section 4.1.2, the binding energy position of the Nb $3d_{5/2}$ core level peak of polycrystalline NbS_{2-x} indicates that niobium atoms in the sulfide are oxidized relative to niobium atoms in the metal. The binding energy position of the S $2p_{3/2}$ core level peak indicates that sulfur atoms in the sulfide are reduced relative to a zero-valent sulfur species. The theoretical energy of formation of the crystalline $NbS_2(s)$ from the separated gas atoms, Nb(g) and 2 S(g), is also too large when compared to the experimental enthalpy.

More realistic enthalpies and charges are obtained when the ionization potentials and atomic parameters of Clementi and Roetti are used to calculate the electronic structure of 2-D

NbS_2. A positive niobium charge of +1.13 and negative sulfur charge of -0.56 are obtained using the parameters of Clementi and Roetti. However, the entire theoretical valence band is shifted to higher binding energies compared to the experimental XPS valence band of NbS_{2-x} when the parameters of Clementi and Roetti are used. These parameters also separate the S 3s band from the bottom of the Nb4d-S3p valence band by ca. 9 eV. Experimentally, the S3s band is separated from the upper Nb4d-S3p valence band by ca. 6 eV.

The ionization potentials and atomic parameters of the S3s, S3p, and Nb4d orbitals obtained by parametrization of the NbS_2 theoretical valence band with the experimental XPS valence band (ESCA atomic parameters) also give a positive niobium charge of +1.75 and negative sulfur charge of -0.87. However, the magnitude of the enthalpy of formation has been decreased by the decrease in the magnitudes of the S3s, S3p, and Nb4d ionization potentials. The theoretical enthalpy of formation is -279.52 kcal/mol as compared to the experimental enthalpy of -391.57 kcal/mol. The top of the valence band in NbS_2 (or the Fermi level in metallic NbS_2) is located at -5.1 eV, whereas the top of the valence band in MoS_2 is located at -5.4 eV.

5.8 Electronic Structure of 3-D RuS_2

Three-dimensional RuS_2, consisting of four RuS_2 molecules per unit cell, was modeled as described in Section 3.6.2. A set of 10 special **k**-points obtained from References 40, were used in the calculation of the theoretical valence band. Radial functions for the valence orbitals involved in this study were represented by Slater-type orbitals using the parameters of Hughbanks and Hoffmann and Clementi and Roetti, Section 3.2 and Table 1. A third calculation was carried out using the S3s and S3p atomic ionization potentials and double zeta coefficients obtained by parametrization of MoS_2, Table 25. The Ru4d atomic ionization potential and double zeta coefficients were obtained by comparison of the theoretically obtained valence band with the experimental XPS valence band of polycrystalline RuS_2 shown in Section 4.2.

5.8.1 Theoretical Valence Band of 3-D RuS_2.

The theoretical valence band for RuS_2 was obtained by first modifying the S3s, S3p, and Ru4d atomic orbital populations by their corresponding photoelectron cross-sections to obtain modified atomic orbital populations, MAOPOP's. Subsequent summation of the S3s, S3p and Ru4d MAOPOP's leads to a RuS_2 theoretical valence band. This method is described in Section 3.3. The ratio of Ru4d to S3p photoelectron cross-sections is 8.62. This ratio is

approximately two times higher than the corresponding Mo4d to S3p photoelectron cross-section ratio. Thus in RuS_2, the Ru4d orbitals will contribute more to the upper Ru4d-S3p valence band region in RuS_2 than the Mo4d orbitals contribute to the upper Mo4d-S3p valence band region in MoS_2. The valence of 3-D RuS_2 is shown in Figure 42a. S3s, S3p and Ru4d modified atomic orbital populations, MAOPOP's, for 3-D RuS_2 are shown in Figure 42b. The theoretical valence band of RuS_2 was obtained using the parameters given in Table 29. The ionization potentials and atomic parameters of the S3s, S3p orbitals obtained by parametrization of the MoS_2 theoretical valence band were used for this calculation, Section 5.6.2. Ru4d double zeta exponents, ζ_i, were obtained from tabulations of Clementi and Roetti. The Ru4d ionization potential and double zeta coefficients were parametrized according to the experimentally obtained XPS valence band of polycrystalline RuS_2. This set of parameters is referred to as the ESCA atomic parameters.

Table 29.

Radial parameters, H_{ii}, ζ_i, and c_i, for the Ru4d, S3s, and S3p atomic orbitals. Parametrization of theoretical and experimental valence bands led to the parameters listed in this table. The numbers in parentheses indicate the value of i.

Atom	Orbital	H_{ii}(eV)	ζ_i	c_i
Ru	4d	-5.065	4.25911(1)	0.42606(1)
			2.09384(2)	0.69271(2)
S	3s	-17.80	2.66221(1)	0.43538(1)
			1.68771(2)	0.60731(2)
S	3p	-8.845	2.33793(1)	0.35338(1)
			1.33331(2)	0.70431(2)

The two lowest energy bands centered around -17.8 eV (see Figures 42a and 42b) consist of mainly S3s orbitals with a small amount of contribution from the Ru4d orbitals. These two bands will be referred to as the S3s bands. In RuS_2, the sulfur atoms occur as dimer pairs, S_2^{-2}, such that the S-S distance of 2.178 Å is smaller than the Ru-S distance of 2.351 Å. Thus, interaction of the two sulfur atoms occurs so that the S3s band which was a single band in the layered NbS_2 and MoS_2 compounds is split into two bands in RuS_2. The highest occupied band (at the top of the valence band) consists of mainly Ru4d character. Ru $4d_{xy}$, $4d_{yz}$, $4d_{zx}$, $4d_{x2-y2}$, and $4d_{z2}$ orbitals contribute to the highest occupied band of the valence band such that the contribution of $4d_{xy} \simeq 4d_{yz} \simeq 4d_{zx} > 4d_{x2-y2} \simeq 4d_{z2}$. One intense band forms the lowest unoccupied portion of the conduction band The lowest unoccupied band

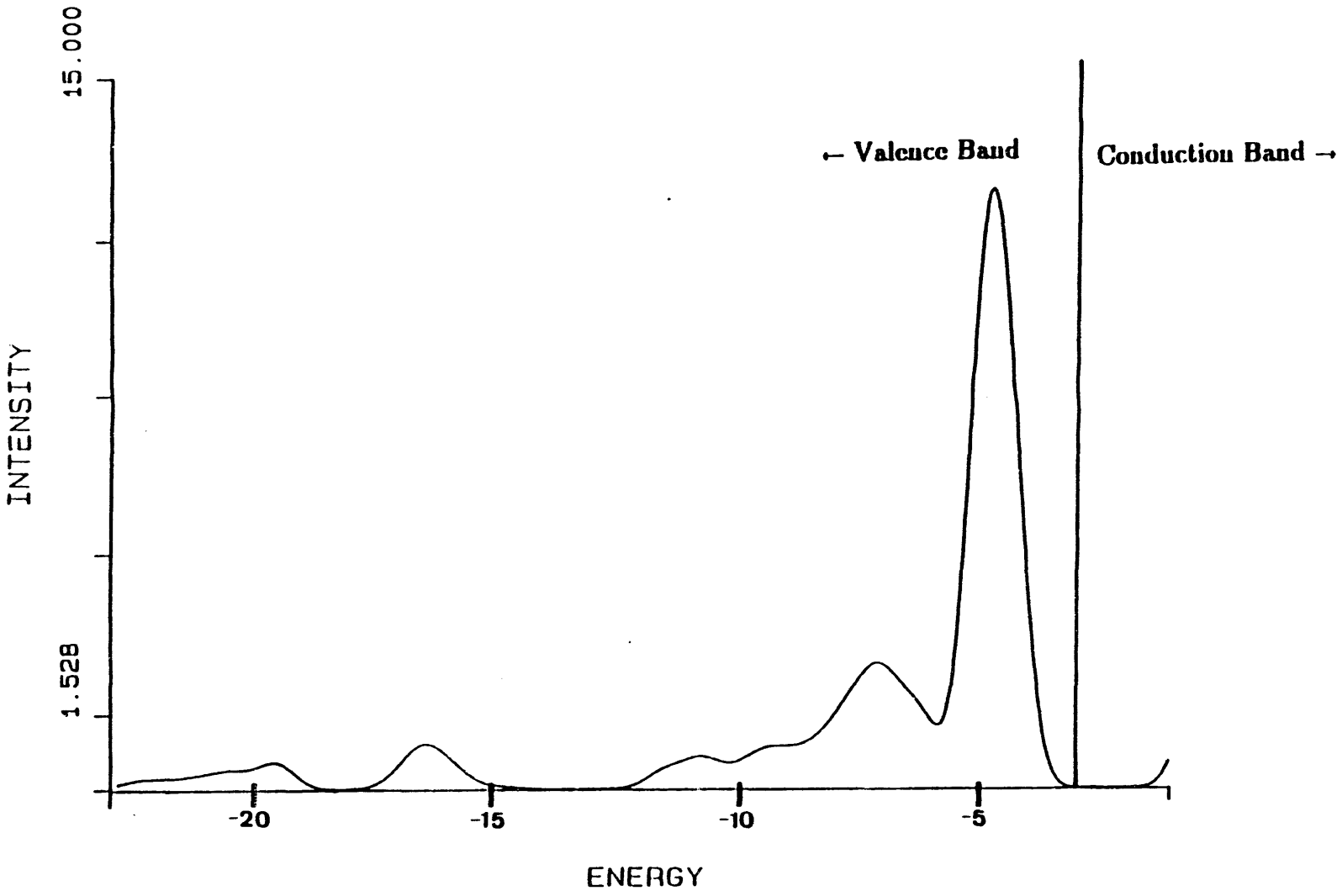

Figure 42a. Theoretical valence band of 3-D RuS_2. The 10 special k-point set and S3s, S3p, and Ru4d ESCA atomic parameters given in Table 29 were used for this calculation.

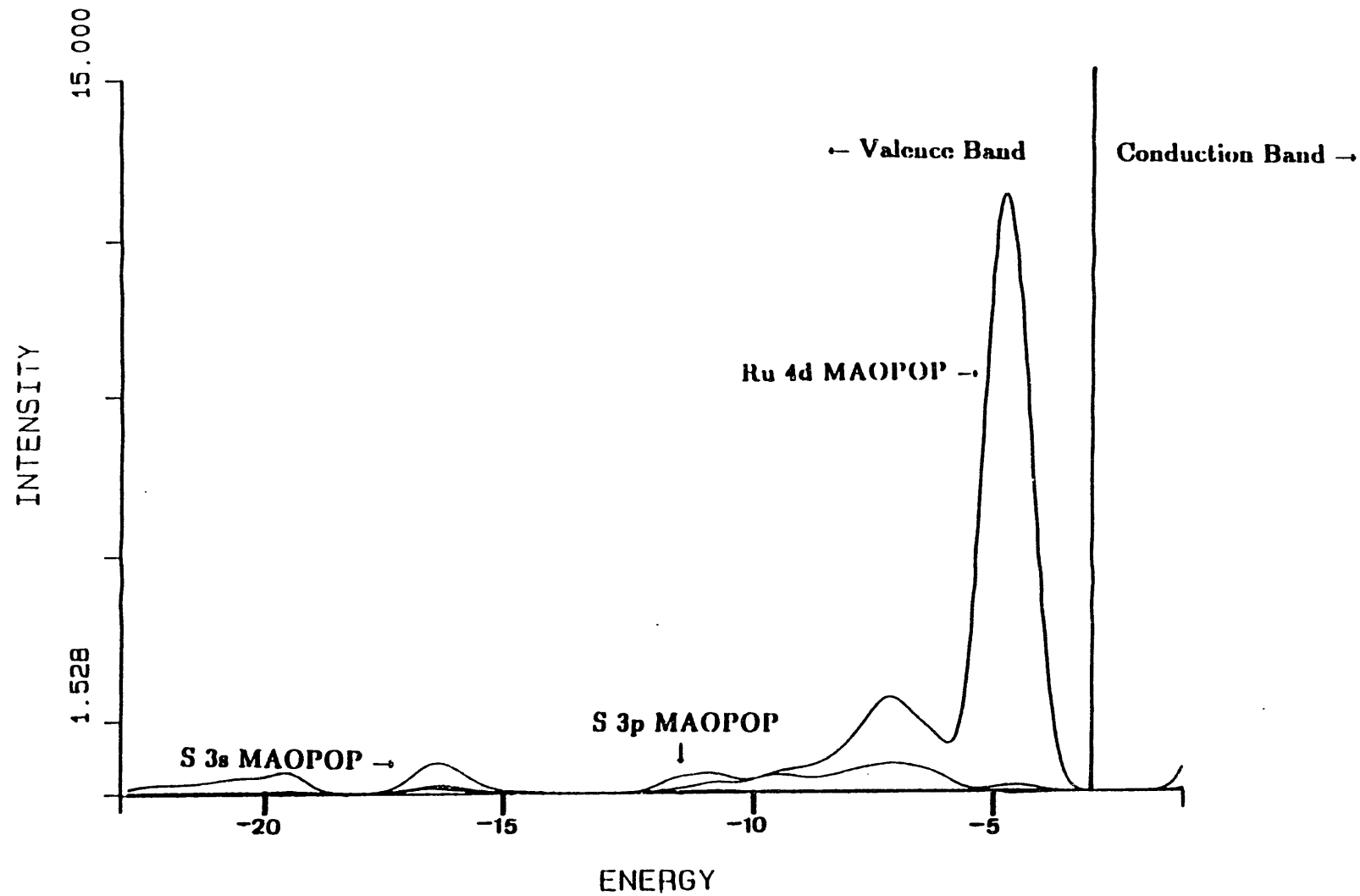

Figure 42b. Theoretical modified atomic orbital populations, MAOPOP's, for the Ru4d and S3s, S3p orbitals of 3 D RuS_2. The 10 special k point set and S3s, S3p, and Ru4d ESCA atomic parameters given in Table 29 were used for this calculation.

(at the bottom of the conduction band) has mainly Ru4d character also. Again, Ru $4d_{xy}$, $4d_{yz}$, $4d_{zx}$, $4d_{x2-y2}$, and $4d_{z2}$ orbitals contribute such that $4d_{x2-y2} \simeq 4d_{z2} > 4d_{xy} \simeq 4d_{yz} \simeq 4d_{zx}$. Crystal field splitting of the d orbitals in a transition metal coordinated by ligands in an octahedral environment occurs such that the $4d_{xy}$, $4d_{yz}$, and $4d_{zx}$ orbitals are degenerate and lie lowest in energy followed by the higher energy degenerate $4d_{x2-y2}$ and $4d_{z2}$. The Ru4d orbitals in RuS_2 follow the crystal field splitting only to a limited extent. S3p orbitals contribute to the lower and center portions of the Ru4d-S3p valence band. The highest occupied band has almost no contribution from the S3s or S3p orbitals.

5.8.2 Comparison of Energies and Charges.

Energies and charges were obtained for each of the theoretical calculations involving different atomic basis sets. The charges and energies for the three sets of calculations are given in Table 30. Calculations involving the atomic parameters of Hughbanks and Hoffmann give

Table 30.

Energies of formation and charges obtained for the three sets of calculations involving different basis sets. H&H=parameters obtained from Hughbanks and Hoffmann, C&R=parameters obtained from Clementi and Roetti, ESCA=parameters obtained by parametrization with the ESCA valence band of RuS_2.

Basis Set	$\Delta U_f^\circ(\frac{kcal}{mol})$	$\Delta H_f^\circ(\frac{kcal}{mol})$	Ru Charge	S Charge
H&H	-364.53	-366.31	-0.58	+0.29
C&R	-227.42	-229.20	-0.96	+0.48
ESCA	-59.61	-61.38	+0.94	-0.47
Experimental	——	-336.07		

unrealistic negative ruthenium and positive sulfur charges of -0.58 and +0.29, respectively. As discussed in Section 4.1.2, the binding energy position of the Ru $3d_{5/2}$ core level peak of polycrystalline RuS_2 does not indicate a large change in oxidation state from the sulfide to ruthenium atoms in the metal. The binding energy position of the S $2p_{3/2}$ core level peak indicates that sulfur atoms in the sulfide are reduced relative to a zero-valent sulfur species. The theoretical energy of formation of the crystalline $RuS_2(s)$ from the separated gas atoms, Ru(g) and 2 S(g), is close to the experimental enthalpy.

When the ionization potentials and atomic parameters of Clementi and Roetti are used to calculate the electronic structure of 3-D RuS_2, the negative charge on the ruthenium and

positive charge on the sulfur atoms remains. The entire theoretical valence band is shifted to higher binding energies compared to the experimental XPS valence band of RuS_2 when the parameters of Clementi and Roetti are used. These parameters also separate the S 3s band from the bottom of the Ru4d–S3p valence band by ca. 3 eV too much.

The ionization potentials and atomic parameters of the S3s, S3p, and Ru4d orbitals obtained by parametrization of the RuS_2 theoretical valence band with the experimental XPS valence band (ESCA atomic parameters) gives a positive ruthenium charge of +0.94 and negative sulfur charge of -0.47. However, the magnitude of the enthalpy of formation has been decreased dramatically by the decrease in the magnitudes of the S3s, S3p, and Nb4d ionization potentials. The theoretical enthalpy of formation is -336.07 kcal/mol as compared to the experimental enthalpy of -61.38 kcal/mol. The top of the valence band in RuS_2 is located at -4.17 eV, whereas the top of the valence band in MoS_2 is located at -5.4 eV.

The experimental enthalpies of formation for the the three disulfides, NbS_2, MoS_2, and RuS_2 are -391.57, -356.37, and -336.07 kcal/mol, respectively. Thus, the order of thermodynamic stability is the following: $NbS_2 > MoS_2 > RuS_2$. Theoretical enthalpies for the three disulfides, NbS_2, MoS_2, and RuS_2, obtained using the ESCA atomic parameters are -279.52, -249.36, and -61.38 kcal/mol. The same order of stability ($NbS_2 > MoS_2 > RuS_2$) is obtained from the theoretical calculations, although the magnitudes of the theoretical enthalpies are too low.

Chapter 6
DISCUSSION

6.1 Orbital Picture of Energy Dispersion.

The orbital character and overlap characteristics of each band shown in Figure **30a** change on proceeding from Γ where $\mathbf{k}=0$ to M where $\mathbf{k}=\frac{1}{2}\mathbf{a}^*$ and to K where $\mathbf{k}=\frac{1}{3}(\mathbf{a}^*+\mathbf{b}^*)$ in the first Brillouin zone. These changes in the crystal orbital wavefunction lead to smooth continuous changes in the binding energy at each point along the directions Γ→M and Γ→K resulting in the energy dispersion curves of Figure **30a**. In this section, the nature of the energy dispersion is investigated by analysis of the crystal orbital coefficients and overlap populations between neighboring atoms. The first system examined will be the 2-D MoS_2 system containing one MoS_2 molecule per unit cell. Structural parameters for this system are given in Table 4. The two sulfur atoms are located in the yz plane as shown in Figure 43. The next system examined is the 3-D MoS_2 crystal and the 1-D $(MoS_2)_5$ linear "crystal" terminating at $(10\bar{1}0)$ and $(10\bar{1}1)$ edges. Differences in the electronic structures of 2-D and 3-D MoS_2 systems are used to study the origin of the indirect gap. Comparison between the 2-D and 1-D systems will be made to study the effect of introducing surface states through termination of MoS_2 at edges. The electronic structures of all of the systems discussed in this section were calculated using the parameters of Hughbanks and Hoffmann (parameters shown in Table 1).[41]

The equation 8c for the crystal orbital consists of linear combinations of atomic orbitals $\chi_\mu(\mathbf{r}-\mathbf{R}_{\mu,p})$ multiplied by a phase factor or Bloch function $\exp(2\pi i\mathbf{k}\cdot\mathbf{R}_p)$. The EHMACPP program provides the user with contributions of the local atomic orbitals to the crystal wavefunction for each energy level at a specific value of the wavevector **k**. Thus, for example in 2-D MoS_2 these atomic coefficients give a local picture of the character and bonding of one molybdenum atom with two neighboring sulfur atoms located in the same unit cell. However, for an accurate orbital picture of the bands the phase factor must be included for atomic orbitals on neighboring unit cells. At the Γ point, the wavevector has a value of zero and thus the phase factor $\exp(2\pi i\mathbf{0}\cdot\mathbf{R}_p)$ is equal to 1. Thus, atomic orbitals on neighboring unit cells have the same orientation in space. However, at the M point the wavevector has a value of $\mathbf{k}=\frac{1}{2}\mathbf{a}^*$ and $\mathbf{k}\cdot\mathbf{R}_p=(\frac{1}{2}\mathbf{a}^*)\cdot(m\mathbf{a}+n\mathbf{b})=\frac{m}{2}$ where m and n are integral multiples of the primitive lattice vectors **a** and **b** respectively (primitive lattice vectors **a**, **b**, **c** and reciprocal lattice vectors $\mathbf{a}^*$, $\mathbf{b}^*$ and $\mathbf{c}^*$ are defined in Section 3.4.1). Then the phase factor at M is $\exp(\pi i m)$ and changes value from +1 when m is an even number (0, ±2, ±4, ±2j) to −1 when m is an odd number

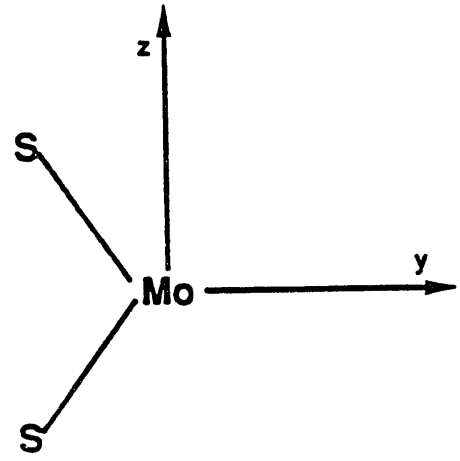

Figure 43. Geometry of the MoS_2 unit in the 2-D MoS_2 system. Sulfur atoms. S_2 and S_3 are located in the yz-plane.

(± 1, ± 3, ± 5, $\pm\{2j+1\}$). The phase factors for the primitive lattice points of 2-D MoS_2 at M are shown in Figure 44a. The white circles indicate a phase of +1 while the black textured circles indicate a phase of -1. At K, the wavevector has a value of $\mathbf{k}=\frac{1}{3}\mathbf{a}^*+\frac{1}{3}\mathbf{b}^*$ and then $\mathbf{k}\cdot\mathbf{R}_p=(\frac{1}{3}\mathbf{a}^*+\frac{1}{3}\mathbf{b}^*)\cdot(m\mathbf{a}+n\mathbf{b})=\frac{(m+n)}{3}$. The phase factor at K is $\exp(2\pi i[m+n]/3)$ and changes in value from 1 when m+n=0, ± 3, ± 6, $\pm 3j$, to $e^{2\pi i/3}$ or 120° out of phase when m+n=. . .-2, 1, 4, 3j+1 to $e^{4\pi i/3}$ or 240° out of phase when m+n=. . .-1, 2, 5, 8, 3j+2. The phase factors for the primitive lattice points of 2-D MoS_2 at K are shown in Figure 44b. The white circles indicate a phase of +1, the black circles indicate a phase of $e^{(2\pi i/3)}$ or 120° and the white squares indicate a phase of $e^{(4\pi i/3)}$ or 240°.

6.1.1 Orbital Picture of Energy Dispersion in 2-D MoS_2.

The nature of the total crystal orbital can be obtained by analysis of the local atomic orbital coefficients with inclusion of the appropriate phase factor for atomic orbitals residing on neighboring unit cells. Local atomic orbital coefficients, individual atomic orbital charges and total charges on the atoms Mo, S_2, and S_3 (see Table 4, S_2 located at $+1.5775\ \hat{z}$ and S_3 located at $-1.5775\ \hat{z}$) in 2-D MoS_2 for Bands #1 through #13 at Γ and M are given in Table 31. In general only atomic orbitals that exhibit a coefficient $>|0.1|$ are shown. At Γ, local atomic orbitals involved in bonding for Band #1 are the Mo5s and S3s orbitals. Local atomic orbitals on neighboring unit cells are in phase with the local atomic orbitals of the first unit cell. Figure 45 reproduces the arrangement of the local atomic orbitals on 7 lattice points of the 2-D MoS_2 lattice for Band #1 at Γ. Overlap between the molybdenum and sulfur atoms is positive +0.19 indicating bonding interaction between the Mo and S atoms in the trigonal prism. Overlap between the S_2 and S_3 atoms is also positive +0.052 indicating weak bonding between sulfur atoms separated by 3.155 Å. Interactions between sulfur atoms separated by 3.155 Å or 2u|c| (where u=0.128252, |c|=12.30 Å) will be referred to as inter-sulfur interactions across the MoS_2 layer, since these involve interactions between a first atomic layer sulfur atom and a third atomic layer sulfur atom eg. S_2-S_3. Interactions between sulfur atoms separated by 3.16 Å or |a| will be referred to as intra-sulfur interactions within the sulfur layer, since these involve interactions between sulfur atoms residing in the same atomic layer eg. S_2-S_2 and S_3-S_3. Intra-sulfur overlap S_2-S_2 and S_3-S_3 is also positive +0.15 indicating bonding interactions between sulfur atoms residing in the first atomic layer and between sulfur atoms residing in the third atomic layer. On proceeding from Γ to M, the energy of Band #1 is destabilized from a minimum at Γ of -24.17 eV to a maximum of -20.43 eV at M. The cause of this destabilization can be traced primarily to the change in intra-sulfur interactions S_2-S_2 and S_3-S_3 from bonding +0.15 at Γ to antibonding -0.061 at M.

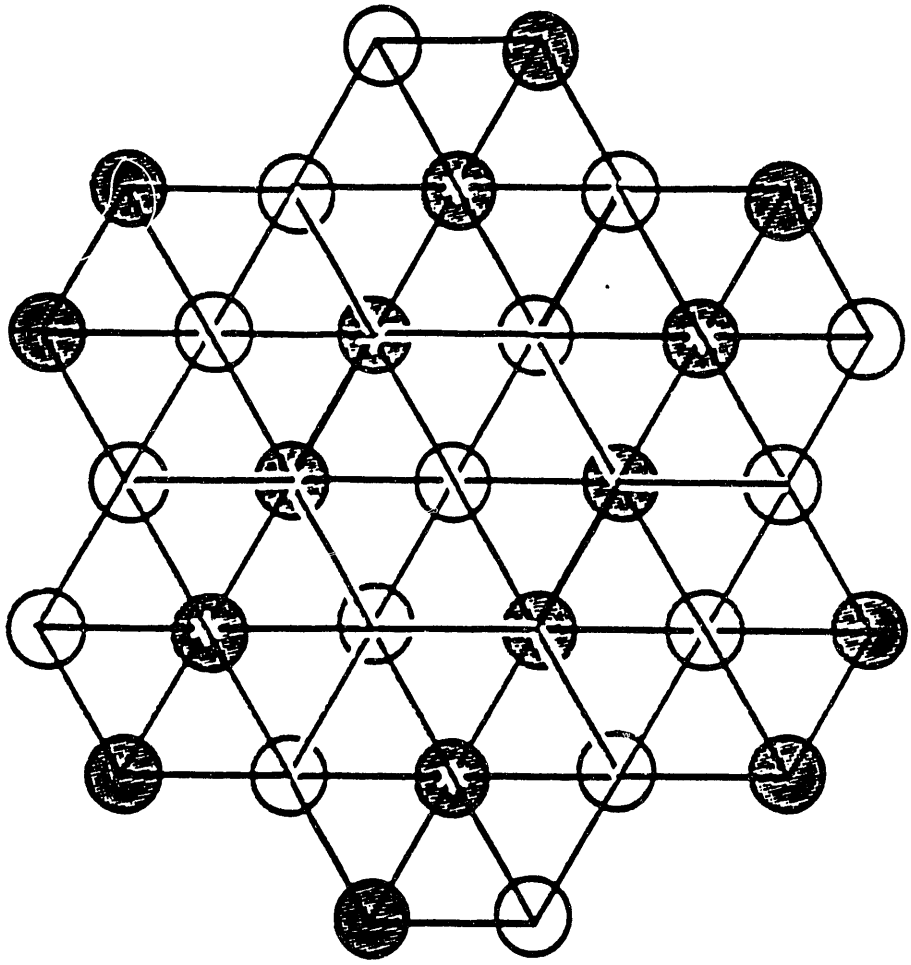

Figure 44a. Phase factor in the real lattice of 2-D MoS_2 at M. White circles indicate a phase $\exp(2\pi i\mathbf{k}\cdot\mathbf{R}_p)$ of +1 while black textured circles indicate a phase of -1. The integers m and n are integral multiples of the primitive lattice vectors **a** and **b** respectively.

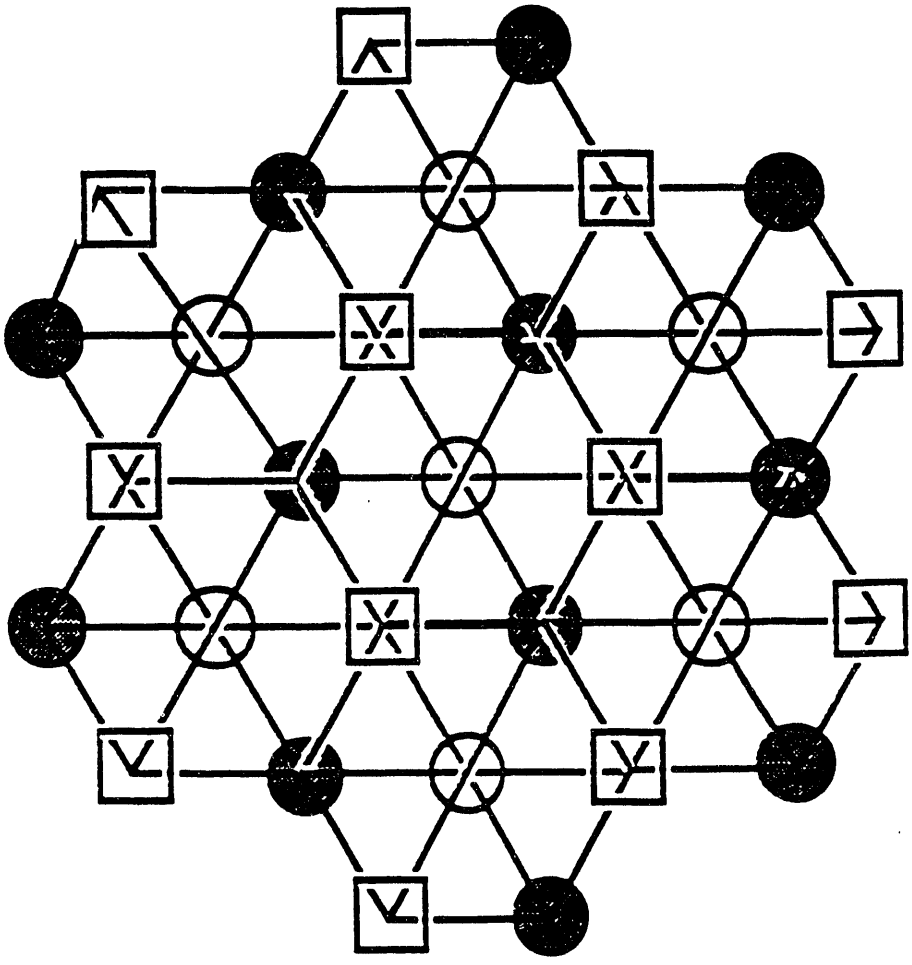

Figure 44b. Phase factor in the real lattice of 2-D MoS_2 at K. White circles indicate a phase $\exp(2\pi i\mathbf{k}\cdot\mathbf{R}_D)$ of -1, black textured circles indicate a phase of $e^{(2\pi i/3)}$ or 120° and white squares indicate a phase of $e^{(4\pi i/3)}$ or 240°. The integers m and n are integral multiples of the primitive lattice vectors **a** and **b** respectively.

Table 31.

Local atomic orbital coefficients, individual atomic orbital charges and total charges on the atoms Mo, S_2, and S_3 in 2-D MoS_2 for Bands #1-#13 at Γ and M. The atomic parameters of Hughbanks and Hoffmann were used in this calculation.

	Γ *Point:* $k=0$				*M Point:* $k=a^*/3$			
Band #	Atomic Orbital	Orbital Coefficient	AO Charge	Atom Charge	Atomic Orbital	Orbital Coefficient	AO Charge	Atom Charge
Band #1	Mo5s	0.11	0.26	0.26	Mo5s	0.14	0.099	0.42
	$Mo4d_{z2}$	0.03	0.0034		$Mo5p_x$	0.11	0.17	
					$Mo4d_{xy}$	0.12	0.075	
	$S_2 3s$	0.54	0.87	0.87	$S_2 3s$	0.58	0.78	0.79
	$S_3 3s$	0.54	0.87	0.87	$S_3 3s$	0.58	0.78	0.79
Band #2	$Mo5p_z$	-0.10	0.21	0.21	$Mo5p_z$	-0.12	0.07	0.49
					$Mo4d_{zx}$	-0.28	0.31	
					$Mo4d_{yz}$	0.16	0.10	
	$S_2 3s$	-0.57	0.89	0.90	$S_2 3s$	-0.60	0.75	0.76
	$S_3 3s$	0.57	0.89	0.90	$S_3 3s$	0.60	0.75	0.76
Band #3	$Mo4d_{z2}$	-0.30	0.33	0.43	$Mo4d_{z2}$	-0.13	0.074	0.37
					Mo5s	-0.16	0.17	
					$Mo4d_{xy}$	-0.082	0.036	
	$S_2 3s$	-0.11	0.011	0.79	$S_2 3p_x$	0.44	0.60	0.81
	$S_2 3p_z$	-0.54	0.78		$S_2 3p_y$	-0.26	0.20	
	$S_3 3s$	-0.11	0.011	0.79	$S_3 3p_x$	0.44	0.60	0.81
	$S_3 3p_z$	0.54	0.78		$S_3 3p_y$	-0.26	0.20	
Band #4	$Mo5p_z$	-0.12	0.11	0.11	$Mo5p_z$	-0.15	0.20	0.30
					$Mo4d_{zx}$	0.13	0.07	
	$S_2 3p_z$	0.68	0.95	0.95	$S_2 3p_x$	0.47	0.63	0.85
					$S_2 3p_y$	-0.27	0.21	
	$S_3 3p_z$	0.68	0.95	0.95	$S_3 3p_x$	-0.47	0.63	0.85
					$S_3 3p_y$	0.27	0.21	
Band #5	$Mo4d_{xy}$	-0.68	1.12	1.14	$Mo4d_{xy}$	-0.26	0.23	0.41
					$Mo4d_{z2}$	0.20	0.12	
					$Mo4d_{x2-y2}$	0.15	0.077	
	$S_2 3p_x$	0.47	0.43	0.43	$S_2 3p_z$	0.58	0.74	0.79
					$S_2 3s$	0.19	0.048	
	$S_3 3p_x$	0.47	0.43	0.43	$S_3 3p_z$	-0.58	0.74	0.79
					$S_3 3s$	0.19	0.048	
Band #6	$Mo4d_{x2-y2}$	-0.68	1.12	1.14	$Mo4d_{x2-y2}$	0.12	0.034	0.30
					$Mo5p_x$	0.15	0.063	
					$Mo5p_y$	0.25	0.19	
	$S_2 3p_y$	0.47	0.43	0.43	$S_2 3p_y$	-0.57	0.64	0.85
					$S_2 3p_x$	-0.33	0.21	
	$S_3 3p_y$	0.47	0.43	0.43	$S_3 3p_y$	-0.57	0.64	0.85
					$S_3 3p_x$	-0.33	0.21	
Band #7	$Mo4d_{zx}$	-0.68	0.97	0.97	$Mo4d_{yz}$	0.49	0.62	0.83
					$Mo4d_{zx}$	0.28	0.21	
	$S_2 3p_x$	0.54	0.52	0.52	$S_2 3p_y$	-0.46	0.44	0.59
					$S_2 3p_x$	-0.26	0.15	
	$S_3 3p_x$	-0.54	0.52	0.52	$S_3 3p_y$	0.46	0.44	0.59
					$S_3 3p_x$	0.26	0.15	

Table 31 (cont).

Local atomic orbital coefficients, individual atomic orbital charges and total charges on the atoms Mo, S_2, and S_3 in 2-D MoS_2 for Bands #1-#13 at Γ and M. The atomic parameters of Hughbanks and Hoffmann were used in this calculation.

	Γ *Point:* $k=0$				*M Point:* $k=a^*/3$			
Band #	Atomic Orbital	Orbital Coefficient	AO Charge	Atom Charge	Atomic Orbital	Orbital Coefficient	AO Charge	Atom Charge
Band #8	$Mo4d_{yz}$	-0.68	0.97	0.97	$Mo4d_{zx}$	0.25	0.19	0.26
					$Mo4d_{yz}$	-0.15	0.06	
	$S_2 3p_y$	0.54	0.52	0.52	$S_2 3p_z$	-0.65	0.82	0.87
					$S_2 3s$	-0.14	0.023	
	$S_3 3p_y$	-0.54	0.52	0.52	$S_3 3p_z$	-0.65	0.82	0.87
					$S_3 3s$	0.14	0.023	
Band #9	$Mo4d_{z2}$	0.91	1.65	1.65	$Mo4d_{z2}$	-0.58	0.68	1.63
					$Mo4d_{xy}$	0.53	0.58	
					$Mo4d_{x2-y2}$	-0.30	0.19	
	$S_2 3p_z$	-0.34	0.17	0.17	$S_2 3p_z$	0.32	0.18	0.18
	$S_3 3p_z$	0.34	0.17	0.17	$S_3 3p_z$	-0.32	0.18	0.18
Band #10	$Mo5p_x$	0.27	0.092	0.96	$Mo4d_{x2-y2}$	-0.94	1.46	1.97
	$Mo4d_{xy}$	-0.74	0.87		$Mo4d_{xy}$	-0.55	0.49	
	$S_2 3p_x$	-0.62	0.52	0.52	$S_2 3p_x$	-0.051	0.0038	0.015
					$S_2 3p_y$	-0.087	0.012	
	$S_3 3p_x$	-0.62	0.52	0.52	$S_3 3p_x$	-0.051	0.0038	0.015
					$S_3 3p_y$	-0.087	0.012	
Band #11	$Mo5p_y$	-0.27	0.092	0.96	$Mo4d_{z2}$	-0.84	1.12	1.85
	$Mo4d_{x2-y2}$	0.74	0.87		$Mo4d_{x2-y2}$	0.32	0.17	
					$Mo4d_{xy}$	-0.55	0.50	
	$S_2 3p_y$	0.62	0.52	0.52	$S_2 3p_y$	0.12	0.016	0.075
					$S_2 3p_x$	-0.20	0.049	
	$S_3 3p_y$	0.62	0.52	0.52	$S_3 3p_y$	0.12	0.016	0.075
					$S_3 3p_x$	-0.20	0.049	
Band #12	$Mo4d_{yz}$	-0.82	1.03	1.03	$Mo4d_{yz}$	-0.79	0.88	1.17
					$Mo4d_{zx}$	-0.46	0.29	
	$S_2 3p_y$	-0.62	0.48	0.48	$S_2 3p_y$	-0.52	0.31	0.41
					$S_2 3p_x$	-0.30	0.10	
	$S_3 3p_y$	0.62	0.48	0.48	$S_3 3p_y$	0.52	0.31	0.41
					$S_3 3p_x$	0.30	0.10	
Band #13	$Mo4d_{zx}$	0.82	1.03	1.03	$Mo4d_{zx}$	-0.83	0.90	1.30
					$Mo4d_{yz}$	0.48	0.30	
					$Mo5p_z$	0.33	0.10	
	$S_2 3p_x$	0.62	0.48	0.48	$S_2 3p_x$	0.30	0.057	0.35
					$S_2 3p_y$	-0.17	0.019	
					$S_2 3p_z$	-0.39	0.15	
					$S_2 3s$	0.41	0.13	
	$S_3 3p_x$	-0.62	0.48	0.48	$S_3 3p_x$	-0.30	0.057	0.35
					$S_3 3p_y$	0.17	0.019	
					$S_3 3p_z$	-0.39	0.15	
					$S_3 3s$	-0.41	0.13	

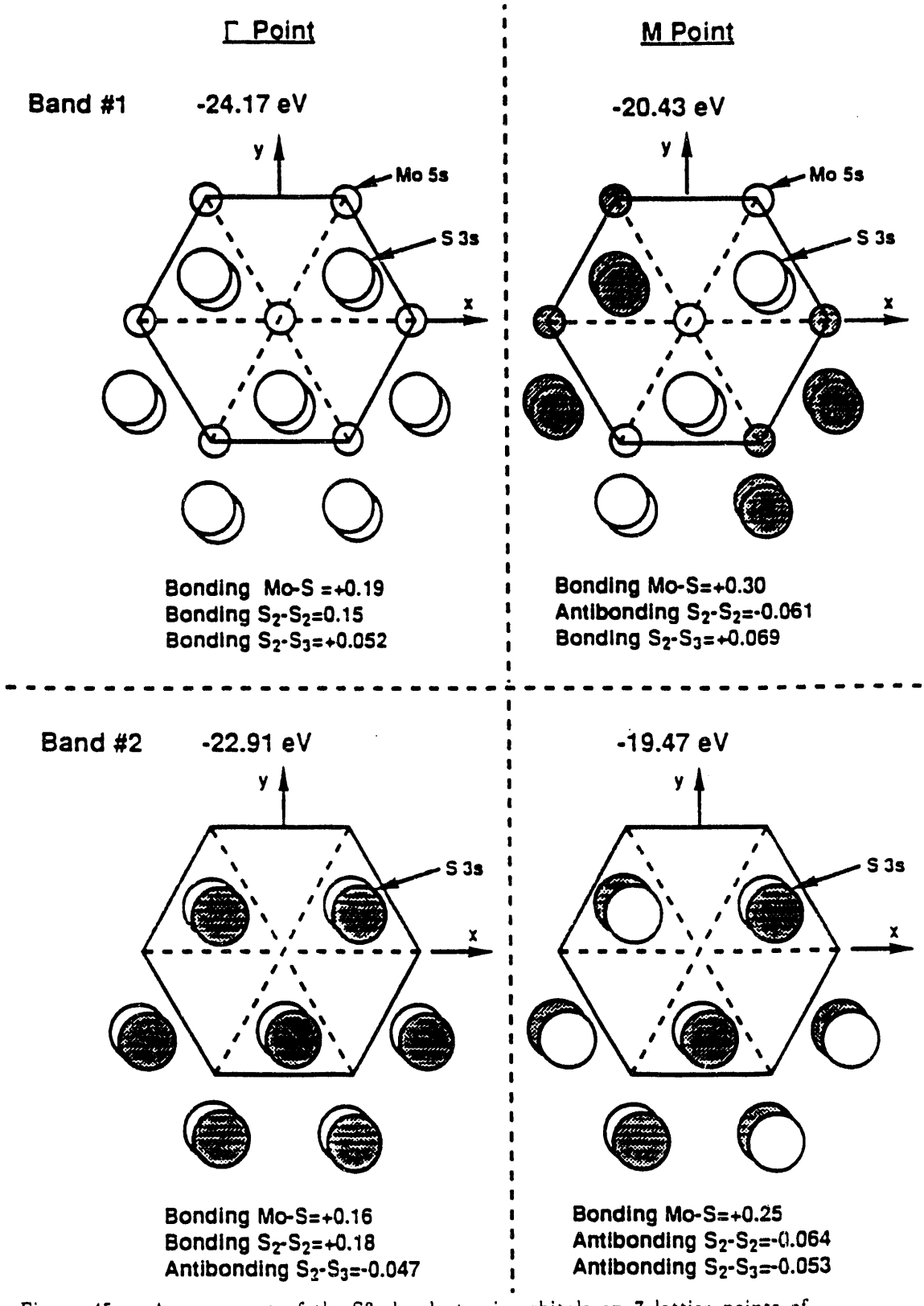

Figure 45. Arrangement of the S3s local atomic orbitals on 7 lattice points of the 2-D MoS_2 lattice for Bands #1 and #2 at Γ and M.

Inter–sulfur interactions S_2–S_3 remain bonding, increasing slightly from +0.052 at Γ to +0.069 at M. Overlap between the molybdenum and sulfur atoms increases from +0.19 to +0.30 at M due to the inclusion of $Mo4d_{xy}$ and $Mo5p_x$ character at M. Intra–sulfur antibonding interactions at M result from the form of the phase factor on neighboring unit cells. A unit cell located at the center of a hexagon is surrounded by 6 neighboring unit cells located at a distance of |**a**| or 3.16 Å. Two of the neighboring unit cells are in phase with the central unit cell while four are out of phase by −1 with the central unit cell. The local atomic orbital coefficients of these four unit cells are then multiplied by the phase −1. A crystal orbital picture of Band #1 at M is shown in Figure 45. Atomic orbital charges indicate that when two electrons occupy Band #1 at Γ, 1.74 electrons or 87% of the electrons are located on the sulfur atoms in the S3s orbitals while 0.26 electrons or 13% are located on the molybdenum atom. At M, 1.58 electrons or 79% of the electrons are located on the sulfur atoms mainly in the S3s orbitals while 0.42 electrons or 21% of the electrons are located on the molybdenum atom. Thus, energy dispersion of this band is mainly due to interactions between the S3s orbitals of neighboring unit cells.

Figure 45 reproduces the arrangement of the S3s local atomic orbitals on 7 lattice points of the 2-D MoS_2 lattice for Band #2 at Γ and M. As shown in Figure 30a, Bands #1 and #2 possess similar, almost parallel dispersion. Overlap between the molybdenum and sulfur atoms in Band #2 is positive +0.16 and +0.25 at Γ and M respectively, indicating bonding interaction between the Mo and S atoms in the trigonal prism. Overlap between the S_2 and S_3 atoms is however now negative −0.047 at Γ and −0.053 at M indicating weak inter–sulfur antibonding between sulfur atoms separated by 3.155 Å. Inter–sulfur interactions, S_2–S_3, in Band #1 are weakly bonding at both Γ and M. Thus, the less stable, less negative energies of Band #2 compared to Band #1 are due primarily to the change in inter–sulfur interactions from bonding for Band #1 to antibonding for Band #2. On proceeding from Γ to M, the energy of Band #2 is destabilized from a minimum at Γ of −22.91 eV to a maximum of −19.47 eV at M. The cause of this destabilization can be traced primarily to the change in intra–sulfur interactions S_2–S_2 and S_3–S_3 from bonding +0.18 at Γ to antibonding −0.064 at M. The change in intra–sulfur interactions from bonding at Γ to antibonding at M is similar for Bands #1 and #2 resulting in parallel dispersion characteristics for the two bands. Overlap between the molybdenum and sulfur atoms increases from +0.16 to +0.25 at M due to the inclusion of $Mo4d_{zx}$ and $Mo4d_{yz}$ character at M. Atomic orbital charges indicate that when two electrons occupy Band #2 at Γ, 1.80 electrons or 90% of the electrons are located on the sulfur atoms primarily in S3s orbitals while 0.21 electrons or 10% are located on the molybdenum atom. At M, 1.52 electrons or 76% of the electrons are located on the sulfur atoms mainly in the S3s orbitals while 0.49 electrons or

24% of the electrons are located on the molybdenum atom mainly on the $Mo4d_{zx}$ and $Mo4d_{yz}$ atomic orbitals. Thus, energy dispersion of this band is mainly due to interactions between the S3s orbitals of neighboring unit cells.

Band #3 (energy dispersion shown in Figure 30a) consists of primarily $Mo4d_{z2}$, S3s and $S3p_z$ character at Γ and $Mo4d_{z2}$, Mo5s, $S3p_x$ and $S3p_y$ character at M. Stabilization of this level from an energy of -15.49 eV at Γ to -16.26 eV at M is mainly due to an increase in bonding between molybdenum and sulfur atoms from +0.16 at Γ to +0.23 at M and between sulfur atoms residing in the same atomic layer (intra-sulfur) from +0.058 at Γ to +0.15 at M. The increase in Mo-S bonding at M results from the better overlap between $S3p_y$ and $S3p_x$ orbitals with $Mo4d_{z2}$ and $Mo4d_{xy}$ orbitals respectively as compared to the overlap of $S3p_z$ orbitals with $Mo4d_{z2}$ orbitals at Γ. Atomic orbital charges indicate that when two electrons occupy Band #3 at Γ, 1.58 electrons or 79% of the electrons are located on the sulfur atoms primarily in $S3p_z$ orbitals while 0.43 electrons or 21% are located on the molybdenum atom in $Mo4d_{z2}$ orbitals. At M, 1.62 electrons or 81% of the electrons are located on the sulfur atoms mainly in $S3p_x$ and $S3p_y$ orbitals while 0.37 electrons or 19% of the electrons are located on the molybdenum atom mainly on the $Mo4d_{z2}$ and Mo5s atomic orbitals. The geometry of the local atomic orbitals of one MoS_2 unit for Bands #3 and #4 at Γ and M are shown in Figure 46.

Band #4 consists of primarily $S3p_z$ and $Mo5p_z$ character at Γ and $S3p_x$, $S3p_y$, $Mo5p_z$, and $Mo4d_{zx}$ character at M. Bonding overlap between molybdenum and sulfur atoms is increased from +0.062 at Γ to +0.21 at M due to the better overlap of $S3p_y$ and $S3p_x$ orbitals with $Mo5p_z$ and $Mo4d_{zx}$ orbitals at M as compared to the overlap of $S3p_z$ orbitals with $Mo5p_z$ at Γ. Atomic orbital charges indicate that when two electrons occupy Band #4 at Γ, 1.9 electrons or 95% of the electrons are located on the sulfur atoms primarily in $S3p_z$ orbitals while 0.11 electrons or 5% are located on the molybdenum atom in $Mo5p_z$ orbitals. At M, 1.70 electrons or 85% of the electrons are located on the sulfur atoms mainly in $S3p_x$ and $S3p_y$ orbitals while 0.30 electrons or 15% of the electrons are located on the molybdenum atom mainly on the $Mo4d_{zx}$ and $Mo5p_z$ atomic orbitals.

Bands #5 and #6 are degenerate at Γ with an energy of -12.80 eV. However on proceeding from Γ to M, the degeneracy of these bands is removed. At M, Band #5 has an energy of -14.18 eV while Band #6 has an energy of -12.61 eV. Band #5 consists of -0.68 $Mo4d_{xy}$ and +0.47 $S3p_x$ character at Γ while Band #6 consists of -0.68 $Mo4d_{x2-y2}$ and +0.47 $S3p_y$. Due to the trigonal prismatic arrangement of six sulfur atoms about a central molybdenum atom, the $Mo4d_{x2-y2}$ and $Mo4d_{xy}$ orbitals have the same symmetry at Γ. At M, Band #5 consists primarily of $Mo4d_{xy}$, $Mo4d_{x2-y2}$, $Mo4d_{z2}$, S3s and $S3p_z$ orbitals. Band #6

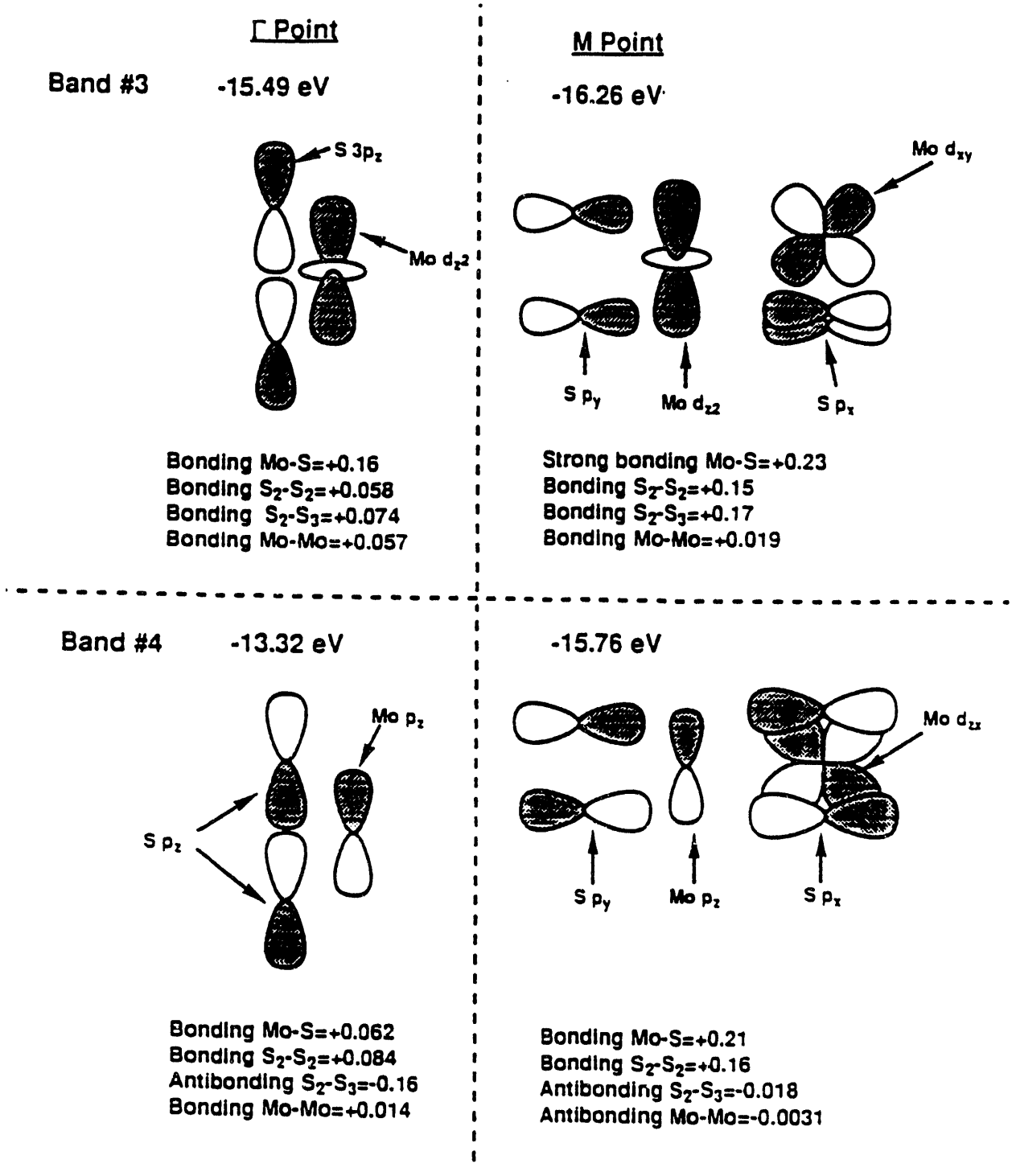

Figure 46. Geometry of the local atomic orbitals of one MoS_2 unit on 2-D MoS_2 for Bands #3 and #4 at Γ and M.

consists primarily of $Mo4d_{x2-y2}$, $Mo5p_x$, $Mo5p_y$, $S3p_y$, and $S3p_x$ orbitals at M. Atomic orbital charges indicate that when two electrons occupy Band #5 at Γ, 0.86 electrons or 43% of the electrons are located on the sulfur atoms, primarily in $S3p_x$ orbitals while 1.14 electrons or 57% are located on the molybdenum atom in $Mo4d_{xy}$ orbitals. At M, 1.58 electrons or 79% of the electrons are located on the sulfur atoms mainly in $S3p_z$ and S3s orbitals while 0.41 electrons or 20.5% of the electrons are located on the molybdenum atom mainly on $Mo4d_{xy}$, $Mo4d_{z2}$ and $Mo4d_{x2-y2}$ atomic orbitals. Atomic orbital charges indicate that when two electrons occupy Band #6 at Γ, again 0.86 electrons or 43% of the electrons are located on the sulfur atoms primarily in $S3p_y$ orbitals while 1.14 electrons or 57% are located on the molybdenum atom in $Mo4d_{x2-y2}$ orbitals. At M, 1.70 electrons or 85% of the electrons are located on the sulfur atoms mainly in $S3p_y$ and $S3p_x$ orbitals while 0.30 electrons or 15% of the electrons are located on the molybdenum atom mainly on the $Mo4d_{x2-y2}$, $Mo5p_x$, and $Mo5p_y$ atomic orbitals. The local geometry of the atomic orbitals resident on one unit of MoS_2 for Bands #5 and #6 at Γ and M is shown in Figure 47.

Bands #7 and #8 are degenerate at Γ with an energy of −11.85 eV. However on proceeding from Γ to M, the degeneracy of these bands is removed. At M, Band #7 has an energy of −13.52 eV while Band #8 has an energy of −12.98 eV. Band #7 consists of −0.68 $Mo4d_{zx}$ and ± 0.54 $S3p_x$ character at Γ while Band #8 consists of −0.68 $Mo4d_{yz}$ and ± 0.54 $S3p_y$. Due to the trigonal prismatic arrangement of six sulfur atoms about a central molybdenum atom, the $Mo4d_{zx}$ and $Mo4d_{yz}$ orbitals have the same symmetry at Γ. At M, Band #7 consists of primarily $Mo4d_{zx}$, $Mo4d_{yz}$, $S3p_x$ and $S3p_y$ orbitals. Band #8 consists of primarily $Mo4d_{zx}$, $Mo4d_{yz}$, $S3p_z$, and S3s orbitals at M. Atomic orbital charges indicate that when two electrons occupy Band #7 at Γ, 1.04 electrons or 52% of the electrons are located on the sulfur atoms primarily in $S3p_x$ orbitals while 0.97 electrons or 48.5% are located on the molybdenum atom in $Mo4d_{zx}$ orbitals. At M, 1.18 electrons or 59% of the electrons are located on the sulfur atoms mainly in $S3p_x$ and $S3p_y$ orbitals while 0.83 electrons or 41.5% of the electrons are located on the molybdenum atom mainly on $Mo4d_{zx}$ and $Mo4d_{yz}$ atomic orbitals. Atomic orbital charges indicate that when two electrons occupy Band #8 at Γ, again 1.04 electrons or 52% of the electrons are located on the sulfur atoms primarily in $S3p_y$ orbitals while 0.97 electrons or 48.5% are located on the molybdenum atom in $Mo4d_{yz}$ orbitals. At M, 1.74 electrons or 87% of the electrons are located on the sulfur atoms mainly in $S3p_z$ and S3s orbitals while 0.26 electrons or 13% of the electrons are located on the molybdenum atom mainly on the $Mo4d_{zx}$ and $Mo4d_{yz}$ atomic orbitals. The local geometry of the atomic orbitals resident on one unit of MoS_2 for Bands #7 and #8 at Γ and M is shown in Figure 48.

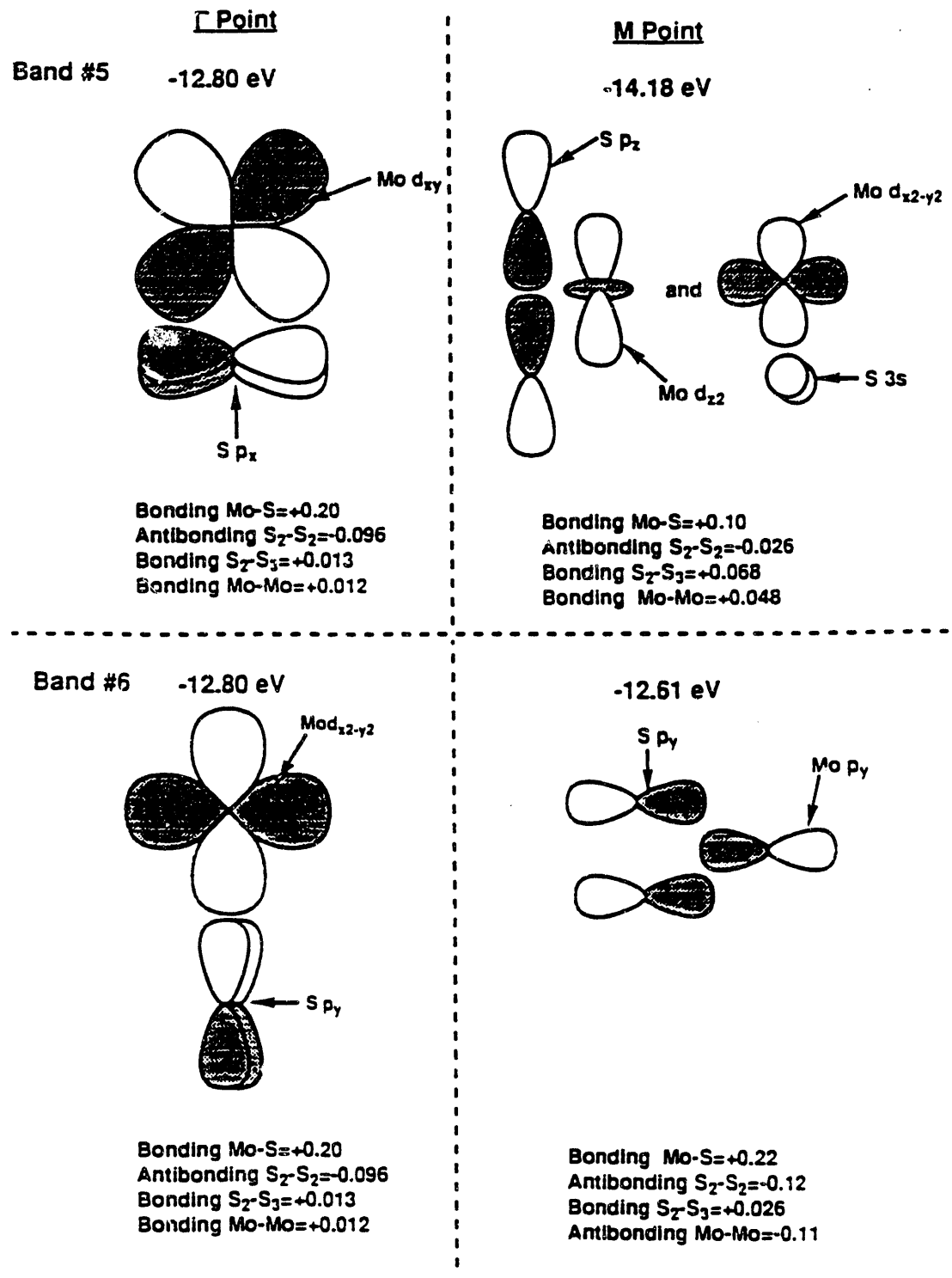

Figure 47. Geometry of the local atomic orbitals of one MoS_2 unit on 2-D MoS_2 for Bands #5 and #6 at Γ and M.

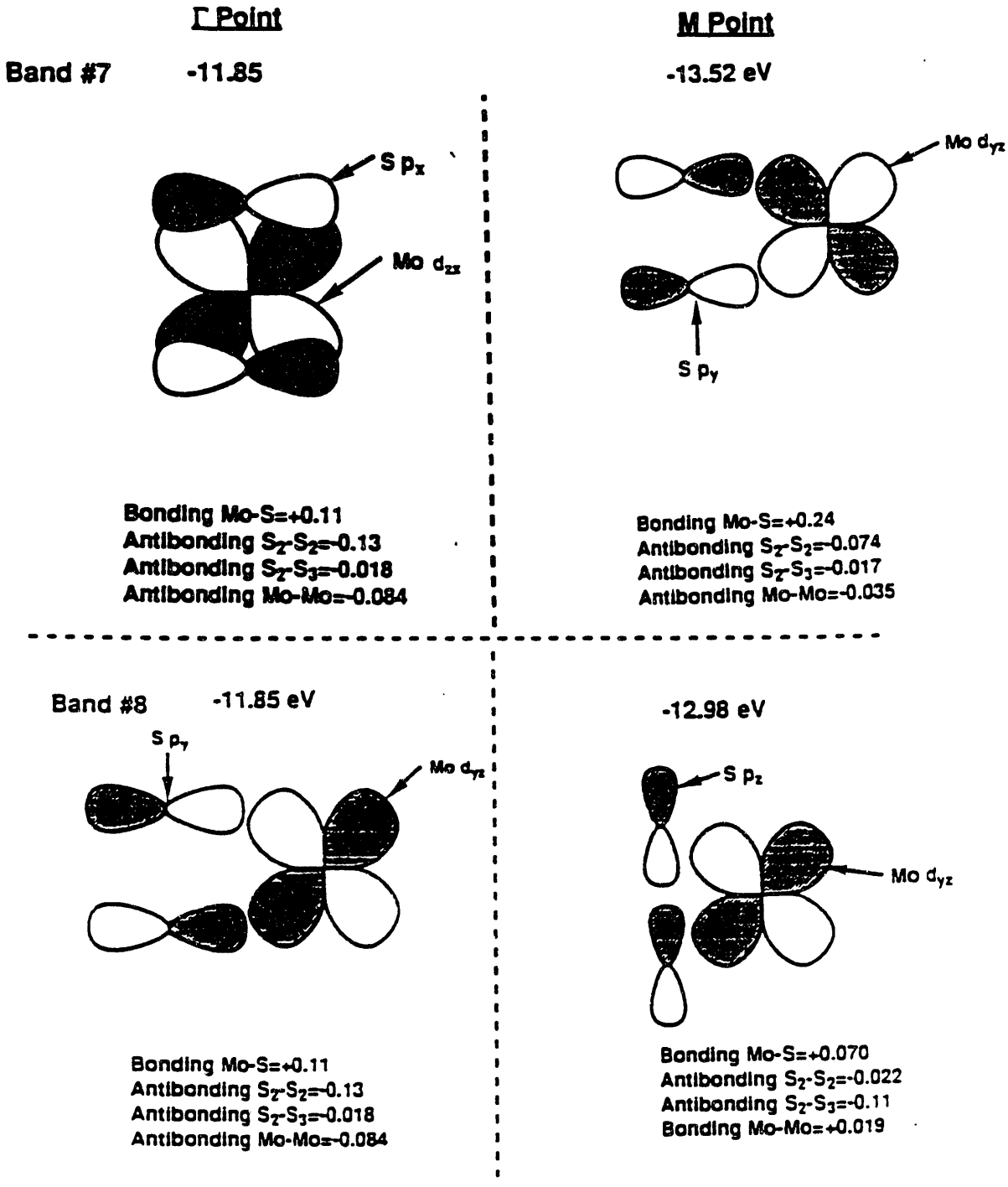

Figure 48. Geometry of the local atomic orbitals of one MoS_2 unit on 2-D MoS_2 for Bands #7 and #8 at Γ and M.

Band #9 is the highest occupied crystal orbital at all points from Γ to M. This band consists of mainly $Mo4d_{z2}$ and $S3p_z$ character at Γ resulting in an energy of -10.68 eV and $Mo4d_{z2}$, $Mo4d_{xy}$, $Mo4d_{x2-y2}$, and $S3p_z$ character at M resulting in a more stable energy of -11.26 eV. In general, the energy stabilization on proceeding from Γ to M is caused by the decrease in molybdenum-sulfur antibonding overlap from -0.20 at Γ to -0.084 at M and from the increase in molybdenum-molybdenum bonding overlap from +0.20 at Γ to +0.27 at M. The geometries of the local molybdenum and sulfur atomic orbitals resident on one MoS_2 unit for Band #9 at Γ and M are shown in Figure 49a. The geometries of the M4d orbitals at 7 lattice points of 2-D MoS_2 at Γ and M are shown in Figure 49b. At Γ the $Mo4d_{z2}$ orbitals are in phase throughout the crystal lattice forming a continuous d_{z2} band resulting in Mo-Mo bonding of +0.20. At M the $Mo4d_{z2}$ orbitals still contribute to Mo-Mo bonding but only in directions bisecting the xy-plane. Incorporation of a large amount of $Mo4d_{xy}$ orbitals that possess bonding overlap in the x-direction leads to a slightly larger amount of Mo-Mo bonding of +0.27. Atomic orbital charges indicate that when two electrons occupy Band #9 at Γ, 0.34 electrons or 17% of the electrons are located on the sulfur atoms primarily in $S3p_z$ orbitals while 1.65 electrons or 83% are located on the molybdenum atom in $Mo4d_{z2}$ orbitals. At M, 0.36 electrons or 18% of the electrons are located on the sulfur atoms mainly in $S3p_z$ orbitals while 1.63 electrons or 82% of the electrons are located on the molybdenum atom mainly on $Mo4d_{z2}$, $Mo4d_{xy}$ and $Mo4d_{x2-y2}$ atomic orbitals. Thus, Band #9 consists of primarily Mo4d character with mixing of the d_{x2-y2}, d_{xy}, and d_{z2} orbitals at M. Previous calculations on MoS_6^{8-} clusters (Appendix B) resulted in splitting of the lowest energy $Mo4d_{z2}$ orbital from the degenerate $Mo4d_{x2-y2}$ and $Mo4d_{xy}$ orbitals by only 0.46 eV (11 kcal/mole). Thus, in the theoretical 2-D MoS_2 system, mixing of these three orbitals does occur at lower symmetry points such as M but not at the high symmetry point Γ. Theoretical modified atomic orbital populations, MAOPOP's, for the Mo4d orbitals in 2-D MoS_2 (using the atomic parameters of H&H) are shown in Figure 29d. The band located at the top of the valence band just below the Fermi level consists of mainly $Mo4d_{z2}$, $Mo4d_{xy}$, and $Mo4d_{x2-y2}$ character such that the contribution of $d_{z2} > d_{xy} > d_{x2-y2}$.

Bands #10 and #11 are degenerate at Γ with an energy of -8.43 eV. Splitting of Bands #10 and #11 occurs as one proceeds from Γ to M until at M, Band #10 has an energy of -9.22 eV while Band #11 has an energy of -8.68 eV. Bands #10 and #11 make up the lowest occupied crystal orbitals at all points from Γ to M. At Γ, Band #10 consists of primarily $Mo4d_{xy}$, $Mo5p_x$ and $S3p_x$ character while Band #11 consists of primarily $Mo4d_{x2-y2}$, $Mo5p_y$ and $S3p_y$ character resulting in degenerate energies at this point in the Brillouin zone.

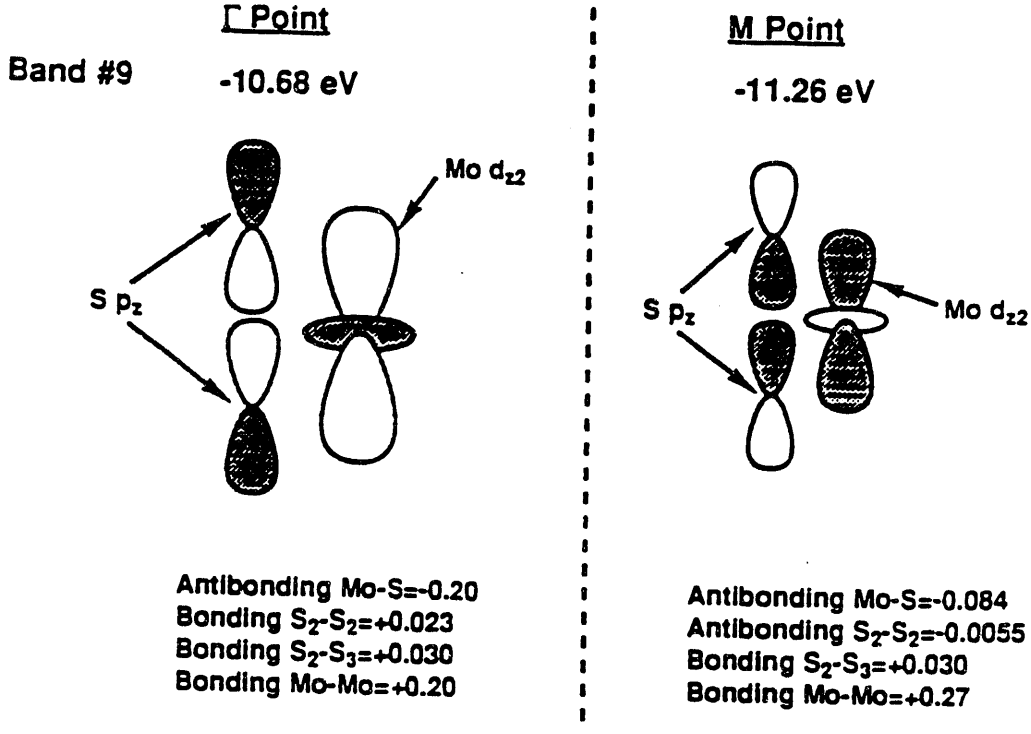

Figure 49a. Geometry of the local atomic orbitals of one MoS_2 unit on 2-D MoS_2 for Band #9 at Γ and M.

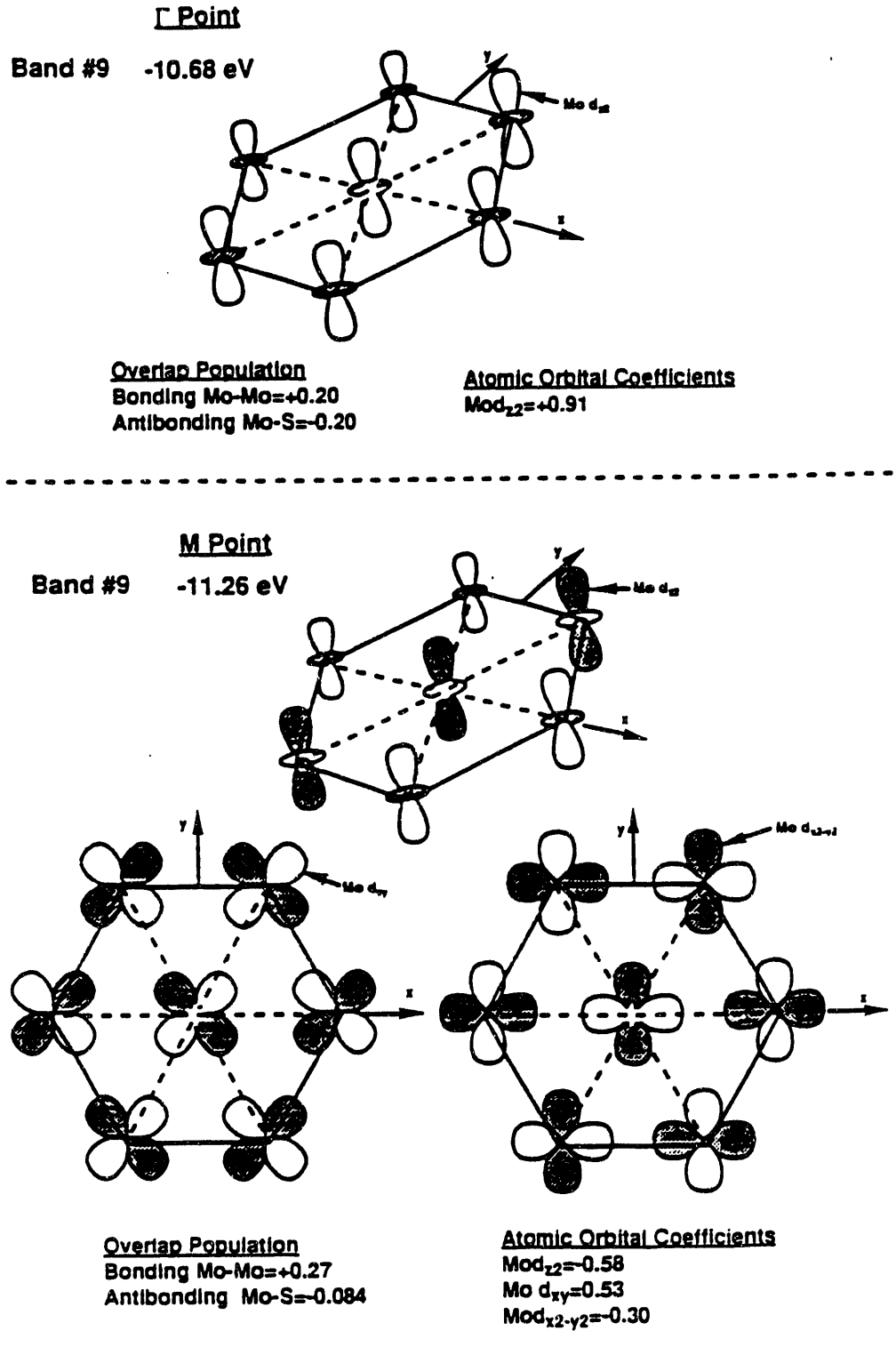

Figure 49b. Arrangement of the Mo4d local atomic orbitals on 7 lattice points of the 2-D MoS_2 lattice for Band #9 at Γ and M.

In general, the energy stabilization on proceeding from Γ to M for Band #10 is caused by the change in molybdenum–sulfur overlap from −0.28 and antibonding at Γ to bonding +0.008 at M. However at the same time, antibonding overlap between neighboring molybdenum atoms increases from −0.077 at Γ to −0.42 at M due to overlap and incorporation of $Mo4d_{x2-y2}$ orbitals. Stabilization on proceeding from Γ to M for Band #11 is caused by the change in molybdenum–sulfur overlap from −0.28 antibonding at Γ −0.13 antibonding at M. At the same time, the antibonding overlap between neighboring molybdenum atoms increases from −0.077 at Γ to −0.30 at M due to overlap and incorporation of $Mo4d_{xy}$ and $Mo4d_{z2}$ orbitals. The geometry of the local molybdenum and sulfur atomic orbitals resident on one MoS_2 unit for Bands #10 and #11 at Γ and M are shown in Figure 50a. The geometries of the M4d orbitals at 7 lattice points of 2-D MoS_2 at Γ and M for Bands #10 and #11 are shown in Figures 50b and 50c respectively. Atomic orbital charges indicate that when two electrons occupy Band #10 at Γ, 1.04 electrons or 52% of the electrons are located on the sulfur atoms primarily in $S3p_x$ orbitals while 0.96 electrons or 48% are located on the molybdenum atom primarily in $Mo4d_{xy}$ orbitals. At M the character of Band #10 has changed dramatically so that only 0.03 electrons or 1.5% of the electrons are located on the sulfur atoms mainly in $S3p_y$ and $S3p_x$ orbitals while 1.97 electrons or 98.5% of the electrons are located on the molybdenum atom mainly on $Mo4d_{xy}$ and $Mo4d_{x2-y2}$ atomic orbitals. Atomic orbital charges indicate that when two electrons occupy Band #11 at Γ, 1.04 electrons or 52% of the electrons are located on the sulfur atoms primarily in $S3p_y$ orbitals while 0.96 electrons or 48% are located on the molybdenum atom primarily in $Mo4d_{x2-y2}$ orbitals. At M the character of Band #11 changes dramatically so that only 0.15 electrons or 7.5% of the electrons are located on the sulfur atoms mainly in $S3p_y$ and $S3p_x$ orbitals while 1.85 electrons or 92.5% of the electrons are located on the molybdenum atom mainly on $Mo4d_{z2}$, $Mo4d_{xy}$ and $Mo4d_{x2-y2}$ atomic orbitals. Thus, Bands #10 and #11 consist of primarily Mo4d character with mixing of the d_{x2-y2}, d_{xy}, and d_{z2} orbitals at M in Band #11. As mentioned above mixing of the $Mo4d_{z2}$ orbital with the $Mo4d_{xy}$ and $Mo4d_{x2-y2}$ orbitals was anticipated from the calculations carried out on MoS_6^{8-} clusters (Appendix B). In the theoretical 2-D MoS_2 system, mixing of these three orbitals does occur at lower symmetry points such as M but not at the high symmetry point Γ. Theoretical modified atomic orbital populations, MAOPOP's, for the Mo4d orbitals in 2-D MoS_2 (using the atomic parameters of H&H) are shown in Figure 29d. The band located at the bottom of the conduction band just above the Fermi level consists of mainly $Mo4d_{z2}$, $Mo4d_{xy}$, and $Mo4d_{x2-y2}$ character such that the contribution of $d_{x2-y2} > d_{xy} \simeq d_{z2}$. This lowest unoccupied band of the valence band represents the derivative of energy dispersion curves Bands #10 and #11 ($\frac{dN}{dE}$).

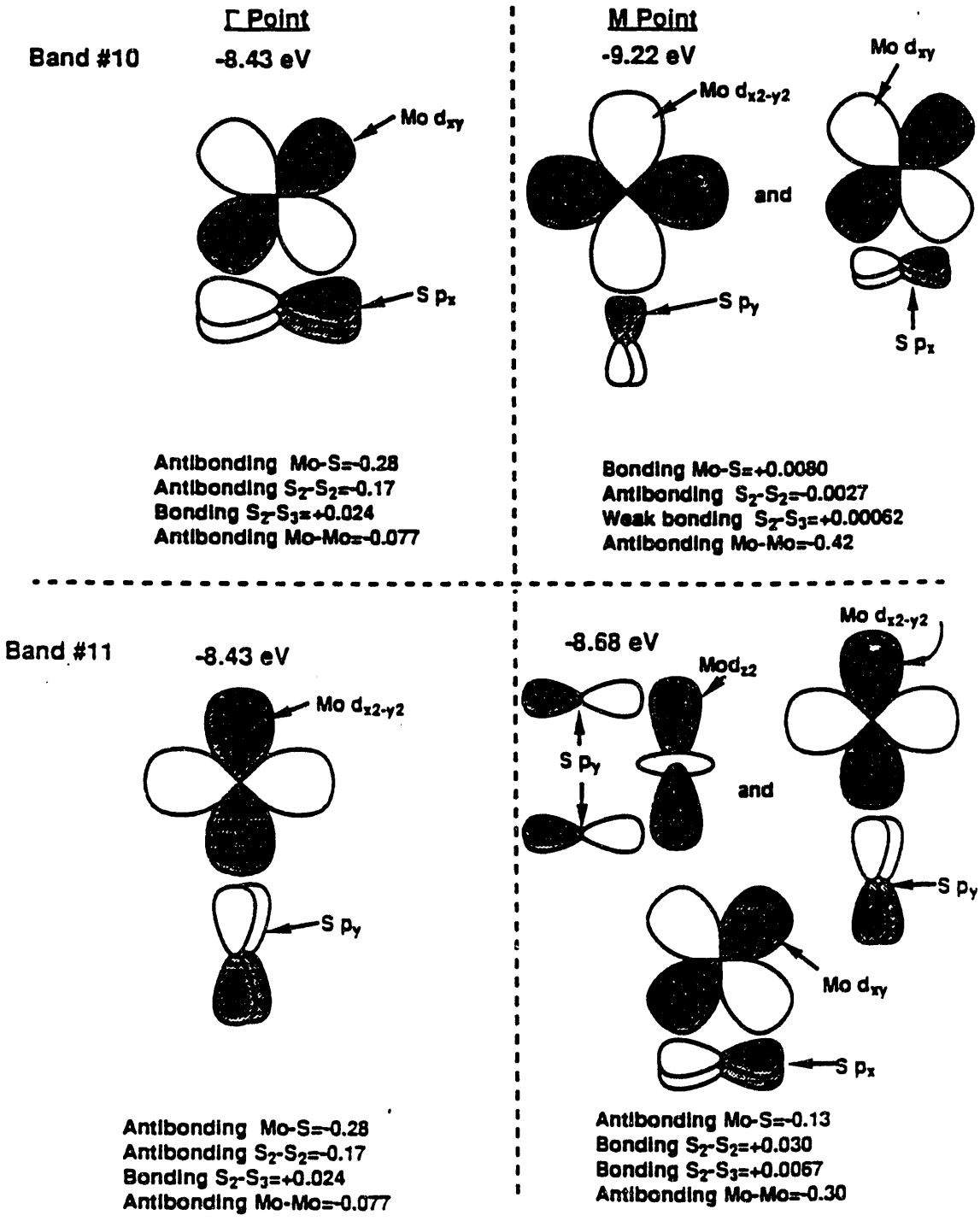

Figure 50a. Geometry of the local atomic orbitals of one MoS_2 unit on 2-D MoS_2 for Bands #10 and #11 at Γ and M.

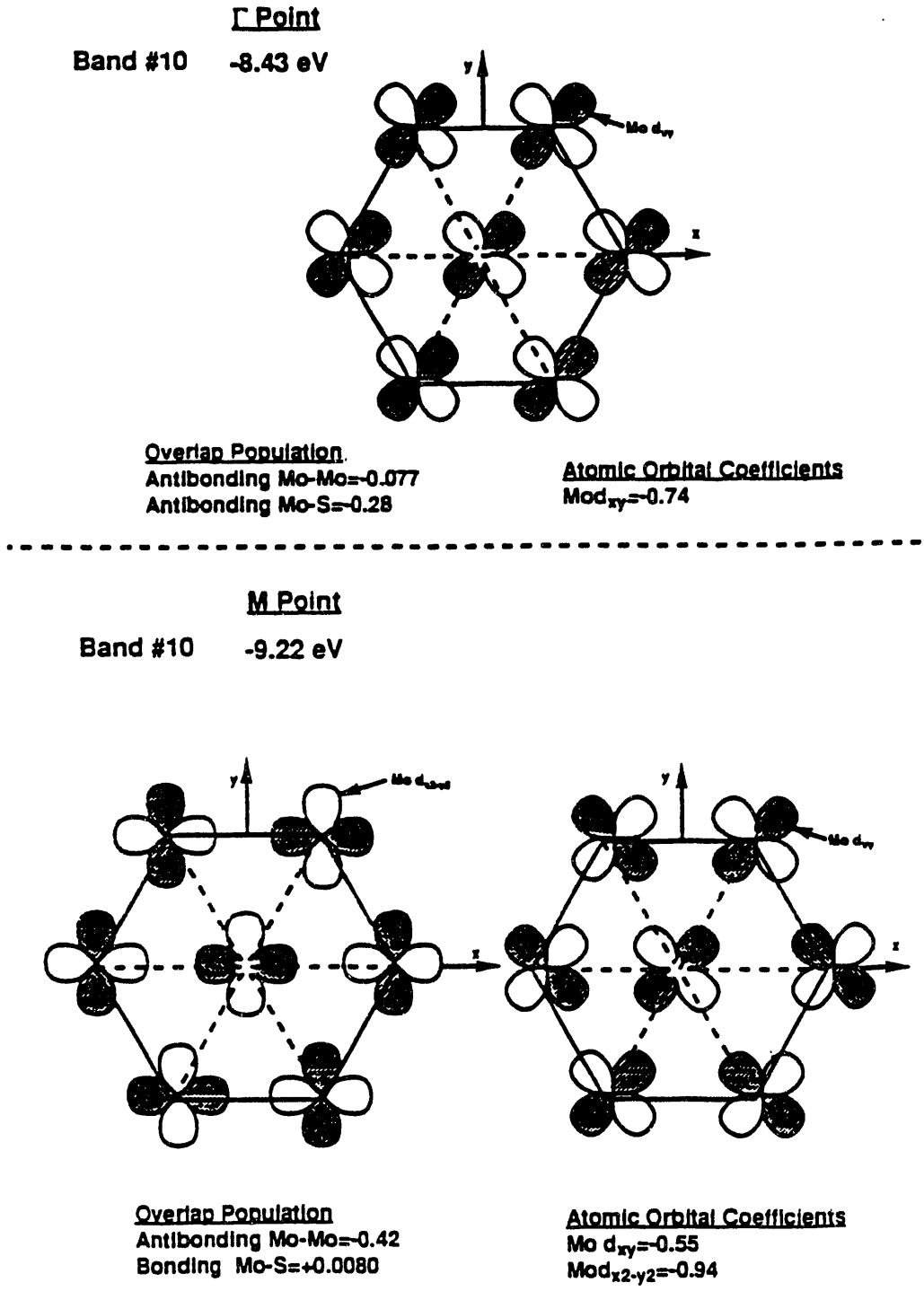

Figure 50b. Arrangement of the Mo4d local atomic orbitals on 7 lattice points of the 2-D MoS_2 lattice for Band #10 at Γ and M.

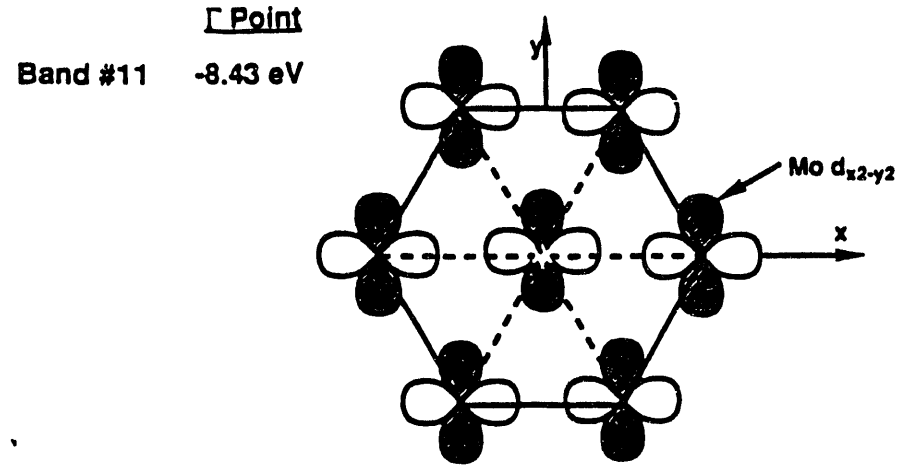

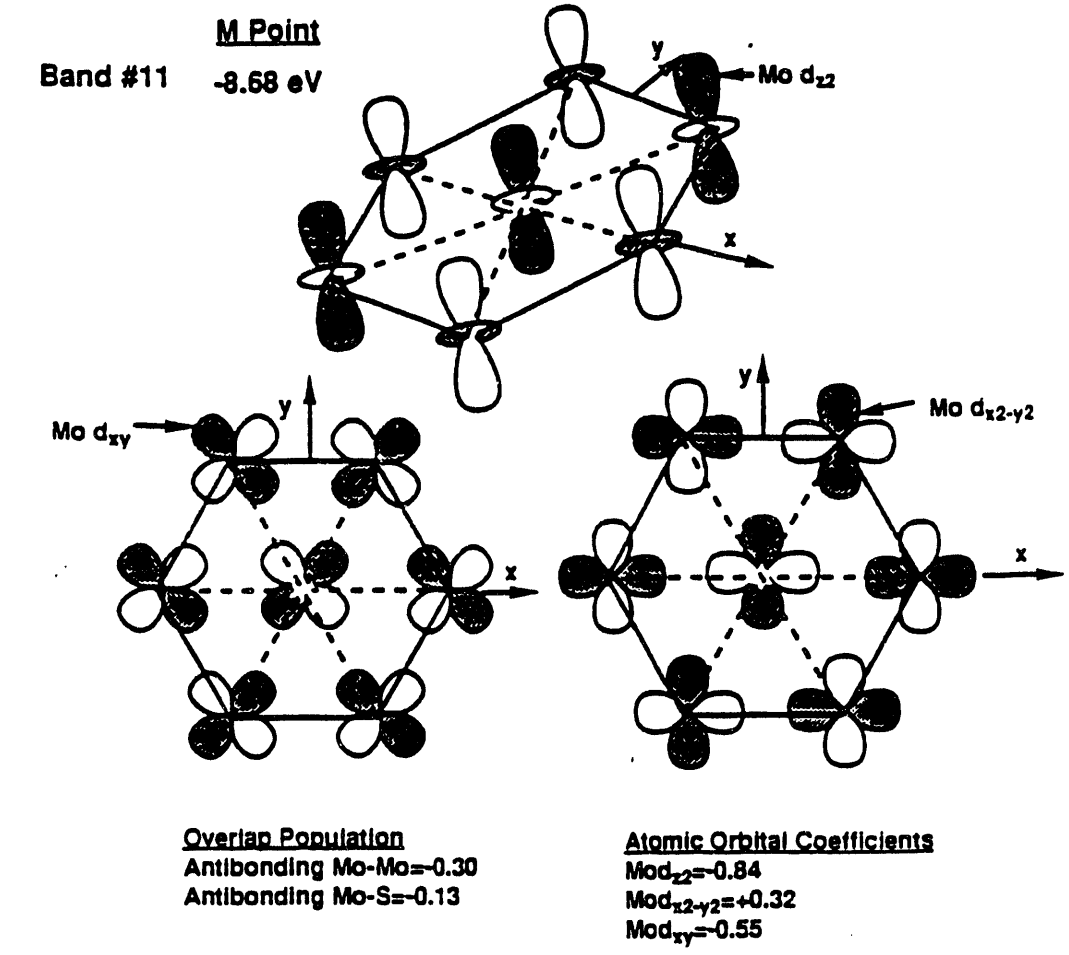

Figure 50c. Arrangement of the Mo4d local atomic orbitals on 7 lattice points of the 2-D MoS_2 lattice for Band #11 at Γ and M.

Bands #12 and #13 are also degenerate at Γ having an energy of -8.04 eV. On proceeding from Γ to M, the degeneracy is lifted such that at M Band #12 has an energy of -6.71 eV and Band #13 has an energy of -2.76 eV. At Γ, Band #12 consists of primarily $Mo4d_{yz}$ and $S3p_y$ character while Band #13 consists of primarily $Mo4d_{zx}$ and $S3p_x$ character resulting in degenerate energies at this point in the Brillouin zone. In general, the energy destabilization on proceeding from Γ to M for Band #12 is caused by the change in molybdenum-sulfur overlap from antibonding -0.16 at Γ to strongly antibonding -0.45 at M. Destabilization on proceeding from Γ to M for Band #13 is caused by the change in molybdenum-sulfur overlap from antibonding -0.16 at Γ to very strongly antibonding -0.89 at M. The geometries of the local molybdenum and sulfur atomic orbitals resident on one MoS_2 unit for Bands #12 and #13 at Γ and M are shown in Figure 51. Atomic orbital charges indicate that when two electrons occupy Band #12 at Γ, 0.96 electrons or 48% of the electrons are located on the sulfur atoms primarily in $S3p_y$ orbitals while 1.03 electrons or 52% are located on the molybdenum atom primarily in $Mo4d_{yz}$ orbitals. At M, 0.82 electrons or 41% of the electrons are located on the sulfur atoms mainly in $S3p_y$ and $S3p_x$ orbitals while 1.17 electrons or 59% of the electrons are located on the molybdenum atom mainly on $Mo4d_{yz}$ and $Mo4d_{zx}$ atomic orbitals. Atomic orbital charges indicate that when two electrons occupy Band #13 at Γ, 0.96 electrons or 48% of the electrons are located on the sulfur atoms primarily in $S3p_x$ orbitals while 1.03 electrons or 52% are located on the molybdenum atom primarily in $Mo4d_{zx}$ orbitals. At M 0.70 electrons or 35% of the electrons are located on the sulfur atoms while 1.30 electrons or 65% of the electrons are located on the molybdenum atom mainly on $Mo4d_{zx}$ and $Mo4d_{yz}$ atomic orbitals. Thus, Bands #12 and #13 consist of primarily Mo4d character with no mixing of the $Mo4d_{zx}$ and $Mo4d_{yz}$ orbitals with the $Mo4d_{x2-y2}$, $Mo4d_{xy}$, and $Mo4d_{z2}$ orbitals. Theoretical modified atomic orbital populations, MAOPOP's, for the Mo4d orbitals in 2-D MoS_2 (using the atomic parameters of H&H) are shown in Figure 29d. The second band of the conduction band consists of primarily $Mo4d_{zx}$ and $Mo4d_{yz}$ character such that the contribution of d_{yz} is greater than that of d_{zx}.

6.1.2 Orbital Picture of Energy Dispersion in 3-D MoS_2.

As indicated in Section 5.2, the energy dispersion curves of the model systems 2-D and 3-D MoS_2 are somewhat different. Addition of the third dimension into the calculation of the energy dispersion curves dramatically affects the band gap of the MoS_2 system. In 2-D MoS_2, the highest occupied crystal orbital of the valence band was located in Band #9 at K. In 3-D MoS_2, the highest occupied crystal orbital of the valence band is located instead in Band #18 at

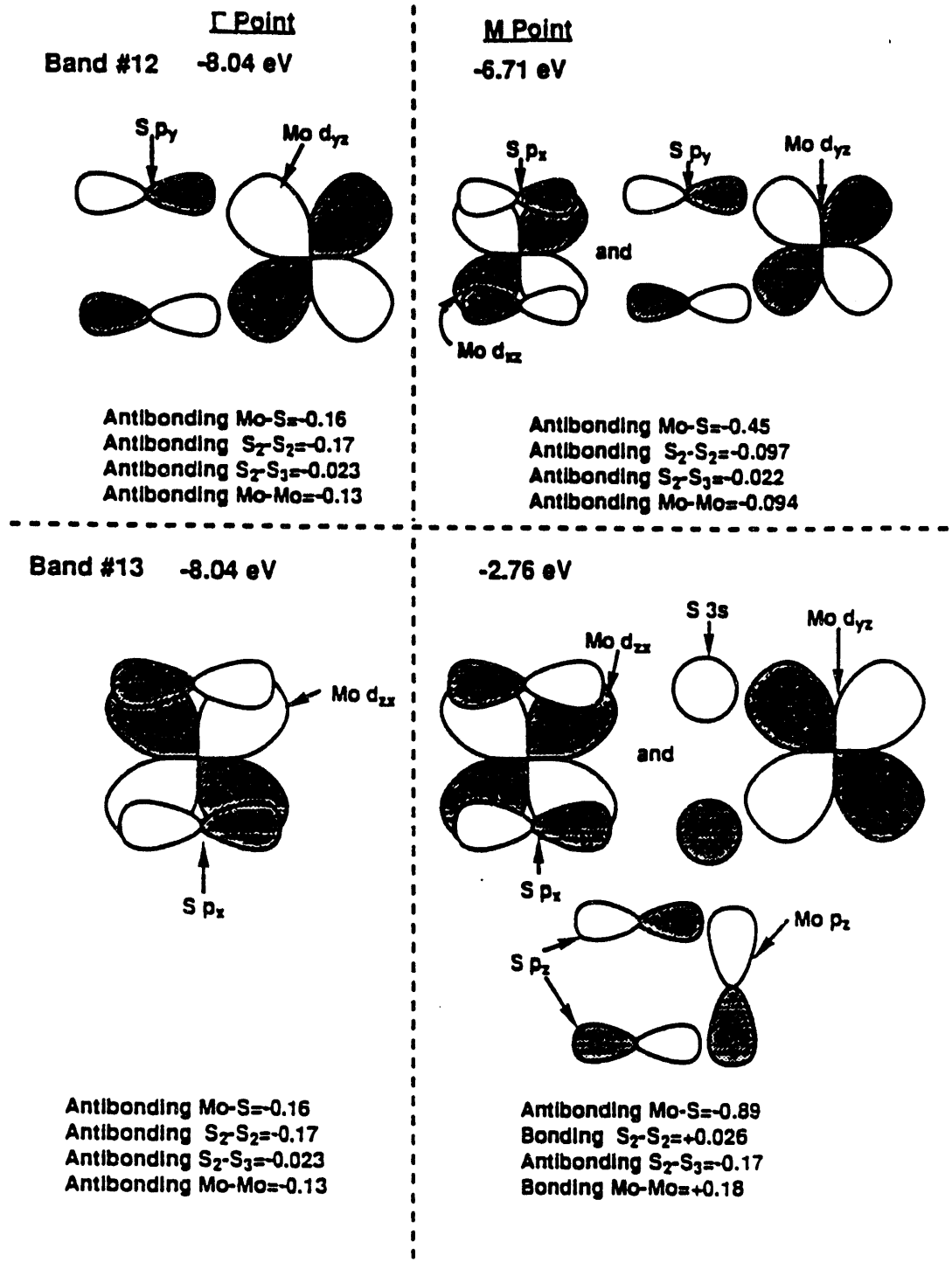

Figure 51. Geometry of the local atomic orbitals of one MoS_2 unit on 2-D MoS_2 for Bands #12 and #13 at Γ and M.

Γ. The lowest point of the conduction band in both the 2-D and 3-D systems occurs at the K point. One important difference between the two model systems is the presence of a direct gap (K→K, 1.19 eV) in the 2-D system and an indirect gap (Γ→K, 0.68 eV) in the 3-D system. Addition of the third dimension adds MoS_2 layers in the c direction. Adjacent MoS_2 layers result in Van der Waals interactions between the layers as well as interactions between the crystal orbitals of each MoS_2 layer. Because of the one-electron nature of the Extended Hückel method, correlation between electrons is not treated. Attractive Van der Waals forces are the result of electron correlations. Thus, absence of correlation also leads to absence and improper treatment of Van der Waals forces. However, interaction of the crystal orbitals on adjacent MoS_2 layers is still treated in the 3-D MoS_2 system. If the atomic orbitals involved in a particular band (or crystal orbital) do not possess a significant component in the c direction (or $\hat{z}$ direction), for instance p_x, p_y, d_{xy} or d_{x2-y2}, then these orbitals will not interact across the wide Van der Waals gap to a significant extent. If the atomic orbitals involved in a particular band do possess a component in the c direction, for instance p_z, d_{z2}, d_{zx}, and d_{yz}, then these orbitals will interact more across the Van der Waals gap. The change from direct to indirect gap on proceeding from 2-D to 3-D MoS_2 is a result of the interaction of crystal orbitals across the Van der Waals gap. In 3-D MoS_2 the highest occupied crystal band (Band #9 in 2-D MoS_2) is split into two bands Bands #17 and #18. Splitting of the highest occupied crystal band at Γ results in the formation of the indirect gap (see Figure 32). Previous theoretical calculations involving 3-D MoS_2 also locate the top of the valence band at Γ.[8,9,10,11,61] Band #17 is stabilized in energy while Band #18 is destabilized in energy. Energy destabilization of Band #18 causes the indirect gap. Band #9 at Γ in 2-D MoS_2 possessed an energy of -10.68 eV. In 3-D MoS_2, Bands #17 and #18 have energies of -10.93 eV and -10.13 eV respectively. Thus at Γ, Band #17 is stabilized by 0.25 eV while Band #18 is destabilized by 0.55 eV. As shown previously for 2-D MoS_2 the highest occupied crystal band, Band #9, at Γ consists of primarily $Mo4d_{z2}$ and $S3p_z$ character. These atomic orbitals each possess a component in the c direction ($\hat{z}$-direction) and are expected to interact across the Van der Waals gap when adjacent MoS_2 layers are added as in 3-D MoS_2. However, the $S3p_z$ orbitals are affected to a greater extent than the $Mo4d_{z2}$ orbitals by introduction of the Van der Waals gap. At K, Band #9 consists of primarily $Mo4d_{x2-y2}$ (-0.68), $Mo4d_{xy}$ (0.68 and 270° phase), $S3p_x$ (0.68 and 270° phase), and $S3p_y$ (0.17) character. These atomic orbitals do not possess a component in the c direction and are not expected to interact significantly across the Van der Waals gap when adjacent MoS_2 layers are added. In 2-D MoS_2 Band #9 at K possessed an energy of -10.65 eV. Band #17 in 3-D MoS_2 has an energy of -10.68 eV and is slightly stabilized by 0.03 eV. At K, Band #18 has an energy of -10.62 eV and is slightly destabilized by 0.03 eV. Major atomic

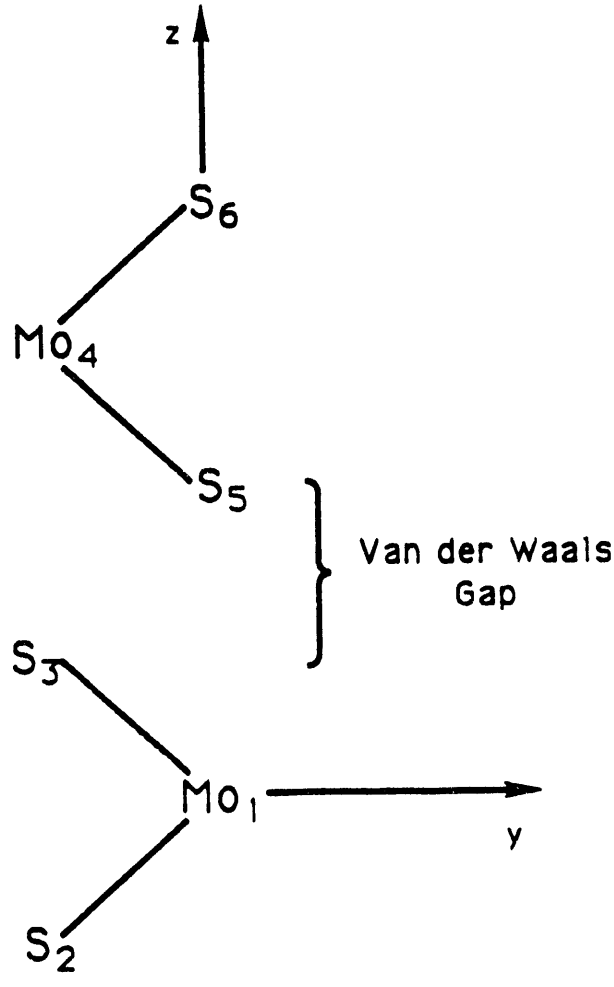

Figure 52. Geometry of the two MoS_2 units in 3-D MoS_2. The $\hat{x}$, $\hat{y}$, and $\hat{z}$ components of each atom are given in Table 4.

Table 32.

Major atomic orbital contributors and individual orbital charges for Bands #17 and #18 at Γ and K for 3-D MoS_2. (*=out of phase by 270°, **=out of phase by 90°)

	Γ *Point:* $k=0$				*M Point:* $k=(a^*+b^*)/3$			
Band #	Atomic Orbital	Orbital Coefficient	AO Charge	Atom Charge	Atomic Orbital	Orbital Coefficient	AO Charge	Atom Charge
Band #17	$Mo_1 4d_{z2}$	0.66	0.89	0.89	$Mo_1 4d_{x2-y2}$	-0.48	0.46	0.93
					$Mo_1 4d_{xy}$	0.48*	0.46	
	$Mo_4 4d_{z2}$	0.66	0.89	0.89	$Mo_4 4d_{x2-y2}$	-0.48	0.46	0.93
					$Mo_4 4d_{xy}$	0.48**	0.46	
	$S_2 3p_z$	0.20	0.055	0.056	$S_2 3p_x$	0.11*	0.018	0.036
					$S_2 3p_y$	0.11	0.018	
	$S_3 3p_z$	-0.20	0.055	0.056	$S_3 3p_x$	0.11*	0.018	0.036
					$S_3 3p_y$	0.11	0.018	
	$S_5 3p_z$	0.20	0.055	0.056	$S_5 3p_x$	0.11*	0.018	0.036
					$S_5 3p_y$	-0.11	0.018	
	$S_6 3p_z$	-0.20	0.055	0.056	$S_6 3p_x$	0.11*	0.018	0.036
					$S_6 3p_y$	-0.11	0.018	
Band #18	$Mo_1 4d_{z2}$	0.60	0.69	0.69	$Mo_1 4d_{x2-y2}$	-0.48	0.45	0.92
					$Mo_1 4d_{xy}$	0.48*	0.45	
	$Mo_4 4d_{z2}$	-0.60	0.69	0.69	$Mo_4 4d_{x2-y2}$	0.48	0.45	0.92
					$Mo_4 4d_{xy}$	0.48*	0.45	
	$S_2 3p_z$	0.32	0.15	0.16	$S_2 3p_x$	0.12*	0.021	0.042
					$S_2 3p_y$	0.12	0.021	
	$S_3 3p_z$	-0.32	0.15	0.16	$S_3 3p_x$	0.12*	0.021	0.042
					$S_3 3p_y$	0.12	0.021	
	$S_5 3p_z$	-0.32	0.15	0.16	$S_5 3p_x$	0.12**	0.021	0.042
					$S_5 3p_y$	0.12	0.021	
	$S_6 3p_z$	0.32	0.15	0.16	$S_6 3p_x$	0.12**	0.021	0.042
					$S_6 3p_y$	0.12	0.021	

orbital contributors and individual orbital charges for Bands #17 and #18 at Γ and K are given for 3-D MoS_2 in Table 32. The geometry of the two MoS_2 units is given in Table 4 and shown in Figure 52.

Bands #17 and #18 possess significant $Mo4d_{z2}$ and $S3p_z$ character at Γ. The arrangement of these orbitals is shown in Figure 53. Stabilization of Band #17 by 0.25 eV is caused by positive interaction between $S3p_z$ orbitals arranged in a trigonal environment across the Van der Waals gap resulting in a small net bonding attraction of +0.019 between the sulfur layers. Destabilization of Band #18 by 0.55 eV is caused by negative interaction between $S3p_z$ orbitals across the Van der Waals gap resulting in a small net antibonding repulsion of -0.062 between the sulfur layers. Interaction between $Mo4d_{z2}$ orbitals is almost zero, since the distance

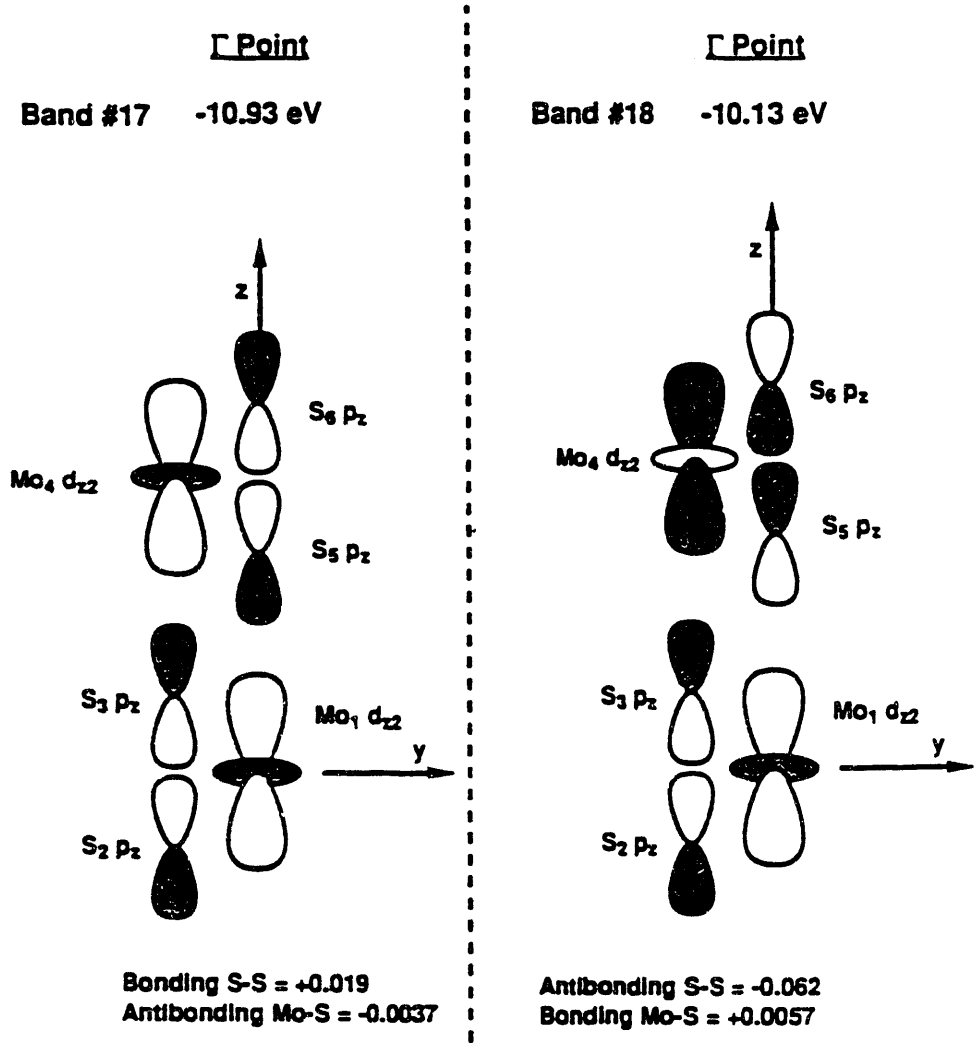

Figure 53. Geometry of the local atomic orbitals of the two MoS_2 units of 3-D MoS_2 for Bands #17 and #18 at Γ.

between molybdenum atoms in adjacent layers is 6.41 Å. At K, Bands #17 and #18 possess significant $Mo4d_{x2-y2}$, $Mo4d_{xy}$, $S3p_x$, and $S3p_y$ character. Band #17 is also stabilized at K but by only 0.03 eV. Stabilization at K is caused by a small positive interaction between the $S3p_x$ and $S3p_y$ orbitals across the Van der Waals gap resulting in weak net bonding attraction of +0.0023 between the layers. Destabilization of Band #18 at K by 0.03 eV is caused by a small negative interaction between the $S3p_x$ and $S3p_y$ orbitals across the Van der Waals gap resulting in a weak net antibonding repulsion of −0.0027 between the layers.

The results indicated above may be open to dispute since as indicated in Section 5.2.1, addition of the third dimension in the form of 3-D MoS_2 reduces the energy of formation of the system. Extended Hückel theory predicts that 2-D MoS_2 with a standard enthalpy of formation of -463.58 kcal/mole is more stable than 3-D MoS_2 with a standard enthalpy of formation of -453.74 eV. As mentioned previously, extended Hückel theory neglects to calculate electron correlation and as such does not treat Van der Waals interactions between adjacent MoS_2 layers. Van der Waals interactions between the layers are expected to be positive and fairly significant. Proper treatment of Van der Waals interactions will probably result in stabilization of the 3-D system when compared to the 2-D system. Previous calculations of Coehoorn et al. on 3-D MoS_2 took sulfur polarization into account qualitatively.[10,11] In this study, the elevation, u, of sulfur atoms above and below the plane of molybdenum atoms was decreased from the experimental value of 0.129 to 0.121. A decrease in u from 0.129 to 0.121 results in an increase of the Van der Waals gap from 2.995 Å to 3.17 Å. An increase in the Van der Waals gap will lead to smaller bonding and antibonding interactions between $S3p_z$ orbitals of adjacent MoS_2 layers. However, whether or not electron correlation is treated correctly does not affect the macroscopic overlap of crystal orbitals on adjacent MoS_2 layers. Extended Hückel theory predicts that the indirect gap results from splitting of the highest occupied crystal band at Γ such that one band is destabilized in energy due to antibonding interactions between $S3p_z$ orbitals across the Van der Waals gap. Inclusion of electron correlation is not expected to change this result. Optical experiments indicate that the band gap of 2H-MoS_2 is indirect with a gap of ~ 1.25 eV.[13] Using the parameters of H&H, solid state Extended Hückel theory predicts an indirect gap of 0.68 eV from Γ→K. Previous theoretical work on MoS_2 positions the indirect gap as occurring from the top of the valence band at Γ to the bottom of the conduction band at T (halfway between Γ and K).[8,9,10] Thus, the position of the highest occupied crystal band in MoS_2 as calculated by Extended Hückel theory is consistent with that calculated using an augmented–spherical–wave method.[10]

6.1.3 Orbital Picture of Edge States in 1-D $(MoS_2)_5$ Systems.

Electronic structures of two 1-D $(MoS_2)_5$ systems terminating at $(10\bar{1}0)$ and $(10\bar{1}1)$ edges were also studied using solid state Extended Hückel theory. The purpose of this study was to identify differences in the valence band and conduction band upon the addition of edge planes into the structure. The first structure, 1-D $(MoS_2)_5$ terminating at $(10\bar{1}0)$ edges, is terminated such that 2-coordinate molybdenum atoms are exposed on the first edge while two 1-coordinate sulfur atoms are exposed on the second edge. A representation of this structure is shown in Figures 12a and 12b. The second structure, 1-D $(MoS_2)_5$ terminating at $(10\bar{1}1)$ edges, is terminated such that 4-coordinate molybdenum and 2-coordinate sulfur atoms are exposed on the first edge while 5-coordinate molybdenum and 1-coordinate sulfur atoms are exposed on the second edge. A representation of this structure is shown in Figures 12c and 12d. As shown in Figures 34a and 35a, the theoretical valence bands of both 1-D $(MoS_2)_5$ systems show an overlap between the valence and conduction bands. In 2-D MoS_2, a system containing no edges, the conduction band was separated from the valence band by a gap leading to semiconductor behavior. Overlap between valence and conduction bands in the 1-D systems can be attributed to the presence of extra states within the band gap region as previously defined for 2-D MoS_2. These extra states will be referred to as edge states since they are mainly localized on the exposed edge atoms.

Energy dispersion curves of 1-D $(MoS_2)_5$ structures are more complicated than those of 2-D MoS_2 due to the larger number of MoS_2 molecules per unit cell. In 2-D MoS_2, energy dispersion curves resulting from extended Hückel calculations consist of 17 bands total due to the use of 17 atomic orbitals as the basis (5, Mo4d; 1, Mo5s; 3, Mo5p; 2, S3s; and 6, S3p). In 1-D $(MoS_2)_5$, energy dispersion curves consist of 85 bands due to the use of 5 MoS_2 molecules per unit cell. Five MoS_2 units possess a total of 90 electrons which will occupy a total of 45 energy levels. Thus, the amount of information obtained from extended Hückel calculations of 1-D $(MoS_2)_5$ systems is very large. In order to identify specific edge states from the multitude of states calculated, some type of criterion had to be used. The criterion chosen identified a state as an edge state if more than 70% of the electrons of its molecular orbital resided specifically on edge atoms. Edge atoms were defined as Mo-0101 (2-coordinate), S-0501 (1-coordinate) and S-0601 (1-coordinate) for the system terminating at $(10\bar{1}0)$ edges and as Mo-0101 (4-coordinate), S-0601 (2-coordinate), Mo-0301 (5-coordinate) and S-0501 (1-coordinate) for the system terminating at $(10\bar{1}1)$ edges. Edge atom positions and coordinations are shown in Figures 12a and 12b for the $(10\bar{1}0)$ terminated structure and in Figures 12c and 12d for the $(10\bar{1}1)$ terminated structure.

Energy dispersion curves of 1-D $(MoS_2)_5$ systems terminating at $(10\bar{1}0)$ and $(10\bar{1}1)$ edges are shown in Figures 54a and 54b respectively. The S3s and Mo4d-S3p valence band regions as well as the lower portion of the conduction band are shown in Figures 54a and 54b. Black circles shown on the energy dispersion curves indicate edge states identified by the criterion discussed above. The Fermi level is also shown and is defined as the energy of the highest occupied crystal orbital. The Fermi level is located at -10.77 eV and -10.65 eV for 1-D $(MoS_2)_5$ systems terminating at $(10\bar{1}0)$ and $(10\bar{1}1)$ edges respectively. Edge states in 1-D $(MoS_2)_5$ terminating at $(10\bar{1}0)$ edges are scattered about the Fermi level at the top of the valence band and at the bottom of the conduction band. Edge states located at the top of the valence band and on the Fermi level will be occupied while edge states located at the bottom of the conduction band (above the Fermi level) will be unoccupied at a temperature of absolute zero. Edge states in 1-D $(MoS_2)_5$ terminating at $(10\bar{1}1)$ edges are also scattered about the Fermi level. However in this system a majority of the edge states are located in the conduction band. Since termination by $(10\bar{1}1)$ edges was found to be more stable by 11.53 kcal/mole than termination by $(10\bar{1}0)$ edges, the $(10\bar{1}1)$ structure will be discussed in detail below.

At Γ or $\mathbf{k}$=0 in 1-D $(MoS_2)_5$ terminating at $(10\bar{1}1)$ edges, edge states are found for Bands #18, #40, #41, #46, #47, and #48. The highest occupied level is expected to be Band #45 at Γ. However due to the overlap of Bands #45 and #46 at $\mathbf{k}$-points intermediate between Γ and K this level would not be occupied at a temperature of absolute zero. The Fermi level energy is -10.65 eV while the energy of Band #45 at Γ is -10.64 eV. Thus, Bands #45, #46, #47, and #48 are located in the conduction bands, while Bands #18, #40, and #41 are located in the valence band. Local atomic orbital coefficients, individual atomic orbital charges and total charges on the atoms of the major contributors to each edge state are shown in Table 33. From the 70% criterion discussed above, at least 1.40 electrons must reside on edge atoms for this state to be termed an edge state. In general only atomic orbitals for edge atoms (Mo-0101, Mo-0301, S-0501, and S-0601) that exhibit a coefficient $>|0.1|$ are shown.

The electrons occupying Band #18 at Γ reside primarily in $Mo_1 4d_{x2-y2}$, $Mo_1 4d_{z2}$, Mo5s and $S_6 3p_z$ and $S_6 3p_y$ orbitals with 67.5% of the electrons localized on the exposed 2-coordinate edge sulfur atom, S_6. Overlap between Mo_1 and S_6 is positive +0.25 leading to bonding between the molybdenum and sulfur atoms residing on Edge 1. Overlap between Mo_1 and an Mo_1 in an adjacent unit cell is bonding +0.062. The electrons occupying Band #40 at Γ reside primarily in $Mo_1 4d_{z2}$, $Mo_1 4d_{x2-y2}$, and $S_6 3p_z$ orbitals with 59.5% of the electrons localized on the exposed 4-coordinate molybdenum atom. The dominant interaction on this edge is antibonding overlap -0.13 between Mo_1 and S_6 and bonding overlap +0.12 between Mo_1 and

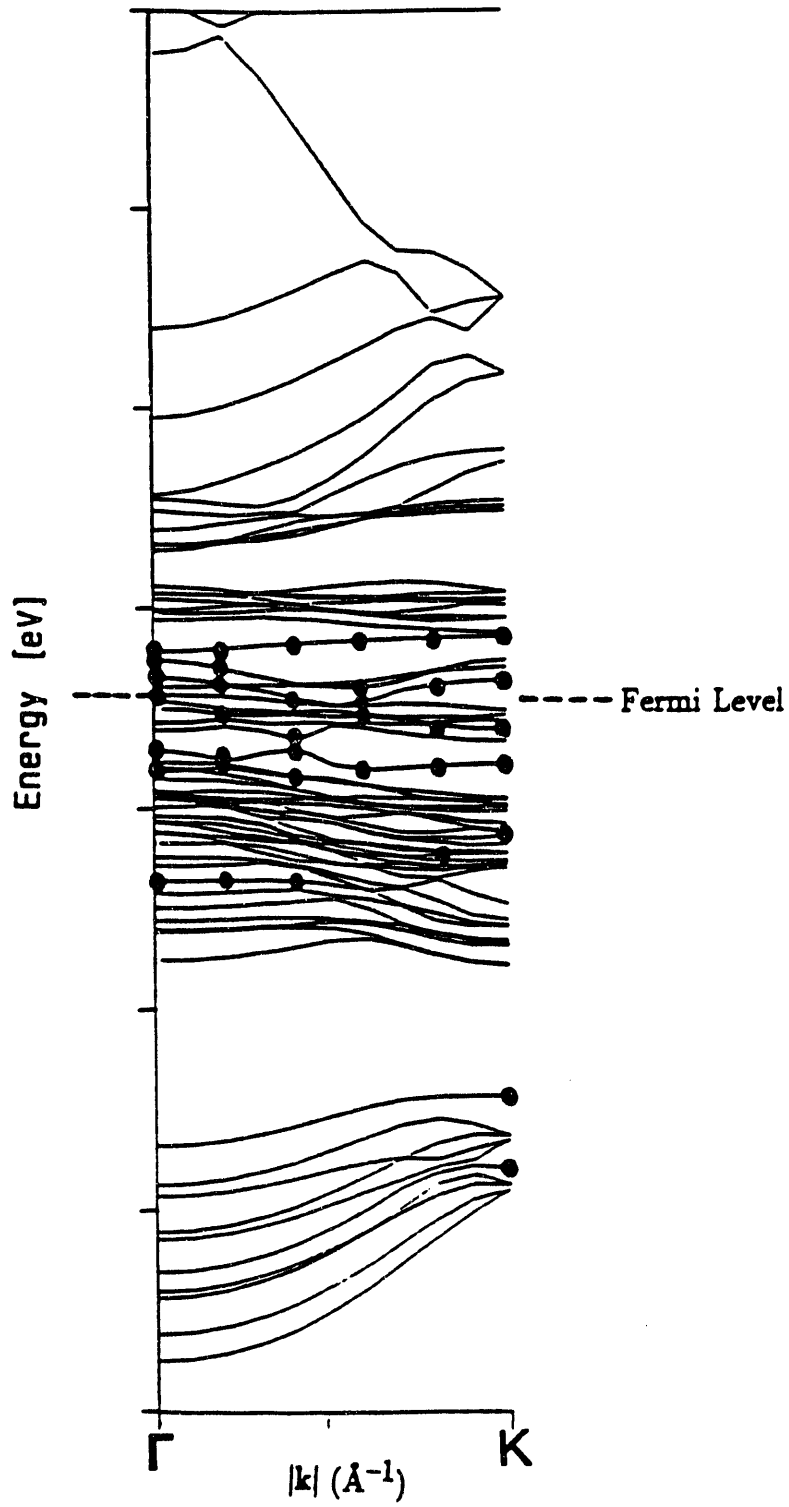

Figure 54a. Energy dispersion curves of 1-D $(MoS_2)_5$ terminating at $(10\bar{1}0)$ edges. The Fermi level is located at -10.77 eV. Black circles indicate edges states carrying more than 70% of the electrons on the following edge atoms: Mo-0101 (2-coordinate), S-0501 (1-coordinate) and S-0601 (1-coordinate).

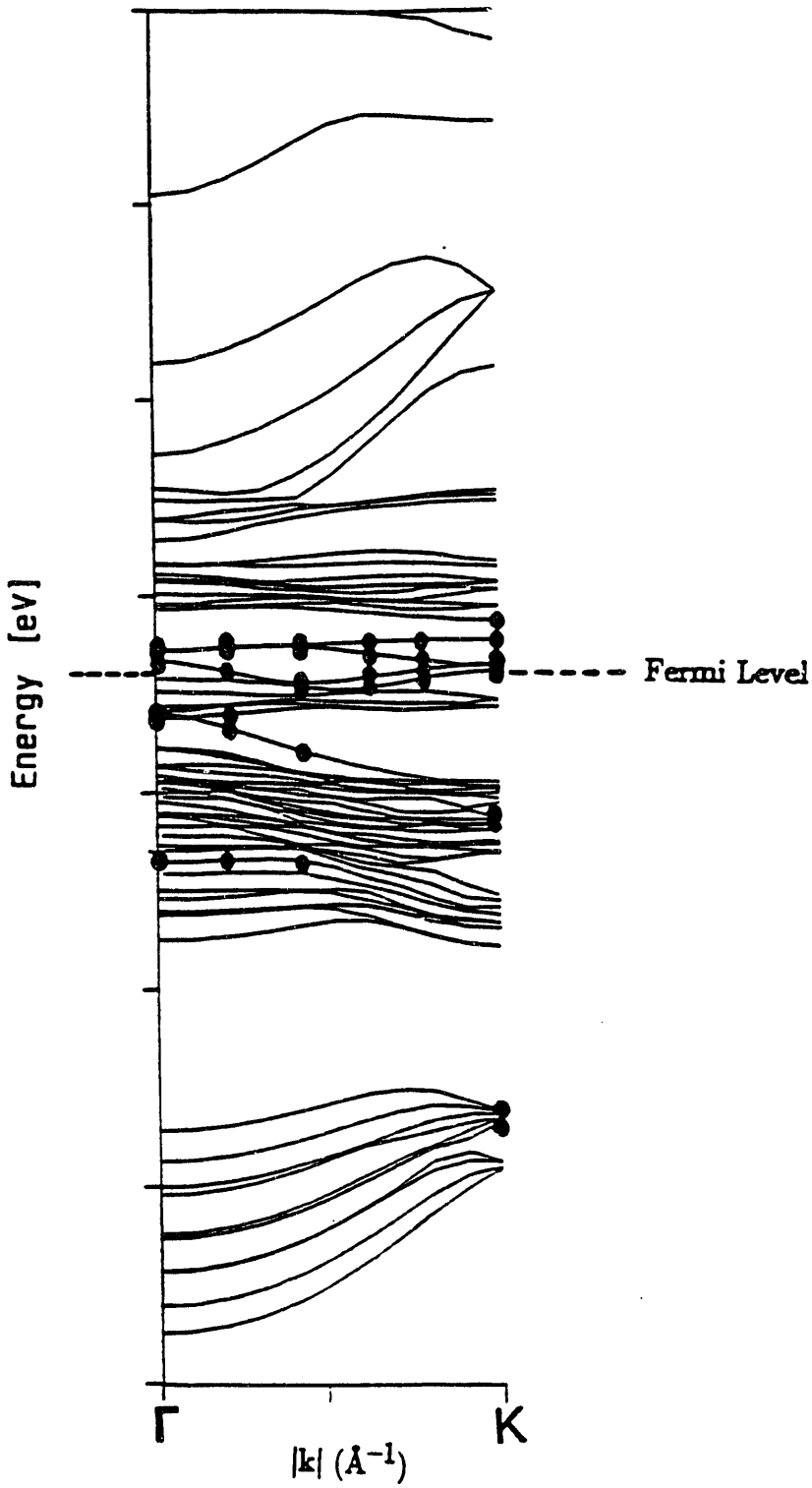

Figure 54b. Energy dispersion curves of 1-D $(MoS_2)_5$ terminating at $(10\bar{1}1)$ edges. The Fermi level is located at -10.65 eV. Black circles indicate edges states carrying more than 70% of the electrons on the following edge atoms: Mo-0101 (4-coordinate), Mo-0301 (5-coordinate), S-0501 (1-coordinate) and S-0601 (2-coordinate).

Table 33.

Local atomic orbital coefficients, individual atomic orbital charges and total charges on edge states of 1-D $(MoS_2)_5$ at Γ. In general only atomic orbitals for edge atoms (Mo-0101, Mo-0301, S-0501, and S-0601) that exhibit a coefficient >|0.1| are shown

Γ *Point: k=0*

Band #	AO	AO Coefficient	AO Charge	Atom Charge
Band #18	$Mo_1 5s$	0.15	0.13	0.40
	$Mo_1 4d_{x2-y2}$	0.24	0.18	
	$Mo_1 4d_{z2}$	-0.17	0.084	
	$S_6 3s$	-0.14	0.0194	1.36
	$S_6 3p_y$	-0.27	0.17	
	$S_6 3p_z$	0.71	1.17	
Band #40	$Mo_1 4d_{z2}$	-0.59	0.69	1.19
	$Mo_1 4d_{x2-y2}$	0.45	0.43	
	$Mo_3 4d_{x2-y2}$	-0.10	0.023	
	$S_6 3p_z$	-0.39	0.25	0.26
Band #41	$Mo_3 5p_x$	0.14	0.04	0.32
	$Mo_3 4d_{xy}$	-0.33	0.23	
	$Mo_3 4d_{zx}$	-0.16	0.049	
	$S_5 3p_x$	0.93	1.47	1.47
Band #46	$Mo_1 3p_z$	-0.16	0.098	1.42
	$Mo_1 4d_{x2-y2}$	-0.48	0.44	
	$Mo_1 4d_{z2}$	-0.51	0.48	
	$Mo_1 4d_{yz}$	-0.44	0.35	
	$S_6 3p_y$	-0.36	0.20	0.20
Band #47	$Mo_1 4d_{xy}$	0.79	1.12	1.78
	$Mo_1 4d_{zx}$	0.60	0.65	
	$S_6 3p_x$	-0.088	0.012	0.012
Band #48	$Mo_3 5s$	-0.16	0.062	1.49
	$Mo_3 5p_y$	0.17	0.099	
	$Mo_3 5p_z$	0.11	0.040	
	$Mo_3 4d_{x2-y2}$	0.29	0.14	
	$Mo_3 4d_{z2}$	0.44	0.36	
	$Mo_3 4d_{yz}$	-0.66	0.79	
	$S_5 3p_y$	-0.26	0.10	0.12
	$S_5 3p_z$	-0.13	0.020	

Mo_1 in an adjacent unit cell. The electrons occupying Band #41 at Γ reside primarily the atoms exposed on Edge 2, $Mo_3 5p_x$, $Mo_3 4d_{xy}$, $Mo_3 4d_{zx}$, and $S_5 3p_x$. In Band #41, 73.5% of the electrons are localized on the $S_5 3p_x$ orbital. Overlap between the exposed molybdenum, Mo_3, and sulfur, S_5, is positive leading to bonding character of +0.12 between the atoms. Overlap between S_5 with sulfur atoms of adjacent unit cells is negative leading to antibonding character of -0.31.

The most interesting states in terms of edge surface states are the unoccupied states that lie above the Fermi level, in this case Bands #46, #47 and #48. When the surface is exposed to adsorbates such as H_2, unoccupied edge states are expected to interact with the molecular orbitals of the adsorbate. If two electrons occupied Band #46 at Γ they would reside primarily on atoms exposed on Edge 1 in the following orbitals: $Mo_1 4d_{x2-y2}$, $Mo_1 4d_{z2}$, $Mo_1 4d_{yz}$, and $S_6 3p_y$. If electrons occupied Band #46, 71% would be localized on the 4-coordinate edge molybdenum atom, Mo_1, while 10% would be localized on the 2-coordinate edge sulfur atom, S_6. Thus, at Γ there is an unoccupied crystal orbital, Band #46, that contains dangling $S_6 3p_y$, $Mo_1 4d_{x2-y2}$, $Mo_1 4d_{z2}$, and $Mo4d_{yz}$ atomic orbitals which could interact with an adsorbate. Overlap between Mo_1 and S_6 is antibonding -0.15 while overlap between the Mo_1 and edge molybdenum atoms in adjacent unit cells is bonding +0.058. Thus, addition of electrons to Band #46 will weaken the total Mo_1-S_6 bond while strengthening the total Mo_1-Mo_1 bond. A hydrogen 1s orbital would be expected to interact favorably with the dangling $S_6 3p_y$ orbital on Edge 1. Thus, a model for adsorption of hydrogen onto S_6 was chosen to occur from the $+\hat{y}$ direction on Edge 1.

Band #47 at Γ can also be termed an edge state since if occupied by two electrons, 89% of the electrons would reside on the 4-coordinate edge molybdenum atom, Mo_1. This band primarily consists of $Mo_1 4d_{xy}$, $Mo_1 4d_{zx}$ and $S_6 3p_x$ orbitals. Overlap of these orbitals is such that weak antibonding Mo_1-S_6 of -0.0032 and stronger antibonding Mo_1-Mo_1 of -0.15 results. If two electrons occupied Band #48 at Γ 74.5% of the electrons would be localized on the 5-coordinate molybdenum, Mo_3, residing on Edge 2. Band #48 primarily consists of $Mo_3 4d_{x2-y2}$, $Mo_3 4d_{z2}$, $Mo_3 4d_{yz}$, $S_5 3p_y$, and $S_5 3p_z$ orbitals. Overlap between Mo_3 and S_5 is antibonding -0.10 while that between Mo_3 atoms on adjacent unit cells is bonding +0.046.

At K or $\mathbf{k}= \mathbf{a}^*/2$ in 1-D $(MoS_2)_5$ terminating at $(10\bar{1}1)$ edges, edge states are found for Bands #5, #10, #30, #32, #45, #46, #47, #48, and #49. Thus, Bands #45, #46, #47, #48 and #49 are located in the conduction band, while Bands #5, #10, #30, and #32 are located in the valence band. Local atomic orbital coefficients, individual atomic orbital charges and total charges on the atoms of the major contributors to each edge state are shown in Table 34. From

Table 34.

Local atomic orbital coefficients, individual atomic orbital charges and total charges on edge states of 1-D $(MoS_2)_5$ at K. In general only atomic orbitals for edge atoms (Mo-0101, Mo-0301, S-0501, and S-0601) that exhibit a coefficient $>|0.1|$ are shown

K Point: $k = a^*/2$

Band #	AO	AO Coefficient	AO Charge	Atom Charge
Band #5	$Mo_1 5p_x$	-0.12	0.14	0.35
	$Mo_1 4d_{xy}$	-0.11	0.047	
	$Mo_1 4d_{zx}$	0.19	0.15	
	$S_6 3s$	-0.85	1.53	1.53
Band #10	$Mo_1 5s$	-0.14	0.092	0.26
	$Mo_1 5p_y$	0.11	0.055	
	$Mo_1 4d_{yz}$	0.11	0.046	
	$S_5 3s$	-0.84	1.44	1.44
Band #30	$Mo_1 4d_{xy}$	-0.19	0.11	0.18
	$Mo_1 4d_{zx}$	0.13	0.055	
	$S_6 3s$	0.21	0.052	1.26
	$S_6 3p_y$	0.18	0.071	
	$S_6 3p_z$	-0.073	1.13	
Band #32	$Mo_3 4d_{x2-y2}$	0.16	0.076	0.24
	$Mo_3 4d_{z2}$	0.11	0.033	
	$Mo_3 4d_{yz}$	0.14	0.060	
	$S_5 3s$	0.18	0.038	1.51
	$S_5 3p_y$	-0.40	0.35	
	$S_5 3p_z$	0.73	1.13	
Band #45	$Mo_1 5p_x$	-0.23	0.25	1.37
	$Mo_1 4d_{xy}$	-0.24	0.11	
	$Mo_1 4d_{zx}$	-0.72	1.01	
	$S_6 3p_y$	0.33	0.17	0.18
Band #46	$Mo_1 4d_{x2-y2}$	0.60	0.67	1.80
	$Mo_1 4d_{z2}$	0.77	1.10	
Band #47	$Mo_3 5p_x$	0.15	0.11	1.60
	$Mo_3 4d_{xy}$	-0.89	1.49	
	$S_5 3p_x$	-0.22	0.064	0.064
Band #48	$Mo_3 5p_y$	-0.14	0.060	1.72
	$Mo_3 5p_z$	-0.15	0.063	
	$Mo_3 4d_{x2-y2}$	-0.66	0.76	
	$Mo_3 4d_{z2}$	0.20	0.074	
	$Mo_3 4d_{yz}$	0.64	0.74	
	$S_5 3p_y$	0.19	0.049	0.069
	$S_5 3p_z$	0.12	0.019	
Band #49	$Mo_1 5p_y$	0.20	0.096	1.41
	$Mo_1 5p_z$	0.15	0.055	
	$Mo_1 4d_{x2-y2}$	-0.65	0.72	
	$Mo_1 4d_{z2}$	0.41	0.29	
	$Mo_1 4d_{yz}$	0.37	0.24	

the 70% criterion discussed above, at least 1.40 electrons must reside on edge atoms for this state to be termed an edge state. In general only atomic orbitals for edge atoms (Mo-0101, Mo-0301, S-0501, and S-0601) that exhibit a coefficient >|0.1| are shown.

At K, the more interesting edge states are those residing at or above the Fermi level, i.e. Bands #45, #46, #47, #48. Thus, these states will be discussed in more detail in the following paragraphs. At a temperature of absolute zero, Band #45 would not be occupied at K because the energy of this level -10.48 eV is higher than the Fermi level energy of -10.65 eV. If Band #45 were occupied by two electrons, 68.5% of the electrons occupying this level would be localized on the four-coordinate edge molybdenum atom, Mo_1. The character of this level is primarily $Mo_1 4d_{zx}$ and $S_6 3p_y$. Overlap between Mo_1 and S_6 is antibonding -0.092 while that between edge Mo_1 atoms on neighboring unit cells is bonding +0.16. At absolute zero, Band #46 is also unoccupied at K but if occupied 90% of the electrons would reside on the four-coordinate edge molybdenum atom, Mo_1, in $Mo4d_{x2-y2}$ and $Mo4d_{z2}$ orbitals. Overlap between Mo_1 and S_6 is weakly antibonding -0.0014 and between Mo_1 atoms on neighboring unit cells is also antibonding -0.026.

Band #47 is also unoccupied at K, but if occupied by two electrons 80% of the electrons would be localized on 5-coordinate molybdenum atoms residing on Edge 2. This band consists of primarily $Mo_3 4d_{xy}$ and $S_5 3p_x$ character. Overlap between Mo_3 and S_5 is antibonding -0.077 while overlap between Mo_3 atoms on adjacent unit cells is bonding +0.15. If occupied 86% of the electrons of Band #48 would reside on edge molybdenum atoms, Mo_3. This band consists of primarily $Mo_3 4d_{x2-y2}$, $Mo_3 4d_{yz}$, $S_5 3p_y$, and $S_5 3p_z$ character. Overlap between Mo_3-S_5 and Mo_3 atoms on adjacent unit cells is antibonding -0.046 and -0.095 respectively. If occupied, 70.5% of the electrons of Band #49 would reside on edge molybdenum atoms, Mo_1. This band consists of primarily $Mo_1 4d_{x2-y2}$, $Mo4d_{z2}$, and $Mo4d_{yz}$ character. Overlap between Mo_1 atoms on adjacent unit cells in antibonding -0.13.

One important aspect is the mixture of $Mo4d_{yz}$ and $Mo4d_{zx}$ orbitals with $Mo4d_{x2-y2}$, $Mo4d_{xy}$ and $Mo4d_{z2}$ orbitals. As discussed for 2-D MoS_2, the $Mo4d_{x2-y2}$ and $Mo4d_{xy}$ orbitals mix with the $Mo4d_{z2}$ orbitals at the top of the valence band and at the bottom of the conduction band. This can be seen from the modified atomic orbital populations, MAOPOP's, of the Mo4d orbitals in Figure 29d. However the Mo4d MAOPOP's for 1-D $(MoS_2)_5$ terminating at $(10\bar{1}1)$ edges, Figure 35c, show that a large amount of $Mo4d_{yz}$ character is present particularly within the region previously defined as the band gap for 2-D MoS_2. The $Mo4d_{zx}$ orbitals mix to a lesser degree within the occupied portion at the top of the valence band. Addition of edges, promotes the mixing of $Mo4d_{yz}$ and $Mo4d_{zx}$ orbitals with the rest of

the Mo4d orbitals. In the case of 1-D $(MoS_2)_5$ terminating at $(10\bar{1}1)$ edges, edges promote the formation of states within the band gap region. These states exhibit primarily Mo4d character from edge molybdenum atoms with a large amount of $Mo4d_{yz}$ character.

6.1.4 Edge States Related to Experimental Results.

The theoretical results discussed above may be used in a discussion of the difference between electronic structures of single crystal and polycrystalline MoS_2. Polycrystalline MoS_2 possesses a larger number of exposed edge molybdenum and sulfur atoms than single crystal MoS_2 due to the higher surface area (~ 60 m^2/gm) and smaller particle size. A study performed by Roxlo et al.[13] looked at the effect on optical absorption of introducing an increasing number of edge sites onto a thin MoS_2 single crystal. Below the energy of the indirect band gap, the amount of absorption increased as the number of edge impurities was increased. This result indicates that with the addition of edges, surface states are appearing in the band gap region. A second study performed by Liang et al.[14] focused on UPS valence band analysis of poorly crystallized MoS_2 samples containing high area edge surfaces. UPS of the poorly crystallized sample showed a tail on the lower binding energy side of the experimental $Mo4d_{z2}$ band in the valence band region. The origin of this tail was attributed to dimerization of molybdenum atoms on reconstructed edge planes. The Mo4d-S3p valence band regions of single crystal and polycrystalline MoS_2 obtained via HR-ESCA in this work are shown in Figure 27b. The area of the S3s region portion of the valence band (this region is not shown) was used for normalization purposes. Differences between the two valence bands include the following: (1) polycrystalline MoS_2 exhibits a higher intensity or tail on the lower binding energy side of the highest occupied crystal band (located at ~ 1.8 eV as measured from the Fermi level of the instrument); (2) the highest occupied crystal band (~ 1.8 eV) decreases in intensity on proceeding from single crystal to polycrystalline MoS_2; and (3) the shape of the third band (located at ~ 4.8 eV) changes in shape. These changes can be explained by looking at the positions and character of the edge states discussed for 1-D $(MoS_2)_5$ terminating at $(10\bar{1}1)$ edges.

The HR-ESCA result that polycrystalline MoS_2 exhibits a higher intensity or tail on the lower binding energy side of the highest occupied crystal band than single crystal MoS_2 is compatible with the UPS results of Liang et al and optical absorption results of Roxlo et al.[13,14] As discussed previously, the 1-D $(MoS_2)_5$ model shows empty edge states residing within the band gap defined previously for 2-D MoS_2. These states are located so close to the Fermi level that population of these states is possible at room temperature. Thus, these states

will be seen by both XPS and UPS. In 1-D $(MoS_2)_5$ terminating at $(10\bar{1}1)$ edges, the Fermi level (or highest occupied crystal orbital) is located at -10.65 eV. The energies of Bands #45, #46 and #47 for 6 points along the direction Γ to K are listed in Table 35. At both Γ and K, Bands #45 and #46 are unoccupied and exhibits energies of -10.64 eV and -10.25 eV at Γ and -10.48 eV and -10.39 eV at K. Thus, these bands are located 0.01 eV and 0.40 eV above the Fermi level at Γ and 0.17 eV and 0.25 eV above the Fermi level at K respectively. However, as one proceeds across **k**-space from Γ to K, Bands #45 and #46 become more stable and drop below the energy of the Fermi level. At $\mathbf{k}=0.2\,\mathbf{a}^*$ both Bands #45 and #46 have energies lower than the Fermi level. However at room temperature (kT=0.026 eV), there is a small probability that bands having energies above the Fermi level energy will be occupied and contribute intensity to the lower binding energy side of the highest occupied crystal band. The probability $f(\epsilon)$ that an electron will be promoted from a position at the Fermi level μ to an energy level ϵ separated from the Fermi level by $\Delta E=\epsilon-\mu$, at a temperature T is governed by the Fermi-Dirac distribution $f(\epsilon)=[\exp(\epsilon-\mu)/kT+1]^{-1}$.[48] Using the Fermi level of -10.65 eV, the energies given in Table 35 for Bands #45, #46 and #47, and the value of kT at room temperature (0.026 eV) the probability for occupation of Bands #45, #46, and #47 was calculated from the Fermi-Dirac distribution. These values are also tabulated in Table 35. Though this is a crude approximation, there seems to be a certain probability for occupation of Bands #45 and #46. Occupation of these levels at room temperature will lead to increased intensity on the lower binding energy side of the highest occupied crystal band. The decrease in intensity of the highest occupied crystal band ($\sim$ 1.8 eV) on proceeding from single crystal to polycrystalline MoS_2 can be attributed to mixing of $Mo4d_{x2-y2}$, $Mo4d_{xy}$, and $Mo4d_{z2}$ orbitals into the edge atom states within the band gap and electron depletion of the highest occupied band due to thermal excitation of electrons to edge states.

Table 35.

Energies in eV and probabilities for electron occupation of Bands #45, #46 and #47 for points along the direction Γ to K in the first Brillouin zone. The Fermi level energy for 1-D $(MoS_2)_5$ terminating at $(10\bar{1}1)$ edges is -10.65 eV. Asterisks indicate energies below the Fermi level.

k-Point	Band #45	f(ε) #45	Band #46	f(ε) #46	Band #47	f(ε) #47
k=0 (Γ)	-10.64	0.40	-10.25	2.1×10^{-9}	-10.10	6.5×10^{-10}
$\mathbf{k}=0.1\mathbf{a}^*$	-10.67*	0.68	-10.49	2.1×10^{-3}	-10.01	2.0×10^{-11}
$\mathbf{k}=0.2\mathbf{a}^*$	-10.79*	1.00	-10.74*	0.97	-9.97	4.4×10^{-12}
$\mathbf{k}=0.3\mathbf{a}^*$	-10.85*	1.00	-10.62	0.24	-10.12	1.4×10^{-9}
$\mathbf{k}=0.4\mathbf{a}^*$	-10.61	0.18	-10.44	3.1×10^{-4}	-10.30	1.4×10^{-6}
$\mathbf{k}=0.5\mathbf{a}^*$(K)	-10.48	1.4×10^{-3}	-10.40	6.7×10^{-5}	-10.35	9.8×10^{-6}

Changes in the valence band located at ~ 4.8 eV can be attributed to edge states identified as Band #18 in Table 33 and Bands #30 and #32 identified in Table 34. Band #18 at Γ is located 3.72 eV below the Fermi level while Bands #30 and #32 at K are located 2.95 eV and 2.87 eV below the Fermi level. The Mo4d-S3p valence band located at ~ 4.8 eV extends from 4 eV to 6 eV. Edge states shown for Bands #18 at Γ and Bands #30 and #32 at K could widen and increase the intensity of this band on the lower binding energy side.

6.2 Electronic Structure of MoS_2: Theory vs. Experiment.

The discussion in Section 6.1 focuses on the electronic structures of 2-D MoS_2, 3-D MoS_2, and 1-D $(MoS_2)_5$ calculated using the Extended Hückel theory and the STO parameters of Hughbanks and Hoffmann (H&H).[41] The theoretical valence band of 2-D MoS_2 is shown in Figure **29b** while the energy dispersion curves are shown in Figures **30a** and **30b**. The 2-D MoS_2 theoretical valence band reproduces some of the features of the experimental valence band (Figure 22b). For instance, the broad band located at ~ -22 eV in the theoretical valence band consists of mainly S3s orbitals. This band shows similar shape in both theoretical and experimental valence bands. However, the S3s band is located too close to the upper portion of the valence band (Mo4d-S3p) compared to the experimental valence band. Also, the Mo4d-S3p portion of the experimental valence band consists of four distinct bands. In the theoretical valence band the Mo4d-S3p region consists of three bands with the center band indicating a certain amount of splitting. The energies obtained from the theoretical calculation indicate that this particular system is a semiconductor. One important feature in the electronic structure calculations is the degree of dispersion of the S3p orbitals. The single zeta S3p radial functions used in this calculation lead to a S3p MAOPOP (see Figure 29c) consisting of two major peaks or bands. This leads to the three-peaked nature of the Mo4d-S3p valence band.

The theoretical energy dispersion curves of 2-D MoS_2 (Figures 30a and 30b) indicate correctly that MoS_2 is a small band gap semiconductor. As discussed in Section 6.1.2, Extended Hückel theory predicts a direct gap for 2-D MoS_2 (K$\rightarrow$K) and an indirect gap for 3-D MoS_2 ($\Gamma\rightarrow$K). Optical absorption experiments indeed indicate that 2H-MoS_2 possesses an indirect gap. The most disturbing feature of the theoretical energy dispersion curves obtained using the H&H parameters is the presence of an energy gap between the highest occupied band (Band #9) and the lower Mo4d-S3p bands (Bands #3-#8). This energy gap indicates no overlap between these bands and separation of the highest occupied band (Band #9) is expected in the theoretical valence band. As shown in Figure 29b, the theoretical valence band does exhibit a band at the top of the valence band well separated from the rest of the Mo4d-S3p bands. The

experimental energy dispersion curves of Mamy et al.[15], reproduced in Figure 30b along with the theoretical curves, do not show a significant gap between the highest occupied band and the lower portion of the Mo4d-S3p valence band. However, curvature of the energy bands at the top and the bottom of the Mo4d-S3p valence band is very similar for both theory and experiment.

In summary, the following features of the electronic structure of MoS_2 were reproduced by Extended Hückel theory using the parameters of H&H: semiconductor nature of 2H-MoS_2, presence of indirect gap, energy dispersion of S3s bands (Bands #1 and #2) and curvature of the energy bands, specifically at the top and bottom of the Mo4d-S3p valence band. The following features were not reproduced by the theory using the parameters of H&H: correct energy position of the entire valence band, relative energy positions of the S3s bands with respect to the Mo4d-S3p bands, overlap between the highest occupied valence band and the lower Mo4d-S3p bands, and four-peaked nature of the Mo4d-S3p portion of the valence band.

For the reasons indicated above, parametrization of the Mo4d, S3p and S3s ionization potentials, H_{ii}, were carried out by comparison with experiment as discussed previously in Section 5.6. Atomic parameters of Clementi and Roetti[42] involving double zeta S3s and S3p STO's were also used in place of the single zeta S3s and S3p STO's of Hughbanks and Hoffmann. Modification of these parameters was also carried out as indicated in Section 5.6.2 to obtain a theoretical valence band which qualitatively reproduces the experimental valence band as shown in Figure 39c. However, the question remains as to whether the parametrization actually changed the orbital character of the energy dispersion bands discussed previously in Section 6.1 Section 6.2.2 will discuss the orbital character of the energy dispersion bands of 2-D MoS_2 obtained using the best fit parameters of Table 25. Also discussed in Section 6.2.1 will be the accuracy of the experimental energy dispersion curves obtained by Mamy et al.[15]

6.2.1 Accuracy of Experimental Energy Dispersion Curves.

Experimental energy dispersion curves of single crystal 2H-MoS_2 obtained by Mamy et al.[15] are compared to theoretical energy dispersion curves of 2-D MoS_2 calculated using solid state Extended Hückel theory and the atomic parameters of Table 25 in Figure 40b. The comparison was made by shifting the experimental curves to more negative binding energies by addition of the work function 4.1 eV.[15] The equation relating the photoelectron kinetic energy E_K and polar angle of detection θ (as measured from the surface normal) to the parallel component of the wavevector $|\mathbf{k}_{||}|$ is shown in equation 18.[57] Energy dispersion curves plot the binding energy E_B versus the parallel component of the wavevector. Since the photoelectron

kinetic energy is used to calculate the value of the wavevector parallel to the crystal surface, the shift in binding energy only serves to shift the entire set of energy dispersion curves by the work function on the binding energy scale.

$$|\mathbf{k}_{||}| = \left(\frac{2mE_K}{h^2}\right)^{\frac{1}{2}} \times \sin\theta \tag{18}$$

$|\mathbf{k}_{||}|$ = parallel component of the wavevector $\mathbf{k}=\mathbf{k}_{||}+\mathbf{k}_{\perp}$
m = electron mass
h = Planck's constant
E_K = photoelectron kinetic energy
θ = polar angle of detection as measured from the surface normal

A limit on the accuracy of the experimental energy dispersion curves can be approximated from the raw data provided in the work of Mamy et al.[15] The raw data are in the form of ultraviolet photoelectron valence band spectra. Errors in the energy position of the peak maxima may lead to errors in both the plotted binding energy and calculated parallel wavevector $|\mathbf{k}_{||}|$. A typical intense peak in the UPS valence band of 2H–MoS_2 obtained by Mamy et al. has a width of approximately 0.22 eV. Thus, the plotted binding energy positions can be in error by as much as ± 0.11 eV. Although the peak positions are probably measured more accurately than ± 0.11 eV, this number will be used to show that even large errors in peak position will lead to small errors in $|\mathbf{k}_{||}|$. The same error occurs in the kinetic energy that is used to calculate the parallel component of the wavevector. Differentiating equation 18 with respect the E_K leads to the expression shown in equation 19. Allowing $\frac{dk}{dE_K}$ to be approximated by $\frac{\Delta k}{\Delta E_K}$ leads to an equation (equation 20) for calculating the error $\Delta|\mathbf{k}_{||}|$ in $|\mathbf{k}_{||}|$ that results from an error of ΔE_K in E_K. Using these expressions and manually measuring the binding

$$\frac{d|\mathbf{k}_{||}|}{dE_K} = \left(\frac{2m}{h^2}\right)^{\frac{1}{2}} \times \sin\theta \times \frac{1}{2} \times (E_K)^{-\frac{1}{2}} \tag{19}$$

$$\Delta|\mathbf{k}_{||}| = \left(\frac{2m}{h^2}\right)^{\frac{1}{2}} \times \sin\theta \times \frac{1}{2} \times \frac{\Delta E_K}{E_K^{1/2}} \tag{20}$$

energies of the UPS peaks, typical errors in $|\mathbf{k}_{||}|$ were approximated. At $\theta=10°$, UPS peaks are located between kinetic energies of 10.56 eV and 15.05 eV corresponding to values of $|\mathbf{k}_{||}|$ between 0.0460 $Å^{-1}$ and 0.0549 $Å^{-1}$ and errors $\Delta|\mathbf{k}_{||}|$ of 2.35×10^{-4} $Å^{-1}$ and 1.97×10^{-4} $Å^{-1}$ respectively. This error represents less than a 1% error in $|\mathbf{k}_{||}|$. At $\theta=40°$, a UPS peak is located at 9.68 eV corresponding to a value of $|\mathbf{k}_{||}|$ of 0.163 $Å^{-1}$ and an error $\Delta|\mathbf{k}_{||}|$ of 9.10×10^{-4} $Å^{-1}$. This error represents an error of $\sim 1\%$ in $|\mathbf{k}_{||}|$. Thus, errors in measurements of the

photoelectron kinetic energy will produce errors in the value of $|k_{||}|$ but the error is insignificant in this experiment. Thus, the experimental energy dispersion curves of Mamy et al accurately represent the true energy dispersion curves.

6.2.2 Orbital Picture of Energy Dispersion in 2-D MoS_2.

Local atomic orbital coefficients, individual atomic orbital charges and total charges on the atoms Mo, S_2, and S_3 in 2-D MoS_2 for Bands #1 through #13 at Γ and M are given in Table 36. This calculation involved the atomic parameters of Table 25 instead of the parameters of Hughbanks and Hoffmann used in the calculations of Section 6.1. In general only atomic orbitals that exhibit a coefficient $>|0.1|$ are shown. Comparison of Table 31 with Table 36 shows that the major character of each band is retained at both Γ and M points. Thus, the switch from the parameters of Hughbanks and Hoffmann to the parameters given in Table 25 does not change the orbital character of the bands.

Small changes in the contribution of each atomic orbital to the overall crystal orbital as evidenced by the tabulated coefficients are seen. For example Band #1 possesses less overall Mo character. In Band #1 at Γ, 99% of the electrons reside on the sulfur atoms. Previously, using the parameters of Hughbanks and Hoffmann, 87% of the electrons resided on the sulfur atoms. This decrease in molybdenum electron density on changing from H&H parameters to those of Table 25 is evidently due to the larger Mo4d–S3s and Mo5s–S3s ionization potential separations in the parameters of Table 25. Dispersion of Bands #1 and #2 is still caused by changes in the intra–sulfur (S_2–S_2) interaction from bonding at Γ to antibonding at M. Also, the stabilization of Band #1 over Band #2 is caused by the change in inter–sulfur (S_2–S_3) interaction from bonding in Band #1 to antibonding in Band #2. The same pictures portraying the geometry of the local atomic orbitals for Bands #1 through #13 at Γ and M shown in Figures 46 through 52 apply for both sets of parameters.

The most important change occurs at the top of the valence band. When the parameters of Table 25 are used to calculate the electronic structure of 2-D MoS_2, overlap occurs between the highest occupied crystal orbital (Band #9) and the lower Mo4d–S3p portion of the valence band (Bands #7 and #8). At M, Band #9 has an energy of -6.21 eV while at Γ, Bands #7 and #8 have energies of -6.06 eV. Thus, overlap between Bands #7 and #8 with Band #9 causes a disappearance of the gap between the highest occupied valence band and the Mo4d–S3p portion of the valence band (see Figure 39c). Figure 39d shows the Mo4d MAOPOP's calculated from the atomic parameters of Table 25. The highest occupied band again consists of Mo4d character such that $d_{z2} > d_{xy} > d_{x2-y2}$. The lowest conduction band

Table 36.

Local atomic orbital coefficients, individual atomic orbital charges and total charges on the atoms Mo, S_2, and S_3 in 2-D MoS_2 for Bands #1-#13 at Γ and M. The atomic parameters of Table 25 were used in this calculation.

	Γ *Point:* $k=0$				*M Point:* $k=a^*/3$			
Band #	Atomic Orbital	Orbital Coefficient	AO Charge	Atom Charge	Atomic Orbital	Orbital Coefficient	AO Charge	Atom Charge
Band #1	Mo5s	0.0028	0.01	0.013	Mo5s	-0.083	0.030	0.20
	$Mo4d_{z2}$	0.0019	0.0029		$Mo5p_x$	-0.058	0.082	
					$Mo4d_{xy}$	-0.075	0.046	
	$S_2 3s$	0.62	0.98	0.99	$S_2 3s$	-0.65	0.90	0.90
	$S_3 3s$	0.62	0.98	0.99	$S_3 3s$	-0.65	0.90	0.90
Band #2	$Mo5p_z$	-0.040	0.076	0.076	$Mo5p_z$	-0.075	0.043	0.28
					$Mo4d_{zx}$	-0.17	0.18	
					$Mo4d_{yz}$	0.10	0.06	
	$S_2 3s$	-0.62	0.95	0.96	$S_2 3s$	-0.64	0.85	0.86
	$S_3 3s$	0.62	0.95	0.96	$S_3 3s$	0.64	0.85	0.86
Band #3	$Mo4d_{z2}$	-0.13	0.12	0.071	$Mo4d_{z2}$	-0.070	0.039	0.028
					Mo5s	0.075	---	
					$Mo4d_{xy}$	-0.057	0.030	
	$S_2 3s$	-0.047	0.0034	0.96	$S_2 3p_x$	0.46	0.74	0.99
	$S_2 3p_z$	-0.55	0.96		$S_2 3p_y$	-0.27	0.25	
	$S_3 3s$	-0.047	0.0034	0.96	$S_3 3p_x$	0.46	0.74	0.99
	$S_3 3p_z$	0.55	0.96		$S_3 3p_y$	-0.27	0.25	
Band #4	$Mo5p_z$	0.14	0.14	0.14	$Mo5p_z$	-0.021	0.026	0.071
					$Mo4d_{zx}$	0.058	0.034	
	$S_2 3p_z$	-0.67	0.93	0.93	$S_2 3p_x$	0.48	0.72	0.96
					$S_2 3p_y$	-0.28	0.24	
	$S_3 3p_z$	-0.67	0.93	0.93	$S_3 3p_x$	-0.48	0.72	0.96
					$S_3 3p_y$	0.28	0.24	
Band #5	$Mo4d_{xy}$	-0.77	1.41	1.43	$Mo4d_{xy}$	0.17	0.15	0.23
	$Mo5p_x$	-0.10	0.018		$Mo4d_{z2}$	-0.13	0.060	
					$Mo4d_{x2-y2}$	-0.10	0.050	
	$S_2 3p_x$	0.40	0.29	0.29	$S_2 3p_z$	-0.63	0.87	0.89
					$S_2 3s$	-0.13	0.017	
	$S_3 3p_x$	0.40	0.29	0.29	$S_3 3p_z$	0.63	0.87	0.89
					$S_3 3s$	-0.13	0.017	
Band #6	$Mo4d_{x2-y2}$	0.77	1.41	1.43	$Mo4d_{x2-y2}$	-0.12	0.031	0.45
	$Mo5p_y$	0.10	0.018		$Mo5p_x$	-0.21	0.10	
					$Mo5p_y$	-0.36	0.30	
	$S_2 3p_y$	-0.40	0.29	0.29	$S_2 3p_y$	0.59	0.58	0.78
					$S_2 3p_x$	0.34	0.19	
	$S_3 3p_y$	-0.40	0.29	0.29	$S_3 3p_y$	0.59	0.58	0.78
					$S_3 3p_x$	0.34	0.19	
Band #7	$Mo4d_{zx}$	0.87	1.42	1.42	$Mo4d_{yz}$	0.55	0.75	1.00
					$Mo4d_{zx}$	0.32	0.25	
	$S_2 3p_x$	-0.44	0.29	0.29	$S_2 3p_y$	-0.45	0.37	0.50
					$S_2 3p_x$	-0.26	0.12	
	$S_3 3p_x$	0.44	0.29	0.29	$S_3 3p_y$	0.45	0.37	0.50
					$S_3 3p_x$	0.26	0.12	

Table 36 (cont).

Local atomic orbital coefficients, individual atomic orbital charges and total charges on the atoms Mo, S_2, and S_3 in 2-D MoS_2 for Bands #1-#13 at Γ and M. The atomic parameters of Table 25 were used in this calculation.

	Γ *Point:* $k=0$				*M Point:* $k=a^*/3$			
Band #	Atomic Orbital	Orbital Coefficient	AO Charge	Atom Charge	Atomic Orbital	Orbital Coefficient	AO Charge	Atom Charge
Band #8	$Mo4d_{yz}$	0.87	1.42	1.42	$Mo4d_{zx}$	0.29	0.094	0.38
					$Mo4d_{yz}$	-0.17	0.28	
	$S_2 3p_y$	-0.44	0.29	0.29	$S_2 3p_z$	-0.69	0.79	0.81
					$S_2 3s$	-0.087	0.0048	
	$S_3 3p_y$	0.44	0.29	0.29	$S_3 3p_z$	-0.69	0.79	0.81
					$S_3 3s$	0.087	0.0048	
Band #9	$Mo4d_{z2}$	-0.95	1.87	1.88	$Mo4d_{z2}$	0.61	0.78	1.81
					$Mo4d_{xy}$	-0.53	0.65	
					$Mo4d_{x2-y2}$	0.30	0.22	
	$S_2 3p_z$	0.26	0.057	0.059	$S_2 3p_z$	-0.26	0.098	0.097
	$S_3 3p_z$	-0.26	0.057	0.059	$S_3 3p_z$	0.26	0.098	0.097
Band #10	$Mo5p_x$	-0.72	0.40	0.94	$Mo4d_{x2-y2}$	-1.01	1.46	1.98
	$Mo4d_{xy}$	0.62	0.53		$Mo4d_{xy}$	-0.59	0.49	
	$S_2 3p_x$	0.72	0.53	0.53	$S_2 3p_x$	-0.043	0.0024	0.0097
					$S_2 3p_y$	-0.075	0.0073	
	$S_3 3p_x$	0.72	0.53	0.53	$S_3 3p_x$	-0.043	0.0024	0.0097
					$S_3 3p_y$	-0.075	0.0073	
Band #11	$Mo5p_y$	-0.72	0.40	0.94	$Mo4d_{z2}$	-0.90	1.12	1.91
	$Mo4d_{x2-y2}$	0.62	0.53		$Mo4d_{x2-y2}$	0.35	0.18	
					$Mo4d_{xy}$	-0.60	0.54	
	$S_2 3p_y$	0.72	0.53	0.53	$S_2 3p_y$	0.12	0.0088	0.044
					$S_2 3p_x$	-0.21	0.027	
	$S_3 3p_y$	0.72	0.53	0.53	$S_3 3p_y$	0.12	0.0088	0.044
					$S_3 3p_x$	-0.21	0.027	
Band #12	$Mo4d_{yz}$	0.70	0.58	0.58	$Mo4d_{yz}$	0.83	0.75	1.00
					$Mo4d_{zx}$	0.48	0.25	
	$S_2 3p_y$	0.87	0.71	0.71	$S_2 3p_y$	0.68	0.38	0.50
					$S_2 3p_x$	0.39	0.13	
	$S_3 3p_y$	-0.87	0.71	0.71	$S_3 3p_y$	-0.68	0.38	0.50
					$S_3 3p_x$	-0.39	0.13	
Band #13	$Mo4d_{zx}$	0.70	0.58	0.58	$Mo4d_{zx}$	-0.87	0.92	1.48
					$Mo4d_{yz}$	0.50	0.31	
					$Mo5p_z$	0.58	0.26	
	$S_2 3p_x$	0.87	0.71	0.71	$S_2 3p_x$	0.35	0.025	0.26
					$S_2 3p_y$	-0.20	0.0084	
					$S_2 3p_z$	-0.46	0.15	
					$S_2 3s$	0.37	0.075	
	$S_3 3p_x$	-0.87	0.71	0.71	$S_3 3p_x$	-0.35	0.025	0.26
					$S_3 3p_y$	0.20	0.0084	
					$S_3 3p_z$	-0.46	0.15	
					$S_3 3s$	-0.37	0.075	

also consists of Mo4d character such that $d_{x2-y2} > d_{xy} \simeq d_{z2}$. The second conduction band consists of Mo4d character such that $d_{yz} > d_{zx}$. A comparison of Figure 39d (atomic parameters of Table 25) with Figure 29d (atomic parameters of Hughbanks and Hoffmann) shows little change in the Mo4d MAOPOP upon changing the atomic parameters. Major changes are seen in the S3p MAOPOP shown in Figures 29c (H&H parameters, single zeta S3s and S3p) and Figure 39b (Table 25 parameters, double zeta S3s and S3p). Double zeta S3p radial functions lead to a 3-peaked S3p MAOPOP that overlaps with the Mo4d MAOPOP to produce a 4-peaked theoretical valence band.

Using the parameters of Table 25, a direct band gap K→K of 1.08 eV was calculated for 2-D MoS_2. Addition of interactions across the Van der Waals gap in the form of 3-D MoS_2 again resulted in calculation of an indirect gap from Γ→0.9 K (close to K) of 0.35 eV. As indicated in Section 5.6.2, the size of the band gap is mainly affected by the Mo4d radial functions. Use of more diffuse Mo4d double zeta functions should increase the size of the band gap.

The empty conduction bands of a natural single crystal of 2H-MoS_2 were studied experimentally by inverse photoemission spectroscopy.[58] In inverse photoemission spectroscopy, a source of electrons injects electrons into the MoS_2 conduction band. Ejection of the conduction band electrons is then detected with reference to the Fermi level of the instrument. The conduction band spectra are representative of the entire MoS_2 Brillouin zone. Two structures of Mo4d character close to the Fermi level were resolved in the conduction band of 2H-MoS_2 . The first structure denoted A_1 was located 1.2 eV above the Fermi level; the second structure denoted A_2 was located 2.4 eV above the Fermi level. Thus, the separation between A_1 and A_2 was 1.2 eV. As shown in Figure 39a and 39c, theoretical conduction bands of 2-D MoS_2 calculated using the parameters of Table 25 show two distinct bands residing above the Fermi level. The first band is located 1.1 eV above the Fermi level (at -3.8 eV) and can be considered to correspond to the A_1 band found in the experiment. The second band is located 3.4 eV above the Fermi level (at -1.4 eV) and can be considered to correspond to the A_2 band found in the experiment. Separation between the two theoretical conduction bands is ca. 2.4 eV as compared to the separation of 1.2 eV in the inverse photoemission experiment. However, the two-peaked nature of the experimental conduction band close to the Fermi level is reproduced by solid state Extended Hückel theory using the parameters of Table 25. As indicated in the preceding section, the experimental conduction band labeled A_1 is predicted by solid state Extended Hückel theory to consist of Mo4d character such that $d_{x2-y2} > d_{xy} \simeq d_{z2}$. The second conduction band labeled A_2 in the experiment is predicted to consist of Mo4d character such

that $d_{yz} > d_{zx}$.

A Raman investigation of polycrystalline MoS_2 carried out under a He atmosphere at 80 K by Polz et al. shows the presence of surface sulfur dimers, S_2^{-2}.[59] A weak band at 529 cm^{-1} was assigned to the S–S stretching mode of disulfide anions. If S_2^{-2} species do in fact exist on MoS_2 edges, then homolytic cleavage of H_2 is probable. The theoretical calculations for 2–D MoS_2 show that interactions between sulfur atoms (both intra– and inter–) do exist in the bulk. Interactions between sulfur atoms existing within the same layer (intra–sulfur interactions, S_2–S_2) cause the energy dispersion of Bands #1 and #2 from Γ to M. The intra–sulfur interactions change from bonding at Γ to antibonding at M. Interactions between sulfur atoms existing across the MoS_2 layer (inter–sulfur interactions, S_2–S_3) cause the energy splitting between Bands #1 and #2. Band #1 is stabilized in energy compared to Band #2 because the inter–sulfur interaction is bonding in Band #1 and antibonding in Band #2. Thus, the theoretical calculations show that S–S interactions are important in the bulk. At edge planes terminating in 1–coordinate sulfur atoms (such as Edge 2 on the 1–D $(MoS_2)_5$ system terminating at $(10\bar{1}0)$ edges) dimerization of the sulfur atoms can be easily envisioned. If the two 1–coordinate edge sulfur atoms relax toward the molybdenum plane, interaction of the sulfur atoms would increase because of the shorter S–S bond length. In bulk MoS_2 the S_2–S_3 bond length is 3.155 Å, however a much shorter S–S bond length is expected to cause the Raman band at 529 cm^{-1}. Raman investigations of the pyritic disulfides, RuS_2, FeS_2, MnS_2 and NiS_2, yielded the following positions for the A_g mode attributed to in–phase S_2 stretching vibrations (also shown are the S–S bond lengths): 390 cm^{-1}, 2.18 Å (RuS_2); 379 cm^{-1}, 2.14 Å (FeS_2); 489 cm^{-1}, 2.09 Å (MnS_2); 480 cm^{-1}, 2.07 Å (NiS_2).[60] Qualitatively, the S–S stretching mode observed for MoS_2 should correspond to a bond length much smaller than 3.155 Å. Theoretical studies of MoS_2 edges using higher level theories involving geometry optimization routines are necessary for determining whether S–S edge dimerization is predicted theoretically.

In summary, the theoretical valence band obtained using the parameters of Table 25 qualitatively reproduces the experimental valence band as shown in Figure 39c. The upper Mo4d–S3p theoretical valence band consists of four distinct peaks, similar to the experimental valence band. The S3p double zeta functions are necessary for a better representation of the MoS_2 valence band. The use of more diffuse S3p double zeta functions increases the overlap between the S3p and Mo4d atomic orbitals leading to the four–peaked nature of the upper valence band. The total width of the Mo4d–S3p theoretical valence band region is ca. 6 eV, the experimental width is also ca. 6 eV. The S3s band is separated from the upper Mo4d–S3p portion of the valence band by ca. 6 eV in both theory and experiment. The two–peaked nature

of the experimental conduction band is also reproduced by the theory. However, the separation between the two lowest lying conduction bands (labeled A_1 and A_2 in the experiment) is larger in the theory 2.4 eV than in the experiment 1.2 eV.

6.2.3 Comparison to Previous Theories.

The tight-binding method including only nearest neighbor interactions was used by Bromley in 1970 and Bromley et al. in 1972 to theoretically calculate the energy dispersion curves of 2-D MoS_2.[7,6] The calculated electronic structure of 2-D MoS_2 was fit to the transmission spectra of 2H-MoS_2 which showed the presence of a pair of excitons just below the fundamental absorption edge. Thus the excitons, whose exact origin in k-space is not experimentally known, were fit to transitions at Γ. The atomic basis set consisted of Mo4d, Mo5s, S3s, and S3p states. These calculations resulted in a theoretical indirect gap from M→Γ. As was discussed in Section 6.1.2, inclusion of interactions across the Van der Waals gap produces splitting of the highest occupied level at Γ. Thus, because of the 2-D nature of this calculation, the indirect gap is very different from that of more recent theoretical studies. Curvature of the highest occupied band and the presence of a gap between the highest occupied valence band and the rest of the Mo4d-S3p are also not consistent with the experimental energy dispersion curves of Mamy et al.[15]

The simplified linear combination of muffin-tin orbitals method was used by Kasowski in 1973 to theoretically calculate the energy dispersion curves of 3-D MoS_2.[8] In this study, the highest occupied valence band was found to overlap with the rest of the Mo4d-S3p valence bands by ca. 0.5 eV. The highest occupied valence band was found to be 2.7 eV wide and was located 1.1 eV below the conduction bands. Due to the 3-D nature of this calculation, an indirect gap was found from Γ→T (1/2 Γ→K). In the direction Γ→A, there is a large splitting of the bands at Γ with corresponding degeneracy at A. This behavior has also been reproduced by solid state Extended Hückel theory (see Section 5.2). In this study, the excitons are attributed to transitions at A. However in this study, only the highest portion of the valence band and the lowest portion of the conduction band are shown.

In 1973 Mattheiss also theoretically calculated the energy dispersion curves of 3-D MoS_2 using first principles augmented-plane-wave theory.[61] In this study, no empirical parameters were used but approximate crystal potentials were derived from neutral-atom charge densities. This study only calculated the electronic structure at high symmetry points Γ, A, K, M and midpoints Σ and T in the Brillouin zone; thus, the curvature of the energy dispersion curves was only approximate. Using this theory, the highest occupied valence band was separated from the

rest of the Mo4d–S3p valence bands by 0.6–0.7 eV. The most important contribution of this paper is a discussion of the Mo4d character at Γ, M and K. Matthiess indicates that the highest occupied valence band consists of d_{z2} character at Γ, d_{z2}, d_{xy} and d_{x2-y2} character at M and d_{xy} and d_{x2-y2} character at K. The same result is obtained when solid state Extended Hückel theory is used to calculate the electronic structure of 2–D MoS_2 (see Sections 6.1 and 6.2). Again, splitting of bands at Γ and degeneracy at A is evident due to the 3–D nature of this calculation.

In 1978, Bullett calculated the electronic structure of 3–D MoS_2 using an approach similar to a simple LCAO approach neglecting 3–center terms and interactions between atoms separated by >5.0 Å.[9] Atomic energy levels for the Mo4d, S3p, and S3s orbitals were located at -5.5 eV, -8.0 eV and -17.8 eV respectively. These values are very close to the atomic ionization potentials found by parametrization of the theoretical 2–D MoS_2 valence band with the HR–ESCA experiment (-6.0 eV, Mo4d; -8.845 eV, S3p; and -17.8 eV, S3s). In this study, the highest occupied valence band of width 1.3 eV overlapped with the lower Mo4d–S3p valence bands by 0.4 eV. Again, splitting of bands at Γ and degeneracy at A is evident due to the 3–D nature of this calculation. An indirect gap of 0.7 eV was found to occur from Γ→T. Bullett also indicates that the highest occupied valence band consists of only d_{z2} character at Γ but contributions from d_{xy} and d_{x2-y2} at other points in the Brillouin zone.

Coehoorn et al. in 1987 also studied the electronic structure of 3–D MoS_2 using an ab initio self–consistent augmented–spherical–wave method.[10,11] In this study, the elevation of sulfur atoms above and below the plane of molybdenum atoms u was changed from the experimental value of 0.129 to 0.121. This was done to take polarization effects into account specifically on the sulfur atoms. In this study an indirect gap from Γ→T (or 0.55 Γ–K) and a direct gap from K→K were found. Band gaps calculated by this method were generally found to be 30–50% smaller than experimental band gaps. Excitons were attributed to direct optical transitions at K.

The studies mentioned above concentrate on assigning the excitons observed in optical spectroscopy to electronic transitions. Valence bands obtained from photoelectron spectroscopy are only qualitatively discussed in terms of the aforementioned electronic structure calculations. The solid state Extended Hückel electronic structure study of MoS_2 undertaken in this thesis was performed in order to better understand the HR–ESCA valence band and character of the energy dispersion curves. As discussed in Section 6.2, the theoretical valence band of MoS_2 obtained using the parameters of Table 25 reproduces the experimental HR–ESCA valence band of MoS_2. As indicated by Matheiss and Bullett, extended Hückel theory predicts that the

highest occupied valence band consists of only d_{z2} character at Γ, d_{z2}, d_{xy} and d_{x2-y2} character at M and d_{xy} and d_{x2-y2} character at K. The Mo4d MAOPOP breakdown of the valence bands and conduction bands (Figure 39d) and the character of each band at Γ and M (Table 36) indicates the complexity of the Mo4d orbital mixing. Extended Hückel theory also predicts the following: splitting of bands at Γ and degeneracy of bands at A upon introducing interactions between crystal orbitals across the Van der Waals gap (3-D MoS_2 model system); Γ as the highest point of the valence band; direct gap at K; and overlap of the highest occupied valence band with the rest of the Mo4d-S3p valence band. One feature not reproduced by solid state Extended Hückel theory is the position of the conduction band. The lowest point of the conduction band occurs at 0.9 K. Thus, the indirect gap is located from Γ→0.9 K instead of from Γ→T.

6.3 Hydrogen Adsorption on MoS_2.

Hydrogen adsorption on MoS_2 surfaces was studied both theoretically and experimentally. Theoretically, hydrogen was adsorbed at various sites on the following systems: 2-D MoS_2, 1-D $(MoS_2)_5$ terminating at $(10\bar{1}0)$ and $(10\bar{1}1)$ edges, $(MoS_2)_{19}$ clusters terminating at $(10\bar{1}0)$ and $(10\bar{1}1)$ edges, and $(MoS_2)_{14}$ clusters terminating at $(10\bar{1}0)$ edges. Experimentally, hydrogen was adsorbed onto polycrystalline MoS_2 and analyzed via HR-ESCA. Section 6.3.1 will discuss the theoretical results while Section 6.3.2 will discuss the theoretical results in terms of the hydrogen adsorption experiment.

6.3.1 Theoretical Results of Hydrogen Adsorption on MoS_2 Systems.

As mentioned previously, most of the theoretical studies were carried out using the parameters of Hughbanks and Hoffmann.[41] The atomic parameters for the H1s orbital were the following: H_{ii}=-13.6 eV and ζ=1.3 au. Atomic ionization potentials for the S3s, S3p and Mo4d orbitals were the following: -20.0 eV, -13.3 eV, and -11.06 eV. Thus, the S3p ionization potential was located 0.30 eV below the H1s ionization potential while the Mo4d ionization potential was located 2.54 eV above the H1s ionization potential. Only hydrogen atom chemisorption (not hydrogen molecule dissociation) was studied theoretically. The purpose of this study is to find relative stability of sites, not relative activation energies.

Theoretical results from hydrogen adsorption onto 2-D MoS_2 are given in Section 5.4 and Table 20. These results indicate that adsorption of hydrogen atoms onto basal plane sulfur atoms (ΔH_{10}=-68.95 kcal/mole) is more thermodynamically feasible than onto basal plane molybdenum atoms (ΔH_{10}=+10.24 kcal/mole). The results of theoretically adsorbing hydrogen

onto 1-D $(MoS_2)_5$ system terminating at $(10\bar{1}1)$ edges are given in Section 5.5 and Table 22. Again, the calculated enthalpies indicate that basal and edge plane sulfur sites are the most thermodynamically favored for hydrogen adsorption. However, a four-coordinate edge molybdenum site is also thermodynamically favored for hydrogen adsorption. Five-coordinate edge and fully coordinated basal plane molybdenum atoms are not thermodynamically favorable sites for hydrogen adsorption. The trend is such that the four-coordinate molybdenum site is more favorable than the five-coordinate molybdenum site which is still more favorable than the six-coordinate molybdenum site.

Results from the $(MoS_2)_{19}$ clusters terminating at $(10\bar{1}0)$ and $(10\bar{1}1)$ edges studied in Appendix B.1.3 and B.1.4 respectively also show similar trends in the hydrogen binding enthalpies (see Table B-5). On the $(MoS_2)_{19}$ cluster terminating at $(10\bar{1}0)$ edges, the most favorable hydrogen adsorption sites are 2-coordinate edge and 4-coordinate edge molybdenum atoms. The next most favorable hydrogen adsorption sites are basal plane and edge plane sulfur sites. Least favorable sites are 2-fold sulfur sites, followed by basal plane molybdenum sites and 3-fold sulfur sites. Caution must be taken when comparing 4-coordinate edge molybdenum sites, Sites S and V, on the $(MoS_2)_{19}$ cluster terminating at $(10\bar{1}0)$ edges with 4-coordinate edge molybdenum sites, Mo-0101 Case B, exposed in a structure terminating at $(10\bar{1}1)$ edges as shown in Figures B-5 and 14b. The four sulfur ligands connected to a 4-coordinate molybdenum site exposed by cluster termination at $(10\bar{1}0)$ edges all reside in the same plane or on the same side of the molybdenum atom. Hydrogen adsorption at this site is more favorable since interaction of adsorbed hydrogen with coordinated sulfur atoms is decreased due to the larger S-H distance. In Table 37, binding enthalpies of hydrogen atoms at representative sites on the various systems are reproduced.

The binding enthalpies indicate that atoms of similar type and coordination adsorb hydrogen with the same strength of interaction. For instance all basal plane sulfur sites possess hydrogen binding enthalpies between 98 kcal/mole and 107 kcal/mole. In general it can be concluded from this set of Extended Hückel calculations that adsorption of hydrogen onto basal plane sulfur sites is slightly more favorable than onto edge plane sulfur sites. However, adsorption of hydrogen onto edge plane molybdenum sites is more favorable than onto basal plane molybdenum sites. As the number of sulfur atoms coordinated to the exposed molybdenum increases so also weakens binding of hydrogen. Thus, the stability of hydrogen adsorption is generally as follows: 2-coordinate Mo > 3-coordinate Mo > 4-coordinate Mo > 5-coordinate Mo > 6-coordinate Mo.

Table 37.

Hydrogen atom binding enthalpies calculated for the following systems: 1-D $(MoS_2)_5$ terminating at $(10\bar{1}1)$ edges and $(MoS_2)_{19}$ clusters terminating at $(10\bar{1}0)$ and $(10\bar{1}1)$ edges. Units are in kcal/mole.

		Hydrogen Binding Enthalpies (kcal/mole):		
		1-D $(MoS_2)_5$	$(MoS_2)_{19}$	$(MoS_2)_{19}$
Atom	Description	$(10\bar{1}1)$	$(10\bar{1}0)$	$(10\bar{1}1)$
Mo	2-coordinate edge (side)	----	-126.12 (E)	----
Mo	4-coordinate edge (side)	----	-118.77 (S)	----
Mo	3-coordinate edge	----	----	-117.97 (Y)
Mo	3-coordinate edge	----	----	-106.70 (Z)
S	3-coordinate basal	-101.87 (S_7)	-106.05 (C)	----
S	3-coordinate basal	-101.70 (S_9)	-102.16 (M)	----
S	3-coordinate basal	-101.60 (S_3)	----	----
S	3-coordinate basal	-98.01 (S_1)	----	----
S	1-coordinate edge (top)	-92.14 (S_5)	-98.30 (L)	----
S	2-coordinate edge (side)	-90.30 (S_6)	-97.09 (T)	----
Mo	4-coordinate edge (side)	-83.84 (Mo_1)	----	-83.50
Mo	5-coordinate edge (side)	----	----	-45.52 (X)
Mo	5-coordinate edge (top)	-37.26 (Mo_3)	----	-39.74 (W)
Mo	6-coordinate basal	-23.16 (Mo_4)	-27.03 (B)	----
Mo	6-coordinate basal	-22.88 (Mo_5)	----	----
Mo	6-coordinate basal	-22.73 (Mo_2)	----	----

However, the relative stability of sulfur sites when compared to molybdenum sites depends on the ionization potentials used for each atomic orbital. The parameters of Hughbanks and Hoffmann place the H1s ionization potential of -13.6 eV just below the S3p ionization potential of -13.3 eV (H&H Mo4d located at -11.06 eV). Interaction of the H1s orbital with the S3p orbital is then very favorable since the energy separation of these levels is only 0.3 eV. A second set of calculations were carried out for hydrogen adsorption on the 1-D $(MoS_2)_5$ system terminating at $(10\bar{1}1)$ edges using the atomic parameters of Table 25. When used to calculate the electronic structure of 2-D MoS_2, the parameters of Table 25 gave the best qualitative fit to the experimental valence band. Atomic ionization potentials for the S3s, S3p, Mo4d and H1s orbitals were the following: -17.80 eV, -8.845 eV, -6.00 eV, and -13.6 eV. The parameters of Table 25 place the H1s ionization potential between the S3s and S3p ionization potentials with S3p-H1s and Mo4d-H1s energy separations of 4.755 eV and 7.6 eV respectively. Interaction of the H1s orbital with the S3p orbitals will no longer be as favorable using the atomic parameters of Table 25. Table 38 lists hydrogen binding enthalpies found on 1-D $(MoS_2)_5$ terminating at $(10\bar{1}1)$ edges for calculations carried out using the parameters of Hughbanks and Hoffmann and the parameters of Table 25.

Table 38.

Hydrogen atom binding enthalpies on 1-D $(MoS_2)_5$ terminating at $(10\bar{1}1)$ edges for Extended Hückel calculations involving the parameters of Hughbanks and Hoffmann (Reference 41) and those of Table 25. Units are in kcal/mole.

Atom	Site	Coordination	ΔH_{15} (H&H)	ΔH_{15} (Table 25)
S-0601	Edge 1	2	-90.30	-72.06
Mo-0101	Edge 1	4	-83.84	-148.84
S-0501	Edge 2	1	-92.14	-57.26
Mo-0301	Edge 2	5	-37.36	-64.60
S-0301	Basal	3	-101.60	-76.51
Mo-0201	Basal	6	-22.73	-27.36

Atomic parameters of Table 25 result in a decrease in stability for hydrogen adsorption at all sulfur sites and an increase in stability for hydrogen adsorption at all molybdenum sites. The most favorable site for hydrogen adsorption when the parameters of Table 25 are used is on 4-coordinate edge molybdenum atoms followed by basal plane sulfur atoms. Basal plane sulfur sites are slightly favored over edge plane sulfur sites. Again, the trend in molybdenum sites is such that lower coordinated edge Mo sites are favored over basal plane sites in the following order: 4-coordinate Mo > 5-coordinate Mo > 6-coordinate Mo. These results indicate that use of Extended Hückel calculations for determining the most favorable adsorbate site must be interpreted with caution. The stability of such sites will depend on the relative energy positions of the adsorbate and surface atomic orbital ionization potentials, H_{ii}.

The theoretical calculations also show that the addition of edges results in more favorable hydrogen adsorption enthalpies on both sulfur and molybdenum atoms. This result is obtained from the comparison of basal plane hydrogen adsorption on 2-D MoS_2 and a study of 1-D $(H\text{-}MoS_2)_5$ in which the hydrogens sit on basal and edge plane sulfur atoms and molybdenum atoms only. As shown in Tables 20 and 23, hydrogen residing on sulfur atoms in 2-D MoS_2 and 1-D $(MoS_2)_5$ terminating at $(10\bar{1}1)$ edges results in the following hydrogen atom binding enthalpies: -68.95 kcal/mole and -93.84 kcal/mole respectively. Hydrogen residing on molybdenum atoms in the 2-D and 1-D systems results in the following hydrogen atom binding enthalpies: +10.24 kcal/mole and -36.50 kcal/mole respectively. In both cases hydrogen adsorption onto the $(MoS_2)_5$ system with a ratio of one hydrogen atom per MoS_2 leads to stabilization of the overall binding enthalpy such that the values obtained are closer to the binding enthalpies for adsorption of hydrogen on basal plane atoms of the 1-D system. The only reasonable explanation for the stabilization is that the addition of edges to the 1-D system modifies not only edge plane atoms but also basal plane atoms such that these sites become

more favorable for reaction with hydrogen. Thus, a MoS_2 system with a large number of edges (such as polycrystalline MoS_2) should adsorb hydrogen more readily than a system with a small number of edges (single crystal MoS_2).

A ^1H NMR study of H_xMoS_α performed by Komatsu and Hall indicated the presence of one Gaussian peak of FWHM ca. 25 ppm and located at a chemical shift of ca. 2 ppm.[21] This peak was attributed to a S–H species; no Mo–H species were detected by ^1H NMR. Komatsu and Hall argue that the presence of hydrogen bonded to paramagnetic Mo^{+3} centers would not be detected due to broadening of the ^1H NMR signal beyond detection. However, the authors continue to argue that if paramagnetic Mo^{+3} centers were present from the reductive adsorption of H_2 on sulfur atoms, then the S–H peak located at ca. 2 ppm would be broadened beyond detection also. The answer seems to lie in the semiconductor nature of the 2H–MoS_2 electronic structure. The theoretical energy dispersion curves indicate that additional electrons will reside in the conduction band of 2–D MoS_2 and in empty edge states at or above the Fermi level in 1–D $(MoS_2)_5$ systems. Thus, in the theoretical 2–D MoS_2 system extra electrons would not be localized on a particular molybdenum atom but would be delocalized on the molybdenum atoms of the lattice. Average charges of 1–D H–$(MoS_2)_5$ systems are given in Tables 24a and 24b. Adsorption of hydrogen on 1–D $(MoS_2)_5$ systems is generally reductive such that the hydrogen is partially oxidized. If hydrogen resides on a sulfur atom, that sulfur atom is generally oxidized while edge 4–coordinate (Mo–0101) and 5–coordinate (Mo–0301) molybdenum atoms are reduced. The only case where hydrogen possesses a negative charge of –0.34 is for adsorption of hydrogen onto 4–coordinate edge Mo–0101. In this case, electrons are transferred from all molybdenum atoms (basal and edge) to the hydrogen atom and edge 2–coordinate sulfur atom S–0601. Thus, although electrons are transferred primarily to the edges, electrons are not localized on a specific molybdenum atom.

Theoretical hydrogen adsorption onto 2– and 4–coordinate molybdenum atoms of the $(MoS_2)_{19}$ cluster terminating at $(10\bar{1}0)$ edges (Appendix B.1.3) results in a Mo–H species with a total negative charge. Electron density for this negative charge is transferred from molybdenum atoms exposed on Edge 1 resulting in an effective oxidation of these molybdenum atoms. Sulfur atoms are unaffected by adsorption onto edge molybdenum atoms. Theoretical hydrogen adsorption onto 1–, 2–, and 3–coordinate sulfur atoms results in a S–H species with a total positive charge. Electron density is transferred from the S–H species to edge and basal plane molybdenum atoms. These theoretical results show that adsorption of hydrogen onto either edge or basal plane molybdenum or sulfur atoms in MoS_2 is more complicated than simple transfer of one electron from hydrogen to a neighboring sulfur atom or molybdenum atom.

Adsorption of hydrogen to molybdenum and sulfur sites affects the entire molybdenum lattice. However, the sulfur lattice is relatively unaffected by adsorption of hydrogen. In general, only sulfur atoms directly bonded to hydrogen are affected by hydrogen adsorption. Thus, the theoretical studies are in general agreement with the statement of Komatsu and Hall that reductive hydrogen adsorption does not localize electrons on a particular molybdenum atom.

The theoretical results are in general agreement with the experimental evidence and conclusions of Komatsu and Hall.[21] Komatsu and Hall suggest that hydrogen molecules are dissociated on coordinatively unsaturated edge sites. Subsequent transfer of hydrogen atoms from edge sites to basal plane sites enables the edge planes to dissociate more hydrogen molecules. The theoretical calculations show that binding of hydrogen to basal plane sulfurs is thermodynamically favorable. Thus, the basal plane of MoS_2 is likely to be covered with hydrogen atoms bound to sulfur atoms. This theoretical result is in agreement with hydrogen uptake experiments that indicate three times larger hydrogen surface areas than nitrogen surface areas and IINS experiments that identify the presence of S–H species.[16]

6.3.2 HR–ESCA of Hydrogen Exposed Polycrystalline MoS_2

Hydrogen adsorption on polycrystalline MoS_2 was examined by HR–ESCA as indicated in Section 2.3.5. The results of this study are given in Section 4.3. Hydrogen adsorption caused all of the core levels to shift to higher binding energies by ca. +0.06—+0.07 eV. A shift of this type indicates that charging of the MoS_2 surface may be occurring upon exposure of the surface to hydrogen. The valence bands of bare and hydrogen exposed MoS_2 are shown in Figure 24. The two spectra are very similar except that the hydrogen exposed sample exhibits extra intensity at the top of the valence band (at ~ 0 eV). This extra intensity at the top of the valence band can be attributed to filling of previously empty edge states at the top of the valence band. Previous experimental results indicate the presence of S–H species that are probably from hydrogen bound to basal plane sulfur atoms. As indicated in Section 5.5.2, theoretical binding of hydrogen to basal plane sulfur sites results in transfer of electrons from the H–S species to edge plane molybdenum atoms. Edge states defined in Section 6.1.3 reside close to the Fermi level and occupation of these states by electrons would lead to increased intensity at the top of the valence band.

Large changes in the MoS_2 valence upon hydrogen adsorption were predicted from solid state Extended Hückel theory (see Section 5.4). These changes were not evident in the experimental HR–ESCA valence bands of bare and hydrogen adsorbed MoS_2. However, the

escape depth of valence band photoelectrons is fairly large, 38 Å for Al K_α radiation. Even at glazing angles the sampling depth was probably close to 7 Å. Thus, the valence band region in this study was probably not sensitive to hydrogen adsorption.

6.4 Electronic Structure of NbS_2 and RuS_2.

As discussed in Section 6.2, the S3s, S3p and Mo4d atomic ionization potentials, H_{ii}, and Slater-type orbital coefficients, c_i, and exponents, ζ_i, were parametrized by using the experimental valence band of MoS_2 obtained via HR-ESCA. An extended Hückel calculation using the atomic parameters listed in Table 25 produces a theoretical valence band that qualitatively reproduces the experimental valence band of MoS_2 (see Figure 39c). Since the S3s and S3p atomic parameters were obtained by comparison with experiment, these parameters are expected to be useful for all transition metal disulfide systems. For instance, the S3s and S3p ionization potentials, H_{ii}, and Slater-type coefficients, c_i, and exponents, ζ_i, used to reproduce the MoS_2 experimental valence band should also reproduce the NbS_2 and RuS_2 experimental valence bands with appropriate choices of Nb4d and Ru4d parameters. Thus, parametrization of the Nb4d and Ru4d ionization potentials were carried out by comparison with experiment as discussed in Sections 5.7 and 5.8. Atomic parameters used in electronic structure calculations of NbS_2 and RuS_2 are given in Tables 27 and 29 respectively. Theoretical valence bands for NbS_2 and RuS_2 are were shown previously in Figures 41a and 42a respectively.

6.4.1 Theoretical Valence Band of NbS_2

The theoretical valence band of 2-D NbS_2 is very similar to that of 2-D MoS_2. The valence band consists of a single S3s band located at ca. 18 eV above the vacuum level and an upper Nb4d-S3p band. The S3s band of 2-D NbS_2 has less dispersion than the S3s band of 2-D MoS_2. The loss of S3s dispersion in 2-D NbS_2 can be attributed to the longer S-S bond distance within the sulfur atomic layers of NbS_2. In NbS_2 the S-S bond distance within the sulfur atomic layers is 3.31 Å, whereas in MoS_2 this distance is 3.16 Å. The highest occupied band is only half occupied ($Nb4d^5$ as compared to $Mo4d^6$) and as a result, 2-D NbS_2 possesses metallic conductivity.

The theoretical valence band of 2-D NbS_2 and experimental valence band of polycrystalline NbS_{2-x} are shown together in Figure 55. Since the NbS_2 work function could not be obtained from the literature, an arbitrary shift of the experimental valence band was carried out. Both the experimental and theoretical valence bands of NbS_2 exhibit four peaks in the Nb4d-S3p valence band region. The highest occupied peak in both cases is well separated

from the rest of the Nb4d-S3p valence band by ca. 2 eV. The S3s, S3p and Nb4d MAOPOP's shown in Figure 41b indicate that the highest occupied band consists of primarily Nb4d character. The S3p MAOPOP shows a large admixture of Nb4d and S3p atomic orbitals in the second band (located at ca. 7 eV) of the Nb4d-S3p valence band. The lower end of the Nb4d-S3p valence band (ca. 9 eV-12 eV) consists of primarily Nb4d character. In MoS_2, the lower end of the Mo4d-S3p valence band consisted of primarily S3p character. The theoretical valence band of NbS_2 reproduces major features of the experimental valence band of polycrystalline NbS_{2-x}. The theoretical S3s band has a FWHM of ca. 2.5 eV while the S3s experimental width is ca. 3.5 eV. Disagreement between theory and experiment could be attributed to the impure nature of the polycrystalline NbS_{2-x} sample. As discussed in Section 4.1.2 and shown in Figure 19, the polycrystalline sample was not stoichiometric and contained a large amount of excess niobium. Core level analysis of the Nb3d and S2p regions showed the presence of 2-3 different niobium oxidation states and 2 different sulfur oxidation states. However, the experimental S3s valence band region of NbS_{2-x} is very similar to that of MoS_2. It seems likely that the valence band of NbS_{2-x} is a fair representation of the valence band of stoichiometric NbS_2.

6.4.2 Theoretical Valence Band of RuS_2.

The theoretical valence band of 3-D RuS_2 and experimental valence band of polycrystalline RuS_2 are shown together in Figure 56. Both the theoretical and experimental valence bands display two bands centered about the ionization potential of the S3s orbitals - 17.80 eV. Both valence bands also show a Ru4d-S3p region consisting of a very intense band located at ca. -4 eV followed by a lower intensity region extending from ca. -6 eV to -12 eV.

The MoS_2 and NbS_2 layered compounds discussed previously displayed a single peak centered at the S3s ionization potential of -17.80 eV. However, RuS_2 exhibits the pyrite structure in which two sulfur atoms exist in the form of a sulfur dimer, S_2^{2-}. The closest S-S bond distance in RuS_2 is the sulfur dimer bond distance of 2.178 Å whereas the closest S-S bond distances in the layered compounds MoS_2 and NbS_2 are 3.155 Å and 2.97 Å respectively. Thus, the S3s region of RuS_2 is split into two bands consisting of primarily S3s character as shown in Figure 42b. The character of the highest occupied band is mainly Ru4d. As discussed in Section 3.3, the theoretical valence band is obtained by summation of the modified atomic orbital populations (MAOPOP's). MAOPOP's are obtained by multiplication of the individual atomic orbital populations by the Scofield cross-section. The Scofield cross-section ratio of Ru4d to S3p is 8.62. Thus, contributions from the Ru4d orbitals will be intensified relative to contributions from the S3p orbitals. The high intensity of the highest occupied band is

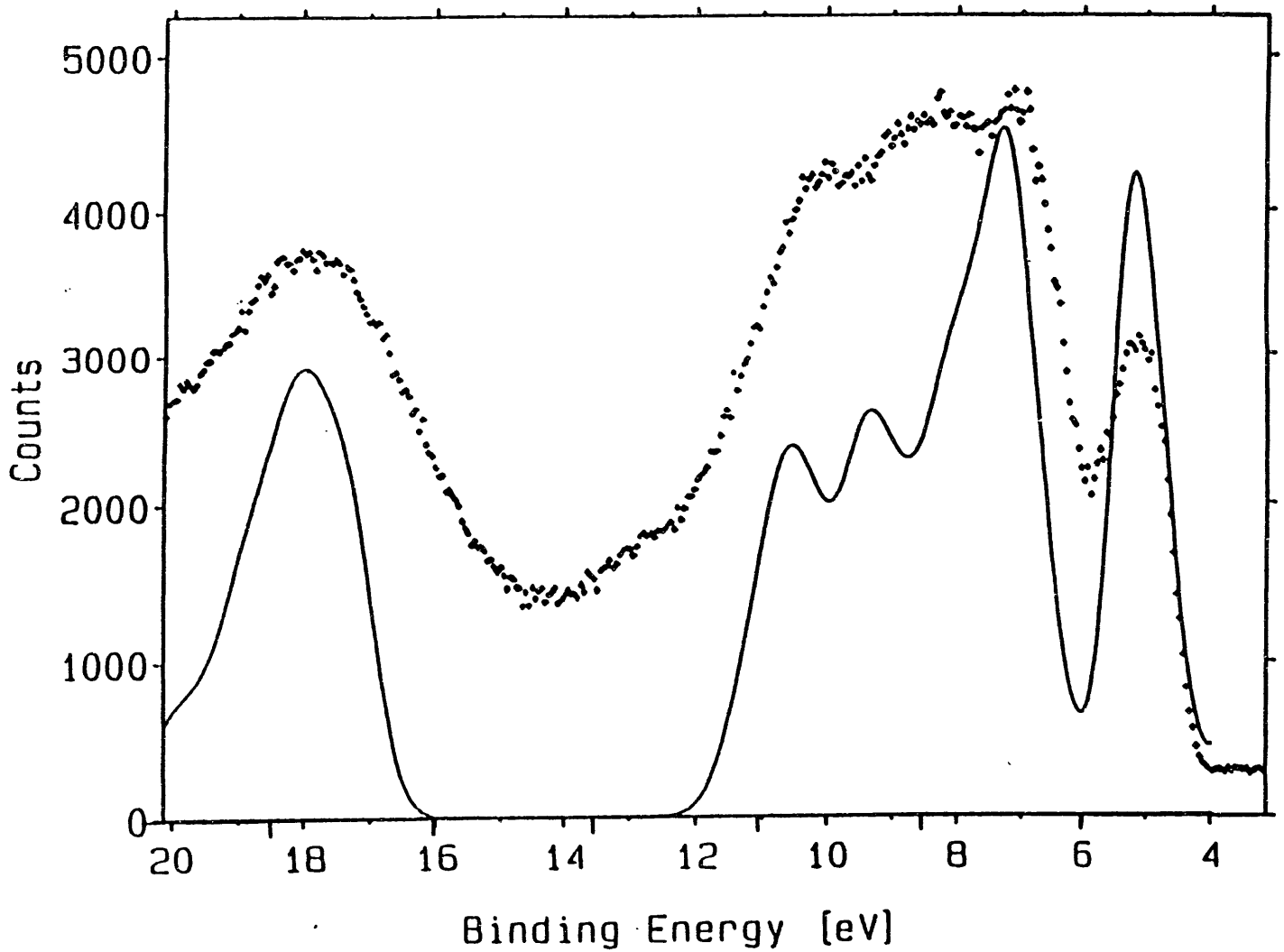

Figure 55. Theoretical valence band of 2-D NbS_2 and experimental HR-ESCA valence band of polycrystalline NbS_{2-x}.

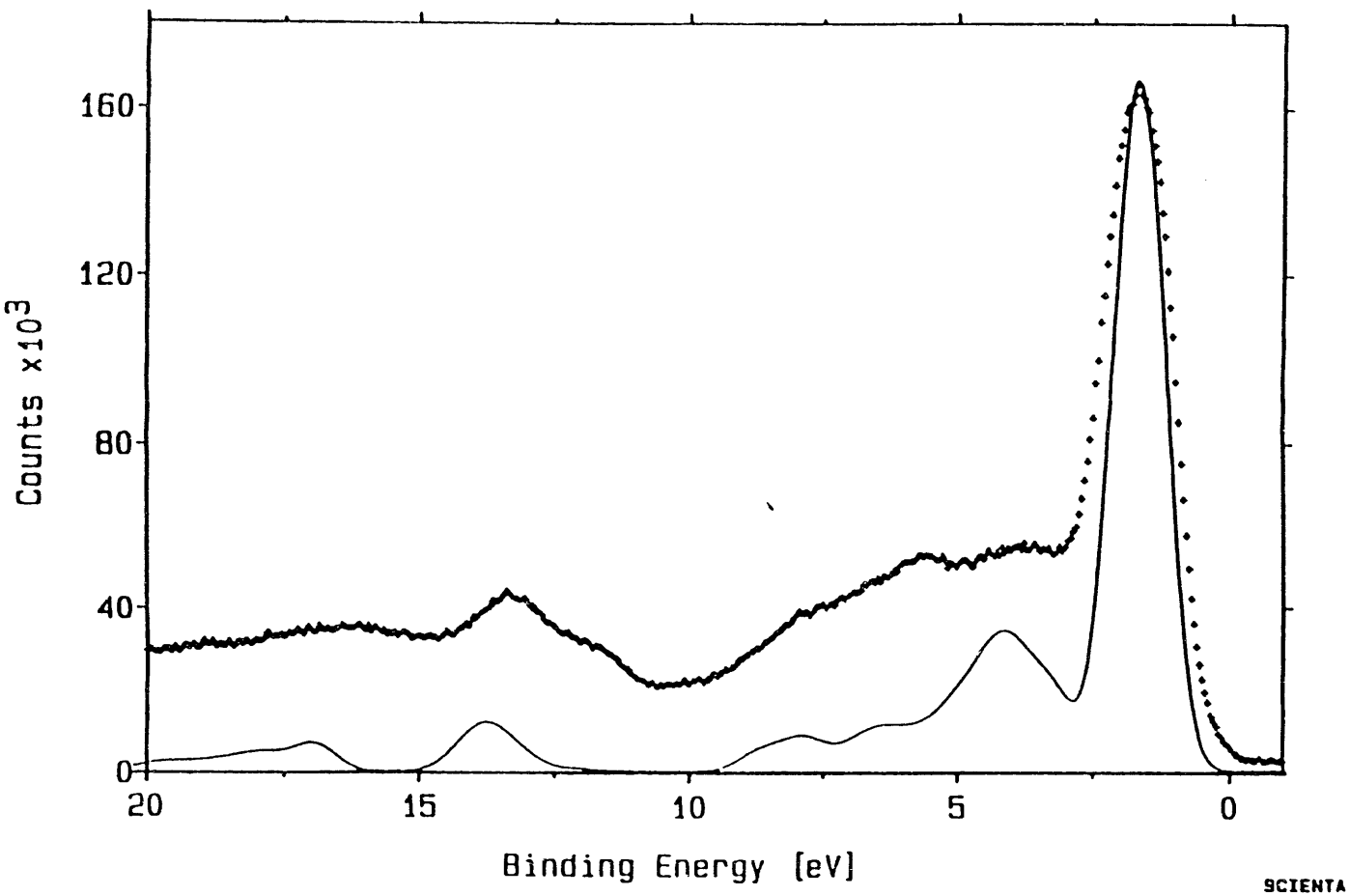

Figure 56. Theoretical valence band of 3-D RuS_2 and experimental HR-ESCA valence band of polycrystalline RuS_2.

primarily due to the large Scofield cross-section of the Ru4d orbitals.

Overall, theoretical valence bands of 2-D NbS_2, 2-D MoS_2 and 3-D RuS_2 calculated using Extended Hückel theory qualitatively reproduce the major features present in the experimental valence bands of polycrystalline NbS_{2-x}, MoS_2 and RuS_2. Parametrization of the S3s and S3p ionization potentials, H_{ii}, and Slater-type orbital coefficients, c_i, and exponents, ζ_i, was carried out using the experimental valence band of MoS_2. The same set of S3s and S3p atomic parameters were used with some agreement between theory and experiment for NbS_2 and RuS_2. In theory, this set of atomic parameters should produce accurate representations of any transition metal disulfide valence band providing that atomic parameters for the transition metal 4d orbitals can be obtained.

6.5 Theoretical Charges Related to Core Level Binding Energy Shifts.

Edge surface species have been detected in previous XPS experiments. Recent studies of Roxlo et al. have focused on lithographically producing stable edge surfaces on molybdenum disulfide single crystals.[62] In this technique a thin film of MoS_2 was cleaved from a single crystal parallel to the basal plane. The thin MoS_2 film was then mounted on a substrate and covered with monodisperse polystyrene spheres. Subsequent Ar^+ ion bombardment followed by removal of the polymer, resulted in removal of MoS_2 not coated by the spheres leaving "posts" of MoS_2 up to a depth of ca. 15 Å. From a transmission electron micrograph, the posts are estimated to be ca. 0.096 μ high (ca. 960 Å) with a diameter of 0.20 μ (ca. 2000 Å). Molybdenum 3d core levels obtained via XPS on lithographically textured MoS_2 samples indicate the presence of two molybdenum oxidation states. The Mo3d core levels of the lithographically textured sample were broadened as compared to the Mo3d core levels of basal plane MoS_2. Curve fitting of the $Mo3d_{5/2}$ peak resulted in two peaks, the first located at 229.0 eV was attributed to bulk Mo^{+4}; the second located at 228.2 eV was attributed to edge molybdenum species that were reduced to Mo^{+3}.

The theoretical studies involving 1-D $(MoS_2)_5$ terminating at $(10\bar{1}0)$ and $(10\bar{1}1)$ edges should predict reduction of coordinatively unsaturated edge molybdenum atoms. Section 5.3.3 discusses the theoretical charges of 1-D $(MoS_2)_5$ systems calculated using the parameters of Hughbanks and Hoffmann (Reference 41). The structure terminating in $(10\bar{1}0)$ edges possesses 2- and 6-coordinate edge molybdenum atoms. If the charges of basal plane molybdenum atoms, Mo-0201, Mo-0401 and Mo-0501 are averaged, an average basal plane molybdenum charge of +0.76 is obtained. The 2- and 6-coordinate edge molybdenum atom (Mo-0101 and Mo-0301) charges are +0.87 and +1.47 respectively. Thus, both edge molybdenums are

oxidized relative to the bulk. The structure terminating in $(10\bar{1}1)$ edges possesses 4- and 5-coordinate edge molybdenum atoms. If the charges of basal plane molybdenum atoms, Mo-0201, Mo-0401 and Mo-0501 are averaged, an average basal plane molybdenum charge of +0.67 is obtained. The 4- and 5-coordinate edge molybdenum atom (Mo-0101 and Mo-0301) charges are +0.69 and +1.25 respectively. Thus, again both edge molybdenums are oxidized relative to the bulk. Solid state Extended Hückel theory using the parameters of Hughbanks and Hoffmann does not correctly predict reduction of coordinatively unsaturated edge molybdenum atoms. Theoretical edge molybdenum atom oxidation instead of reduction could be attributed to the use of Hughbanks and Hoffmann atomic parameters instead of the ESCA parameters of Table 25. Errors could also be introduced if in the real system, sulfur atoms attached to coordinatively unsaturated edge molybdenum atoms relax as evidenced by the Raman detection of the S_2 species. Then, edge geometries used in the theoretical 1-D $(MoS_2)_5$ systems would be incorrect. As mentioned previously, higher levels of theory that include geometry optimization are necessary for determining whether relaxation can be predicted theoretically. The XPS study of Roxlo et al. showed only the Mo3d levels of lithographically textured edges of MoS_2. It would be interesting to see the corresponding S2p region of these edges. As indicated in Section 4.1.3, $S2p_{3/2}$ photoelectron peaks for pyritic (S_2^{-2}) and layered (S^{-2}) compounds appear at binding energies of 162.5 eV and 161.8 eV respectively. If as predicted from Raman, S_2 species do exist on MoS_2 edges then XPS should be able to detect these species since the separation between S_2^{-2} and S^{-2} species is 0.70 eV.

When the parameters of Table 25 are used in the calculation of 1-D $(MoS_2)_5$ terminating at $(10\bar{1}1)$ edges, a result consistent with the experimental XPS of MoS_2 edges is obtained. Charges on the molybdenum atoms, Mo-0101, -0201, -0301, -0401, and -0501 are the following: +0.95, +1.16, +1.68, +1.09, and +1.26. If the charges of basal plane molybdenum atoms, Mo-0201, Mo-0401 and Mo-0501 are averaged, an average basal plane molybdenum charge of +1.17 is obtained. The 4- and 5-coordinate edge molybdenum atom charges are +0.95 and +1.68 respectively. Thus, the 5-coordinate edge molybdenum atom is oxidized relative to the bulk while the 4-coordinate edge molybdenum atoms is reduced relative to the bulk. Thus, in solid state extended Hückel calculations, charges, energies and binding enthalpies depend highly on the atomic orbital parameters of the basis set.

The most reasonable theoretical charges for MoS_2, NbS_2, and RuS_2 systems were obtained when the atomic parameters of Tables 25, 27 and 29 were used as input. For MoS_2, theoretical charges for both 2-D and 3-D systems were calculated. In layered 2-D MoS_2, theoretical molybdenum and sulfur charges were the following: +0.99 and -0.50. While in

layered 3-D MoS_2, theoretical molybdenum and sulfur charges were the following: +1.33 and -0.67. Thus, addition of layers in the c direction increased charge transfer from molybdenum to sulfur species. In layered 2-D NbS_2, theoretical niobium and sulfur charges were the following: +1.75 and -0.87. Theoretical charges of 3-D NbS_2 are also expected to display increased charge transfer from niobium to sulfur species upon addition of layers in the c direction. In pyritic 3-D RuS_2, theoretical ruthenium and sulfur charges were the following: +0.94 and -0.47.

Binding energies for the $S2p_{3/2}$ core levels obtained via HR-ESCA for pyritic RuS_2 and layered MoS_2 and NbS_2 were the following: 162.59 eV, 161.88 eV and 161.82 eV respectively. Thus, sulfur atoms in both layered and pyritic structures are reduced relative to a zero-valent species. However, sulfur atoms in layered compounds are reduced to a greater extent than sulfur atoms in pyritic compounds. As mentioned in Section 4.1.3, the S2p core levels can be used to distinguish pyritic-type sulfur from layered-type sulfur. Theoretical charges show the same trend in sulfur oxidation state as the HR-ESCA experiment. Since the escape depth of S2p photoelectrons is fairly large ca. 36 Å (see Section 2.3.1), theoretical charges of 3-D systems should be compared to the HR-ESCA experiment. Theoretical sulfur charges of layered 3-D MoS_2 and pyritic 3-D RuS_2 are -0.67 and -0.47 respectively. Thus experimentally and theoretically, sulfur atoms in MoS_2 are reduced relative to sulfur atoms in RuS_2.

Experimental HR-ESCA positions the $Mo3d_{5/2}$ core level of polycrystalline MoS_2 at 229.05 eV. Thus in polycrystalline MoS_2, molybdenum appears at a higher binding energy relative to a molybdenum species in the metallic state ($Mo3d_{5/2}$ positioned at 227.7 eV). The +1.35 shift in $Mo3d_{5/2}$ binding energy from molybdenum metal to MoS_2 indicates oxidation of the molybdenum in MoS_2. In 3-D MoS_2, the theoretical charge on molybdenum is +1.33. Thus experimentally and theoretically, molybdenum atoms in MoS_2 are oxidized relative to molybdenum metal. Experimental HR-ESCA positions the $Ru3d_{3/2}$ core level of polycrystalline RuS_2 at 279.96 eV (see Section 4.1.3). However, previous XPS investigations on sulfided $RuCl_3$ supported on Al_2O_3 place the $Ru3d_{5/2}$ core level at 280.2 eV.[63] The $Ru3d_{5/2}$ core level of ruthenium metal was located at 280.05 eV. Thus the Ru3d core levels do not shift significantly upon oxidation. The theoretical charge on ruthenium in 3-D RuS_2 is +0.94. Thus experimentally and theoretically, ruthenium atoms in RuS_2 are oxidized relative to ruthenium metal. Errors in the $Ru3d_{5/2}$ binding energy position of this study could have been due to inaccurate calibration of the HR-ESCA.

Experimental and theoretical trends in transition metal and sulfur oxidation states agreed qualitatively. However, quantitative agreement between theory and experiment depends on the component parts of the charge potential model developed by Siegbahn and reproduced in

Equation 15. Binding energy shifts vary with changes in oxidation states and potentials. Thus, theoretical calculations of HR–ESCA binding energy shifts depend on the accuracy of theoretical charges and on correctly calculating the potential in ionic solids. This potential depends on correctly choosing a unit cell that does not possess a dipole moment. Further evaluation of the potentials in transition metal disulfides is needed before exact correlation of the experimental binding energy shifts with theoretical charges can be made.

6.6 Angle Resolved HR–ESCA of Single Crystal MoS_2.

Use of angle resolved ESCA for studies of molybdenum coordination in MoS_2 is only feasible for basal plane molybdenum atoms. Due to the high stability of the basal plane, edge planes larger than the spot size analyzed by the SCIENTA ESCA–300 spatial lens have not been synthesized. The spatial lens is used to magnify the area of the sample from which electrons are detected. In this study, pass energies of 75 eV were used resulting in an analyzed sample area of 3.9 mm $\times$ 110 μ. As mentioned above, recent studies of Roxlo et al. have focused on lithographically producing stable edge surfaces on molybdenum disulfide single crystals.[62] Although, the lithography produces well ordered edge planes (0.096 μ high and 0.20 μ in diameter), these planes are still smaller than the spot size analyzed by the spatial lens. At this time, angle resolved HR–ESCA of MoS_2 edge surfaces is not feasible.

As discussed in Section 4.3.3, forward focusing of molybdenum photoelectrons by basal plane sulfur atoms is seen for single crystal MoS_2. At a constant polar angle of 49°, intense maxima in $Mo3d_{5/2}$ and $Mo3d_{3/2}$ photoelectron area occurs at azimuthal angles of 5° and 72° see Figure 28d. Due to inaccuracies in the azimuthal rotational control knob, the exact value of the azimuthal angle may be in error. However despite the inaccuracies of the azimuthal angle, the relative difference between these two directions is 67°, very close to the expected difference of 60°. Forward focusing of second atomic layer molybdenum photoelectrons by first atomic layer sulfur atoms at a constant polar angle of 49° is predicted to occur at the following azimuthal angles: 0°, 120°, and 240°. These three angles correspond to directions parallel to the three Mo–S bonds. Forward focusing of fifth atomic layer molybdenum photoelectrons by fourth atomic layer sulfur atoms at a constant polar angle of 49° is also predicted to occur at the following azimuthal angles: 60°, 180°, and 300°. Thus at a constant polar angle of 49°, maxima in Mo3d photoelectron area are expected every 60°. At this point forward focusing of second atomic layer molybdenum photoelectrons by first atomic layer sulfur atoms can not be distinguished from forward focusing of fifth atomic layer molybdenum photoelectrons by fourth atomic layer sulfur atoms. Intuitively, forward focusing of fifth atomic layer molybdenum photoelectrons would be

expected to exhibit decreased photoelectron area compared to forward focusing of second atomic layer molybdenum photoelectrons by first atomic layer sulfur atoms due to a higher probability for multiple scattering events. Theoretical simulation of forward focusing on MoS_2 that includes multiple scattering effects would help in differentiating the two previously discussed cases.

In Figures 28a, 28b, and 28c are shown the $Mo3d_{5/2}$ (and $Mo3p_{3/2}$ in 28a and 28c) photoelectron areas versus polar angle at constant azimuthal angles of 0°, 30° and 60° respectively. As mentioned previously, designation of the azimuthal angle was arbitrary. In this study, the 0° azimuth (Figure 28a) corresponds approximately to the position of the 5° maximum in the previous study of photoelectron area versus azimuthal angle (see Figure 29d). The 60° azimuth (Figure 28c) corresponds approximately to the position of the 72° maximum shown also in Figure 29c. The 30° azimuth corresponds to a direction intermediate between the two previous and close to the position of the minimum in $Mo3d_{5/2}$ photoelectron intensity seen in Figure 29d. In Table 17a is shown a tabulation of the polar angles, azimuthal angles, and distance between emitter and scatterer for forward focusing of molybdenum photoelectrons. The closest emitter to scatterer distance is found for forward focusing of second atomic layer molybdenum photoelectrons by first atomic layer sulfur atoms and for fifth atomic layer molybdenum photoelectrons by fourth atomic layer sulfur atoms. Both types of forward focusing will be seen at polar angles of 49.1°. Intense maxima in $Mo3d_{5/2}$ and $Mo3p_{3/2}$ photoelectron area are seen at polar angles of 0° and 48° for the 0° azimuth (Figure 28a). Intense maxima in $Mo3d_{5/2}$ and $Mo3p_{3/2}$ photoelectron area are seen at polar angles of −2° and 47° for the 60° azimuth (Figure 28c). The aforementioned polar angle maxima are very close to the forward focusing maxima of 0° and 49.1° calculated from the MoS_2 basal plane geometry. Intense maxima in $Mo3d_{5/2}$ photoelectron area are seen at −3° and 36° for the 30° azimuth (Figure 28b). The most notable feature of this study is the minimum in $Mo3d_{5/2}$ photoelectron intensity at a polar angle of 48° for the 30° azimuth and corresponding maximum at a polar angle of $\sim 48°$ for the 0° and 60° azimuth. A maximum is also observed at a polar angle of 36° for the 30° azimuth. Again, using the values of Table 17a, this maximum could be attributed to forward focusing of fifth atomic layer molybdenum photoelectrons by first and or third atomic layer sulfur atoms at polar angles of 39.3° and 34.6° respectively. For the 0° azimuth, smaller maxima occur at approximately 14°, 31° and 37°. For the 60° azimuth, smaller maxima occur at approximately 12° and 30°. The smaller maxima could originate from either of the following processes: forward focusing or first order diffraction from forward focusing.

As indicated in Table 17b, forward focusing of sulfur photoelectrons is also expected to occur at various polar and azimuthal angles on basal plane MoS_2. However the sulfur core

levels are of much weaker intensity than the Mo3d core levels. Thus, trends in S2p photoelectron area will be less easily observed. A preliminary study was performed on basal plane MoS_2 where the Mo3d, S2p and S2s photoelectron areas were followed versus polar and azimuthal angles. Maxima in S2p photoelectron area were observed but were not as well defined as the corresponding Mo3d maxima (for example see Figure 28d). Thus, the core levels of molybdenum were primarily used in these studies.

Chapter 7
CONCLUSIONS

7.1 General Conclusions.

With reference to the questions posed in the Introduction (Chapter 1), the following general conclusions can be drawn from the theoretical and experimental results: (1) Solid state Extended Hückel theory can be used to assess the dispersion characteristics and orbital nature of the MoS_2 energy dispersion curves. (2) Addition of edges to theoretical MoS_2 systems results in the formation of unoccupied edge states at or above the Fermi level. (3) Theoretical binding enthalpies for hydrogen atom adsorption on MoS_2 systems indicate that basal plane sulfur sites and coordinatively unsaturated edge molybdenum sites are thermodynamically favorable. The relative stability of sulfur sites compared to molybdenum sites depends on the relative positions of the H1s, S3s, S3p, and Mo4d ionization potentials. (4) Parametrization of the S3s, S3p and Mo4d ionization potentials and Slater-type orbital coefficients, c_i, and exponents, ζ_i, with the HR-ESCA MoS_2 valence band led to qualitative agreement between theoretical and experimental valence bands. (5) Use of the parametrized S3s and S3p ionization potentials, coefficients and exponents for electronic structure calculations of RuS_2 and NbS_2 led to qualitative agreement between theoretical and experimental valence bands. (6) Theoretical sulfur charges in general reflected the trend in S2p binding energy shifts for layered and pyritic transition metal disulfides. At this point, direct correlation between theoretical charges and experimental HR-ESCA binding energy shifts was not made. (7) Angle resolved HR-ESCA of single crystal MoS_2 was carried out. Forward focusing of Mo3d photoelectrons by first layer and fourth layer sulfur atoms was observed at a polar angle of 49° and at azimuthal angles separated by 60°. Each of these conclusions will be discussed in more detail in the following paragraphs.

7.1.1 Orbital Character

Extended Hückel theory has been successfully used to assess the dispersion characteristics and orbital nature of the MoS_2 energy dispersion curves. A direct gap (K→K) was calculated for the 2-D MoS_2 system while an indirect gap (Γ→K) was calculated for the 3-D MoS_2 system. Electronic structure calculations of 3-D MoS_2 involved interactions of crystal orbitals across the Van der Waals gap resulting in splitting of the highest occupied band at Γ. Theoretical destabilization of 3-D MoS_2 compared to 2-D MoS_2 can be traced to larger energy destabilization of bands involving antibonding overlap of crystal orbitals across the Van der Waals gap versus smaller energy stabilization of bands involving bonding overlap of crystal

orbitals across the Van der Waals gap. Van der Waals interactions involving electron correlation are not included in Extended Hückel theory which is essentially a one-electron theory. Addition of attractive Van der Waals forces into the theoretical calculations in the form of treatment of electron correlation should stabilize 3-D MoS_2 with respect to 2-D MoS_2.

7.1.2 Addition of Edges to MoS_2

Electronic structure studies of 1-D $(MoS_2)_5$ systems led to the conclusion that addition of edges results in the formation of unoccupied edge states at and above the Fermi level. HR-ESCA valence band comparisons of single crystal and polycrystalline MoS_2 show higher intensity on the low binding energy side of the experimental $Mo4d_{z2}$ band (the highest occupied band) in the sample containing a higher number of edge sites, polycrystalline MoS_2. Below the edge of the indirect gap, optical absorption also increased as the number of edge impurities was increased. The theoretical calculations show that occupation of edge states located at or above the Fermi level will contribute to higher intensity on the low binding energy side of the highest occupied band. Edge states residing at or above the Fermi level possess mainly Mo4d character with some mixture of $Mo4d_{yz}$ and $Mo4d_{zx}$ orbitals from edge molybdenum atoms.

7.1.3 MoS_2 Hydrogen Adsorption

Binding enthalpies for hydrogen adsorption on molybdenum and sulfur sites on various molybdenum disulfide systems were calculated. Of the sulfur sites, fully-coordinated basal plane sites were favored over 1-coordinate and 2-coordinate edge sites on all of the systems studied. Basal plane sulfur sites on systems terminating in edges were favored over basal plane sites of an infinite sheet. Of the molybdenum sites, 2-, 3-, 4- and 5-coordinate edge sites were favored in that order over fully-coordinated basal plane sites. Basal plane molybdenum sites on systems terminating in edges were favored over basal plane sites of an infinite sheet. The relative stability of the sulfur sites compared to the molybdenum sites depended on the relative positions and separations of the S3s, S3p, Mo4d ionization potentials from the H1s ionization potential of -13.6 eV. The parameters of Hughbanks and Hoffmann placed the S3p orbitals at -13.3 eV, 0.3 eV from the H1s orbitals. Use of the atomic parameters of Hughbanks and Hoffmann tended to stabilize the sulfur sites relative to the molybdenum sites. Thus, the order of stability (in terms of binding enthalpy) was as follows: 2-coordinate edge Mo > 3-coordinate edge Mo > 3-coordinate basal plane S > 1- and 2-coordinate edge S > 4-coordinate edge Mo > 5-coordinate edge Mo > 6-coordinate basal plane Mo. The parameters of Table 25 placed the S3p orbitals at -8.845 eV, 4.755 eV from the H1s orbitals. Use of the atomic parameters of Table 25 tended to

destabilize the sulfur sites and stabilize the molybdenum sites relative to the calculations involving the parameters of Hughbanks and Hoffmann. The order of stability was as follows: 4–coordinate edge Mo > 3–coordinate basal plane S > 2–coordinate edge S > 5–coordinate edge Mo > 1–coordinate edge S > 6–coordinate basal plane Mo.

The theoretical hydrogen results lend support to the conclusions of Komatsu and Hall (Reference 21). Komatsu and Hall conclude from their experimental evidence that edge dissociation of hydrogen is followed by diffusion of hydrogen atoms to basal plane sites. The calculations show that coordinatively unsaturated edge molybdenum atoms and basal plane sulfur atoms are thermodynamically favorable for binding of hydrogen. Thus it is possible that hydrogen molecules are initially dissociated on 2–, 3–, 4–, or 5–coordinate edge molybdenum atoms. Subsequent transfer of hydrogen atoms from edge sites to basal plane sulfur sites enables the edge planes to dissociate more hydrogen molecules. IINS experiments of H_xMoS_2 samples indicate the presence of S–H bonds.[17,18] The calculations indicate that these sites are probably hydrogen bound to basal plane sulfur.

Charge transfer due to hydrogen adsorption onto molybdenum and sulfur sites in 1–D $(MoS_2)_5$ terminating at $(10\bar{1}1)$ edges and a $(MoS_2)_{19}$ cluster terminating at $(10\bar{1}0)$ edges was also studied. Adsorption onto 2– and 4–coordinate molybdenum sites resulted in transfer of electrons from bulk and edge molybdenum atoms to the negatively charged Mo–H species. Adsorption of hydrogen onto edge and basal plane sulfur atoms resulted in transfer of electrons from the positively charged S–H species to basal plane and edge molybdenum atoms. Thus, transfer or depletion of electrons was provided by the molybdenum lattice while the sulfur lattice was relatively unaffected. This result is consistent with the comments of Komatsu and Hall (Reference 21) on reductive hydrogen adsorption.

HR–ESCA valence band analysis of hydrogen exposed polycrystalline MoS_2, indicated extra intensity at the top of the valence band. Due to the large basal plane area, most of the bound hydrogen is probably found on basal plane sulfur atoms. Theoretical binding of hydrogen to basal plane sulfur sites results in transfer of electrons from the S–H species to edge plane molybdenum atoms. Edge states reside at or above the Fermi level and occupation of these states by electrons leads to increased intensity at the top of the valence band.

7.1.4 Parametrization of Theoretical MoS_2 Valence Band

Comparison of 2–D MoS_2 theoretical valence bands with the experimental HR–ESCA valence band of polycrystalline MoS_2 led to parametrization of the S3s, S3p and Mo4d atomic

ionization potentials, H_{ii}, Slater-type coefficients, c_i, and exponents, ζ_i. Theoretical valence bands were obtained by summation of modified atomic orbital populations, MAOPOP's. MAOPOP's were obtained by multiplication of individual atomic orbital populations by the appropriate Scofield cross-sections. The theoretical valence band of 2-D MoS_2 calculated using Extended Hückel theory and the atomic parameters of Table 25 qualitatively reproduces the experimental HR-ESCA valence band of polycrystalline MoS_2. The theoretical conduction band of 2-D MoS_2 also qualitatively reproduces the experimental inverse photoemission spectroscopy conduction band of single crystal MoS_2.

7.1.5 Theoretical NbS_2 and RuS_2 Valence Bands

The S3s and S3p atomic parameters found from parametrization of 2-D MoS_2 were also used to study the theoretical valence bands of 2-D NbS_2 and 3-D RuS_2. The theoretical valence bands of 2-D NbS_2 and 3-D RuS_2 calculated using solid state Extended Hückel theory and the atomic parameters of Tables 27 and 29, qualitatively reproduce the experimental HR-ESCA valence bands of polycrystalline NbS_{2-x} and RuS_2. However, the theoretical S3s region of 2-D NbS_2 was found to exhibit a smaller full width at half maximum than the experimental S3s region.

7.1.6 Theoretical Sulfur Charges Related to Experimental Binding Energy Shifts

Theoretical sulfur charges in general reflected the trend in S2p binding energy shifts for layered and pyritic transition metal disulfides. Binding energies for the $S2p_{3/2}$ core levels obtained via HR-ESCA for pyritic RuS_2 and layered MoS_2 were the following: 162.59 eV and 161.88 eV. Theoretical sulfur charges of pyritic 3-D RuS_2 and layered 3-D MoS_2 are -0.47 and -0.67 respectively. Thus experimentally and theoretically, sulfur atoms in MoS_2 are reduced relative to sulfur atoms in RuS_2. At this point, direct correlation between theoretical charges and experimental HR-ESCA binding energy shifts was not made.

7.1.7 Angle Resolved HR-ESCA of Single Crystal MoS_2

Angle resolved HR-ESCA of single crystal MoS_2 showed the existence of forward focusing at a polar angle of ca. 49° and at azimuthal angles separated by 60°. Forward focusing of second atomic layer molybdenum photoelectrons by first atomic layer sulfurs was shown to occur at the following azimuthal angles: 0°, 120° and 240° (arbitrary designation of 0°). Forward focusing of fifth atomic layer molybdenum photoelectrons by fourth atomic layer sulfurs was

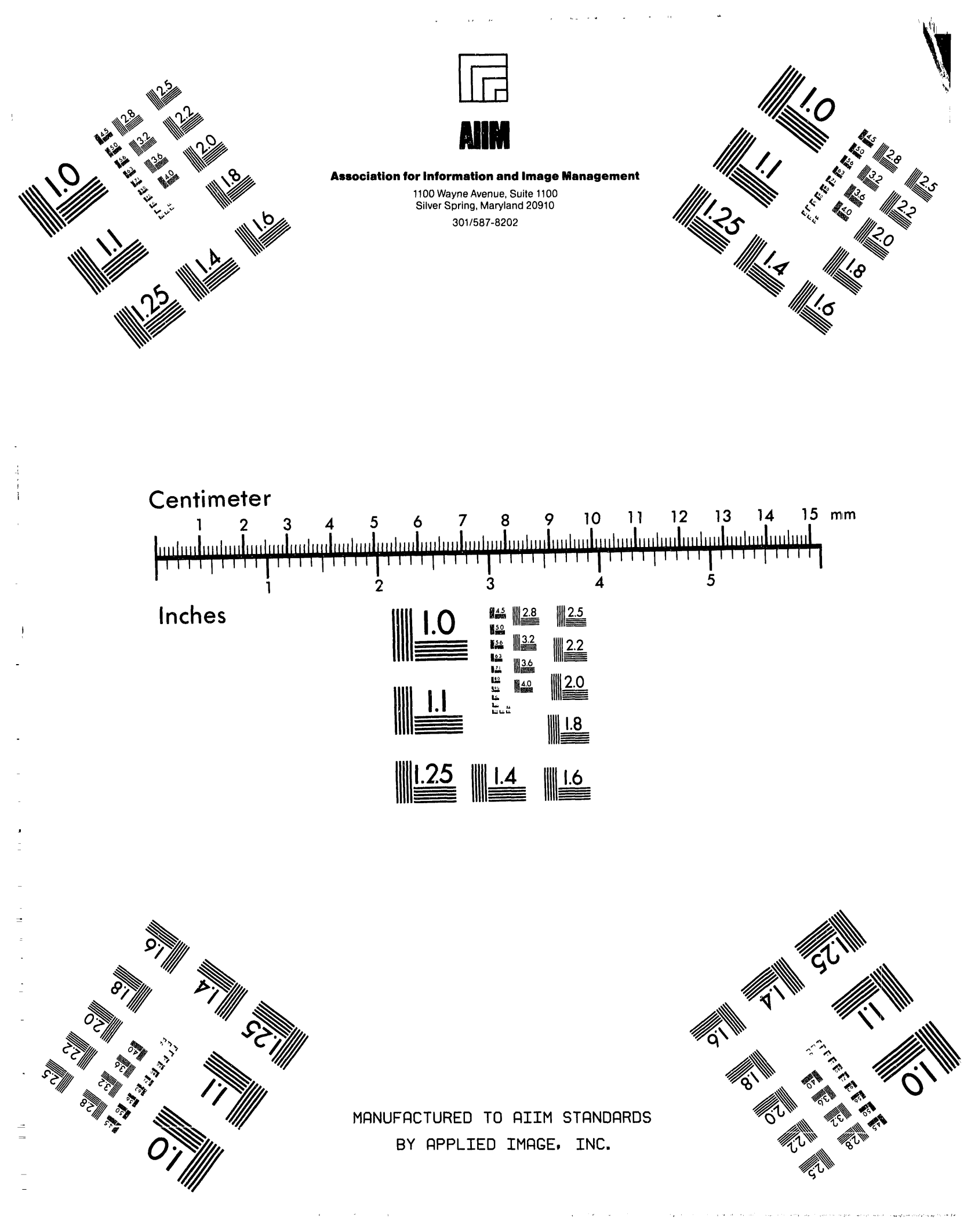
AIIM
Association for Information and Image Management
1100 Wayne Avenue, Suite 1100
Silver Spring, Maryland 20910
301/587-8202
Centimeter
Inches
MANUFACTURED TO AIIM STANDARDS
BY APPLIED IMAGE, INC.

4 of 4

shown to occur at the following angles: 60°, 180° and 300°. Thus in MoS_2, forward focusing predominates even when the molybdenum atom is located 7.73 Å from the surface. Due to the high stability of the basal plane, edge planes larger than the spot size analyzed by the SCIENTA ESCA-300 spatial lens have not been synthesized. At this time, angle resolved HR-ESCA of MoS_2 edge surfaces is not feasible.

Although the theoretical work discussed in this report is fairly complete, some experimental work on single crystal and polycrystalline MoS_2 could be carried out to support the theoretical results. For instance, energy dispersion of the S3s bands in MoS_2 has been theoretically predicted from solid state Extended Hückel theory. A simple UPS experiment of single crystal MoS_2 using a He_{II} source would show whether the S3s bands, shown as Bands #1 and #2 for the 2-D MoS_2 system, do in fact show the dispersion characteristics predicted by solid state Extended Hückel theory. As mentioned previously, hydrogen adsorption experiments detected only hydrogen bound sulfur species, S-H. A good *in situ* optical absorption experiment of MoS_2 hydrogen exposure needs to be carried out to complete the hydrogen studies.

DISCLOSURE

Portions of this work have been published in the following article:

"Structure and Surface Properties of Sulfides," K. Klier, M. Richards and R. G. Herman, in Synthesis and Properties of New Catalysts: Utilization of Novel Materials, Components, and Synthetic Techniques, ed. by W. Corcoran, Jr., M. J. Ledoux, and J. R. Knox, Materials Research Society, 157 (1990).

REFERENCES

1. C.W. Curtis and D.R. Cahela, Energy & Fuels, 3, 168 (1989).

2. T.A. Pecoraro and R.R. Chianelli, J. Catal., 67, 430 (1981).

3. J. G. Santiesteban, C. E. Bogdan, R. G. Herman, and K. Klier, 9th International Congress on Catalysis, 561 (1988).

4. M.A. Mays, Pure & Appl. Chem., 61, 1373 (1989).

5. J.W. Pasterczyk, L.E. Iton, M. Winterer, T.R. Krause, S.A. Johnson, and V.A. Maroni, Symposium on Natural Gas Upgrading II, San Francisco Mtg., Volume 37, (The Division of Petroleum Chemistry, Inc. ACS, Washington, D.C.: April, 1992) p. 349.

6. R.A. Bromley, R.B. Murray, and A.D. Yoffe, J. Phys. C, 5, 759 (1972).

7. R.A. Bromley, Phys. Lett., 33A, 242 (1970).

8. R.V. Kasowski, Phys. Rev. Lett., 30, 1175 (1973).

9. D.W. Bullett, J. Phys. C, 11, 4501 (1978).

10. R. Coehoorn, C. Haas, J. Dijkstra, C.J.F. Flipse, R.A. de Groot, and A. Wold, Phys. Rev. B, 35, 6195 (1987).

11. R. Coehoorn, C. Haas, and R.A. de Groot, Phys. Rev. B, 35, 6203 (1987).

12. A.B. Anderson, Z.Y. Al-Saigh, and W.K. Hall, J. Phys. Chem., 92, 803 (1988).

13. C.B. Roxlo, R.R. Chianelli, H.W. Deckman, A.F. Ruppert, and P.P. Wong, J. Vac. Sci. Technol. A, 5, 555 (1987).

14. K.S. Liang, G.J. Hughes, and R.R. Chianelli, J. Vac. Sci. Technol. A, 2, 991 (1984).

15. R. Mamy, A. Boufelja, and B. Carricaburu, Phys. Stat. Sol. b, 141, 467 (1987).

16. C.J. Wright, C. Sampson, D. Fraser, R.B. Moyes, and P.B. Wells, J.C.S. Faraday I, 76, 1585 (1980).

17. C. Sampson, J.M. Thomas, S. Vasudevan, and C.J. Wright, Bull. Soc. Chim. Belg., 90, 1215 (1981).

18. S. Vasudevan, J.M. Thomas, C.J. Wright, and C. Sampson, J. Chem. Soc., Chem Commun., 419 (1982).

19. A. Blackburn and P.A. Sermon, J. Chem. Tech. Biotechnol., 33A, 120 (1983).

20. P. N. Jones, E. Knözinger, W. Langel, R.B. Moyes, and J. Tomkinson, Surf. Sci., 207, 159 (1988).

21. T. Komatsu and W. K. Hall, J. Phys. Chem., 95, 9966 (1991).

22. S. Harris, Chem. Phys., 67, 229 (1982).

23. N.A.W. Holzwarth, S. Harris, and K.S. Liang, Phys. Rev. B, 32, 3745 (1985).

24a. W.F. Egelhoff, Jr., Phys. Rev. B, 30, 1052 (1984);

24b. W.F. Egelhoff, Jr., J. Vac. Sci. Technol., A2, 350 (1984).

25. H.C. Poon and S.Y. Tong, Phys. Rev. B, 30, 6211 (1984).

26. W. F. Egelhoff, Jr., Sol. State & Mat. Science, 16, 213 (1990).

27. A. P. Kadwela, G. S. Herman, D. J. Friedman, C. S. Fadley, and J. J. Rehr, Physica Scripta, 41, 948 (1990).

28. M.-L. Xu, J. J. Bartman and M. A. Van Hove, Phys. Rev. B., 39, 8275 (1989).

29. J. G. Santiesteban, "Alcohol Synthesis From Carbon Monoxide and Hydrogen Over MoS_2-Based Catalysts," Ph.D. Dissertation, (Department of Chemistry, Lehigh University: May 1989).

30. T.A. Pecoraro and R.R. Chianelli, J. Catal., 67, 430 (1981).

31. D. R. Lide, ed., "CRC Handbook of Chemistry and Physics," 71^{st} ed., (CRC Press, Boca Raton: 1990).

32 P.W. Atkins, "Physical Chemistry," 3rd ed., (W. H. Freeman and Co., New York: 1986), p.779.

33. M. Kieke, "Preparation and Characterization of Niobium Disulfide Catalysts," M.S. thesis, (Department of Chemistry, Lehigh University: Dec. 1991).

34. B. D. Cullity, "Elements of X-Ray Diffraction," 2nd ed., (Reading, Massachusetts: Addison-Wesley Publishing Company, Inc., 1978).

35. P. T. Clarke, "Standard Stereograms for Materials Science," (London: Her Majesty's Stationary Office, 1976).

36. A. G. Knapp, Surf. Sci., 34, 289 (1973).

37. M. P. Seah and W. A. Dench, Surf. and Int. Anal., 1, 2 (1979).

38. M.-H. Whangbo, M. Evain, T. Hughbanks, M. Kertesz, S. Wijeyesekera, C. Wilker, C. Zheng, and R. Hoffmann, "Extended Hückel Molecular, Crystal and Properties Package," QCPE 571.

39. R. Hoffmann, J. Chem. Phys., 39, 1397 (1963).

40a. D.J. Chadi and M.L. Cohen, Phys. Rev. B, 8, 5747 (1973).

40b. H.J. Monkhorst and J.D. Pack, Phys. Rev. B, 13, 5188 (1976).

40c. D.J. Chadi, Phys. Rev. B, 16, 1746 (1977).

40d. J.D. Pack and H.J. Monkhorst, Phys Rev. B, 16, 1748 (1977).

41. T. Hughbanks and R. Hoffmann, J. Am. Chem. Soc., 105, 1150 (1983).

42. E. Clementi and C. Roetti, Atomic Data and Nuclear Data Tables, 14, 177 (1974).

43. R. H. Williams and A. J. McEvoy, Phys. Stat. Sol. B, 47, 217 (1971).

44. C. A. Papageorgopoulos, Surf. Sci., 75, 17 (1978).

45. J. H. Scofield, J. Elec. Spectr. Rel. Phen., 8, 129 (1976).

46. U. Gelius in "Electron Spectroscopy," ed. D. A. Shirley (North–Holland Pub.Co., Amsterdam: 1971), 311.

47. J. A. Wilson and A. D. Yoffe, Advan. Phys., 18, 193 (1969).

48. C. Kittel, "Introduction to Solid State Physics," 6^{th} ed., (John Wiley & Sons, New York: 1986).

49. Sutarno, O. Knop, and K. I. G. Reid, Can. J. Chem., 45, 1391 (1967).

50. A. Eucken, "Landolt–Bőrstein," 1(4), (Springer–Verlag, Berlin: 1955), 32.

51. N. Elliott, J. of Chem. Phys., 33, 903 (1960).

52. C. D. Wagner, W. M. Riggs, L. E. Davis, J. F. Moulder, and G. E. Muilenberg, "Handbook of X–ray Photoelectron Spectroscopy," (Perkin–Elmer Corp., Eden Prairie, Minnesota: 1979).

53. D. Briggs and M.P. Seah, "Practical Surface Analysis," Volume 1 (John Wiley & Sons, New York: 1990).

54. D. Briggs and M. P. Seah, "Practical Surface Analysis," 2nd ed., (John Wiley & Sons, New York: 1933).

55. T. D. Henson, D. Sarid, and L. S. Bell, The Royal Microscopical Society, (1988).

56. K. C. Mills, "Thermodynamic Data for Inorganic Sulphide, Selenides and Tellurides," (Butterworths, London: 1974).

57. N.V. Smith in "Photoemission in Solids I", ed. M. Cardona and L. Ley, (Springer–Verlag, Berlin: 1978), 242.

58. M. Sancrotti, L. Braicovich, C. Chemelli, and G. Trezzi, Sol. State. Commun., 66, 593 (1988).

59. J. Polz, H. Zeilinger, B. Müller, and H. Knözinger, J. Catal., 120, 22 (1989).

60. S. S. Lin, Y. S. Huang, C. R. Huang, and M. C. Lee, Sol. St. Comm., 69, 589 (1989).

61. L. F. Mattheiss, Phys. Rev. Lett., 30, 784 (1973).

62. C. B. Roxlo, H. W. Deckman, J. Gland, S. D. Cameron, R. R. Chianelli, Science, 235, 1629 (1987).

63. J. A. De Los Reyes, S. Göbölös, M. Vrinat, and M. Breysse, Catal. Lett., 5, 17 (1990).

64. R. Huisman, R. De Jonge, C. Haas, and F. Jellinek, J. Sol. State Chem., 3, 56 (1971).

65. I. N. Levine, "Quantum Chemistry", 3rd ed., (Allyn and Bacon, Inc., Boston, Mass.: 1983).

Appendix A

CALCULATION OF ENERGIES OF FORMATION FROM EHMACPP

A.1 Energy of Formation of 2-D MoS_2.

$$Mo^0\,(g) \rightarrow Mo^{+6}(g) + 6\,e- \qquad \Delta U_1 = 6 \times I_{4d} \qquad \text{A.1.1}$$

$$2 \times \left\{ S^0\,(g) \rightarrow S^{+6}(g) + 6\,e- \qquad \Delta U_2 = (4 \times I_{3p}) + (2 \times I_{3s}) \right\} \qquad \text{A.1.2}$$

$$Mo^{+6}(g) + 2\,S^{+6}(g) + 18\,e- \rightarrow MoS_2(s) \qquad \Delta U_3 = \text{EHT Energy} \qquad \text{A.1.3}$$

$$Mo^0(g) + 2\,S^0(g) \rightarrow MoS_2(s) \qquad \Delta U_4 = \Delta U_1 + (2 \times \Delta U_2) + \Delta U_3 \qquad \text{A.1.4}$$

The energy of 2-D MoS_2 can be obtained from the above reaction scheme. The energy of reaction A.1.3, ΔU_3, is calculated from solid state extended Hückel theory by placing all of the electrons into the lowest energy levels. For instance, in the case of 2-D MoS_2, there is one MoS_2 per unit cell. Each molybdenum and sulfur atom brings 6 electrons to the system. Thus, there are 18 electrons per MoS_2 unit. These electrons fill the 9 lowest energy crystal orbitals. By addition of the lowest 9 energy levels with subsequent multiplication by 2 one obtains the energy of reaction A.1.3, ΔU_3. The other energies, ΔU_1 and ΔU_2, are obtained from the ionization potentials, H_{ii}, input into the program for the Mo4d and S3s, 3p orbitals. The energy of formation, ΔU_4, is obtained by addition of the energies of reaction A.1.1, A.1.2, and A.1.3. Energies can be converted into enthalpies through the relationship $\Delta H = \Delta U + \Delta nRT$. In this relationship, Δn=the number of gas molecules (or atoms) in the product minus the number of gas molecules (or atoms) in the reactants, R=ideal gas constant, and T=temperature in Kelvin.

A.2 Energy of Formation of 1-D $(MoS_2)_5$ Systems.

$$5 \times \left\{ Mo^0\,(g) \rightarrow Mo^{+6}(g) + 6\,e- \qquad \Delta U_1 = 6 \times I_{4d} \right\} \qquad \text{A.2.1}$$

$$10 \times \left\{ S^0\,(g) \rightarrow S^{+6}(g) + 6\,e- \qquad \Delta U_2 = (4 \times I_{3p}) + (2 \times I_{3s}) \right\} \qquad \text{A.2.2}$$

$$5\,Mo^{+6}(g) + 10\,S^{+6}(g) + 90\,e- \rightarrow (MoS_2)_5(s) \quad \Delta U_5 = \text{EHT Energy} \qquad \text{A.2.3}$$

$$5\,Mo^0(g) + 10\,S^0(g) \rightarrow (MoS_2)_5(s) \qquad \Delta U_6 = (5 \times \Delta U_1) + (10 \times \Delta U_2) + \Delta U_5 \qquad \text{A.2.4}$$

The energy of 1-D $(MoS_2)_5$ can be obtained from the reaction scheme given above. The energy of reaction A.2.3, ΔU_5, is calculated from solid state extended Hückel theory by placing all of the electrons into the lowest energy levels. In $(MoS_2)_5$ there are 90 electrons and as a result 45 of the lowest energy levels will be filled. The energy of formation for $(MoS_2)_5$, ΔU_6

reaction A.2.4, can be divided by 5 to obtain an energy of formation per MoS_2 unit. This number can then be compared to the energy of formation of MoS_2, A.1.4.

A.3 Energy of Formation of 2-D H-MoS_2.

$Mo^0\,(g) \rightarrow Mo^{+6}(g) + 6\,e^-$	$\Delta U_1 = 6 \times I_{4d}$	A.3.1
$2 \times \{S^0\,(g) \rightarrow S^{+6}(g) + 6\,e^-$	$\Delta U_2 = (4 \times I_{3p}) + (2 \times I_{3s})\}$	A.3.2
$H^0\,(g) \rightarrow H^+(g) + 1\,e^-$	$\Delta U_7 = I_{1s}$	A.3.3
$Mo^{+6}(g) + 2\,S^{+6}(g) + H^+(g) + 19\,e^- \rightarrow H\text{-}MoS_2(s)$	ΔU_8=EHT Energy	A.3.4
$Mo^0(g) + 2\,S^0(g) + H^0(g) \rightarrow H\text{-}MoS_2(s)$	$\Delta U_9 = \Delta U_1 + (2 \times \Delta U_2) + \Delta U_7 + \Delta U_8$	A.3.5

The energy of formation of 2-D H-MoS_2 can be obtained from the reaction scheme given above. This reaction scheme is similar to that for the formation of 2-D MoS_2, Section A.1, except for the addition of the hydrogen atom. The binding energy of hydrogen atoms on the 2-D MoS_2 system, ΔU_{10}, can be obtained from a scheme incorporating the energy of formation of the bare surface, ΔU_4, and the energy of formation of the hydrogen covered surface, ΔU_9. This reaction scheme is given in equations A.3.6–A.3.8.

$Mo^0(g) + 2\,S^0(g) + H^0(g) \rightarrow H\text{-}MoS_2(s)$	ΔU_9	A.3.6
$MoS_2(s) \rightarrow Mo^0(g) + 2\,S^0(g)$	$-\Delta U_4$	A.3.7
$MoS_2(s) + H^0(g) \rightarrow H\text{-}MoS_2(s)$	$\Delta U_{10} = \Delta U_9 - \Delta U_4$	A.3.8

The binding energy of a hydrogen molecule with the MoS_2 surface can also be obtained from the dissociation energy of the hydrogen molecule, ΔU_{11}, and ΔU_{10}. This energy can be found from the reaction scheme given in equations A.3.9–A.3.11. Thus, a theoretical prediction as to whether a hydrogen molecule has a thermodynamic tendency to adsorb on the surface can be made. Enthalpies can be obtained from the relationship, $\Delta H = \Delta U + \Delta nRT$, as discussed in A.1.

$\frac{1}{2}\,H_2(g) \rightarrow H^0\,(g)$	ΔU_{11}	A.3.9
$MoS_2(s) + H^0(g) \rightarrow H\text{-}MoS_2(s)$	ΔU_{10}	A.3.10
$MoS_2(s) + \frac{1}{2}\,H_2(g) \rightarrow H\text{-}MoS_2(s)$	$\Delta U_{12} = \Delta U_{11} + \Delta U_{10}$	A.3.11

A.4 Energy of Formation of 1-D H-$(MoS_2)_5$ Systems.

$5 \times \{Mo^0\ (g) \rightarrow Mo^{+6}(g) + 6\ e^-$	$\Delta U_1\}$	A.4.1
$10 \times \{S^0\ (g) \rightarrow S^{+6}(g) + 6\ e^-$	$\Delta U_2\}$	A.4.2
$H^0(g) \rightarrow H^+(g) + 1\ e^-$	ΔU_7	A.4.3
$5\ Mo^{+6}(g) + 10\ S^{+6}(g) + H^+(g) + 91\ e^- \rightarrow (MoS_2)_5(s)$	ΔU_{13}=EHT Energy	A.4.4
$5\ Mo^0(g) + 10\ S^0(g) + H^0(g) \rightarrow H\text{-}(MoS_2)_5(s)$	ΔU_{14}	A.4.5

The energy of formation of a 1-D H-$(MoS_2)_5$ system can be obtained from the reaction scheme given above. In equation A.4.5 ΔU_{14}, the energy of formation of H-$(MoS_2)_5$, is equal to the following sum: $(5 \times \Delta U_1)+(10 \times \Delta U_2)+\Delta U_7+\Delta U_{13}$. The binding energy of hydrogen atoms on the $(MoS_2)_5$ surface (or edges) can be obtained from the reaction scheme given in equations A.4.6–A.4.8. Binding energies of hydrogen molecules on the 1-D $(MoS_2)_5$ surface can be obtained from the reaction scheme given in equations A.4.9–A.4.11.

$5\ Mo^0(g) + 10\ S^0(g) + H^0(g) \rightarrow H\text{-}(MoS_2)_5(s)$	ΔU_{14}	A.4.6
$(MoS_2)_5(s) \rightarrow 5\ Mo^0(g) + 10\ S^0(g)$	$-\Delta U_6$	A.4.7
$(MoS_2)_5 + H^0(g) \rightarrow H\text{-}(MoS_2)_5(s)$	$\Delta U_{15}=\Delta U_{14}-\Delta U_6$	A.4.8

$\frac{1}{2}\ H_2(g) \rightarrow H^0\ (g)$	ΔU_{11}	A.4.9
$(MoS_2)_5(s) + H^0(g) \rightarrow H\text{-}(MoS_2)_5(s)$	ΔU_{15}	A.4.10
$(MoS_2)_5(s) + \frac{1}{2}\ H_2(g) \rightarrow H\text{-}(MoS_2)_5(s)$	$\Delta U_{16}=\Delta U_{11}+\Delta U_{15}$	A.4.11

Appendix B
EXTENDED HÜCKEL CLUSTER CALCULATIONS

B.1 Molybdenum Disulfide Cluster Calculations.

Calculations of the electronic structure of MoS_6^{n-} (where n=0 , 2, 4, 6, 8) trigonal prisms and stoichiometric $(MoS_2)_n$ clusters have been carried out using the extended Hückel method described previously in Section 3.1. Ionization potentials H_{ii}, orbital exponents ζ_i and orbital coefficients c_i for the Mo5s, Mo5p, Mo4d and S3s, S3p valence orbitals were taken from the work of Hughbanks and Hoffmann (Reference 41) and are given in Table 1.

B.1.1 Trigonal Prismatic MoS_6^{n-} Clusters.

The electronic structure of the trigonal prismatic MoS_6^{n-} cluster was studied first by varying the negative charge n on the cluster. Geometric parameters for the atoms of the MoS_6^{n-} cluster are given in Table B-1. Parameters for this cluster are taken from the solid state geometry of crystalline 2H-MoS_2. In this geometry, the symmetry of the MoS_6^{n-} trigonal prism is D_{3h}. The angle, θ, existing between the C_3 axis and the Mo-S bonds is 49.515°.

Table B-1

Cartesian coordinates of the atoms in a MoS_6^{n-} trigonal prism. The coordinates are obtained from the solid state lattice parameters (**a**, **b**, **c**, u) of crystalline 2H-MoS_2. Units are in Å.

Atom	x	y	z
Mo	0.	0.	0.
S_1	1.580000	-0.912213	1.5775
S_2	1.580000	-0.912213	-1.5775
S_3	-1.580000	-0.912213	1.5775
S_4	-1.580000	-0.912213	-1.5775
S_5	0.	1.824427	1.5775
S_6	0.	1.824427	-1.5775

Energy level diagrams for the MoS_6^{n-} cluster and the NbS_6^{n-} cluster are shown in Figure B-1. The NbS_6^{n-} cluster will be discussed in Section B.2. Ligand field theory predicts a splitting of the d orbitals when a molybdenum atom is coordinated to six sulfur ligands in a trigonal prismatic environment. This theory predicts that the Mo4d_{z2} orbital is split from the degenerate 4d_{x2-y2} and 4d_{xy} orbitals which are split from the degenerate 4d_{zx} and 4d_{xy} orbitals. In $(MoS_6)^{n-}$ clusters this splitting occurs in the following energy order: $d_{z2} < d_{x2-y2}$, $d_{xy} < d_{zx}$, d_{yz}. Molecular orbital (MO) #25 has an energy of -9.98 eV and consists primarily of Mo4d_{z2}

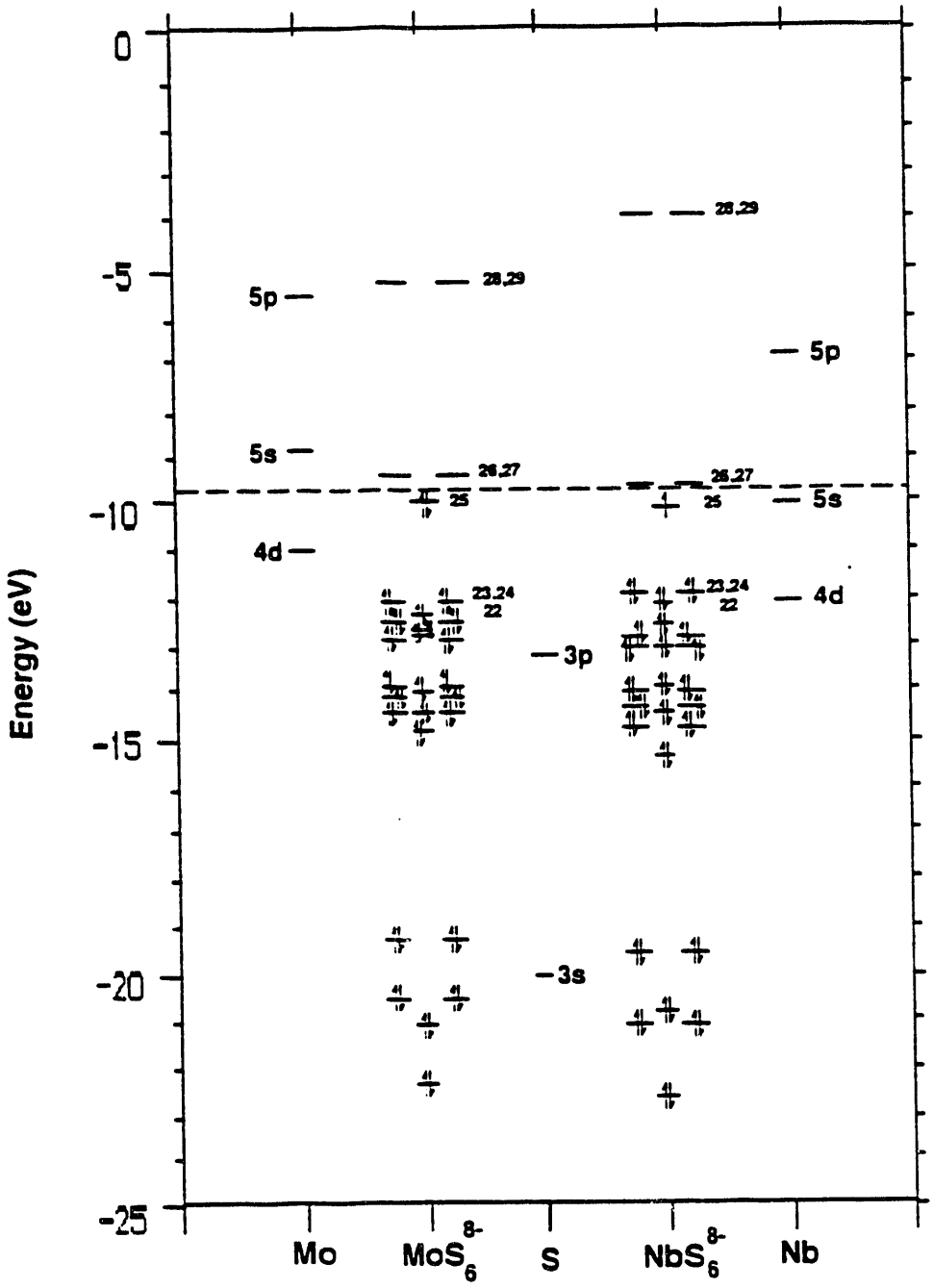

Figure B-1 Energy level diagrams of the MoS_6^{n-} and NbS_6^{n-} clusters. Energy values are in eV.

character (−0.9732) and S3p character such that the six Mo–S bonds are antibonding. For MO #25, the contribution of the Mo4d_{z2} orbital to the total wavefunction can be obtained from the Mo4d_{z2} coefficient resulting from the extended Hückel calculation. The total wavefunction for each energy level is made up of linear combinations of atomic orbitals (LCAO's) such that $\psi_j = \sum_i c_{ij}\chi_i$ where j=the index of the molecular orbital, i=the index of the atomic orbital, χ_i=atomic orbital i, c_{ij}=contribution of atomic orbital i to molecular orbital j, and ψ=total wavefunction for energy level j. For molecular orbital #25, the Mo4d_{z2} coefficient is −0.9732. Thus, MO #25 consists of primarily Mo4d_{z2} character. When the charge on the $(MoS_6)^{n-}$ cluster is 8−, the 25^{th} level is fully occupied by two electrons and is the highest occupied molecular orbital (HOMO) of the cluster. Molecular orbitals #26 and #27 are degenerate and have an energy of −9.52 eV. Molecular orbital #26 consists primarily of Mo4d_{xy} (−0.9110) and S3p character while MO #27 consists primarily of Mo4d_{x2-y2} (+0.9110) and S3p character. The d_{xy} (#26) and d_{x2-y2} (#27) levels are split from the d_{z2} (#25) level by 0.46 eV. Molecular orbitals #26 and #27 are the lowest unoccupied molecular orbitals (LUMO's) in the MoS_6^{8-} cluster. Molecular orbitals #28 and #29 are degenerate with an energy of −5.24 eV. Molecular orbital #28 consists of primarily Mo4d_{yz} (−0.9478) and S3s and S3p character while Mo #29 consists primarily of Mo4d_{zx} (+0.9478) and S3s and S3p character. The d_{yz} (#28) and d_{zx} (#29) levels are split from the d_{xy} (#26) and d_{x2-y2} (#27) levels by 4.28 eV. The large splitting of the Mo4d_{yz} and Mo4d_{zx} levels in MoS_6^{n-} clusters would seem to preclude mixing of these d levels with the other d levels. However, the d_{x2-y2} and d_{xy} degenerate levels are split from the d_{z2} level by only 0.46 eV in the MoS_6^{n-} cluster and mixing of these levels could occur in crystal orbitals. For instance in the 2-D MoS_2 system discussed in Section 5.1.1, the theoretical modified atomic orbital populations, MAOPOP's, for the Mo4d orbitals (Figure 27d) shows that the highest occupied crystal band consists of contributions from the Mo4d_{z2}, 4d_{xy}, and 4d_{x2-y2} orbitals in the following order: 4d_{z2}> 4d_{xy}> 4d_{x2-y2}. The lowest unoccupied crystal band consists of contributions from the same three Mo4d orbitals in the following order: 4d_{x2-y2}> 4d_{z2} $\simeq$ 4d_{xy}. The next lowest unoccupied band consists of contributions from only the Mo4d_{yz} and Mo4d_{zx} orbitals. Thus in 2-D MoS_2 systems, the d_{x2-y2} and d_{xy} levels mix with the d_{z2} level but these levels are still well separated from the d_{zx} and d_{yz} levels.

The gross electron population on the central molybdenum atom was studied as a function of the charge on the MoS_6^{n-} cluster. The gross electron populations on the molybdenum atom and the sulfur ligands for each charge are tabulated in Table B-2. As the cluster charge was increased from 0 to −6, the molybdenum gross electron population remained constant at a value of 3.94 while the sulfur gross electron population increased from 6.34 to 7.34.

However, when the cluster charge was increased from -6 to -8, the molybdenum gross electron population increased to 5.66 while the sulfur gross electron population increased by only 0.05 to 7.39. The reason for this change is apparent when the orbital character of molecular orbitals 21 to 25 is examined. Molecular orbitals 21, 22, 23, and 24 primarily consist of contributions from the 6 sulfur ligand 3p atomic orbitals. Thus, occupation of these levels by electrons does not change the overall molybdenum electron population but does increase the overall sulfur electron population. However, molecular orbital 25 consists of mainly molybdenum $4d_{z2}$ (-0.9732) with small contributions from the S3p atomic orbitals. Thus, occupation of this level by electrons will primarily increase the overall molybdenum electron population.

Table B-2

Gross electron populations of the central molybdenum atom and the sulfur ligands in the MoS_6^{n-} cluster as a function of the cluster charge, n. Also shown are the total number of electrons and the level of the highest occupied molecular orbital (HOMO) for each charge.

n	0	2	4	6	8
Total # e-	42	44	46	48	50
HOMO	21	22	23	24	25
Mo Gross e- Population	3.94	3.94	3.94	3.94	5.66
S Gross e- Population	6.34	6.68	7.01	7.34	7.39

A second study involved changing the angle (θ) between the C_3 axis and the Mo-S bond in the trigonal prismatic MoS_6^{8-} cluster while allowing the Mo-S bond distance to remain constant at 2.412 Å. In crystalline 2H-MoS_2, this angle has a value of 49.515°. Extended Hückel energies and Mo gross electron populations were calculated as a function of this angle where the angle was varied from 10° to 80° in increments of 10°. The results of this study are tabulated in Table B-3. As indicated in Table B-3, the MoS_6^{n-} cluster energy and Mo gross electron population decrease on changing the angle from 10° to 50°. As the angle is increased from 50° to 80°, the cluster energy and Mo gross electron population again increase. Figure B-2 plots the variation in the cluster energy vs the change in the angle between the C_3 axis and the Mo-S and Nb-S bonds. The NbS_6^{8-} cluster will be discussed in greater detail in Section B.2. A minimum in energy is obtained at θ=50° very close to the solid state angle of 49.515°. Thus, extended Hückel theory correctly predicts the geometry of the trigonal prism. The cause of the energy destabilization at θ<50° and θ>50° is due to the repulsion of electrons on the sulfur zligands. At small and large values of θ, sulfur ligands are located in close proximity to each

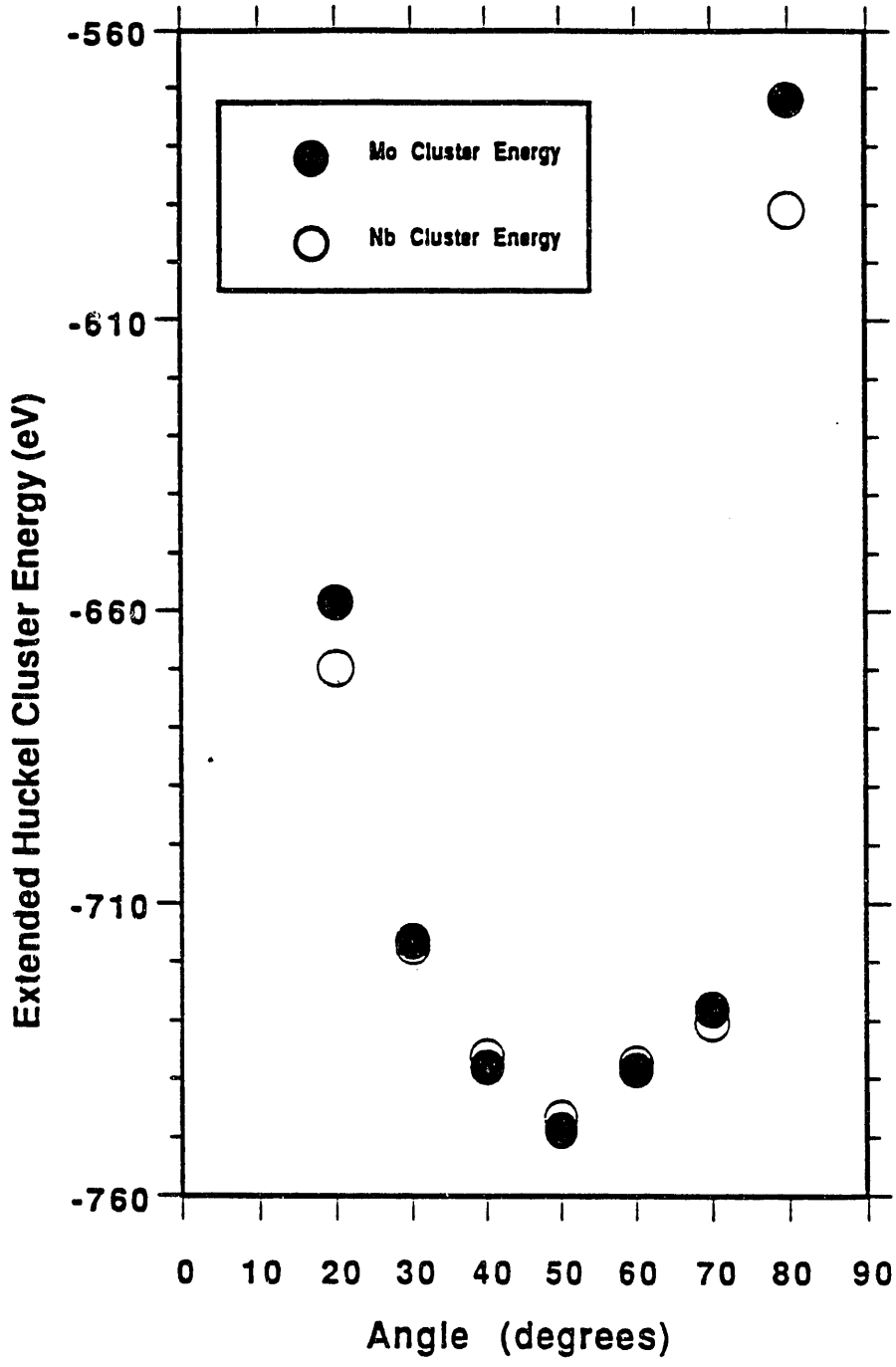

Figure B-2 Variation of the Extended Hückel energy as a function of the angle (θ) between the C_3 axis and the Mo–S and Nb–S bonds in MoS_6^{8-} and NbS_6^{8-}.

Table B-3

Extended Hückel energies and Mo and S gross electron populations as a function of the angle (θ) between the C_3 axis and Mo-S bond in MoS_6^{8-}.

θ	E(EHT), eV	Mo e- pop	S e- pop
10	-403.68	17.72	5.38
20	-658.51	14.07	5.99
30	-716.49	10.65	6.56
40	-738.04	7.29	7.12
50	-748.72	5.66	7.39
60	-738.39	9.24	6.79
70	-728.11	10.21	6.63
80	-572.03	13.73	6.04

other, due to repulsion of electrons residing on these ligands, electrons are transferred from the sulfur ligands to the central molybdenum atom of the cluster. Hence the large Mo gross electron population at small and large θ values. At θ=50°, the sulfur ligands are located almost at the maximum distance from each other. Thus, repulsion of electrons residing on the sulfur ligands is decreased and the gross electron population of the sulfur ligands reaches a maximum while that of the central molybdenum reaches a minimum.

If the splitting of the Mo4d levels is examined by a crystal-field calculation a minimum in energy is not obtained at 50° but rather at 58°. The crystal field splitting of the Mo4d levels in a MoS_6 trigonal prism was studied by R. Huisman et al in 1971.[67] In this study the five initially degenerate d levels of Mo are split into three levels E_0 ($4d_{z2}$), $E_{\pm 1}$($4d_{zx}$ and $4d_{yz}$), and $E_{\pm 2}$ ($4d_{x2-y2}$ and $4d_{xy}$) by the presence of the six point charges (Ze, Z=charge) representing the six sulfur ligands of the trigonal prism. The energy levels are given in Equations B-1, B-2, and B-3 and the parameters A, B, $\bar{r}^2$, and $\bar{r}^4$ are defined in Equations B-4, B-5, and B-6 respectively. The constant R represents the Mo-S bond distance of 2.412 Å while θ is the angle between the C_3 axis of the trigonal prism and the Mo-S bond.

$$E_0 = 2A\bar{r}^2 + 6B\bar{r}^4 \tag{B-1}$$

$$E_{\pm 1} = A\bar{r}^2 - 4B\bar{r}^4 \tag{B-2}$$

$$E_{\pm 2} = -2A\bar{r}^2 + B\bar{r}^4 \tag{B-3}$$

$$A = \left(\frac{3}{7}\right) \times \left(3\cos^2\theta - 1\right) \times \left(\frac{e^2Z}{4\pi\epsilon_0 R^3}\right) \tag{B-4}$$

$$B = \left(\frac{1}{28}\right) \times \left(35\cos^4\theta - 30\cos^2\theta + 3\right) \times \left(\frac{e^2Z}{4\pi\epsilon_0 R^5}\right) \tag{B-5}$$

$$\bar{r}^k = \int_0^\infty |R(r)|^2 \, r^{k+2} \, dr \tag{B-6}$$

If the Mo4d double zeta STO's of Hughbanks and Hoffmann (ζ_1=4.54, ζ_2=1.90, c_1=c_2=0.5899, Table 1) are used to obtain the $\bar{r}^k$ values of equation B-6 the values for $\bar{r}^2$ and $\bar{r}^4$ are the following: 3.21 $Å^2$ and 22.5 $Å^4$ respectively. The values of A and B and thus E_0, $E_{\pm 1}$, and $E_{\pm 2}$ then depend on the angle θ between the C_3 axis and the Mo-S bond. If the angle θ is varied from 40° to 65°, the ordering of the levels changes dramatically. At θ=40°, a crystal field calculation predicts that the degenerate $E_{\pm 2}$ levels are more stable than the E_0 level which is more stable than the degenerate $E_{\pm 1}$ levels (-5.02 eV, -0.05 eV, and 5.04 eV respectively). As the angle θ is increased from 40° to 46°, the degenerate $E_{\pm 2}$ levels destablilze in energy while the E_0 level stabilizes in energy. At θ>46°, the E_0 level is more stable than the degenerate $E_{\pm 2}$ levels. At θ=50°, close to the solid state value of 49.515°, the energies of the E_0, $E_{\pm 2}$, and $E_{\pm 1}$ levels are the following: -4.47 eV, -2.32 eV, and 4.56 eV. However, the energy of the E_0 level does not reach a minimum until $\theta \simeq 58°$. At this angle the energies of the E_0, $E_{\pm 2}$, and $E_{\pm 1}$ levels are the following: -5.43 eV, 0.13 eV, and 2.58 eV, respectively. Since the lowest level E_0 is occupied by two electrons, the lower energy of this level at $\theta \simeq 58°$ indicates a stable structure at this angle. Thus, a crystal field calculation of the splitting of the Mo4d levels by ligands in a trigonal prismatic environment is not sufficient to produce the correct angle between the C_3 axis and the Mo-S bond.

B.1.2 Stoichiometric $(MoS_2)_x$ Clusters.

The stability of $(MoS_2)_x$ clusters was studied as a function of the number of MoS_2 units or cluster size, x. The energy and gross electron populations of the central molybdenum and sulfur atoms were followed as a function of x. Figure B-3 shows the geometry of the largest cluster calculated, $(MoS_2)_{19}$. Table B-4 lists the structures studied as well as the energy per MoS_2 unit and the Mo and S gross electron populations. As the cluster size increases from 1 to 19, the energy of formation per MoS_2 unit decreases indicating stabilization of the larger clusters. The energy of formation of an infinite cluster with no edges, 2-D MoS_2, is -463.58 kcal/mole. Thus, 2-D MoS_2 is energetically the most stable structure calculated. Addition of van der Waals interactions was studied in the $(MoS_2)_{14}$ cluster. This cluster consists of two $(MoS_2)_7$ layers separated by the van der Waals spacing 2.995 Å. Addition of van der Waals interactions destabilizes the structure by 3.44 kcal/mole. This result is similar to the destabilization of the 3-D MoS_2 structure by 9.84 kcal/mole when compared to the 2-D MoS_2 structure discussed in Section 5.2.1.

Destabilization of the $(MoS_2)_{14}$ cluster and 3-D MoS_2 structure relative to the $(MoS_2)_7$ and 2-D MoS_2 structure respectively is mainly due to the antibonding interaction of the

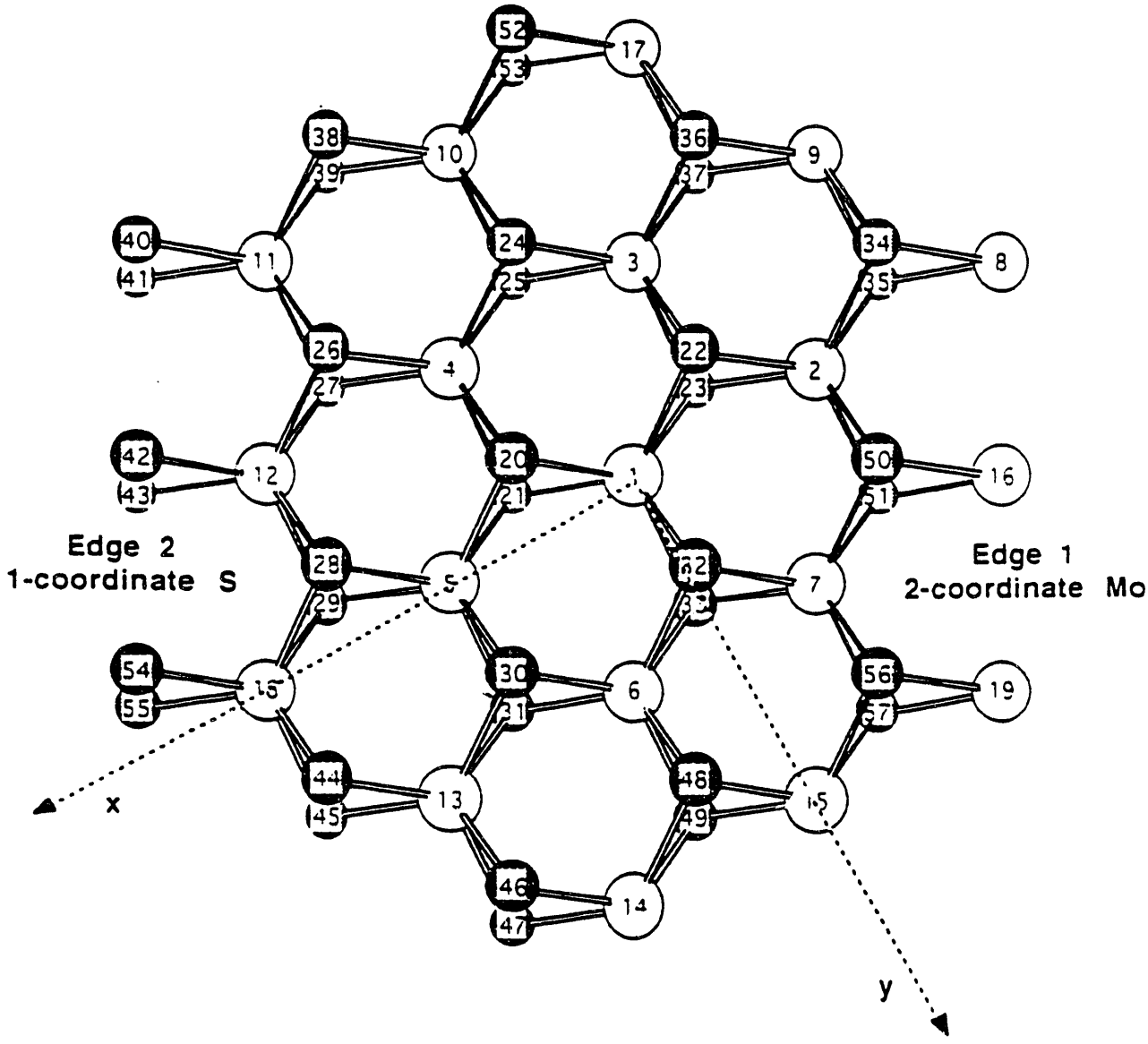

Figure B-3 Top view of the $(MoS_2)_{19}$ cluster terminating at the $(10\bar{1}0)$ edges. The edges of this cluster contain 2-coordinate Mo, 4-coordinate Mo, 1-coordinate S and 2-coordinate S. White Circles=Mo and Black Textured Circles=S.

Table B-4

Energy and gross electron populations of $(MoS_2)_x$ clusters as a function of the cluster size x.

Cluster	x	Description	$\Delta U/x$ ($\frac{kcal}{mole}$)	Gross Electron Populations: Mo-0101	S-0101
MoS_2	1	1 layer	-336.73	3.81	7.10
$(MoS_2)_7$	7	1 layer	-412.30	4.81	6.23
$(MoS_2)_{16}$	16	1 layer	-426.02	5.18	6.26
$(MoS_2)_{19}$	19	1 layer	-431.85	5.20	6.26
2-D MoS_2	∞	No edges	-463.58	5.44	6.28
$(MoS_2)_{14}$	14	2 layers of $(MoS_2)_7$	-408.86	4.82	6.19

molecular orbitals and crystal orbitals across the van der Waals gap. Van der Waals interactions or forces are not treated by extended Hückel theory. Van der Waals forces are a result of the attractive potentials arising from dipole–dipole, dipole–induced dipole, and induced dipole–induced dipole interactions. Induced dipole–induced dipole interactions (or dispersion forces) can be thought of as arising from an instantaneous dipole moment on one atom which subsequently induces an instantaneous dipole moment (induced dipole) on a second atom. Thus, electrons on the second atom sense and are affected by the presence of electrons on the first atom. Dispersion forces result from the instantaneous correlation between the motions of the electrons in one atom with the motions of the electrons in a second atom. In quantum mechanical calculations, correlation of electrons is treated by the occurence of a potential energy term in the true Hamiltonian $\hat{H}$ of $\frac{1}{2}\sum_{i \neq j}\frac{e^2}{|r_i - r_j|}$ where the double sum is over all of the i, j electrons in the system and $|r_i - r_j|$ is the difference in position of the two electrons i and j. For many electron systems such as the $(MoS_2)_{14}$ cluster and the 3-D MoS_2 structure, treatment of correlation is not computationally feasible. Extended Hückel theory treats the valence electrons as separate from the core level electrons and approximates the true hamiltonian as a sum of one electron hamiltonians. Correlation of electrons and thus van der Waals forces arising from the potential energy term involving electron–electron repulsion in the true hamiltonian is not treated explicitly in this theory. Background information for van der Waals forces and correlation was obtained from Reference 68.

When the central molybdenum (Mo-0101) gross electron populations are examined for the various cluster sizes, the population can be seen to increase as the cluster size increases. The increase levels off at higher cluster sizes and the highest population is obtained for $(MoS_2)_\infty$

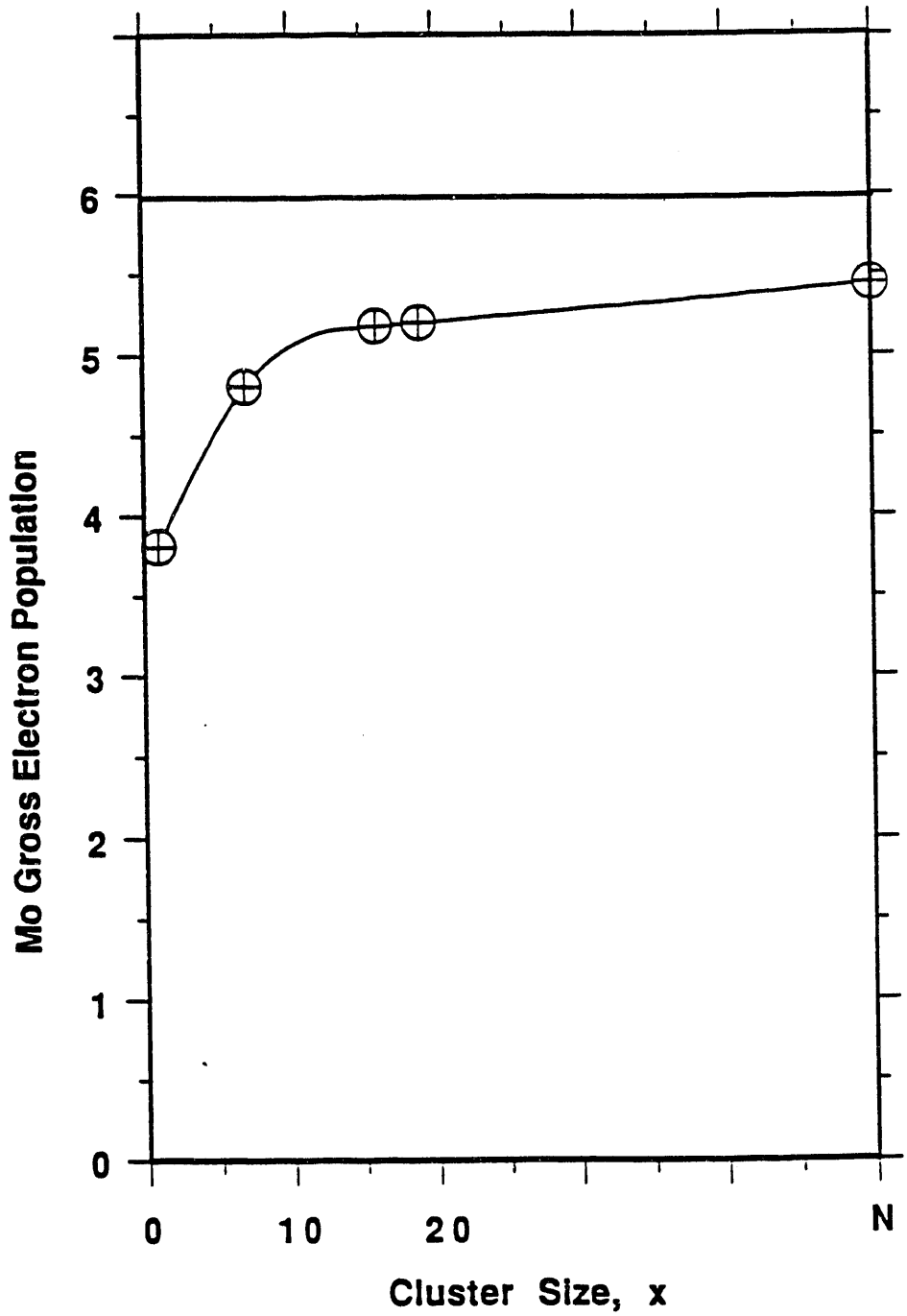

Figure B–4 Plot of the central molybdenum (Mo-0101) gross population vs. cluster size x for $(MoS_2)_x$ clusters. The Mo gross population reaches a maximum at 2-D MoS_2 or $(MoS_2)_\infty$.

(infinite cluster size no edges) modeled as 2-D MoS_2. Figure B-4 plots the central molybdenum (Mo-0101) gross electron population vs. cluster size for the cluster given in Table B-4.

B.1.3 Hydrogen Adsorption on $(MoS_2)_{19}$ Clusters Terminating at $(10\bar{1}0)$ Edges.

As discussed in the Introduction, the mechanism of hydrogen adsorption on polycrystalline MoS_2 is only poorly understood. Experimental studies such as neutron scattering and differential scanning calorimetry identify two different sites for hydrogen adsorption. Neutron scattering identifies a S-H bending mode that occurs upon occupation of the first site. However, no experiments have ever directly identified hydrogen bonded to molybdenum atoms. The IINS experiments of hydrogen adsorbed on polycrystalline MoS_2 carried out by Sampsom et al[17] and Vasudevan et al[18] identified an excitation at 872 cm^{-1} that was attributed to deformation modes of either Mo-O-H or Mo-H. The Mo-O-H species was thought to be the cause of this excitation since the excitation persisted even after exposure to air for a period of 4 weeks. In order to gain insight into possible hydrogen adsorption sites, extended Hückel calculations were carried out on $(MoS_2)_{19}$ clusters with hydrogen atoms placed at various basal and edge plane Mo and S atom sites. The 18 hydrogen sites studied are shown in Figure B-5 where the sites are labeled alphabetically. The $(MoS_2)_{19}$ cluster terminating at (1010) edges shown in Figure B-3 indicates the numerical labeling of the molybdenum (#1→#19) and sulfur (#20→#57) atoms. Sulfur atoms located on the top basal plane possess even numbers while those located on the opposite or lower basal plane possess odd numbers. No attempt was made at minimization of the H-$(MoS_2)_{19}$ energy with respect to the Mo-H and S-H bond distances. The Mo-H and S-H bond distances used were 1.7 Å and 1.35 Å respectively. The reasons for choosing the aforementioned Mo-H and S-H bond distances are given in Section 3.4.5.

The results of the hydrogen adsorption calculations are shown in Table B-5. The binding enthalpy was calculated as discussed in Appendix A.4. The sites are tabulated in order of increasing binding enthalpy and a description of the hydrogen adsorption site is given including the type of bond resulting from placement of hydrogen at each site and the original coordination of the closest atom. The descriptors side and top in the column labeled Bond in Table B-5 indicate the direction of the bonded hydrogen. On the $(MoS_2)_{19}$ basal plane, the Mo and S atoms are fully coordinated and hydrogen atoms are most likely to approach the surface from the top in the +z direction, perpendicular to the basal plane. On the cluster edges, the atoms are not fully coordinated and the descriptor side defines the approach of hydrogen as opposite that of the coordinated atoms.

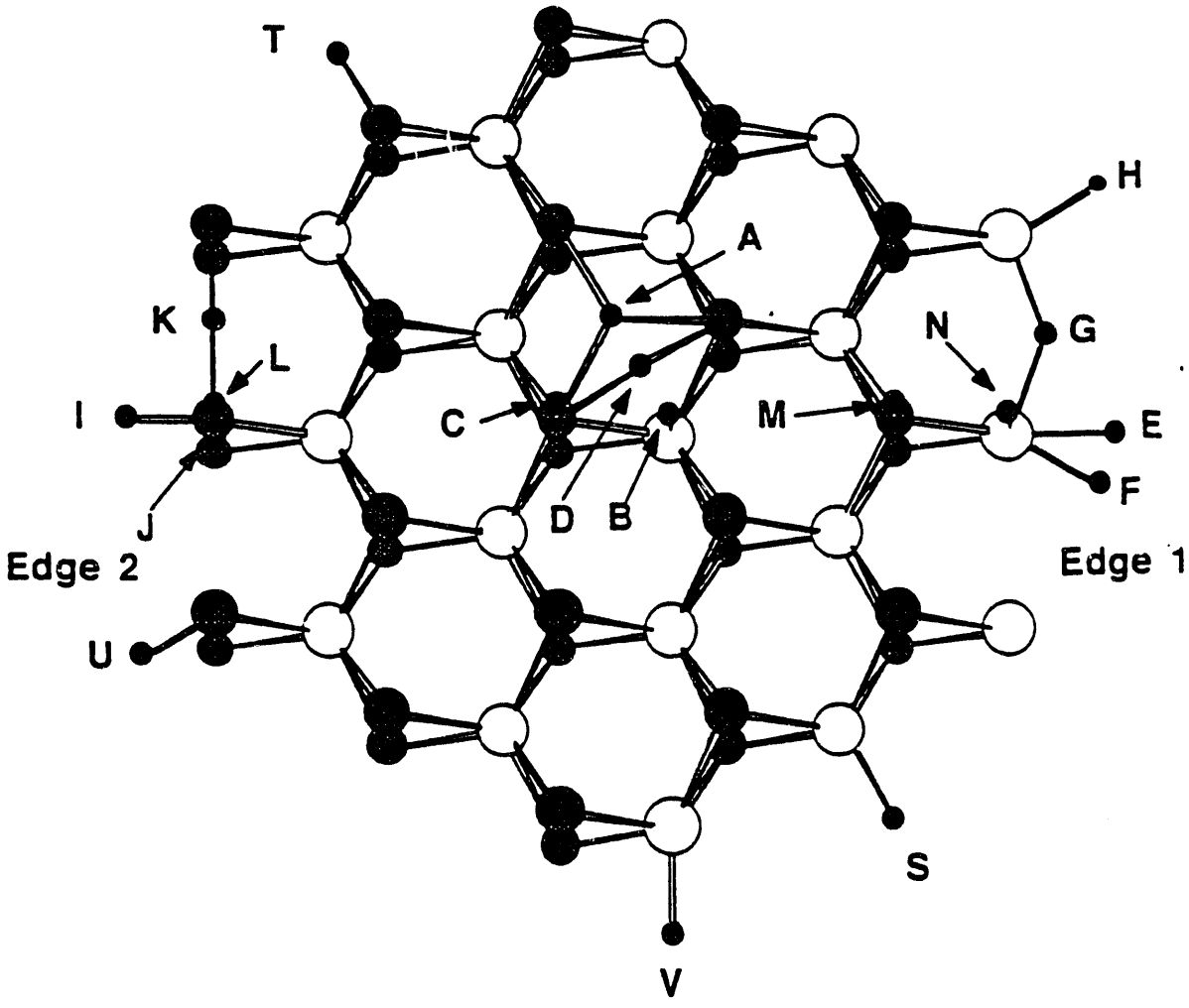

Figure B-5 The 18 hydrogen sites (identified alphabetically) studied on the $(MoS_2)_{19}$ cluster terminating in $(10\bar{1}0)$ type edges. White Circles=Mo, Black Circles=H, and Black Textured Circles=S.

Table B-5

Binding enthalpies of hydrogen atoms on the $(MoS_2)_{19}$ cluster terminating at the $(10\bar{1}0)$ edge. Hydrogen sites are labeled alphabetically and the position of each site on the cluster is shown in Figure B-5. The description gives the Mo or S atom number and coordination prior to hydrogen bonding. The bond gives the bond type and direction of the bonded hydrogen.

#	Site	$\Delta H(\frac{kcal}{mole})$	Description	Bond
1	E	-126.12	2-coordinate edge Mo_{16}	Mo-H side
2	H	-123.47	2-coordinate edge Mo_8	Mo-H side
3	F	-121.71	2-coordinate edge Mo_{16}	Mo-H side
4	G	-121.16	2-coordinate edge $Mo_{8,16}$	Mo-H-Mo side
5	S	-118.77	4-coordinate edge Mo_{15}	Mo-H side
6	V	-115.37	4-coordinate edge Mo_{14}	Mo-H side
7	C	-106.05	3-coordinate basal S_{20}	S-H top
8	M	-102.16	3-coordinate basal S_{50}	S-H top
9	L	-98.30	1-coordinate edge S_{42}	S-H top
10	T	-97.09	2-coordinate edge S_{38}	S-H side
11	I	-96.84	1-coordinate edge S_{42}	S-H side
12	U	-93.79	1-coordinate edge S_{54}	S-H side
13	N	-63.96	2-coordinate edge Mo_{16}	Mo-H top
14	K	-61.57	1-coordinate edge $S_{40,42}$	S-H-S
15	D	-42.56	3-coordinate basal $S_{20,22}$	S-H-S
16	J	-38.95	1-coordinate edge $S_{42,43}$	S-H-S
17	B	-27.03	6-coordinate basal Mo_1	Mo-H top
18	A	-16.29	3-coordinate basal $S_{20,22,24}$	3-fold S site

Theoretical hydrogen adsorption on $(MoS_2)_{19}$ clusters containing exposed 2-coordinate Mo, 4-coordinate Mo, 1-coordinate S and 2-coordinate S shows that the most thermodynamically favorable sites for hydrogen to adsorb are on exposed 2-coordinate and 4-coordinate Mo atoms. The approach of hydrogen from the side opposite the coordinated sulfur atoms is favored over the approach of hydrogen from the top close to coordinated S atoms. This situation is exemplified by a comparison of the binding enthalpies of sites E and N. Both sites involve binding of hydrogen to a 2-coordinate exposed Mo atom. However, in site E the hydrogen is bonded from the side opposite the coordinated S atoms and in site N the hydrogen is bonded from the top (+z direction) 1.83 Å away from one of the 2 coordinated S atoms. The

binding enthalpies for sites E and N are -126.12 and -63.96 kcal/mole respectively. Thus, the proximity of hydrogen to both a molybdenum (d_{Mo-H}=1.7 Å) and a sulfur atom (d_{S-H}=1.83 Å) decreases the stability of site N when compared to site E. Site B involves the binding of hydrogen from the top to a basal plane molybdenum atom. Binding of hydrogen to this position places the hydrogen atom 1.83 Å away from three of the sulfur atoms coordinated to the molybdenum. The binding enthalpy of site B is -27.03 kcal/mole, even lower than that of site N where the hydrogen was close to only one sulfur atom. Both 2-coordinate and 4-coordinate exposed Mo atoms are favorable sites for hydrogen adsorption but the feasibility of hydrogen adsorption on 5-coordinate exposed Mo atoms can not be studied with the $(MoS_2)_{19}$ cluster terminating at the $(10\bar{1}0)$ edges. A second $(MoS_2)_{19}$ structure terminating at $(10\bar{1}1)$ edges and containing 4-coordinate exposed Mo as well as 5-coordinate exposed Mo will be used for this study. This study will be discussed in Section B.1.4.

When hydrogen is bound to a molybdenum atom at site E (2-coordinate edge Mo_{16}), the electron densities on the bound molybdenum atom (Mo_{16}) and the hydrogen atom are increased. Upon theoretical hydrogen adsorption, the electron density on the molybdenum increases from 5.00 to 5.22 (-0.22) while the electron density on the hydrogen increases from 1.00 to 1.43 (-0.43). Thus, the total charge on the Mo-H species is -0.65 and can be represented as $Mo^{\delta 1^-}H^{\delta 2^-}$ where $\delta 1^-$=-0.22 and $\delta 2^-$ = -0.43. The extra electron density on Mo_{16} and H is mainly transferred from the neighboring edge molybdenum atoms, Mo_8 and Mo_{19}. These two molybdenum atoms have decreased in electron density from 5.98 to 5.70 (+0.28) upon hydrogen adsorption at site E. Thus, electron density is transferred from edge molybdenum atoms, Mo_8 and Mo_{19}, to the hydrogen bound edge molybdenum atom, Mo_{16}, and the hydrogen. The sulfur atoms in the lattice are relatively unaffected by hydrogen bound to a molybdenum atom.

When hydrogen is bound to a molybdenum atom at site H (2-coordinate edge Mo_8), the electron density on the hydrogen atom is increased from 1.00 to 1.43 (-0.43). However, the electron density on the bound molybdenum atom (Mo_8) is decreased from 5.98 to 5.65 (+0.33). Thus, the total charge on the Mo-H species is -0.10 and can be represented as $Mo^{\delta 1^+}H^{\delta 2^-}$ where $\delta 1^+$= +0.33 and $\delta 2^-$=-0.43. Many of the molybdenum atoms near edge 1 (the edge on which hydrogen is adsorbed) are affected slightly (either reduced or oxidized by less than 0.06 electrons) by the adsorption of hydrogen. However, the electron density on edge 2-coordinate Mo_{19} is decreased from 5.98 to 5.77 (+0.21). Again, the sulfur atoms in the lattice are unaffected by hydrogen adsorption onto a molybdenum atom.

When hydrogen is bound to a molybdenum atom at site S (4-coordinate edge Mo_{15}),

the electron density on the hydrogen is increased from 1.00 to 1.42 (−0.42). However, the electron density on the bound molybdenum atom (Mo_{15}) is relatively unaffected (+0.02) by the presence of hydrogen. Thus, the total charge on the Mo–H species is −0.40 and can be represented as Mo–$H^{\delta 2^-}$ where $\delta 2^- = -0.42$. Again, only the electron densities on the molybdenum atoms are affected by hydrogen adsorption. The electron densities on edge molybdenum atoms, Mo_8, Mo_{16}, and Mo_{19} are decreased from 5.98 to 5.75 (+0.23), 5.00 to 4.96 (+0.04), and 5.98 to 5.76 (+0.22). The electron density on bulk molybdenum atoms specifically Mo_6 and Mo_7 is slightly increased from 5.06 to 5.16 (−0.10) and 4.86 to 4.96 (−0.10). Thus, electrons are transferred away from the molybdenum atoms exposed on edge 1 to the hydrogen atom and a few bulk molybdenum atoms.

When hydrogen is bound to a molybdenum at site V (4–coordinate edge Mo_{14}), the electron density on the bound molybdenum atom (Mo_{14}) and the hydrogen atom is increased. The electron density on the molybdenum atom increases from 4.46 to 4.64 (−0.18) while that on the hydrogen atom increases from 1.00 to 1.41 (−0.41). Thus, the total charge on the Mo–H species is −0.59 and can be represented as $Mo^{\delta 1^-}$–$H^{\delta 2^-}$ where $\delta 1^- = -0.18$ and $\delta 2^- = -0.41$. Again, the electron densities on edge molybdenum atoms, Mo_8, Mo_{16}, and Mo_{19} are decreased from 5.98 to 5.73 (+0.25), 5.00 to 4.92 (+0.08), and 5.98 to 5.67 (+0.31). The electron densities of bulk molybdenum atoms Mo_6 and Mo_{13} is slightly increased from 5.06 to 5.17 (−0.11) and 4.78 to 4.91 (−0.13). Thus, in all four cases (sites E, H, S, and V) hydrogen adsorption from the side onto edge molybdenum atoms produces a Mo–H species with a total negative charge. Electron density for this negative charge is, for the most part, transferred from molybdenum atoms exposed on edge 1 resulting in an effective oxidation of these molybdenum atoms. Sulfur atoms are unaffected by adsorption onto edge molybdenum atoms.

The next most stable sites for binding of hydrogen on the $(MoS_2)_{19}$ cluster terminating at $(10\bar{1}0)$ edges are on top and side sulfur sites. In on top sites the hydrogen is bound in the z direction to one sulfur atom at a distance of 1.35 Å. Thus, closest molybdenum atoms are located at a large distance (3.45 Å) from the sulfur bound hydrogen atom. In side sites the hydrogen is bound to sulfur atoms on the side opposite coordinated molybdenum atoms. Sites C, M, and L are examples of hydrogen bonded to sulfur atoms from the top. Sites I, U, and T are examples of hydrogen bonded to edge sulfur atoms from the side. Overall, hydrogen bonded from the top to sulfur atoms is more stable than hydrogen bonded from the side. Another interesting feature resulting from these calculations is the stability of basal plane sulfur sites eg. site C. Introduction of edges consisting of exposed sulfur atoms does not provide more stable sulfur sites than the basal plane.

When hydrogen is bound to a sulfur atom at site C (3-coordinate basal S_{20}), the electron density on the bound sulfur atom (S_{20}) and the hydrogen atom is decreased. The electron density on the sulfur atom decreases from 6.26 to 5.40 (+0.86) while that on the hydrogen atom decreases from 1.00 to 0.90 (+0.10). Thus, the total charge on the S-H species is +0.96 and can be represented as $S^{\delta 1^+}H^{\delta 2^+}$ where $\delta 1^+$=+0.86 and $\delta 2^+$=+0.10. No other sulfur atoms are affected by the binding of hydrogen to a basal plane sulfur atom. Electron densities of the edge molybdenum atoms, Mo_8 and Mo_{19} are decreased from 5.98 to 5.89 (+0.09) and 5.98 to 5.89 (+0.09). The electron densities of edge Mo_{16} and bulk molybdenum atoms Mo_1, Mo_2 and Mo_7 are increased by -0.30, -0.14, -0.13, and -0.13 respectively. Thus, electron density is transferred from the S-H species and edge Mo_8 and Mo_{19} to bulk Mo_1, Mo_2, and Mo_7 and edge Mo_{16}.

When hydrogen is bound to a sulfur atom at site M (3-coordinate basal S_{50}), the electron density of the bound sulfur atom (S_{50}) and the hydrogen atom is decreased. The electron density on the sulfur atom decreases from 6.19 to 5.40 (+0.79) while that on the hydrogen atom decreases from 1.00 to 0.90 (+0.10). Thus, the total charge on the S-H species is +0.89 and can be represented as $S^{\delta 1^+}H^{\delta 2^+}$ where $\delta 1^+$=+0.79 and $\delta 2^+$=+0.10. No other sulfur atoms are affected by the binding of hydrogen to a basal plane sulfur atom. Electron densities of the edge molybdenum atoms, Mo_8 and Mo_{19} are decreased from 5.98 to 5.81 (+0.17) and 5.98 to 5.81 (+0.17). The electron densities of edge Mo_{16} and bulk molybdenum atoms Mo_2 and Mo_7 are increased by -0.47, -0.16, and -0.16 respectively. Thus, electron density is transferred from the S-H species and edge Mo_8 and Mo_{19} to bulk Mo_2, Mo_7 and edge Mo_{16}.

When hydrogen is bound to a sulfur atom at site T (2-coordinate edge S_{38}), the electron density on the bound sulfur atom (S_{38}) and the hydrogen atom is decreased. The electron density on the sulfur atom decreases from 6.76 to 5.97 (+0.23) while that on the hydrogen atom decreases from 1.00 to 0.90 (+0.10). Thus, the total charge on the S-H species is +0.33 and can be represented as $S^{\delta 1^+}H^{\delta 2^+}$ where $\delta 1^+$=+0.23 and $\delta 2^+$=+0.10. The sulfur atom S_{39} is only slightly affected (+0.04) by the binding of hydrogen in close vicinity. No other sulfur atoms are affected by the binding of hydrogen to a basal plane sulfur atom. In this case electrons are transferred from the S-H species to the opposite side of the $(MoS_2)_{19}$ cluster. Edge molybdenum atoms and basal plane molybdenum atoms residing on or close to edge 1 are reduced by transfer of electrons upon hydrogen adsorption.

When hydrogen is bound to a sulfur atom at site I (1-coordinate edge S_{42}), the electron density on the bound sulfur atom (S_{42}) and the hydrogen atom is decreased. The electron

density on the sulfur atom decreases from 7.30 to 6.46 (+0.84) while that on the hydrogen atom decreases from 1.00 to 0.87 (+0.13). Thus, the total charge on the S–H species is +0.97 and can be represented as $S^{\delta 1^+}\!\!-\!\!H^{\delta 2^+}$ where $\delta 1^+$=+0.84 and $\delta 2^+$=+0.13. No other sulfur atoms are affected by the binding of hydrogen to this edge sulfur atom. In this case electrons are transferred from the S–H species to the opposite side of the $(MoS_2)_{19}$ cluster. Edge molybdenum atoms and basal plane molybdenum atoms residing on or close to edge 1 are reduced by transfer of electrons upon hydrogen adsorption.

When hydrogen is bound to a sulfur atom at site U (1–coordinate edge S_{54}). the electron density on the bound sulfur atom (S_{54}) and the hydrogen atom is decreased. The electron density on the sulfur atom decreases from 7.32 to 6.50 (+0.82) while that on the hydrogen atom decreases from 1.00 to 0.87 (+0.13). Thus, the total charge on the S–H species is +0.95 and can be represented as $S^{\delta 1^+}\!\!-\!\!H^{\delta 2^+}$ where $\delta 1^+$=+0.82 and $\delta 2^+$=+0.13. No other sulfur atoms are affected by the binding of hydrogen to this sulfur atom. In the three cases involving binding of hydrogen to edge sulfur atoms (sites T, I, and U), electrons are transferred from the S–H species to the opposite side of the $(MoS_2)_{19}$ cluster. Edge molybdenum atoms and basal plane molybdenum atoms residing on or close to edge 1 are reduced by transfer of electrons upon hydrogen adsorption.

Hydrogen adsorption onto two–fold sulfur sites such as sites D, J, and K involved the adsorption of hydrogen into a position intermediate between two sulfur atoms such that a S–H–S type bond is the result. Again for the three sites studied no attempt at optimization of the two S–H bond distances by varying the bond angle (or the elevation of the H above the plane of the sulfur atoms) was attempted in these structures. In the D and K positions, the hydrogen atom is located in the plane of the two sulfur atoms and the result is a linear S–H–S linkage. The distance of the hydrogen atom from each sulfur atom is 1.58 Å. Hydrogen located at site J also results in a linear S–H–S linkage but the two S–H bond distances are slightly smaller, 1.5775 Å. Hydrogen bound to sulfur atoms at site K is also located 2.88 Å from the two molybdenum atoms. However, hydrogen atoms bound at sites D and J are also located 1.82 Å from nearest molybdenum atoms. Thus due to the larger Mo–H distance for a hydrogen atom bound at site K, the binding enthalpy of a hydrogen atom at this site (–61.57 kcal/mole) is more negative than at sites D and J. Sites D and J have lower binding enthalpies of –42.56 and –38.95 kcal/mole respectively due to the proximity of molybdenum atoms to hydrogen atoms residing on these sites.

The least stable site for hydrogen binding was found to be site A. Hydrogen in this position is bound in a 3–fold sulfur site such that the hydrogen is located at the center of an

equilateral triangle formed by the three basal plane sulfur atoms. Hydrogen located at site A results in three equal S–H bond distances of 1.82 Å and three equal Mo–H bond distances of 2.41 Å. Destabilization of this site results from the proximity of the three sulfur atoms and three molybdenum atoms to a hydrogen atom bound at this site.

B.1.4 Hydrogen Adsorption on $(MoS_2)_{19}$ Clusters Terminating at $(10\bar{1}1)$ Edges.

The $(MoS_2)_{19}$ cluster terminating at $(10\bar{1}1)$ edges is shown in Figure B–6. The exposed edges of this cluster consist of 3–coordinate, 4–coordinate and 5–coordinate Mo as well as 1–coordinate and 2–coordinate S. Calculation of the energies of formation, ΔU_f°, of the two $(MoS_2)_{19}$ clusters terminating at the $(10\bar{1}0)$ and $(10\bar{1}1)$ edges gives the following values: –431.85 and –434.97 kcal/mole, respectively. Thus, the cluster terminating at $(10\bar{1}1)$ edges is more stable than the cluster terminating at $(10\bar{1}0)$ edges by 3.12 kcal/mole. The stability of clusters terminating at $(10\bar{1}1)$ edges over $(10\bar{1}0)$ edges is consistent with previous results on 1–D $(MoS_2)_5$ systems terminating at the same edges. These results are presented in Section 5.3.2. The results of this study show that termination of the 1–D $(MoS_2)_5$ structure at $(10\bar{1}1)$ edges is more stable by 11.5 kcal/mole than termination at $(10\bar{1}0)$ edges.

At this point, only six hydrogen adsorption sites, E, I, W, X, Y, and Z were studied on the $(MoS_2)_{19}$ cluster terminating at $(10\bar{1}1)$ edges. These sites are shown in Figure B–7. Site E again involves hydrogen binding to a 4–coordinate exposed Mo atom. The Mo–H distance is 1.7 Å but at this position, the hydrogen is located 2.41 Å away from two sulfur atoms. Site I involves binding of a hydrogen atom from the side to an exposed 1–coordinate sulfur atom at a distance of 1.35 Å. The binding enthalpies of sites E and I on the $(10\bar{1}1)$ cluster are –83.50 and –91.77 kcal/mole respectively. Site I on the $(10\bar{1}1)$ structure is similar to site I on the $(10\bar{1}0)$ structure but the binding enthalpies still differ and are –91.77 and –96.84 kcal/mole respectively. Site E on the $(10\bar{1}1)$ structure is not equivalent to site E on the $(10\bar{1}0)$ structure due to the different termination planes. In the $(10\bar{1}0)$ structure, the exposed Mo atom is 2–coordinate whereas in the $(10\bar{1}1)$ structure the exposed Mo atom is 4–coordinate. Comparison can be made between sites S and V on the $(10\bar{1}0)$ structure and site E on the $(10\bar{1}1)$ structure. Hydrogen binding at sites S and V resulted in binding enthalpies of –118.77 and –115.37 kcal/mole respectively. Thus, site E on the $(10\bar{1}1)$ structure possesses a much lower binding enthalpy than sites S and V on the $(10\bar{1}0)$ structure. The destabilization of site E on the $(10\bar{1}1)$ structure with respect to sites S and V can be attributed to the smaller S–H distances and the overall "screening" of the molybdenum site by four sulfur ligands that is present on occupation of site E. Occupation of site E on the $(10\bar{1}1)$ cluster places the hydrogen atom close to two adjacent

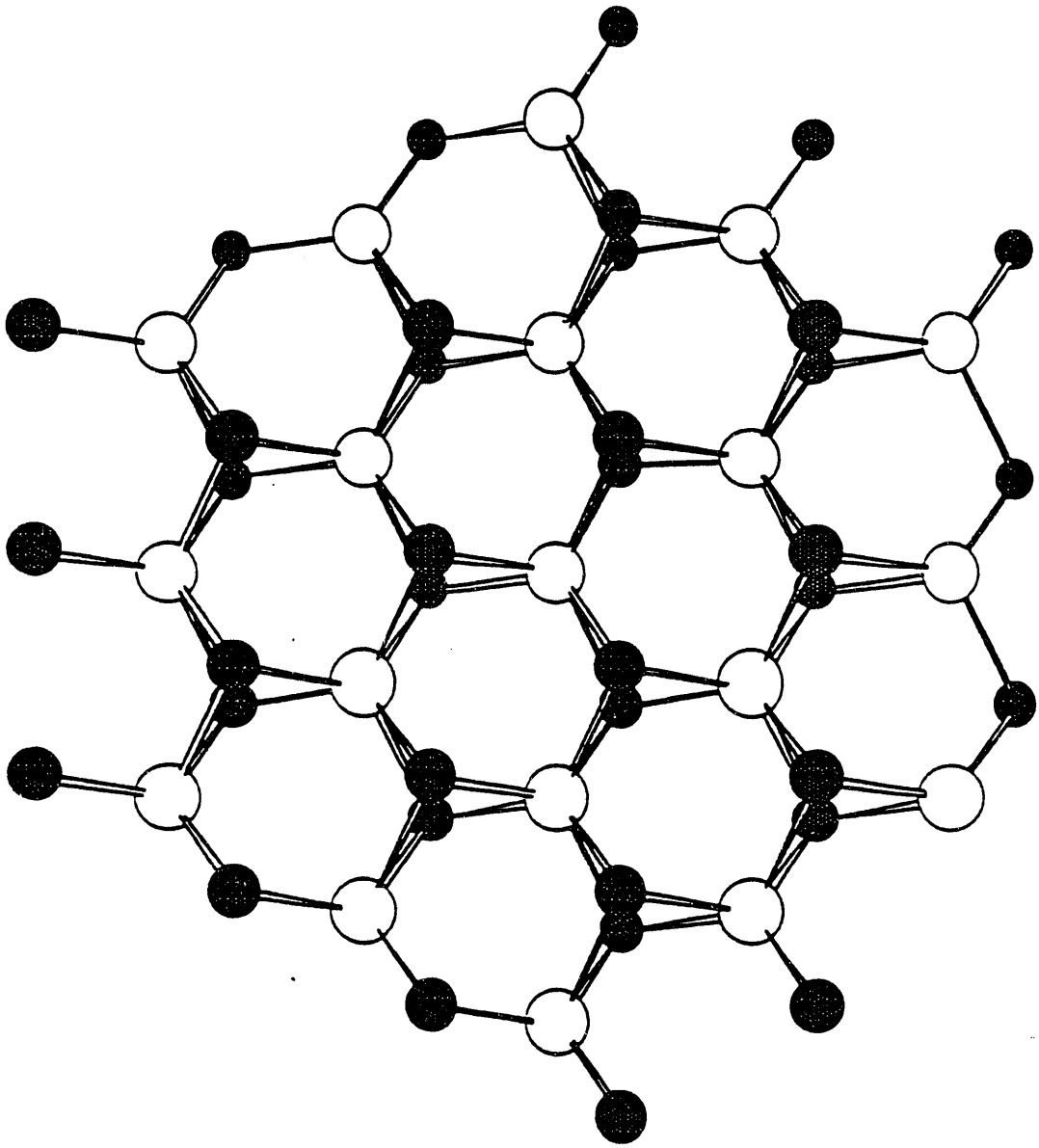

Figure B–6 Representation of the $(MoS_2)_{19}$ cluster terminating at $(10\bar{1}1)$ edges. White Circles=Mo and Black Textured Circles=S.

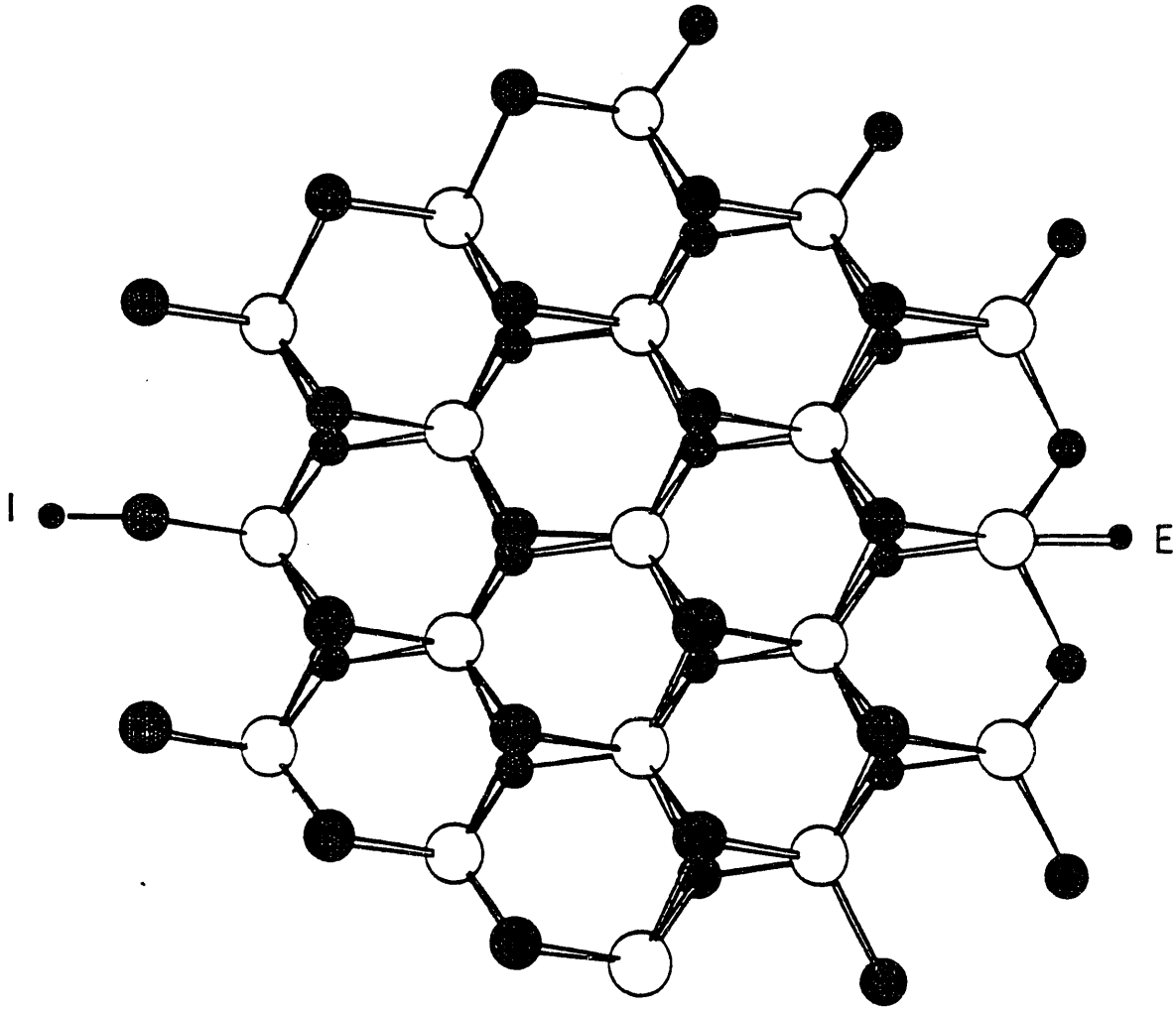

Figure B–7 The two hydrogen adsorption sites. E and I, studied on the $(MoS_2)_{19}$ cluster terminating at $(10\bar{1}1)$ edges. White Circles=Mo. Black Circles=H and Black Textured Circles=S.

sulfur atoms while sites S and V on the $(10\bar{1}0)$ cluster position the hydrogen far from the nearest sulfur atoms.

Sites W and X both involve binding of hydrogen to a 5-coordinate edge molybdenum atom (Mo_9) at a distance of 1.7 Å. Site W involves binding of a hydrogen atom to the molybdenum from the top placing the hydrogen atom 1.83 Å away from two 3-coordinate sulfur atoms. Site X involves binding of a hydrogen atom from the side placing the hydrogen atom 1.58 Å from a 1-coordinate edge sulfur atom. Sites Y and Z both involve binding of hydrogen to a 3-coordinate edge molybdenum atom (Mo_{14}) at a distance of 1.7 Å. Both sites involve binding of the hydrogen atom from the side but site Z places the hydrogen atom 2.82 Å away from one sulfur atom whereas site Y involves placing the hydrogen atom 2.95 Å away from the nearest sulfur atom. Hydrogen binding enthalpies for sites W, X, Y, and Z are the following: -39.74, -45.52, -117.97, and -106.70 kcal/mole respectively. Thus, binding of hydrogen to 3-coordinate edge molybdenum sites is more stable than 5-coordinate edge molybdenum atoms. Between the two $(MoS_2)_{19}$ clusters terminating in $(10\bar{1}0)$ and $(10\bar{1}1)$ edges, binding of hydrogen to molybdenum atoms ranging in coordination from 2 to 6 has been studied. A qualitative comparison of these binding enthalpies can be made. Binding enthalpies of hydrogen to 2-, 3-, 4-, 5-, and 6-coordinate molybdenum atoms are the following: -126.12 (Site E, $(10\bar{1}0)$), -117.97 (Site Y, $(10\bar{1}1)$), -83.50 (Site E, $(10\bar{1}1)$), -45.52 (Site X, $(10\bar{1}1)$) and -27.03 (Site B, $(10\bar{1}0)$). The most stable molybdenum hydrogen binding sites appear to be 2-, 3-, and 4-coordinate edge molybdenum atoms. In general, as the number of sulfur ligands attached to the molybdenum atom increases, the stability of hydrogen binding enthalpy decreases. Binding enthalpies for hydrogen adsorption on 1-D $(MoS_2)_5$ structures terminating at $(10\bar{1}1)$ edges (discussed in Section 5.5) result in more negative binding enthalpies for 4-coordinate molybdenum atoms (-83.84 kcal/mole) than for 5-coordinate molybdenum atoms (-37.26 kcal/mole) in agreement with the results on the $(MoS_2)_{19}$ cluster terminating at $(10\bar{1}1)$ edges.

The study of hydrogen adsorption on $(MoS_2)_{19}$ clusters terminating at $(10\bar{1}1)$ edges is incomplete. A study of hydrogen adsorption on the more stable $(10\bar{1}1)$ cluster will not be complete unless binding enthalpies of hydrogen adsorption sites paralleling those studied on the $(10\bar{1}0)$ cluster are calculated. For instance, an interesting comparison would be between the binding enthalpy of hydrogen at site C on the $(10\bar{1}0)$ and $(10\bar{1}1)$ clusters. The sulfur atom exposed to hydrogen at site C is fully coordinated and is located far from the terminated edges. Thus, this sulfur atom can be considered as representative of basal plane sulfur atoms. The expectation is that occupation of site C should result in similar binding enthalpies on the two structures.

B.1.5 Hydrogen Adsorption on $(MoS_2)_{14}$ Clusters.

The $(MoS_2)_{14}$ cluster terminating at $(10\bar{1}0)$ edges was used to examine hydrogen adsorption at various sites in the van der Waals gap between the $(MoS_2)_7$ layers. The $(MoS_2)_{14}$ structure as well as five of the seven hydrogen adsorption sites are shown in Figure B-8. Hydrogen adsorption sites are labeled alphabetically and include sites A, B, C, and E in which hydrogen resides in the middle of the van der Waals gap at different locations and environments. Site D on the $(MoS_2)_{14}$ cluster is similar to site E on the $(MoS_2)_{19}$ cluster terminating at $(10\bar{1}0)$ edges. Site F on the $(MoS_2)_{14}$ cluster is similar to site C on the $(MoS_2)_{19}$ cluster involving binding of hydrogen to a basal plane sulfur atom. Site G is similar to Site F in that hydrogen is bound to a basal plane sulfur atom but within the van der Waals gap. The binding enthalpies are given in decreasing stability in Table B-6.

Table B-6

Binding enthalpies of hydrogen on $(MoS_2)_{14}$ clusters terminating at $(10\bar{1}0)$ edges. This structure consists of two $(MoS_2)_7$ clusters separated by the van der Waals gap.

#	Site	$\Delta H(\frac{kcal}{mole})$	Description	Bond
1	D	-124.10	2-coordinate edge Mo	Mo-H
2	F	-101.96	3-coordinate basal S	S-H
3	G	-92.88	3-coordinate basal S within van der Waals gap	S-H
4	C	-76.59	1-coordinate edge S	S-H—Mo
5	B	-71.92	3-coordinate S	S-H—Mo
6	A	-43.06	3-coordinate S	S-H
7	E	-14.36	1-coordinate S	S-H-S

Site A is arranged such that hydrogen resides in the middle of the van der Waals gap 1.75 Å from a 3-coordinate sulfur in the first $(MoS_2)_7$ cluster and 2.18 Å from two 1-coordinate sulfur atoms in the second $(MoS_2)_7$ cluster. A hydrogen atom at site B is located 1.50 Å from a 1-coordinate sulfur atom in the first $(MoS_2)_7$ cluster, 2.36 Å from a 1-coordinate and two 3-coordinate sulfur atoms and 3.08 Å from a molybdenum in the second $(MoS_2)_7$ cluster. A hydrogen atom residing at site C is located 3.08 Å from a 2-coordinate molybdenum atom in the first $(MoS_2)_7$ cluster and 1.50 Å from a 1-coordinate S atom in the second $(MoS_2)_7$ cluster. A hydrogen atom residing at site D is located 1.7 Å from a 2-coordinate molybdenum atom in the first $(MoS_2)_7$ cluster. As mentioned previously, this site is similar to site E in the $(MoS_2)_{19}$

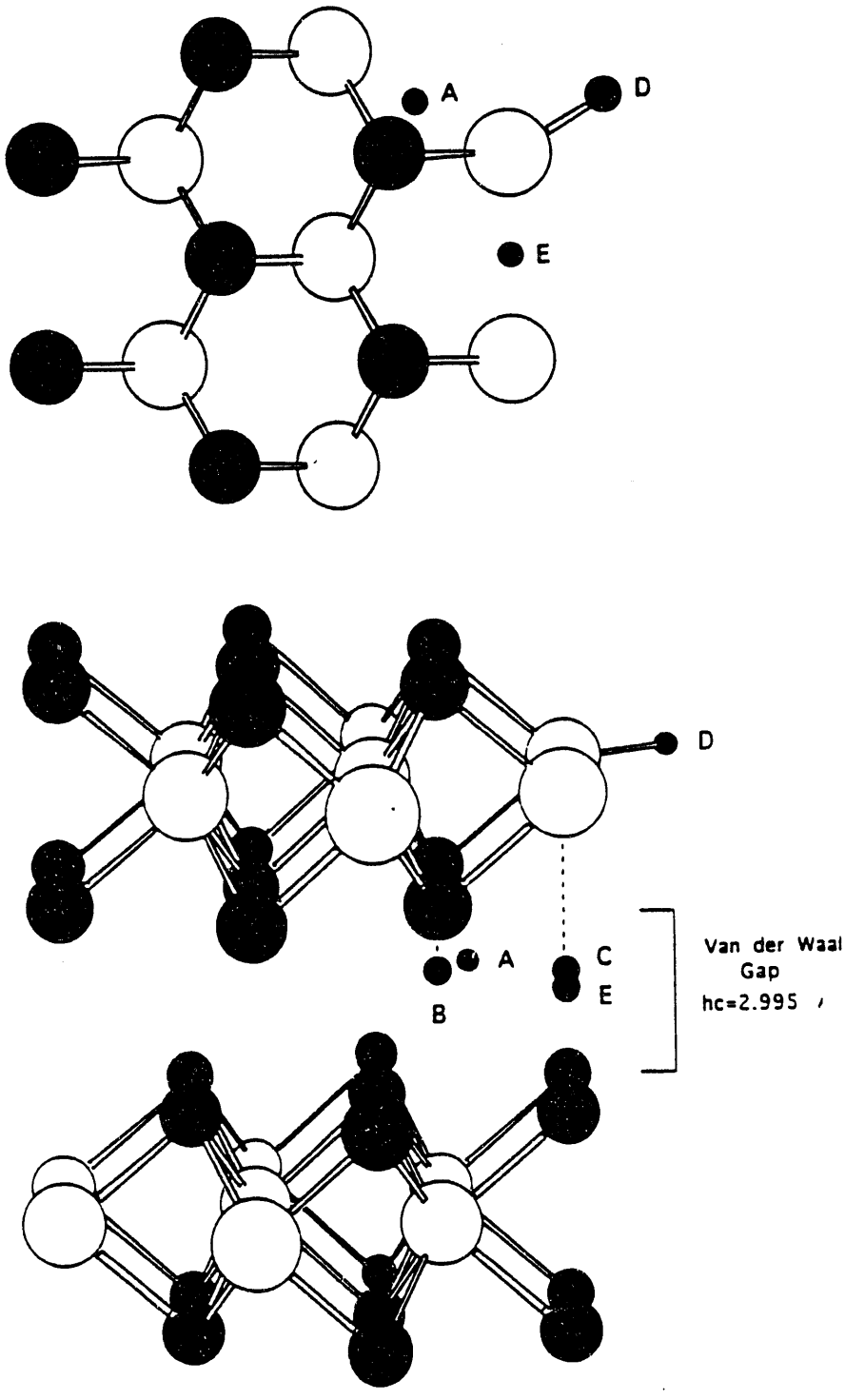

Figure B-8 Representation of the $(MoS_2)_{14}$ cluster terminating at $(10\bar{1}0)$ edges and the five hydrogen sites studied. This structure consists of two $(MoS_2)_7$ clusters separated by the van der Waals gap. a) $(MoS_2)_{14}$ viewed from the top (parallel to the $\hat{z}$ axis) b) $(MoS_2)_{14}$ viewed from the side.

cluster terminating at $(10\bar{1}0)$ edges. A hydrogen atom residing at site E in the $(MoS_2)_{14}$ cluster is located 2.23 Å from two 1-coordinate sulfur atoms in the second $(MoS_2)_7$ cluster and 2.88 Å and 3.46 Å from two 3-coordinate sulfur atoms and two 2-coordinate molybdenum atoms in the first $(MoS_2)_7$ cluster respectively. A hydrogen atom residing at site F is located 1.35 Å from a 3-coordinate basal plane sulfur atom in the first $(MoS_2)_7$ cluster. Site F in the $(MoS_2)_{14}$ cluster is similar to site C in the $(MoS_2)_{19}$ cluster. A hydrogen atom residing at site G is located 1.35 Å from a basal plane sulfur atom and resides between the two $(MoS_2)_7$ clusters, within the van der Waals gap. Thus, a hydrogen atom bound to site G is also located 2.46 Å from three 3-coordinate basal plane sulfur atoms residing on the second $(MoS_2)_7$ cluster.

Hydrogen atoms located at site D on the $(MoS_2)_{14}$ cluster have a binding enthalpy of -124.10 kcal/mole. Since hydrogen adsorption on the $(MoS_2)_7$ cluster was not studied, this binding enthalpy will be compared to occupation of a similar site, site E, on the $(MoS_2)_{19}$ cluster. This value is very close to the binding enthalpy, -126.12 kcal/mole, of hydrogen residing at site E on the $(MoS_2)_{19}$ cluster terminating at $(10\bar{1}0)$ edges. Thus, the use of one MoS_2 layer to model edge and basal plane hydrogen binding sites in the $(MoS_2)_{19}$ studies is justified by this result. Addition of Van der Waals interactions should not change the energy ordering of the hydrogen binding sites in the $(MoS_2)_{19}$ clusters.

In the $(MoS_2)_{14}$ cluster sites F and G result in binding enthalpies of -101.96 and -92.88 kcal/mole respectively. These sites are similar to site C on the $(MoS_2)_{19}$ cluster terminating at $(10\bar{1}0)$ edges where hydrogen is bound from the top (z-direction) to a basal plane sulfur atom with a S-H distance of 1.35 Å. Occupation of site C in the $(MoS_2)_{19}$ cluster results in a binding enthalpy of -106.05 kcal/mole. Thus, site F on the $(MoS_2)_{14}$ cluster has a similar although slightly more positive binding enthalpy than site C on the $(MoS_2)_{19}$ cluster. The destabilization of site F can be attributed to the smaller cluster size of the $(MoS_2)_7$ layer compared to the $(MoS_2)_{19}$ layer. In the $(MoS_2)_{19}$ cluster, the central sulfur atom is surrounded by a greater number of MoS_2 units and is located farther from the terminated edges resulting in larger amount of bulk-like character when compared to the central sulfur atom of the $(MoS_2)_7$ cluster. Occupation of site G on the $(MoS_2)_{14}$ cluster results in binding of hydrogen to a basal plane sulfur atom and places the hydrogen between the two $(MoS_2)_7$ layers within the van der Waals gap. Thus, destabilization of site G compared to site F is due to the interactions of hydrogen with sulfurs across the van der Waals gap located at a S-H distance of 2.46 Å.

In the $(MoS_2)_{14}$ cluster sites C and B result in similar hydrogen binding enthalpies of -76.59 and -71.92 kcal/mole respectively. These sites are similar to sites C, M, and L on the $(MoS_2)_{19}$ cluster terminating at $(10\bar{1}0)$ edges where hydrogen is bound from the top (z-

direction) to basal plane and edge plane sulfur atoms with a S–H bond distance of 1.35 Å. Occupation of sites C, M, and L results in binding enthalpies of -106.05, -102.16, and -98.30 kcal/mole respectively. Thus, the sites C, M, and L on the $(MoS_2)_{19}$ cluster are more stable than sites C and B on the $(MoS_2)_{14}$ cluster. Destabilization of sites C and B on the $(MoS_2)_{14}$ cluster may be due to the increased S–H distance of 1.5 Å that results from placing the hydrogen in the middle of the van der Waals gap. As mentioned previously, the energy of the hydrogen containing clusters was not minimized with respect to the S–H distance and in most cases a constant S–H bond distance of 1.35 Å was used. However for the $(MoS_2)_{19}$ cluster terminating at $(10\bar{1}0)$ edges, the binding enthalpy of position C (hydrogen adsorbed on top of a basal plane sulfur atom) was calculated at S–H distances greater than 1.35 Å. These results are shown in Table B–7. In general as the S–H bond distance increased, the binding enthalpy also became less negative indicating a destabilization of the site. Thus, part of the destabilization of sites C and B on the $(MoS_2)_{14}$ structure can be attributed to the increased S–H bond distance of these sites. Sulfur atoms located 2.36 Å away from hydrogen atoms at sites C and B may also affect the binding enthalpy of these sites.

Table B–7

Binding enthalpies of hydrogen residing at site C on the $(MoS_2)_{19}$ cluster terminating at $(10\bar{1}0)$ edges as a function of the S–H distance.

S–H Distance (Å)	Binding Enthalpy, ΔH_f° ($\frac{kcal}{mole}$)
1.35	-106.05
1.425	-98.84
1.5	-91.31

Sites A and E are the least stable hydrogen sites on the $(MoS_2)_{14}$ cluster. Part of the destabilization may again be due to the large S–H distances. These sites can be compared to the 2-fold (K, D, J) and 3-fold (A) hydrogen sites on the $(MoS_2)_{19}$ cluster terminating at $(10\bar{1}0)$ edges. These sites have the least stable binding enthalpy on the $(MoS_2)_{19}$ cluster and a similar situation occurs for sites A and E on the $(MoS_2)_{14}$ cluster.

B.1.6 Hydrogen Approaches to $(MoS_2)_{19}$ Clusters

In experiments studying hydrogen adsorption, hydrogen molecules not hydrogen atoms approach the polycrystalline MoS_2 surface. The molecule is either heterolytically or homolytically dissociated to produce either S–H and Mo–H or two S–H surface species. Since the previous theoretical study involving hydrogen atom adsorption on a $(MoS_2)_{19}$ cluster

indicated that adsorption of hydrogen onto 2- and 4-coordinate edge molybdenum atoms was thermodynamically favored, this study focuses on approaches of hydrogen for heterolytic cleavage. Again, no attempt was made to minimize the cluster energy with respect to the S-H and Mo-H bond distances. S-H and Mo-H bond distances of 1.35 Å and 1.7 Å were used in this study. The three final binding states of hydrogen molecule are shown in Figure B-9 a, b, and c. Approach O (Figure B-9a) is the final state that would result from heterolytic cleavage of a hydrogen molecule that approached from the top (H-H bond parallel to the basal plane and approaching perpendicular to the basal plane in the z-direction). Approach P (Figure B-9b) is the final state that would result from heterolytic cleavage of a hydrogen molecule that approached edge 1 with its H-H bond parallel to the bond between the exposed molybdenum atom and a sulfur atom. Approach R (Figure B-9c) is the final state that would result from heterolytic cleavage of a hydrogen molecule that approached the edge from the side (H-H bond and approach parallel to the basal plane).

The binding enthalpies of hydrogen atoms and molecules to the $(MoS_2)_{19}$ cluster terminating at $(10\bar{1}0)$ edges resulting from the three different approaches indicated above are shown in Table B-8. Approach O results in a final state that has hydrogen atoms positioned at

Table B-8

Binding enthalpies of hydrogen atoms and molecules to the $(MoS_2)_{19}$ cluster terminating at $(10\bar{1}0)$ edges resulting from Approaches O, P, R and S (discussed below).

	Binding Enthalpy, $\Delta H^{\circ}(\frac{kcal}{mole})$:	
Approach	Atoms (2H(g))	Molecules (H_2(g))
O	-177.30	-73.10
P	-192.88	-88.68
R	-105.07	+0.87
S	-193.49	-89.29

sites M and N on the $(MoS_2)_{19}$ cluster. The previous study of individual hydrogen atom adsorption onto the $(MoS_2)_{19}$ cluster at sites M and N results in binding enthalpies of -102.16 and -63.96 kcal/mole respectively. Assuming no change in the adsorption characteristics of the cluster upon hydrogen adsorption, an overall binding enthalpy of -166.12 kcal/mole is obtained from the addition of M and N binding enthalpies. This value compares well to the value of -177.30 kcal/mole found for Approach O. The most stable final state results from hydrogen approaching by Approach P. This approach results in a hydrogen atom bonded to a fully coordinated sulfur atom from the side and to a hydrogen atom bonded to a 2-coordinate

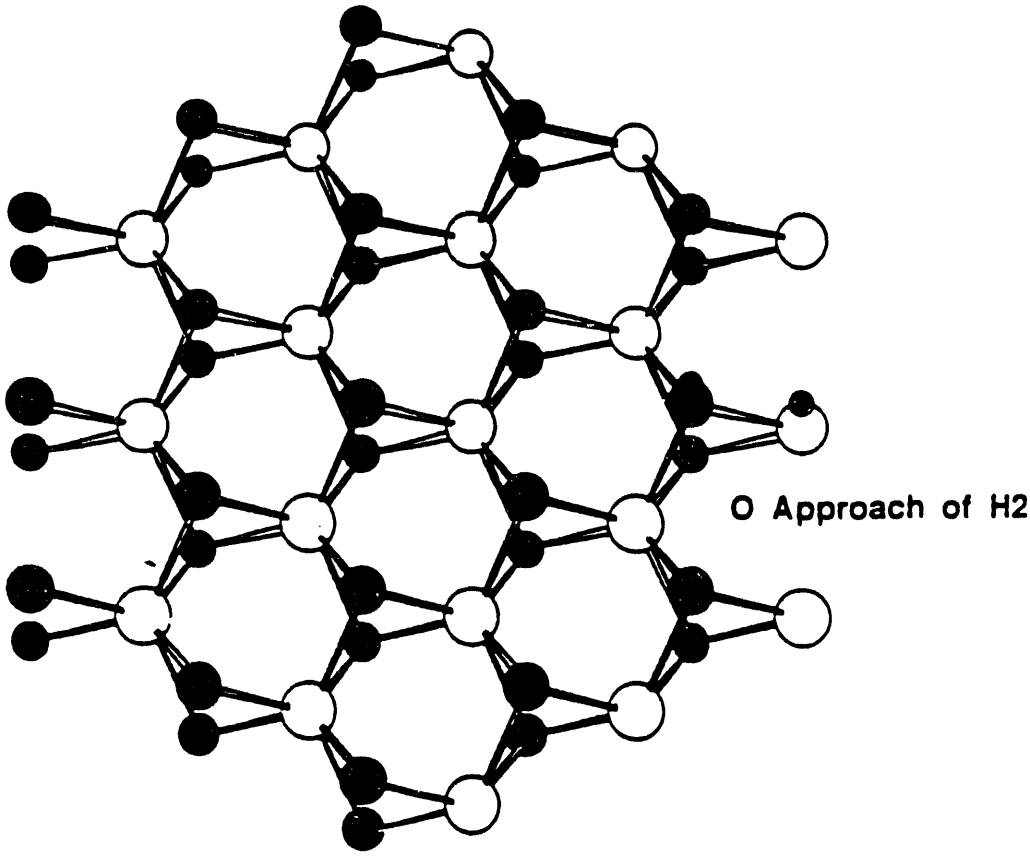

Figure B-9a Schematic representation of the final state resulting from heterolytic cleavage of a hydrogen molecule incoming by Approach O toward a $(MoS_2)_{19}$ cluster terminating at $(10\bar{1}0)$ edges.

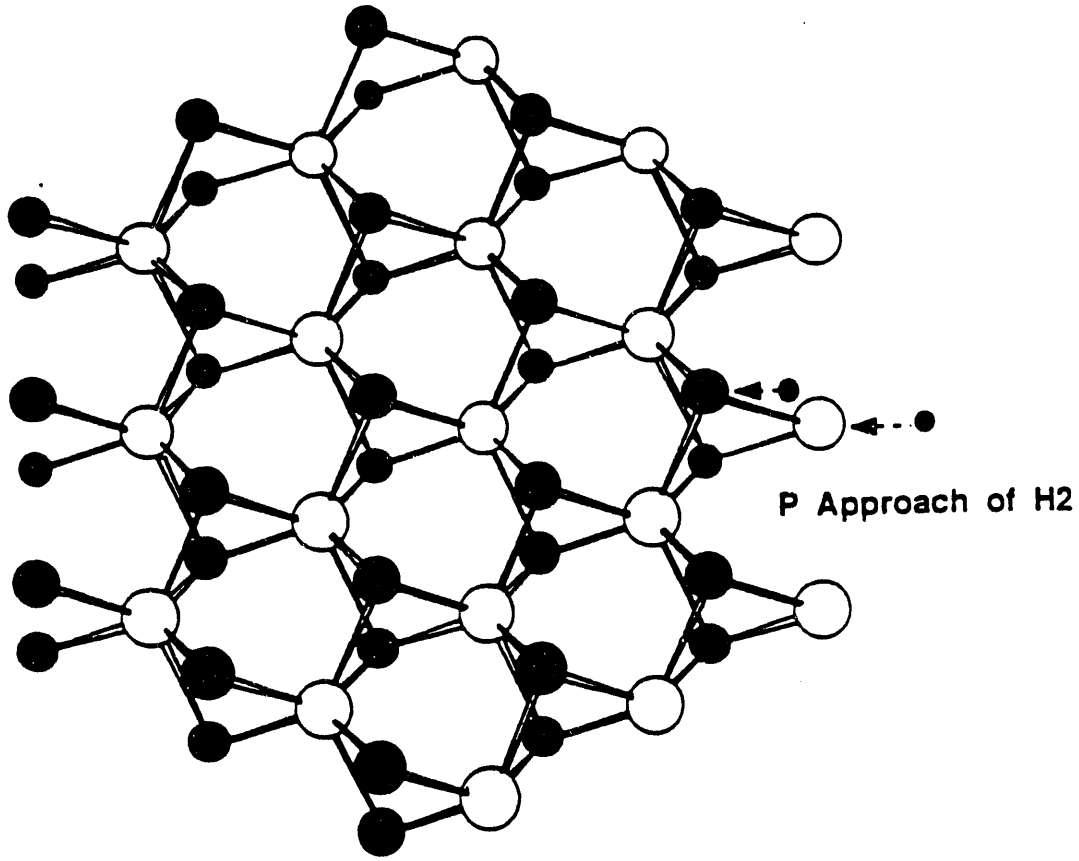

Figure B-9b Schematic representation of the final state resulting from heterolytic cleavage of a hydrogen molecule incoming by Approach P toward a $(MoS_2)_{19}$ cluster terminating at $(10\bar{1}0)$ edges.

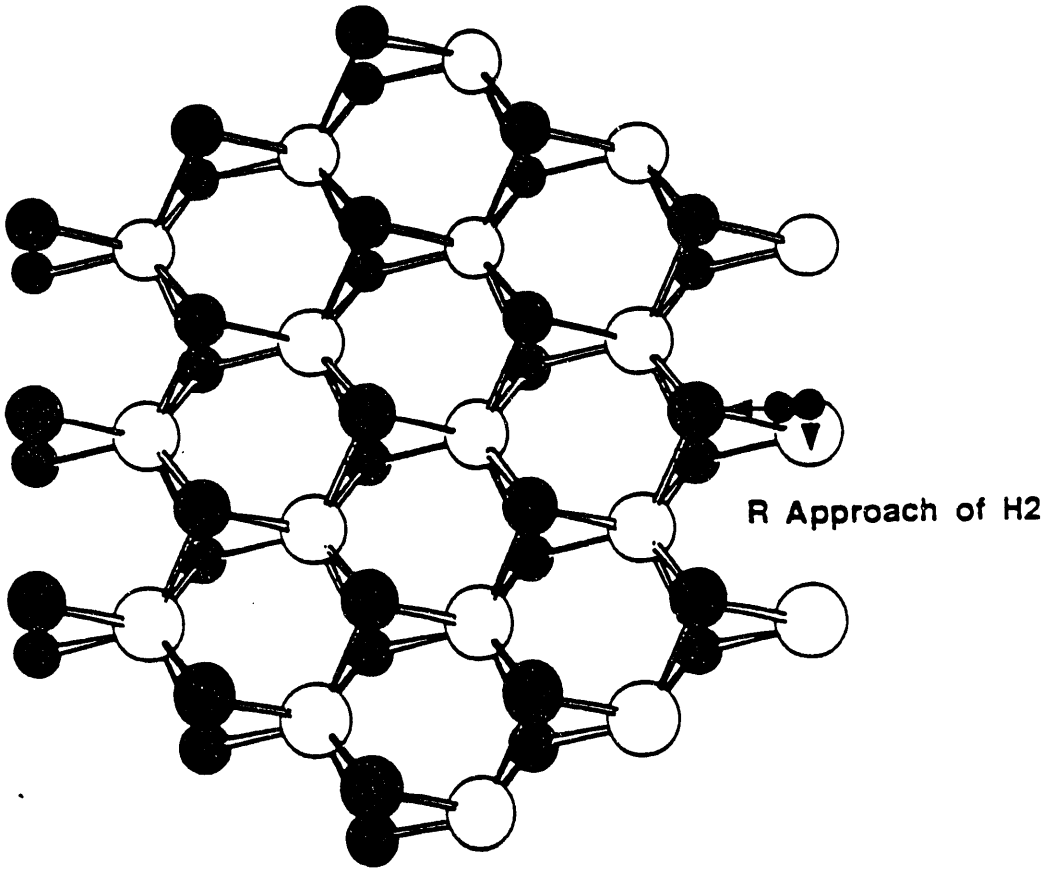

Figure B-9c Schematic representation of the final state resulting from heterolytic cleavage of a hydrogen molecule incoming by Approach R toward a $(MoS_2)_{19}$ cluster terminating at $(10\bar{1}0)$ edges.

molybdenum atom from the side. The molybdenum site resulting from Approach P is the same as site E on the $(MoS_2)_{19}$ cluster terminating at $(10\bar{1}0)$ edges. Site E was found to be the most stable site on the $(MoS_2)_{19}$ cluster terminating at $(10\bar{1}0)$ edges. Approaches O and R both result in occupation of the less thermodynamically stable molybdenum site N. Thus Approach P is more stable due to the stability of the final occupied molybdenum site. The sulfur site occupied by Approaches P and R does not have an analogous site in the previous hydrogen atom study. However, this site should not be as stable as the sulfur site (M) occupied by Approach O since a hydrogen atom in this site is positioned 1.78 Å from an adjacent molybdenum atom. Thus heterolytic cleavage of a hydrogen molecule by Approach R results in occupation of the less thermodynamically favorable molybdenum and sulfur sites.

Homolytic cleavage of hydrogen on 1–coordinate sulfur atoms residing on the second edge of the $(MoS_2)_{19}$ cluster terminating at $(10\bar{1}0)$ edges was also studied. Coordination of the second edge is shown in Figure B–3. The local geometry of the H_2–$(MoS_2)_{19}$ cluster resulting from homolytic cleavage of hydrogen on this edge (referred to as Approach S) is shown in Figure B–10a. Approach S (Figure B–10a) is the final state that would result from homolytic cleavage of a hydrogen molecule that approached Edge 2 with its H–H bond parallel to the $(10\bar{1}0)$ plane and perpendicular to the basal plane. This approach results in hydrogen atom and molecule binding enthalpies of –193.49 and –89.29 kcal/mole respectively. The binding enthalpy of homolytic Approach S is slightly more negative than that of heterolytic Approach P. However due to the semiempirical nature of the calculations, both Approaches P and S are equally feasible.

A second homolytic hydrogen approach (Approach A) to Edge 2 is shown in Figure B–10b. In this study, the distance of the hydrogen molecule from the two edge sulfur atoms was varied so that a decrease in the S–H distance was accompanied by a corresponding increase in the H–H bond distance. Binding enthalpies along with S–H and H–H bond distances are shown in Table B–9.

From this study it is evident that changes in the S–H bond distance dramatically effect the hydrogen binding enthalpies. Previous calculations of hydrogen atom adsorption on the $(MoS_2)_{19}$ surface used a constant S–H bond distance of 1.35 Å. From Table B–9, the S–H bond distance that minimizes the hydrogen binding enthalpy is 0.78 Å. The binding enthalpy resulting from a S–H bond distance of 1.35 Å when approximated from the binding enthalpies given above is ca. 180–185 kcal/mole (rough approximation assuming a linear relationship between the R=1.0 and the R=1.5 Å points). When this homolytic binding enthalpy is compared to those resulting from heterolytic cleavage of hydrogen due to Approaches O, P and

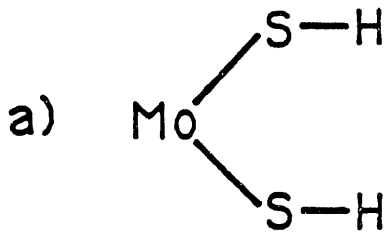

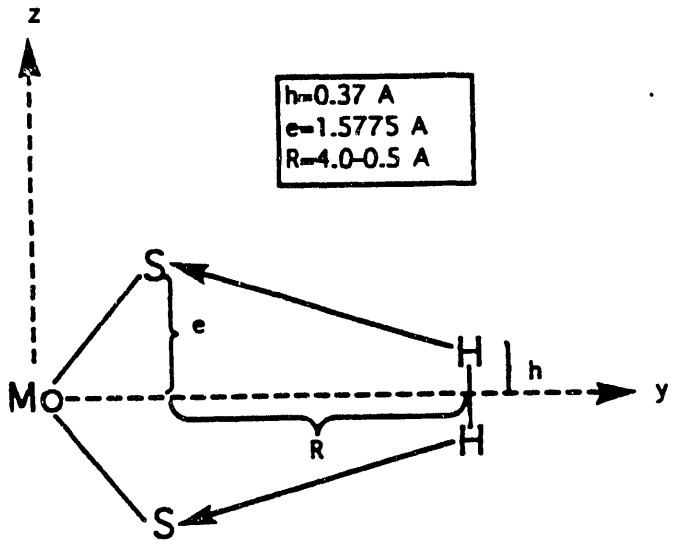

b) Homolytic Approach of H_2 to MoS_2.

Figure B-10 Local geometries of the two H_2-$(MoS_2)_{19}$ clusters resulting from homolytic approaches S and A of hydrogen molecules to Edge 2. a) Approach S and b) Approach A.

Table B-9

Binding enthalpies and corresponding S-H and H-H bond distances obtained from homolytic cleavage of a hydrogen molecule on two 1-coordinate sulfur atoms residing on the second edge of the $(MoS_2)_{19}$ cluster terminating at $(10\bar{1}0)$ edges.

R (Å)	d_{H-S} (Å)	d_{H-H} (Å)	ΔH° ($\frac{kcal}{mole}$)
3.0	3.13	1.34	-107.47
2.0	2.09	1.95	-69.99
1.5	1.57	2.25	-155.83
1.0	1.04	2.55	-243.82
0.75	0.78	2.70	-260.69
0.50	0.52	2.85	-247.37

R, heterolytic cleavage of hydrogen on edge 1 is still favored by Approach P. A parallel study of hydrogen approaches to $(MoS_2)_{19}$ clusters terminating at $(10\bar{1}1)$ edges was not carried out.

B.1.7 Hydrogen Adsorption on MoS_2 Molecule

Hydrogen adsorption on an MoS_2 molecule possessing the solid state geometry of crystalline MoS_2 was also studied to parallel the study of hydrogen adsorption on $(MoS_2)_{19}$ clusters. The geometry of the MoS_2 molecule and attached hydrogens is shown in Table B-10. The hydrogen labeled H(1) is attached to the molybdenum atom from the side with a Mo-H bond distance of 1.7 Å while hydrogens labeled H(2) and H(3) are attached to the sulfur atoms from the side with a S-H bond distance of 1.35 Å. The following three hydrogen adsorbed systems were studied and are shown in Figure B-11: H(1)-MoS_2, MoS_2-H(2), and MoS_2-H(2)H(3). The binding enthalpies of the hydrogen adsorbed systems are shown in Table B-11.

Table B-10

Cartesian coordinates of the MoS_2 molecule and attached hydrogens. Hydrogen labeled H(1) is attached to the molybdenum atom from the side while the hydrogens labeled H(2) and H(3) are attached to the sulfur atoms S(1) and S(2) from the side.

Atom	x	y	z
Mo	0.	0.	0.
S(1)	0.	1.824427	1.5775
S(2)	0.	1.824427	-1.5775
H(1)	0.	-1.7	0.
H(2)	0.	3.174427	1.5775
H(3)	0.	3.174427	-1.5775

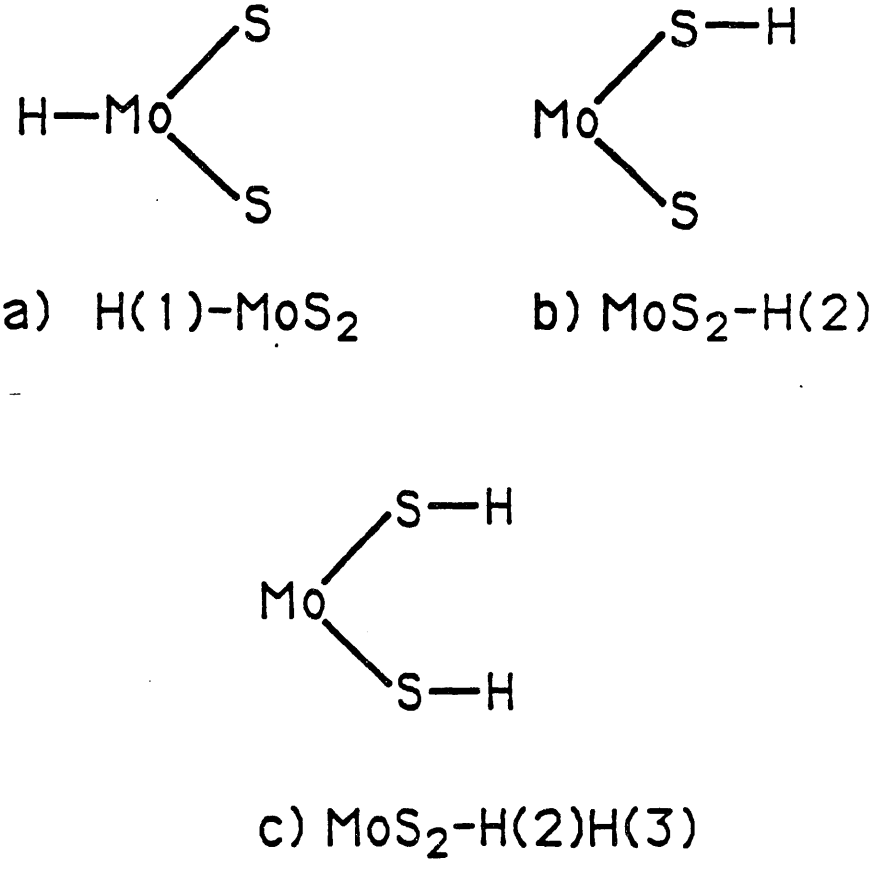

Figure B-11 Arrangement of the atoms in the following hydrogen adsorbed MoS_2 systems: a) H(1)-MoS_2, b) MoS_2-H(2), and c) MoS_2-H(2)H(3).

Table B-11

Binding enthalpies of hydrogen adsorbed on an MoS_2 molecule. H(1) indicates hydrogen attached to Mo, H(2) indicates hydrogen attached to S(1) and H(3) indicates hydrogen attached to S(2).

	System	$\Delta\dot{H}(\frac{kcal}{mole})$
1)	H(1)-MoS_2	-122.79
2)	MoS_2-H(2)	-90.36
3)	MoS_2-H(2)H(3)	-180.18

The binding enthalpies of the H(1)-MoS_2 and MoS_2-H(2) systems can be compared to the hydrogen binding enthalpies on sites E and I of the $(MoS_2)_{19}$ cluster terminating at $(10\bar{1}0)$ edges. The binding enthalpies of hydrogen on site E and in the H(1)-MoS_2 system are -126.12 and -122.79 kcal/mole respectively. The binding enthalpies of hydrogen on site I and in the MoS_2-H(2) system are -96.84 and -90.36 kcal/mole respectively. Hydrogen binding enthalpies found for the MoS_2 molecule and edge sulfur and molybdenum atoms of the $(MoS_2)_{19}$ cluster compare well. Thus, the MoS_2 molecule can be used to approximate the behavior of some edge atoms of the $(MoS_2)_{19}$ cluster specifically, 1-coordinate sulfur atoms and 2-coordinate molybdenum atoms. The third system studied, MoS_2-H(2)H(3), approximates the structure resulting from homopolar splitting of a hydrogen molecule by sulfur atoms. The binding enthalpy of this system can be compared to the binding enthalpies of the structures resulting from heterolytic splitting of a hydrogen molecule by Approaches O, P, and R. The binding enthalpy of hydrogen atoms on the MoS_2-H(2)H(3) system is -180.18 kcal/mole. Approaches O and R on the $(MoS_2)_{19}$ system have less negative binding enthalpies (-177.30 and -105.07 kcal/mole respectively) than the MoS_2-H(2)H(3) system. However, Approach P results in a stronger binding enthalpy of -192.88 kcal/mole. From this study, a preliminary conclusion on the mechanism of hydrogen splitting would be that heterolytic splitting of hydrogen on $(10\bar{1}0)$ edges of MoS_2 is favored over homolytic splitting of hydrogen on the same edges when the hydrogen approaches with its H-H bond parallel to the $(10\bar{1}0)$ plane. However, other systems terminating in different edge planes, such as $(10\bar{1}1)$, may produce different results. Thus, further calculations must be carried out before a more general conclusion of heterolytic vs. homolytic cleavage of hydrogen on MoS_2 is reached.

B.1.8 Hydrogen Approaches to the MoS_2 Molecule.

Since the previous study involved hydrogen atom adsorption onto an isolated molecule

of MoS_2, this study focuses on approaches of hydrogen for heterolytic and homolytic cleavage. The following six different hydrogen approaches or paths were studied and are shown schematically in Figure B-12: a) Path A, b) Path B, c) Path C, d) Path D, e) Path E, and f) Path F. Paths A, E, and F result in homolytic cleavage of the hydrogen molecule on the two sulfur atoms. Paths B, C, and D result in heterolytic cleavage of the hydrogen molecule on a molybdenum and a sulfur atom. In all cases the hydrogen molecule is initially positioned at R_0 4.0 Å away from the atoms of interest in the $\hat{y}$ direction. Paths A and B are similar in that when the hydrogen molecule is moved closer to the atoms of interest, a decreased S-H or Mo-H distance is accompanied by an increased H-H distance. Paths C, D, E, and F are similar in that when the hydrogen molecule is moved closer to the atoms of interest, a decreased S-H or Mo-H distance is not accompanied by an increased H-H distance. The H-H distance is kept constant in these cases with a value of 0.74 Å for Paths C and E and with a value of 0.05 Å for Paths D and F.

The relative energies of the systems resulting from the paths discussed above were calculated for different values of R. In each case the value of R was decreased from its initial value of 4.0 Å to a final value of 0.5 Å or 0.0. The relative energy or binding energy of hydrogen molecule to the MoS_2 molecule (shown in equation B-7) was calculated from the individual extended Hückel energies of the components. The energy of the MoS_2 molecule, E_{MoS_2} was calculated to be -267.36 eV and was obtained from an extended Hückel calculation of the molecule in the geometry of the particular path under study. The energy of the H_2 molecule, E_{H_2}, was calculated to be -35.13 eV when the H-H separation was 0.74 Å. In Table B-12 are shown the S-H and H-H bond distances as well as the relative energy, E_{rel}, for each value of R for Path A. Table B-13 shows the S-H, Mo-H, and H-H bond distances as well as the relative energy for each value of R in Path B. Tables B-14, B-15, B-16, and B-17 show S-H and relative energies for Paths C, D, E, and F respectively.

$$H_2(g) + MoS_2(s) \rightarrow H_2MoS_2(s) \quad \Delta\dot{U} \text{ or } E_{rel} = E_{H_2MoS_2} - (E_{MoS_2} + E_{H_2}) \quad \text{(B-7)}$$

The relative energies of Path A for the MoS_2, $(MoS_2)_{19}$ and NbS_2 systems are plotted vs. R in Figure B-13. The approach of hydrogen by Path A to all three systems is similar as can be seen from the trends in relative energy. One promising result is the parallel behavior of the MoS_2 and $(MoS_2)_{19}$ systems. Thus, the MoS_2 molecule may be used to model the behavior of the $(MoS_2)_{19}$ cluster for homolytic cleavage of hydrogen. However, one disturbing result comes from the position of the relative energy minimum in all three plots. The relative energy

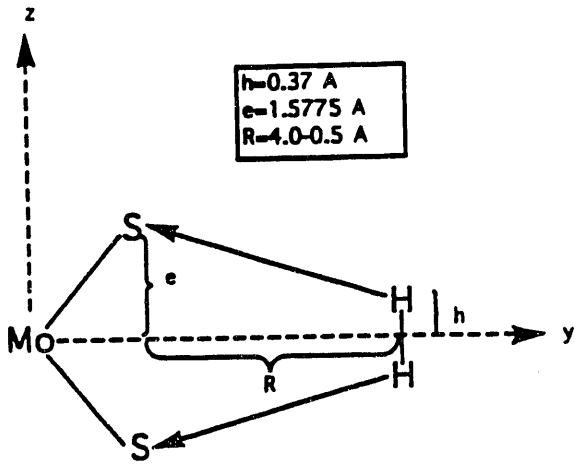

Path A: Homolytic Approach of H_2 to MoS_2.

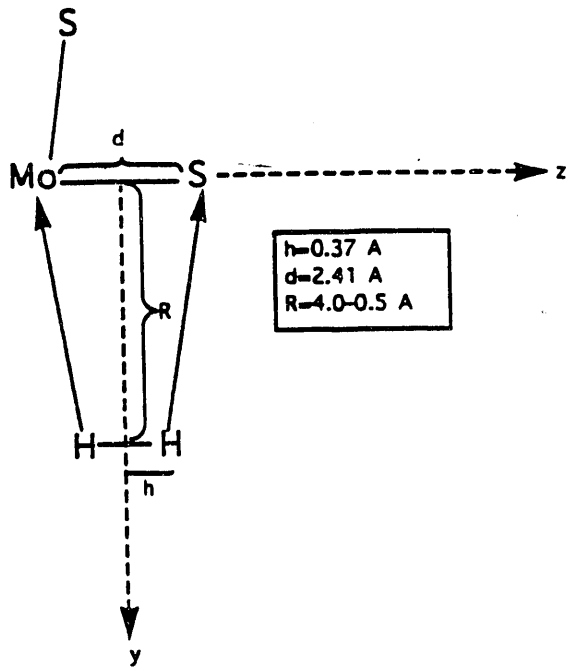

Path B: Heterolytic Approach of H_2 to MoS_2.

Figure B-12 Schematic representation of the six different hydrogen paths for the approach of a hydrogen molecule to the MoS_2 molecule. a) Path A, b) Path B. c) Path C. d) Path D, e) Path E, and f) Path F.

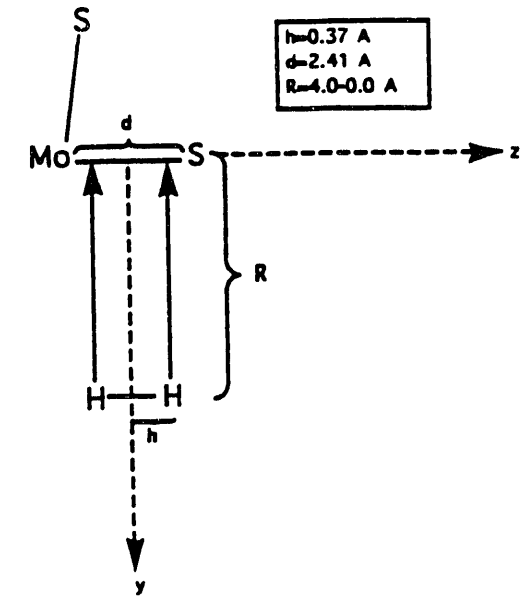

Path C: Heterolytic approach of H_2 to MoS_2 with a fixed H-H separation of 0.74 A.

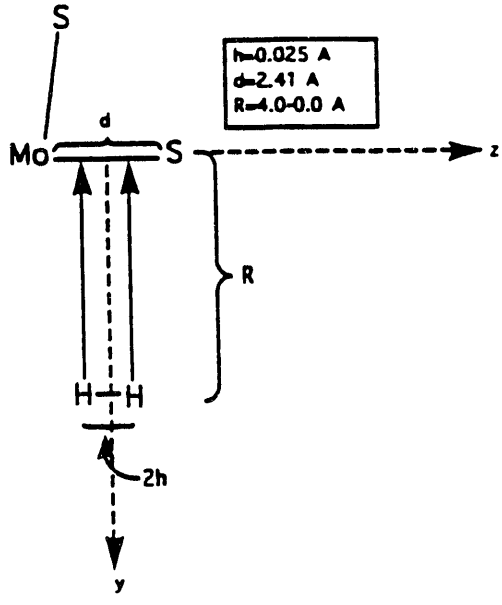

Path D: Heterolytic approach of H_2 to MoS_2 with a fixed H-H separation of 0.05 A.

Figure B-12 Schematic representation of the six different hydrogen paths for the approach of a hydrogen molecule to the MoS_2 molecule. a) Path A. b) Path B. c) Path C. d) Path D. e) Path E. and f) Path F.

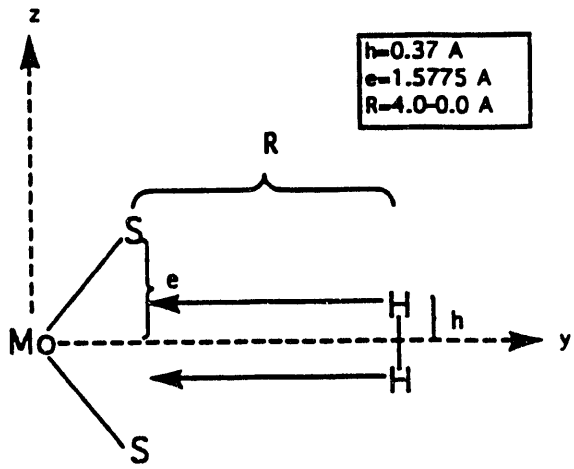

Path E: Homolytic approach of H_2 to MoS_2 with a fixed H-H separation of 0.74 A.

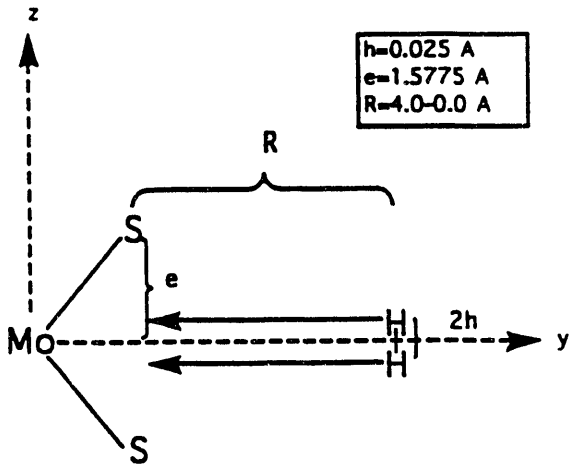

Path F: Homolytic approach of H_2 to MoS_2 with a fixed H-H separation of 0.05 A.

Figure B-12 Schematic representation of the six different hydrogen paths for the approach of a hydrogen molecule to the MoS_2 molecule. a) Path A. b) Path B, c) Path C, d) Path D, e) Path E, and f) Path F.

Table B-12

S-H and H-H bond distances as well as the relative energy, E_{rel}, for each value of R for the homolytic approach of a hydrogen molecule to MoS_2 by Path A, Figure B-12a.

R(Å)	E_{rel} (eV)	S-H (Å)	H-H (Å)
4.00	0.001	4.18	0.74
3.50	1.665	3.66	1.04
3.00	3.3235	3.13	1.34
2.50	4.427	2.61	1.65
2.00	4.8427	2.09	1.95
1.75	3.9729	1.83	2.10
1.50	1.8964	1.57	2.25
1.25	-0.2219	1.31	2.40
1.00	-1.9057	1.04	2.55
0.75	-2.6615	0.78	2.70
0.50	-2.0920	0.52	2.85

Table B-13

S-H, Mo-H and H-H bond distances as well as the relative energy, E_{rel}, for each value of R for the heterolytic approach of a hydrogen molecule to MoS_2 by Path B, Figure B-12b.

R(Å)	E_{rel} (eV)	Mo-H, S-H (Å)	H-H (Å)
4.00	0.0015	4.09	0.74
3.50	1.1468	3.58	0.95
3.00	2.372	3.06	1.16
2.50	3.5943	2.55	1.37
2.00	3.1778	2.04	1.58
1.75	1.7426	1.79	1.68
1.50	0.1062	1.53	1.78
1.25	-1.4233	1.28	1.89
1.00	-2.2082	1.02	1.99
0.75	-2.2083	0.77	2.10
0.50	-1.0141	0.51	2.20

Table B-14

S-H and Mo-H bond distances as well as the relative energy, E_{rel}, for each value of R for the heterolytic approach of a hydrogen molecule to MoS_2 by Path C, Figure B-12c. Path C retains a constant H-H distance of 0.74 Å.

R(Å)	E_{rel} (eV)	S-H, Mo-H (Å)
4.00	0.00	4.09
3.00	0.06	3.11
2.50	0.32	2.64
2.00	1.18	2.17
1.75	1.87	1.94
1.50	2.47	1.72
1.25	2.74	1.50
1.00	2.88	1.30
0.75	3.26	1.12
0.50	4.16	0.97
0.25	5.48	0.87
0.00	5.85	0.84

Table B-15

S-H and Mo-H bond distances as well as the relative energy, E_{rel}, for each value of R for the heterolytic approach of a hydrogen molecule to MoS_2 by Path D, Figure B-12d. Path D retains a constant H-H distance of 0.05 Å.

R(Å)	E_{rel} (eV)	S-H, Mo-H (Å)
4.00	-2.25	4.17
3.00	-2.20	3.22
2.50	-1.98	2.76
2.00	-1.15	2.32
1.75	-0.24	2.11
1.50	1.08	1.91
1.25	2.62	1.72
1.00	3.92	1.55
0.75	4.79	1.40
0.50	5.26	1.28
0.25	5.40	1.21
0.00	5.51	1.18

Table B-16

S-H bond distances as well as the relative energy, E_{rel}, for each value of R for the homolytic approach of a hydrogen molecule to MoS_2 by Path E, Figure B-12e. Path E retains a constant H-H distance of 0.74 Å.

R(Å)	E_{rel} (eV)	S-H (Å)
4.00	0.00	4.18
3.00	0.04	3.23
2.50	0.19	2.78
2.00	0.76	2.34
1.75	1.38	2.13
1.50	2.28	1.93
1.25	3.04	1.74
1.00	3.10	1.57
0.75	2.91	1.42
0.50	2.92	1.31
0.25	3.11	1.23
0.00	3.53	1.21

Table B-17

S-H bond distances as well as the relative energy, E_{rel}, for each value of R for the homolytic approach of a hydrogen molecule to MoS_2 by Path F, Figure B-12f. Path F retains a constant H-H distance of 0.05 Å.

R(Å)	E_{rel} (eV)	S-H (Å)
4.00	-2.25	4.29
3.00	-2.22	3.38
2.50	-2.07	2.94
2.00	-1.48	2.53
1.75	-0.81	2.34
1.50	0.25	2.16
1.25	1.72	1.99
1.00	3.31	1.85
0.75	4.54	1.72
0.50	5.42	1.63
0.25	5.94	1.57
0.00	6.19	1.55

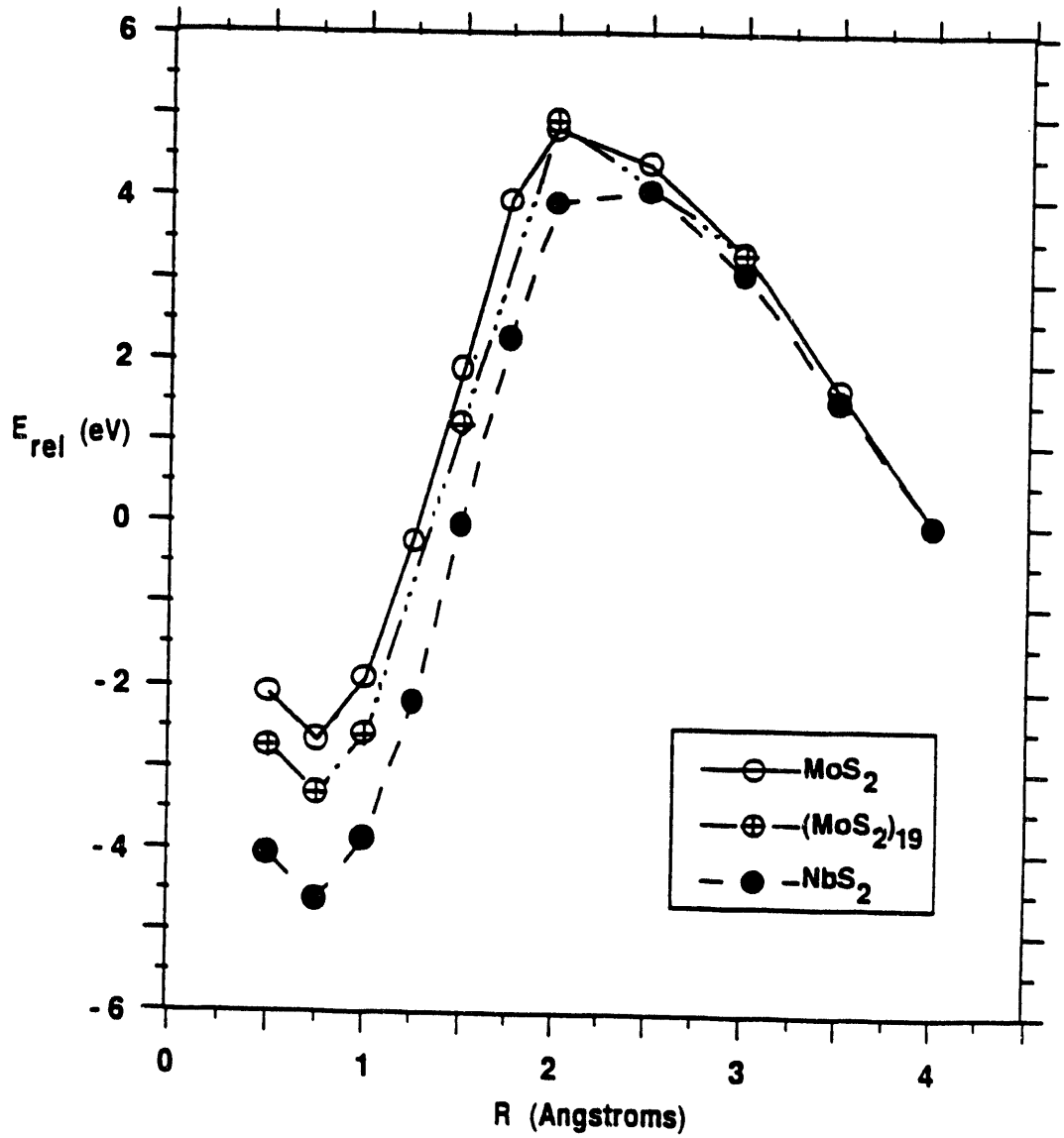

Figure B-13 Relative energies of homolytic hydrogen dissociation via Path A for the MoS_2, $(MoS_2)_{19}$ and NbS_2 systems plotted vs. R. The geometry of Path A is shown in Figure B-12a.

minimum occurs at a value of R equal to 0.75 Å and corresponds to a S–H bond distance of 0.78 Å for both the MoS_2 and $(MoS_2)_{19}$ systems. A S–H bond distance of 1.35 Å was used for the majority of hydrogen calculations carried out prior to this study. From Table B–12, a S–H bond distance of 1.35 Å would correspond to a relative energy less negative than –0.22 eV.

The relative energies of Paths A and B are plotted vs. R for the MoS_2 system in Figure B–14. Notice that the relative energy minimum for Path B is located between values of R equal to 0.75 Å and 1.00 Å corresponding to Mo–H (and S–H) bond distances of 0.77 Å and 1.02 Å respectively. Thus, extended Hückel theory again predicts that the most stable Mo–H and S–H bond distances are much lower than the previously used values of 1.7 Å and 1.35 Å. The difference between the lowest relative energies for Paths A and B is 0.45 eV such that Path A has the more negative energy. Homolytic cleavage of H_2 by MoS_2, Path A, is thus favored over heterolytic cleavage of H_2 by MoS_2, Path B, by 0.45 eV ($\sim$ 10 kcal/mole).

The relative energies of Paths A, E, and F for the MoS_2 system are plotted vs. R in Figure B–15. Of the three homolytic Paths A, E, and F, Path A results in the most negative relative energy and thus is the most favorable path for hydrogen adsorption. Path E, with a constant H–H bond distance of 0.74 Å, has a relative energy equal to zero at R=4.0 Å. Thus, at this distance the H_2 and MoS_2 molecules act as isolated species. As the value of R is decreased from 4.0 Å to 0.0 Å along Path E, the relative energy becomes more positive until a value of +3.53. eV is reached at 0.0 Å. Thus, adsorption of hydrogen while retaining a constant H–H bond distance of 0.74 Å along Path E is not thermodynamically feasible. Path F, with a constant H–H bond distance of 0.05 Å, has a relative energy equal to –2.25 eV at R=4.0 Å. As the value of R is decreased from 4.0 Å to 0.0 Å along Path F, the relative energy becomes more positive until a value of +6.19 eV is reached at 0.0 Å. Thus, adsorption of hydrogen via Path F (as calculated in Extended Hückel theory) is only feasible when the hydrogen molecule (retaining a H–H bond distance of 0.05 Å) is located far from the MoS_2 at a distance of 4.0 Å. The negative relative energy at R=4.0 Å for Path F can be traced to the stability of a hydrogen molecule retaining a H–H bond of 0.05 Å in extended Hückel calculations. Extended Hückel theory incorrectly predicts an energy minimum at a H–H bond distance of 0.05 Å for H_2 and not at the experimentally correct H–H bond distance of 0.74 Å. The difference between the energy of a hydrogen molecule with bond distances of 0.05 Å and 0.74 Å is $\sim$ –2.3 eV close to the stabilization of Path F at R=4.0 Å.

The relative energies of Paths B, C, and D for the MoS_2 system are plotted vs. R in Figure B–16. Of the three heterolytic Paths B, C, and D, Path B results in the most negative relative energy. Path C, with a constant H–H bond distance of 0.74 Å, has a relative energy

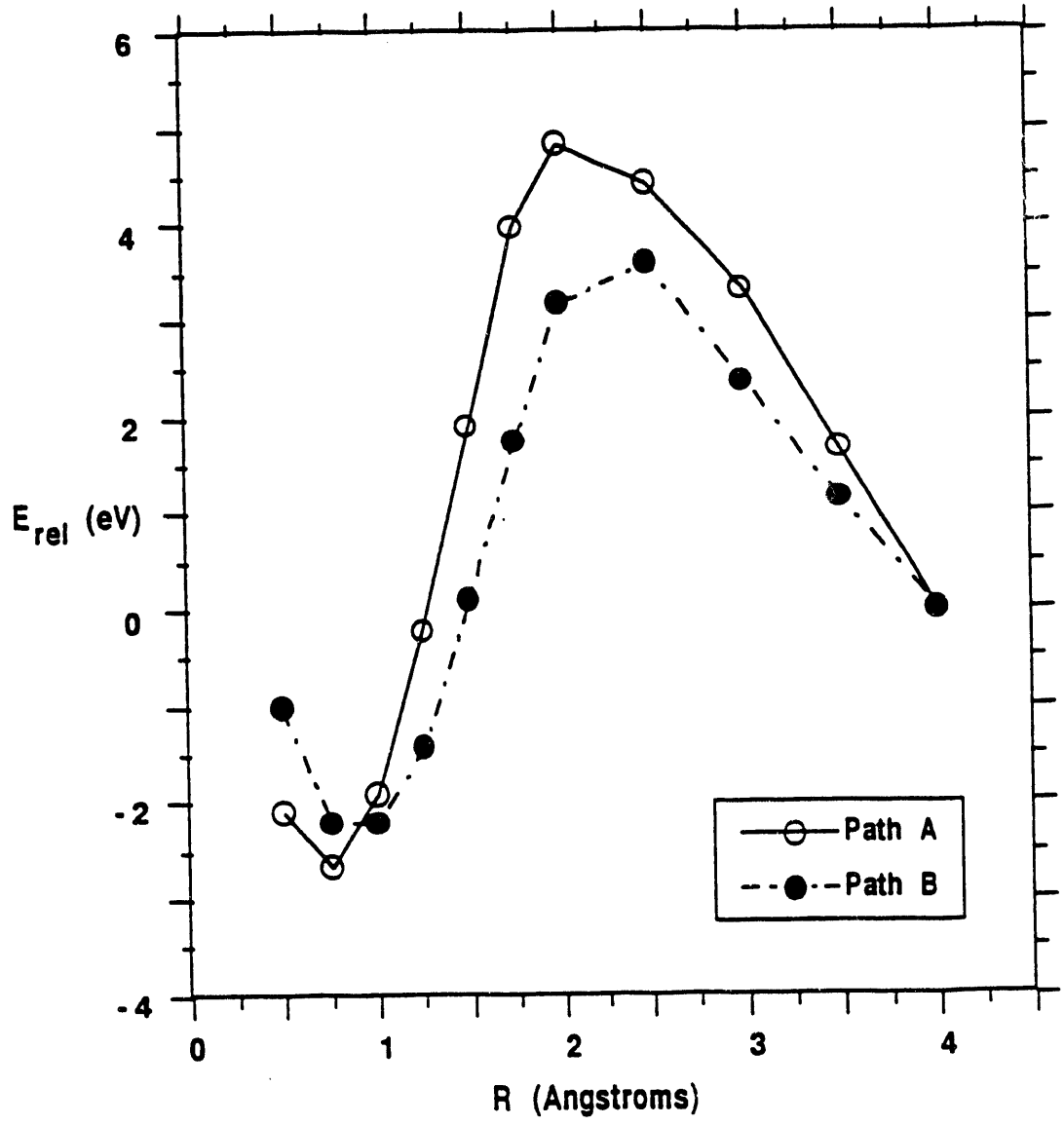

Figure B-14 Relative energies of Paths A and B are plotted vs. R for the MoS_2 system. The geometries of homolytic Path A and heterolytic Path B are shown in Figures B-12a and B-12b.

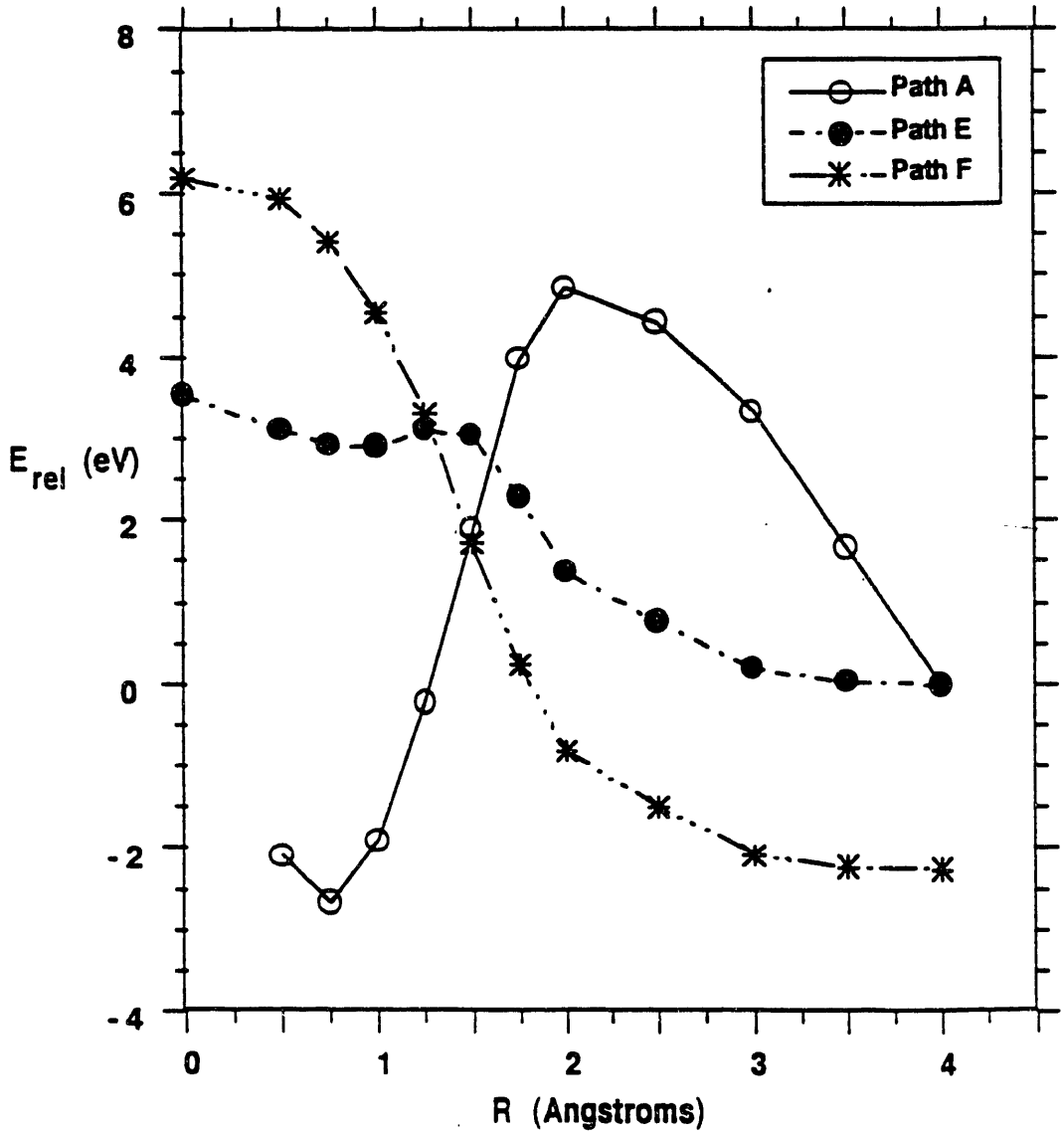

Figure B-15 Relative energies for the homolytic Paths A, E, and F plotted vs. R for the MoS_2 system. Geometries of Paths A, E, and F are shown in Figures B-12a, B-12e, and B-12f.

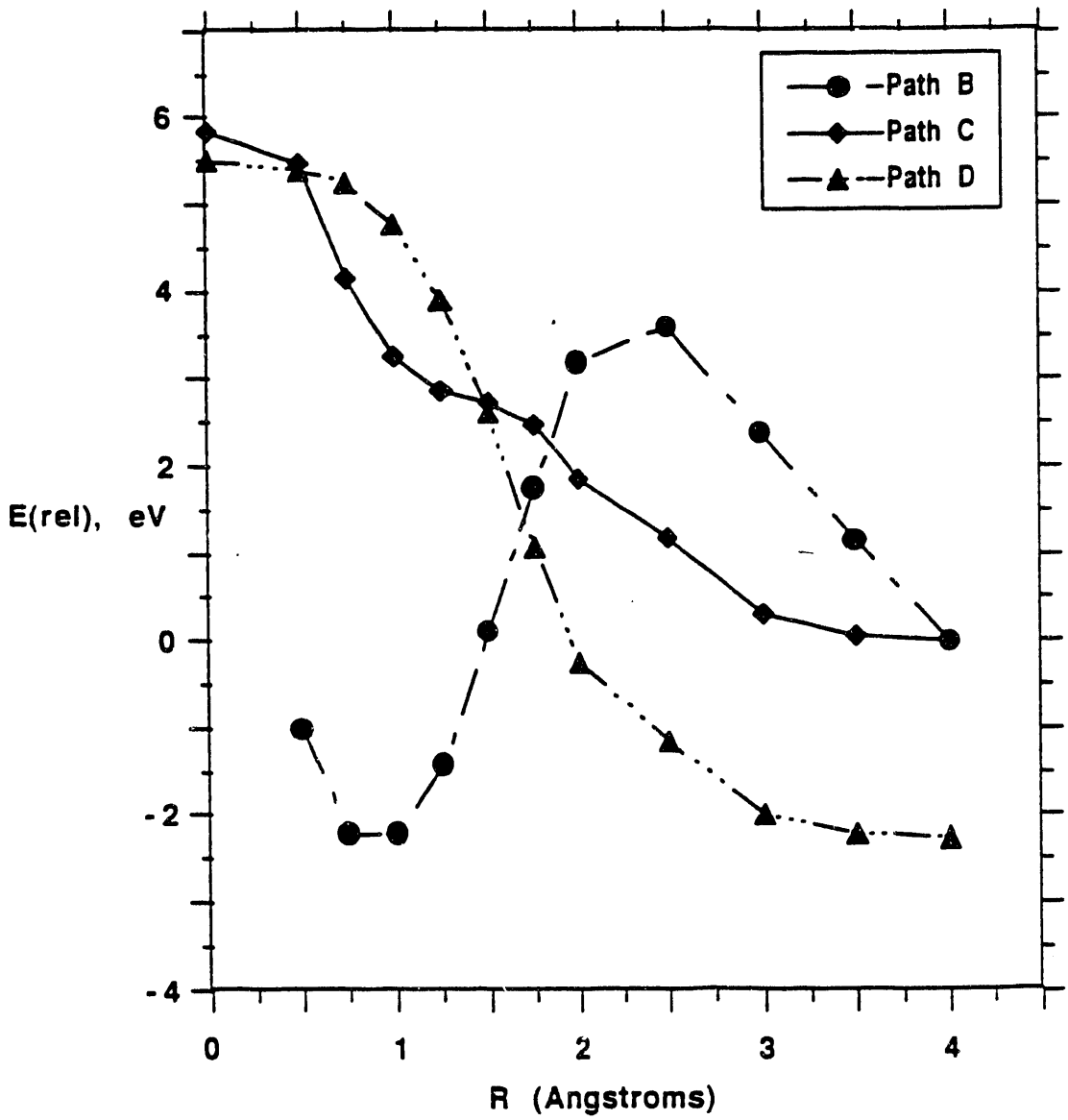

Figure B-16 Relative energies for the heterolytic Paths B, C, and D plotted vs. R for the MoS_2 system. Geometries of Paths B, C, and D are shown in Figures B-12b, B-12c, and B-12d.

equal to zero at R=4.0 Å. Thus, at this distance the H_2 and MoS_2 molecules act as isolated species. As the value of R is decreased from 4.0 Å to 0.0 Å along Path C, the relative energy becomes more positive until a value of +5.85 eV is reached at 0.0 Å. Thus, adsorption of hydrogen while retaining a constant H-H bond distance of 0.74 Å along Path C is not thermodynamically feasible. Path D, with a constant H-H bond distance of 0.05 Å, has a relative energy equal to -2.25 eV at R=4.0 Å. As the value of R is decreased from 4.0 Å to 0.0 Å along Path D, the relative energy becomes more positive until a value of +5.41 eV is reached at 0.0 Å. Thus, adsorption of hydrogen via Path D is only feasible when the hydrogen molecule (retaining a H-H bond distance of 0.05 Å) is located far from the MoS_2 at a distance of 4.0 Å. The negative relative energy at R=4.0 Å for Path D can again be traced to the stability of a hydrogen molecule retaining a H-H bond of 0.05 Å in extended Hückel calculations. The cause of the negative relative energies for Path F are due to the difference between the energy of a H_2 molecule having a H-H bond distance of 0.05 Å and one having a H-H bond distance of 0.74 Å.

The results of this study indicate that homolytic cleavage of a hydrogen molecule is slightly favored over heterolytic cleavage ($\sim$ 10 kcal/mole) on MoS_2 molecules. Homolytic cleavage on both MoS_2 and $(MoS_2)_{19}$ clusters follows a similar path. However, homolytic cleavage on the $(MoS_2)_{19}$ clusters is favored over that on the MoS_2 molecule by +0.66 eV ($\sim$ 15 kcal/mole).

B.2 Niobium Disulfide Cluster Calculations

Electronic structure calculations of niobium disulfide clusters $(NbS_2)_X$ were also carried out using the extended Hückel method described previously in Section 3.1. Ionization potentials H_{ii}, orbital exponents ζ_i and orbital coefficients c_i for the Nb 5s, Nb5p, Nb4d and S3s, S3p valence orbitals were taken from the work of Hughbanks and Hoffmann (Reference **41**) and are given in Table 1 (Section 3.2).

B.2.1 Trigonal Prismatic NbS_6^{n-} Clusters.

The electronic structure of the trigonal prismatic NbS_6^{n-} cluster was studied first by varying the negative charge n on the cluster. Geometric parameters for the atoms of the NbS_6^{n-} cluster are given in Table B-18. Parameters for this cluster are taken from the solid state geometry of crystalline 2H-NbS_2. In this geometry, the symmetry of the NbS_6^{n-} trigonal prism is D_{3h}. The angle, θ, existing between the C_3 axis and the Nb-S bonds is 52.127°.

Table B-18

Cartesian coordinates of the atoms in an NbS_6^{n-} trigonal prism. The coordinates are obtained from the solid state lattice parameters (**a**, **b**, **c**, u) of crystalline 2H-NbS_2. Units are in Å.

Atom	x	y	z
Nb	0.	0.	0.
S_1	1.655	-0.955515	1.48625
S_2	1.655	-0.955515	-1.48625
S_3	-1.655	-0.955515	1.48625
S_4	-1.655	-0.955515	-1.48625
S_5	0.	1.911029	1.48625
S_6	0.	1.911029	-1.48625

The energy level diagram for the NbS_6^{n-} cluster is similar to the diagram for the MoS_6^{n-} cluster Figure B-1. Due to the trigonal prismatic environment imposed by the 6 sulfur ligands the Nb 4d orbitals are split in the following order: $d_{z2} < d_{x2-y2}$, $d_{xy} < d_{zx}$, d_{yz}. When the charge on the NbS_6^{n-} cluster is 8-, the 25^{th} level is only half occupied by one electron and is the highest occupied molecular orbital (HOMO). Levels 26 and 27 are the doubly degenerate lowest unoccupied molecular orbitals (LUMOs) of the cluster.

Molecular orbital #25 has an energy of -10.17 eV and consists primarily of $Nb4d_{z2}$ character (-0.9404) and S3p character such that the six Mo-S bonds are antibonding. Molecular orbitals #26 and #27 are degenerate and have an energy of -9.58 eV. Molecular orbital #26 consists primarily of $Nb4d_{x2-y2}$ (0.8753) and some S3p character while MO #27 consists primarily of $Nb4d_{xy}$ (-0.8753) and some S3p character. The d_{x2-y2} (#26) and d_{xy} (#27) levels are separated from the d_{z2} (#25) by 0.59 eV. Molecular orbitals #28 and #29 are degenerate with an energy of -3.90 eV. Molecular orbital #28 consists primarily of $Nb4d_{zx}$ (-0.9583), S3s and S3p character while MO #29 consists primarily of $Nb4d_{yz}$ (0.9583), S3s, and S3p character. The d_{zx} (#28) and d_{yz} (#29) levels are separated from the d_{xy} (#27) and d_{x2-y2} (#26) levels by 5.68 eV. The large splitting of the $Nb4d_{yz}$ and $Nb4d_{zx}$ levels in NbS_6^{n-} clusters would seem to preclude mixing of these d levels with the other d levels. However, the d_{x2-y2} and d_{xy} degenerate levels are separated from the d_{z2} level by only 0.59 eV in the NbS_6^{n-} cluster and mixing of these levels could occur in certain systems. For instance in the 2-D NbS_2 system discussed in Section 5.7, the highest occupied band consists of contributions from the $Nb4d_{z2}$, $4d_{xy}$, and $4d_{x2-y2}$ orbitals in the following order: $4d_{z2} > 4d_{xy} > 4d_{x2-y2}$. The lowest unoccupied crystal band consists of contributions from the same three Nb4d orbitals in the following order: $4d_{x2-y2} > 4d_{z2} \simeq 4d_{xy}$. The next lowest unoccupied band consists of contributions from only the $Nb4d_{yz}$ and Nb $4d_{zx}$ orbitals. Thus in 2-D NbS_2 systems, the d_{x2-y2} and d_{xy} levels mix

with the d_{z2} level but these levels are still well separated from the d_{zx} and d_{yz} levels.

The gross electron population on the central niobium atom was studied as a function of the charge on the NbS_6^{n-} cluster. The gross electron populations on the niobium atom and the sulfur ligands for each charge are tabulated in Table B-19. As the cluster charge is increased

Table B-19

Gross electron populations of the central niobium atom and the sulfur ligands in the NbS_6^{n-} cluster as a function of the cluster charge n. Also shown ar the total number of electrons and the level of the highest occupied molecular orbital (HOMO) for each charge.

n	0	2	4	6	8
Total # e-	41	43	45	47	49
HOMO	20.5	21.5	22.5	23.5	24.5
Nb Gross e- Population	4.98	5.00	5.03	5.06	5.82
S Gross e- Population	6.00	6.33	6.66	6.99	7.20

from 0 to -6, the niobium gross electron population increased slowly from 4.98 to 5.06 ($\sim$ 0.02-0.03 per each addition of 2 e-) however the sulfur gross electron population increased from 6.00 to 6.99 ($\sim$ 0.33 per each addition of 2e-). However, when the cluster charge was increased from -6 to -8, the niobium gross electron population increased from 5.06 to 5.82. At the same time, the sulfur gross electron population increased from 6.99 to 7.20 ($\sim$ 0.20 for the addition of 2e-). The reason for this change is apparent when the orbital character of molecular orbitals 21 to 25 is examined. Molecular orbitals 21, 22, 23, and 24 primarily consist of contributions from the 6 sulfur ligand 3p atomic orbitals. Thus, occupation of these levels by electrons does not change the overall niobium electron populations much but does increase the overall sulfur electron population. However, molecular orbital 25 consists of mainly niobium $4d_{z2}$ with small contributions from the S3p atomic orbitals. When the charge is increased from -6 to -8, the first electron is placed in the 24^{th} level and the second is placed in the 25^{th} level. Addition of the first electron increases the sulfur gross electron population while addition of the second electron increases the niobium gross electron population.

A second study involved changing the angle (θ) between the C_3 axis and the Nb-S bond in the trigonal prismatic NbS_6^{8-} cluster while allowing the Nb-S bond distance to remain constant at 2.421 Å. In crystalline 2H-NbS_2, this angle has a value of 52.127°. Extended Hückel energies and Nb gross electron populations were calculated as a function of this angle

where the angle was varied from 10° to 80° in increments of 10°. The results of this study are tabulated in Table B-20. As indicated in Table B-20, the NbS_6^{8-} cluster energy and Nb gross electron population decrease on changing the angle from 10° to 50°. As the angle is increased from 50° to 80°, the cluster energy and Nb gross electron population again increase. A similar situation is seen in MoS_6^{8-} clusters Section B.1.1. The minimum energy is obtained for θ=50°, close to the solid state angle of 52.127°. Thus, extended Hückel theory correctly predicts the geometry of the NbS_6^{8-} trigonal prism. The trends in the extended Hückel energy and Nb gross electron population is similar for both the NbS_6^{8-} and MoS_6^{8-} trigonal prisms. A more in depth description of the trends is given in Section B.1.1.

Table B-20

Extended Hückel energies and Nb and S gross electron populations as a function of the angle (θ) between the C_3 axis and Nb–S bond in NbS_6^{8-}.

θ	E(EHT), eV	Nb e- pop	S e- pop
10	-434.08	17.71	5.22
20	-669.83	13.57	5.90
30	-717.15	10.41	6.43
40	-736.35	7.21	6.96
50	-746.79	5.82	7.20
60	-737.40	9.43	6.60
70	-730.27	10.21	6.46
80	-590.87	13.85	5.86

B.2.2 Stoichiometric $(NbS_2)_x$ Clusters.

The stability of $(NbS_2)_x$ clusters was studied as a function of the number of NbS_2 units or cluster size x. The energy and gross electron populations of the central niobium and sulfur atoms were followed as a function of x. Geometry parameters (a, b, c, u) were obtained from the solid state structure of crystalline NbS_2 and are discussed in Section 3.5.2. Figure B-17 shows the geometry of the largest cluster calculated, $(NbS_2)_{19}$ terminating at $(10\bar{1}0)$ edges. This structure is similar to the $(MoS_2)_{19}$ structure terminating at $(10\bar{1}0)$ edges (shown in Figure B-3) except that the bond distances and atom separations are different. Table B-21 lists the structures studied as well as the energy/NbS_2 unit and the Nb and S gross electron populations.

As the cluster size increases from 1 to 19, the energy of formation per NbS_2 unit decreases indicating stabilization of the larger clusters. The energy of formation of an infinite cluster with no edges, 2-D NbS_2, is -533.37 kcal/mole. Thus, 2-D NbS_2 is energetically the most stable structure calculated. The addition of interactions across the van der Waals gap was

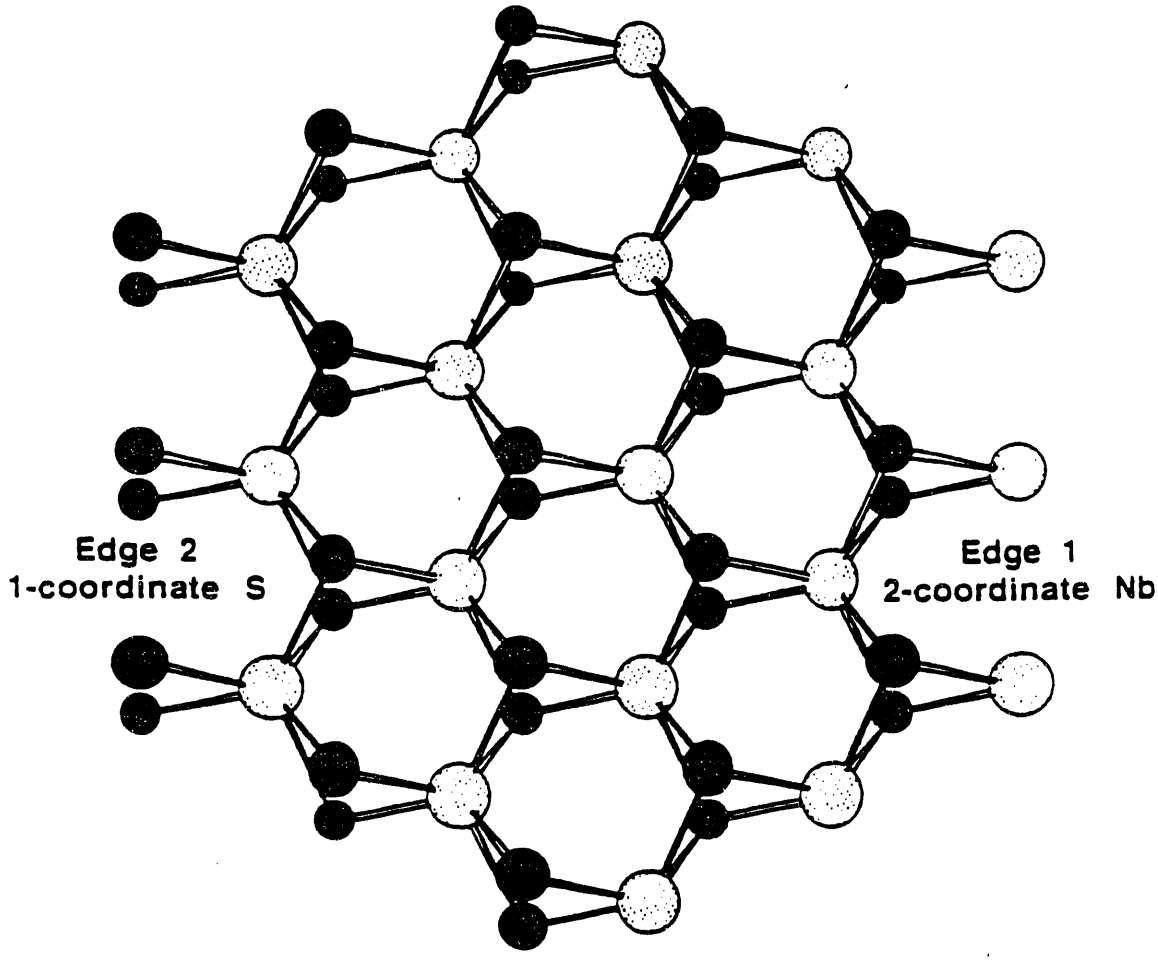

Figure B-17 Top view of the $(NbS_2)_{19}$ cluster terminating at $(10\bar{1}0)$ edges. The edges of this cluster contain 2-coordinate Nb, 4-coordinate Nb, 1-coordinate S and 2-coordinate S. White Textured Circles=Nb and Black Textured Circles=S.

Table B-21

Energy and gross electron populations for bulk Nb and S atoms of $(NbS_2)_x$ cluster as a function of the cluster size x.

Cluster	x	Description	$\Delta U/x$ ($\frac{kcal}{mole}$)	Gross Electron Populations: Nb-0101	S-0101
NbS_2	1	1 layer	-322.78	4.04	6.48
$(NbS_2)_7$	7	1 layer	-451.04	5.18	5.82
$(NbS_2)_{16}$	16	1 layer	-475.99	5.06	5.74
$(NbS_2)_{19}$	19	1 layer	-485.77	5.14	5.77
2-D NbS_2	∞	No edges	-533.37	5.43	5.79
$(NbS_2)_{14}$	14	2 layers of $(NbS_2)_7$	-449.89	5.19	5.76

studied in the $(NbS_2)_{14}$ cluster. This cluster consists of two $(NbS_2)_7$ layers separated by the van der Waals spacing 2.9725 Å. Addition of interactions across the van der Waals gap destabilizes the $(NbS_2)_{14}$ cluster by 1.15 kcal/mole when compared to the $(NbS_2)_7$ cluster containing no van der Waals gap. This result is similar to the destabilization of the $(MoS_2)_{14}$ cluster by +3.44 kcal/mole when compared to the $(MoS_2)_7$ cluster (presented in Section B.1.2). Destabilization of the NbS_2 cluster is less than that of the corresponding MoS_2 cluster. This result reflects the difference of TS_2 layer stacking in the c direction between NbS_2 and MoS_2. In MoS_2, stacking of S-Mo-S layers in the c direction positions sulfur atoms beneath and above molybdenum atoms in adjacent layers. In NbS_2, stacking of S-Nb-S layers in the c direction positions niobium atoms beneath and above niobium atoms in adjacent layers. The closest Mo-S distance across the van der Waals gap is 4.57 Å while the closest Nb-S distance across the gap is 4.85 Å. Increased Nb-S distances across the van der Waals gap in NbS_2 systems decrease the destabilizing effect of the antibonding interactions between the cluster orbitals across the gap in extended Hückel calculations. The destabilizing effect upon the addition of interactions across the van der Waals gap arises due to the neglect of electron correlation which would result in the inclusion of attractive van der Waals forces. Extended Hückel theory does not treat correlation and thus neglects to calculate the stability of structures containing van der Waals gaps relative to structures with no van der Waals gap.

B.2.3 Hydrogen Adsorption on $(NbS_2)_{19}$ Clusters Terminating at $(10\bar{1}0)$ Edges.

Extended Hückel calculations were carried out on $(NbS_2)_{19}$ clusters terminating at (1010) edges with hydrogen atoms placed at various basal and edge plane Nb and S sites. The

18 hydrogen sites studied previously on the $(MoS_2)_{19}$ (Figure B-5) cluster were again studied on the $(NbS_2)_{19}$ cluster. No attempt was made at minimization of the H-$(NbS_2)_{19}$ energy with respect to the Nb-H and S-H bond distances. The Nb-H and S-H bond distances used were 1.7 Å and 1.35 Å respectively.

The results of the hydrogen adsorption calculations are shown in Table B-22. The binding enthalpy was calculated as discussed in Appendix A.4. The sites are tabulated in order of increasing binding enthalpy and a description of the hydrogen adsorption site is given including the type of bond resulting from placement of hydrogen at each site and the original coordination of the closest atom. The descriptors side and top in the column labeled Bond in Table B-22 describe the direction of the bonded hydrogen. On the $(NbS_2)_{19}$ basal plane, the Nb and S atoms are fully coordinated and hydrogen atoms are most likely to approach the surface from the top in the +z direction, perpendicular to the basal plane. On the cluster edges, the atoms are not fully coordinated and the descriptor defines the approach of hydrogen as opposite that of the coordinated atoms.

Theoretical hydrogen adsorption on $(NbS_2)_{19}$ clusters containing exposed 2-coordinate Nb, 4-coordinate Nb, 1-coordinate S and 2-coordinate S shows that the most thermodynamically favorable sites for hydrogen to adsorb are on basal plane sulfur atoms (specifically site C) located far from the edges (bulk sulfur atoms). This result is very different from the previous calculations on $(MoS_2)_{19}$ clusters terminating at $(10\bar{1}0)$ edges. In these clusters, the most favorable site for hydrogen adsorption was on 2-coordinate edge molybdenum atoms with hydrogen bound to the side opposite the coordinated sulfur ligands (specifically site E). The main reason for this change in adsorption behavior is due to the stabilization of hydrogen bonded to sulfur sites producing S-H bonds relative to hydrogen bonded to niobium sites producing Nb-H sites. For example, consider site E (Mo-H and Nb-H) in the $(MoS_2)_{19}$ and $(NbS_2)_{19}$ clusters with binding enthalpies of -126.12 and -121.59 kcal/mole, respectively. Site E is destabilized by $\sim$ -4.53 eV on changing the transition metal from Mo to Nb. Next, consider site C (S-H) in the $(MoS_2)_{19}$ and $(NbS_2)_{19}$ clusters with binding enthalpies of -106.05 and -125.97 kcal/mole respectively. Site C is stabilized by $\sim$ 19.92 kcal/mole on changing the transition metal from Mo to Nb. In the $(NbS_2)_{19}$ cluster, sites C, M, L, T, I, and U, or sites containing S-H type linkages, are stabilized by $\sim$ 20 kcal/mole. Sites E, H, F, and G, or sites containing Nb-H type linkages, are destabilized by $\sim$ 1-5 kcal/mole. Thus, the adsorption behavior of $(NbS_2)_{19}$ clusters favors both edge niobium and sulfur sites as well as basal plane sulfur sites.

Table B-22

Binding enthalpies of hydrogen atoms on the $(NbS_2)_{19}$ cluster terminating at the $(10\bar{1}0)$ edge. Hydrogen sites are labeled alphabetically and the position of each site on the cluster is shown in Figure B-5. The description gives the Nb or S atom number and coordination prior to hydrogen bonding. The bond gives the bond type and direction of the bonded hydrogen.

#	Site	$\Delta H(\frac{kcal}{mole})$	Description	Bond
1	C	-125.97	3-coordinate basal S_{20}	S-H top
2	H	-122.02	2-coordinate edge Nb_8	Nb-H side
3	L	-121.69	1-coordinate edge S_{42}	S-H top
4	E	-121.59	2-coordinate edge Nb_{16}	Nb-H side
5	I	-121.53	1-coordinate edge S_{42}	S-H side
6	M	-120.19	3-coordinate basal S_{50}	S-H top
7	U	-119.04	1-coordinate edge S_{54}	S-H side
8	S	-117.94	4-coordinate edge Nb_{15}	Nb-H side
9	T	-117.46	2-coordinate edge S_{38}	S-H side
10	G	-116.71	2-coordinate edge $Nb_{8,16}$	Nb-H-Nb side
11	V	-116.32	4-coordinate edge Nb_{14}	Nb-H side
12	F	-116.16	2-coordinate edge Nb_{16}	Nb-H side
13	K	-81.38	1-coordinate edge $S_{40,42}$	S-H-S
14	N	-76.70	2-coordinate edge Nb_{16}	Nb-H top
15	J	-53.22	1-coordinate edge $S_{42,43}$	S-H-S
16	D	-52.51	3-coordinate basal $S_{20,22}$	S-H-S
17	B	-44.45	6-coordinate basal Nb_1	Nb-H top
18	A	-25.86	3-coordinate basal $S_{20,22,24}$	3-fold S site

When hydrogen is bound to a sulfur atom at site C (3-coordinate basal S_{20}) in the $(NbS_2)_{19}$ cluster, the electron density on the bound sulfur atom (S_{20}) and the hydrogen atom is decreased. The electron density on the sulfur atom decreases from 5.77 to 5.03 (+0.74) while that on the hydrogen atom decreases from 1.00 to 0.91 (+0.09). Thus, the total charge on the S-H species is +0.83 and can be represented as $S^{\delta 1^+}\!\!-\!\!H^{\delta 2^+}$ where $\delta 1^+$=+0.74 and $\delta 2^+$=+0.09. The only other sulfur atom affected by the binding of a hydrogen atom to a basal plane sulfur atom at site C is sulfur S_{21}, located on the opposite side of the cluster 3.155 Å from S_{20}. The electron density of this sulfur atom also decreases from 5.77 to 5.70 (+0.07). Electron densities of the three niobium atoms attached to the hydrogen adsorbed sulfur atom (S_{20}) Nb_1, Nb_4, and Nb_5 are increased from 5.14 to 5.22 (-0.08), 4.87 to 4.95 (-0.08) and 4.87 to 4.95 (-0.08). The fully coordinated niobium atoms, Nb_3 and Nb_6, also experience an increase in electron density from 5.06 to 5.17 (-0.11). Edge 4-coordinate niobium atoms, Nb_9, Nb_{14}, Nb_{15}, and Nb_{17} also experience an increase in electron density by -0.05. Thus, electron density is transferred from the S-H species to bulk niobium atoms close to the S-H site. The edge consisting of exposed 2-coordinate niobium atoms is not affected by adsorption of hydrogen to site C.

When hydrogen is bound to a niobium atom at site H (2-coordinate edge Nb_8), the electron density on the hydrogen atom is increased from 1.00 to 1.31 (-0.31). The electron density on the bound niobium atom (Nb_8) is increased from 5.68 to 6.04 (-0.36). Thus, the total charge on the Nb-H species is -0.67 and can be represented as $Nb^{\delta 1^-}\!\!-\!\!H^{\delta 2^-}$ where $\delta 1^-$= -0.36 and $\delta 2^-$=-0.31. The extra electron density on the Nb-H species is transferred from bulk niobium atoms (Nb_1, Nb_3, Nb_4, Nb_5, and Nb_6) and 4-coordinate edge niobium atoms (Nb_9, Nb_{15}, Nb_{17}). Thus, electron density is transferred from bulk and edge niobium atoms to the Nb-H species.

When hydrogen is bound to a niobium atom at site E (2-coordinate edge Nb_{16}), the electron density on the hydrogen atom is increased from 1.00 to 1.31 (-0.31). The electron density on the bound niobium atom (Nb_{16}) is increased from 5.34 to 5.73 (-0.39). Thus, the total charge on the Nb-H species is -0.70 and can be represented as $Nb^{\delta 1^-}\!\!-\!\!H^{\delta 2^-}$ where $\delta 1^-$= -0.39 and $\delta 2^-$=-0.31. The extra electron density on the Nb-H species is transferred from bulk niobium atoms (Nb_1, Nb_3, Nb_4, Nb_5, and Nb_6) and 4-coordinate edge niobium atoms (Nb_9, Nb_{14}, Nb_{15}, Nb_{17}). Thus, electron density is transferred from bulk and edge niobium atoms to the Nb-H species.

When hydrogen is bound to a sulfur atom at site I (1-coordinate edge S_{42}) in the $(NbS_2)_{19}$ cluster, the electron density on the bound sulfur atom (S_{42}) and the hydrogen atom is decreased. The electron density on the sulfur atom decreases from 6.59 to 5.81 (+0.78) while

that on the hydrogen atom decreases from 1.00 to 0.87 (+0.13). Thus, the total charge on the S–H species is +0.91 and can be represented as $S^{\delta 1^+}H^{\delta 2^+}$ where $\delta 1^+$=+0.78 and $\delta 2^+$=+0.13. The only other sulfur atom affected by the binding of a hydrogen atom to an edge sulfur atom at site I is sulfur S_{43}, located on the opposite side of the cluster 3.155 Å from S_{42}. The electron density of this sulfur atom also decreases from 6.59 to 6.47 (+0.12). Electron densities of the bulk niobium atoms Nb_1, Nb_3, Nb_4, Nb_5, and Nb_6 increase by -0.06, -0.10, -0.06, -0.06, and -0.10 electrons respectively. The four 4–coordinate niobium atoms Nb_9, Nb_{14}, Nb_{15}, and Nb_{17} also increase in electron density by -0.06 electrons. Thus, again electron density is transferred from the S–H species to bulk niobium atoms and 4–coordinate edge niobium atoms.

In general when hydrogen adsorbs onto a sulfur atom residing in the $(NbS_2)_{19}$ cluster, electrons are transferred from the positively charged S–H species to 4–coordinate edge niobium and bulk niobium atoms. When a hydrogen atom adsorbs onto a niobium atom in the $(NbS_2)_{19}$ cluster, electrons are transferred to the negatively charged Nb–H species from 4–coordinate edge niobium and bulk niobium atoms. In either case the excess charge imposed by the Nb–H or S–H species is distributed more uniformly over bulk and 4–coordinate niobium atoms. In general when hydrogen adsorbs onto a sulfur atom residing in the $(MoS_2)_{19}$ cluster, electrons are transferred from the positively charges S–H species to the edge containing exposed 2–coordinate molybdenum atoms (Edge 1).

B.2.4 Hydrogen Adsorption on $(NbS_2)_{19}$ Clusters Terminating at $(10\bar{1}1)$ Edges.

The $(NbS_2)_{19}$ cluster terminating at $(10\bar{1}1)$ edges is similar to the $(MoS_2)_{19}$ cluster shown in Figure B–6. Exposed edges consist 3–coordinate Nb, 4–coordinate Nb, 5–coordinate Nb, 1–coordinate S and 2–coordinate S. Energies of formation of the two $(NbS_2)_{19}$ clusters terminating at $(10\bar{1}0)$ and $(10\bar{1}1)$ edges are as follows: -485.76 and -496.65 kcal/mole. Thus, the cluster terminating at $(10\bar{1}1)$ edges is more stable than the cluster terminating at $(10\bar{1}0)$ edges by 10.89 kcal/mole. A stabilization of 3.12 kcal/mole was found in the $(MoS_2)_{19}$ system.

Two hydrogen adsorption sites, E and I, were studied on the $(NbS_2)_{19}$ cluster terminating at $(10\bar{1}1)$ edges. These sites are shown in Figure B–7. Site E again involves hydrogen binding to a 4–coordinate edge Nb atom. Site I involves binding of a hydrogen atom from the side to an exposed 1–coordinate sulfur atom. The binding enthalpies of sites E and I on the $(10\bar{1}1)$ cluster are -82.94 and -113.76 kcal/mole respectively. Site I is similar on both the $(10\bar{1}0)$ and the $(10\bar{1}1)$ structures and thus the binding enthalpies have not too different values -121.53 and -113.76 kcal/mole respectively. Site E on the $(10\bar{1}1)$ structure is not equivalent to site E on the $(10\bar{1}0)$ structure due to the different coordination of the niobium (4–

coordinate in the former and 2-coordinate in the latter). Comparison can be made between sites S and V on the $(10\bar{1}0)$ structure and site E on the $(10\bar{1}1)$ structure. Hydrogen binding at sites S and V resulted in binding enthalpies of -117.94 and -116.32 kcal/mole respectively. Thus, site E on the $(10\bar{1}1)$ structure possesses a much more negative binding enthalpy than sites S and V. Destabilization of site E on the $(10\bar{1}1)$ structure can be attributed to the smaller S-H distances present on occupation of site E. Occupation of site E on the $(10\bar{1}1)$ cluster places the hydrogen atom close to two adjacent sulfur atoms while sites S and V on the $(10\bar{1}0)$ cluster position the hydrogen far from the nearest sulfur atoms.

B.2.5 Hydrogen Adsorption on NbS_2 Molecule

Hydrogen adsorption on an NbS_2 molecule possessing the geometry of crystalline NbS_2 was also studied to parallel the study of hydrogen adsorption on $(NbS_2)_{19}$ clusters. This study is similar to the MoS_2 molecule study discussed in Section B.1.7. The following three hydrogen adsorbed systems were studied and are shown for the MoS_2 molecule in Figure B-10: H(1)-NbS_2 and NbS_2-H(2). The binding enthalpies of the hydrogen adsorbed systems are shown in Table B-23.

Table B-23

Binding enthalpies of hydrogen adsorbed on an NbS_2 molecule. H(1) indicates hydrogen attached to Nb and H(2) indicates hydrogen attached to S(1).

	System	$\Delta\dot{H}\left(\frac{kcal}{mole}\right)$
1)	H(1)-NbS_2	-121.07
2)	NbS_2-H(2)	-120.74

The binding enthalpies of the H(1)-NbS_2 and NbS_2-H(2) systems can be compared to the hydrogen binding enthalpies on sites E and I of the $(NbS_2)_{19}$ cluster terminating at $(10\bar{1}0)$ edges. The binding enthalpies of hydrogen on site E and in the H(1)-NbS_2 system are -121.59 and -121.07 kcal/mole respectively. The binding enthalpies of hydrogen on site I and in the MoS_2-H(2) system are -121.53 and -120.74 kcal/mole respectively. Hydrogen binding enthalpies found for the NbS_2 molecule and edge sulfur and niobium atoms of the $(NbS_2)_{19}$ cluster compare well. Thus, the NbS_2 molecule can be used to approximate the behavior of certain edge atom sites of the $(NbS_2)_{19}$ cluster specifically, 1-coordinate sulfur atoms and 2-coordinate niobium atoms.

B.2.6 Hydrogen Approaches to the NbS_2 Molecule.

Since the previous study involved hydrogen atom adsorption onto an isolated molecule of NbS_2, this study focuses on approaches of hydrogen for heterolytic and homolytic cleavage. The following two different hydrogen approaches or paths were studied and are shown schematically for MoS_2 in Figure B-12: a) Path A and b) Path B. In the case of NbS_2 the parameters e and d shown in Figure B-12 have values of 1.4862 Å and 2.42 Å respectively. Path A results in homolytic cleavage of the hydrogen molecule by two sulfur atoms while Path B results in heterolytic cleavage of the hydrogen molecule on a molybdenum and a sulfur atom. In both cases the hydrogen molecule is initially positioned at R_0 4.0 Å away from the atoms of interest in the $\hat{y}$ direction. Paths A and B are similar in that when the hydrogen molecule is moved closer to the atoms of interest, a decreased S-H or Nb-H distance is accompanied by an increased H-H distance.

The relative energies of the systems resulting from the paths discussed above were calculated for different values of R. In each case the value of R was decreased from its initial value of 4.0 Å to a final value of 0.5 Å. The relative energy or binding energy of hydrogen molecule to the NbS_2 molecule (shown in equation B-2) was calculated from the individual extended Hückel energies of the components. The energy of the NbS_2 molecule, E_{NbS_2} was calculated to be -260.90 eV and was obtained from an extended Hückel calculation of the NbS_2 molecule in the geometry of the particular path under study. The energy of the H_2 molecule, E_{H_2}, was calculated to be -35.13 eV when the H-H separation was 0.74 Å. In Table B-24 are shown the S-H and H-H bond distances as well as the relative energy, E_{rel}, for each value of R for Path A. Table B-25 shows the S-H, Mo-H, and H-H bond distances as well as the relative energy for each value of R in Path B.

$$H_2(g) + NbS_2(s) \rightarrow H_2NbS_2(s) \quad \Delta U^{\circ} \text{ or } E_{rel} = E_{H_2NbS_2} - (E_{NbS_2} + E_{H_2}) \quad \text{(B-1)}$$

The relative energy of homolytic Path A for the NbS_2 system is plotted vs. R in Figure B-13. The approach of hydrogen by Path A to the sulfurs of NbS_2 results in a minimum relative energy of -4.63 eV at R=0.75 Å corresponding to a S-H bond distance of 0.78 Å. This result is consistent with the position of the previous minimum found for the MoS_2 and $(MoS_2)_{19}$ systems. Thus, extended Hückel predicts that the most stable S-H bond distance in transition metal disulfides is 0.78 Å. The binding energy of hydrogen by homolytic Path A is more negative by 1.97 eV ($\sim$ 45.4 kcal/mole) on NbS_2 than on MoS_2. Thus, homolytic cleavage of hydrogen seems more likely on NbS_2 than on MoS_2.

Table B-24

S-H and H-H bond distances as well as the relative energy, E_{rel}, for each value of R for the homolytic approach of a hydrogen molecule to NbS_2 by Path A, shown for MoS_2 in Figure B-12a.

R(Å)	E_{rel} (eV)	S-H (Å)	H-H (Å)
4.00	0.0012	4.15	0.74
3.50	1.5365	3.63	1.02
3.00	3.0816	3.11	1.30
2.50	4.0922	2.60	1.58
2.00	3.9384	2.08	1.86
1.75	2.2744	1.82	2.00
1.50	-0.0208	1.56	2.14
1.25	-2.2087	1.30	2.27
1.00	-3.8725	1.04	2.41
0.75	-4.6297	0.78	2.55
0.50	-4.0604	0.52	2.69

Table B-25

S-H, Nb-H and H-H bond distances as well as the relative energy, E_{rel}, for each value of R for the heterolytic approach of a hydrogen molecule to NbS_2 by Path B, shown for MoS_2 in Figure B-12b.

R(Å)	E_{rel} (eV)	S-H (Å)	H-H (Å)
4.00	0.0027	4.09	0.74
3.50	1.1584	3.58	0.95
3.00	2.4061	3.07	1.16
2.50	3.6321	2.55	1.37
2.00	2.5124	2.04	1.58
1.75	0.9666	1.79	1.69
1.50	-0.6523	1.53	1.79
1.25	-2.0214	1.28	1.90
1.00	-2.8286	1.02	2.00
0.75	-2.7280	0.77	2.11
0.50	-1.4002	0.51	2.21

The relative energies of Paths A and B are plotted vs. R for the NbS_2 system in Figure B–18. Notice that the relative energy minimum for Path B is located between values of R equal to 0.75 Å and 1.00 Å corresponding to Nb–H (and S–H) bond distances of 0.77 Å and 1.02 Å respectively. Thus, extended Hückel theory again predicts that the most stable Nb–H and S–H bond distances are much lower than the previously used values of 1.7 Å and 1.35 Å. The difference between the lowest relative energies for Paths A and B is 1.80 eV such that Path A has the more negative energy. Homolytic cleavage of H_2 by NbS_2, Path A, is thus favored over heterolytic cleavage of H_2 by NbS_2, Path B, by 1.80 eV ($\sim$ 41.5 kcal/mole). Homolytic cleavage of H_2 by MoS_2, Path A, is also favored over heterolytic cleavage of H_2 by MoS_2, Path B, by 0.45 eV ($\sim$ 10 kcal/mole). Thus, both MoS_2 and NbS_2 studies favor homolytic cleavage of H_2 over heterolytic cleavage of H_2.

B.3 Ruthenium Disulfide Cluster Calculations.

Calculations of the electronic structure of stoichiometric $(RuS_2)_{18}$ clusters have been carried out using the extended Hückel method described previously in Section 3.1. Ionization potentials H_{ii}, orbital exponents ζ_i and orbital coefficients c_i for the Ru5s, Ru5p, Ru4d and S3s, S3p valence orbitals were taken from the work of Hughbanks and Hoffmann (Reference 37) and are given in Table 1.

B.3.1 Stoichiometric $(RuS_2)_{18}$ Clusters.

Stoichiometric $(RuS_2)_{18}$ clusters were studied to obtain the energy of formation. Parameters for this cluster were taken from the solid state geometry of crystalline RuS_2 described previously in Section 3.6. Calculated and experimental enthalpies of formation per TS_2 unit for each of the transition metal disulfide clusters studied are tabulated in Table B–26. Experimental and theoretical enthalpies of formation do not compare well. However, trends in the stability of the transition metal disulfide species are similar. Theoretical and experimental enthalpies predict the following stability order: $NbS_2 > MoS_2 > RuS_2$.

Table B–26

Theoretical and experimental enthalpies of formation per TS_2 unit for the following clusters: $(MoS_2)_{19}$, $(NbS_2)_{19}$ and $(RuS_2)_{18}$. Units are in kcal/mole.

Cluster	Theoretical ΔH_f°	Experimental ΔH_f°
$(NbS_2)_{19}$	-487.55	-391.57
$(MoS_2)_{19}$	-433.63	-356.37
$(RuS_2)_{18}$	-331.84	-336.07

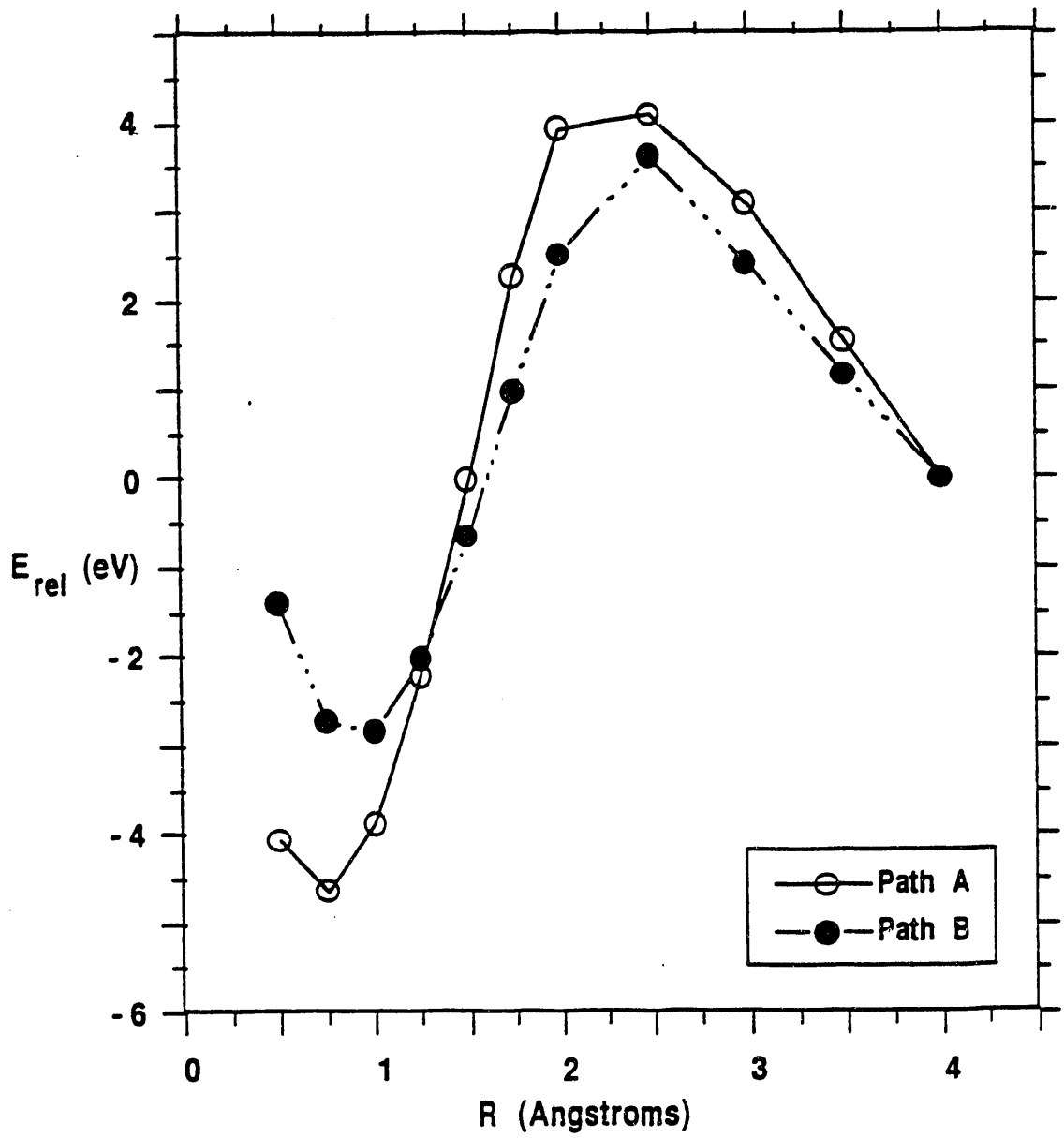

Figure B-18 Relative energies of Paths A and B are plotted vs. R for the NbS_2 system. The geometries of homolytic Path A and heterolytic Path B are shown in Figures B-12a and B-12b.

DATE
FILMED
8/13/93
END